Dierk Raabe
Computational Materials Science

WILEY-VCH

Computational Materials Science: The Simulation of Materials, Microstructures and Properties By Dierk Raabe
Copyright © 1998 Wiley-VCH Verlag GmbH
ISBN: 3-527-29541-0

Further Titles of Interest:

R. W. Cahn, P. Haasen, E. J. Kramer (Eds.)
Materials Science and Technology
A Comprehensive Treatment
in 18 Volumes

Dierk Raabe

Computational Materials Science

The Simulation of Materials Microstructures and Properties

WILEY-VCH

Weinheim • New York • Chichester
Brisbane • Singapore • Toronto

Dr. Dierk Raabe
Department for Materials Science & Engineering
Carnegie Mellon University
Room 3317, Wean Hall
Pittsburgh, PA 15213-3890, USA
and
Institut für Metallkunde und Metallphysik
RWTH Aachen
Kopernikusstraße 14
52056 Aachen, Germany

This book was carefully produced. Nevertheless, authors, editors and publisher do not warrant the information contained therein to be free of errors. Readers are advised to keep in mind that tatements, data, illustrations, procedural details or other items may inadvertently be inaccurate.

Library of Congress Card No.: applied for

British Library Cataloguing-in-Publication Data: applied for

Deutsche Bibliothek Cataloguing-in-Publication Data:
Raabe, Dierk:
Computational materials science : the simulation of materials,
microstructures and properties / Dierk Raabe. - Weinheim ; New York ;
Chichester ; Brisbane ; Singapore ; Toronto : Wiley-VCH, 1998
ISBN 3-527-29541-0

© WILEY-VCH Verlag GmbH. D-69469 Weinheim (Federal Republic of Germany), 1998.
Printed on acid-free and chlorine-free paper.
All rights reserved (including those of translation in other languages). No part of this book may be reproduced in any form - by photoprinting, microfilm, or any other means - nor transmitted or translated into machine language without written permission from the publishers. Registered names, trademarks, etc. used in this book, even when not specifically marked as such, are not to be considered unprotected by law.
Printing: betz-druck gmbh, D-64291 Darmstadt.
Bookbinding: Wilhelm Osswald & Co, D-67433 Neustadt.
Printed in the Federal Republic of Germany.

Foreword

In writing a text on simulation in Materials Science, Dr. Raabe is taking an important step in the development of Computational Materials Science and Engineering. This aspect of the field has been slowly but surely taking root and has attracted a number of researchers to the area. It is a mark of the increasing importance of the computational approach that we now have this carefully thought out compendium of simulation techniques. He discusses not just the theoretical and numerical basis for each technique but also gives the context for where each method is appropriate. It is notable that he has actively used and published on many of the methods that he discusses. Moreover, the range of length (and time) scales is appropriately broad in a way that corresponds to the breadth of our discipline, which deals with everything from civil engineering structures such as bridges to electronic devices that are a few atoms wide. Materials science often deals with competing, complex mechanisms, and it is very useful to have a third tool available to complement theory and experiment in order to verify or test our understanding. Even such basic needs as equilibrium phase relationships will depend on computational methods with sparse experimental verification. For thosé of us with a strong interest in microstructure, it is very exciting to see microstructural prediction catch up to the successes of continuum methods in heat flow, fluid flow and mechanical deformation. In writing this text, Dierk Raabe is to be thanked for providing us with such a complete review of computational methods in Materials Science and Engineering.

A. D. (Tony) Rollett, Department Head, Materials Science and Engineering,
Carnegie Mellon University, Pittsburgh, April 1998

Author's Preface

The recent advance of numerical prediction methods in nearly all domains of materials science and engineering has established a new, exciting, interdisciplinary approach which is often referred to as "computational materials science". It brings together elements from materials science, physics, computer science, mathematics, chemistry, and mechanical engineering. For instance, simulations in the field of materials physics concentrate on the investigation of lattice and defect dynamics at the atomic scale using molecular dynamics and Monte Carlo methods. Materials-related simulations in the field of mechanical engineering focus on large-scale construction problems, using finite element methods where the microstructure is incorporated by using averaging constitutive laws. In contrast to these examples, the classical domain of materials science can be seen in the investigation of lattice defects and their interactions at the mesoscale. Performing simulations on this particular scale is a great challenge, in that it must bridge enormous space and time scales and provide concepts to describe adequately complex many-body interaction phenomena. For this purpose a variety of new concepts has been developed which enables one to handle the interaction of many individual lattice defects in a more or less discrete manner at dimensions *above* the atomic scale and *below* the macroscopic scale. These so-called mesoscale simulation methods include deterministic and probabilistic cellular automata with global and local transformation rules, Ginzburg–Landau-type phase field kinetic methods, dislocation dynamics, polycrystal and non-linear crystal plasticity finite element models, geometrical and component models, topological network or vertex models, and multistate kinetic Potts-type Monte Carlo approaches. However, classical techniques such as molecular dynamics, Metropolis Monte Carlo, and conventional finite element simulations are also used extensively.

Although an increasing body of excellent conference proceedings, monographs, and journals are available covering particular aspects of computational materials science, no comprehensive overview of that field exists (see General Reading). This contribution aims to fill that gap. It gives a review of modern approaches to the space- and time-discretized simulation of materials microstructures, together with the respective theoretical backgrounds, that currently prevail in materials science. Particular emphasis is placed on the fundamentals of space- and time-discretized simulations of materials microstructures at the mesoscale.

The book comprises five Parts. Part I is entitled Introduction and Fundamentals. After the Introduction it concentrates on aspects which are scale-independent, namely, definitions and notions used in modeling and simulation, and fundamentals of solving differential equations. The sequence of the ensuing Parts reflects the spatial and temporal hierarchy of microstructure, i.e., it presents simulation methods at the nanoscopic–microscopic (Part II), microscopic–mesoscopic (Part III), and mesoscopic–macroscopic levels

(Part IV). The last chapter provides a review of integrated, i.e., of scale-bridging, modeling and simulation (Part V). Part II (on the nano–micro level) focuses on the various Metropolis Monte Carlo and molecular dynamics approaches. Part III (on the micro–meso level) concentrates on dislocation dynamics, Ginzburg–Landau-type diffuse phase field kinetic methods, cellular automata, multistate and kinetic Potts models, geometrical and component models, and topological network and vertex models. Part IV (on the meso–macro level) presents large-scale finite element and finite difference and polycrystal models. The chapters are complemented by a discussion of typical applications in the field of materials science and representative examples.

Due to the fact that it is particularly those simulations that predict microstructure evolution and microstructure–property relations at the micro–mesoscale, the theoretical concepts and methods in Part III are discussed in greater detail and furnished with elementary examples from plasticity, recrystallization and grain growth phenomena, solid-state diffusion, and phase transformation.

The Appendices present a list of suggested general reading, some basic aspects of computer science, advanced empirical techniques such as fuzzy logic and artificial neuronal networks, and a brief introduction to percolation theory.

The book addresses students at the graduate and undergraduate levels, lecturers, materials scientists and engineers, as well as materials-oriented physicists, chemists, mathematicians, and mechanical engineers. Any offer of criticism, advice, or example that might help to improve this text will be highly appreciated.

This book was written during my time at the Institut für Metallkunde und Metallphysik at Rheinisch-Westfälische Technische Hochschule Aachen and at the Department of Materials Science and Engineering at Carnegie Mellon University in Pittsburgh. My warmest thanks are due to my mentors Prof. Dr. G. Gottstein and Prof. Dr. Dr. h.c. K. Lücke, who have steadily promoted and profoundly stimulated my work. I am particularly indebted to Prof. Dr. H. Mughrabi, Prof. Dr. D. J. Srolovitz, Dr. U. F. Kocks, and Prof. Dr. A. D. Rollett for discussions and a number of helpful comments. Furthermore, I am grateful to Prof. Dr. D. M. Barnett, Prof. Dr. M. Berveiller, Prof. Dr. W. Blum, Prof. Dr. Y. Bréchet, Prof. Dr. U. Glatzel, Dr. P. Gumbsch, Prof. Dr. J. P. Hirth, Prof. Dr. P. Neumann, Prof. Dr. W. Mao, Prof. Dr. H. Mecking, Dr. D. Rönnpagel, the late Prof. Dr. J. Schlipf, Prof. Dr. S. Schmauder, Prof. Dr. L. Shvindlerman, Prof. Dr. Z. Sun, Prof. Dr. L. Tóth, and Prof. Dr. P. van Houtte for stimulating discussions and fruitful comments.

I am deeply grateful to my friends and colleagues at the Institut für Metallkunde und Metallphysik, especially to the computer simulation group. Moreover, I would like to express my warmest thanks to the computer maintenance and programming group, especially to M. Loeck. The generous financial support of the Deutsche Forschungsgemeinschaft, particularly through the Sonderforschungsbereich 370 "Integrative Werkstoffmodellierung" (Collaborative Research Center on Integrated Modeling of Materials) and through the Heisenberg stipend, has to mentioned here with gratitude. The kind support and the hospitality of the Department of Materials Science and Engineering at Carnegie Mellon University is gratefully acknowledged. Finally, I would like to thank Dr. J. Ritterbusch and M. Petersen of Wiley-VCH for their kind and valuable advise.

Dierk Raabe, Berlin, February 1998

About the Author

Dierk Raabe graduated at the Institut für Metallkunde und Metallphysik at Rheinisch-Westfälische Technische Hochschule Aachen in 1990. After his Dissertation in 1992 he worked in Aachen as a lecturer and group head in the fields of computational materials science, textures, and composites. After his Habilitation in the field of physical metallurgy and metal physics in 1997 he received a Heisenberg stipend from the Deutsche Forschungsgemeinschaft and joined the Department of Materials Science and Engineering at Carnegie Mellon University as a visiting scientist. The author received a VDEh scholarship by Verein Deutscher Eisenhüttenleute (German Society for Iron and Steel), the Springorum Memorial Medal and the Borchers Medal of RWTH Aachen, the Adolf-Martens Award of the Bundesanstalt für Materialforschung und -prüfung (German Institute for Materials Research and Testing), the Friedrich-Wilhelm Award of RWTH Aachen, the Masing Memorial Award of the Deutsche Gesellschaft für Materialkunde DGM (German Society for Materials Science), the Best Paper Award 1995 of *Steel Research*, and the International Young Scientist and Engineer Award of ICOTOM (International Conference on Textures of Materials). His current research interests are in the fields of polycrystal plasticity, recrystallization, grain growth, textures, and composites. He has organized various international conferences on computational materials science and is chairman of the research group on computer simulation in materials science of the Deutsche Gesellschaft für Materialkunde DGM. The author has taught in the field of physical metallurgy and metal physics, including courses on computational materials science at the Rheinisch-Westfälische Technische Hochschule Aachen and, together with Richard Smith, at Carnegie Mellon University. The author can be reached at raabe@andrew.cmu.edu or at raabe@imm.rwth-aachen.de.

Contents

Abreviations Used Frequently
In Computational Materials Science XV
In Computer Science XVI

Symbols XVII
Material Constants A 1
Material Constants B 2

I Introduction and Fundamentals **3**

1 Introduction **5**

2 Modeling and Simulation in Materials Science **13**
2.1 Some Notions 13
2.2 The Basic Idea behind Modeling 13
2.3 The Generalized State Variable Concept 14
2.3.1 Concepts for Models beyond the Atomic Scale 14
2.3.2 Independent Variables 15
2.3.3 State Variables or Dependent Variables 15
2.3.4 Kinematic Equations 16
2.3.5 Equations of State 16
2.3.6 Structure Evolution Equations 17
2.3.7 Parameters 17
2.3.8 Examples of Phenomenological Modeling Concepts 18
2.3.9 Analytical Model and Numerical Counterpart 18
2.4 Numerical Modeling and Simulation 20
2.5 Categories of Models 23
2.5.1 Spatial Scale 23
2.5.2 Spatial Dimension 23
2.5.3 Spatial Discretization 24
2.5.4 Predictive Character 26
2.5.5 Descriptive Character 27
2.5.6 Path-Dependence 27
2.6 Round-Robin Tests 28

3 Fundamentals and Solution of Differential Equations 29
3.1 Introduction to Differential Equations . . . 29
3.2 Solution of Partial Differential Equations . . . 32
3.3 Fundamentals of the Finite Difference Method . . . 34
3.3.1 Discretization of Time . . . 34
3.3.2 Numerical Errors of Finite Difference Methods . . . 34
3.3.3 Euler Methods . . . 35
3.3.4 Leap-Frog Method . . . 38
3.3.5 Predictor–Corrector Methods . . . 38
3.3.6 Crank–Nicholson Method . . . 39
3.3.7 Runge–Kutta Methods . . . 40
3.4 Fundamentals of the Finite Element Method . . . 41
3.4.1 Discretization and Basic Procedure . . . 41
3.4.2 The Ritz Variational Method . . . 44

II Simulation Techniques at the Nano–Micro Scale 47

4 Fundamentals 49

5 Statistical Mechanics in Atomic-Scale Simulations 53

6 Monte Carlo Simulation and Integration 61
6.1 Introduction and Fundamentals . . . 61
6.2 Some Historical Remarks . . . 63
6.3 Random Numbers . . . 64
6.4 Random Walk Simulation . . . 65
6.5 Hit-or-Miss Random Sampling Integration . . . 66
6.6 Simple or Naive Sampling — Nonweighted Monte Carlo Integration . . . 68
6.7 Importance Sampling — Weighted Monte Carlo Integration . . . 71
6.8 The Metropolis Monte Carlo Method . . . 73
6.8.1 Fundamentals of the Algorithm . . . 73
6.8.2 The Metropolis Method for Canonical and Microcanonical Ensembles 74
6.8.3 The Metropolis Method for Grandcanonical Ensembles . . . 75
6.9 Spin Monte Carlo Models . . . 75
6.9.1 Introduction . . . 75
6.9.2 $\frac{1}{2}$ Spin Ising Model . . . 76
6.9.3 Heisenberg Spin Model . . . 77
6.9.4 Lattice Gas Spin Model . . . 78
6.9.5 q-State Potts Spin Model . . . 78
6.9.6 Ising-Related Spin Models — the MFA, CVM, and BWG Models . 78
6.10 Lattice Types . . . 79
6.11 Errors of Monte Carlo Methods . . . 80
6.12 Application of the Monte Carlo Method in Materials Science . . . 81
6.13 Examples of the Monte Carlo Method in Materials Science . . . 84
6.13.1 Simulation of Surface Segregation . . . 84
6.13.2 Simulation of Phase Transition in Polymers . . . 84
6.13.3 Simulation of Thin Film Deposition . . . 84

7 Molecular Dynamics **87**
7.1 Introduction . . . 87
7.2 Models of Interatomic Potentials . . . 88
7.2.1 Introduction and Fundamentals . . . 88
7.2.2 Empirical Pair Potentials and Weak Pseudopotentials . . . 90
7.2.3 Isotropic Many-Body Pair-Functional Potentials . . . 92
7.2.4 Shell Model . . . 93
7.2.5 Bond Order Potentials . . . 94
7.2.6 Tight-Binding Potentials . . . 95
7.2.7 Local Electron Density Functional Theory . . . 97
7.3 Equations of Motion for Atomic Systems . . . 98
7.3.1 Fundamentals . . . 98
7.3.2 Constant Pressure . . . 99
7.3.3 Constant Temperature . . . 101
7.4 Integration of the Equations of Motion . . . 101
7.5 Boundary Conditions . . . 102
7.6 Application of Molecular Dynamics in Materials Science . . . 104
7.7 Examples of Molecular Dynamics Simulations in Materials Science . . . 106
7.7.1 Simulation of Chain Dynamics in Polymers . . . 106
7.7.2 Simulation of Brittle Fracture . . . 107
7.7.3 Simulation of Wafer Bonded Silicon Interfaces . . . 107
7.7.4 Simulation of Void Formation during Thin Film Deposition . . . 109
7.7.5 Simulation of Interaction of Dislocations with Grain Boundaries . 109

III Simulation Techniques at the Micro–Meso Scale **111**

8 Introduction **113**

9 Discrete Dislocation Statics and Dynamics **119**
9.1 Introduction . . . 119
9.2 Linear Elasticity Theory for Crystal Plasticity . . . 121
9.2.1 Introduction . . . 121
9.2.2 General Concepts of Elasticity Theory . . . 122
9.2.3 Equilibrium Equations . . . 126
9.2.4 Compatibility Equations . . . 127
9.2.5 Hooke's Law — the Linear Relationship between Stress and Strain 128
9.2.6 Elastic Energy . . . 133
9.2.7 Green's Tensor Function in Elasticity Theory . . . 133
9.2.8 Airy's Scalar Stress Function in Elasticity Theory . . . 136
9.3 Dislocation Statics . . . 137
9.3.1 Introduction . . . 137
9.3.2 2D Field Equations for Infinite Dislocations in an Isotropic Linear Elastic Medium . . . 138
9.3.3 2D Field Equations for Infinite Dislocations in an Anisotropic Linear Elastic Medium . . . 140
9.3.4 3D Field Equations for Dislocation Segments in an Isotropic Linear Elastic Medium . . . 142
9.3.5 3D Field Equations for Dislocation Segments in an Anisotropic Linear Elastic Medium . . . 146

9.4 Dislocation Dynamics . . . 151
9.4.1 Introduction . . . 151
9.4.2 Newtonian Dislocation Dynamics . . . 152
9.4.3 Viscous and Viscoplastic Dislocation Dynamics . . . 164
9.5 Kinematics of Discrete Dislocation Dynamics . . . 167
9.6 Dislocation Reactions and Annihilation . . . 168
9.7 Application of Dislocation Statics and Dynamics in Materials Science . . . 170
9.8 Examples of Dislocation Dynamics Simulations in Materials Science . . . 171
9.8.1 Two-Dimensional Dynamics . . . 171
9.8.2 Three-Dimensional Dynamics . . . 173

10 Ginzburg–Landau-Type Phase Field Kinetic Models 177
10.1 Introduction . . . 177
10.2 Diffusional Phase Transformation . . . 179
10.2.1 The Phenomenological Laws of Diffusion . . . 179
10.2.2 Ostwald Ripening and Gibbs–Thomson Equation . . . 181
10.2.3 Lifshitz–Slyozov–Wagner Theory . . . 184
10.3 Continuum Phase Field Kinetic Models . . . 186
10.3.1 Cahn–Hilliard and Allen–Cahn Model . . . 186
10.3.2 Thermal Fluctuation . . . 191
10.3.3 Landau Energy Density Functional . . . 191
10.3.4 Solution of the Linearized CHGL theory . . . 192
10.4 Microscopic Phase Field Kinetic Model . . . 193
10.5 Consideration of Elastic Stresses . . . 195
10.6 Application of Phase Field Kinetic Models in Materials Science . . . 197
10.7 Examples of Phase Field Simulations in Materials Science . . . 199
10.7.1 Simulation of Spinodal Decomposition . . . 199
10.7.2 Simulation of Grain Growth . . . 199

11 Cellular Automata 201
11.1 Introduction and Fundamentals . . . 201
11.2 Versatility of Cellular Automata in Materials Science . . . 204
11.3 Formal Description of Cellular Automata . . . 205
11.4 Probabilistic Cellular Automata . . . 208
11.5 Lattice Gas Cellular Automata . . . 209
11.6 Mesh Types for Cellular Automaton Simulations . . . 212
11.7 Optimization of Cellular Automata with Respect to Storage Limitation . 212
11.8 Cellular Automata and Monte Carlo . . . 213
11.9 Simulation of Non-Equilibrium Phenomena . . . 214
11.9.1 Thermodynamic Aspects . . . 214
11.9.2 Kinetic Aspects . . . 215
11.9.3 Deterministic Cellular Automaton Solution . . . 217
11.9.4 Probabilistic Cellular Automaton Solution . . . 218
11.10 Application of Cellular Automata in Materials Science . . . 219
11.11 Examples of Cellular Automaton Simulations in Materials Science . . . 221
11.11.1 Simulation of Recrystallization by Use of a CA with Deterministic Transformation Rules . . . 221
11.11.2 Simulation of Recrystallization and Coarsening by Use of a CA with Stochastic Transformation Rules . . . 221

12 Mesoscale Kinetic Monte Carlo and Potts Models 225
12.1 Introduction and Fundamentals 225
12.2 Influence of Grid Size and Symmetry 228
12.3 Application of Multistate and Kinetic Potts Models in Materials Science . 229
12.4 Examples of Potts Simulations in Materials Science 229
12.4.1 Grain Coarsening Phenomena 229
12.4.2 Recrystallization 231

13 Geometrical and Component Models 233
13.1 Introduction 233
13.2 Geometrical Model 233
13.3 Component Model 234
13.4 Application of Geometrical and Component Models in Materials Science . 235
13.5 Examples of Geometrical and Component Simulations in Materials Science 237

14 Topological Network and Vertex Models 239
14.1 Introduction and Fundamentals 239
14.2 Application of Topological and Vertex Models in Materials Science 241
14.3 Examples of Topological and Vertex Simulations in Materials Science . . . 242
14.3.1 Vertex Model for Recovery and Recrystallization 242
14.3.2 Toplogical Network Model for Grain Growth 244

IV Simulation Techniques at the Meso–Macro Scale 247

15 Introduction 249

16 Finite Element and Difference Methods at the Meso–Macroscale 251
16.1 Introduction and Fundamentals 251
16.2 The Equilibrium Equation in FE Simulations 253
16.3 Finite Elements and Shape Functions 253
16.4 Assemblage of the Stiffness Matrix 255
16.5 Solid-State Kinematics 258
16.6 Conjugate Stress–Strain Measures 261
16.7 Finite Difference Methods at the Macroscale 261
16.8 Application of FE and FD Methods in Materials Science 263
16.9 Examples of Finite Element Simulations in Materials Science 265
16.9.1 Crystal Plasticity Finite Element Simulation 265
16.9.2 Finite Element Simulation of Solidification 265

17 Polycrystal Elasticity and Plasticity Models 267
17.1 Introduction and Fundamentals 267
17.2 Homogenization Models for Polycrystals 268
17.3 Constitutive Models for Polycrystals 270
17.4 Voigt Model of Homogeneous Elastic Strain 273
17.5 Reuss Model of Homogeneous Elastic Stress 274
17.6 Hashin–Shtrikman Homogenization for Polycrystal Elasticity 275
17.7 Eshelby's Inclusion Approach 276
17.8 Kröner's Self-Consistent Approach 280
17.9 Taylor Full-Constraints Model for Homogeneous Strain in Polycrystals . . 280

17.10 Bishop–Hill Polycrystal Model 286
17.11 Taylor Relaxed-Constraints Models 287
17.12 Sachs Model for Homogeneous Stress in Polycrystals 288
17.13 Statistical Grain Interaction Model 289
17.14 Viscoplastic Polycrystal Modeling 290
17.15 Generalized Self-Consistent Polycrystal Models 291
17.16 Simulation of Local Orientation Gradients by Use of Polycrystal Theory . 294
17.17 Application of Polycrystal Models in Materials Science 296
17.18 Examples of Polycrystal Simulations in Materials Science 297
17.18.1 Simulation of the Elastic Constants of Steels 297
17.18.2 Comparison of Polycrystal Homogenization Approaches 298
17.18.3 Simulation of Textures in Iron-Aluminides 298
17.18.4 Combination of Texture and FE Simulation 298

V Integrated Modeling and Simulation 301

18 Fundamentals 303

19 Space and Time Scales in Microstructure Simulation 305

VI Appendices 309

A General Reading 311

B Computer Classification 315

C Advanced Empirical Methods 319
C.1 Artificial Neural Networks 319
C.2 Fuzzy Set Theory 321

D Percolation Theory 325
D.1 Fundamentals 325
D.2 Bond, Site, and Bootstrap Percolation 325

Abbreviations Used Frequently In Computational Materials Science

Abbreviation	Translation
bcc	body-centered cubic
BWG	Bragg–Williams–Gorsky model
CA	cellular automata
CCA	classical cellular automata
CH	Cahn–Hilliard theory
CRSS	critical resolved shear stress
CVM	cluster variation method
DFT	discrete Fourier transform
DOF	degree of freedom
EAM	embedded atom method
fcc	face-centered cubic
FC	full-constraints Taylor model
FD/FDM	finite difference method
FE/FEM	finite element method
FFT	fast Fourier transform
FHP	Frisch–Hasslacher–Pomeau
GCA	generalized cellular automata
GL	Ginzburg–Landau form
HF	Hartree–Fock approach
IMS	integrated modeling and simulation
LAP	Los Alamos Plasticity code
LCAO	linear combination of atomic orbitals
LD	lattice dynamics
LDF	local electron density functional theory
LIM	linear iteration method
LJ	Lennard–Jones potential
MC	Monte Carlo method
MD	molecular dynamics
MFA	molecular field approximation
MRT^2	Metropolis–Rosenbluth–Rosenbluth–Teller–Teller method
NIM	natural iteration method
NN	nearest neighbor
NNN	next nearest neighbor
ODF	orientation distribution function
PC	Portevin–Le Chatelier (dynamic strain aging)
RX	recrystallization
RC	relaxed-constraints Taylor model
RVE	representative volume element
SC	self-consistent model

Abbreviations Used Frequently In Computer Science

Abbreviation	Translation
ANN	artificial neural networks
AP	array processor
ASCII	American standard code of information interchange
ASIC	application-specific integrated circuit
bit	binary digit
BLAS	basic linear algebra subroutines
byte	smallest adressable memory unit, 8 bit + 1 test bit
CISC	complex instruction set computer
CM	connection machine
CMOS	complementary metal oxide semiconductor
CMOSFET	complementary metal oxide field-effect transistor
CPI	cycles per instruction
CPU	central processor unit
ECL	emitter-coupled logic
FLOP/s	floating point operations per second
Gbyte	10^9 (Giga) byte
GFLOP/s	10^9 (Giga) floating point operations per second
GSI	Giga-scale integration
HPF	high-performance FORTRAN
IC	integrated circuit
LSI	large-scale integration
MESFET	semiconductor field-effect transistor
MFLOP/s	10^6 (Mega) floating point operations per second
MIMD	multiple instruction stream–multiple data stream
MIPS	million instructions per second
MISD	multiple instruction stream–single data stream
MLP	multilayer perceptron (neural network)
MOSFET	metal oxide field-effect transistor
MPP	massively parallel programed
MSI	mid-scale integration
RISC	reduced instruction set computer
SISD	single instruction stream–single data stream
SIMD	single instruction stream–multiple data stream
SOM	self-organizing map (neural network)
SSI	small-scale integration
TFLOP/s	10^{12} (Tera) floating point operations per second
ULSI	ultra large-scale integration
VLIW	very long instruction word
VLSI	very large-scale integration

Symbols

Symbol	Meaning
a	chemical activity
A	unit area
$\boldsymbol{A}$, A_{ijkl}	fourth-rank accommodation tensor in self-consistent models
Å	Ångstrøm, 10^{-10} m
A_{MP}	interface area between matrix and precipitation
A^{z}	Zener's anistropy ratio
$\boldsymbol{b}$, b_i	Burgers vector
B	magnetic field
B^{el}	elastic bulk modulus
C_{60}	Buckminster fullerene, containing 60 C atoms
c	velocity of sound
c, c_p, c_V	heat capacity (isobaric, isochoric)
c_{vac}	equilibrium concentration of vacancies
$c^{\mathrm{M}}(R)$	matrix concentration near the surface of a precipitation with radius R
$\boldsymbol{C}$, C_{ijkl}	fourth-rank stiffness tensor
$\boldsymbol{C}'$, C'_{ijkl}	Hashin–Shtrikman stiffness tensor variable
$\tilde{\boldsymbol{C}}$, $\tilde{C}'_{ijkl}$	Hashin–Shtrikman stiffness tensor
p	pressure
$\tilde{D}_i$	chemical diffusion coefficient of component i
D^{gb}	grain boundary diffusion constant
D	diffusion constant; subgrain size
$\mathfrak{E}$	error of approximate FEM solutions
E	elastic modulus
E_{d}	energy of the dislocation core
E_{kin}	kinetic energy
E_{pot}	potential energy
$\boldsymbol{E}^{\mathrm{G}}$	Green–Lagrange strain tensor
$\boldsymbol{F}$, F_i	force vector
$\boldsymbol{F}$, $r_{i,j} = \partial r_i/\partial x_j$	deformation gradient tensor
$\dot{\boldsymbol{F}}$, $\dot{r}_{i,j} = \partial \dot{r}_i/\partial x_j$	deformation gradient rate tensor
F	Helmholtz free energy
$\tilde{F}$	Helmholtz free energy functional
$f(c)$	Helmholtz free energy density
$\boldsymbol{g} = \boldsymbol{g}(\varphi_1, \phi, \varphi_2)$	orientation, rotation matrix
$\Delta\boldsymbol{g} = \Delta\boldsymbol{g}(\varphi_1, \phi, \varphi_2)$	misorientation
G	Gibbs free enthalpy
g	Gibbs free enthalpy density
G_0	surface-dependent part of Gibbs free enthalpy
G_{A}	surface-independent part of Gibbs free enthalpy
$G_{ij}(\boldsymbol{x}, \boldsymbol{x}') = G_{ij}(\boldsymbol{x} - \boldsymbol{x}')$	time-independent Green's tensor function
$\hbar = h/(2\pi)$	Planck's constant divided by 2π
H	enthalpy
H^{f}	enthalpy of formation

H^{m}	enthalpy of migration
$\mathcal{H}$	Hamilton energy operator
$\mathcal{H}_{\mathrm{Ising}}$	Hamiltonian in Ising models
$\mathcal{H}_{\mathrm{Potts}}$	Hamiltonian in Potts models
$\boldsymbol{H}$, $u_{i,j} = \partial u_i/\partial x_j$	displacement gradient tensor
$\dot{\boldsymbol{H}}$, $\dot{u}_{i,j} = \partial \dot{u}_i/\partial x_j$	velocity gradient tensor
$\{hkl\}\langle uvw\rangle$	Miller indices (slip systems, crystal orientation)
I_1, I_2, I_3	invariants of the stress tensor
I	diffusion flux through precipitate surface
$\boldsymbol{I}$	unit tensor
J_1, J_2, J_3	invariants of the stress deviator
J	exchange interaction energy
j	particle flux, net number of particles which pass through a plane of unit area in time
j_B^α	flux of particle type B in phase α
$\boldsymbol{K}^{\mathrm{elem}}$	element stiffness matrix (FEM)
k_{B}	Boltzmann constant
$\boldsymbol{L}^*$	interaction tensor in self-consistent models
$\hat{L}_{ij}$	symmetric matrix of kinetic operators
L	Lagrange–Euler function
M_{ij}^{s}	matrix of the geometry coefficients which relates the resolved shear stress to the stress tensor
m	mass, strain rate sensitivity, mobility
M	magnetization, Taylor factor
$\boldsymbol{M}$, M_{ij}	matrix of mobility coefficients; symmetric part of the generalized Schmid factor
$\hat{M}_{ij}$	symmetric Onsager kinetic operator matrix
$\boldsymbol{n}$, n_i	unit normal vector
n_0	equilibrium value of the electron density
N	particle number in a canonical ensemble
$N\ V\ T$	macrocanonical ensemble
$N\ V\ E$	microcanonical ensemble
N, P, T	isobaric-isothermal ensemble
N_i	ith particle or atom
N_{L}	Loschmidt number, $6.02\,10^{23}\,/mol$, Avogadro's constant
N, V, ξ	grandcanonical ensemble
$\boldsymbol{p}_1, \ldots, \boldsymbol{p}_N$	set of momentum vectors of all N particles in a canonical ensemble
$\boldsymbol{r}_1, \ldots, \boldsymbol{r}_N$	set of position vectors of all N particles in a canonical ensemble
$P(\langle s_i\rangle)$	probability of a configuration $\langle s_i\rangle$
$P_i(+)$, $P_i(-)$	single-site probabilities for "spin up" (+) and "spin down" (-)
$P_{\mathrm{nc}}(\boldsymbol{k}, \boldsymbol{i})$	cluster-type correlated probability
$\boldsymbol{P}$, P_i	body force vector
$\mathbf{p}_i$	momentum vector of the ith particles in a canonical ensemble
ps	pico second, 10^{-12} s
q_{TF}	reciprocal of the Thomas-Fermi screening length

q_{D}	radius of a Debye sphere
q_{exp}	experimentally observed quantity q
$\langle q(\boldsymbol{\Gamma}(t))\rangle_{\mathrm{time}}$	time average
$\langle q\rangle_{\mathrm{ens}}$	ensemble average of a quantity q
Q	activation energy
Q_{m}	activation energy of grain boundary mobility
$\boldsymbol{q}$, q_i	Rodrigues vector
$\boldsymbol{R}$, R_{ij}	rigid-body rotation
R	particle radius in the Gibbs–Thomson equation
$1/R$	crystal curvature
$\mathbf{r}_i$	position vector of the ith particle in a canonical ensemble
$1/R^{\mathrm{c}}$	cell wall curvature
S_i	microstructure parameter
$\boldsymbol{S}$, S_{ijkl}	fourth-rank compliance tensor
$\boldsymbol{S}'$, S'_{ijkl}	Hashin–Shtrikman compliance tensor variable
$\widetilde{\boldsymbol{S}}$, $\widetilde{S}'_{ijkl}$	Hashin–Shtrikman compliance tensor
t_{w}	waiting time in front of obstacles
t_{g}	gliding time between obstacles
T	temperature
T, V, μ	grandcanonical ensemble
T_{c}	Curie temperature
$\boldsymbol{T}$, T_i	traction vector
U	internal energy
$U(\Omega)$	cohesive energy contribution in a pair potential
V	volume
v_{F}	Fermi velocity of electrons
v	interface velocity
W	elastic energy density
$w(\boldsymbol{\Gamma})$	probability function
$(\boldsymbol{zz})_{ij}$	symmetric Christoffel stiffness matrix
$(\boldsymbol{zz})_{ij}^{-1}$	inverse of the Christoffel stiffness matrix
Z	zustandsintegral, canonical partition function

Greek Symbols

β	$1/(k_{\mathrm{B}}T)$
χ	coupling factor in self-consistent models
Δ	Laplace operator; increment
δ_{ij}	Kronecker symbol
$\eta(\boldsymbol{r},t)$	structure variable in kinetic field models
$\boldsymbol{\varepsilon}$, ε_{ij}	strain tensor
ε_{ii}	dilatation, trace of the strain tensor
$\dot{\boldsymbol{\varepsilon}}$, $\dot{\varepsilon}_{ij}$	strain rate tensor
ϵ_{ijk}	totally antisymmetric Levi–Civita permutation operator
$\boldsymbol{\Gamma}(t)$	vector in phase space
γ^{c}	specific energy of subgrain walls
γ	activity coefficient

γ^t	shear on slip system t
$\dot{\gamma}^t$	shear rate on slip system t
κ	positive constant related to interfacial constants
$\mathbf{\Lambda}$	second Piola–Kirchhoff tensor
Λ	interface mobility
λ	Lamé's constant, obstacle spacing
μ	modulus of rigidity, shear modulus; chemical potential
$\mu_{\mathrm{A}}^{\gamma}$	chemical potential of atom type A in phase γ
∇	nabla operator
ν	Poisson's ratio
φ_1, ϕ, φ_2	Euler angles
ω_D	Debye frequency
Ω	average atomic volume
$\mathbf{\Omega}$	plastic spin
$\boldsymbol{\omega}$, ω_{ij}	rigid-body rotation, antisymmetric part of the displacement gradient tensor
$\dot{\boldsymbol{\omega}}$, $\dot{\omega}_{ij}$	rigid-body rotation rate
ϱ	dislocation density; mass density
ϱ_{i}	dislocation density in the cell interior
ϱ_{w}	dislocation density in the cell walls
$\rho(\mathbf{\Gamma})$	phase space density, probability density
σ_{AM}	specific interface energy between matrix and particle
$\boldsymbol{\sigma}$, σ_{ij}	stress tensor
σ_{ii}	trace of the stress tensor
σ^{h}	hydrostatic stress
$\boldsymbol{\sigma}^{\mathrm{c}}$, σ_{ij}^{c}	microscopic or local stress tensor (crystal)
$\boldsymbol{\sigma}^{\mathrm{e}}$, σ_{ij}^{e}	macroscopic stress tensor (external, matrix)
Θ	Debye temperature
τ_t	resolved shear stress on slip system t
τ_t^{crit}	critical resolved shear stress on slip system t
ϕ	Airy stress function
$\psi_{ij}(r_{ij})$	pair potential
$\xi(x,t)$	Langevin noise term

Material Constants A

Element	Lattice	a [Å]	c [Å]	T_m [K]	E [GPa]	ν	ϱ [gcm^{-3}]	D_0 [cm^2s^{-1}]	Q [eV]
Ag	fcc	4.09		1234	83	0.37	10.5	0.400	1.92
Al	fcc	4.05		933	70	0.34	2.70	1.300	1.55
Au	fcc	4.08		1336	78	0.44	19.32	0.090	1.81
Be	hex	2.27	3.59	1560	305	0.05	1.85	1.370	1.13
Cd	hex	2.98	5.62	594	50	0.44	8.64	0.050	0.79
Cr	bcc	2.88		2163	279	0.21	7.14	0.200	3.19
Co	hcp	2.51	4.07	1765	206	0.31	8.89	0.830	2.95
Cu	fcc	3.62		1356	130	0.34	8.93	0.200	2.05
Fe	bcc	2.87		1809	211	0.29	7.87	5.800	2.92
K	bcc	5.32		337	4	0.35	0.86	0.310	0.42
Mg	hcp	3.21	5.21	923	44	0.29	1.74	1.300	1.40
Mo	bcc	3.15		2888	325	0.30	10.28	0.100	4.01
Na	bcc	4.29		371	9	0.32	0.97	0.240	0.46
Nb	bcc	3.30		2740	104	0.38	8.58	12.000	4.57
Ni	fcc	3.52		1728	202	0.31	8.91	1.300	2.91
Pb	fcc	4.95		600	16	0.44	11.34	0.280	1.05
Pt	fcc	3.92		2062	170	0.39	21.45	0.330	2.95
Sn	tet	5.83		505	54	0.33	7.29	0.780	1.13
Ta	bcc	3.30		3269	185	0.35	16.67	0.120	4.29
Ti	hex	2.95	4.68	1948	116	0.32	4.51	$6 \cdot 10^{-8}$	1.27
U	orth	5.88		1403	120	0.23	18.70	0.002	4.97
V	bcc	3.03		2175	127	0.36	6.09	0.011	2.64
W	bcc	3.17		3683	411	0.28	19.26	5.600	5.92
Zn	hex	2.66	4.95	693	105	0.29	7.14	0.130	0.95
Zr	hex	3.23	5.15	2125	96	0.33	6.51	0.002	1.65

a	lattice constant	hex	hexagonal
bcc	body-centered cubic	Lattice	lattice structure (300 K)
c	lattice constant normal to basal plane	ort	orthorhombic
D_0	factor of self diffusion	Q	activation energy of self diffusion
eV	electron volt	T_m	melting point
E	elastic bulk modulus (300 K)	tet	tetragonal
fcc	face-centered cubic	ν	Poisson's ratio (300 K)
hcp	$\approx$ hexagonal close packed	ϱ	density (300 K)

Material Constants B

Element	c_p $[cal\,(g\,K)^{-1}]$	σ $[(\mu\Omega\,m)^{-1}]$	P	T_b $[K]$	M	T_D $[K]$	ES	N $[10^{22} cm^{-3}]$
Ag	0.056	62.5	1.9	2483	107.87	225	$4d^{10}\,5s$	5.85
Al	0.215	36.2	1.5	2723	26.98	428	$3s^2\,3p$	6.02
Au	0.031	45.0	2.4	3243	196.97	165	$5d^{10}\,6s$	5.90
Be	0.450	15.2	1.5	3043	9.01	1440	$2s^2$	12.10
Cd	0.055	13.1	1.7	1038	112.40	209	$4d^{10}\,5s^2$	4.64
Cr	0.110	6.7	1.6	2938	51.97	630	$3d^5\,4s$	8.33
Co	0.099	11.1	1.8	3173	58.93	445	$3d^7\,2s^2$	8.97
Cu	0.092	56.0	1.9	2868	63.54	343	$3d^{10}\,4s$	8.45
Fe	0.110	10.0	1.8	3273	55.85	470	$3d^6\,4s^2$	8.50
K	0.177	13.3	0.8	1033	39.10	91	$4s$	1.40
Mg	0.250	21.7	1.2	1380	24.31	400	$3s^2$	4.30
Mo	0.061	21.0	1.8	5833	95.94	450	$4d^5\,5s$	6.42
Na	0.295	20.0	0.9	1165	22.99	158	$3s$	2.65
Nb	0.065	6.3	1.6	3573	92.91	275	$4d^4\,5s$	5.56
Ni	0.105	11.5	1.8	3003	58.71	450	$3d^8\,4s^2$	9.14
Pb	0.031	4.8	1.8	1998	207.19	105	$6s^2\,6p^2$	3.30
Pt	0.032	9.0	2.2	4803	195.09	240	$5d^9\,6s$	6.62
Sn	0.054	8.3	1.8	2543	118.69	200	$5s^2\,5p^2$	3.62
Ta	0.036	6.5	1.5	5698	180.95	240	$5d^3\,6s^2$	5.55
Ti	0.126	3.5	1.5	3533	47.90	420	$3d^2\,4s^2$	5.66
U	0.028	1.6	1.7	4091	238.03	207	$5f^3\,6d\,7s^2$	4.80
V	0.120	5.3	1.6	3723	50.94	380	$3d^3\,4s^2$	7.22
W	0.032	18.0	1.7	6203	183.85	400	$5d^4\,6s^2$	6.30
Zn	0.092	16.5	1.6	1179	65.37	327	$3d^{10}\,4s^2$	6.55
Zr	0.066	2.5	1.4	3853	91.22	291	$4d^2\,5s^2$	4.29

c_p	specific heat (300 K – 400 K)	σ	electrical conductivity (300 K)
ES	electronic structure	T_b	boiling point (760 Torr)
N	atomic concentration (300 K)	T_D	Debye temperature
M	atomic weight	P	Pauling's electronegativity

Part I

Introduction and Fundamentals

Computational Materials Science: The Simulation of Materials, Microstructures and Properties By Dierk Raabe
Copyright © 1998 Wiley-VCH Verlag GmbH
ISBN: 3-527-29541-0

Chapter 1

Introduction

Modern materials science is based on the fundamental experience that the properties of materials are not unalterably determined by their average chemical composition but they are to a large extent influenced by their microstructure. This applies particularly for their mechanical and electromagnetic properties. Thus, modern "materials research" is often used as a synonym for "microstructure research".

While the evolutionary direction of microstructure is prescribed by thermodynamics, its actual evolution path is selected by kinetics. It is this strong influence of thermodynamic non-equilibrium mechanisms that entails the large variety and complexity of microstructures typically encountered in engineering materials. It is an essential observation that it is not those microstructures that are close to *equilibrium*, but often those that are in a highly *non-equilibrium* state that provide particularly advantageous material property profiles.

Microstructure can be defined as the totality of all thermodynamic non-equilibrium lattice defects on a space scale that ranges from Ångstrøms (e.g. non-equilibrium foreign atoms)[1] to meters (e.g. sample surface) (Haasen 1984). Its temporal evolution ranges from picoseconds (dynamics of atoms) to years (corrosion, creep, fatigue). It is one major aim of materials science to quantitatively relate macroscopic sample behavior to microstructure. This goal imposes the task of identifying and describing those lattice defects, including their collective static and dynamic behavior, that are responsible for specific macroscopic properties. Figures 1.1 and 1.2 show that the characteristic scales which are associated with the various lattice defects establish a certain hierarchy of microstructure.

This sequence, however, merely reflects a spatial rather than a crisp physical classification[2]. Following this length scale hierarchy, the various levels of microstructure modeling can be roughly grouped into the nanoscopic, microscopic, mesoscopic, and macroscopic regimes. In this context the term *nanoscopic* refers to the atomic level, *microscopic* to lattice defects ensembles below the grain scale, *mesoscopic* to lattice defect ensembles at the grain scale, and *macroscopic* to the sample geometry. Of course, this subdivision is to a certain extent arbitrary. As will be discussed later, various alternative subdivisions are conceivable.

[1] In pure metals, only vacancies or certain foreign atoms provide sufficient entropy to compensate their enthalpy of formation or solution, respectively $c_{vac}(T \lessapprox T_{melt}) \approx 10^{-4}$.

[2] For instance, *small* defects, such as dopants, can have a *larger* influence on strength or conductivity than *large* defects such as preciptates.

Computational Materials Science: The Simulation of Materials, Microstructures and Properties By Dierk Raabe
Copyright © 1998 Wiley-VCH Verlag GmbH
ISBN: 3-527-29541-0

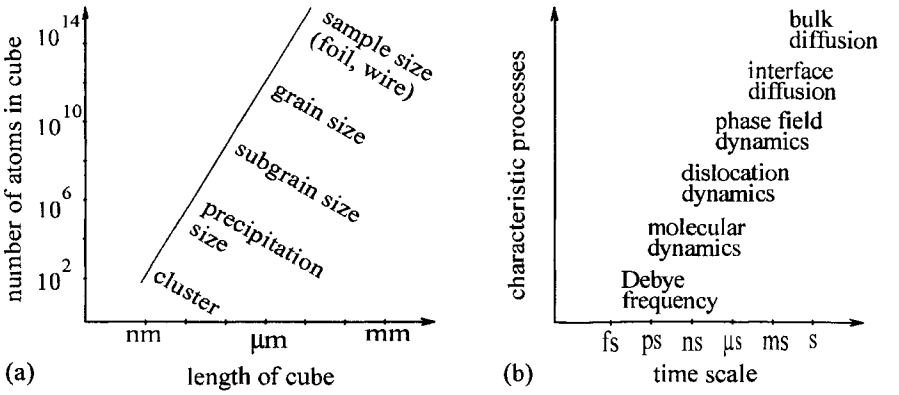

Figure 1.1: Some characteristic space and time scales, (a) number of atoms in a cube, (b) characteristic times of typical simulation problems.

Due to the large spatial and temporal spread of microstructural ingredients and the complexity of possible interaction phenomena among the various lattice defects, a quantitative physical prediction of microstructure evolution and of relevant microstructure–property relations increasingly requires the employment of modeling and simulation (Figures 1.1, 1.2; Tables 1.1, 1.2, and 1.3). This applies particularly when closed analytical expressions cannot be formulated, and when the investigated problem is not easily accessible to experiments. Furthermore, as far as practical engineering aspects are concerned, the use of numerical approaches with predictive power reduces the huge number of experiments typically required in optimizing materials and designing new processes. Progress in the simulation of materials and corresponding manufacturing processes thus facilitates and accelerates the development and optimization of new products.

By using a concept which could be referred to as the "generalized state variable approach", the method of modeling and simulation can be defined in terms of a small number of characteristic steps (see also Section 2.3).

First one defines a set of independent variables and a set of dependent variables. In advanced discrete microstructure models the independent variables typically quantify time and space. The dependent variables are referred to as state variables (Kocks et al. 1975). These must be chosen in a way to allow a sufficiently precise quantification of the material properties under investigation. Subsequently, the mathematical model is formulated. It typically consists of a set of state equations which express certain properties of the material in terms of a given set of state variables, and a set of evolution equations which describe the changes of the values of the state variables as functions of the independent variables. In materials mechanics the state equations typically cover the statics of microstructures, while the evolution equations describe their kinetics. These sets of equations are often accompanied by expressions that reflect the kinematics of the material under the constraints imposed by the manufacturing process or experiment considered.

The selection of adequate state variables, state equations, and evolution equations can be made heuristically, on the basis of theoretical ab-initio concepts, or on the basis of phenomenological observations. This selection represents the most important steps in modeling and reflects the particular physical approach that is made by the researcher to

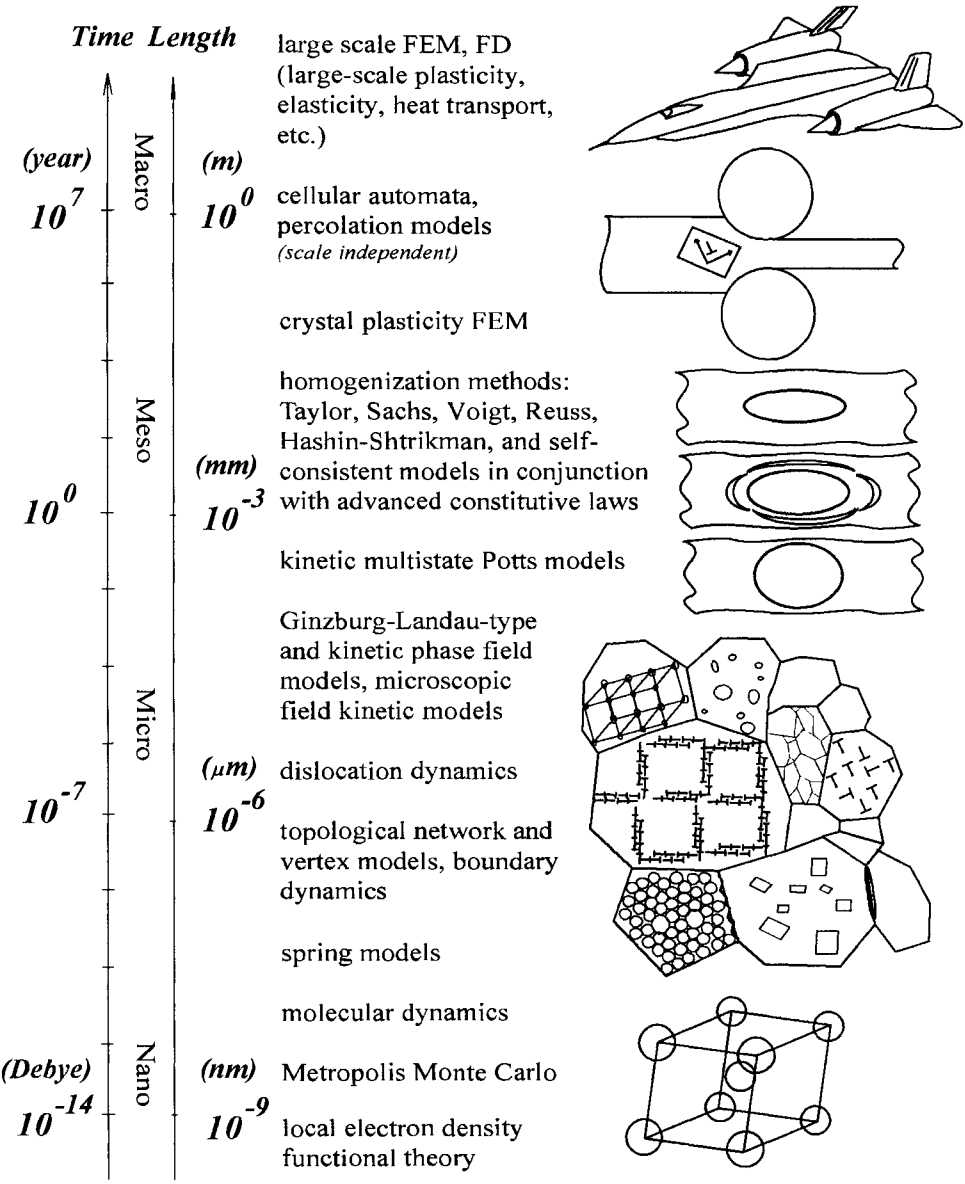

Figure 1.2: Typical space and time scales and simulation methods in computational materials science.

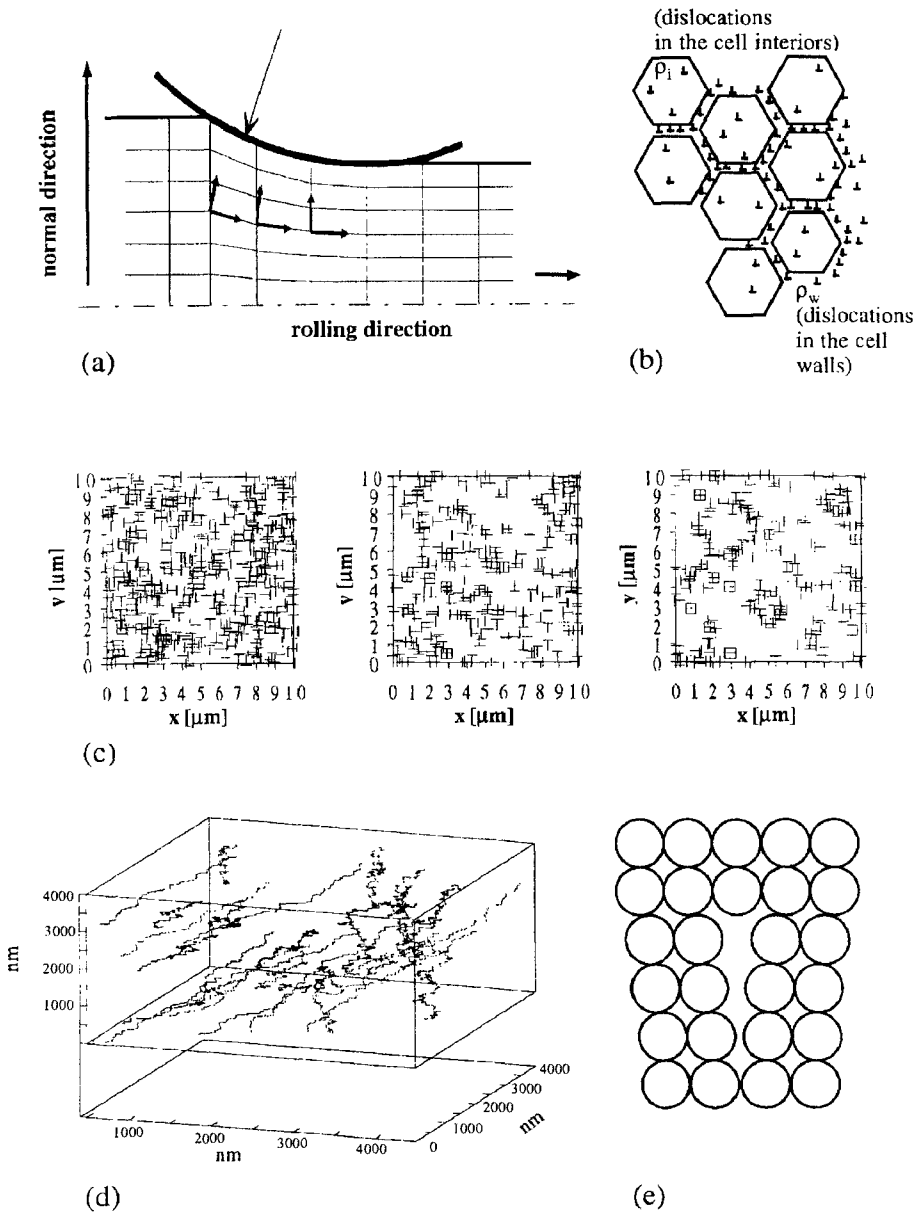

Figure 1.3: Alternative approaches to simulate crystal plasticity at various scales: (a) two-dimensional finite element simulation; (b) statistical constitutive simulations based on the original kinematical one-parameter model (Kocks, Mecking) and their extensions to more-parameter descriptions (Mughrabi, Estrin, Argon); (c) two-dimensional dislocation dynamics; (d) three-dimensional dislocation dynamics; (e) molecular dynamics.

Table 1.1: Space scales and methods in materials simulation, nano–micro level.

Scale [m]	Simulation method	Typical applications
$10^{-10} - 10^{-6}$	Metropolis Monte Carlo	thermodynamics, diffusion, ordering
$10^{-10} - 10^{-6}$	cluster variation method	thermodynamics
$10^{-10} - 10^{-6}$	Ising model	magnetism
$10^{-10} - 10^{-6}$	Bragg-Williams-Gorsky model	thermodynamics
$10^{-10} - 10^{-6}$	molecular field approximation	thermodynamics
$10^{-10} - 10^{-6}$	molecular dynamics (embedded atom, shell, empirical pair, bond order, effective medium, and second moment potentials)	structure and dynamics of lattice defects
$10^{-12} - 10^{-8}$	ab-initio molecular dynamics (tight-binding potentials, local density functional theory)	materials constants, structure and dynamics of simple lattice defects

approximate the problem being addressed. After setting up this framework of variables and equations, which are usually in the form of differential equations, adequate boundary- and initial-value conditions must be formulated which are in accord with the problem under investigation and which turn the initial model into a well-defined mathematical formulation. The final numerical (or analytical) *solution* of such a well-posed problem can be referred to as simulation or numerical (or analytical) experimentation.

The employment of numerical methods in materials science is promoted by the ever-increasing capability of computer systems in terms of speed and information storage, and by the growing demands for quantitative predictions in industry and research. The scientific branch that has matured within this interdisciplinary field, bringing together approaches from materials science, physics, computer science, mathematics, chemistry, and mechanical engineering, is often referred to as "computational materials science".

Computer simulation nowadays complements most if not all fields of materials science and engineering. For instance, simulations in materials physics aim at predicting microstructural phenomena at the atomic scale using ab-initio molecular dynamics and Monte Carlo methods. Simulations in materials science pertaining to mechanical engineering typically focus on large-scale construction problems using finite element approaches where the microstructure is reduced to the incorporation of averaging constitutive laws.

In contrast to these examples, the original domain of materials science is the investigation of lattice defect ensembles at the mesoscale. The use of simulations in this particular field represents a great challenge, in that it must bridge enormous space and time scales and provide concepts to adequately describe complex many-body interaction phenomena. For this purpose a number of new concepts have been developed which enable one to handle the interaction of many individual lattice defects in a more or less discrete fashion. The latter aspect is of special interest, since most microstructural evolution phenomena are highly nonlinear and entail self-organization on a microstructural scale (Haken 1978; Khachaturyan 1983; Kubin 1988; Martin and Kubin 1992).

In contrast to atomic-scale molecular dynamics and Monte Carlo simulations, most mesoscale approaches are formulated as continuum models, but often with a discrete consideration of lattice defects. The methods include deterministic and probabilistic cellular

Table 1.2: Space scales and methods in materials simulation, micro–meso level.

Scale [m]	Simulation method	Typical applications
$10^{-10} - 10^{0}$	cellular automata	recrystallization, grain growth, and phase transformation phenomena, fluid dynamics, crystallograhpic texture, crystal plasticity
$10^{-7} - 10^{-2}$	spring models	fracture mechanics
$10^{-7} - 10^{-2}$	vertex models, network models, grain boundary dynamics	subgrain coarsening, recrystallization, secondary recrystallization, nucleation, recovery, grain growth, fatigue
$10^{-7} - 10^{-2}$	geometrical, topological, and component models	recrystallization, grain growth, secondary recrystallization, crystallographic textures, solidification, crystal topology
$10^{-9} - 10^{-4}$	dislocation dynamics	crystal plasticity, recovery, microtexture, dislocation patterning, thermal activation
$10^{-9} - 10^{-5}$	kinetic Ginzburg–Landau-type phase field models	diffusion, interface motion, precipitation formation and coarsening, polycrystal and polyphase grain coarsening phenomena, isostructural and non-isostructural phase transformation, type II superconductivity
$10^{-9} - 10^{-5}$	multistate kinetic Potts models	recrystallization, grain growth, phase transformation, crystallographic textures

Table 1.3: Space scales and methods in materials simulation, meso–macro level.

Scale [m]	Simulation method	Typical applications
$10^{-5} - 10^{0}$	large-scale finite element, finite difference, linear iteration, and boundary element methods	averaged solution of differential equations at the macroscopic scale (mechanics, electromagnetic fields, hydrodynamics, temperature fields)
$10^{-6} - 10^{0}$	crystal plasticity finite element models, finite elements with advanced constitutive laws considering microstructure	microstructure mechanics of complex alloys, fracture mechanics, textures, crystal slip, solidification
$10^{-6} - 10^{0}$	Taylor–Bishop–Hill, relaxed constraints, Sachs, Voigt, and Reuss models, Hashin–Shtrikman model, Eshelby and Kröner-type self-consistent models	polyphase and polycrystal elasticity and plasticity, microstructure homogenization, crystallographic textures, Taylor factors, crystal slip
$10^{-8} - 10^{0}$	cluster models	polycrystal elasticity
$10^{-10} - 10^{0}$	percolation models	nucleation, fracture mechanics, phase transformation, current transport, plasticity, superconductivity

automata which may account for both short-range (local) and long-range (global) interactions, Ginzburg–Landau-, Cahn–Hilliard-, and Allen–Cahn-type phase field methods, dislocation dynamics, polycrystal and nonlinear crystal plasticity finite element models, topological network and vertex models, boundary dynamics, and multistate kinetic Potts methods. However, classical techniques such as molecular dynamics, Metropolis Monte Carlo, and conventional finite element simulations are also used extensively.

Advanced microstructure simulations should meet three major requirements. First, they should enable one to use, or even derive, advanced path-independent microstructure–property relations with quantitative validity. Second, they should provide insight into the underlying thermodynamic and path-dependent physical principles that govern the complex nature of microstructure evolution at the various space and time scales. Third, they should allow one, at least in certain cases, to replace and complement experimentation by simulation.

In engineering terms microstructure simulations should thus provide a convenient means of predicting and understanding material properties and microstructure evolution for technical applications under conditions that have not yet been studied or that are not amenable to experiments. To fulfill these requirements and at the same time to optimize the predictive power of models, the various numerical methods are increasingly complemented by the concept of integrated modeling and simulation (Gottstein 1996). This term characterizes the coupling of computer codes with the aim of bridging the scale discrepancies between different simulation levels. This can be achieved by either *simultaneous* integration (direct integration) or *sequential* integration (Raabe 1997). The first notion means that various interacting simulation codes, which may use different numerical techniques, are employed simultaneously in one computer experiment. The second term describes the alternative method of an adequate parameter-transfer between simulations that are used sequentially.

Since microstructure evolution is path-dependent, concepts of integrated modeling and simulation should include as many of the microstructurally relevant processing steps and parameters as possible. However, such a procedure requires the incorporation of various space and time scales which can differ by some orders of magnitude. One reasonable approach for combining various scales consists in the incorporation of constitutive laws that have been derived from non-averaged, i.e. space- and time-discretized, simulations on the appropriate smaller scale. In such a concept, the results obtained from simulations on a certain scale are averaged and condensed before being considered at the next scale. This means that the phenomenological character of the model equations used in each step increases with increasing scale.

However, there is also a more direct way of bridging scale discrepancies. Some of the simulation techniques mentioned above were originally confined to particular space and time scales. This applies especially to methods which reveal intrinsic physical scaling parameters, e.g. molecular dynamics and some Monte Carlo methods. In contrast, most mesoscale models are continuum approaches, i.e. they are *not* intrinsically calibrated and have thus a larger potential for spanning time and length scales. In this context especially the various crystal plasticity finite element, cellular automaton, dislocation dynamics, boundary dynamics, and multistate Potts[3] models are of importance.

For instance, the finite element technique is designed to provide approximate solutions to coupled sets of partial differential equations subject to appropriate boundary- and initial-value conditions. Its application in computational materials science was orig-

[3]Monte Carlo method with a delta-type Hamiltonian for the identification of interfaces.

inally confined to solving elastic and simple plastic problems at the macroscopic level using averaging constitutive laws and the conditions for equilibrium and compatibility. However, through the introduction of improved constitutive laws, i.e. elements of crystal plasticity, finite element methods are nowadays increasingly capable of considering material heterogeneity also at the mesoscopic level. This trend in finite element simulations points from the macroscopic to the mesoscopic scale. For the Potts model, which has its roots in the stochastic Metropolis Monte Carlo method, the reverse applies. By mapping generalized spin numbers to discrete domains which comprise cells with identical spin, it enables one to extend the use of the Monte Carlo algorithm to the description of interfaces. This approach points from the microscopic to the mesoscopic scale.

The material in this book should assist the reader in selecting appropriate simulation methods and critically estimating the plausibility of the predictions. Both aspects are important, since one often encounters different concepts for simulating the same problem. For instance, in the field of plasticity, one can use finite element methods, statistical kinematical simulations, discrete dislocation dynamics, molecular dynamics, or combinations of these (Figure 1.3).

Besides the numerous technical details that will be reviewed in the following chapters, the selection of appropriate simulation techniques should be accompanied by the following more general considerations:

Scales: What are the physical time and length scales of the phenomenon?
Microstructure: Is it necessary to incorporate microstructure?
Analytical solution: Is it possible to solve the problem analytically?
Experimental data: Are experimental data available to check the predictions?
Independent variables: Which variables should serve as independent variables?
Dependent variables: Which variables should serve as dependent variables?
Model approach: Should a first-principles, phenomenological, or empirical model approach be used?
Model parameters: Do the required parameters have any physical meaning and are corresponding experimental or theoretical data available?
Boundary conditions: Which boundary- and initial-value conditions are adequate?
Realistic conditions: Are particular boundary- and initial-value conditions known?
Discretization: What degree of spatial and temporal discretization is required?
Simulation scale: Which simulation method is suited for the scale addressed?
Error tolerance What degree of precision is required? Which error can be tolerated?
Deterministic/stochastic: Is the phenomenon deterministic or stochastic?
Atomistic/continuum: Should an atomistic or continuum model be used?
Combination of scales: Is it required to combine various space and/or time scales?
Integrated simulation: What is the appropriate integrated simulation method to bridge the various space and/or time scales?
Simulation code: Are existing simulation codes available?
Comparison: Were the chosen simulation methods quantitatively compared with experiments, analytical solutions, and/or competitive numerical approaches?
Programing language: Which programing language, compiler, commercially available solver, etc. should be used?
Speed: Which is the fastest simulation method?
Price: Which is the cheapest simulation method?
Computer power: How much computer power is available for the simulation?
Data analysis: What methods must be used to analyze and present the data?

Chapter 2

Modeling and Simulation in Materials Science

2.1 Some Notions

The words "modeling" and "simulation" are often distinguished by somewhat arbitrary arguments or they are simply used synonymously. This lack of clarity reflects that theoretical concepts and technical facilities encountered in computational materials science develop faster than semantics. For elaborating a common language in this field, a less ambiguous definition of both concepts might be helpful.

In current scientific understanding the word "modeling" (model (Latin, Italian): copy, replica, exemplar) often covers two quite different meanings, namely, model formulation and numerical modeling. The latter term is frequently used as a synonym for numerical simulation (simulare (Latin): fake, duplicate, mimic, imitate). Thus, apart from the possibility of using these notions synonymously, this chapter addresses some definitions which appear reasonable, at least in the context of microstructure simulation.

2.2 The Basic Idea behind Modeling

The general intention of a scientific inquiry is to obtain an understanding and a control of some parts of the universe (Rosenblueth and Wiener 1945). However, most parts of the real world are neither sufficiently obvious nor simple that they could be grasped and controlled without *abstraction*.

Scientific abstraction consists in replacing the part of the real world under investigation by a model. This process of designing models can be regarded as the most general and original principle of modeling. It describes the classical scientific method of formulating a simplified imitation of a real situation with preservation of its essential features. In other words, a model describes a part of a real system by using a *similar* but *simpler* structure. Abstract models can thus be regarded as the basic starting point of theory. However, it must be underlined that there exists no such thing as a unified exact method of deriving models. This applies particularly for the materials sciences, where one deals with a large variety of scales and mechanisms.

Computational Materials Science: The Simulation of Materials, Microstructures and Properties By Dierk Raabe
Copyright © 1998 Wiley-VCH Verlag GmbH
ISBN: 3-527-29541-0

The ensuing sections present some general ideas about modeling concepts. Special emphasis is placed on the presentation of the generalized state variable concept. This approach, which is well established in the field of constitutive plasticity modeling (Argon 1975; Kocks et al. 1975), builds models in terms of well-defined sets of state variables and corresponding state and evolution equations. State equation concepts can serve as a tool in designing the basic structure of models at various scales.

Although a large number of articles and monographs exist on modeling and simulation, only a few authors have reflected on the nature and the fundamental concepts of modeling. Interesting contributions in that context were made by Rosenblueth and Wiener (1945), who contemplated the philosophical side of modeling, by Koonin (1986), and by Bellomo and Preziosi (1995), who gave a concise mathematical definition of modeling.

2.3 The Generalized State Variable Concept

2.3.1 Concepts for Models beyond the Atomic Scale

The rather broad definition of the very nature of modeling given above seems to be a compelling scientific concept for the general case and is presumably in good accord with the reader's own experience. Unfortunately, this crisp concept becomes somewhat vague when used in materials science, due to the large spread of scales. Possibly the best approach to model the evolution of microstructures consists in discretely solving the equations of motion of all atoms in the material portion of interest (Chapter 7). Such an approach provides the coordinates and velocities of all atoms at any instant, i.e. it predicts the temporal evolution of the entire microstructure. The more detailed the description of the interatomic forces in such simulations, the smaller is the need for additional empirical model ingredients. In contrast, models beyond that scale have to incorporate averaging continuum approximations which are often much more phenomenological in nature than the more ab-initio assumptions made at the atomic scale.

While atomistic methods thus indeed prevail in microstructure simulations at the nanoscale, they are not tractable at the meso- and macroscale where at least 10^{23} atoms are involved. Even when using simple radially symmetric interatomic pair potentials, atomistic simulations are at present confined to not much more than 10^8 atoms. Thus, for modeling microstructural phenomena beyond the nanoscopic scale, one must drop the idea of predicting the motions of single atoms and switch to continuum models. Since real microstructures tend to be highly complex, it can be a non-trivial and at the same time crucial task to extract those state variables out of the many observables that properly characterize microstructural phenomena at a continuum scale.

For obtaining a reasonable simplification of the microstructure to be modeled it is often first necessary to investigate the real system by experimental observation, to formulate logical heuristic assumptions, or to conduct theoretical ab-initio arguments. From the physical picture so obtained, one has to derive a phenomenological constitutive description, including the main physical mechanisms, that allows one to characterize the system behavior at a level beyond the atomic scale.

The phenomenological picture must then be translated into a mathematical model. Using an approach which can be referred to as the "generalized state variable concept", this procedure requires the definition or appropriate selection of independent variables, state variables (which are sometimes termed "dependent variables"), kinematic equations, equations of state, evolution equations, physical parameters, boundary- and initial-value

Table 2.1: Ingredients required in formulating mathematical models in materials science.

Step	Ingredient
1.	*Independent variables*, e.g. time and space.
2.	*State variables*, i.e. intensive and extensive or implicit and explicit dependent variables, e.g. temperature, dislocation density, displacement, or concentration.
3.	*Kinematic equations*, i.e. functions that describe the coordinate changes of mass points without considering the actual forces, e.g. equations for computing strain and rotation from displacement gradients under consideration of constraints.
4.	*State equations*, i.e. path-independent functions that describe the actual state of the material in terms of the values of the dependent variables.
5.	*Evolution equations*, i.e. path-dependent functions that describe the evolution of microstructure in terms of the change in the values of the dependent variables.
6.	*Physical parameters.*
7.	*Boundary- and initial-value conditions.*
8.	*Numerical algorithms* or *analytical methods* to solve the framework set up by 1–7.

conditions, and appropriate algorithms (Table 2.1). Such a basic phenomenological framework of variables and equations forms the backbone of many microstructure models.

2.3.2 Independent Variables

The independent variables can, by definition, be freely chosen. In advanced microstructure models, time t and space $\boldsymbol{x} = (x_1, x_2, x_3)$ typically serve as independent variables. For instance, molecular dynamics simulations predict the deterministic trajectory of the system in phase space by calculating the positions $\boldsymbol{x}_i$ and velocities $\dot{\boldsymbol{x}}_i$ of all i atoms in the system at each moment. Discrete dislocation dynamics simulations, which average out the atomistic nature of the material by reducing the direct atomic interactions to linear continuum elasticity, calculate the exact positions $\boldsymbol{x}_j$ and velocities $\dot{\boldsymbol{x}}_j$ of all j dislocations (in two dimensions; 2D) or dislocation segments (in three dimensions; 3D) at each instant. Advanced crystal plasticity finite element simulations track the stress and strain state in each material portion as a function of crystal orientation and constitutive behavior, discretely in time and space.

2.3.3 State Variables or Dependent Variables

The state variables are functions of the independent variables. Their value determines the state of a system at any instant, irrespective of their history. In classical thermodynamics they usually occur as extensive, i.e. mass-dependent, or intensive, i.e. mass-independent, quantities.

In microstructure mechanics one often encounters a further distinction, namely, that between explicit and implicit state variables (Swaerengen and Holbrook 1985). While explicit state variables define *local* microstructural features of the material such as particle or grain size, implicit state variables are defined as mesoscopic or macroscopic *averages*. The latter type of state variable has gained particular relevance in considering microstructural properties in finite element calculations.

State variables in material models are often tensor-valued variables which depend on space and time, such as the displacement $\boldsymbol{u} = (u_1, u_2, u_3) = \boldsymbol{u}(\boldsymbol{x}, t)$ which is a tensor of first rank, or strain $\boldsymbol{\varepsilon} = \boldsymbol{\varepsilon}(\boldsymbol{x}, t)$ which is a tensor of second rank. However, scalar state quantities, such as the dislocation density in statistical Kocks–Mecking-type plasticity models, the concentrations of the chemical constituents in Cahn–Hilliard-type simulations, or the density of bosons in Ginzburg–Landau calculations, are admissible as well.

Phenomenological models for predicting the behavior of complex commercial alloys, polymers, or composites often require a considerable number of state variables. For instance, a description of the flow stress of a metal-matrix composite or of a superalloy could consider the solute concentrations of the ingredients, the dislocation density in all phases, the interface spacing, and the particle size and distribution. The disadvantage associated with such detailed *phenomenological* descriptions involving many variables is that they spoil the original idea of finding a transparent *physical* model. In other words, using too many state variables can turn a physical into an empirical polynomial model, where the state variables serve as mere fitting quantities. An increasing number of state variables thus often reduces the physical significance of each of these variables. Although multivariable approaches can be helpful in the field of industrial modeling, where the materials and the manufacturing processes are often too complicated to allow a transparent description, they are less desirable in physically oriented microstructure simulations. The art of constitutive modeling can thus be demonstrated in finding a balance between adjustable parameters (Section 2.3.7) and state variables with a crisp physical significance.

2.3.4 Kinematic Equations

Kinematic equations for solids are used to calculate quantities such as strain, strain rate, rigid-body spin, or rate of crystal reorientation under consideration of externally or internally imposed constraints[1]. The kinematic constraints are usually defined by the manufacturing or experimental process being investigated. For instance, during rolling it is not admissible for any material portion near the surface to undergo displacements perpendicular to the rolling plane.

2.3.5 Equations of State

Equations of state relate a property of interest, such as the electrical resistivity, the flow stress, or the free enthalpy, to the actual values of the state variables (Table 2.1). Since the state variables are usually functions of the independent variables, the values of the state equations depend on them as well. In discrete material simulations the state of a material can thus be described with the resolution of the independent variables. Equations of state generally represent path-independent functions. That means they provide a general means of calculating materials properties from adequate state variable values irrespective of their origin and history. Hence, data input to state equations can be derived both by simulation and by experiment. Microstructural equations of state usually quantify the material response to external or internal changes in the values of the dependent variables. This means that state equations *characterize* the material. For instance, the dependence

[1] The rigid-body rotation of the continuum (skew symmetric part of the displacement gradient tensor) is not necessarily identical to the crystal rotation. This discrepancy is due to kinematic subtleties arising from the crystallographic nature of slip and from what is defined as the reference set of axes (van Houtte and Aernoudt 1975; Kocks and Chandra 1982; Argon 1986; Leffers and Lebensohn 1996).

Table 2.2: Some typical state equations in computational materials science.

State quantity	State variable(s)	State equation
stress	strain or displacement	Hooke's law
flow stress	uniform dislocation density, Taylor factor	Taylor equation in Kocks–Mecking-type models
flow stress	dislocation density in the cell walls and cell interiors	advanced statistical two- and three-parameter plasticity models
interatomic potential	interatomic spacing	radially symmetric interatomic pair potentials
interatomic potential	interatomic spacing and angular position	tight-binding potentials
free energy	concentration of atoms or bosons	free energy Landau form in Ginzburg–Landau-type models

of flow stress on displacement is entirely different for a liquid, an elastic-rigid-plastic body, a viscoplastic material, or a creeping solid. Typical examples of state equations are the interatomic potential and force functions in molecular dynamics, Hooke's law of elasticity in dislocation dynamics, nonlinear elasticity laws in polymer mechanics, the relations between flow stress and dislocation density in constitutive plasticity laws, and the free energy functional in the Ginzburg–Landau and related microstructural phase field models.

2.3.6 Structure Evolution Equations

The next step consists in predicting the evolution of the microstructure as a function of the independent variables. For this purpose one must either *measure* the values of the state variables consecutively for each set of independent variables, or incorporate additional model equations which allow one to *calculate* the changes of the state variables. Such expressions are referred to as "evolution equations", or "structure evolution equations". These are equations that steadily update the values of the state variables as a function of the independent variables. It is a fundamental feature of microstructure that it is in thermodynamic non-equilibrium, i.e. the governing evolution equations are generally path-dependent and thus not equations of state. This means they may usually not be written as total differentials. Typical structure evolution equations are Newton's law of motion in molecular and dislocation dynamics, or classical rate equations such as the heat and diffusion equation.

2.3.7 Parameters

The state variables in the state equations are weighted, based on parameters. These should have a physical meaning and be amenable to experiment and/or theory.

Identifying appropriate parameters and incorporating their correct values are among the most crucial tasks in any simulation. This applies particularly in the field of mesoscale materials simulations, where the values of parameters can depend considerably on other

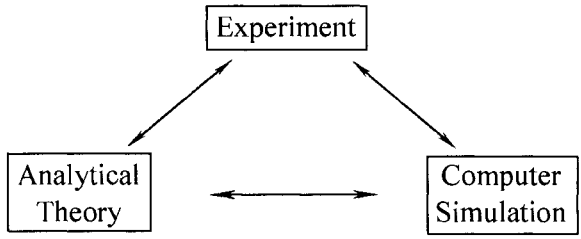

Figure 2.1: Schematic illustration of the relations between analytical models, simulation, and experiment according to Binder (1991a).

parameters and on the state variables themselves. This means that the underlying state equations contain nonlinearities and/or are coupled with other state equations. Furthermore, many material parameters have a very strong direct influence, such as in the field of thermal activation where they occur in the argument of exponential functions. For instance, the activation energy of grain boundary motion occurs in an exponential term and can depend strongly on the misorientation of the neighboring crystals, on the inclination of the boundary plane, and on the concentration of foreign atoms in the boundary.

Depending on the desired precision, parameters can be incorporated in a more or less detailed fashion. For instance, the elastic constants can be considered either by simply employing the scalar Lamé constants (isotropy) or by including the components of the fourth-rank elasticity tensor (anisotropy) together with their respective temperature coefficients. Diffusion coefficients can be used as scalar bulk quantities or in tensorial form with different values parallel to different crystal axes.

2.3.8 Examples of Phenomenological Modeling Concepts

The aforementioned sets of kinematic, state, and evolution equations in the form of algebraic, differential, and/or integral expressions establish, together with appropriate state and independent variables, a mathematical state variable model (Andersen and de Hoog 1976; Avula et al. 1983; Williams 1985; Smith 1987; Neelamkavil 1987; Szekely and Wahnsiedler 1988; Bellomo and Preziosi 1995). The totality of the equations and parameters that altogether characterize the particular response of a material is often referred to as the set of constitutive equations or constitutive laws (Argon 1975; Krawietz 1986; Kocks 1987; Andersen et al. 1987; Krausz and Krausz 1996).

Figures 2.1, 2.2, 2.3, and 2.4 show flowcharts which present some more or less overlapping approaches to define modeling and simulation. The generalized state variable approach to the definition of both terms, as outlined above, is presented in Figure 2.5.

2.3.9 Analytical Model and Numerical Counterpart

The above considerations concerning modeling concepts do not imply any technical details of the way in which the resulting set of governing equations can be solved. A number of the simpler statistical models can be employed without using numerical methods (Table 2.1). In contrast, most modern discrete models of microstructure dynamics consist of large numbers of coupled differential equations so that their application requires numerical

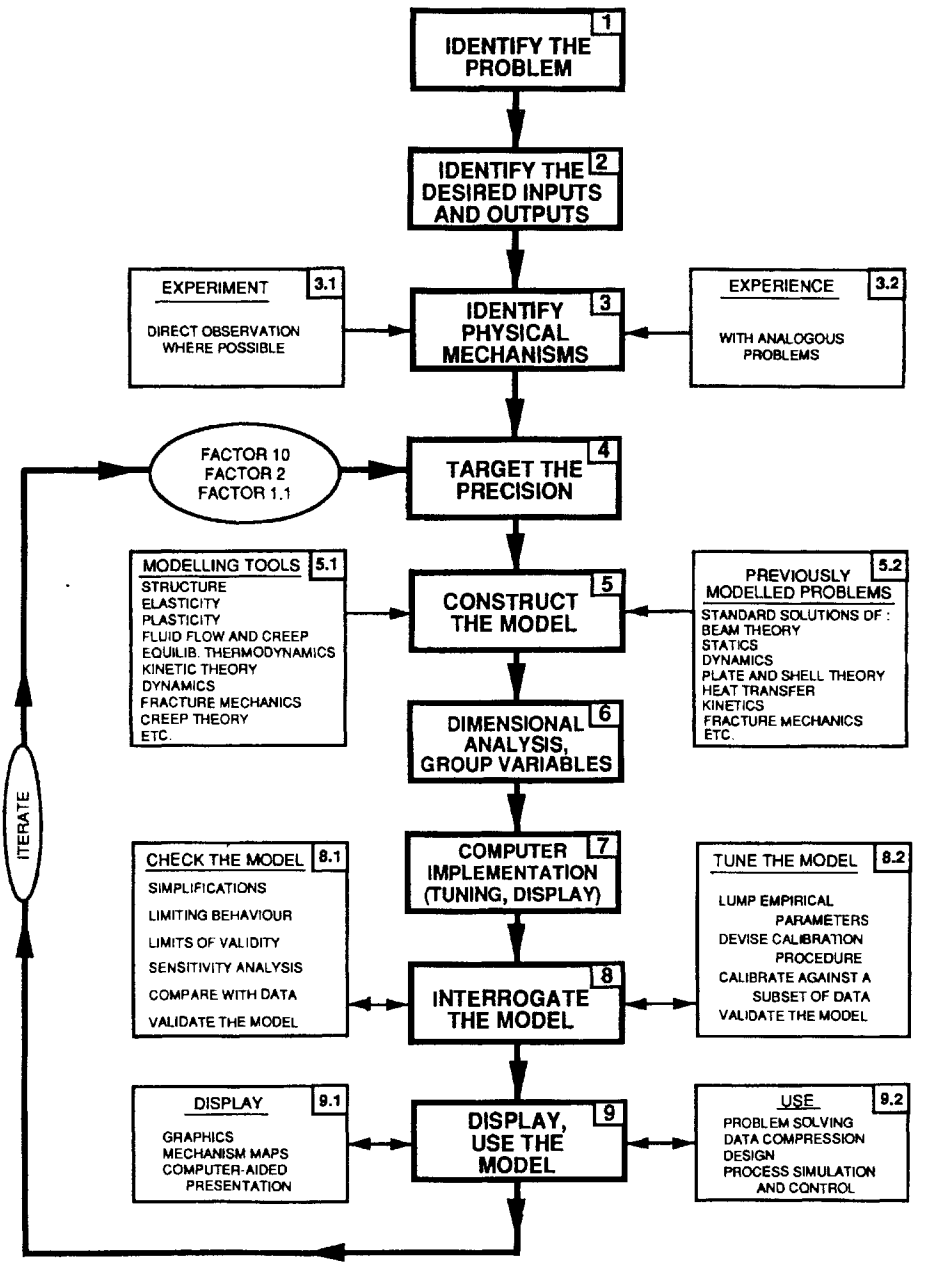

Figure 2.2: Flowchart illustrating stages in the process of modeling according to Ashby (1992).

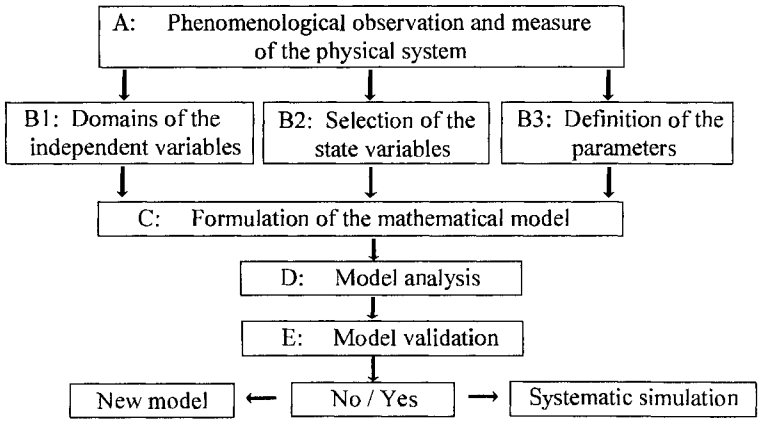

Figure 2.3: Flowchart illustrating stages in the process of modeling according to Bellomo and Preziosi (1995).

tools. In this context it should be recalled that the original, mostly analytical, mathematical model is not exactly identical to its numerical counterpart. Depending on the underlying analytical expressions, the exactness of the corresponding numerical solution can depend on a number of parameters such as truncation, series expansion, discretization (integration, differentiation), statistical, ergodic, or programing errors. However, even in complex models it is sometimes possible to derive analytical solutions to simple cases and use them for scrutinizing corresponding numerical predictions.

2.4 Numerical Modeling and Simulation

The considerations discussed above fall into the domain of model formulation or model design. The second often-encountered meaning of modeling is the numerical solution of the governing equations associated with models. This procedure can be referred to as "numerical modeling" or "simulation". Both terms paraphrase the solution of a set of mathematical expressions, i.e., of a number of path-dependent and path-independent functions, which quantify the underlying model formulation using appropriate boundary- and initial-value conditions. Although both numerical modeling and simulation basically address the same activity, they are often used in a somewhat different fashion.

One common approach is to use the notion "numerical modeling" for the entire procedure of model formulation and program code generation, while the term "simulation" is often used in the sense of numerical experimentation. In this picture, modeling comprises the entire phenomenological, theoretical, and conceptual work including progamming, while simulation describes the mere application of the program under conditions that map essential parameters of real processes, i.e. under different boundary- and initial-value conditions. This definition is in line with a suggestion of Ashby (1992) who described "simulation" as the "... study of the dynamic response of a modeled system by subjecting the model to inputs which simulate real events..."; see Figure 2.2.

An additional approach to distinguish between the two terms is to consider the scale addressed. It is a frequent (although not logical) observation that the term "numerical modeling" is primarily used to describe the numerical solution of macroscopic or meso-

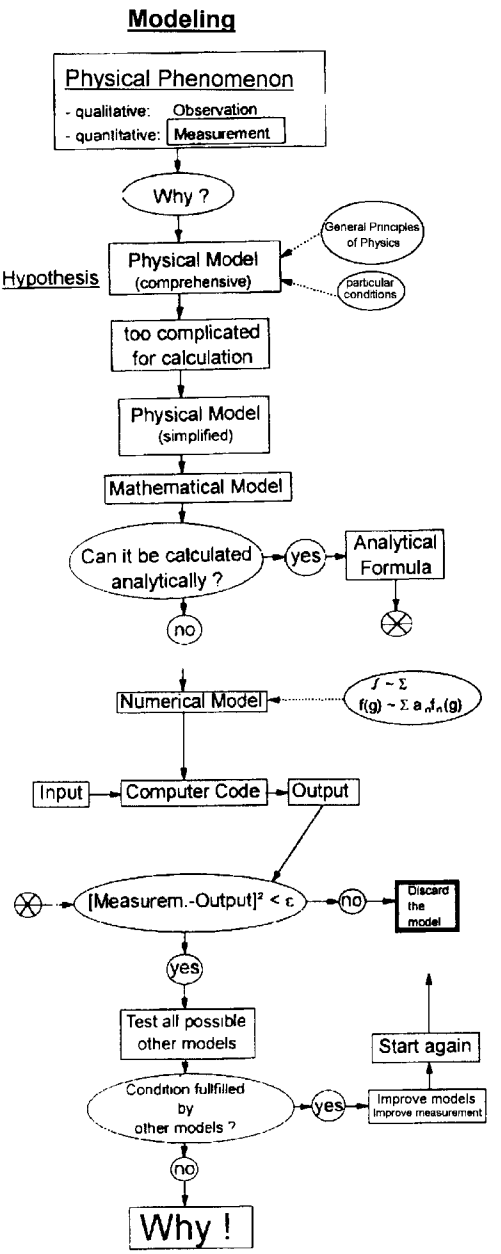

Figure 2.4: Flowchart illustrating stages in the process of modeling according to Bunge (1997).

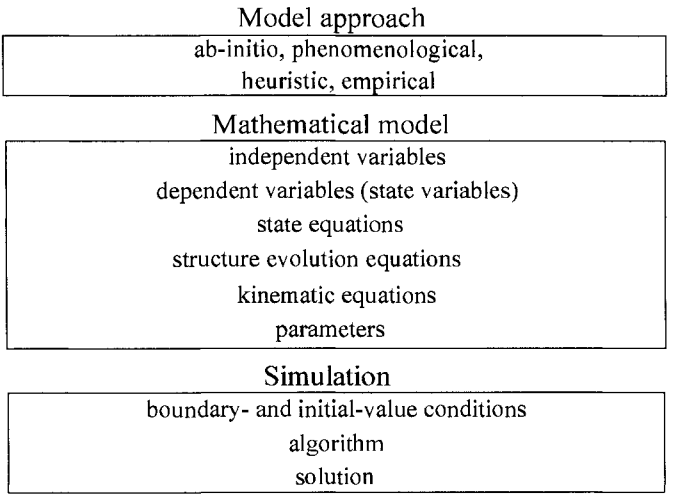

Figure 2.5: Flowchart illustrating stages in the process of modeling and simulation according to the generalized state variable approach.

scopic, rather than microscopic models. Model calculations in the microscopic regime are often referred to as "simulation". For instance, one is inclined to say that the atomic positions and velocities as described by molecular dynamics are obtained by simulation rather than by modeling (microscopic regime, single atoms). On the other hand, if say the kinematical Kocks–Mecking approach is used for the calculation of flow curves, it is common to speak of modeling (macroscopic regime, global dislocation densities). However, if the same flow curves are described using space- and time-discretized calculations involving single dislocations or even dislocation segments, one is prone to speak of simulation (microscopic–mesoscopic regime, discrete dislocations).

This somewhat inconsistent and arbitrary use of the terms "modeling" and "simulation" can serve as a starting point to elaborate arguments that permit a more commensurate distinction between the two notions, as follows.

An obvious dissimilarity between modeling and simulation lies in the fact that many classical models do not require the employment of computers but can be rendered into a closed form to be solved analytically. However, models that can be solved by means of analytical techniques are often not discrete in space. For instance, a number of plasticity models that can predict dislocation densities and stresses do not incorporate the exact positions of the individual dislocation segments.

The reverse often applies for simulation, where the governing analytical expressions are typically known for *one* individual defect or particle but not for the *global* ensemble. For instance, there are no expressions with a closed analytical solution which allow one to predict the exact actual positions and velocities of all atoms in a moving high-angle grain boundary. This problem can only be tackled by solving Newton's equation of motion for a larger number of atoms. This means that simulations typically provide numerical solutions to problems that can be dismantled into a large number of individual microscopic events. Therefore, the notion of "simulation" frequently appears in conjunction with the space-discretized solution of *many-body problems* (e.g. many atoms, vacancies, molecules,

dislocations, dislocation segments, or finite elements) (Raabe 1997). As the quintessence of these considerations, the following definitions are suggested to distinguish simulation from numerical modeling.

Microstructure simulations provide numerical results to models which are formulated as microscopic or mesoscopic many-body problems by solving the algebraic, differential, or integral expressions that reflect the behavior of the considered elementary lattice defects (real physical defects) or quasi-defects (artificial microscopic system elements) with a high degree of spatial and temporal discretization. Microstructure simulation can thus be interpreted as a tool for the numerical prediction of microstructure evolution at the lattice-defect or quasi-lattice-defect level.

Numerical (analytical) modeling of microstructure provides numerical (analytical) solutions to macroscopic models by solving the algebraic, differential, or integral expressions that govern the behavior of global lattice defect ensembles with a high degree of temporal, but low degree of spatial, discretization.

The above considerations imply that numerical modeling is typically faster than simulation when applied to identical physical problems at the same level, i.e. numerical modeling can cover larger space and time scales. Such an advantage can be crucial, especially in industrial applications. However, numerical modeling is often less discrete in space and thus provides less predictive power on the local scale.

2.5 Categories of Models

2.5.1 Spatial Scale

Various more or less precise approaches are conceivable to classify microstructure models (Table 2.3). Often they are simply grouped according to their underlying characteristic scale. A coarse spatial subdivision would suggest four classes of models, namely, macroscopic, mesoscopic, microscopic, and nanoscopic models. The term macroscopic refers to the sample geometry, mesoscopic to lattice defect ensembles at the grain scale, microscopic to lattice defects ensembles below the grain scale, and nanoscopic to the atomic level. Of course, such spatial categories and their definitions are rather arbitrary. For instance, one can just as well choose three instead of four classes, using one for the macroscopic scale, one for the mesoscopic scale, and one for the atomistic scale. A similar classification approach was used to organize this book into chapters (nano–micro, micro–meso, meso–macro). Details of such spatial categories are apparent from Figures 1.1 and 1.2, and Tables 1.1–1.3.

2.5.2 Spatial Dimension

A second possible approach to identifying model categories accounts for the spatial dimension of a model (one-, two-, and three-dimensional). In computational materials science two- and three-dimensional models prevail. The difference between them can be of substantial relevance for an appropriate interpretation of the results. For instance, a correct incorporation of slip system geometry and of dislocation interactions cannot be made in two-dimensional simulations but requires a three-dimensional treatment. This is important in Taylor-type simulations or the more complex crystal plasticity finite element codes. Even in conventional finite element simulations the discrepancies between the predictions obtained in two and three dimensions can be significant. For instance, in

Table 2.3: Characteristic features of simulations.

Classification aspect	Type of model
spatial scale	macroscopic, mesoscopic, microscopic, nanoscopic
spatial dimension	one-, two-, three-dimensional
spatial discretization	continuum, atomistic
predictive character	deterministic, stochastic/probabilistic, statistical
descriptive character	first-principles, phenomenological, empirical
path-dependence	kinetic, static

two-dimensional finite element simulations of rolling processes the transverse broadening of the sheet is typically neglected. An extension of dislocation dynamics from two to three dimensions allows one to correctly describe dislocation multiplication, i.e. the activation of a Frank–Read source or of a pole mechanism. This is not possible in two-dimensional simulations. Similar arguments occur in the discussion of grain topologies arising from mesoscale and atomistic simulations involving interfaces.

2.5.3 Spatial Discretization

Concerning the degree of spatial discretization, two basic classes can be identified, namely, continuum and atomistic models (Table 2.3). Continuum models average out the nature of single atoms by using differential equations that describe the material response in a mean macroscopic fashion under consideration of phenomenological or empirical constitutive equations and the constraints imposed by equilibrium, compatibility, and conservation laws. Typical examples of continuum models are classical finite element (Courant 1943; Zienkiewicz and Morgan 1983; Livesley 1983; Rao 1989), polycrystal (Taylor 1938; Bishop and Hill 1951), self-consistent (Eshelby 1961; Kröner 1961), certain deterministic cellular automata[2] (von Neumann 1963), dislocation dynamics (Devincre 1996), topological vertex (Humphreys 1992a), and phase field models (Cahn and Hilliard 1958).

In recent years various refinements were introduced to particularly enrich large-scale continuum models with microstructural ingredients. Typical examples of such advanced methods are anisotropic finite element models which consider crystal plasticity, crystallographic texture, and the topology and morphology of the microstructure (Becker 1991; Karhausen and Kopp 1992; Wulf et al. 1993; McHugh et al. 1993a; Schmauder 1994; Wang et al. 1994; Dawson et al. 1994; Beaudoin et al. 1996; Sarma and Dawson 1996; Schmauder and Raabe 1996; Schmauder and Weichert 1996; Wulf et al. 1996)[3].

Typical examples of advanced polycrystal models are relaxed-constraints Taylor-type approaches which consider statistical (Schmitter 1991b) or local grain interactions (Wagner 1995), deformation banding, and grain fragmentation (Lee and Duggan 1993; Leffers 1994). According to van Houtte (1996a) these models have in common that they quantify

[2]Since cellular automata are not intrinsically calibrated, they cannot be generally classified as continuum-type approaches. Depending on the underlying physical model, they can also occur as atomistic models.

[3]The field of advanced finite element models is often referred to as computational micromechanics (McHugh et al. 1993a) or computational microstructure mechanics (Schmauder 1995). The latter notion seems somewhat more appropriate, since the former one is already reserved for the field of mechanical engineering at the microscopic level.

the degree of strain relaxation and local interaction between crystals statistically in terms of certain penalty terms. These can be derived on the basis of geometrically necessary dislocations or more continuum-type considerations. Advanced self-consistent schemes take into account grain shape (Thiem et al. 1986) and dislocation cell structures (Muller et al. 1994a).

Advanced continuum plasticity models are capable of discretely simulating the dynamics of individual dislocations considering both time and the actual position of each defect as independent variables. The literature in this field can be classified into simulations in two dimensions (2D) and three dimensions (3D). 2D calculations can be carried out either with flexible dislocations which are constrained to lie in their glide plane (Foreman and Makin 1966; Bacon et al. 1973; Scattergood and Bacon 1975; Altintas 1978; Rönnpagel 1987; Rönnpagel et al. 1993; Mohles and Rönnpagel 1996), or with non-flexible infinite straight dislocations which can leave their glide plane (Neumann 1971; Lépinoux and Kubin 1987; Ghoniem and Amodeo 1989; Gulluoglu et al. 1989; Amodeo 1990; Gulluoglu et al. 1990; Gulluoglu and Hartley 1992; Lubarda et al. 1993; van der Giessen and Needleman 1995; Raabe and Roters 1995; Wang and LeSar 1995; Roters and Raabe 1996; Raabe et al. 1996; Roters and Raabe 1997; Zacharopoulos et al. 1997). While the first type of 2D simulation provides a top view into the glide plane, the second one provides a lateral perspective parallel to the dislocation tangent. 3D simulations are independent of such geometrical constraints (Demir et al. 1992; Devincre and Condat 1992; Kubin et al. 1992; Kubin 1993a; Devincre and Kubin 1994; Rhee et al. 1994; Raabe 1995a; Raabe 1995b; Devincre 1996; Fivel et al. 1996; Hirth 1996; Raabe 1996a; Raabe 1996b; Rönnpagel 1996; Raabe 1998a).

Topological network, vertex, or boundary dynamics models which are based on incorporating the kinetic properties of subgrain walls and large-angle grain boundaries as underlying defects are increasingly used to mimic the incipient stages of recrystallization (Humphreys 1992a), low-cycle fatigue (Draheim and Gottstein 1996a), and grain growth (Adams et al. 1997).

Sophisticated approaches to the simulation of diffusional phase transformations and competitive particle ripening processes are based on the Ginzburg–Landau-type kinetic phase field models (Cahn and Hilliard 1965; Khachaturyan 1968; Allen and Cahn 1979; Chen 1995). Substantial progress in the continuum description of recrystallization phenomena was attained through the introduction of modified deterministic cellular automata (Hesselbarth and Göbel 1991; Pezzee and Dunand 1994; Marx and Raabe 1995; Raabe et al. 1996; Sheldon and Dunand 1996; Marx et al. 1996; Marx 1998; Reher 1998).

If a more detailed prediction of microstructural features is addressed, continuum-type models must be replaced by atomistic models which provide a better spatial resolution and usually incorporate fewer phenomenological assumptions when compared with their continuum counterparts.

Typical examples of atomistic models are classical molecular dynamics and Monte Carlo methods. In contrast to classical molecular dynamics (Alder and Wainwright 1959; Verlet 1967; Daw and Baskes 1984), modern atomistic approaches have increasingly gained momentum through the use of more realistic potential functions and substantially enhanced computer power (Finnis et al. 1988; Sutton and Balluffi 1995). First-principles ab-initio models even aim at approximate solutions of the Schrödinger equation for a limited number of atoms. Variants of the ab-initio approach are provided by molecular dynamics in conjunction with tight-binding or local density functional theory (Hohenberg and Kohn 1964; Kohn and Sham 1965; Car and Parinello 1985; Ballone et al. 1988), and by variational quantum Monte Carlo methods (Ballone 1989). The numerical perfor-

mance of most first-principles models is still too slow for the computation of microstructure evolution. However, they are of increasing importance in predicting elementary physical materials properties and the basic structure and behavior of simple lattice defects (Sutton 1996; Voter 1996).

2.5.4 Predictive Character

Another possible method of classifying models is by their predictive character.

Deterministic models are based on such algebraic or differential equations as state and evolution equations that describe microstructure evolution in an unambiguous and strictly reproducible fashion. Stochastic models incorporate probabilistic steps particularly in the description of structure evolution. Statistical models are usually not discrete in space and are therefore addressed only briefly in this book.

Stochastic models were originally designed to mimic canonical ensembles by performing a large number of computer experiments using random numbers. Their extension to space-discretized simulations of microstructure was especially promoted by rendering the Ising model for the calculation of magnetic domains into the multistate Potts model which allows one to simulate interfaces by mapping domains of identical generalized spin. Typical examples of conventional stochastic models are the Potts model (1952)[4], the Metropolis (1953) Monte Carlo method, and probabilistic cellular automata (Grassberger et al. 1984; Kinzel 1985).

In recent years various improvements were suggested which allow one to extend microscopical stochastic concepts to space-discretized microstructure simulations. Typical examples of space-discretized stochastic approaches are Monte Carlo models for the investigation of diffusion and short-range ordering (Binder 1991a), kinetic Potts models for simulating microstructural non-equilibrium transformation phenomena (Anderson et al. 1984; Srolovitz et al. 1986; Rollett et al. 1989; Doherty et al. 1990; Glazier et al. 1990; Tavernier and Szpunar 1991a; Rollett et al. 1992; Peczak 1995; Holm et al. 1996), improved probabilistic cellular automata (Wolfram 1986), stochastic percolation models for studying normal and superconducting current paths, microplasticity, diffusion, fracture mechanics, and properties of porous media (Stauffer 1991; Stauffer and Aharony 1992; Sahimi 1994; Kuo and Gupta 1995), and advanced simulations of dislocation dynamics which consider thermal activation in terms of a Langevin force (Rönnpagel et al. 1993; Mohles and Rönnpagel 1996).

Statistical models are typically not discrete in space. Thus, they are not so much within the scope of this book and only briefly discussed. Famous statistical kinematical models of plasticity were published by Argon (1975) and Kocks, Argon, and Ashby (1975). Typical examples of advanced microstructural constitutive models are modern approaches to the kinematical theory which incorporate a variety of relevant microstructural parameters in the kinetic equation of state and more elaborate structural evolution principles (Mughrabi 1980; Mecking and Kocks 1981; Mughrabi 1983; Estrin and Mecking 1984; Prinz and Argon 1984; Mughrabi et al. 1986; Gottstein and Argon 1987; Kuhlmann-Wilsdorf and Hansen 1991; Blum 1993). Corresponding efforts were made to extend the classical kinematical theory to the description of stage IV and stage V strain hardening (Anongba et al. 1993; Argon and Haasen 1993; Zehetbauer and Seumer 1993).

[4]The notions of q-state and multistate Potts model are used synonymously. They both describe (kinetic) Monte Carlo models which use a delta-type Hamiltonian and a number of q generalized spin states.

Furthermore, a new group of nonlinear and stochastic structural evolution theories was suggested to render earlier models more physically plausible and at the same time in better accord with experiments that show plastic instabilities (Kocks 1985; Schlipf 1992; Kubin 1993b; Kubin 1996).

Classical metallurgical kinetic concepts are those that describe discontinuous transformations such as recrystallization with statistical treatment of topology (Kolmogorov 1937; Avrami 1939; Johnson and Mehl 1939). In the domain of non-equilibrium transformation kinetics these classical statistical approaches were extended to more general microstructural path models (Juul Jensen et al. 1985; Marthinsen et al. 1989; Vandermeer and Rath 1989; Furu and Nes 1990; Marthinsen et al. 1990; Vandermeer and Rath 1990; Vandermeer et al. 1991).

2.5.5 Descriptive Character

Another classification scheme can be introduced by distinguishing between first-principles, phenomenological, and empirical concepts.

First-principles models aim to capture the underlying mechanism or feature of a system with a minimum set of assumptions and phenomenological laws. Typical examples are furnished by simulations based on local density functional theory (Hohenberg and Kohn 1964; Kohn and Sham 1965; Car and Parinello 1985; Ercolessi et al. 1986; Ballone et al. 1988). It is clear that even first-principles models must incorporate some assumptions without deriving them or proving their validity in detail. For instance, even atomic scale simulations based on local density functional theory implicitly use the adiabatic Born–Oppenheimer approximation (Chapter 4). However, the number of such phenomenological ingredients is limited as much as possible.

Most simulations in computational materials science are phenomenological, i.e. they use state and evolution equations in accord with certian physical phenomena. In such approaches most atomic details such as the electronic structure are typically averaged out without neglecting the relevant properties of the underlying lattice defects.

Empirical approaches provide a more or less precise mathematical fit to a set of experimental observations. Thus they typically do not incorporate the properties of the underlying lattice defects. While the process of phenomenologically formulating models can be regarded as an essential step in that it must be decided which state variables are of strong and which of little influence on the system behavior, empirical models do not distinguish between important and unimportant contributions.

While phenomenological models thus have a certain predictive capability, empirical methods do not have real power to predict (Ashby 1992). Consequently, there is no obvious reason to classify purely empirical approaches as models[5]. Improvements in the systematic application of empirical approaches were achieved through the advent of fuzzy set theory and artificial neuronal network methods (see Appendix).

2.5.6 Path-Dependence

Models can focus on static or kinetic aspects (or on both). The main purpose of static simulations is the calculation of path-independent material properties as a function of certain extensive and intensive state variables. Purely static calculations can only give a

[5]In this context it should be underlined that nearly all microstructure models, except for ab-initio simulations, use certain empirical input data, such as elastic constants, electrical conductivity, etc. (Ashby 1992; Bunge 1997).

shapshot of the material behavior for a given microstructure. However, they can neither predict any path-dependent behavior nor provide a temporal update of the values of the state variables. This restriction implies that static simulations are generally concerned with equations of state rather than with structure evolution equations. For instance, the simulation of thermodynamic quantities or the prediction of improved mechanical equations of state in dislocation theory can be achieved by static simulations which do not show any temporal scaling and thus no *evolution* of microstructure. In contrast, kinetic simulations can predict both the path-dependent evolution of microstructure and the material properties at any time.

2.6 Round-Robin Tests

Apart from the numerous technical and physical aspects of modeling and simulation, there exists an important non-scientific problem associated with this field, namely, the psychological barrier to accepting the validity of models that have been suggested by competitive authors (Bunge 1997). It is indeed a typical observation in computational materials science that an increasing number of models is gradually introduced to tackle identical metallurgical phenomena, often without careful comparison with other existing approaches. The notion of "comparison" in this context does not mean merely to list some common or distinguishing features of competitive models, but to compare *quantitatively* the predictions on the basis of identical input data. Such quantitative procedures are well established in comparing data that are obtained by experimentation, but are rarely performed in computational materials science (Royer et al. 1991; Wagner et al. 1991; Tóth et al. 1997). Although an approach to introduce a certain standardization of simulation codes under consideration of different methods was made by the Los Alamos group through the free distribution of the Los Alamos Plasticity (LAP) code (Kocks et al. 1987), the use of quantitative round-robin tests might be a reasonable complementation of current simulation activities. For instance, a round-robin test for the comparison of polycrystal plasticity models should cover the following aspects:

1. The simulations should address a standard material with properly defined metallurgical characteristics, such as chemistry, grain size, grain shape, strength, precipitation size, and distribution, etc.
2. If the models require an input from a tensile, compression, or multiaxial mechanical test, they should use the same data.
3. All predictions should be compared with one set of experimental results, that were obtained under properly defined conditions.
4. The input data should contain an identical set of discretized orientations.
5. The orientation distribution functions that are derived from the output data should be computed by using the same method (Gauss or Lorentz functions, spherical harmonics, etc.).
6. The data should be presented in the same way.
7. The comparison should be discussed and published.

Chapter 3

Fundamentals and Solution of Differential Equations

3.1 Introduction to Differential Equations

Many of the laws encountered in materials science are most conveniently formulated in terms of differential equations. Deriving and solving differential equations are thus among the most common tasks in modeling material systems.

Differential equations are equations involving one or more scalar or tensorial dependent variables, independent variables, unknown functions of these variables, and their corresponding derivatives. Equations which involve unknown functions that depend on only one independent variable are referred to as ordinary differential equations (Abramovitz and Segun 1964; Hartman 1964; Arrowsmith and Place 1982; Bronstein and Semendjajev 1987). If the equations involve unknown functions that depend on more than one independent variable they are referred to as partial differential equations (Farlow 1982; Haberman 1983). The "order" of a differential equation is the highest order of any of the derivatives of the unknown functions in the equation. Equations involving only the first derivatives are referred to as first-order differential equations. Equations involving the second derivatives are referred to as second-order differential equations. Second- and higher-order differential equations such as

$$\frac{\mathrm{d}^2 u(t)}{\mathrm{d}t^2} = f(u,t) \tag{3.1}$$

can be transformed into a coupled set of lower-order equations by substitution:

$$\frac{\mathrm{d}v(t)}{\mathrm{d}t} = f(u,t) \qquad v = \frac{\mathrm{d}u(t)}{\mathrm{d}t} \tag{3.2}$$

In these equations u is the state variable which is a function of the independent time variable t, v is the first time derivative of u, and f a function of u and v, respectively. For instance, the frequently occurring problem of (one-dimensional) motion of a particle or dislocation segment of effective mass m under a force field $f(x,t)$ in the x-direction is

Computational Materials Science: The Simulation of Materials, Microstructures and Properties By Dierk Raabe
Copyright © 1998 Wiley-VCH Verlag GmbH
ISBN: 3-527-29541-0

described by the second-order differential equation

$$m \frac{\mathrm{d}^2 x(t)}{\mathrm{d}t^2} = f(x,t) \tag{3.3}$$

If one defines the particle momentum

$$p(x,t) = m \frac{\mathrm{d}x(t)}{\mathrm{d}t} \tag{3.4}$$

equation (3.3) becomes the two coupled first-order equations (Hamilton's equations)

$$\frac{\mathrm{d}x(t)}{\mathrm{d}t} = \frac{p}{m} \qquad \frac{\mathrm{d}p(x,t)}{\mathrm{d}t} = f(x,t) \tag{3.5}$$

Differential equations which contain only linear functions of the independent variables are called "linear differential equations". For these equations the superposition principle applies. That means linear combinations of solutions which satisfy the boundary conditions are also solutions to the differential equation satisfying the same boundary conditions. Differential equations which involve nonlinear functions of the independent variables are denoted as "nonlinear differential equations" (Struble 1962; Andronov et al. 1973; Jordan and Smith 1987). For such equations the superposition principle does not apply.

Most problems in computational materials science lead in their mathematical formulation to "partial differential equations" which involve both space and time as independent variables. Usually, one is interested in particular solutions of partial differential equations which are defined within a certain range of the independent variables and which are in accord with certain initial-value and boundary-value conditions. In this context it is important to emphasize that a problem which is in the form of a differential equation and boundary conditions must be well posed. That means only particular initial and boundary conditions transform a partial differential equation into a solvable problem.

Partial differential equations can be grouped according to the type of additional conditions which are required in formulating a well-posed problem. This classification scheme will be outlined in the following for the important group of linear second-order partial differential equations with two independent variables, say x_1 and x_2. The general form of this equation is

$$A \frac{\partial^2 u}{\partial^2 x_1} + B \frac{\partial^2 u}{\partial x_1 \partial x_2} + C \frac{\partial^2 u}{\partial^2 x_2} + D \frac{\partial u}{\partial x_1} + E \frac{\partial u}{\partial x_2} + F\,u + G = 0 \tag{3.6}$$

where $A = A(x_1,x_2)$, $B = B(x_1,x_2)$, $C = C(x_1,x_2)$, $D = D(x_1,x_2)$, $E = E(x_1,x_2)$, $F = F(x_1,x_2)$, and $G = G(x_1,x_2)$ are given functions of the independent variables x_1 and x_2. It is stipulated that the functions $A(x_1,x_2)$, $B(x_1,x_2)$, and $C(x_1,x_2)$ never be equal to zero at the same point (x_1,x_2). In analogy to the classification of higher-order curves in analytical geometry which are described by

$$a\,{x_1}^2 + b\,x_1 x_2 + c\,{x_2}^2 + d\,x_1 + e\,x_2 + f = 0\,, \qquad a^2 + b^2 + c^2 \neq 0 \tag{3.7}$$

equation (3.6) can for given values $\hat{x}_1$, $\hat{x}_2$, of the variables x_1 and x_2 assume hyperbolic, parabolic, or elliptic character. Roughly speaking, hyperbolic differential equations involve second-order derivatives of opposite sign when all terms are grouped on one side, parabolic differential equations involve only a first-order derivative in one variable, but

have second-order derivatives in the remaining variables, and elliptic differential equations involve second order derivatives in each of the independent variables, each of the derivatives having equal sign when grouped on the same side of the equation.

hyperbolic partial differential equation	$4\,A\,(\hat{x}_1,\hat{x}_2)\;C\,(\hat{x}_1,\hat{x}_2) < B^2\,(\hat{x}_1,\hat{x}_2)$
parabolic partial differential equation	$4\,A\,(\hat{x}_1,\hat{x}_2)\;C\,(\hat{x}_1,\hat{x}_2) = B^2\,(\hat{x}_1,\hat{x}_2)$
elliptic partial differential equation	$4\,A\,(\hat{x}_1,\hat{x}_2)\;C\,(\hat{x}_1,\hat{x}_2) > B^2\,(\hat{x}_1,\hat{x}_2)$

In that context it must be considered that, since $A(x_1,x_2)$, $B(x_1,x_2)$, and $C(x_1,x_2)$ depend on independent variables, the character of the differential equation may vary from point to point. The approach to group differential equations according to the character of their discriminant $(4\,A\,C - B^2)$ is due to its importance in substituting mixed derivatives by new independent variables. The fundamental classification scheme outlined here for second-order partial differential equations can be extended to coupled sets of nonlinear higher-order partial differential equations with more than two independent variables.

Classical examples of the three types of differential equations are the wave equation for the hyperbolic class, the heat or diffusion equation and the time-dependent Schrödinger equation for the parabolic class, and the Laplace and time-independent Schrödinger equation for the elliptic class. In three dimensions and rectangular coordinates they can be written:

$$\text{wave equation} \qquad \frac{\partial^2 u}{\partial t^2} - c^2\left(\frac{\partial^2 u}{\partial x_1^2} + \frac{\partial^2 u}{\partial x_2^2} + \frac{\partial^2 u}{\partial x_3^2}\right) = 0$$

$$\text{diffusion equation} \qquad \frac{\partial u}{\partial t} - D\left(\frac{\partial^2 u}{\partial x_1^2} + \frac{\partial^2 u}{\partial x_2^2} + \frac{\partial^2 u}{\partial x_3^2}\right) = 0$$

$$\text{Laplace equation} \qquad \frac{\partial^2 u}{\partial x_1^2} + \frac{\partial^2 u}{\partial x_2^2} + \frac{\partial^2 u}{\partial x_3^2} = 0$$

where x_1, x_2, and x_3 are the spatial variables, t the temporal variable, u the state variable, D the diffusion coefficient[1] which is assumed to be positive and independent of the concentration, and c the propagation velocity of the wave. It is worth mentioning that for stationary processes where $\partial u/\partial t = 0$, the diffusion (heat) equation changes into the Laplace equation. In cases where under stationary conditions sinks or sources appear in the volume being considered, the diffusion equation changes into the Poisson equation:

$$\text{Poisson equation} \qquad \frac{\partial^2 u}{\partial x_1^2} + \frac{\partial^2 u}{\partial x_2^2} + \frac{\partial^2 u}{\partial x_3^2} - f(x_1,x_2,x_3) = 0$$

which in two dimensions is identical to the differential equation for the description of the transverse displacement of a membrane. An important differential equation similar to the Poisson equation is the Helmholtz equation, which contains both the dependent function itself and its second spatial derivative:

$$\text{Helmholtz equation} \qquad \frac{\partial^2 u}{\partial x_1^2} + \frac{\partial^2 u}{\partial x_2^2} + \frac{\partial^2 u}{\partial x_3^2} + \alpha\, u = 0 \qquad \alpha = const.$$

[1] The assumption that the diffusion coefficient is independent of the concentration applies only for certain systems and very small concentrations. In real materials the value of the diffusion coefficient is, first, a tensor quantity and, second, highly sensitive to the concentration. A more detailed discussion of solid-state diffusion with consideration of the concentration dependence of the diffusion coefficient as well as sinks and sources is given in Chapter 10.

Using the more general Laplace operator $\Delta = \nabla^2$ instead of rectangular coordinates and $\dot{u}$ and $\ddot{u}$ for the first- and second-order time derivatives, respectively, the above equations can be rewritten in a more compact notation:

$$\begin{aligned} \ddot{u} - c^2\,\Delta u &= 0 \\ \dot{u} - D\,\Delta u &= 0 \\ \Delta u &= 0 \\ \Delta u - f &= 0 \\ \Delta u + \alpha\, u &= 0 \end{aligned}$$

Hyperbolic and parabolic partial differential equations typically describe non-stationary, i.e. time-dependent problems. This is indicated by the use of the independent variable t in the corresponding equations. For solving non-stationary problems one must define initial conditions. These are values of the state variable and its derivative which the solution should assume at a given starting time t_0. These initial conditions could amount to $u(x_1, x_2, x_3, t_0)$ and $\dot{u}(x_1, x_2, x_3, t_0)$ for the wave equation and $u(x_1, x_2, x_3, t_0)$ for the diffusion or heat equation. If no constraints are given to confine the solutions to particular spatial coordinates, i.e. $-\infty < x_1, x_2, x_3 < +\infty$, the situation represents a pure initial-boundary problem.

In cases where additional spatial conditions are required, such as $u(x_{10}, x_{20}, x_{30}, t)$ for the wave equation, and $u(x_{10}, x_{20}, x_{30}, t)$ or $(\partial u/\partial x_1)$ $(x_{10}, x_{20}, x_{30}, t)$, $(\partial u/\partial x_2)$ $(x_{10}, x_{20}, x_{30}, t)$, and $(\partial u/\partial x_3)$ $(x_{10}, x_{20}, x_{30}, t)$ for the diffusion equation, or a combination of both, one speaks of a "boundary-initial-value problem".

Models that are mathematically described in terms of elliptic partial differential equations are typically independent of time, thus describing *stationary* situations. The solutions of such equations depend only on the boundary conditions, i.e. they represent pure boundary-value problems. Appropriate boundary conditions for the Laplace or stationary heat and diffusion equation, respectively, $\Delta u = 0$, can be formulated as Dirichlet boundary conditions or as Neumann boundary conditions. Dirichlet boundary conditions mean that solutions for the state variable u are given along the spatial boundary of the system. Neumann boundary conditions mean that solutions for the first derivative $\partial u/\partial x_n$ are given normal to the spatial boundary of the system. If both the function and its normal derivative on the boundary are known, the border conditions are referred to as Cauchy boundary conditions.

3.2 Solution of Partial Differential Equations

The solution of partial differential equations by use of analytical methods is only possible in a limited number of cases. Thus, one usually has to resort to numerical methods (Cohen 1962; Abramovitz and Segun 1964; Botha and Pinder 1983; Engeln-Müllges 1988). In the following sections a number of techniques are presented that allow one to obtain approximate numerical solutions to initial- and boundary-value problems.

Numerical methods to solve complicated initial-value and boundary-value problems have in common the discretization of the independent variables (typically time and space) and the transformation of the continuous derivative into its discontinuous counterpart, i.e., its finite difference quotient. Using these discretization steps amounts to recasting the continuous problem expressed by differential equations with an infinite number of

unknowns, i.e., function values, into an discrete algebraic one with a finite number of unknown parameters which can be calculated in an approximate fashion.

Numerical methods to solve differential equations which are essentially defined through *initial* rather than *boundary* values, i.e. which are concerned with time derivatives, are often referred to as finite difference techniques. Most of the finite difference simulations addressed in this book are discrete not only in time but also in space. Finite difference methods approximate the derivatives that appear in differential equations by a transition to their finite difference counterparts. This applies for the time and the space derivatives. Finite difference methods do not use polynomial expressions to approximate functions.

Classical textbooks suggest a substantial variety of finite difference methods (Cohen 1962; Abramovitz and Segun 1964; Botha and Pinder 1983; Engeln-Müllges 1988). Since any simulation must balance optimum calculation speed and numerical precision, it is not reasonable generally to favor one out of the many possible finite difference solution techniques for applications in computational materials science. For instance, parabolic large scale bulk diffusion or heat transport problems can be solved by using a simple central difference Euler method (Section 3.3.3), while the solution of the equations of particle motion in molecular dynamics is usually achieved by using the Verlet (Section 7.4) or the Gear predictor–corrector method (Section 3.3.5). In most cases, it is useful to select a discretization method with respect to the properties of the underlying differential equations, particularly to the highest occurring order of derivative.

A second group of numerical means of solving differential equations comprises the various finite element methods. These methods are designed to solve numerically both complex boundary-value and initial-value problems. They have in common the spatial discretization of the area under consideration into a number of finite elements, the temporal discretization in cases where time-dependent problems are encountered, and the approximation of the true spatial solutions in the elements by polynomial trial functions. These features explain why they are referred to as finite element techniques.

Although both the finite difference and the finite element techniques can handle space and time derivatives, the latter approach is more sophisticated in that it uses trial functions and a minimization routine. Thus, the finite difference techniques can be regarded as a subset of the various more general finite element approximations (Zienkiewicz and Morgan 1983; Zienkiewicz and Taylor 1989).

Many finite difference and particularly most finite element methods are sometimes intuitively associated with the solution of large-scale problems. Although this association is often true for finite element methods which prevail at solving meso- and macroscale boundary-value problems in computational materials science, it must be underlined that such general associations are inadequate. Finite difference and finite element methods represent mathematical approximation techniques. They are generally *not* intrinsically calibrated to any physical length or time scale. Scaling parameters are introduced by the physics of the problem addressed but not by the numerical scheme employed to solve a differential equation. Owing to this fact, the fundamentals of the various finite difference and finite element techniques are not presented together with the macro-, meso-, micro-, or nanoscale simulation methods discussed in the ensuing chapters, but treated separately in this chapter.

A subsequent part of the book provides a more detailed discussion of typical applications of the finite difference and the finite element method for materials simulations at the macro- and mesoscale (Chapter 16). Detailed monographs on partial differential equations and their numerical solution have been published by Forsythe and Wasow (1960), Richtmyer and Morton (1967), Dettman (1969), Marsal (1976), and Boas (1983).

3.3 Fundamentals of the Finite Difference Method

3.3.1 Discretization of Time

The finite element and the finite difference methods are related in that they both allow one to discretize partial differential equations and solve them under appropriate initial- and boundary-value conditions. However, since the finite difference methods do not require the use of polynomial trial functions and a minimization procedure, they are presented here at the beginning in order to provide an introductory overview of numerical approaches to solving differential equations. Since finite difference methods were originally designed to solve initial-value problems, the present section concentrates on the numerical approximation of functions that are described by differential equations which contain time derivatives.

When numerically solving initial-value problems one encounters two fundamental problems that the computer cannot handle: first, the mapping of the independent variable time, which is continuous rather than discrete, and second, the evaluation of derivatives which are defined through a limit process. Consequently, each finite difference technique is based on two main numerical approximations, namely, the discretization of time from a continuous measure into tiny intervals of length $h = \Delta t$, and the replacement of the differential equation by the corresponding difference equation.

The first derivative $\mathrm{d}u/\mathrm{d}t$ of a function $u(t)$ is at t_0 defined through the limit of a difference quotient:

$$\left.\frac{\mathrm{d}u}{\mathrm{d}t}\right|_{t=t_0} = \lim_{h\to 0} \frac{u(t_0+h)-u(t_0)}{h} \tag{3.8}$$

The transformation of this continuous derivative into its finite difference quotient

$$\frac{\Delta u}{h} = \lim_{\Delta t\to h\neq 0} \frac{u(t_0+h)-u(t_0)}{h} \tag{3.9}$$

is a discrete method since its objective is restricted to satisfying the governing equation discretely rather than continuously. The given example belongs to the category of linear *one-step* finite difference discretizations because it involves only two consecutive stations.

3.3.2 Numerical Errors of Finite Difference Methods

The two simplifications generally inherent in any finite difference method, viz., the discretization of time and the replacement of the differential quotient by its difference quotient, can entail various types of numerical errors[2].

The "truncation error" is the amount by which the exact solution of the continuous differential equation fails to satisfy the approximate equation. It is calculated as the norm of the difference between the solution to the continuous differential equation and the solution to the discretized difference equation divided by the time interval used in the numerical algorithm.

[2]Most finite difference simulations addressed in this book are discrete not only in time but also in space. Such space-discretized finite difference simulations show additional errors that arise from the discretization of space and the replacement of the spatial differential quotients by their discretized spatial counterparts. In practice, these errors can exceed those arising from the discretization of time, for instance in Ginzburg–Landau or Cahn–Hilliard-type phase field simulations which contain strong concentration or structure gradients across diffuse interfaces.

It is clear that the deviation between the analytical solution obtained for the continuous differential equation and that obtained numerically from the approximate equation should degrade by gradually refining the time step of the calculation. This property is referred to as the "consistency" of an approximate method. A finite difference approximation is called consistent with the differential equation if the truncation error goes to zero as the time interval goes to zero. If all approximate solutions to a given differential equation are consistent, the numerical scheme is called a "convergent" method.

In this context it should be added that in the case of space-discretized finite difference simulations, such as are encountered in the fields of dislocation dynamics (Section 9.4), diffusional phase transformations (Section 10.2), and recrystallization (Section 11.9), there can be considerable residual errors due to the discretization of space, irrespective of the decrease in the time intervals.

Because of the limited precision of computers another numerically introduced error must be considered, namely, the "round-off error". This error is not identical to the truncation error. While the latter stems from the limitation in transforming the difference quotient into a differential quotient (equations (3.8) and 3.9)), the former is due to the discretization of time. In contrast to truncation errors which are generally reduced with a decreasing time interval, round-off errors can even increase with decreasing time intervals. This becomes clear in a simple example where the time steps are physically given by real numbers in units of seconds such as 1.3, 1.6, 1.9, 2.2, and so on, but numerically for some reason these are reduced to integers, i.e. to 1, 1, 1, 2, and so on. For very small time steps it is clear that such round-off errors can entail substantial accumulated deviations from the analytical result. In order to keep this error as small as possible, finite difference computer codes should generally work with double precision.

A further important criterion in evaluating the quality of a finite difference scheme is its stability. The investigation of the stability of the solution quantifies whether the errors discussed above will accumulate and amplify without limit during the computation or not.

Thorough reviews on the numerical aspects and the errors associated with finite difference techniques have been published by Forsythe and Wasow (1960), Richtmyer and Morton (1967), and Bellomo and Preziosi (1995).

3.3.3 Euler Methods

As a starting point for explaining the various finite difference schemes it is useful to recall a simple initial-value problem:

$$\frac{\mathrm{d}u}{\mathrm{d}t} = f(u,t) \tag{3.10}$$

where the state variable u depends only on the independent time variable t. When the initial condition is given by $u(t_0) = u_0$, the above equation can be written in integral form,

$$u(t) = u_0 + \int_{t_0}^{t_n} f\left(s, u(s)\right) \mathrm{d}s \tag{3.11}$$

The general strategy to solve this integral consists in dividing the interval $[t_0, t_n]$ into a large number, n, of equally spaced subintervals of length $h = (t_n - t_0)/n$. Partitioning the time in the above integral into such discrete intervals

$$[t_0, t_n] = [t_0, t_1] \cup [t_1, t_2] \cup \ldots \cup [t_{n-1}, t_n] \tag{3.12}$$

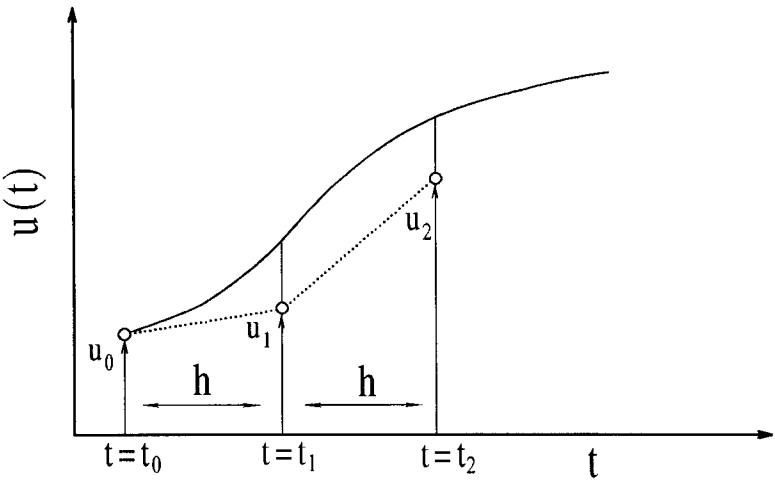

Figure 3.1: Explicit or forward Euler method.

leads to a discretized equivalent of equation (3.11):

$$u(t) = u_0 + \sum_{j=0}^{n-1} \int_{t_j}^{t_{j+1}} f\left(s, u(s)\right) \mathrm{d}s \tag{3.13}$$

The simplest method to approximate the time derivative $\mathrm{d}u/\mathrm{d}t$ at the time t_i is to identify the local tangent at point t_i with the slope calculated from the two subsequent values of the state variables $u_i = u(t_i)$ and $u_{i+1} = u(t_{i+1})$, and the time interval $h = t_{i+1} - t_i$ (Figure 3.1).

$$\frac{\mathrm{d}u}{\mathrm{d}t}(t_i) \approx \frac{u_{i+1} - u_i}{h} \tag{3.14}$$

Quantifying the truncation error[3] shows that it is linearly proportional to the chosen time interval h. This means that equation (3.14) can be rewritten

$$\frac{\mathrm{d}u}{\mathrm{d}t}(t_i) = \frac{u_{i+1} - u_i}{h} + O(h) \tag{3.15}$$

Combining equation (3.14) with equation (3.10) rewritten for the time t_i

$$\frac{\mathrm{d}u}{\mathrm{d}t}(t_i) = f(u_i, t_i) \tag{3.16}$$

leads to

$$u_{i+1} = u_i + h\, f(u_i, t_i) \tag{3.17}$$

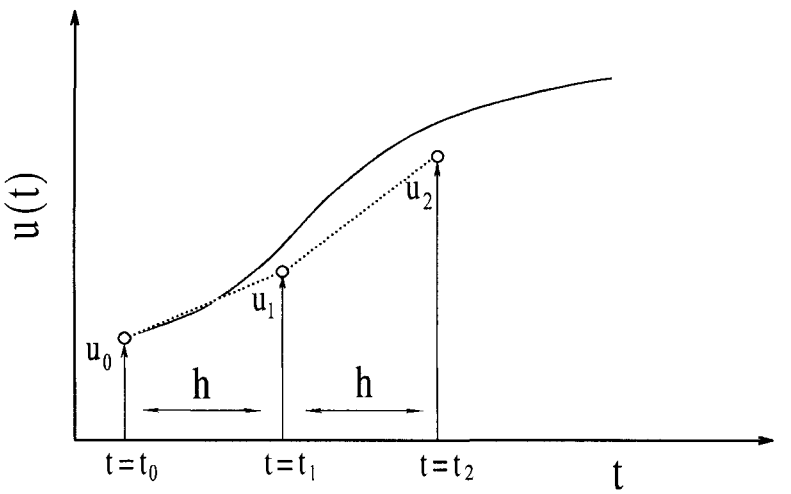

Figure 3.2: Implicit or backward Euler method.

This method is referred to as "forward" or "explicit" Euler method since the value u_{i+1} is given directly in terms of some previously computed value of the state variable u_i.

The "backward" or "implicit" Euler method differs from the explicit method in the evaluation of f in (t_{i+1}, u_{i+1}) rather than in (u_i, t_i) (Figure 3.2). The value of the state variable u after $(i+1)$ steps then amounts to

$$u_{i+1} = u_i + h\, f(u_{i+1}, t_{i+1}) \tag{3.18}$$

The implicit Euler method generally leads to a similar truncation error as the explicit approach, i.e.

$$\frac{\mathrm{d}u}{\mathrm{d}t}(t_i) = \frac{u_i - u_{i-1}}{h} + O(h) \tag{3.19}$$

Although the implicit Euler algorithm looks at first very similar to the explicit method, it is computationally less efficient. This is evident from equation (3.18), where the unknown u_{i+1} appears on both sides of the equation, i.e., the expression must be transformed before its solution. This is not the case for the explicit Euler method, equation (3.17), which can be solved directly since the value of u_i is already known. However, the implicit Euler method is more stable than the explicit one and is thus preferred in certain cases irrespective of its lower efficiency.

The various Euler methods can also be derived by using the Taylor (1715) formula which allows one to express the change in the state variable $u(t_0 + h) - u(t_0)$ in terms of a series expansion

$$u(t_0 + h) - u(t_0) = \sum_{j=1}^{n-1} \frac{h^j}{j!} \frac{\mathrm{d}^j u(t_0)}{\mathrm{d}t^j} + \mathfrak{H}_n \tag{3.20}$$

[3] A quantification of the round-off error is not possible here, since it depends on the relation between the chosen time intervals and the precision of the computer being used.

where $\mathfrak{H}_n$ is the residual error of the expansion in the case of $n < \infty$. Conducting the Taylor expansion for three subsequent equidistant points $t_{i-1} = t_i - h$, t_i, and $t_{i+1} = t_i + h$ leads to three equations:

$$\begin{aligned} u_{i-1} - u_i &= -h\,\frac{\mathrm{d}u_i}{\mathrm{d}t} + \frac{h^2}{2!}\,\frac{\mathrm{d}^2u_i}{\mathrm{d}t^2} - \frac{h^3}{3!}\,\frac{\mathrm{d}^3u_i}{\mathrm{d}t^3} + \frac{h^4}{4!}\,\frac{\mathrm{d}^4u_i}{\mathrm{d}t^4} - \ldots \\ u_i - u_i &= 0 \\ u_{i+1} - u_i &= h\,\frac{\mathrm{d}u_i}{\mathrm{d}t} + \frac{h^2}{2!}\,\frac{\mathrm{d}^2u_i}{\mathrm{d}t^2} + \frac{h^3}{3!}\,\frac{\mathrm{d}^3u_i}{\mathrm{d}t^3} + \frac{h^4}{4!}\,\frac{\mathrm{d}^4u_i}{\mathrm{d}t^4} + \ldots \end{aligned} \tag{3.21}$$

For instance, dividing the last of these equations by h leads to an expression similar to that obtained for the forward Euler method, equation (3.15).

$$\frac{\mathrm{d}u_i}{\mathrm{d}t} = \frac{u_{i+1} - u_i}{h} - \frac{h}{2}\,\frac{\mathrm{d}^2u_i}{\mathrm{d}t^2} - \frac{h^2}{6}\,\frac{\mathrm{d}^3u_i}{\mathrm{d}t^3} - \frac{h^3}{12}\,\frac{\mathrm{d}^4u_i}{\mathrm{d}t^4} - \ldots \tag{3.22}$$

The truncation error in this expansion is characterized by the lowest-order term in h. Equivalent Taylor-type derivations can be made for the backward and the central difference quotients (see below).

3.3.4 Leap-Frog Method

A general reduction of the truncation error as compared with the first-order explicit and implicit Euler methods can be achieved by using the more symmetric second-order "central difference" or "leap-frog" method:

$$\frac{\mathrm{d}u}{\mathrm{d}t}(t_i) = \frac{u_{i+1} - u_{i-1}}{2h} + O(h^2) \tag{3.23}$$

In this finite difference method the value of the variable u at time t_{i+1} is calculated by

$$u_{i+1} = u_{i-1} + 2h\,f(u_i, t_i) \tag{3.24}$$

Depending on the required accuracy higher-order central difference algorithms can also be formulated.

3.3.5 Predictor–Corrector Methods

The predictor–corrector method is a finite difference method that in its simplest form includes a forward Euler method which is referred to as the "predictor", and a subsequent correction of the predicted result which is named the "corrector". The procedure can be used in an iterative manner. Together with the Verlet algorithm, it represents the most common method of integrating the equations of motion in molecular dynamics.

The predictor–corrector method proceeds by first estimating the value of the state variable u at time t_{i+1} using an explicit Euler step (Section 3.3.3).

$$u_{i+1}^{\mathfrak{E}} = u_i + h\,f(u_i, t_i) \tag{3.25}$$

This step is referred to as the predictor, since it provides a first prediction of the value of u at t_{i+1} which is here denoted by $u_{i+1}^{\mathfrak{E}}$. In a second step this value is modified by using the implicit algorithm

$$u_{i+1} = u_i + h\,f(u_{i+1}^{\mathfrak{E}}, t_{i+1}) \tag{3.26}$$

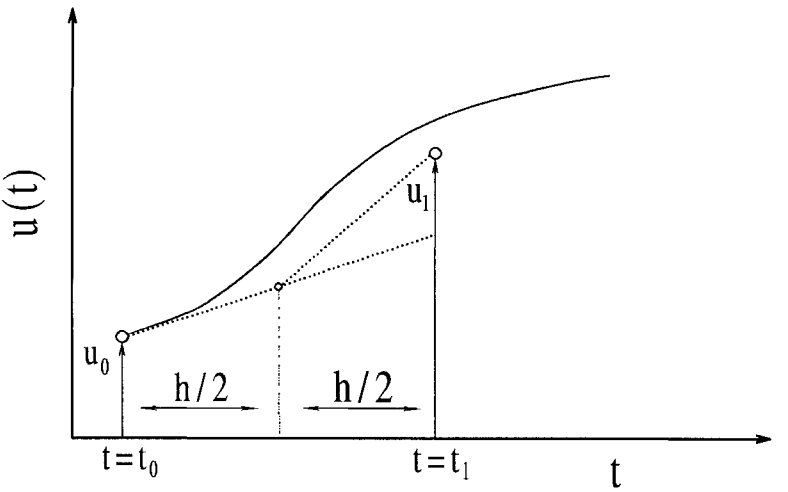

Figure 3.3: Crank–Nicholson method.

This step is named the corrector, since it changes the initial explicit prediction of u_{i+1}. Using the second step, equation (3.26), more than once turns the predictor–corrector method into an iterative technique. This process, which does not affect the order of the finite difference method, is called correcting to convergence:

$$u_{i+1}^{\mathfrak{E}} = u_i + h\, f(u_i, t_i)$$

$$n \text{ times} \left\{ \begin{array}{l} u_{i+1} = u_i + h\, f(u_{i+1}^{\mathfrak{E}}, t_{i+1}) \\ u_{i+1}^{\mathfrak{E}} = u_{i+1} \end{array} \right. \tag{3.27}$$

Iterative predictor–corrector methods prevail as finite difference algorithms in molecular dynamics, fluid dynamics, and simulations of diffusion.

3.3.6 Crank–Nicholson Method

The Crank–Nicholson method is a second-order finite difference method. It consists in averaging the values of f in t_i and t_{i+1}. The value of the state variable u at time t_{i+1} amounts to

$$u_{i+1} = u_i + \frac{h}{2}\left[f(u_i, t_i) + f(u_{i+1}, t_{i+1})\right] \tag{3.28}$$

This method corresponds to proceeding for half the time interval along the derivative determined at time t_i and for the remaining part along the derivative at t_{i+1}. Mathematically, this technique is identical to the trapezoidal rule. The truncation error shows a decay which is proportional to h^2 (Figure 3.3). The Crank–Nicholson method can also be transformed into a predictor–corrector formulation where the first evaluation of

$u_{i+1}^{\mathfrak{E}}$ is achieved by a forward Euler method and the second one by using the averaging Crank–Nicholson step.

$$u_{i+1}^{\mathfrak{E}} = u_i + h\, f(u_i, t_i)$$

$$n \text{ times} \left\{ \begin{array}{l} u_{i+1} = u_i + \frac{h}{2}\left[f(u_i, t_i) + f(u_{i+1}^{\mathfrak{E}}, t_{i+1})\right] \\ u_{i+1}^{\mathfrak{E}} = u_{i+1} \end{array} \right. \tag{3.29}$$

The iterative ($n = 1...$) predictor–corrector combination of the explicit Euler method and the Crank–Nicholson step can also be referred to as the second-order Runge–Kutta method.

3.3.7 Runge–Kutta Methods

The Crank–Nicholson method introduced above, which is essentially based on a modified Euler algorithm, can be regarded as a special second-order case of the more general Runge–Kutta method. In fact, all the previously discussed methods have in common that they express the solution in terms of the derivative which is calculated for different times. Thus, all Euler-based methods are often classified as generalized Runge–Kutta algorithms. The Runge–Kutta formulation of the Crank–Nicholson method, equation (3.29), can be written

$$\begin{aligned} u_{i+1} &= u_i + \frac{h}{2}\left[F_1 + F_2\right] \\ F_1 &= f(u_i, t_i) \\ F_2 &= f(u_i + hF_1, t_i + h) \end{aligned} \tag{3.30}$$

In their most general form the functions at different stations amount to

$$F_n = f\left[u_i + h\left(A_{n1}\, F_1 + A_{n2}\, F_2 + ... + A_{n\,n-1}\, F_{n-1}\right), t_i + a_n\, h\right] \qquad n = 1, ..., o \tag{3.31}$$

where a_n and A_{nm} are coefficients and o the order of the Runge–Kutta approximation.

Equation (3.31) reveals a certain similarity to the Taylor formula, which allows one to express the change of the dependent variable $u(t_0 + h) - u(t_0)$ as a series expansion, equation (3.20). While the Taylor expansion is carried out on *one* point, the Runge–Kutta method uses derivatives on *various* points. However, the coefficients a_n and A_{nm} in equation (3.31) can indeed be derived by replacing the functions by Taylor series expansions. Comparing the coefficients of both forms leads to a system of linear equations which can then be solved. Thus, the term with the highest order in the Taylor expansions determines the order of the Runge–Kutta algorithm. Following this procedure the coefficients of the fourth-order Runge–Kutta formula amount to

$$\begin{aligned} u_{i+1} &= u_i + \frac{h}{6}\left[F_1 + 2F_2 + 2F_3 + F_4\right] \\ F_1 &= f(u_i, t_i) \\ F_2 &= f(u_i + \frac{h}{2}F_1, t_i + \frac{h}{2}) \\ F_3 &= f(u_i + \frac{h}{2}F_2, t_i + \frac{h}{2}) \\ F_4 &= f(u_i + h\,F_3, t_i + h)\,. \end{aligned} \tag{3.32}$$

3.4 Fundamentals of the Finite Element Method

3.4.1 Discretization and Basic Procedure

The finite element method is a general numerical means for obtaining approximate solutions in space to boundary- and initial-value problems. It is based on generating the governing differential equations and their discretized algebraic counterparts of the problem under investigation using a variational formulation with the course of the state variable being approximated by appropriate interpolation functions (Figure 3.4).

While conventional analytical variational methods aim to find a solution by using a single polynomial expression which is valid throughout the whole domain considered (sample), finite element methods, which are used in cases where the sample shape is complicated, aim to find a solution by constructing approximations within each of a number of subdomains which are called "finite elements". Finite element methods thus spatialy discretize the entire domain of interest, which may have nearly arbitrary geometry, into an assembly of relatively simply shaped elements which fill the entire domain without gaps and without overlap. The subdomains are interconnected at joints which are referred to as nodes. The form, size, and orientation of the finite elements depends on a number of parameters, for instance on the sample shape.

The interpolation functions are defined in a piecewise manner. This can be done by employing different coefficients or even different functions (mostly linear functions or simple polynomials) in the various elements from which the total domain is developed. This amounts to assuming a piecewise linear or polynomial solution over the entire domain under consideration. The interpolation functions, which are also called "trial" or "ansatz" functions, usually describe the course of the state variable in an element in terms of its node values. Most finite element methods use these functions to map both the state variable and the topology of the element which, by definition, is then referred to as an isoparametric element. Trial functions for isoparametric elements are therefore also referred to as "shape" or "form functions" (see Chapter 16).

Since the finite element method approximates the real course of the considered state variables in each element by polynomials, the elements must be smaller the simpler these functions are. The use of higher-order polynomials usually allows one the employment of larger subdomains. Thus the element size depends also on the chosen polynomial interpolation functions. Depending on the domain to be investigated, linear or polynomial functions of second or third order are typically used. Finally, the element size must be reduced in regions where strong gradients of the state variable are expected. Less critical areas allow a courser mesh in order to reduce computation time. Aspects such as the initial discretization procedure or the mesh updating depend on the programmer's experience and are biased by their phenomenological knowledge of the simulated process. For instance, the coordinate transformation associated with the updating of a finite element mesh during a simulated large-strain plastic deformation process is often referred to as the most important component of a successful finite element solution.

In two dimensions a simple quadratic interpolation function could amount to

$$u = a_{00} + a_{10}\,x_1 + a_{01}\,x_2 + a_{11}\,{x_1}^2 + a_{12}\,x_1 x_2 + a_{22}\,{x_2}^2 \tag{3.33}$$

In the general case the coefficients a_{00}, a_{10}, a_{01}, a_{11}, a_{12}, and a_{22} differ from element to element, which means the approximate solution is defined piecewise. For obtaining a *steady* course of the approximation, the values of u at a particular point on the element boundary $\hat{x}_1, \hat{x}_2$ which belongs to two neighboring finite elements i and j must be identical,

replacement of continuum sample by an assemblage of subdomains (finite elements)
formulation of constitutive laws
selection of simple polynomial interpolation functions to map the element topology and to approximate the course of state variable in the elements
use of variational principle to describe the problem under investigation
splitting of system integral into subintegrals over individual elements
replacement of continuum state variable in integrals by interpolation functions
loop over each integration point (element nodes) within an element to assemble system of element equations containing element stiffness, load, and unknown state variable
assemblage of system of global equations from element equations containing system stiffness, load, and unknown state variable
consideration of boundary conditions
solution of global system of equations for unknown state variable field
calculation of state equation values from state variables

Figure 3.4: Important steps in the finite element method.

i.e., $u^i(\hat{x}_1, \hat{x}_2) = u^j(\hat{x}_1, \hat{x}_2)$. A steady course of the first derivative of u on the element boundaries is not generally required. For obtaining a better approximation one must use higher-order polynomials or reduce the element size.

In the next step one defines a number of nodes in terms of their coordinates in each individual element. A node that is positioned on an element boundary belongs to at least two elements. The number of nodes defined in each finite element equals the number of coefficients in the chosen interpolation function. Using the quadratic ansatz polynomial defined by equation (3.33) thus requires the definition of six nodes in each subdomain.

In the ensuing step the unknown coefficients of the ansatz function a_{00}, a_{10}, a_{01}, a_{11}, a_{12}, and a_{22} are expressed in terms of the respective values of the state variable u at the six nodes u_1, u_2, u_3, u_4, u_5, and u_6,

$$\begin{aligned} u = {} & f_1(u_1, u_2, u_3, u_4, u_5, u_6) + f_2(u_1, u_2, u_3, u_4, u_5, u_6)\, x_1 + \\ & f_3(u_1, u_2, u_3, u_4, u_5, u_6)\, x_2 + f_4(u_1, u_2, u_3, u_4, u_5, u_6)\, {x_1}^2 + \\ & f_5(u_1, u_2, u_3, u_4, u_5, u_6)\, x_1\, x_2 + f_5(u_1, u_2, u_3, u_4, u_5, u_6)\, {x_2}^2 \end{aligned} \tag{3.34}$$

where $u_\alpha = u_\alpha^i(x_1, x_2)$, i.e. $\alpha = 1, 2, ..., 6$ is the number of the node with the position (x_1, x_2) in the element i. Thus, $u_1 = u_1^i(x_1, x_2)$, $u_2 = u_2^i(x_1, x_2)$, $u_3 = u_3^i(x_1, x_2)$, $u_4 = u_4^i(x_1, x_2)$, $u_5 = u_5^i(x_1, x_2)$, and $u_6 = u_6^i(x_1, x_2)$.

The next step consists in the transformation of the original differential equation, which usually describes the problem addressed, into an equivalent integral formulation by use of a variational principle. This task is referred to as the "inverse" problem of the calculus of variation. While the original variational problem consists in identifying a function, say

principle of minimum potential energy (Dirichlet variational principle)
principle of virtual work
Markov's principle (upper bound theory)
Hill's principle (lower bound theory)
Hamilton's principle

Figure 3.5: Some examples of general variational principles.

$u(x)$, which minimizes or maximizes a given functional, i.e.,

$$I(u) = \int_{x_0}^{x_1} f\left(x, u, \mathrm{d}u/\mathrm{d}x\right) \mathrm{d}x \stackrel{!}{=} extr \tag{3.35}$$

the inverse problem is to construct such a functional for a given differential equation, the Euler–Lagrange function of which is $u(x)$.

For obtaining approximate solutions, the polynomial trial functions for the unknown state variables are then substituted into these integrals. Since the approximate solutions obtained by using ansatz polynomials are typically not equal to the correct analytical solutions, one requires certain criteria to minimize the deviation. For solving large-scale material problems the basis for obtaining approximate solutions is mostly provided by minimizing certain energy functionals (see details in Chapter 16). The incorporation of the ansatz functions into these functionals results in a system of equations which represents a discretized counterpart of the underlying continuous partial differential equations and whose solution is the discrete solution at the nodes.

In the domain of solid mechanics two energy criteria prevail, namely, the variational virtual work or virtual displacement principle which is often used for nonlinear material response, and the minimum potential energy principle which is often employed for linear material response (Figure 3.5).

The latter method is often referred to as the Dirichlet variational principle[4]. For a first introduction simpler minimization procedures such as a least-squares fit method are also conceivable. However, in either case it is first required to transform the differential equation into its corresponding integral form, equation (3.35), and to substitute the unknown function by a trial or interpolation function. For instance, solving the one-dimensional boundary-value problem expressed by the differential equation

$$\frac{\mathrm{d}^2 u}{\mathrm{d}x^2} = u \tag{3.36}$$

with given boundary values $u(x = a) = u_a$ and $u(x = b) = u_b$ is equivalent to finding a function $u(x)$ for the definite integral which fits the boundary conditions and at the same time minimizes the value

$$\int_a^b \left[u^2 + \left(\frac{\mathrm{d}u}{\mathrm{d}x}\right)^2\right] \mathrm{d}x \tag{3.37}$$

[4]It can be shown that the variational potential energy principle of Dirichlet is equivalent to the virtual displacement principle (Curnier 1994), see Chapter 16.

Such problems, which are referred to as "variational" problems, have already been addressed by Euler and Lagrange. Ritz tackled this task by expressing u in terms of a series of unknown coefficients c_0, c_1, c_2,...,c_n and a set of given functions $\Phi_1(x)$, $\Phi_2(x)$,...,$\Phi_n(x)$ in the form

$$u = c_0 + c_1\,\Phi_1(x) + c_2\,\Phi_2(x) + \ldots + c_n\,\Phi_n(x) \tag{3.38}$$

By transforming the original differential equation into the integral expression (equations (3.36) and (3.37)), one obtains the value of the integral as a function of the coefficients. These can then determined so as to minimize the value of the integral.

The original approach was introduced by Ritz in order to minimize the deviation between the correct and the approximate solutions over the *entire* domain addressed. Thus, the original Ritz method focuses on achieving the best possible correspondence between the correct and the approximate solutions over the entire system directly in one step. However, this technique entails the disadvantage that in two- and three-dimensional domains where $\Phi_i(x_1, x_2)$ or $\Phi_i(x_1, x_2, x_3)$ are used instead of $\Phi_i(x_1)$, the consideration of irregular boundary conditions is less tractable.

Thus, the initial Ritz method was modified so to approximate the solution piecewise rather than over the entire domain. This amounts to transforming the integral in equation (3.37) into a sum of integrals over subdomains:

$$\int_a^b \left[u^2 + \left(\frac{\mathrm{d}u}{\mathrm{d}x}\right)^2\right] \mathrm{d}x = \int_{a=a_0}^{a_1} \left[u^2 + \left(\frac{\mathrm{d}u}{\mathrm{d}x}\right)^2\right] \mathrm{d}x + \int_{a_1}^{a_2} \left[u^2 + \left(\frac{\mathrm{d}u}{\mathrm{d}x}\right)^2\right] \mathrm{d}x + \ldots + \int_{a_{n-1}}^{b=a_n} \left[u^2 + \left(\frac{\mathrm{d}u}{\mathrm{d}x}\right)^2\right] \mathrm{d}x$$

$$\text{where } a = a_0 < a_1 < a_2 < \ldots < a_n = b \tag{3.39}$$

Each interval $a_{i-1} < x < a_i$ can then be understood to be the ith finite element and the polynomial interpolation functions for the unknown state variables can be substituted into the corresponding integrals. This technique leads to a minimization of the error in a piecewise fashion at particular nodes rather than to a minimization of the total, i.e., of the integral deviation over the entire domain in one step.

The Ritz method in its finite element version originally worked with a relatively simple minimization routine. This approach can be improved by minimizing the deviation between the correct and the approximate solutions after multiplication with a so-called weighting function. Further details on the application of variational methods in the finite element method are presented in the monographs of Courant (1943), Livesley (1983), Zienkiewicz and Morgan (1983), Rao (1989), Zienkiewicz and Taylor (1989), Rowe, Sturgess, Hartley, and Pillinger (1991), and Zienkiewicz and Taylor (1991).

3.4.2 The Ritz Variational Method

In the preceding section the basic ideas of the variational calculus and the finite element method were outlined. However, before addressing applications of finite element simulations at the meso- and macroscale in Chapter 16, it is helpful first to present the basic ingredients of the technique by using a simple *analytical* example that allows clarification of the underlying principles. This makes the method more transparent and prepares for the ensuing chapters.

The task to be solved is the analytical approximation of the solution to a simple boundary-value problem using the classical Ritz method considering only one element. The starting point of the calculation is a one-dimensional ordinary second-order differential equation which was formulated to describe adequately the material problem being addressed. It is assumed that the analytical solution of this differential equation is not known:

$$\frac{\mathrm{d}^2 u}{\mathrm{d}x^2} = 12\,K\,x^2 \tag{3.40}$$

In this equation the function u, which can be referred to as state or dependent variable, depends on the independent variable x. K is a parameter, for instance a material constant. The differential equation is complemented by two boundary conditions, say

$$\begin{aligned} u(x=0) &= 0 \\ u(x=1) &= K \end{aligned} \tag{3.41}$$

The next step is to select a simple polynomial trial function $a(x)$. Although there exists no general rule for the selection of suitable ansatz functions, one can often yield a good estimate by using functions that reflect the material behavior, at least on a phenomenological basis. In order to keep the approximation as simple as possible, one can use a quadratic form such as

$$a(x) = A\,x^2 + B\,x + C \tag{3.42}$$

where A, B, and C are constants. In the next step one has to consider the boundary conditions given by equation (3.41).

$$\begin{aligned} a(x=0) = A\,x^2 + B\,x + C = 0 \quad &\Longrightarrow \quad C = 0 \\ a(x=1) = A\,x^2 + B\,x = K \quad &\Longrightarrow \quad B = K - A \end{aligned} \tag{3.43}$$

Thus, by combining equations (3.41) and (3.42), one obtains

$$a(x) = A\,x^2 + (K - A)\,x \tag{3.44}$$

Now one has to use the ansatz function for an approximate solution of the original differential equation, i.e.

$$\frac{\mathrm{d}^2 u}{\mathrm{d}x^2} - 12\,K\,x^2 = 0 \tag{3.45}$$

is transformed into

$$\frac{\mathrm{d}^2 a}{\mathrm{d}x^2} - 12\,K\,x^2 = 2\,A - 12\,K\,x^2 \neq 0 \tag{3.46}$$

Obviously, the solution is not correct since the right-hand side of equation (3.46) is not equal to zero. The deviation $2A - 12Kx^2$, which is referred to as the error of the approximation, is indicated by $\mathfrak{E}(x)$.

According to Ritz, the next step in the improvement of the approximate solution now consists in the procedure of minimization of the error given by $\mathfrak{E}(x)$. Since we do not have any detailed information of the material behavior or of the type of process addressed, except that given by equations (3.40) and (3.41), the minimization of the integrated

quadratic error $\mathfrak{E}(x)$ with respect to A represents the simplest possible approach. This can be put formally by writing

$$Q = \int_0^1 \mathfrak{E}(x)^2 \mathrm{d}x \tag{3.47}$$

The minimization within the interval described by the boundary conditions can be written

$$\frac{\partial Q}{\partial A} = 2\int_0^1 \mathfrak{E}(x)\frac{\partial \mathfrak{E}(x)}{\partial A}\,\mathrm{d}x = 2\int_0^1 \left(2A - 12Kx^2\right) 2\,\mathrm{d}x \;=\; 0 \tag{3.48}$$

By integration of equation (3.48) one obtains $A = 2K$. Thus, the originial polynomial ansatz function (equation (3.42)), amounts after optimization with respect to minimizing the quadratic error in the range $x = 0$ to $x = 1$ to

$$a(x) = 2\,Kx^2 - K\,x \tag{3.49}$$

As is evident from this example, the approximation could be improved by either using higher-order polynomial ansatz functions or by subdividing the original element into a number of smaller elements. A further modification can be introduced by changing the minimization procedure. Instead of using the minimization of the quadratic error, one could introduce some weighting function $w(x)$ to transform equation (3.48) into

$$\int_{x_0}^{x_1} \mathfrak{E}(x)\,w(x)\,\mathrm{d}x = 0 \tag{3.50}$$

The use of special weighting functions leads to the so-called Galerkin method. Further examples of variational approaches are given in the works of Forsythe and Wasow (1960), Richtmyer and Morton (1967), Dettman (1969), Marsal (1976), Boas (1983), DeVries (1994), and Bellomo and Preziosi (1995).

Part II

Simulation Techniques at the Nanoscopic–Microscopic Scale

Computational Materials Science: The Simulation of Materials, Microstructures and Properties By Dierk Raabe
Copyright © 1998 Wiley-VCH Verlag GmbH
ISBN: 3-527-29541-0

Chapter 4

Fundamentals

The prediction of microstructures at the atomic scale requires the solution of a Schrödinger wave equation for about 10^{23} nuclei and their electronic shells[1]. Such a differential equation must be equipped with a Hamiltonian describing all particle interactions occurring. For a single particle in a potential $U(\mathbf{r})$ with mass m and coordinates $\mathbf{r}$ whose wave function is $\Psi(\mathbf{r},t)$ the time-dependent Schrödinger equation assumes the form

$$-\frac{\hbar^2}{2m}\nabla^2\Psi(\mathbf{r},t) + U(\mathbf{r})\,\Psi(\mathbf{r},t) = \mathrm{i}\hbar\,\frac{\partial\Psi(\mathbf{r},t)}{\partial t} \tag{4.1}$$

where $\hbar = h/(2\pi)$ and h is Planck's constant. $\Psi(\mathbf{r},t)$ has the interpretation that $|\Psi(\mathbf{r},t)|^2$ $\mathrm{d}r_x\,\mathrm{d}r_y\,\mathrm{d}r_z$ is the probability that the particle may be observed in the volume element $\mathrm{d}r_x\,\mathrm{d}r_y\,\mathrm{d}r_z$ at any particular time.

For a bound particle in an eigenstate of energy E_k, equation (4.1) may be separated into a time-dependent and a time-independent part

$$\Psi(\mathbf{r},t) = \psi_k(\mathbf{r})\,\exp\left(-\mathrm{i}\,\frac{E_k t}{\hbar}\right) \tag{4.2}$$

The time-independent Schrödinger equation is, by substitution,

$$-\frac{\hbar^2}{2m}\nabla^2\psi(\mathbf{r})_k + U(\mathbf{r})\,\psi(\mathbf{r})_k = E_k\,\psi(\mathbf{r})_k \tag{4.3}$$

In analogy to the classical energy equation, this time-independent expression can be regarded as an operator equation, with $\mathrm{i}\hbar\nabla$ replacing the classical momentum p in the expression $p^2/(2m)$ for the kinetic energy

$$\mathcal{H}\,\psi(\mathbf{r})_k = E_k\,\psi(\mathbf{r})_k \tag{4.4}$$

where $\mathcal{H}$ is the Hamilton operator. The analogy to the classical description may be used to generalize equation (4.3) to cases with N particles, including their mutual interactions:

$$-\frac{\hbar^2}{2}\left(\sum_i \frac{1}{m_i}\nabla_i^2\right)\psi(\mathbf{r}_1,\mathbf{r}_2,...,\mathbf{r}_N)_k + U(\mathbf{r}_1,\mathbf{r}_2,...,\mathbf{r}_N)_k\psi(\mathbf{r}_1,\mathbf{r}_2,...,\mathbf{r}_N)_k = E_k\,\psi(\mathbf{r}_1,\mathbf{r}_2,...,\mathbf{r}_N)_k \tag{4.5}$$

[1] neglecting relativistic effects and energy contributions arising from spin magnetic moments.

Computational Materials Science: The Simulation of Materials, Microstructures and Properties By Dierk Raabe
Copyright © 1998 Wiley-VCH Verlag GmbH
ISBN: 3-527-29541-0

For instance, a material consisting of i electrons of mass m_e with a negative unit charge $q_e = -e$ and the spatial coordinates $\mathbf{r}_{e_i}$, and j nuclei of mass m_n with a positive charge $q_n = z_n\, e$ and the spatial coordinates $\mathbf{r}_{n_j}$, can be described by the eigenvalue wave equation

$$
\begin{aligned}
&-\frac{\hbar^2}{2m_e}\sum_i \nabla_i^2\, \psi(\mathbf{r}_{e_1}, \mathbf{r}_{e_2}, \ldots, \mathbf{r}_{e_i}, \mathbf{r}_{n_1}, \mathbf{r}_{n_2}, \ldots, \mathbf{r}_{n_j})_k \\
&\qquad - \frac{\hbar^2}{2}\sum_j \frac{1}{m_{nj}} \nabla_j^2\, \psi(\mathbf{r}_{e_1}, \mathbf{r}_{e_2}, \ldots\ldots, \mathbf{r}_{e_i}, \mathbf{r}_{n_1}, \mathbf{r}_{n_2}, \ldots, \mathbf{r}_{n_j})_k \\
&+ \left(\sum_{\substack{i1,i2 \\ i1\neq i2}} \frac{e^2}{|\mathbf{r}_{e_{i1}} - \mathbf{r}_{e_{i2}}|} + \sum_{i,j} \frac{z_j\, e^2}{|\mathbf{r}_{e_i} - \mathbf{r}_{n_j}|} + \sum_{\substack{j1,j2 \\ j1\neq j2}} \frac{z_{j1}\, z_{j1}\, e^2}{|\mathbf{r}_{n_{j1}} - \mathbf{r}_{n_{j2}}|} \right) \psi(\mathbf{r}_{e_1}, \mathbf{r}_{e_2}, \ldots, \\
&\qquad \mathbf{r}_{e_i}, \mathbf{r}_{n_1}, \mathbf{r}_{n_2}, \ldots, \mathbf{r}_{n_j})_k = E_k\, \psi(\mathbf{r}_{e_1}, \mathbf{r}_{e_2}, \ldots, \mathbf{r}_{e_i}, \mathbf{r}_{n_1}, \mathbf{r}_{n_2}, \ldots, \mathbf{r}_{n_j})_k \qquad (4.6)
\end{aligned}
$$

The terms that appear in this Hamilton operator suggest a distinction between those material properties that are determined by the lattice dynamics ($\mathbf{r}_{n_j}$, $\hbar^2/(2m_{nj})$, e.g., propagation of acoustic waves, thermal expansion, the non-electronic part of the specific heat, thermal conductivity of semiconductors and ceramics, and structural defects, and those that are determined by the electronic system ($\mathbf{r}_{e_i}$, $\hbar^2/(2m_{ei})$, e.g. electrical conductivity, thermal conductivity of metals, and superconductivity. At first view such a concept seems somewhat inaccurate, because it is the wave functions of the electrons and thus the electronic charge density that determine the position of the atomic nuclei. However, decoupling the motions of the light electrons from those of the heavy nuclei can be justified by the fact that the relaxation time of the electrons is typically three orders of magnitude below that of the atomic nuclei. This amounts to a situation where the electronic system practically remains in its ground-state irrespective of the positions of the nuclei. This concept is referred to as the adiabatic or Born–Oppenheimer approximation.

Its employment in the present case allows one to approximate the exact wave function ψ in equation (4.6) as a product of two separate wave functions, where one portion describes the dynamics of the electrons φ and a second portion describes the dynamics of the nuclei ϕ, $\psi(\mathbf{r}_{e_1}, \mathbf{r}_{e_2}, \ldots, \mathbf{r}_{e_i}, \mathbf{r}_{n_1}, \mathbf{r}_{n_2}, \ldots, \mathbf{r}_{n_j}) = \varphi(\mathbf{r}_{e_1}, \mathbf{r}_{e_2}, \ldots, \mathbf{r}_{e_i})\, \phi(\mathbf{r}_{n_1}, \mathbf{r}_{n_2}, \ldots, \mathbf{r}_{n_j})$. This approach amounts to separating the dynamics of the heavy constituents (nuclei) from that of the light ones (electrons). The corresponding Schrödinger equation is

$$
\begin{aligned}
&\left(-\frac{\hbar^2}{2\, m_e}\sum_i \nabla_i^2 + \sum_{\substack{i1,i2 \\ i1\neq i2}} \frac{e^2}{|\mathbf{r}_{e_{i1}} - \mathbf{r}_{e_{i2}}|} + \sum_{i,j} \frac{z_j\, e^2}{|\mathbf{r}_{e_i} - \mathbf{r}_{n_j}|} \right) \varphi(\mathbf{r}_{e_1}, \mathbf{r}_{e_2}, \ldots, \mathbf{r}_{e_i})_{k_e} \\
&\qquad = E^e_{k_e}\, \varphi(\mathbf{r}_{e_1}, \mathbf{r}_{e_2}, \ldots, \mathbf{r}_{e_i})_{k_e} \qquad (4.7)
\end{aligned}
$$

for the electronic system with the eigenvalues E_{k_e} and

$$
\begin{aligned}
&\left(-\frac{\hbar^2}{2}\sum_j \frac{1}{m_n} \nabla_j^2 + \sum_{\substack{j1,j2 \\ j1\neq j2}} \frac{z_{j1}\, z_{j2}\, e^2}{|\mathbf{r}_{n_{j1}} - \mathbf{r}_{n_{j2}}|} + \sum_{i,j} \frac{z_j\, e^2}{|\mathbf{r}_{e_i} - \mathbf{r}_{n_j}|} \right) \phi(\mathbf{r}_{n_1}, \mathbf{r}_{n_2}, \ldots, \mathbf{r}_{n_j})_{k_n} \\
&\qquad = E^n_{k_n}\, \phi(\mathbf{r}_{n_1}, \mathbf{r}_{n_2}, \ldots, \mathbf{r}_{n_i})_{k_n} \qquad (4.8)
\end{aligned}
$$

for the nuclei with the eigenvalues E_{k_n}.

Approximate solutions of equation (4.7) using Hartee–Fock or local electron density functional theory form the basis of electronic ground state calculations with fixed coordinates for the nuclei. Since the exact ground state wave function will have a lower energy than any other admissible wave function, it is straightforward to express these theories in a variational form. Equation (4.8) is the starting point for the prediction of atomic configurations with instantaneously equilibrated electrons (Chapter 7).

This part of the book deals mainly with atomic-scale structure and distribution function simulations, i.e., with approximations to equation (4.8) and their discrete or statistical numerical solution. The solution methods can be principally grouped into probabilistic and deterministic approaches. While the first class is usually referred to as Monte Carlo methods, the second one is referred to as molecular dynamics. Energy band calculations for many-electron systems with fixed nuclei will only briefly be discussed in Section 7.2.7. In computational materials science, Monte Carlo methods are most widely used to determine stochastically equilibrium states for known distribution functions or to solve directly integral formulations of the equation of motion (Metropolis et al. 1953; Hammersley and Handscomb 1964; Binder 1984; Kalos and Whitlock 1986; Suzuki 1987).

When used in a statistical fashion the Monte Carlo technique mimics a canonical ensemble by performing a large number of successive stochastic computer experiments using uncorrelated random numbers which form a Markov chain. This allows one to explore within reasonable computation time a large number of states in phase space. Most Monte Carlo methods use weighted schemes, i.e, the transition probabilities between configurations are visited according to their proper statistical relevance. By assuming ergodic system behavior, averages can be obtained as pseudo-time averages along the trajectory in phase space. Monte Carlo techniques are particularly useful in calculating state function values and correlation functions on the basis of adequate Hamiltonians.

Statistical Monte Carlo integrations represent classical methods for the prediction of equilibrium configurations, i.e. of path-independent properties of canonical ensembles. Howver, they also gain momentum as approximation methods for the simulation of path-dependent behavior such as is often investigated in the field of microstructure dynamics. It must be clearly underlined that Monte Carlo methods are *not* principally confined to equilibrium predictions but can be used to solve any differential equation which can be turned into an integral form. The original idea of the various Monte Carlo approaches is to provide a probabilistic means for numerical integration. In general, they are thus not intrinsically scaled to the atomistic regime but can be used at any scale, provided they are applied to an appropriate probabilistic model.

Typical examples of non-atomistic Monte Carlo applications lie in the field of transport and phase transformation phenomena. The extension of Monte Carlo predictions to applications in the field of microstructure simulation was particularly promoted by the modification of the Ising lattice model for the simulation of magnetic domains to the multistate Potts model for the simulation of generalized domains (Potts 1952; Wu 1982). This approach, which is often referred to as the q-state Potts model, uses *generalized* instead of binary spin numbers. This allows one to map discretely various types of domains by regions of identical spin. In microstructure simulation these domains can be interpreted as areas of similarly oriented material with negligible interaction energy between identical neighbors and a non-negligible interaction between dissimilar neighbors. The latter case can be used to identify internal interfaces. In the Potts lattice model, each simulation step is carried out using the conventional Metropolis Monte Carlo algorithm, but with an underlying delta-type Hamiltonian which accounts for dissimilar lattice neighbors. Structure evolution is reflected by the transient behaviour of the system, i.e., by the mesoscopic

evolution of the domain size and shape. While original Monte Carlo approaches were confined to simulating the values of path-independent state functions, they are now through the q-state Potts model a convenient means in simulating path-dependent microstructure evolution. When using an internal kinetic measure such as the number of Monte Carlo steps, counted in units of lattice sites, Ising- and Potts-type Monte Carlo models are sometimes referred to as kinetic Monte Carlo models (Anderson et al. 1984; Srolovitz et al. 1984; Grest et al. 1988; Srolovitz et al. 1988; Rollett et al. 1989; Glazier et al. 1990; Anderson and Rollett 1990; Holm et al. 1996). Kinetic Potts-type simulations of domain growth and shrinkage are often employed to predict microstructure evolution at the mesoscale. They are therefore discussed in Chapter 12, which deals with mesoscale simulations. The various Monte Carlo methods are described with special regard to their application at the atomic scale in the first major chapter of this part (Chapter 6).

Most of the molecular dynamics methods are based on turning equation (4.8) into a classical form by replacing the quantum mechanical expression for the kinetic energy by the classical momentum term

$$\frac{1}{2}\sum_j \frac{p^2}{m_j} + U = \sum_j m_j v_j^2 + U = E \tag{4.9}$$

and solving it for a nucleus in the potential U using Newton's law of motion:

$$m\frac{\partial v}{\partial t} = -\nabla U \tag{4.10}$$

A number of typical more or less empirical potentials will be discussed in Section 7.2. While Monte Carlo techniques prevail in simulations of equilibrium properties, molecular dynamics approaches are mainly used to solve discretely the equation of motion. They are hence of particular importance in the prediction of the dynamics of lattice defects (Alder and Wainwright 1959; Verlet 1967; Catlow and Mackroth 1982; Hoover 1986; Allen and Tildesley 1989; Tersoff et al. 1989; Mark et al. 1992; Broughton et al. 1993; Sutton and Balluffi 1995). In contrast to the probabilistic nature of the Monte Carlo technique, the molecular dynamics method is deterministic.

Under the assumption of ergodic system behavior (Halmos 1955; Farquhar 1964; Bedford et al. 1991), thermodynamic quantities can be calculated as time averages of the simulation. Thus the molecular dynamics technique allows one to mimic both thermodynamics and path-dependent dynamics of many-body interaction phenomena at the atomic scale (Alder and Wainwright 1960; Rahman 1964; Verlet 1968). At first sight the deterministic character of molecular dynamics simulations therefore seems to be superior to the stochastic Monte Carlo technique. However, molecular dynamics has its limitations in statistics: both Monte Carlo and molecular dynamics compute averages along their respective trajectories in configuration space. However, in multidimensional systems with up to $6N$ degrees of freedom Monte Carlo integrations allow one to visit a larger number of states along their stochastic trajectory than molecular dynamics simulations along their deterministic trajectory. This means that with molecular dynamics much less of the phase state is actually accessible as compared with Monte Carlo. Furthermore, the assumption of ergodic system behavior which justifies time integration for obtaining averages has never been unambiguously proven (Farquhar 1964).

However, the great value of molecular dynamics lies in its capability to predict microstructure dynamics at a scale that is not, or only with great effort, amenable to experimentation. It is the only deterministic simulation method that provides insight into the path-dependence of microstructure evolution at an atomistic level.

Chapter 5

Statistical Mechanics in Atomic-Scale Simulations

Atomic-scale simulations can be used to predict equilibrium and transient thermodynamic states, correlation functions, and the dynamics of atoms. This is achieved through the discrete or statistical numerical calculation of many-body[1] interaction phenomena. The mutual interaction of the particles being considered is usually quantified in terms of appropriate Hamiltonians.

Often, it is desirable to extract data of macroscopic relevance from such atomic-scale simulations. This requires the use of adequate statistical methods. This chapter deals with the conversion of detailed microscopic information, such as is obtained from atomic-scale simulations, into macroscopic information. The quantitative tools for this procedure are provided by statistical mechanics.

The field of statistical mechanics can be devided into two main branches, namely equilibrium statistical mechanics, which deals with the derivation of the laws of thermodynamics and calculation of the values of thermodynamic state functions and other equilibrium properties of systems in terms of their atomistic properties, and non-equilibrium statistical mechanics, which deals with the approach of systems to thermodynamic equilibrium, the derivation of macroscopic transport equations and their coefficients, and other non-equilibrium properties of systems in terms of their atomistic properties. While the first area can be referred to as "statistical thermodynamics", the second can be termed "statistical kinetics".

In this chapter the fundamentals of equilibrium statistical mechanics as required in formulating and analyzing atomic-scale simulations will be briefly reviewed, based on the work of Maxwell, Boltzmann, and Gibbs. Some aspects of non-equilibrium statistical mechanics will be touched upon as well. More detailed contributions about statistical mechanics have been published by Boltzmann (1905), Hill (1956), Reif (1965), Wannier (1966), Pointon (1967), Kestin and Dorfman (1971), Münster (1974), Ludwig (1979), Landau and Lifshitz (1980), Reichl (1980), Binder (1984), Binder and Heermann (1988), Atkins (1986), Allen and Tildesley (1989), and Honerkamp and Römer (1993).

[1] A body, in this context, is any material portion below the continuum scale and above the electronic scale, i.e. body ≡ atom or molecule.

Computational Materials Science: The Simulation of Materials, Microstructures and Properties By Dierk Raabe
Copyright © 1998 Wiley-VCH Verlag GmbH
ISBN: 3-527-29541-0

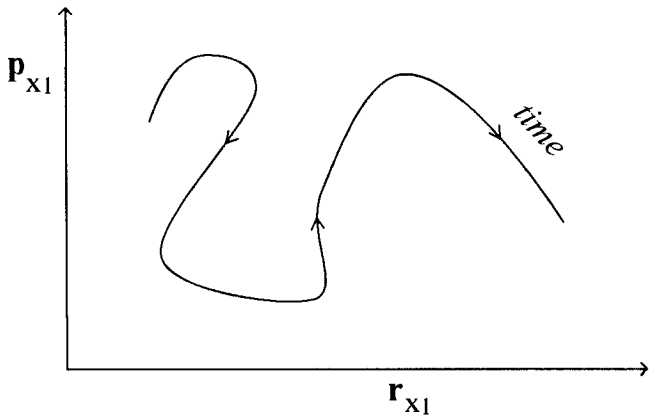

Figure 5.1: Motion of a point in a two-dimensional phase space. The diagram only maps the temporal evolution of two coordinates, $\mathbf{r}_{x_1}(t)$ and $\mathbf{p}_{x_1}(t)$, out of the $6N$ coordinates, $\mathbf{r}_{x_1}(t)$, $\mathbf{r}_{x_2}(t)$, ..., $\mathbf{r}_{x_N}(t)$, $\mathbf{p}_{x_1}(t)$, $\mathbf{p}_{x_2}(t)$, ..., $\mathbf{p}_{x_N}(t)$. The arrows indicate the continuous increase of time.

The microscopic thermodynamic state of a classical, i.e., of a nonquantum atomic gas consisting of N particles in translational motion is given by the three components of the particle position vectors $\mathbf{r}_1, ..., \mathbf{r}_N$ and by the three components of the particle velocity or respective momentum vectors $\mathbf{p}_1, ..., \mathbf{p}_N$. The number of atoms encountered in real systems is of the order of 10^{23}. From an atomistic point of view one thus deals with a huge microscopic data set of at least 6×10^{23} numbers required to determine fully the macroscopic state of a system. These $6N$ components, or degrees of freedom (DOF), of the position and momentum vectors can be thought of as coordinates in a multidimensional space which is referred to as phase space. Depending on the prescribed macroscopic system parameters, i.e., on the underlying state function, one usually deals with a Gibbs phase space or a Helmholtz phase space. At any instant in its temporal evolution the system can be characterized by a specific set of data points, say particle velocities and positions, in phase space (Figure 5.1). This vector set can be put together to form the $6N$ dimensional quantity $\mathbf{\Gamma}(t)$:

$$\mathbf{\Gamma}(t) = \{\, \mathbf{r}_1(t), ..., \mathbf{r}_N(t), \mathbf{p}_1(t), ..., \mathbf{p}_N(t) \,\} \tag{5.1}$$

Each point in phase space represents a typical system at any particular instant of time. Due to the $6N$ possible coordinates, the phase space for classical particles is sometimes denoted as $\mathbf{\Gamma}_{6N}(t)$ or simply $\mathbf{\Gamma}$. Of course, further microscopic degrees of freedom that appear in nonclassical Hamiltonians, such as the particle spin, can be considered as well. Writing $\mathbf{\Gamma}(t)$ in differential form leads to the expression

$$\begin{aligned} d\mathbf{\Gamma}(t) = {} & d\mathbf{r}_{x_1}(t) \cdot d\mathbf{r}_{y_1}(t) \cdot d\mathbf{r}_{z_1}(t) \cdot d\mathbf{r}_{x_2}(t) \cdot d\mathbf{r}_{y_2}(t) \cdot d\mathbf{r}_{z_2}(t) \cdot ... \\ & ... \cdot d\mathbf{r}_{x_N}(t) \cdot d\mathbf{r}_{y_N}(t) \cdot d\mathbf{r}_{z_N}(t) \cdot d\mathbf{p}_{x_1}(t) \cdot d\mathbf{p}_{y_1}(t) \cdot d\mathbf{p}_{z_1}(t) \cdot d\mathbf{p}_{x_2}(t) \cdot d\mathbf{p}_{y_2}(t) \cdot d\mathbf{p}_{z_2}(t) \cdot ... \\ & ... \cdot d\mathbf{p}_{x_N}(t) \cdot d\mathbf{p}_{y_N}(t) \cdot d\mathbf{p}_{z_N}(t) \end{aligned} \tag{5.2}$$

where $\mathbf{r}_{x_1}(t)$ represents the x component of the position vector $\mathbf{r}$ of particle 1 as a function of time t, and $\mathbf{p}_{x_1}(t)$ is the x component of the momentum vector $\mathbf{p}$ of particle 1 as a

Table 5.1: Ensemble types in Monte Carlo and molecular dynamics.

Ensemble	Prescribed parameters
macrocanonical	particle number, volume, temperature
microcanonical	particle number, volume, energy
grandcanonical	volume, temperature, chemical potential
isobaric–isothermal	particle number, pressure, temperature

function of time t. This can be rewritten more compactly as

$$\mathrm{d}\Gamma(t) = \mathrm{d}\mathbf{r}^{3N}(t)\ \mathrm{d}\mathbf{p}^{3N}(t) \tag{5.3}$$

The quantitiy $\mathrm{d}\Gamma(t)$ can be regarded as a volume element about the point $\Gamma(t)$ in phase space. The temporal evolution of a system can be characterized by the time trajectory of $\Gamma(t)$ in phase space. While kinetic Monte Carlo simulations provide states along a stochastic trajectory which is usually calculated by importance sampling, i.e. by a weighted sampling scheme, molecular dynamics simulations provide states along a deterministic trajectory which is calculated by solving the classical equations of motion of all particles involved.

For obtaining a more macroscopic picture of a system consisting of 10^{23} particles, a detailed microscopic analysis including the individual coordinates, velocities, orientations, and angular velocities of the molecules is often neither tractable nor required. The central idea of statistical mechanics thus consists in the replacement of the $6\,N$ microscopic parameters for the characterization of the thermodynamic state by a few macroscopic parameters, such as the particle number N, volume V, temperature T, energy E, chemical potential μ, heat capacity c, or pressure P. In cases where certain macroscopic system parameters are prescribed, this can be achieved by calculating averages from the fluctuating microscopic parameters of the individual particles.

Calculating averages makes sense because the number of possible microstates considerably exceeds the number of macrostates. In other words, one macrostate can be realized by a multiplicity of microstates, i.e. the particles must satisfy the same prescribed macroscopic constraints but may differ in their microscopic states. Using averages thus follows the belief that the macroscopic properties of a system consisting of a large number of interacting particles is not sensitive to the details in its microscopic, i.e. atomistic, states.

Furthermore, the calculation of average data which are in the following text denoted by $\langle q \rangle$ reflects the essential experimental experience of identifying particles with an average behavior with a larger probability than those with non-average properties. This means that macroscopically observed quantities q_{exp} can be set equal to the system averages $\langle q \rangle$.

The analysis of averages in addition to the fine details of atomistic simulations allows one to correctly consider externally imposed macroscopic constraints, such as pressure or volume, and check the consistency of the resulting predictions with respect to the values of these state variables. This means that in the field of microstructure simulation, statistical mechanics complements and controls the prediction of individual positions and velocities.

The set of all points in phase space together with their respective probabilities establishes an ensemble (Table 5.1). In other words, an ensemble characterizes the probabilities of all microscopic states that are allowed within certain macroscopic constraints, which are represented by a set of externally imposed macroscopic parameters. In the area of

equilibrium statistical mechanics one deals with stationary ensembles. Depending on the prescribed set of macroscopic conditions, one speaks of a "macrocanonical" or simply a "canonical" stationary ensemble (N, V, T prescribed), a "microcanonical" stationary ensemble (N, V, E prescribed), a "grandcanonical" stationary ensemble (V, T, μ prescribed), or an "isobaric–isothermal" stationary ensemble (N, P, T prescribed). While in the canonical, microcanonical, and isobaric–isothermal ensembles the concentration of the elementary constituents is fixed, in grandcanonical systems it depends on the prescribed chemical potential.

The macrocanonical or canonical ensemble is typically prescribed in Monte Carlo simulations where N particles are in a box with volume V which is embedded in a heat bath with constant temperature T. The total energy and the system pressure may fluctuate around some average value. The characteristic function of the canonical ensemble is the Helmholtz free energy $F(N, V, T)$.

The microcanonical ensemble with N particles in a box with volume V and a fixed total energy E prevails in molecular dynamics simulations. The system temperature and pressure may fluctuate around some average value. The characteristic function of the microcanonical ensemble is the entropy $S(N, V, E)$.

The grandcanonical ensemble with a prescribed temperature T, a given chemical potential μ, and a fixed volume V is typically implemented in Monte Carlo simulations. The system energy, the pressure, and the number of individual particles may fluctuate around some average value. The characteristic function of the grandcanonical ensemble is the Massieu function $J(\mu, V, T)$.

The isobaric–isothermal ensemble with a given temperature T, pressure D, and number of particles N is typically realized in Monte Carlo simulations. The total energy and the system volume may fluctuate. The characteristic function of the isobaric–isothermal ensemble is the Gibbs free energy $G(N, P, T)$ (Figure 5.2).

Statistical data can be obtained from a microscopic set of particles by calculating either time averages or ensemble averages. The equivalence of these averages is the subject of the ergoden theory. The use of time averages $\langle q \rangle_{\text{time}}$ follows the assumption that a macroscopically observed quantity q_{exp} is insensitive to temporal fluctuations of the microstates.

$$\langle q \rangle_{\text{time}} = q_{\text{exp}} = \langle q\,(\mathbf{\Gamma}(t)) \rangle_{\text{time}} = \lim_{t_{\text{exp}} \to \infty} \frac{1}{t_{\text{exp}}} \int_{t_0}^{t_0 + t_{\text{exp}}} q\,(\mathbf{\Gamma}(t))\ \mathrm{d}t \tag{5.4}$$

Correspondingly, the validity of ensemble averages $\langle q \rangle_{\text{ens}}$ is based on the assumption that a macroscopically observed quantity q_{exp} is insensitive to phase space fluctuations of the microstates. In other words, the ensemble average can be determined by replacing the time average $\langle q \rangle_{\text{time}}$, given by equation (5.4), by an average taken over all members of the ensemble, $\langle q \rangle_{\text{ens}}$, frozen at a particular time $t = t_{\text{fix}}$.

$$\langle q \rangle_{\text{ens}} = q_{\text{exp}} = \langle\, q\,(\mathbf{\Gamma}(t{=}t_{\text{fix}}))\,\rangle_{\text{ens}} = \int_{\mathbf{\Gamma}} q\,(\mathbf{\Gamma})\ \rho\,(\mathbf{\Gamma})\ \mathrm{d}\mathbf{\Gamma} \tag{5.5}$$

where $\rho\,(\mathbf{\Gamma}) = \rho(\mathbf{r}_1, ..., \mathbf{r}_N, \mathbf{p}_1, ..., \mathbf{p}_N)$ is the probability distribution function. It is sometimes also referred to as the phase space distribution function or simply as the distribution function. $\rho\,(\mathbf{\Gamma})$ is proprtional to the probability that, for a given macrostate, the system is at $t = t_0$ in a microstate the phase space point of which lies within a volume element of the phase space, $\mathrm{d}\mathbf{\Gamma}$, about the point $\mathbf{\Gamma}$. Since the microstate must definitely exist

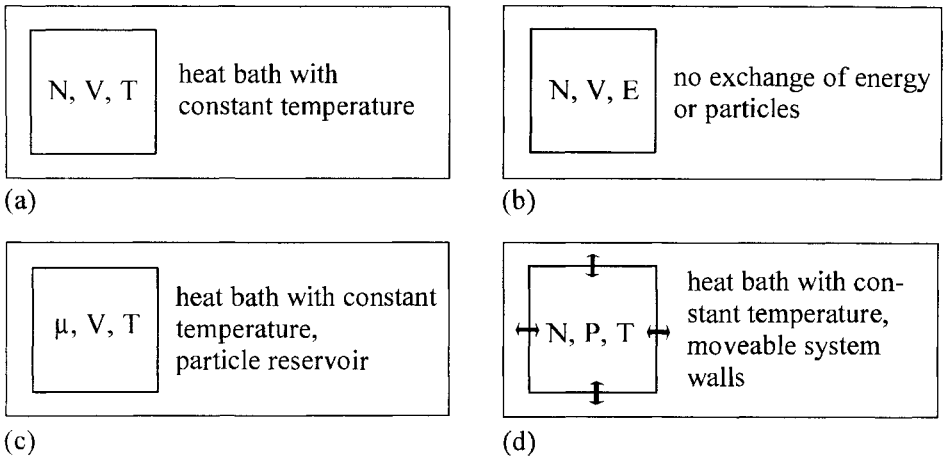

Figure 5.2: Typical ensembles in atomic-scale Monte Carlo and molecular dynamics simulations: (a) canonical or macrocanonical ensemble (N, V, T prescribed, Helmholtz free energy $F(N,V,T)$ as characteristic function); (b) microcanonical ensemble (N, V, E prescribed, entropy $S(N,V,E)$ as characteristic function); (c) grandcanonical ensemble (V, T, μ prescribed, Massieu function $J(\mu,V,T)$ as characteristic function); (d) isobaric–isothermal ensemble (N, P, T prescribed, Gibbs free energy $G(N,P,T)$ as characteristic function).

somewhere in phase space, the integral of the distribution function over the phase space amounts to 1:

$$\int_{\Gamma} \rho(\Gamma)\, \mathrm{d}\Gamma = 1 \tag{5.6}$$

From the classical formulation of the Liouville equation it follows that, if $\rho(\Gamma)$ represents an equilibrium ensemble, then its time-dependence completely vanishes, i.e., it is a function only of the conserved quantities of motion.

$$\frac{\partial \rho(\Gamma)}{\partial t} = 0 \tag{5.7}$$

The Liouville theorem can be regarded as a conservation law for probability density. This means that any equilibrium ensemble characterized in terms of a constant $\rho(\Gamma)$ represents a stationary ensemble.

The phase space density function depends on the system Hamiltonian,

$$\rho(\Gamma) = f(\mathcal{H}(\Gamma)) \tag{5.8}$$

with

$$\mathcal{H}(\Gamma) = E_{\mathrm{pot}}(\mathbf{r}_1, ..., \mathbf{r}_N) + E_{\mathrm{kin}}(\mathbf{p}_1, ..., \mathbf{p}_N) \tag{5.9}$$

where $E_{\mathrm{pot}}(\mathbf{r}_1, ..., \mathbf{r}_N)$ is the potential energy and $E_{\mathrm{kin}}(\mathbf{p}_1, ..., \mathbf{p}_N)$ the kinetic energy.

The phase space density function for a canonical system $\rho_{\mathrm{NVT}}(\mathbf{\Gamma})$ is conveniently described in terms of the probability $w(\mathbf{\Gamma})$ to observe a particle with energy $\mathcal{H}(\mathbf{\Gamma})$ and the canonical zustandsintegral or canonical partition function[2] Z_{NVT}.

The basic assumption of statistical mechanics is that all microstates of a system that have the same energy are equally probable. In the classical canonical description the probability can be expressed in terms of the Boltzmann factor. The probability density $w_{\mathrm{NVT}}(\mathbf{\Gamma})$, which describes the non-normalized statistical weight with which the canonical phase space configuration $\mathbf{\Gamma}$ occurs in thermal equilibrium, can be written

$$w_{\mathrm{NVT}}(\mathbf{\Gamma}) = \frac{1}{N!\,h^{3N}} \exp\left(-\beta\,\mathcal{H}(\mathbf{\Gamma})\right) \tag{5.10}$$

where β is $1/(k_{\mathrm{B}}\,T)$ with k_{B} the Boltzmann constant and $1/(N!)$ the normalization factor which takes into account that for N identical particles a permutation of particle indices does not lead to a change in the quantum state. The factor $1/(h^{3N})$ accounts for the Heisenberg uncertainty, where h^{3N} can be regarded as the volume of tiny cells in phase space below which the position and momentum vectors can no longer be determined at the same time.

The canonical partition function Z_{NVT}, which integrates the weights over all states in phase space, plays the role of a normalizing factor,

$$Z_{\mathrm{NVT}} = \int_{\mathbf{\Gamma}} w_{\mathrm{NVT}}(\mathbf{\Gamma})\;\mathrm{d}\mathbf{\Gamma} = \frac{1}{N!\,h^{3N}} \int_{\mathbf{\Gamma}} \exp\left(-\beta\,\mathcal{H}(\mathbf{\Gamma})\right)\,\mathrm{d}\mathbf{\Gamma} \tag{5.11}$$

The canonical phase space density function $\rho_{\mathrm{NVT}}(\mathbf{\Gamma})$ can then be written as a nomalized weight distribution function, namely

$$\rho_{\mathrm{NVT}}(\mathbf{\Gamma}) = \frac{w(\mathbf{\Gamma})}{Z_{\mathrm{NVT}}} = \frac{\exp\left(-\beta\,\mathcal{H}(\mathbf{\Gamma})\right)}{\int_{\mathbf{\Gamma}} \exp\left(-\beta\,\mathcal{H}(\mathbf{\Gamma})\right)\;\mathrm{d}\mathbf{\Gamma}} \tag{5.12}$$

In the case of discrete energies $\mathcal{H}(\mathbf{\Gamma})$ and distinguishable non-quantum particles which show a behavior in accord with the Maxwell–Boltzmann distribution, it is convenient to write the canonical partition function as a sum rather than an integral:

$$Z_{\mathrm{NVT}} = \sum_{\mathbf{\Gamma}} \exp\left(-\beta\,\mathcal{H}(\mathbf{\Gamma})\right) \tag{5.13}$$

The canonical ensemble average $\langle q\rangle_{\mathrm{NVT}}$ for a property q can then be written

$$\langle q\rangle_{\mathrm{NVT}} = \langle\, q\left(\mathbf{\Gamma}(t{=}t_{\mathrm{fix}})\right)\rangle_{\mathrm{NVT}} = \sum_{\mathbf{\Gamma}} \rho_{\mathrm{NVT}}(\mathbf{\Gamma})\;q(\mathbf{\Gamma}) = \frac{\sum_{\mathbf{\Gamma}} w(\mathbf{\Gamma})\;q(\mathbf{\Gamma})}{\sum_{\mathbf{\Gamma}} w(\mathbf{\Gamma})} \tag{5.14}$$

The microcanonical probability density $w_{\mathrm{NVE}}(\mathbf{\Gamma})$, which describes the non-normalized statistical weight with which the microcanonical phase space configuration $\mathbf{\Gamma}$ occurs in thermal equilibrium, can be written

$$w_{\mathrm{NVE}}(\mathbf{\Gamma}) = \frac{1}{N!\,h^{3N}}\,\delta\left(\mathcal{H}(\mathbf{\Gamma}) - E\right) \tag{5.15}$$

[2]Planck referred to it as the zustandsintegral, i.e. sum over states; this is where the symbol Z comes from.

where E is the system energy and δ the Dirac delta function. The microcanonical partition function Z_{NVE} amounts to

$$Z_{\mathrm{NVE}} = \int_{\Gamma} w_{\mathrm{NVE}}(\mathbf{\Gamma})\, \mathrm{d}\mathbf{\Gamma} = \frac{1}{N!\, h^{3N}} \int_{\Gamma} \delta(\mathcal{H}(\mathbf{\Gamma}) - E)\, \mathrm{d}\mathbf{\Gamma} \tag{5.16}$$

In the case of discrete energies the microcanonical partition function can be written as a sum:

$$Z_{\mathrm{NVE}} = \sum_{\Gamma} \delta(\mathcal{H}(\mathbf{\Gamma}) - E) \tag{5.17}$$

The probability density of the grandcanonical ensemble $w_{\mu\mathrm{VT}}(\mathbf{\Gamma})$ is

$$w_{\mu\mathrm{VT}}(\mathbf{\Gamma}) = \frac{1}{N!\, h^{3N}} \exp(-\beta\, (\mathcal{H}(\mathbf{\Gamma}) - \mu N)) \tag{5.18}$$

where μ is the specified chemical potential and N the number of particles. The grandcanonical partition function $Z_{\mu\mathrm{VT}}$ amounts to

$$Z_{\mu\mathrm{VT}} = \int_{\Gamma} w_{\mu\mathrm{VT}}(\mathbf{\Gamma})\, \mathrm{d}\mathbf{\Gamma} = \frac{1}{N!\, h^{3N}} \int_{\Gamma} \exp(-\beta\, (\mathcal{H}(\mathbf{\Gamma}) - \mu N))\, \mathrm{d}\mathbf{\Gamma} \tag{5.19}$$

For discrete energies the grandcanonical partition function can be written as a sum:

$$Z_{\mu\mathrm{VT}} = \sum_{\Gamma} \sum_{\mathrm{N}} \exp(-\beta\, (\mathcal{H}(\mathbf{\Gamma}) - \mu N)) = \sum_{\mathrm{N}} \exp(\beta \mu N)\; Z_{\mathrm{NVT}} \tag{5.20}$$

The probability density of the isobaric-isothermal ensemble $w_{\mathrm{NPT}}(\mathbf{\Gamma})$ is

$$w_{\mathrm{NPT}}(\mathbf{\Gamma}) = \frac{1}{N!\, h^{3N}\, \Omega_0} \exp(-\beta\, (\mathcal{H}(\mathbf{\Gamma}) + PV)) \tag{5.21}$$

where Ω_0 is a volume constant, P the pressure, and V the volume. The isobaric-isothermal partition function Z_{NPT} amounts to

$$Z_{\mathrm{NPT}} = \int_{V} \int_{\Gamma} w_{\mathrm{NPT}}(\mathbf{\Gamma})\, \mathrm{d}\mathbf{\Gamma}\, \mathrm{d}V = \frac{1}{N!\, h^{3N}\, \Omega_0} \int_{V} \int_{\Gamma} \exp(-\beta\, (\mathcal{H}(\mathbf{\Gamma}) + PV))\, \mathrm{d}\mathbf{\Gamma}\, \mathrm{d}V \tag{5.22}$$

In the case of discrete energies the isobaric-isothermal partition function can be written as a sum:

$$Z_{\mathrm{NPT}} = \sum_{\Gamma} \sum_{V} \exp(-\beta\, (\mathcal{H}(\mathbf{\Gamma}) + PV)) = \sum_{V} \exp(-\beta P V)\; Z_{\mathrm{NVT}} \tag{5.23}$$

The partition function is a fundamental quantity which allows one to calculate various thermodynamic state functions in thermodynamic equilibrium. For instance, the Helmholtz free energy F is proportional to the logarithm of the canonical partition function, i.e.

$$F = -k_{\mathrm{B}} T \ln Z_{\mathrm{NVT}} = -k_{\mathrm{B}} T \ln \sum_{\Gamma} \exp(-\beta \mathcal{H}(\mathbf{\Gamma})) \tag{5.24}$$

The Gibbs free energy G is proportional to the logarithm of the isobaric-isothermal partition function, i.e.

$$G = -k_{\mathrm{B}}T \ln Z_{\mathrm{NPT}} = -k_{\mathrm{B}}T \ln \sum_{r} \sum_{V} \exp(-\beta \ (\mathcal{H}(\Gamma) + PV)) \tag{5.25}$$

From these two main state functions some further useful thermodynamic relations can be derived. For instance, the internal energy U can be written as derivative of the canonical partition function,

$$U = -\frac{\partial \ln Z_{\mathrm{NVT}}}{\partial \beta} \tag{5.26}$$

and the entropy S and pressure P as derivatives of the free energy,

$$\begin{aligned} S &= -\left(\frac{\partial \ln F}{\partial T}\right)_V \\ P &= -\left(\frac{\partial \ln F}{\partial V}\right)_T \end{aligned} \tag{5.27}$$

where V is the volume.

An important theorem that relates the average of the canonical or macrocanonical ensemble (N, V, T) to the average of the microcanonical ensemble (N, V, E) is denoted as the "thermodynamic limit". It states that, if apart from phase transition in the two ensembles, when both the number of particles N and the volume V are increased to infinity, the averages of both ensembles are equal. However, computer simulations can only be are performed for finite-sized systems. The deviation between averages of infinite and finite-sized systems decays with $1/N$, where N is the number of particles being considered.

Chapter 6

Monte Carlo Simulation and Integration

6.1 Introduction and Fundamentals

The various techniques commonly referred to as Monte Carlo methods comprise direct approaches to mimic stochastic events which can be decomposed into isolated processes and statistical approaches to integrate multidimensional definite integrals numerically. Monte Carlo simulations are generally concerned with large series of computer experiments using uncorrelated random numbers (Hammersley and Handscomb 1964; Shreider 1966; Binder 1984; Kalos and Whitlock 1986; Koonin 1986; Binder and Heermann 1988; Allen and Tildesley 1989; Binder 1991a; Yeomans 1992; Pang 1997).

Usually, Monte Carlo models can be dismantled into three characteristic steps (Figure 6.1). In the first step, the physical problem under investigation is translated into an analogous probabilistic or statistical model[1]. In the second step, the probabilistic model is solved by a numerical stochastic sampling experiment including a large number of arithmetical and logical operations. In the third step, the data obtained are analyzed using statistical methods.

Due to the extensive employment of stochastic sampling, the development of the Monte Carlo method was closely connected with the progress in computer technology. The stochastic character of this method requires huge series of uncorrelated random numbers. The validity of this approach is covered by the central limit theorem of probability theory.

Depending on the distribution from which the random numbers are selected for a numerical integration experiment, one can distinguish simple (naive) sampling from importance sampling Monte Carlo methods. The former method (simple sampling) uses an equal distribution of the random numbers. The latter (importance sampling) employs

[1]Probabilistic processes describe situations where the spatial and/or temporal evolution of a system is not unequivocally described by a set of equations transforming one state into another (which would be referred to as a deterministic process) but determined by random or quasi-random processes. Under such conditions the state of a system can only be predicted with a certain probability. It must be noted in this context that the term "random process" does not literally mean that the underlying physical mechanisms are truly random. It only means that it is in models often much more efficient to incorporate certain deterministic processes via a pseudo-stochastic process than to solve exactly the equations of motion of all particles in the system.

Computational Materials Science: The Simulation of Materials, Microstructures and Properties By Dierk Raabe
Copyright © 1998 Wiley-VCH Verlag GmbH
ISBN: 3-527-29541-0

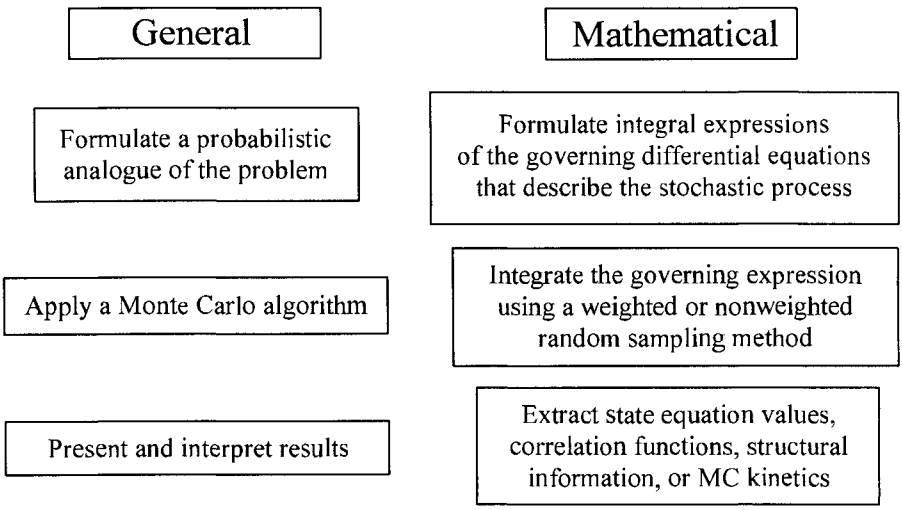

Figure 6.1: Important steps in Monte Carlo modeling.

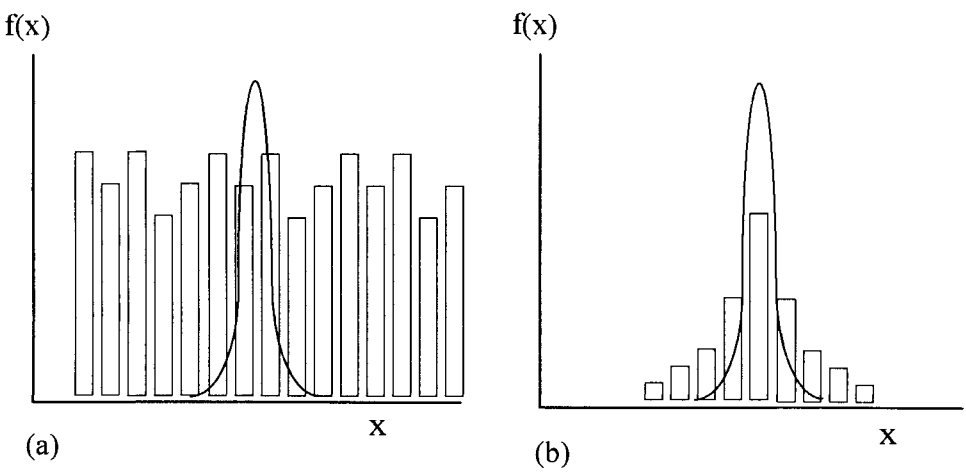

Figure 6.2: Schematic illustration of a nonweighted (a) and a weighted (b) random sampling method. For numerical integration purposes the weighted sampling scheme is much more effective than the nonweighted approach. The columns indicate the weighted frequency of chosen x-values (not the values of the integrand) for which the integrand values are calculated.

Sampling Method
Simple (nonweighted) sampling, importance (weighted) sampling
Lattice Type
cubic, hexagonal, Voronoi, Bethe/Cayley, Kagome, etc.
Spin Model
Ising model, q-state Potts model, lattice gas model, Heisenberg model
Energy Operator
exchange energy, elastic energy, chemical potential, magnetic field, etc.

Figure 6.3: Some criteria to classify Monte Carlo simulation methods.

a distribution which is accommodated to the problem being investigated. Importance sampling thus means that a large weight is used in those regions where the integrand has large values, and a small weight in those regions where it assumes small values.

For instance, in order to integrate effectively a Gauss type decaying symmetric function by stochastic sampling, it is useful to sample integrand values with a large weight around its symmetry center rather than in regions where the function assumes negligible values. Figure 6.2 clearly shows that the nonweighted integration by random sampling requires a much larger number of trials to approximate the true integral than the weighted scheme.

In the field of computational materials science, the simple sampling technique is often employed in percolation models as a nonweighted stochastic integration method. Importance sampling is the underlying principle of the Metropolis Monte Carlo algorithm (Metropolis et al. 1953), which is in the form of the q-state Potts model also widely used in microstructure simulation (Srolovitz 1986; Rollett et al. 1989; Holm et al. 1996).

Monte Carlo simulation methods can be roughly grouped according to the sampling technique employed, the spatial lattice, the spin model, and, connected with that, the quantities that enter the energy operator (Figure 6.3). Of course, other classification schemes are conceivable as well (Potts 1952; Metropolis et al. 1953; Hammersley and Handscomb 1964; Shreider 1966; Wu 1982; Binder 1984; Kalos and Whitlock 1986; Koonin 1986; Allen and Tildesley 1989; Binder and Stauffer 1987; Suzuki 1987; Binder 1991a; Binder 1991b; Heermann and Burkitt 1991; Yeomans 1992).

This chapter addresses the main sampling algorithms (simple sampling and importance sampling), some lattice types (cubic, Bethe, Kagomé, etc.), the main spin or local interaction models and their Hamiltonians (Ising, Potts, lattice gas, Heisenberg), and finally some typical applications and examples in the field of materials science.

6.2 Some Historical Remarks

The first substantial contribution to what one would today denote as the Monte Carlo approach was published by Lord Kelvin (1901), who used this method for a discussion of the Boltzmann equation. The systematic development of the Monte Carlo technique as a simulation tool dates from 1944. During their work on the Manhattan project[2] S. Ulam and J. von Neumann introduced Monte Carlo simulations to mimic the uncorrelated spatial diffusion of neutrons in fissile materials (random walk problem). Independently,

[2]Development and assemblage of the first atomic bombs from 1943 at Los Alamos National Laboratory, New Mexico, USA, under the direction of J. Robert Oppenheimer.

J.E. Mayer suggested a similar numerical method to calculate integrals by use of a non-weighted random sampling procedure. It was especially the novel contribution of these reserachers to realize that determinate problems can be tackled by finding an adequate probabilistic analogue which may then be solved by random walk-type many-particle simulations or by random sampling of adequate integral formulations.

The main idea of solving state function integrals by randomly sampling from a non-uniform distribution of numbers was introduced in the 1950s by N. Metropolis, A.W. Rosenbluth, M.N. Rosenbluth, A.T. Teller, and E. Teller (1953). A similar method was independently suggested by B. Alder, J. Kirkwood, S. Frankel, and V. Lewinson (see comments in the article by Metropolis et al.).

The fact that these techniques are based on the use of random numbers rather than deterministic algorithms possibly led to the name Monte Carlo, indicating the stochastic character of the method. Other sources, however, say that S. Ulam's uncle went each year to Monte Carlo for gambling and so gave the method its name.

6.3 Random Numbers

Monte Carlo methods can be used both to simulate stochastic many-body phenomena and integrate functions by random sampling using large series of uncorrelated random numbers which form a Markov chain. It is clear that the reliability of Monte Carlo predictions is dependent on the randomness of the numbers employed.

In digital computers one can generate random numbers by producing an integer number which exceeds a reserved portion of computer memory and by omitting the leading bits or extracting the middle bits of this integer number. In fact, according to the original idea of Metropolis and von Neumann, all pseudo-random number generators exploit a fixed word length in a digital computer. Following a suggestion of Lehmer (1951), a pseudo-random sequence can be generated through a modulo operation that cuts off the leading bits of a large integer number that requires memory in excess of its reserved word length. This method of generating random numbers is referred to as the congruential method. Mathematically it can be described in terms of the recursive algorithm

$$(a\,R + c)\,\text{modulo}\,n \;\longmapsto\; R \tag{6.1}$$

where R is the random number, n a large integer number, a a multiplier the digits of which should not show a regular pattern, and c a number that should have no nontrivial factor in common with n.

The algorithm is started with a so-called "seed" number R_0 the value of which can be chosen arbitrarily. If the program is run more than once and a different source of random numbers is required each time, it is sensible to set the seed number to the last value attained by R on the preceding program execution or to set it to the current machine time. If one plans to rerun a simulation program with the same random number sequence, one must simply start with the same seed number each time. In the next step R is multiplied by a. The value of a should be chosen in accord with three rules: First, if n is a power of 2, i.e., if a binary computer is used, one should pick a so that a modulo $8 = 5$. Second, a should preferably be chosen between $0.01\,n$ and $0.99\,n$. Third, the digits of a should not display a simple, regular pattern. In the next step one adds a number c to the product of R and a. c should have no factor in common with n. For instance, one may choose $c = 1$ or $c = a$. The number m should be of the order of the word length of the computer, e.g. 2^{30}.

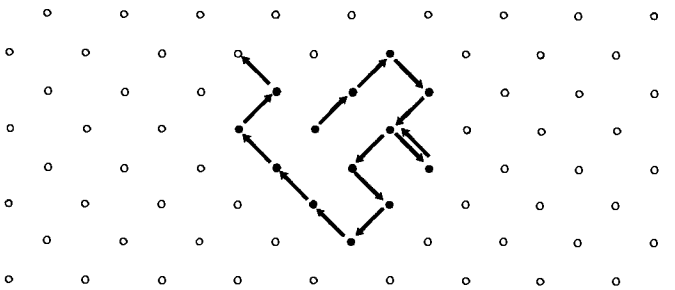

Figure 6.4: Two-dimensional random walk problem.

Random number generators are usually provided by mathematical program libraries. These algorithms, which are mostly based on the method described above, typically provide random numbers that are uniformly distributed in the interval $[0, 1]$. Such a sequence of numbers is referred to as being uniformly distributed in $[0, 1]$ if no subset of the interval contains more than its share of the numbers. This means that the number of elements that fall inside a certain subinterval of $[0, 1]$ should depend only on the size of the subinterval and not on where it is located.

Random numbers provided by digital computer cannot be truly random because the manner in which they are generated is completely deterministic. Stochastic elements are simply simulated by algorithms providing sequences with a large periodicity. For this reason, random numbers produced by computer algorithms are usually referred to as pseudo-random numbers. The periodicity in most pseudo-random sequences generated on machines with a 32-bit word length is of the order of n, i.e. of 2^{30}. This is sufficient for many applications, since the error of Monte Carlo simulations decays in proportion to $n^{-1/2}$, where n is the number of random trials. Another concern is that coordinates in an n-dimensional space, generated by pseudo-random algorithms, often fall onto a relatively small number of hyperplanes. Furthermore, it often observed that certain pairs of two subsequent digits occur more often than expected for a truly random sequence. Improved results can be achieved by combining different random number generators.

More detailed overviews on the generation, use, and portability of pseudo-random numbers where published by Lehmer (1951), Hammersley and Handscomb (1964), Kinderman and Monahan (1977), Schrage (1979), Binder and Stauffer (1987), Binder (1991b), Leva (1992), Press and Teukolsky (1992), Chen and Yang (1994), and Knuth (1997).

6.4 Random Walk Simulation

The earliest computational utilization of Monte Carlo methods was not the numerical approximation of multidimensional integrals but the imitation of stochastic diffusion-type processes which can be decomposed into a number of successive and uncorrelated processes (Figure 6.4). The first example of such topological numerical experiments was the simulation of random walk problems in the field of neutron diffusion by Ulam and von Neumann. Using a Monte Carlo method they simulated the spatial net diffusion of thermal neutrons through the radiation shield around fissile materials by randomly changing their flight direction after each collison event. Cases where such changes in direction can be idealized as mutually uncorrelated events are referred to as "random walk" problems.

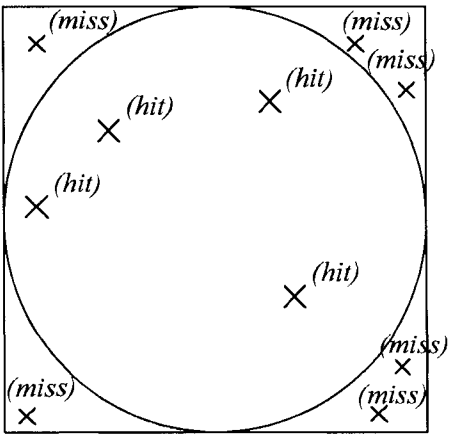

Figure 6.5: Hit-or-miss technique to determine the integral of a circle.

Pure random walk simulations are based on the assumption that the diffusion proceeeds by the succession of purely stochastical single events, i.e. no external or internal fields that may bias the diffusion towards any particular direction, are considered. For instance, the uncorrelated diffusion of an intrinsic vacancy can be described by a random walk. However, advanced spatial Monte Carlo simulations can also describe diffusion processes and percolation problems where the successive events are not uncorrelated and/or where the changes in direction are linked to certain barriers in energy or chemical concentration.

6.5 Hit-or-Miss Random Sampling Integration

The hit-or-miss technique is the oldest and simplest Monte Carlo method for the approximation of definite integrals. Within certain limits, it even works without the use of digital computers. Instead of directly calculating and averaging a large number of integrand values at randomly chosen function arguments (see Section 6.6), the hit-or-miss method proceeds by randomly generating coordinates of arbitrary dimension and investigating whether the corresponding points lie beyond or below a given integrand function. For a large number of shots, the number of hits divided by the sum of all the trial shots approximates the relative value of the integral.

The simple sampling Monte Carlo hit-or-miss procedure can be demonstrated by estimating the relative value of the integral of a circle (Figure 6.5). In a first step, a circle of radius $|\boldsymbol{r}| = 1$ is embedded in a square that extends to $-1 < x < +1$ and $-1 < y < +1$ in such a manner that both areas overlap entirely, i.e. their center coordinates $(0, 0)$ are identical. In a second step, a number of trial shots is generated by choosing pairs of random numbers which are interpreted as coordinates in the field described above. In order to confine the trial shots to the area prescribed by the square, both the x- and the y-coordinates are chosen from a uniform distribution within the range $(-1, +1)$. Third, it is investigated whether the randomly chosen point lies within the circle or not. The relative value of the integral is then calculated by dividing the number of hits, n_{hit}, by

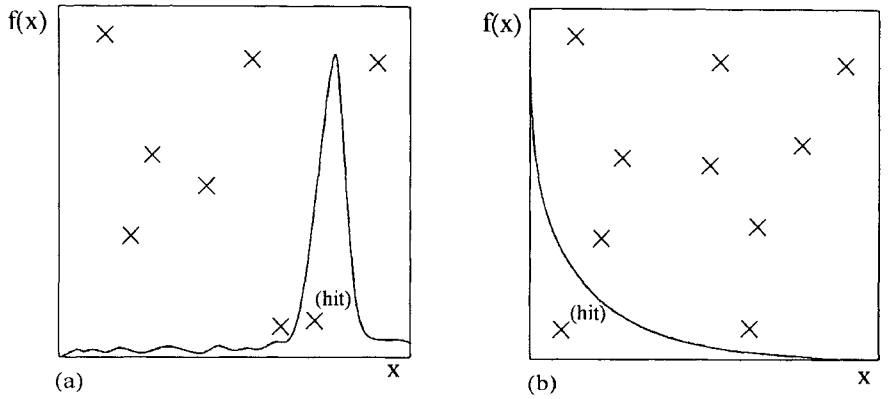

Figure 6.6: Hit-or-miss technique to determine the integral of a delta-type function (a) and of a Boltzmann-type function (b). In both examples the simple sampling hit-or-miss integration method is clearly inefficient.

the number of all trial shots, n_{all}:

$$\frac{\text{area of the circle}}{\text{area of the square}} = \frac{n_{\text{hit}}}{n_{\text{all}}} \tag{6.2}$$

One can reduce the integration time by exploiting the symmetry of the numerical experiment. For instance, in the above example it suffices to select the random x and y trial values only from a quarter of the total area using the uniform interval $(0, 1)$. The relative value of the integral then amounts to

$$\frac{\text{area of the circle}}{\text{area of the square}} = \frac{n'_{\text{hit}}}{n'_{\text{all}}} \tag{6.3}$$

where n'_{hit} and n'_{all} are the number of hits and the number of all trial shots in the reduced area. It is clear that the precision of this numerical approximation depends on the number of trials. Using only two trial shots the relative estimate would amount to 0%, 50%, or 100%, respectively, which is far from the value of $\pi/4 \approx 78.5\%$.

When integrating a more complicated function, the simple sampling hit-and-miss method is evidently impractical (Figure 6.6). For instance, the approximate integration of a delta-type (a) or Boltzmann function (b) is inefficient because one selects random coordinates over the entire region (outer integral) instead of choosing them from the relatively small domain which is of interest (inner integral). In such cases only a very small fraction of the trial shots lies within regions where the function substantially contributes to the integral.

The efficiency of stochastic sampling can thus be improved by choosing random numbers from a domain which has a similar altough not necessarily equal shape to the function to be integrated. This is the basic idea of the importance sampling integration method and will be addressed in Section 6.7.

6.6 Simple or Naive Sampling — Nonweighted Monte Carlo Integration

Provided that a sufficiently large quantity of pseudo-random numbers is involved, the Monte Carlo approach can be efficiently used for the approximation of the values of higher-dimensional definite integrals (Hammersley and Handscomb 1964; Allen and Tildesley 1989). The simple or naive sampling Monte Carlo techniques comprise all integration methods which choose the random numbers from a uniform distribution (Gardiner 1985; Binder and Stauffer 1987).

To start with a simple example let us consider the following one-dimensional definite integration problem

$$\mathfrak{I} = \int_a^b h(x)\,\mathrm{d}x \tag{6.4}$$

A numerical value of this integral can be found by dividing the interval $[a, b]$ evenly into a number of n slices or subintervals with $x_0 = a$ and $x_n = b$ and summing over the corresponding discrete function values. The mean value $\tilde{\mathfrak{I}}$ of the true integral $\mathfrak{I}$ is then

$$\mathfrak{I} \approx \tilde{\mathfrak{I}} = (b-a)\,\frac{1}{n}\sum_{i=1}^{n} h\left(x_i\right) \tag{6.5}$$

As will be shown later (Section 6.11), the statistical error in this numerical approximation of the integral decreases in proportion to $1/\sqrt{n}$, i.e. the deviation between the approximate and the true integral vanishes as n increases to infinity. This means that the value of the integral $\int_a^b h(x)\mathrm{d}x$ can be approximated by the average of the n function values $h(x_1)$, $h(x_2)$,...,$h(x_n)$, provided that n is a very large number. This method is equivalent to approximating the integral by sampling integrand values from a discrete set of n evenly distributed coordinates $x_1, x_2, ..., x_n$ in the region $[a, b]$ with an equal weight at each of these points. This integration method can be referred to as "deterministic sampling".

On the other hand, instead of choosing regular subintervals in the region $[a, b]$, one can sample and average integrand values at m randomly chosen coordinates $x_1, x_2, ..., x_m$, which are selected from a uniform distribution in the interval $[a, b]$, to achieve an equally valid approximation of the integral (Figure 6.7). This method requires a large chain of m uncorrelated random numbers (Markov chain) in the interval being investigated. The corresponding integrand values at these points can be regarded as a set of statistical samples,

$$\mathfrak{I} \approx \tilde{\mathfrak{I}}_{\mathrm{MC}}\,, = (b-a)\,\frac{1}{m}\sum_{j=1}^{m} h\left(x_j\right) \tag{6.6}$$

where $\mathfrak{I}$ is the true value of the integral and $\tilde{\mathfrak{I}}_{\mathrm{MC}}$ its approximation by statistical sampling. In order to achieve a high efficiency of this method it is desirable that $m \ll n$. The validity of this approach, which can be referred to as "random sampling", is covered by the central limit theorem of probability theory. The statistical error in the numerical approximation of the integral by random sampling decays in proportion to $1/\sqrt{m}$. Monte Carlo methods which select the arguments at which the integrand values are calculated from a uniform distribution in the region being investigated are called simple, naive, or nonweighted random sampling methods. The random numerical sampling method is, for

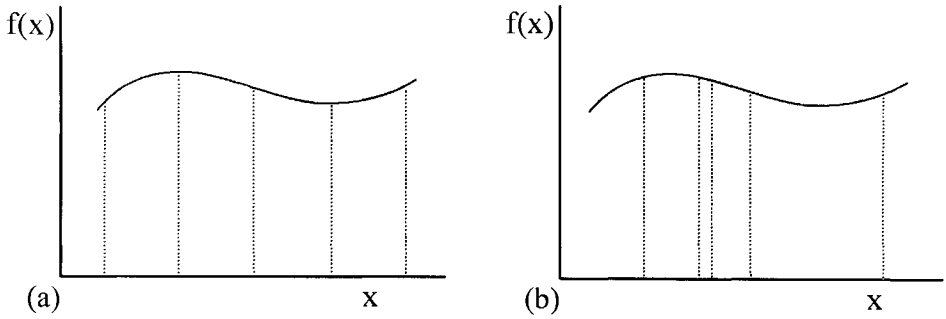

Figure 6.7: Nonweighted numerical integration methods; (a) integration using equally sized subintervals (deterministic sampling); (b) integration using randomly sized subintervals (random or stochastic sampling).

the approxiation of low-dimensional integrals, much less effective compared with classical deterministic methods. For instance the trapezoid rule yields, for a number of m steps, an error of $1/m^2$ which is much better than the error of $1/\sqrt{m}$ which is associated with the Monte Carlo approximation. However, the real advantage of random sampling methods lies in the approximation of higher-dimensional integrals, such as encountered in the field of many-body dynamics and statistical mechanics (see Chapter 5). While the integration error of the Monte Carlo method in higher-dimensional systems will still scale with $1/\sqrt{m}$, the error that is associated with the trapezoid rule yields a magnitude of $1/m^{2/D}$, where D is the dimension.

The concept of integration by random sampling can be easily extended to k-dimensional integrands, e.g.

$$\int_{a_1=0}^{b_1=1}\int_{a_2=0}^{b_2=1}\cdots\int_{a_k=0}^{b_k=1} h(x_1,x_2,...,x_k)\,\mathrm{d}x_1\mathrm{d}x_2...\mathrm{d}x_k \approx \frac{1}{s}\sum_{i=1}^{s} h(x_{1_i},x_{2_i},...,x_{k_i}) \quad (6.7)$$

where $(x_{1_i},x_{2_i},...,x_{k_i}) = \boldsymbol{x}_i$ is the ith out of a set of s uncorrelated sampling vectors, each consisting of k randomly selected and equally weighted components. The vectors represent sample points in the multidimensional body described by the integral.

If the integral is not of length 1 in each dimension but, say, bounded by $[a_1,b_1]$, $[a_2,b_2]$,..., $[a_k,b_k]$, where a_i and b_i can assume any values, then the average of $h(x_{1_i},x_{2_i},$ $...,x_{k_i})$ over s randomly distributed vectors with components in the intervals $[a_1,b_1]$, $[a_2,b_2]$,...,$[a_k,b_k]$ is not simply an approximation for the integral but rather for its value divided by the multidimensional region that it fills, i.e.

$$\frac{1}{s}\sum_{i=1}^{s} h(x_{1_i},x_{2_i},...,x_{k_i}) \approx$$
$$\frac{1}{(b_1-a_1)(b_2-a_2)...(b_k-a_k)}\int_{a_1}^{b_1}\int_{a_2}^{b_2}\cdots\int_{a_k}^{b_k} h(x_1,x_2,...,x_k)\,\mathrm{d}x_1\mathrm{d}x_2...\mathrm{d}x_k \quad (6.8)$$

A typical application of high-dimensional Monte Carlo integration methods lies in the field of atomic-scale many-body simulations, where data of macroscopic relevance must be extracted from a large set of microscopic data by use of statistical mechanics. For

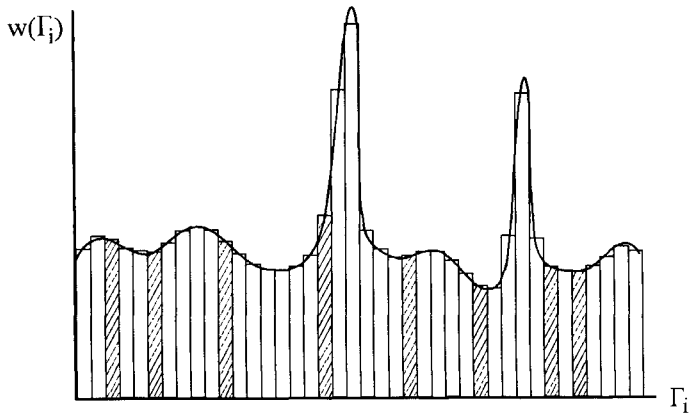

Figure 6.8: Integration of the discretized ensemble probability density function $w_{\text{ens}}(\mathbf{\Gamma}_i)$ using a nonweighted, i.e. simple sampling method. Averages calculated from the marked integrand values will yield a poor approximation of the true integral.

instance, in the case of discrete energies the canonical ensemble average $\langle q \rangle_{\text{NVT}}$ for a property q can be written

$$\langle q \rangle_{\text{NVT}} = \sum_{\mathbf{\Gamma}} \rho_{\text{NVT}}(\mathbf{\Gamma})\ q(\mathbf{\Gamma}) \tag{6.9}$$

where $\mathbf{\Gamma} = \mathbf{r}_1, ..., \mathbf{r}_N, \mathbf{p}_1, ..., \mathbf{p}_N$ is the phase space configuration or point in phase space and the operator $\rho_{\text{NVT}}(\mathbf{\Gamma})$ the canonical probability or phase space distribution function (Chapter 5). This equation can be rewritten in terms of the canonical probability density $w_{\text{NVT}}(\mathbf{\Gamma})$,

$$\langle q \rangle_{\text{NVT}} = \frac{\sum_{\mathbf{\Gamma}} w(\mathbf{\Gamma})\ q(\mathbf{\Gamma})}{\sum_{\mathbf{\Gamma}} w(\mathbf{\Gamma})} \tag{6.10}$$

Reformulating this equation for a Monte Carlo integration using a number of s discrete sampling vectors $\mathbf{\Gamma}_i$ leads to

$$\langle q \rangle_{\text{NVT}} \approx \langle q \rangle_{\text{MC}} = \frac{\sum_{i=1}^{s} w(\mathbf{\Gamma}_i)\ q(\mathbf{\Gamma}_i)}{\sum_{i=1}^{s} w(\mathbf{\Gamma}_i)} = \frac{\sum_{i=1}^{s} \exp(-\beta\, \mathcal{H}(\mathbf{\Gamma}_i))\ q(\mathbf{\Gamma}_i)}{\sum_{i=1}^{s} \exp(-\beta\, \mathcal{H}(\mathbf{\Gamma}_i))} \tag{6.11}$$

where $\beta = 1/k_{\text{B}}T$, $\mathcal{H}$ the system Hamiltonian, and $\langle q \rangle_{\text{MC}}$ the Monte Carlo approximation for the true value of $\langle q \rangle_{\text{NVT}}$.

Figure 6.8 shows that the random sampling method can be inefficient in cases where the integrand is not a smooth function in phase space. The integrand, which is in this example the discretized probability density function $w_{\text{NVT}}(\mathbf{\Gamma}_i)$, has some peaks, which are in part not detected by the random sampling procedure (marked slices). Generalizing this example means that the simple or naive sampling method will be inefficient in cases where certain local values of the ensemble weight factor $w_{\text{ens}}(\mathbf{\Gamma}_j) / \sum_i^s w_{\text{ens}}(\mathbf{\Gamma}_i)$ taken at coordinates $\mathbf{\Gamma}_j$, substantially deviate from the average value. This is particularly the case in statistical mechanics, where the canonical Boltzmann density function $w_{\text{ens}}(\mathbf{\Gamma}) = \exp(-\beta\, \mathcal{H}(\mathbf{\Gamma}))$ is very small in most regions of the configuration space. The elimination of this shortcoming through the introduction of the weighted random sampling method is the topic of the next section.

6.7 Importance Sampling — Weighted Monte Carlo Integration

Most average quantities that describe the state of many-body systems can be expressed in integral form (Chapter 5). For choosing adequate integration methods some properties of such averages should be considered. First, the averages are multidimensional integrals since they depend on the independent coordinates and momentum vectors of N particles ($6N$ variables for an atomic gas). Second, the integrands can vary by several orders of magnitude, as is evident from the Boltzmann term in the partition function. This means that some configurations make large contributions to the integrals while other configurations are of negligible importance. Third, the chosen method should generally allow one to integrate steep, e.g. delta-type, functions, as encountered for instance in the phase space density of the microcanonical ensemble.

Conventional numerical integration methods under such conditions are often neither sufficiently fast nor precise. Even the simple sampling Monte Carlo integration method discussed above, which uses a limited number of uniformly distributed integrand values, is not sufficient in such cases since it has difficulties in correctly integrating the phase density function with its extreme variations. On the other hand, one should consider that the integration by sampling is very efficient at integrating smooth functions. For instance, if the integrand is a constant, one only needs one single point to have the exact value of the integral from the simple sampling integration. Similar considerations apply if the function to be integrated is smooth and close to a constant, so that a good approximation can be found with only a small number of sampled integrand values.

This idea of turning an arbitrarily steep integrand function into a very smooth function and adjusting the integration interval is the main background of the importance sampling approach. In other words, the extension of the simple or naive sampling to the importance sampling method introduces the main improvement of using weighted integrands. This means that the selected pseudo-random numbers are chosen from a non-uniform distribution. This procedure allows one to concentrate the function evaluation in regions of space that make relevant contributions to the integral (Metropolis et al. 1953).

The introduction of a weighting function $g(x)$ for the estimation of an integral $\mathfrak{I}$ can be written

$$\mathfrak{I} = \int_a^b h(x)\,\mathrm{d}x = \int_a^b \left[\frac{h(x)}{w(x)}\right] w(x)\,\mathrm{d}x \tag{6.12}$$

If one now changes variables from x to, say, $y(x)$

$$y(x) = \int_0^x g(x')\,\mathrm{d}x' \tag{6.13}$$

the integral turns into

$$\mathfrak{I} = \int_{y(x=a)}^{y(x=b)} \frac{h\left(y(x)\right)}{g\left(y(x)\right)}\,\mathrm{d}y \tag{6.14}$$

The Monte Carlo approximation of this integral then proceeds as above, namely by averaging the discrete values of $h\left(y(x)\right)/g\left(y(x)\right)$ at a random sampling of n points uniformly distributed in y over the interval $[a, b]$

$$\tilde{\mathfrak{I}} \approx \left(y\left(x=b\right) - y\left(x=a\right)\right) \frac{1}{n} \sum_{i=1}^{n} \frac{h\left(y(x)_i\right)}{g\left(y(x)_i\right)} \tag{6.15}$$

The introduction of a weighting function into the Monte Carlo method can be clarified in terms of a simple analytical example: The integral $\mathfrak{I}$ of a function $h(x)$ between a and b can be written

$$\mathfrak{I} = \int_a^b h(x)\,\mathrm{d}x \tag{6.16}$$

Assuming $h(x) = \exp(-x/2)$, equation (6.16) amounts to

$$\mathfrak{I} = \int_a^b \exp\left(-\frac{x}{2}\right)\mathrm{d}x \tag{6.17}$$

At first, a second function $g(x)$ must be found that has a similar course to the original function $h(x)$ in the region considered, i.e. $h(x) \approx g(x)$. In the example the exponential function $\exp(-x/2)$ can be approximated by a series expansion of the form $1-x/2+x^2/2-x^3/6+\ldots \approx 1-x/2$. Considering the interval $[a=0, b=1]$ and using the substitutional function $g(x) = 1 - x/2$ the original integral can be rewritten

$$\mathfrak{I} = \int_a^b \frac{h(x)}{g(x)}\,g(x)\,\mathrm{d}x = \int_{y(x=a)}^{y(x=b)} \frac{h(y)}{w(y)}\,\mathrm{d}y = \int_{y(x=a)}^{y(x=b)} \frac{\exp\left(-\frac{x}{2}\right)}{1-\frac{x}{2}}\,\mathrm{d}y \tag{6.18}$$

Using

$$y(x) = \int_0^x g(x')\,\mathrm{d}x' = \int_0^x \left(1-\frac{x'}{2}\right)\mathrm{d}x' = x - \frac{x^2}{4} \tag{6.19}$$

and

$$x = 2\left(1+\sqrt{1-y}\right) \tag{6.20}$$

The original integral can can then be rewritten

$$\mathfrak{I} = \int_{x=0}^{x=1} \exp\left(-\frac{x}{2}\right)\,\mathrm{d}x = \int_{y=0}^{y=3/4} \frac{\exp\left(-\left(1+\sqrt{1-y}\right)\right)}{\sqrt{1-y}}\mathrm{d}y \tag{6.21}$$

This example shows that the substitution of the variables modifies the integration boundaries and also the form of the integrand. Thus, instead of selecting random values for x that are equally distributed between a and b and using them for the simple sampling Monte Carlo integration of the original function $h(x)$, one selects equally distributed random numbers for y and integrates the weighted function $h(x)/g(x)$. In cases where these values of y are well distributed one thus encounters the relatively simple task of integrating a function $h(x)/g(x)$ which is close to one.

In the following sections the Metropolis Monte Carlo method which is based on using weighting functions for state function will be explained for canonical ensembles with constant chemical composition and for grandcanonical ensembles with variable chemical composition. The weighting function in these classical cases usually assumes a Boltzmann-type form. This reflects the fact that the probability distribution of non-quantum particles is exponentially dependent on their energy. Furthermore, various applications of the Metropolis algorithm will be discussed. In recent years various advanced Metropolis-type methods have been proposed. Among these, especially the Monte Carlo algorithm in conjunction with atomic potentials (Bacher et al. 1992) and the so-called inverse Monte Carlo method (Livet 1987; Desplat et al. 1996) are increasingly gaining momentum.

6.8 The Metropolis Monte Carlo Method

6.8.1 Fundamentals of the Algorithm

The Metropolis Monte Carlo algorithm is a weighted, i.e. an importance random sampling method for generating states of a system in a particular statistical ensemble which is characterized by its limiting probability distribution in thermal equilibrium $\rho_{\text{ens}}(\mathbf{\Gamma})$ (see Chapter 5). In systems with constant chemical composition (canonical, microcanonical, and isothermal-isobaric ensembles) the probability distribution is a function of the system Hamiltonian. In systems with variable chemical composition (grandcanonical ensembles) it is a function of the chemical potential.

The thermodynamic state of a system of N classical particles can be characterized in terms of the three components of the position vectors $\mathbf{r}_1, ..., \mathbf{r}_N$ and by the three components of the particle momentum vectors $\mathbf{p}_1, ..., \mathbf{p}_N$. These $6\,N$ components can be regarded as the components of a vector $\mathbf{\Gamma}$ in a $6\,N$-dimensional phase space.

Two ensemble states $\mathbf{\Gamma}_i$ and $\mathbf{\Gamma}_j$ are linked by a transition probability π_{ij} which quantifies the probability that the system will move from state i to state j. The value of the probability density function for the ith state of a system is given by $\rho_{\text{ens}}(\mathbf{\Gamma}_i)$ and that of the jth state by $\rho_{\text{ens}}(\mathbf{\Gamma}_j)$. The Metropolis Monte Carlo solution for the components of this transition matrix $\boldsymbol{\pi}$ is

$$\pi_{ij} = \begin{cases} \alpha_{ij} & \text{if} \quad \rho_{\text{ens}}(\mathbf{\Gamma}_j) \geq \rho_{\text{ens}}(\mathbf{\Gamma}_i) \qquad i \neq j \\ \alpha_{ij}\left(\rho_{\text{ens}}(\mathbf{\Gamma}_j)/\rho_{\text{ens}}(\mathbf{\Gamma}_i)\right) & \text{if} \quad \rho_{\text{ens}}(\mathbf{\Gamma}_j) < \rho_{\text{ens}}(\mathbf{\Gamma}_i) \qquad i \neq j \\ 1 - \sum_{i \neq j} \pi_{ij} & \text{if} \quad \rho_{\text{ens}}(\mathbf{\Gamma}_j) = \rho_{\text{ens}}(\mathbf{\Gamma}_i) \qquad i = j \end{cases} \tag{6.22}$$

where $\boldsymbol{\alpha}$ is the symmetrical and stochastic matrix of the Markov chain. The rule for calculating the components of $\boldsymbol{\pi}$ for cases where $\rho_{\text{ens}}(\mathbf{\Gamma}_j) < \rho_{\text{ens}}(\mathbf{\Gamma}_i)$ shows that the Metropolis algorithm only requires the knowledge of the ratio $\rho_{\text{ens}}(\mathbf{\Gamma}_j)$ / $\rho_{\text{ens}}(\mathbf{\Gamma}_i)$ and does not require the knowledge of ensemble partition function Z_{NVT} (see Chapter 5). Using the symmetry properties of the matrix α one can show that

$$\sum_j \pi_{ij} = 1 \tag{6.23}$$

and

$$\rho_{\text{ens}}(\mathbf{\Gamma}_i)\,\pi_{ij} = \rho_{\text{ens}}(\mathbf{\Gamma}_j)\,\pi_{ji} \tag{6.24}$$

Equation (6.23) essentially reflects that each state $\mathbf{\Gamma}_i$ must exist somewhere in phase space. Equation (6.24) represents the principle of microscopic reversibility. It can be used to demonstrate that the limiting distribution of the Markov chain is the probability density distribution function $\rho_{\text{ens}}(\mathbf{\Gamma})$.

The Metropolis algorithm proceeds by randomly or systematically choosing a new trial state $\mathbf{\Gamma}_j$, sampling the stochastic matrix according to

$$\alpha = \frac{1}{\mathcal{N}} \tag{6.25}$$

where $\mathcal{N}$ is the number of possible particle positions, and evaluating the configurational energy change according to the ratio $\rho_{\text{ens}}(\mathbf{\Gamma}_j)$ / $\rho_{\text{ens}}(\mathbf{\Gamma}_i)$ of the probability densities $\rho_{\text{ens}}(\mathbf{\Gamma}_j)$ and $\rho_{\text{ens}}(\mathbf{\Gamma}_i)$. The next two sections demonstrate how the Metropolis solution to the transition matrix is usually identified for ensembles with constant or variable chemical composition.

6.8.2 The Metropolis Method for Canonical and Microcanonical Ensembles

In the Metropolis Monte Carlo approach each of the N ensemble atoms is assigned an initial position. Subsequently, the Hamiltonian for this configuration is calculated. The reconfiguration of this starting system depends on the prescribed macroscopical values. In canonical and microcanonical systems the number of the elementary constituents is prescribed.

In Monte Carlo models with variable particle positions one hypothesizes a new configuration by arbitrarily or systematically choosing one atom located at, i say, and proposing that it be moved to a temporary trial position, j say. The move is indicated by $i \rightarrow j$. It brings the system from point $\mathbf{\Gamma}_i$ to point $\mathbf{\Gamma}_j$ in phase space. Depending on the particular particle interaction being considered the displacement will change the system energy from $\mathcal{H}(\mathbf{\Gamma}_i)$ to $\mathcal{H}(\mathbf{\Gamma}_j)$. However, such an arbitrary displacement of an atom does not affect the composition of the system.

The move is accepted with a certain probability. In canonical and microcanonical ensembles one computes the change in the system Hamiltonian $\Delta\mathcal{H}(\mathbf{\Gamma}_{i\rightarrow j})$ that is associated with the new configuration[3],

$$\Delta\mathcal{H}(\mathbf{\Gamma}_{i\rightarrow j}) = \mathcal{H}(\mathbf{\Gamma}_j) - \mathcal{H}(\mathbf{\Gamma}_i) \tag{6.26}$$

where $\mathcal{H}(\mathbf{\Gamma}_j)$ is the Hamiltonian associated with the trial state and $\mathcal{H}(\mathbf{\Gamma}_i)$ the Hamiltonian associated with the originial state. This new atomic arrangement is then evaluated according to the following rules.

If the new energy value is *smaller* than the preceding one, the move would bring the system to a state of lower energy. Hence, the move is immediately accepted and the displaced particle remains in its new position.

However, if the new energy value *exceeds* the preceding one, the move is accepted only with a certain probability $(\rho_{\text{ens}}(\mathbf{\Gamma}_j)/\rho_{\text{ens}}(\mathbf{\Gamma}_i))$ which is in canonical systems described by a Boltzmann factor (Chapter 5).

$$(\rho_{\text{ens}}(\mathbf{\Gamma}_j)/\rho_{\text{ens}}(\mathbf{\Gamma}_i)) = \exp(-\beta\,\Delta\mathcal{H}(\mathbf{\Gamma}_{i\rightarrow j})) \tag{6.27}$$

where β is $1/(k_{\text{B}}\,T)$. The probability of accepting the configurational change for a positive value of $\Delta\mathcal{H}(\mathbf{\Gamma}_{i\rightarrow j})$ is then proportional to

$$p_{i\rightarrow j} \propto \exp(-\beta\,\Delta\mathcal{H}(\mathbf{\Gamma}_{i\rightarrow j})) \tag{6.28}$$

According to Metropolis et al. (1953) one now generates a random number ξ between 0 and 1 and determines the new configuration according to the following rule:

$$\xi \begin{cases} \leq \exp(-\beta\,\Delta\mathcal{H}(\mathbf{\Gamma}_{i\rightarrow j})) : & \text{the move is accepted} \\ > \exp(-\beta\,\Delta\mathcal{H}(\mathbf{\Gamma}_{i\rightarrow j})) : & \text{the move is not accepted} \end{cases} \tag{6.29}$$

If the new configuration is rejected one counts the original position as a new one and repeats the process by using some other arbitrarily chosen atom.

[3]In an alloy it is not required to calculate the entire internal energy of the new configuration but only the new value of the mixing energy.

6.8.3 The Metropolis Method for Grandcanonical Ensembles

In grandcanonical ensembles the concentration of the elementary constituents is not prescribed. One hypothesizes a new configuration j by arbitrarily choosing one atom and proposing that it be exchanged by an atom of a different kind. This procedure affects the chemical composition of the system.

Again, the move is accepted with a certain probability. In a grandcanonical ensemble one computes the energy change $\Delta U(\mathbf{\Gamma}_{i\to j})$ that is associated with the change in composition. The new configuration is evaluated according to the following criteria: If the new energy value is smaller than the preceding one, the move is accepted. However, if the new energy value exceeds the preceding one, the move is accepted with a certain probability.

The probability of accepting the compositional change in a grandcanonical ensemble is for a positive value of $\Delta U(\mathbf{\Gamma}_{i\to j})$ proportional to

$$p_{i\to j} \propto \exp\left(-\beta\, \Delta U(\mathbf{\Gamma}_{i\to j})\right) \tag{6.30}$$

where ΔU is the change in the sum of the mixing energy and the chemical potential of the mixture. The decision about which configuration is accepted is then made according to equation (6.22). If the new configuration is rejected one counts the original position as a new one and repeats the process by using some other arbitrarily or systematically chosen atom.

6.9 Spin Monte Carlo Models

6.9.1 Introduction

Models in which the degrees of freedom reside on a discrete spatial lattice and interact locally arise in several areas of solid-state physics and materials science. The energy variation in such approaches typically occurs by the flip of particle spins rather than by the displacment and/or exchange of particles. They are of great value in predicting the cooperative behavior of many-body systems by assigning particles with specific properties to the lattice sites (Figure 6.9).

The simplest of these models is the $\frac{1}{2}$ spin Ising model, which can be regarded as a crude approximation of a magnetic material or a binary alloy. The q-state Potts model represents a generalized or multispin version of the original Ising model where the spins can represent more or less arbitrary properties. Simulation on the basis of the Potts spin model are of particular relevance in the field of mesoscale computational materials science (Chapter 12). Further models that are important are the lattice gas and the Heisenberg approach. Related approaches which are of particular relevance in computational materials science are the molecular field approximation (MFA), the cluster variation method (CVM), and the Bragg–Williams–Gorsky (BWG) models.

The evolution and the thermodynamic properties of these spin lattice models are usually calculated by randomly flipping the spins of particles that reside at arbitrary lattice sites and weighting the resulting energy changes using a Metropolis Monte Carlo sampling approach.

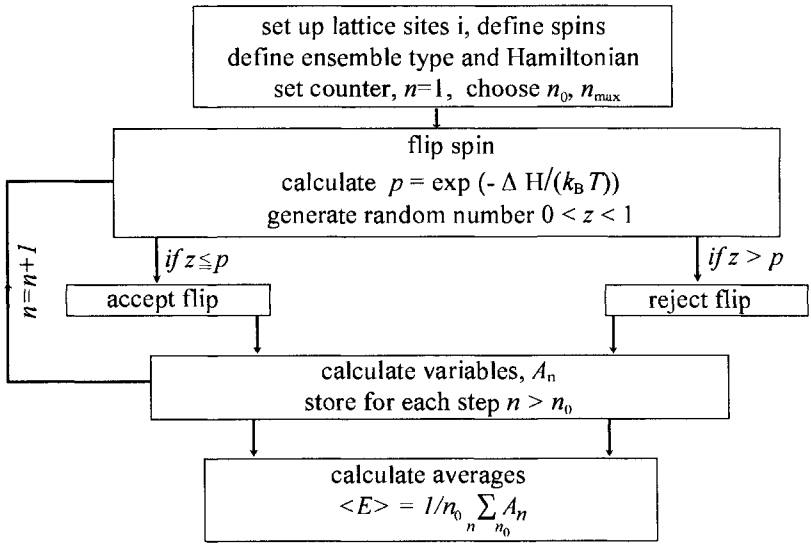

Figure 6.9: Flowchart illustrating the basic steps in a Monte Carlo simulation for simple spin models. The energy variation in such approaches typically occurs by the flip of particle spins rather than by the displacment and/or exchange of particles. The system takes n_0 steps to reach equilibrium. The total number of steps is n_{max}.

6.9.2 $\frac{1}{2}$ Spin Ising Model

In an $\frac{1}{2}$ spin Ising lattice model the internal system energy is calculated as the sum of pair-interaction energies between the atoms or molecules that are attached to the nodes of a regular lattice (Huang 1963; Binder 1984; Koonin 1986; Binder 1991a; Yeomans 1992). If one translates that into magnetic language, the Ising model consists of a discrete set of spin degrees of freedom interacting with each other and with an external magnetic field.

The original Ising model was confined to the consideration of nearest-neighbor interactions. However, the extension of this concept to including additional interactions with the next-nearest neighbors is straightforward (see Figure 11.2). Ising models which consider such long-range interactions are sometimes referred to as extended Ising models.

The original Ising model is a pertinent means of studying ferromagnetic ordering of the elementary magnetic moments in solids. The spin variable S_i defined at each lattice point i may assume two different states, namely "spin up", $S_i = +1$, or "spin down", $S_i = -1$. This mimics the spin $\frac{1}{2}$ situation, although the spins are taken to be classical degrees of freedom and do not impose the angular momentum commutation rules characteristic of a quantum description. The extension of the Ising model to a true quantum approach is realized in the Heisenberg model (Section 6.9.3). Since the spin on each lattice site can assume only two values, the Ising model lends itself very well to studying atomic configurations of a binary alloy in a periodic structure. The spin is then a representation of the occupation of a particular lattice site (Trohidou and Blackman 1990; Ferrenberg and Landau 1991; Wansleben and Landau 1991; Zhang and Yang 1993; Wang and Young 1993; Heuer 1993; Hasenbusch and Pinn 1994; Andersson et al. 1994; Wingert and Stauffer 1995; Gu et al. 1996; Scholten and Kaufman 1997; Schur and Blote 1997)

For a classical Ising ensemble for ferromagnetic ordering, the Hamiltonian derived from the interaction energies between nearest neighbors can be written

$$\mathcal{H}_{\text{Ising}} = -J \sum_{\langle i,j \rangle} S_i\, S_j \; - B \sum_i S_i \; , \qquad S_i = \pm 1 \tag{6.31}$$

where J is the effective interaction energy, B some intensive[4] thermodynamic field variable, e.g. the magnetic field, $\langle i,j \rangle$ the sum over nearest-neighbor pairs, and S_i the spin variable that points in the direction of the local magnetic moment at lattice site i.

For a ternary metallurgical Ising system with the constituents A, B, and C the Hamiltonian $\mathcal{H}_{ABC}$ can be written

$$\begin{aligned}\mathcal{H}_{ABC} = \sum_n \frac{1}{2}\{ & N_{AB}^k \left(2V_{AB}^k - V_{AA}^k - V_{BB}^k\right) + \\ & N_{AC}^k \left(2V_{AC}^k - V_{AA}^k - V_{CC}^k\right) + N_{BC}^k \left(2V_{BC}^k - V_{BB}^k - V_{CC}^k\right)\} + \\ & N_A \left(\sum_k V_{AA}^k \frac{z^k}{2}\right) + N_B \left(\sum_k V_{BB}^k \frac{z^k}{2}\right) + N_C \left(\sum_k V_{CC}^k \frac{z^k}{2}\right)\end{aligned} \tag{6.32}$$

where N_{AB}^k is the number of AB pairs in the sphere k (e.g. NN or NNN), and V_{ij} the respective interaction energy between two constituents i and j. The total number of atoms of one type, say A, amounts to

$$N_A = \frac{1}{z^k}\left(2N_{AA} + N_{AB}^k + N_{AC}^k\right) \tag{6.33}$$

where z^k is the coordination number of sphere k. From equation (6.32) the mixing energy of a ternary alloy can be calculated.

6.9.3 Heisenberg Spin Model

The Ising model is restricted to applications where the spin vector can only lie parallel or antiparallel to the direction of quantization introduced by the magnetic field. This implies that the Hamiltonian of an Ising model can only prove useful in describing a magnet which is highly anisotropic in spin space.

However, in real systems, fluctuation of the spin away from the axis of quantization must inevitably occur to some degree. An appropriate Hamiltonian suggested by Heisenberg amounts to

$$\mathcal{H}_{\text{Heis}} = -J_{\parallel} \sum_{\langle i,j \rangle} S_i^{x_3}\, S_j^{x_3} \; - J_{\perp} \sum_{\langle i,j \rangle} \left(S_i^{x_1}\, S_j^{x_1} \; + S_i^{x_2}\, S_j^{x_2}\right) - B \sum_i S_i^{x_3} \; , \quad S_i = \pm 1 \tag{6.34}$$

where x_1, x_2, and x_3 are Cartesian axes in spin space, J_i the anisotropic interaction energy, and B the external field. For $J_{\perp} = 0$ one regains the classical Ising model, equation (6.31). The most fundamental difference between the Heisenberg model and the Ising model is that for the former the spin operators do not commute. Thus, the Heisenberg model can be regarded as a quantum mechanical rather than a classical spin model.

[4]Independent of the volume.

6.9.4 Lattice Gas Spin Model

The original lattice gas spin approach is a model where the sites of a regular lattice can be vacant or occupied by an atom or molecule.

A variable, say $t_i = 1, 0$, is used to indicate whether the site is occupied or unoccupied. The Hamiltonian can then be written

$$\mathcal{H}_{\text{gas}} = -J_{\text{int}} \sum_{\langle i,j \rangle} t_i t_j - \mu_{\text{int}} \sum_i t_i \,, \qquad t_i = 0, 1 \tag{6.35}$$

where J_{int} is the nearest-neighbor interaction energy, which favors neighboring sites being occupied, and μ_{int} the chemical potential which controls the number of atoms at each site. Since the lattice gas Hamiltonian represents an ordinary two-state operator, it can be transformed into a conventional Ising model.

6.9.5 q-State Potts Spin Model

The q-state Potts spin model is of particular relevance in the field of mesoscale prediction of transformation phenomena. A more detailed discussion is therefore given in Part III on micro–mesoscale simulation techniques (Chapter 12).

The basic idea of the Potts model consists in replacing the binary spin variable as used in the Ising model by a generalized variable S_i which can assume one out of q possible states, and by accounting only for the interaction between dissimilar neighbors. The Hamiltonian can thus be written

$$\mathcal{H}_{\text{Potts}} = -J_{\text{int}} \sum_{\langle i,j \rangle} \left(\delta_{S_i S_j} - 1 \right) \,, \qquad S_i = 1, 2, ..., q \tag{6.36}$$

The delta-type Hamiltonian has a vanishing exchange interaction energy between neighboring sites with identical spins and nonvanishing exchange interaction between sites with unlike spins.

6.9.6 Ising-Related Spin Models — the MFA, CVM, and BWG Models

The numerical prediction of basic metallurgical thermodynamics, i.e. of phase diagrams, increasingly concentrates on the use of microscopical methods. Among these, the Ising and Potts spin models, discussed above, are especially of relevance. They are usually solved using Monte Carlo algorithms.

In addition to these classical methods some related models have more recently been suggested, viz. the Bragg–Williams–Gorsky (BWG) model, the molecular field approximation (MFA), and the cluster variation method (CVM). In contrast to the Ising and Potts models they are typically solved by linear iteration methods or by using the Newton–Raphson algorithm.

Both the MFA and the CVM[5] are based on Ising- or Potts-type arrangements considering first or first and next-nearest neighbors (Brout 1965; Smart 1966; Bennett 1986; Inden 1974; Kikuchi 1974; Ceder et al. 1989; Schön and Inden 1996). The solution of MFA and CVM models is not usually obtained by using the importance sampling technique but by the so-called natural iteration method (NIM) (Inden 1974; Kikuchi 1974).

[5]The BWG model is a point approximation in a hierarchy of the CVM (Ackermann et al. 1989).

For an Ising ferromagnet, equation (6.31), the free energy can be found from the minimum of the functional

$$F = U - TS_c = \sum_{S_i=\pm 1} \mathcal{H}_{\text{Ising}}(\langle S_i \rangle)\ P(\langle S_i \rangle) + k_B T \sum_{S_i=\pm 1} P(\langle S_i \rangle) \ln P(\langle S_i \rangle) \quad (6.37)$$

where U is the internal energy, S_c the configurational entropy, and $P(\langle S_i \rangle)$ the probability that a particular configuration $\langle S_i \rangle$ occurs. Minimizing equation (6.37) with respect to P leads to the canonical distribution

$$P_e(\langle S_i \rangle) \propto \exp\left(-\frac{\mathcal{H}_{\text{Ising}}(\langle S_i \rangle)}{k_B T}\right) \quad (6.38)$$

The MFA method is now defined by factorizing the probability $P(\langle S_i \rangle)$ of a spin configuration of the entire lattice into a product containing single-site probabilities P_i. In a ferromagnetic Ising-type system these can assume only two states, namely, $P_i(+) = (1+M)/2$, or $P_i(-) = (1-M)/2$. $P_i(+)$ is the probability that at site i the spin is up and $P_i(-)$ that it is down. The magnetization is calculated by $M = P(+) - P(-)$. Summing the contributions to the Ising Hamiltonian, equation (6.31), over all possible values of $P_i(+)$ and $P_i(-)$, i.e. $J_{ij} S_i S_j P_i P_j$, yields $J_{ij} M^2$ which reduces the expression for the Helmholtz free energy, equation (6.37), to a quadratic function of the magnetization. A minimization of this free energy function leads to an expression describing a second-order phase transition at the Curie temperature T_c.

The factorization of the configuration probability $P(\langle S_i \rangle)$ into single-site probabilities $P_i(+)$ and $P_i(-)$ does not consider the possible correlation in the probabilities of different sites. The cluster variation method (CVM) improves the uncorrelated MFA concept by approximating the configuration probability $P(\langle S_i \rangle)$ by cluster rather than single-site probabilities (Khachaturyan 1983; Binder and Stauffer 1987).

Cluster-type correlated probabilities $P_{nc}(k,i)$ describe the probability that at a lattice site i a particular spin configuration k occurs that includes n spins in a cluster of geometric configuration c. The cluster geometry c may simply include one particular nearest neighbor, a triangle, or a tetrahedron, etc. The spin configuration variable k amounts to $k_{\text{Ising}} = 1, ..., 2^n$ in the case of the Ising ferromagnet $k_{\text{Pott}} = 1, ..., Q^n$ for the q-state Potts model. It is worth noting that the CVM, when based on the Potts model, is similar to the probabilistic cellular automaton technique. On the basis of the correlated probabilities $P_{nc}(k,i)$ a Helmholtz free energy expression similar to equation (6.37) is derived which can be used to simulate phase transition phenomena (Inden 1974; Khachaturyan 1983; Ackermann et al. 1986; Ackermann et al. 1989; Binder 1991c) and the magnetic specific heat capacity (Schön and Inden 1996).

6.10 Lattice Types

Figure 6.10 shows some typical spatial lattices that are frequently used in Monte Carlo, cellular automaton (Chapter 11), and percolation simulations (Appendix). Particularly in simulations which account for local interactions among neighbors, the type of lattice employed can have a substantial influence on the predictions.

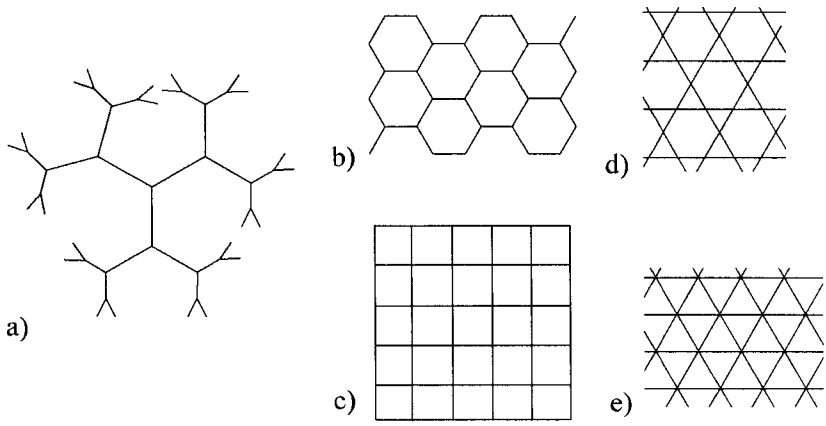

Figure 6.10: Some regular spatial lattices used in Monte Carlo, cellular automaton, and percolation simulations. (a) Bethe/Cayley lattice (coordination number $k = 3$) (lattice without closed circuits; all sites except those on the perimeter have the same number of neighbors); (b) honeycomb lattice ($k = 3$); (c) square lattice ($k = 4$); (d) Kagomé lattice ($k = 4$); (e) triangular lattice ($k = 6$).

6.11 Errors of Monte Carlo Methods

The main errors that can occur in Monte Carlo approximations may arise from the random number generator and from statistics. Random numbers that are provided by digital computers are not truly uncorrelated but can show periodic behavior. It is therefore useful to check the periodicity of such sequences before employing them massively.

The statistical uncertainty associated with numerical Monte Carlo experiments can be discussed in terms of the central limit theorem for large numbers. Considering the original integral $\mathfrak{I}$ in the interval $[0, 1]$

$$\mathfrak{I} = \int_0^1 h(x)\,\mathrm{d}x \tag{6.39}$$

and its stochastic quadrature approximation

$$\tilde{\mathfrak{I}} \approx \frac{1}{n}\sum_{i=1}^{n} h(x_i) \tag{6.40}$$

one obtains by conventional statistics

$$\sigma_{\mathfrak{I}}^2 \approx \frac{1}{n}\sigma_h^2 = \frac{1}{n}\left[\frac{1}{n}\sum_{i=1}^{n} h(x_i)^2 - \left(\frac{1}{n}\sum_{i=1}^{n} h(x_i)\right)^2\right] \tag{6.41}$$

where σ_h^2 is the variance in h, i.e. a measure of the extent to which h deviates from its average value over the region of integration. This formula reveals two very important statistical aspects of Monte Carlo approximations. First, the error decreases as $n^{-1/2}$.

Second, the precision of the approximation increases with decreasing σ_h^2. This means that the best stochastic quadrature is achieved when the function is as smooth as possible.

Monte Carlo integration methods are for the approxiation of low-dimensional integrals much less effective when compared with classical deterministic methods. For example, the trapezoid quadrature yields for n steps an error of $1/n^2$. This result is better than the error of $n^{-1/2}$ which is associated with the Monte Carlo approximation. However, the main advantage of the Monte Carlo integration method lies in the approximation of higher-dimensional integrals (see Chapter 5). While the integration error of the Monte Carlo method in higher-dimensional systems will still scale with $n^{-1/2}$, the error associated with the trapezoid method yields an error of $1/n^{2/D}$, where D is the dimension.

6.12 Application of the Monte Carlo Method in Materials Science

This section gives a number of classical or recently published references on applications of Monte Carlo simulations related to various domains of materials science. Of course, the list can by no means be complete but it may serve as a bibliography for getting more acquainted with some examples of the recent original literature in this field. The examples listed are mainly about surface and interface phenomena, diffusion, phase transformation, polymers, epitaxial growth and structure, heterophase interfaces, crystal growth, fracture, and materials thermodynamics. The full citations are given in the References at the end of the book.

Field of application	Reference
classics	Potts (1952)
	Metropolis, Rosenbluth, Rosenbluth, Teller, and Teller (1953)
	Hammersley and Handscomb (1964)
	Shreider (1966)
	Wu (1982)
	Kalos and Whitlock (1986)
	Koonin (1986)
	Binder and Stauffer (1987)
	Suzuki (1987)
	Binder (1991a)
	Allen and Tildesley (1989)
	Heermann and Burkitt (1991)
	Yeomans (1992)
surface structure and diffusion	de Miguel, Ferron, and Cebollada (1988)
	Jiang and Ebner (1989a)
	Cheng and Yeung (1991)
	Smilauer, Wilby, and Vvedensky (1993)
	Zhang, Detch, and Metiu (1993)
polymers	Bruns, Motoc, and O'Driscol (1981)
	Baumgärtner (1984a)
	Milik and Orszagh (1989)
	Reiter, Zifferer, and Olaj (1990)
	Cifra, Karasz, and MacKnight (1992)

	Toral and Chakrabarti (1993)
	Kamide, Iijima, and Shirataki (1994)
	Haas, Hilfer, and Binder (1995)
	Smith, Russell, and Kaiser (1996)
	Peng, Sommer, and Blumen (1996)
	Wang, Wang, and Wu (1997)
epitaxial growth	Kew, Wilby, and Vvedensky (1993)
and structure	Plotz, Hingerl, and Sitter (1994)
	Tagwerker, Plotz, and Sitter (1995)
heterophase interfaces	Schmid and Binder (1992)
	Frontera, Vives, and Planes (1995)
	Li and Ming (1997)
Potts model	*see references in Chapter 12*
Ising model	Trohidou and Blackman (1990)
	Ferrenberg and Landau (1991)
	Wansleben and Landau (1991)
	Zhang and Yang (1993)
	Wang and Young (1993)
	Heuer (1993)
	Andersson, Mattsson, and Svedlindh (1994)
	Hasenbusch and Pinn (1994)
	Wingert and Stauffer (1995)
	Gu, Chakraborty, and Lebowitz (1996)
	Scholten and Kaufman (1997)
	Schur and Blote (1997)
crystal growth,	Saito and Ueta (1989)
morphology,	Jiang and Ebner (1989b)
and texture	Cheng, Tang, and Tang (1989)
	Liu, Jin, and Ming (1989)
	Li, Jun, and Ming (1991)
	Zhu and Smith (1992a)
	Zhu and Smith (1992b)
	Cheng and Coller (1992)
	Cheng (1993)
	Kotrla and Levi (1994)
	Li, Peng, and Ming (1995)
	Morhacova (1995)
	Papajova, Nemeth, and Vesely (1995)
	Grandjean, Massies, and Leroux (1996)
	Smith (1997)
grain boundaries	Seki, Seidman, Oh, and Foiles (1991a)
	Seki, Seidman, Oh, and Foiles (1991b)
	Alba and Whaley (1992)
	Udler and Seidman (1993)
	Radhakrishnan and Zacharia (1995)
	Tabet and Ledra (1996)
	Saito (1997)
fracture	Cox (1989)

	Shimamura, Kuriyama, and Kashiwagi (1990)
	Ochiai, Peters, and Schulte (1991)
	Fernandez, Chao, and Amo (1992)
	Pieracci (1997)
diffusion	Limoge and Bocquet (1988)
	Rupsky, Iordanova, and Apostolov (1990)
	Salomons and de Fontaine (1990)
	Gladyszewski and Gladyszewski (1991)
	Übing and Gomer (1991a)
	Übing and Gomer (1991b)
	Übing and Gomer (1991c)
	Kutner and Bogusz (1992)
	Frontera, Vives, and Planes (1993)
	Mattsson, Engberg, and Wahnstrom (1993)
	Sommer, Schulz, and Trautenberg (1993)
	Qin and Murch (1993)
	Guo, Zhong, and Peng (1994)
	Cao (1994)
	Gongalez-Miranda, Labarta, and Puma (1994)
	Pekalski and Ausloos (1994)
	Ausloos and Pekalski (1995)
	Chen, Gomez, and Freeman (1996)
	Wang, Rickman, and Chou (1996)
	Kosztin, Faber, and Schulten (1996)
phase diagrams	Bichara and Inden (1991)
	Tetot, Finel, and Ducastelle (1991)
	Dunweg and Landau (1993)
	Fiig, Anderson, and Lingard (1993)
	Farooq and Khwaja (1993)
	Khanna, Welberry, and Withers (1993)
	Silverman, Zunger, and Adler (1995a)
	Silverman, Zunger, and Adler (1995b)
phase transformation	Castan and Lindgard (1989)
	Reynolds, Kaletta, and Ertl (1989)
	Roland and Grant (1989)
	Quade, Hupper, and Scholl (1994a)
	Saul, Treglia, and Legrand (1994a)
	Zamkova and Zinenko (1994)
	Guenin, Clapp, and Rifkin (1996)
	Schön and Inden (1996)
	Tadaki, Kinoshita, and Hirotsu (1997)
BWG, MFA, CVM	Brout (1965)
	Smart (1966)
	Inden (1974)
	Kikuchi (1974)
	Bennett (1986)
	Ceder, De Graef, and Delaey (1989)
	Schön and Inden (1996)

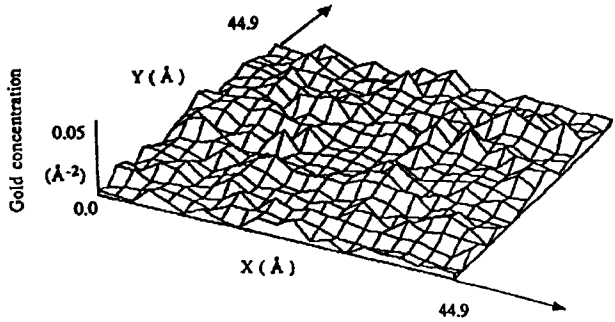

Figure 6.11: Distribution of Au atoms in a Pt-1*at.*% Au alloy in the (002) lattice plane which is adjacent to a 5° [100] twist boundary (Seki et al. 1991).

6.13 Examples of the Monte Carlo Method in Materials Science

6.13.1 Simulation of Surface Segregation

The Monte Carlo method has been widely used to predict chemical segregation effects in interfaces and on surfaces. Figure 6.11 shows the distribution of Au atoms in a Pt-1*at.*% Au alloy in the (002) lattice plane which is immediately adjacent to the interface generated by a 5° [100] twist boundary (Seki et al. 1991). The Monte Carlo simulation was conducted using an embedded atom potential. The plot shows the density of the Au atoms in units of [number of Au atoms $\mathring{A}^{-2}$]. The simulation considers the periodical presence of primary grain boundary dislocations in the interface. The distribution of the Au atoms show a hill-and-valley topology which can be attributed to these dislocations.

6.13.2 Simulation of Phase Transition in Polymers

Numerous applications of the Monte Carlo method deal with phase transition phenomena in polymers (Bruns et al. 1981; Baumgärtner 1984a; Baumgärtner 1984b). Relevant questions in this context are the kinetics and the topology associated with chain interactions. Figure 6.12 shows schematically some typical situations where chain interactions in polymers play an important role in microstructure formation. The progress and the topology of polymerization in such materials can be simulated using a non-overlapping Monte Carlo random walk type algorithm which describes the evolution of the polymer chain orientation. Figure 6.13 as an exemple shows the phase transition of a polymer from the isotropic to the nematic phase.

6.13.3 Simulation of Thin Film Deposition

Kinetic variants of the Monte Carlo method have been used to simulate the formation of fiber textures during thin film deposition (Smith 1997). Figures 6.14 and 6.15 show simulated textures and microstructures with different ratios of the binding energy to the surface atoms belonging to different crystallographic orientations.

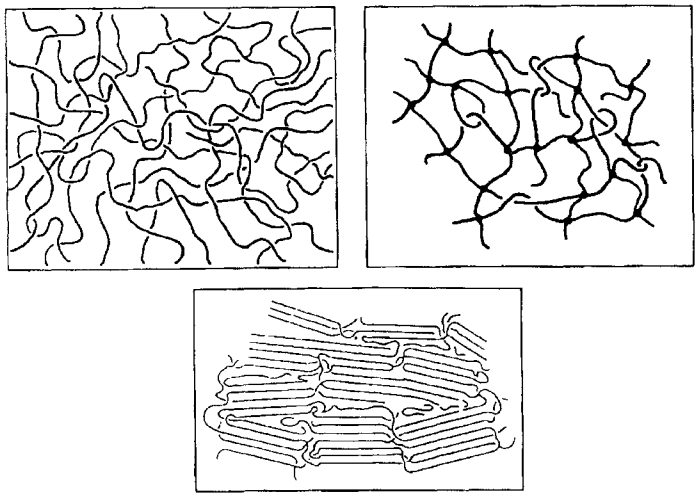

Figure 6.12: Schematic representation of some typical situations where chain interactions in polymers play a role in the formation of microstructures.

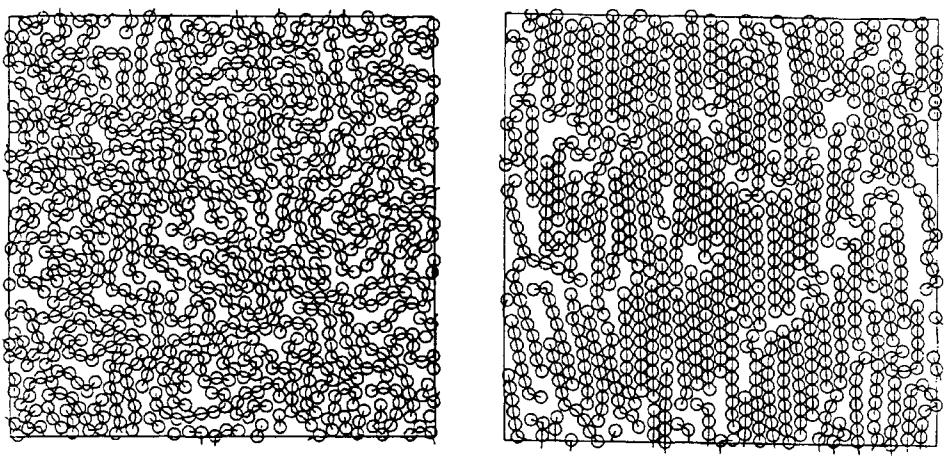

Figure 6.13: Phase transition of a polymer from the isotropic to the nematic phase (Baumgärtner 1984).

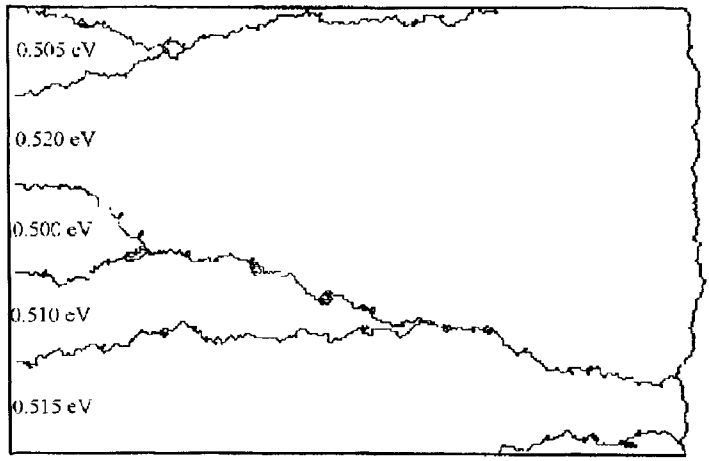

Figure 6.14: Simulated thin film microstructure obtained from film grown onto a five-grain substrate at 600 K at a deposition rate of 1 monolayer every 100 s. The local surface binding energies for these grains are given in eV in the picture (Smith 1997).

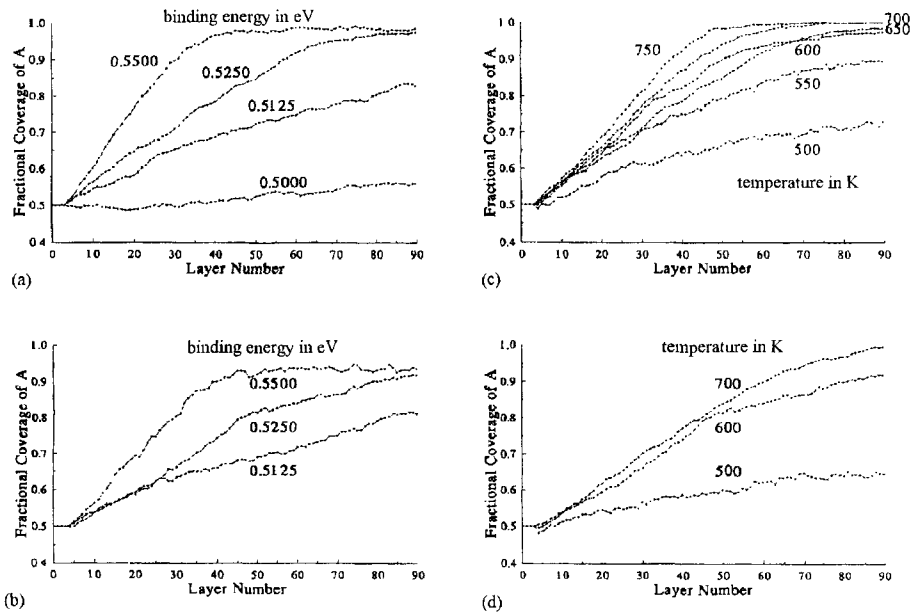

Figure 6.15: Simulated kinetics of texture formation (fractional coverage of component A) during thin film growth as a function of surface binding energy and temperature; (a) 600 K, 1 monolayer every 100 s; (b) 600 K, 1 monolayer every 10 s; (c) 0.525 eV / 0.5 eV, 1 monolayer every 100 s; (d) 0.525 eV / 0.5 eV, 1 monolayer every 10 s (Smith 1997).

Chapter 7

Molecular Dynamics

7.1 Introduction

Besides the various Monte Carlo algorithms (Metropolis et al. 1953), the molecular dynamics method represents the second main simulation technique for the solution of many-body interaction phenomena at the atomistic level (Alder and Wainwright 1959; Rahman 1964; Verlet 1967; Parinello and Rahman 1981; Hoover 1986; Lutsko et al. 1988a; Sankey and Niklewski 1989; Allen and Tildesley 1989).

While the Metropolis Monte Carlo method is a statistical probabilistic approach that penetrates the phase space along a Markov chain in a stochastic manner, molecular dynamics represents a deterministic technique and tracks the individual motion of each of the particles. The original path-independent Monte Carlo algorithm is confined to the computation of equilibrium thermodynamic quantities. It does not predict material dynamics at the nanoscale[1]. Conversely, the validity of ensemble average predictions obtained by molecular dynamics is limited by statistics and based on the assumption of system ergodicity.

Molecular dynamics simulations mimic elementary atomistic path-dependent processes by solving the equations of motion of all particles. An exact treatment of this many-body problem would require the formulation and solution of a Schrödinger wave equation for all atoms considered, accounting for the interactions among the charged constituents (nuclei, electrons) and their kinetic energies (see Chapter 4). However, it can be shown that a quasi-classical treatment of the atomic interactions and the resulting dynamics in terms of potentials and the classical equation of motion, as realized in most molecular dynamics aproaches, is consistent, within certain limits, with the solution of the Schrödinger equation. The analogy can essentially be derived by separating the time-dependent from the time-independent part of the Schrödinger equation, by using the adiabatic Born–Oppenheimer approximation for splitting the wave function into one part to describe the dynamics of the light electrons and another part to describe the dynamics of the heavy nuclei, and by replacing the quantum mechanical expression for the kinetic energy by the classical momentum term.

[1] It is possible to introduce a kinetic quantity into Monte Carlo simulations by tracking the number of Monte Carlo steps and dividing it by the number of lattice sites. Corresponding approaches are referred to as kinetic Monte Carlo models.

Computational Materials Science: The Simulation of Materials, Microstructures and Properties By Dierk Raabe
Copyright © 1998 Wiley-VCH Verlag GmbH
ISBN: 3-527-29541-0

This means that the simulation of atomic configurations with instantaneously equilibrated electrons in their ground state merely requires an adequate incorporation of the forces among the atoms, expressed as derivatives of more or less empirical interatomic potential functions. The time evolution of the ensemble is then computed by integrating the equations of motion in a discrete fashion using time steps of $\approx 10^{-14}$–10^{-15} s. The method involves the calculation of the present position and velocity of each individual atom, and its position and velocity a small time later. Typical scaling parameters of molecular dynamics simulations are Ångstrøms – nanometers for the atomic spacing, 10^{-5}–10^{-3} ps for the elementary oscillation period, and 10^3–10^9 for the number of particles involved (Allen and Tildesley 1989; Catlow et al. 1990; Allen and Tildesley 1992; Kirchner et al. 1996; Voter 1996). It is worth noting that most molecular dynamics simulations cover a real time below 1 nanosecond. The maximum number of atoms or molecules that can be dealt with is determined by the complexity of the interatomic forces being considered.

The underlying potentials reflect the interaction among the atoms and are usually quantified in terms of the relative position of two or more atoms (Verlet 1967). They can include a variety of parameters such as the charges, the polarizabilities of the ions, or the local atomic density (Finnis and Sinclair 1984; Vitek and Srolovitz 1989; Finnis and Rühle 1993; Haberlandt et al. 1995; Sutton and Balluffi 1995; Sutton 1996). The forces are computed in each elementary calculation step as the derivatives of the interaction potentials arising from the presence of the other atoms which lie within a certain cut-off radius around the atom considered.

While in simple pair potentials (Morse, Lennard–Jones, Buckingham) only the direct interaction between *two* atoms is considered and added up for a certain sphere with a radius of about four atoms, in modern many-body potentials the influence of the density of the neighboring atoms is also quantified in terms of an additional attractive force. Depending on the number of particles and potential employed, optimized computer codes for molecular dynamics can be used on personal computers, workstations, and mainframes dealing with as many as 10^8–10^9 particles.

The plan of this chapter is as follows. First, a brief survey is given on some typical potential functions used in molecular dynamics. Second, the equations of motion are discussed with respect to their application in atomic systems. Third, some aspects of finite difference methods are addressed, as required in the integration of the equations of motion. Fifth, some comments are made about the use of boundary conditions. Finally, some typical applications and examples are reviewed.

7.2 Models of Interatomic Potentials

7.2.1 Introduction and Fundamentals

The binding forces among atoms determine the material structure and its intrinsic mechanic and electromagnetic properties. In solid-state physics and bonding chemistry, four different types of interatomic bonds are usually recognized, namely metallic, ionic, covalent, and van der Waals[2]. Except for some special cases such as the cohesion between neighboring {0002} planes in graphite, the van der Waals force is very weak and can often be neglected in materials simulations. Its contribution to cohesion is usually more than

[2]Sometimes the interatomic cohesion that is transmitted through a hydrogen atom is referred to as an additional binding type. It is very important in organic chemistry (DNA helix, water) but less relevant in physical metallurgy.

one order of magnitude smaller as compared with the other binding types. The remaining three types can be classified into bonding with electron delocalization into itinerant states forming large molecular orbitals (metallic, covalent), and bonding with electron transfer from one ion to another (ionic).

These three main bonding classes represent phenomenological idealizations of real systems, where mixed bonding conditions prevail. For instance, in most transition metals directional covalent terms complement the pure metallic bond. Since the pioneering work of Hume-Rothery and Cottrell it has been the aim of materials scientists to quantitatively predict the bonding and thus the structure of real materials on the basis of the interatomic forces (Cottrell 1988; Pettifor and Cottrell 1992; Pettifor 1993). With the advent of quantum mechanics it became clear that any quantitative bonding theory must involve the nonclassical behavior of the valence electrons which bind the atoms together. Thus, for predicting the bond between atoms one has to solve Schrödinger's equation for a many-body problem ($\approx 10^{23}$ particles) (Chapter 4). It is obvious that such a procedure is not tractable because of the large number of atoms involved. For this reason a variety of approximations of interatomic potentials has been developed to describe the interactions among the atoms more or less phenomenologically (equations (4.1)–(4.8).

The analogy between the full quantum mechanical treatment and the classical method of using empirical potentials and the equation of motion is justified on the basis of some assumptions. These are the separation of the time-dependent from the time-independent solution of the complete Schrödinger equation, the Born–Oppenheimer approximation, and the replacment of the quantum mechanical momentum by the classical momentum. These approximations enable one to transfer the potentials used from one atomic environment to another. The latter aspect is not necessarily straightforward from an electronic point of view (Sutton and Balluffi 1995). Especially in the simulation of real materials containing lattice defects such as solute foreign atoms, dislocations, and interfaces, considerable fluctuations in the electronic structure can appear, due to changes in the local atomic configuration.

However, it is commonly accepted that, in order to understand some basic physical concepts that occur in classical atomic ensembles, including structural defects such as dislocation cores or internal interfaces, the fine details of the potentials might not be crucial. For instance, the fundamental relationship between the core structure of screw dislocations in body-centered cubic metals and their mobility was elucidated by molecular dynamics simulations using pair potentials (Vitek 1968; Vitek 1976). Although these relatively simple functions provided only approximate information about the bonding of the real material, the simulations were of significant value in later interpretations of the plasticity of body-centered cubic metals (Sesták and Seeger 1978; Christian 1983).

The potential concept enables the researcher to carry out nanoscale molecular dynamics simulations with as many as 10^6–10^8 atoms, provided sufficient computational resources are available. Of course, such quantities do not yet allow a full mesoscale treatment of materials, which would involve as many as 10^{23} atoms, but it represents the best possible approach to reveal atomistic mechanisms and intrinsic structural properties. This information can then be incorporated at a larger scale to formulate and solve continuum mesoscale models.

A large variety of interatomic potentials is currently being used in simulating lattice defects. They range from generic radially symmetric empirical pair interactions (Lennard-Jones 1924; Morse 1929; Torrens 1972; Tersoff et al. 1989), to non radially symmetric bonds, which are helpful in simulating lattice defects in the technically relevant transition metals, to more fundamental approaches such as the semi-empirical tight-binding

potentials which display the same angular momentum as real atomic orbitals (Sutton and Balluffi 1995; Voter 1996), to local density functional theory (Hohenberg and Kohn 1964; Kohn and Sham 1965). It should be emphasized that the formulation of adequate potentials is not only required in molecular dynamics, but increasingly gains momentum in conjunction with Metropolis Monte Carlo and cluster variation types of simulations. This chapter reviews these concepts particularly with respect to their relevance in the field of microstructure simulation and discusses their respective properties and predictive potential. Thorough reviews on the various potentials and their theoretical backgrounds and limitations have been published by Torrens (1972), Hoover (1986), Finnis et al. (1988), Vitek and Srolovitz (1989), Sutton and Balluffi (1995), and Voter (1996).

7.2.2 Empirical Pair Potentials and Weak Pseudopotentials

Most molecular dynamics simulations between the 1950s and the 1980s used empirical radially symmetric pair potentials to describe the interactions of atoms (Erginsoy et al. 1964; Rahman 1964). In these early classical potential functions the interaction energy and force between an atom and its neighbors is given by the sum of each of the pairwise contributions, but no additional cohesive pseudopotential contributions are involved. The parameters occurring in such expressions are obtained by fitting empirical potential functions to intrinsic material parameters such as the elastic constants, crystal structure, cohesive energy, stacking fault energy, or lattice parameter, to bulk properties. The underlying potential functions are usually of a more or less arbitrary exponential or higher-order polynomial form.

These classical potentials are mostly used to simulate basic structural aspects, for instance single lattice defects and their dynamics. Due to their simple mathematical structure they are particularly preferred when a large number of atoms must be considered. Owing to the physical meaning of the empirical terms involved (Pauli repulsion, dipole–dipole attraction) classical pair potentials represent a good characterization of monoatomic closed-shell gases such as argon or helium.

One can distinguish between two types of pair potentials. The first group, which is referred to as classical pair potentials, describes the total energy of the system, but involves no further cohesive term. The second group, which is referred to as isotropic weak pseudopotentials, describes energy changes of the system associated with structural changes and includes a further cohesive term.

Classical pair potentials fully determine the *total energy* of a system without considering any further cohesive terms that arise from the interaction with atoms far away from the particle considered (Vitek 1996). The atoms are regarded as mass points which have a central interaction with their nearest neighbors (Lennard-Jones 1924; Morse 1929; Torrens 1972). The interaction of any pair of atoms depends only on their spacing. This implies that such potentials are principally radially symmetric and independent of the angular position of other atoms in the vicinity. The required constants are obtained by fitting material properties that are accessible in experiments. The classical pair potential can be written

$$E_{\text{tot}} = \frac{1}{2} \sum_{i=1 \neq j}^{N} \sum_{j=1 \neq i}^{N} \psi_{ij}\left(r_{ij}\right) \tag{7.1}$$

where $r_{ij} = \mid \boldsymbol{r}_{ij} \mid$ is the spacing between two atoms i and j and ψ_{ij} the pair potential. The simplest classical pair potential without any cohesive interaction is the hard sphere

model which can be written

$$\psi_{ij}(r_{ij}) = \begin{cases} = \infty & \text{for } r_{ij} \leq r_0 \\ = 0 & \text{for } r_{ij} > r_0 \end{cases} \tag{7.2}$$

where r_0 is the inner cut-off radius which can be interpreted as the radius of the hard sphere. A smoother potential with both repulsive and attractive components is the Lennard–Jones potential, which was developed for inert gases. It contains an empirical attractive term, which mimics a van der Waals type of bond dominating at large distances, and an empirical repulsive term, which mimics the Coloumb interaction of the nuclei and the Pauli repulsion arising from the quantum exclusion of the electrons dominating at short distances.

$$\psi_{ij}(r_{ij}) = \frac{C_{\mathrm{LJ1}}}{r_{ij}^n} - \frac{C_{\mathrm{LJ2}}}{r_{ij}^m} \tag{7.3}$$

This potential is mostly used in the so-called 12–6 form (Vitek 1996) where $n = 12$ and $m = 6$. The constants amount to $C_{\mathrm{LJ1}} = 4\epsilon\sigma^n$ and $C_{\mathrm{LJ2}} = 4\epsilon\sigma^m$ where ϵ and σ are adjustable parameters (Broughton et al. 1993). A similar description is given by the Morse potential,

$$\psi_{ij}(r_{ij}) = C_{\mathrm{M1}} \left\{ \exp(-2\alpha(r_{ij} - r_0)) - 2\exp(-\alpha(r_{ij} - r_0)) \right\} \tag{7.4}$$

where α, C_{M1}, and r_0 are adjustable parameters. The classical pair potentials are particularly pertinent in simulating ionic systems, fullerenes (C_{60}), and cases where van der Waals bonding prevails, such as molecule crystals (Morse 1929; Lennard-Jones 1924; Torrens 1972; Vitek and Srolovitz 1989). Some details of pair potentials are discussed in the overview article of Vitek (1996).

The second type of pair potential addressed in this section describes energy changes associated with configurational variation at constant average atom density, rather than the total energy of the system. It can be described by the more general equation

$$E_{\mathrm{tot}} = \frac{1}{2} \sum_{i=1 \neq j}^{N} \sum_{j=1 \neq i}^{N} \psi_{ij}(r_{ij}) + U(\Omega) \tag{7.5}$$

where $U(\Omega)$ is the cohesive contribution to the total energy and Ω the average density of the material (Torrens 1972; Vitek 1996). This view corresponds to the picture of a pseudopotential representing the ion cores in simple s–p bonded metals, such as lithium, sodium, potassium, magnesium, and aluminum. The total energy is then assumed to be composed of a large density-dependent but structure-independent part $U(\Omega)$, and a structure-dependent part that is represented by the pair interactions $\psi_{ij}(r_{ij})$ (Voter 1996). One should note that the pseudopotential approach is not identical to the various many-body potentials such as the embedded atom method. The latter methods consider the *local* rather than the *average* density of the material (Daw and Baskes 1984).

Although allowing us fast computations of atomistic problems with consideration of as many as 10^8 particles, the classical pair potentials have some major drawbacks. For instance, if the cohesive energy per atom is correctly described, the vacancy formation energy is not, and vice versa (Finnis and Rühle 1993). Furthermore, the inadequate prediction of the Cauchy discrepancy represents a major shortcoming of the classical pair potentials when used for metals. For describing the linear anisotropic elastic behavior of

cubic metals, one requires three constants, e.g. C_{1111} (C_{11}), C_{1122} (C_{12}), and C_{2323} (C_{44}). These elastic constants are the second spatial derivatives of the potential (Honerkamp and Römer 1993). Using the corresponding analytical expressions shows that the value $C_{1122} - C_{2323}$ amounts to $2\,\mathrm{d}U/\mathrm{d}\Omega + \Omega\,\mathrm{d}^2U/\mathrm{d}\Omega^2$ (Finnis and Rühle 1993). It follows hence that for the first type of pair potentials, equation (7.1), the Cauchy relation $C_{1122} = C_{2323}$ applies. However, for the second type of pair potentials, equation (7.5), the Cauchy relation does not usually hold. While the Cauchy relation is often satisfied for van der Waals solids and ionic crystals, it is generally wrong for cubic metals. This is evident from a simple estimation. For numerous metals Poisson's ratio amounts to $\nu \approx 1/3$ and the Zener ratio to $A \approx 1$ (isotropic limit, observed only for tungsten). For cubic metals the former constant is given by $\nu = C_{1122}/(C_{1111} + C_{1122})$ and the latter one by $A = 2\,C_{2323}/(C_{1111} - C_{1122})$. By using both equations in the isotropic limit, one obtains $C_{1122} - C_{2323} = C_{2323}/2 \neq 0$. For hexagonal and trigonal metals, where the Cauchy relations amount to $C_{1133} = C_{2323}$ and $3\,C_{1122} = C_{1111}$, similar deviations to those for cubic materials occur. The observed discrepancy among the elastic constants of metal crystals can only be fitted if the model is constrained by the boundary condition to a lattice parameter that is smaller than its equilibrium value (Sutton 1996). The second type of classical empirical interatomic force description, using pseudopotentials, contains a large average density-dependent contribution. However, for simulating lattice defects the assumption of a homogeneous density is mostly incorrect.

Finally, it must be emphasized that classical pair potentials are radially symmetric. Therefore, they cannot reflect the directional nature of the bonding. However, directionality of the bonding can be essential for simulating lattice defect dynamics of transition metals. The presence of d-electrons near the Fermi level spoils this simple model of a radial symmetry (Finnis et al. 1988; Pettifor 1993; Finnis and Rühle 1993). However, for metals in which cohesion is provided by the outermost s and p electrons forming free electron bands with small gaps at the Brillouin zone boundaries due to weak ionic pseudopotentials, the isotropic limit works better than in the case of transition metals (Sutton and Balluffi 1995).

7.2.3 Isotropic Many-Body Pair-Functional Potentials

The various isotropic many-body or simply pair-functional potentials represent a refined class of empirical or semi-empirical potentials. Most of these models share the principal view that the cohesion energy of an atom is largely determined by the local electron density at the site into which that atom is placed (Friedel 1952). The contribution to the electron density at that site is due to the neighboring atoms. The decohesion energy is in most of these approaches represented by a pair potential type of contribution that largely reflects the electrostatic repulsion. Isotropic many-body potentials are valuable both to study complex systems that are intractable with more rigorous methods, and to study generic properties that do not depend so much on the details of the energetics (Raeker and DePristo 1991; Daw et al. 1993; Foiles 1996).

Important versions of these approaches are the second moment (Cyrot-Lackmann 1967), the effective medium (Norskov and Lang 1980), the embedded atom (Daw and Baskes 1983), the glue (Ercolessi et al. 1986), and the Finnis–Sinclair (Finnis and Sinclair 1984) models. This class of models is sometimes also referred to as pair-functional methods (Foiles 1996). According to the above-mentioned physical concept, these models all have the following functional form for the total energy E_{tot} at zero temperature (Finnis and

Rühle 1993; Sutton and Balluffi 1995; Foiles 1996):

$$E_{\text{tot}} = \sum_{i}^{N} F(\varrho_i) + \frac{1}{2} \sum_{i=1 \neq j}^{N} \sum_{j=1 \neq i}^{N} V(r_{ij}) \tag{7.6}$$

where $F(\varrho_i)$, which is sometimes referred to as the embedding or glue function, models the attractive interaction as a function of the local electron density into which the considered atom is placed. The term $V(r_{ij})$ describes a pairwise isotropic interatomic potential function which is essentially repulsive and depends only on the atomic spacing r_{ij}. $V(r_{ij})$ is usually fitted from experimental data (Finnis et al. 1988; Vitek and Srolovitz 1989). The embedding function F is a square root in the second moment and in Finnis–Sinclair potentials. The square-root behavior is derived from a simplified tight-binding model of electronic densities of states. In the embedded atom method and similar approaches, the embedding function is derived from the energy of an atom embedded in a homogeneous free-electron gas of the local density ϱ_i at the atomic site (Daw and Baskes 1984). In either case the embedding function is a negative concave function of ϱ_i.

$$\varrho_i = \sum_{j=1 \neq i}^{N} \phi(r_{ij}) \tag{7.7}$$

This function can be interpreted as the charge at the ith nucleus due to the spherical symmetric electronic charge densities ϕ of the neighboring atoms. The equivalence of the embedded atom and Finnis–Sinclair approximations in the tight-binding theory of metallic cohesion has been discussed by Ackland, Finnis, and Vitek (1988).

As pointed out by various authors (Finnis and Rühle 1993; Sutton and Balluffi 1995), the isotropic many-body potentials are very similar in behavior and almost as straightforward to compute as classical pair potentials (involving an increase by a factor of two in computation time as compared with pair potentials). The main limitation of the early radially symmetric many-body potentials is that they do not account for the directional nature of the bond. Thus, the covalent contributions (d orbitals) of the transition metal bonds cannot be adequately described. The same applies for silicon with its half-filled sp bands, which form covalent bonds with an angular character. Consequently, neither the negative Cauchy pressure nor the stability of non-closely packed lattice structures can be adequately predicted (Foiles 1996).

However, the main advantage of the various isotropic many-body potentials is the incorporation of the approximate variation of the bond strengths with the atomic coordination. Increasing the coordination decreases the strength of each of the individual bonds that the atom forms and increases the bond length (Foiles 1996). Stimulated by the requirement to include binding anisotropy, but to avoid the computational efforts associated with tight-binding approaches (which consider bond directionality), angle-dependent many-body potentials are increasingly in use (Baskes 1992; Moriarty 1994; Voter 1996).

7.2.4 Shell Model

The shell model provides a potential form that is mainly used for atomistic simulations of materials with dominant ionic or covalent binding contributions. For instance, it is employed for molecular dynamics simulations of purely ionic solids, oxides, silicates, and purely covalent materials.

The shell model can be regarded as a derivative of the pair-functional models, but based on a more ionic picture. The total energy E_{tot} is expressed as a sum of the one-body $E_i(r)$, two-body $V(r_{ij})$, and higher-order $U(r_{ij}, r_{jk}, r_{ki})$ interactions.

$$E_{\text{tot}} = \sum_{i}^{N} E_i(r) + \sum_{i<j}^{N} V(r_{ij}) + \sum_{i<j<k}^{N} U(r_{ij}, r_{jk}, r_{ki}) \tag{7.8}$$

where r is the lattice spacing and r_{ij} the spacing between the atoms i and j (Stoneham et al. 1996).

The first term in equation (7.8) is interpreted as a rearrangement energy, which is required to convert a free-space ion into a crystal ion. It can be expressed as a function of the ion's distance to the nearest neighbor:

$$E_{\text{rearr}}(r) = E_0 + \exp\left(-\frac{r}{R_{\text{rearr}}}\right) \tag{7.9}$$

where the value of R_{rearr} can be determined empirically from Born–Mayer potentials. The pair interaction term is usually provided by a Born–Mayer form.

7.2.5 Bond Order Potentials

The main idea of the bond order formalism is the derivation of a general potential function that can describe the atomic interaction for materials with different chemical bonding and different structure (Abell 1985; Tersoff 1986; Brenner 1990; Brenner 1993; Brenner 1996). Starting from chemical pseudopotential theory and a localized-orbital basis set, Abell (1985) gave an analytical expression for the binding energy E_i of each atom in a translational periodic structure as a function of the nearest-neighbor distance r.

$$E_i = \frac{1}{2} \sum_{j=1}^{Z} \left(q\, V_{\text{rep}}(r) + b\, V_{\text{att}}(r)\right) \tag{7.10}$$

where Z is the number of nearest neighbors, q the number of valence electrons per atom, b the bond order, $V_{\text{rep}}(r)$ a function that describes the near-neighbor two-center repulsive interatomic force, and $V_{\text{att}}(r)$ its attractive counterpart (Brenner 1996).

The bond order b is independent of the bond length. It can be calculated as the sum of the squares of the molecular coefficients on neighboring atoms. The magnitude of the bond order characterizes the strength of the chemical bond. It depends on the inverse square root of the coordination number, i.e.

$$b \propto \frac{1}{\sqrt{Z}} \tag{7.11}$$

According to Abell (1985) the repulsive and attractive terms are best approximated by exponential functions, so that equation (7.10) can be written

$$E_i = \frac{1}{2} \sum_{j=1}^{Z} \left(C_{\text{bo1}} \exp(-\sigma r) - \frac{1}{\sqrt{Z}} C_{\text{bo2}} \exp(-\lambda r)\right) \tag{7.12}$$

where C_{bo1}, C_{bo2}, σ, and λ must be fitted from experiment.

7.2.6 Tight-Binding Potentials

Tight-binding potentials are approaches that lie between the more ab-initio local density functional theory (Section 7.2.7) and the more empirical isotropic many-body pair-functional potentials (Section 7.2.3). The tight-binding method represents the simplest possible approach to incorporating quantum mechanical principles into the calculation of the potential (Sutton and Balluffi 1995; Kohan and Ceder 1996). In contrast to the free-electron model it is based on using non- or weakly-overlapping atomic basis functions. Consequently, tight-binding solutions are based on formulating wave functions as linear combinations of atomic orbitals (LCAO) or plane wave basis sets. The atomic-like orbitals which serve as basis functions in the LCAO method display the same angular momentum as true atomic orbitals but with radial dependencies (Sutton and Balluffi 1995). As will be shown below, combination of the atomic functions enables one to describe delocalized states and hence to reproduce the band structure.

In contrast to most of the empirical and semi-empirical potentials discussed in the previous sections, tight-binding potentials account for the directional nature of the bond (particularly under the influence of p- and d-atomic orbitals), for the consideration of the bonding and antibonding states, and for energy changes as a result of atomic displacements.

Using linear combinations of atomic orbitals the wave function of the nth eigenstate of a system $\Psi^{(n)}$ can be written

$$\psi^{(n)} = \sum_{i}^{N} c_i^{(n)} \phi_i \tag{7.13}$$

where N is the number of atomic basis functions and ϕ_i the ith basis function. For instance, in a molecule consisting of two atoms 1 and 2, ϕ_1 would be the wave function of a valence electron for the Hamiltonian $\mathcal{H}_1$ associated with atom 1,

$$\mathcal{H}_1 \, \phi_1 \; = \; E \, \phi_1 \tag{7.14}$$

and ϕ_2 the wave function of a valence electron for the Hamiltonian $\mathcal{H}_2$ associated with atom 2,

$$\mathcal{H}_2 \, \phi_2 \; = \; E \, \phi_2 \tag{7.15}$$

with

$$\mathcal{H} = \left(\frac{\hbar^2}{2\,m} \nabla^2 \; + \; v(r) \right) \tag{7.16}$$

where $\hbar$ is $h/(2\pi)$, ∇ the nabla operator, m the effective mass of the electron, and $v(r)$ a electrostatic pseudopotential experienced by an electron with the energy E.

The series expansion coefficients $c_i^{(n)}$ in equation (7.13) are determined by substituting the combined wave function $\psi^{(n)}$ into the Schrödinger equation:

$$\mathcal{H} \sum_{i}^{N} c_i^{(n)} \phi_i \; = \; E^{(n)} \sum_{i}^{N} c_i^{(n)} \phi_i \tag{7.17}$$

where $\mathcal{H}$ is the Hamiltonian of the total system and $E^{(n)}$ the expected energy of the nth eigenstate. By assuming orthogonality and normalization of the N basis functions

$$\int_{\text{vol}} \widetilde{\phi}_i \, \mathcal{H} \, \phi_i \; \mathrm{d}V \; = \; 1 \tag{7.18}$$

one obtains N secular equations of the form

$$\sum_{j}^{N} \mathcal{H}_{ij}\, c_j^{(n)} = E^{(n)}\, c_i^{(n)} \tag{7.19}$$

with $\mathcal{H}_{ij}$ being the Hamiltonian matrix component which is defined in terms of the volume integral

$$\mathcal{H}_{ij} = \int_{\text{vol}} \widetilde{\phi}_i\, \mathcal{H}\, \phi_j \, \mathrm{d}V \tag{7.20}$$

The N secular equations represent an eigenvalue problem which is solved by matrix diagonalization. As a result one obtains the eigenvalues and the eigenvectors which are the coefficients of the linear combination ansatz. Since the eigenvectors can have non-zero values throughout the solid, the technique of linearly combined atomic orbitals allows one to describe delocalized states and thus to reproduce the band structure.

Because of Pauli's principle each eigenstate can hold two electrons with opposite spin. If the system contains $2\,z$ electrons, only the z lowest eigenvalues will be occupied at $T = 0$ K. All other states are unoccupied. The band energy then amounts to

$$E_{\text{band}} = 2 \sum_{n=1}^{z} E^{(n)} \tag{7.21}$$

Combining this expression with the secular equations, equation (7.19) leads to

$$E_{\text{band}} = \sum_{ij} 2 \sum_{n=1}^{z} c_i^{(n)}\, \widetilde{c}_j^{(n)}\, \mathcal{H}_{ji} = \sum_{ij} \rho_{ij}\, \mathcal{H}_{ji} \tag{7.22}$$

where ρ_{ij} is the ij component of the density matrix:

$$\rho_{ij} = 2 \sum_{n=1}^{z} c_i^{(n)}\, \widetilde{c}_j^{(n)} \tag{7.23}$$

The significance of these matrix elements lies in the fact that they are the coefficients of the charge density function, which can be expressed in terms of a sum of atomic charge densities and bond charge densities. The off-diagonal matrix elements, which are referred to as bond orders, enable one to calculate the number of electrons in the bonding and antibonding states.

$$\rho_{ij} + \rho_{ji} = m_{\text{bond}} - n_{\text{antibond}} = 2 \sum_{n=1}^{z} \left(c_j^{(n)}\, \widetilde{c}_i^{(n)} + c_i^{(n)}\, \widetilde{c}_j^{(n)} \right) \tag{7.24}$$

In the simplest variant the resulting force on an atom can then be calculated assuming the Hellmann–Feynman theorem

$$\frac{\delta E_{band}}{\delta x_k} = \sum_{ij} \left(\rho_{ij} \frac{\partial \mathcal{H}_{ji}}{\partial x_k} + \rho_{ji} \frac{\partial \mathcal{H}_{ij}}{\partial x_k} \right) \tag{7.25}$$

where δx_k is an infinitesimal shift of atom k in the x direction (Esterling 1986; Sankey and Niklewski 1989). For a more detailed description of the tight-binding approach the reader is referred to the book by Sutton and Balluffi (1995).

7.2.7 Local Electron Density Functional Theory

The treatment of the local electron density functional theory does not belong, strictly speaking, in a chapter which deals with potentials to mimic the interactions and dynamics of atoms. Its main difference from classical molecular dynamics methods lies in the fact that it treats the dynamics of the electrons rather than that of the atoms. Of course, both are closely connected (equation (4.6)), but the employment of the adiabatic Born–Oppenheimer approximation artificially separates the complete Schrödinger wave equation into a portion which describes the dynamics of the electrons and a portion which describes the dynamics of the nuclei.

While classical molecular dynamics methods deal with approximate solutions to the simplified Schrödinger equation which only accounts for the dynamics of the heavy nuclei and leaves the electrons generally in their ground state, electron dynamics simulations deal with approximate solutions to a simplified Schrödinger equation which accounts only for the dynamics of the light electrons, but with the nuclei positions remaining unchanged.

The starting point of the local electron density functional theory is the fundamental theorem of Hohenberg and Kohn (1964) and Kohn and Sham (1965) stating that the total ground state energy of an electronic many-body system is a functional of the electronic charge density. This concept, by concentrating on the electron density rather than on the many-body wave function, allows one to formulate an *effective* Schrödinger equation. This effective wave equation is similar to the Hartree–Fock approach except that each electron now experiences an additional attractive potential. In principle this approach of Hohenberg and Kohn (1964) and Kohn and Sham (1965) gives a late physical justification to treating each electron quasi-independently of the other particles. This is done by replacing the electron–electron Coulomb interaction by an effective single-particle potential. This charge density functional method accounts for all correlations between the electrons so that any given electron is surrounded by a hole or exclusion zone which forbids any other electron to enter. Since the exact shape of this exclusion region is unknown, one replaces the exact hole by an approximate hole which an electron would have in a homogeneous electron gas of equal density to that experienced by the considered electron at any particular instant (Hohenberg and Kohn 1964; Kohn and Sham 1965; Miyazaki et al. 1991). This procedure of approximating the exclusion zone is the basis of the local electron density functional method (Lundquist and March 1983; Callaway and March 1984; Moriarty 1988; Jones and Gunnarsson 1989; Parr and Yang 1989; Pettifor and Cottrell 1992). The effective Schrödinger equation can then be written

$$\left(\frac{\hbar^2}{2\,m}\nabla^2 + v_{\mathrm{H}}(\boldsymbol{r}) + v_{\mathrm{hole}}(\boldsymbol{r})\right)\psi_i(\boldsymbol{r}) = E_i\,\psi_i(\boldsymbol{r}) \tag{7.26}$$

where $\boldsymbol{r}$ is the position vector of the electron (the potentials are not necessarily radially symmetric), $v_{\mathrm{H}}(\boldsymbol{r})$ the Hartree–Fock potential arising from the electrostatic Coulomb interaction imposed by the ions and electrons, and $v_{\mathrm{hole}}(\boldsymbol{r})$ the additional attractive potential arising from the exclusion zone.

The total energy can be written

$$U = \sum_i E_i - \frac{1}{2}\int\!\!\int \frac{e^2\,\rho(\boldsymbol{r})\,\rho(\boldsymbol{r}')}{4\,\pi\varepsilon_0\,\mid \boldsymbol{r}-\boldsymbol{r}'\mid}\,\mathrm{d}\boldsymbol{r}\,\mathrm{d}\boldsymbol{r}' - \int \rho(\boldsymbol{r})\,\left(v_{\mathrm{hole}}\left(\rho(\boldsymbol{r})\right) - \epsilon_{\mathrm{hole}}\left(\rho(\boldsymbol{r})\right)\right)\mathrm{d}\boldsymbol{r} + U_{\mathrm{ion-ion}} \tag{7.27}$$

where $\epsilon_{\text{hole}}(\rho(\boldsymbol{r}))$ is the exchange and correlation energy per electron of a homogeneous electron gas of density $\rho(\boldsymbol{r})$, and e the elementary charge. Various applications using the local electron density functional method have been published by Miyazaki, Ishii, and Terakura (1991), Sommers, Doniach, and Fu (1991), Tanatar (1992), Khein and Singh (1995), Duffy, Chong, and Dupuis (1995), Guan, Casida, and Salahub (1995), Cordero and Alonso (1997), Trautwein, Antony, and Grodzicki (1997), and Valderrama, Ludena, and Hinze (1997).

7.3 Equations of Motion for Atomic Systems

7.3.1 Fundamentals

This section is devoted to the formulation of the classical equations of motion for a system of N atoms or molecules that interact through a well-defined potential model function (Alder and Wainwright 1959; Verlet 1967)

The most fundamental form in which to write the equations of motion for conservative systems[3] with holonomic constraints[4] is given by the Lagrangian formulation in conjunction with Hamilton's principle of least action (Hoover 1986; Allen and Tildesley 1989). The Lagrange–Euler function L is defined in terms of the kinetic and potential energy and is considered to be a function of generalized coordinates $\boldsymbol{x}$ and their time derivatives $\dot{\boldsymbol{x}}$. The generalized coordinates can be complicated functions of the space coordinates.

Denoting the kinetic energy by E_{kin} and the potential energy by E_{pot}, the Lagrange–Euler function can be written

$$L = E_{\text{kin}} - E_{\text{pot}} \tag{7.28}$$

While the potential energy depends on $\boldsymbol{x}$, the kinetic energy depends on $\dot{\boldsymbol{x}}$.

The Lagrangian formulation of the equation of motion can be derived by using Hamilton's least action principle, which states that in conservative systems the motion of a mass element between any two fixed space–time points is that which minimizes the integral of L relative to slightly different, varied motions.

$$\int L\,\mathrm{d}t \to \min. \qquad \text{or equivalently} \qquad \int \delta L\,\mathrm{d}t = 0 \tag{7.29}$$

Since L depends explicitly upon both the generalized coordinates $\boldsymbol{x}$ and their time derivative $\dot{\boldsymbol{x}}$, the variation has the form

$$\int \delta L\,\mathrm{d}t = 0 = \int \left[\left(\frac{\partial L}{\partial \boldsymbol{x}}\right)\delta \boldsymbol{x} + \left(\frac{\partial L}{\partial \dot{\boldsymbol{x}}}\right)\left(\frac{\mathrm{d}\delta \boldsymbol{x}}{\mathrm{d}t}\right)\right]\mathrm{d}t \tag{7.30}$$

where the derivative $(\mathrm{d}\delta\boldsymbol{x}/\mathrm{d}t)$ can be integrated by parts with respect to time, because the integral $\delta\boldsymbol{x}$ is known to vanish at the two endpoints. Then, since the form of the variation that results, namely $\int [(\partial L/\partial \boldsymbol{x}) - (\mathrm{d}/\mathrm{d}t)\ (\partial L/\partial \dot{\boldsymbol{x}})]\ \delta\boldsymbol{x}\,\mathrm{d}t$, contains the arbitrary variation $\delta\boldsymbol{x}$, the coefficient of $\delta\boldsymbol{x}$ must vanish at all times in the interval. This leads then to the Lagrangian form of the equation of motion,

$$\frac{\mathrm{d}}{\mathrm{d}t}\left(\frac{\partial L}{\partial \dot{x}_i}\right) - \left(\frac{\partial L}{\partial x_i}\right) = 0 \tag{7.31}$$

[3]Conservative systems are systems with constant energy.

[4]In mechanics, holonomic constraints mean geometric rather than kinetic constraints.

The equations of motion can be formulated equivalently using the Hamiltonian instead of the Lagrangian form. Hamilton's mechanics are also suitable to describe the time-reversible motion of mass elements in conservative systems under holonomic constraints. However, in the Hamilton form the conjugate momenta $\boldsymbol{p}$ appear instead of the velocities $\dot{\boldsymbol{x}}$ in the equations of motion. It can be constructed from the Lagrange form through

$$\boldsymbol{p} = \frac{\partial L(\boldsymbol{x}, \dot{\boldsymbol{x}})}{\partial \dot{\boldsymbol{x}}} \qquad \text{and} \qquad H(\boldsymbol{x}, \boldsymbol{p}) = (\dot{\boldsymbol{x}}\, \dot{\boldsymbol{p}}) - L \tag{7.32}$$

Assuming a simple isotropic pair potential (Section 7.2.2), the total potential energy E_{pot} is given by

$$E_{\text{pot}} = \frac{1}{2} \sum_{i=1 \neq j}^{N} \sum_{j=1 \neq i}^{N} \Psi\left(\mid \boldsymbol{x}_i - \boldsymbol{x}_j \mid\right) \tag{7.33}$$

where Ψ is the interatomic potential, which depends only on the magnitude of the spacing $\boldsymbol{x}_i - \boldsymbol{x}_j$ between neighboring atoms. In this expression the suffix $i = 1, 2, ..., N$ represents the ith atom[5] and *not* the ith component of the vector $\boldsymbol{x}$. The kinetic energy is given by

$$E_{\text{kin}} = \sum_{i=1}^{N} m_i\, \dot{\boldsymbol{x}}_i^T\, \dot{\boldsymbol{x}}_i \tag{7.34}$$

where m_i is the mass of the ith atom and $\dot{\boldsymbol{x}}_i^T$ the transpose of $\dot{\boldsymbol{x}}_i$.

Applying the Lagrange formalism to the simplest possible case yields Newton's equation of motion for a particle at $\boldsymbol{r}_i$ (in Cartesian coordinates)

$$m_i\, \ddot{\boldsymbol{r}}_i = -\frac{1}{2} \sum_{i=1 \neq j}^{N} \frac{\mathrm{d}\Psi\left(\mid \boldsymbol{r}_i - \boldsymbol{r}_j \mid\right)}{\mathrm{d}\boldsymbol{r}_i} \tag{7.35}$$

It is an important issue to compare atomic scale simulation results with experimental observations. For this purpose molecular dynamics simulations can be equipped with Lagrangians for the consideration of environmental constraints, such as constant pressure, constant temperature, or constant bond length. The consideration of constant pressure was addressed by Andersen (1980), of variable box shape at constant pressure by Parinello and Rahman (1981), of constant temperature by Nosé (1984b), and of constant bond length by Ryckaert, Ciccotti, and Berendsen (1977). The constant-pressure and the constant-temperature schemes will be introduced below.

7.3.2 Constant Pressure

According to Andersen (1980) a constant-pressure environment can be realized by introducing the instantaneous volume of the system Ω. The effective Euler–Lagrange function in the hydrostatic pressure case with constant cell shape can then be written

$$L = \sum_{i=1}^{N} \frac{m_i}{2} D^2\, \dot{\boldsymbol{q}}_i^2 - \sum_{i=1}^{N} \sum_{j>i}^{N} \Psi\left(\mid D\, \boldsymbol{q}_{ij} \mid\right) + \frac{M_{\text{W}}}{2} \dot{\Omega}^2 - \Omega\, p_0 \tag{7.36}$$

[5]The vector notation $\boldsymbol{x}_j$ must not be confused with the notation x_j. The former expression denotes the position vector $\boldsymbol{x}$ of the jth atom. The latter term gives merely the jth component of a position vector $\boldsymbol{x}$.

where M_W the effective mass of the cell wall which is associated with the expansion and contraction of the volume Ω of the simulation box and p_0 the external pressure. The last two terms in this equation deal with the constant pressure being imposed. The coordinates of the atoms $\boldsymbol{q}_i$ are rescaled with the dimension of the simulation cell, $D = \Omega^{1/3}$, since the spacing between any two atoms changes with D and the coordinates independent of the volume can then be given by $\boldsymbol{q}_i = \boldsymbol{r}_i/D$.

An important generalization of the constant-pressure scheme which allows one to deal with a variable shape of the simulation cell was introduced by Parinello and Rahman (1981). According to their approach the Euler–Lagrange function in the hydrostatic pressure case can be written

$$L = \frac{1}{2}\sum_{i=1}^{N} m_i \dot{\boldsymbol{q}}_i^T \boldsymbol{G}\dot{\boldsymbol{q}}_i - \sum_{i=1}^{N}\sum_{j>i}^{N} \Psi\left(\mid \boldsymbol{q}_{ij} \mid\right) + \frac{1}{2} M_W \operatorname{Tr}\left(\dot{\mathfrak{H}}^{\mathrm{T}}\dot{\mathfrak{H}}\right) - \Omega p_0 \tag{7.37}$$

where $\mathfrak{H}$ is the matrix formed by the vectors of the simulation cell, M_W the effective mass of the cell wall, Tr the trace of the matrix product $\left(\dot{\mathfrak{H}}^{\mathrm{T}}\dot{\mathfrak{H}}\right)$, and p_0 the external pressure. The cell matrix is calculated according to

$$\mathfrak{H} = [\boldsymbol{a}, \boldsymbol{b}, \boldsymbol{c}] \tag{7.38}$$

Consequently, the matrix $\left(\dot{\mathfrak{H}}^{\mathrm{T}}\dot{\mathfrak{H}}\right)$ amounts to

$$\left(\dot{\mathfrak{H}}^{\mathrm{T}}\dot{\mathfrak{H}}\right) = \begin{pmatrix} \dot{\boldsymbol{a}}\cdot\dot{\boldsymbol{a}} & \dot{\boldsymbol{a}}\cdot\dot{\boldsymbol{b}} & \dot{\boldsymbol{a}}\cdot\dot{\boldsymbol{c}} \\ \dot{\boldsymbol{b}}\cdot\dot{\boldsymbol{a}} & \dot{\boldsymbol{b}}\cdot\dot{\boldsymbol{b}} & \dot{\boldsymbol{b}}\cdot\dot{\boldsymbol{c}} \\ \dot{\boldsymbol{c}}\cdot\dot{\boldsymbol{a}} & \dot{\boldsymbol{c}}\cdot\dot{\boldsymbol{b}} & \dot{\boldsymbol{c}}\cdot\dot{\boldsymbol{c}} \end{pmatrix} \tag{7.39}$$

The position of the ith atom in real space expressed through the cell vectors $\boldsymbol{a}$, $\boldsymbol{b}$, and $\boldsymbol{c}$ can then be written

$$\boldsymbol{q}_i = \mathfrak{H}\,\boldsymbol{r}_i \tag{7.40}$$

The interatomic spacing that enters the potential can then be expressed as

$$\boldsymbol{q}_{ij} = \mathfrak{H}\left(\boldsymbol{r}_i - \boldsymbol{r}_j\right) \tag{7.41}$$

The matrix $\boldsymbol{G}$ can be written

$$\boldsymbol{G} = \mathfrak{H}^{\mathrm{T}}\,\mathfrak{H} \tag{7.42}$$

where T indicates the transposed matrix form. The volume of the simulation cell Ω is given by

$$\Omega = \det \mathfrak{H} \tag{7.43}$$

and its orientation by

$$\boldsymbol{\Sigma} = \Omega\left(\mathfrak{H}^{\mathrm{T}}\right)^{-1} \tag{7.44}$$

7.3.3 Constant Temperature

Constant-pressure molecular dynamics simulations are usually performed with a constant-temperature environment as additional constraint. The constant-temperature method proceeds by rescaling the velocities of the atoms during the simulation to ensure the relation between the total kinetic energy and the temperature of the canonical system. It can be shown that this rescaling is equivalent to a force constraint up to the first order in the time step. The force is equivalent to an artificial frictional force, which is proportional to the velocity of the atom. According to Nosé (1984b) the corresponding Lagrangian can be written

$$L = \sum_{i=1}^{N} \frac{m_i}{2} s^2 \dot{q}_i^2 - \sum_{i=1}^{N} \sum_{j>i}^{N} \Psi\left(| q_{ij} |\right) + \frac{m_s}{2} \dot{s}^2 - F\, k_{\mathrm{B}} T \ln |s| \tag{7.45}$$

where s, $\dot{s}$, and m_s are the coordinate, velocity, and effective mass of an introduced fictitious variable that calibrates the kinetic energy and the time step in order to have the constraint of the canonical ensemble satisfied and F is the total number of degrees of freedom of the system.

Combining the constant-pressure with the constant-temperature scheme results in an effective Langrangian of the form

$$L = \sum_{i=1}^{N} \frac{m_i}{2} s^2 D^2 \dot{q}_i^2 - \sum_{i=1}^{N} \sum_{j>i}^{N} \Psi\left(| D q_{ij} |\right) + \frac{m_s}{2} \dot{s}^2 - F\, k_{\mathrm{B}} T \ln |s| + \frac{M_{\mathrm{W}}}{2} \dot{\Omega}^2 - \Omega\, p_0 \tag{7.46}$$

7.4 Integration of the Equations of Motion

For a given potential the N equations of motion can be solved by using a finite difference algorithm. The fundamentals of finite difference methods were discussed in Chapter 3. The Gear predictor–corrector and the time-reversible Verlet algorithms are the methods that are frequently used in molecular dynamics. The first method was presented in Chapter 3. The latter approach will be discussed briefly below (Verlet 1967).

The Verlet technique allows one to calculate the actual position r_i and velocity $\dot{r}_i$ of the ith atom at time t in Cartesian coordinates (in the general Lagrange formalism the Cartesian coordinates r must be distinguished from the generalized coordinates x). The displacement in the vicinity of t can be described by a Taylor expansion:

$$r_i(t+\delta t) = r_i(t) + \dot{r}_i(t)\delta t + \frac{1}{2}\ddot{r}_i(t)(\delta t)^2 + \frac{1}{3!}\dddot{r}_i(t)(\delta t)^3 + \frac{1}{4!}\ddddot{r}_i(t)(\delta t)^4 + \ldots \tag{7.47}$$

$$r_i(t-\delta t) = r_i(t) - \dot{r}_i(t)\delta t + \frac{1}{2}\ddot{r}_i(t)(\delta t)^2 - \frac{1}{3!}\dddot{r}_i(t)(\delta t)^3 + \frac{1}{4!}\ddddot{r}_i(t)(\delta t)^4 \mp \ldots \tag{7.48}$$

By adding equations (7.47) and (7.48) one obtains an expression for the position of the ith atom as a function of its acceleration,

$$\begin{aligned} r_i(t+\delta t) &= 2r_i(t) - r_i(t-\delta t) + \ddot{r}_i(t)(\delta t)^2 + \frac{2}{4!}\ddddot{r}_i(t)(\delta t)^4 + \ldots \\ &\approx 2r_i(t) - r_i(t-\Delta t) + \ddot{r}_i(t)(\Delta t)^2 \end{aligned} \tag{7.49}$$

The required acceleration of the ith atom is calculated from the conservative force $\boldsymbol{F}_i$, the atomic mass m_i, and, if $T \neq 0$, a thermodynamic friction coefficient $\xi(t)$. The force is obtained as a derivative of the respective potential. The velocity of the atom is calculated by subtracting equation (7.47) from equation (7.48).

$$\dot{\boldsymbol{r}}_i(t) \approx \frac{\boldsymbol{r}_i(t+\Delta t) - \boldsymbol{r}_i(t-\Delta t)}{2\Delta t} \tag{7.50}$$

According to these equations the Verlet algorithm can be started if the first two positions of the atoms are known. However, in typical molecular dynamics simulations, only the initial positions and initial velocities are given. Therefore, one first needs a method to calculate the second set of atomic positions before one can start the recursive Verlet algorithm. A common practice to overcome this problem is to treat the force during the first two simulated time steps as a constant and to apply conventional kinematics, i.e.

$$\boldsymbol{r}_i(t+\Delta t) \approx \boldsymbol{r}_i(t) + \Delta t\, \dot{\boldsymbol{r}}_i(t) + \frac{(\Delta t)^2}{2}\, \ddot{\boldsymbol{r}}_i(t) \tag{7.51}$$

7.5 Boundary Conditions

The formulation of adequate boundary conditions for molecular dynamics simulations should consider two main aspects (Wolf and Yip 1992). First, to reduce the efforts for computation (computation time, coding convenience, required random access memory), the size of the simulation box should be as small as possible. On the other hand, the simulation cell should be large enough to exclude the possibility that any kinetic disturbance can re-enter the block leading to an artificial perturbation of the lattice defects being investigated. Furthermore, the box must be large enough to provide reliable statistics. An adequate compromise between both requirements must be found and carefully checked. Second, a physically realistic coupling accounting for volume expansion, strain compatibility, and stress equilibrium between the surrounding and the simulation cell should be considered.

In cases where bulk properties of the material or simple lattice defects without intrinsic periodicity and without long-range interactions are studied one tyically uses simple periodic, i.e. cyclic boundary conditions. Periodic boundary conditions reduce the influence of surface effects on the simulation results.

To use periodic boundary conditions in a simulation of N particles confined to a volume Ω, one can assume that this volume is only a small portion of the sample. The volume Ω is referred to as the "primary cell". It is representative of the bulk material. The bulk sample is assumed to be composed of the primary cell surrounded by exact replicas of itself. These replica cells are referred to as the "image cells" (Figure 7.1). Each cell in the array which consists of the primary cell and the image cells can be identified by a translation vector $\boldsymbol{t}$. The length of the cell L and the translation vectors allow one to describe the positions and velocities of all image particles outside the primary cell as a function of the positions and velocities of the particles inside the primary cell.

$$\begin{aligned} \boldsymbol{r}_i^{\mathrm{im}\,j} &= \boldsymbol{r}_i^{\mathrm{pr}} + L\,\boldsymbol{t}^j \\ \dot{\boldsymbol{r}}_i^{\mathrm{im}\,j} &= \dot{\boldsymbol{r}}_i^{\mathrm{pr}} \end{aligned} \tag{7.52}$$

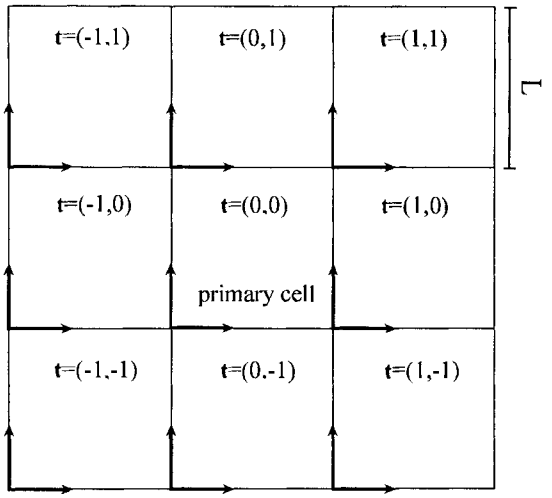

Figure 7.1: Cell array and translation vectors for periodic boundary conditions in two dimensions.

where L is the length of the cell, $\boldsymbol{t}^j$ the cell translation vector of cell j, $\boldsymbol{r}_i^{\mathrm{im}\,j}$ the position vector of the ith image particle in image cell j, $\boldsymbol{r}_i^{\mathrm{pr}}$ the position vector of the ith particle in the primary cell, $\dot{\boldsymbol{r}}_i^{\mathrm{im}\,j}$ the velocity vector of the ith image particle in image cell j, and $\dot{\boldsymbol{r}}_i^{\mathrm{pr}}$ the velocity vector of the ith particle in the primary cell.

In the domain of grain boundary and dislocation simulations physical periodicity can occur naturally, e.g. in large-angle grain boundaries containing a high density of coincidence site lattice points or in low angle grain boundaries consisting of regular arrays of dislocations. Especially in such cases, the superimposition of artificial periodicity makes simulations senseless, irrespective of the quality of the potential employed.

For simulating the dynamics of lattice defects and acoustic waves in materials, the Born–van Kármán, the antiperiodic Möbius, or the generalized helical periodic border conditions are typically used (Sutton 1996). For investigating dislocation emission from crack tips, Kohlhoff, Gumbsch, and Fischmeister (1991) and Gumbsch (1996a) have introduced an integrated method of combining a finite element frame with molecular dynamics simulations. In a similar line, Tadmore, Phillips, and Ortiz (1996) have suggested a mixed atomistic and continuum model for treating the deformation of solids.

Although molecular dynamics is deterministic, it contains a stochastic element, viz. the starting configuration. It should be assured in each molecular dynamics simulation, therefore, before the filtering of relevant data, that the system has passed its relaxation time. The relaxation period can be considerably shortened by choosing a reasonable starting configuration. This can be achieved by prescribing a minimum spacing between the atoms and by using an initial velocity field in accord with the Maxwell distribution.

Various possible boundary conditions in molecular dynamics simulations of lattice defects have been discussed for first-order phase transitions (Binder 1991c), dislocation cores (Vitek 1976), cascade formation and irradiation damage (Bacon 1996), grain boundaries (Wolf and Yip 1992; Finnis and Rühle 1993; Sutton and Balluffi 1995; Sutton 1996), and crack tips (Gumbsch 1996a).

7.6 Application of Molecular Dynamics in Materials Science

A large number of researchers have used molecular dynamics to simulate materials at an atomic scale. In the field of materials science, structural investigations of lattice defects and phase transformations prevail. In this context special attention was devoted to both homophase and heterophase interfaces, dislocations, cracks, interfacial segregation, misfit dislocations, secondary grain boundary dislocations, and structural domains in polymers. Furthermore, substantial contributions were published on the atomic scale synthesis or design of materials. In this context stress was placed particularly on metals, polymers, and ceramics. A number of relevant contributions which were published during recent years are listed in the following table. Of course, the list can by no means be complete but it may serve as a bibliography for getting better acquainted with some examples of the classical and recent original literature in this field. The full citations are given in the bibliography at the end of the book.

Field of application	Reference
classics and fundamentals	Alder and Wainwright (1959)
	Rahman (1964)
	Verlet (1967)
	Verlet (1968)
	Parinello and Rahman (1981)
	Hoover (1986)
	Lutsko, Wolf, and Yip (1988a)
	Sankey and Niklewski (1989)
	Allen and Tildesley (1989)
	Catlow, Parker, and Allen (1990)
	Heermann and Burkitt (1991)
	Allen and Tildesley (1992)
	Daw, Foiles, and Baskes (1993)
	Kirchner, Kubin, and Pontikis (1996)
	Voter (1996)
Environment conditions	Ryckaert, Ciccotti, and Berendsen (1977)
	Andersen (1980)
	Parinello and Rahman (1981)
	Nosé (1984b)
	Nosé (1984a)
structure of misfit dislocations	Wolf, Foiles, and Fischmeister (1991)
	Vitek, Gutekunst, and Rühle (1995)
structure and mobility of interfaces	Lutsko, Wolf, and Yip (1988a)
	Chen, Srolovitz, and Voter (1989)
	Foiles (1989)
	Paxton and Sutton (1989)
	Phillpot, Lutsko, and Wolf (1989b)
	Phillpot, Lutsko, and Wolf (1989a)
	de Hosson and Vitek (1990)
	Jhan and Bristowe (1990)

	Campbell, Gumbsch, and King (1992)
	Weinberg, Shamsuzzoha, and Deymier (1992)
	Wolf and Yip (1992)
	Hofmann and Finnis (1994)
	Majid, Counterman, and Balluffi (1994)
	Vitek, Wang, and Bassani (1994)
	Liu and Plimpton (1995a)
	Liu and Plimpton (1995b)
	Schmidt, Ernst, and Vitek (1995)
	Sutton and Balluffi (1995)
	Dawson, Bristowe, and White (1996)
	Yan, Ernst, and Chen (1996)
structure and energy of lattice dislocations	Vitek (1974)
	Pestman, de Hosson, and Vitek (1989)
	Huang, Meyer, and Pontikis (1990)
	Duesbery and Richardson (1991)
	Huang, Meyer, and Pontikis (1991)
	Pestman, de Hosson, and Vitek (1991)
	Vitek and Igarashi (1991)
	Bigger, McInnes, and Sutton (1992)
	Khantha, Vitek, and Pope (1992)
	Vitek (1992)
	Joos, Ren, and Duesbery (1994)
	Bulatov, Yip, and Argon (1995)
	Hamilton, Daw, and Foiles (1995)
	Hamilton and Foiles (1995)
	Zhang, Wang, and Tang (1995)
	Chen and Ding (1996)
	von Boehm and Nieminen (1996)
	Justo, Bulatov, and Yip (1997)
	Xu and Moriarty (1997)
segregation effects	Kelires and Tersoff (1989)
	Srolovitz, Wang, and Najafabadi (1993)
	Wang, Najafabadi, and Srolovitz (1993)
	Menyhard, Yan, and Vitek (1994)
	Rittner, Foiles, and Seidman (1994)
structure of microcracks	Jokl, Vitek, and McMahon (1989)
	Hoagland, Daw, and Foiles (1990)
	Kohlhoff, Gumbsch, and Fischmeister (1991)
	Zhang and Wang (1996)
	Gumbsch, Zhou, and Holian (1997)
thin films and surfaces	Salik (1985)
	Müller (1985)
	Gilmer, Grabow, and Bakker (1990)
	Loisel, Lapujoulade, and Pontikis (1991)
	Harrison, Colton, and Brenner (1993)
	Sinnott, Colton, and Brenner (1994)
	Finnis, Kaschner, and Scheffler (1995)

	Goringe and Sutton (1996)
	Pinches and Tildesley (1996)
	Smith and Srolovitz (1996)
	Goringe, Clark, and Sutton (1997)
heterophase interfaces	Lutsko, Wolf, and Yip (1988b)
	Gumbsch, Daw, and Foiles (1991)
	Holzman, Adams, and Foiles (1991)
	Duffy, Harding, and Stoneham (1992)
	Hong, Smith, and Srolovitz (1992)
	Duffy, Harding, and Stoneham (1993)
	Stoneham, Ramos, and Sutton (1993)
	Duffy, Harding, and Stoneham (1994)
	Floro, Thompson, and Bristowe (1994)
	Hong, Smith, and Srolovitz (1994)
	Majid, Counterman, and Bristowe (1994)
	Duffy, Harding, and Stoneham (1995)
	Finnis, Kruse, and Schönberger (1995)
	Duffy, Harding, and Stoneham (1996)
	Finnis (1996)
	Kruse, Finnis, and Gillan (1996)
materials design	Chen, Voter, and Albers (1990)
	Pettifor (1990)
	Pettifor (1992)
	Hammonds, McDonald, and Tildesley (1993)
	Robertson, Brenner, and White (1995)
	Godwin, Horsfield, and Sutton (1996)
atomistics and finite elements	Kohlhoff, Gumbsch, and Fischmeister (1991)
	Gumbsch (1996b)
	Gumbsch (1996a)
	Tadmore, Phillips, and Ortiz (1996)
	Tadmore, Ortiz, and Phillips (1996)

7.7 Examples of Molecular Dynamics Simulations in Materials Science

7.7.1 Simulation of Chain Dynamics in Polymers

The atomic-scale dynamics of monomers and polymers has been widely investigated using molecular dynamics and Monte Carlo methods. Particular attention has been drawn to the simulation of the motion and reaction of single chains. While considerable progress in the understanding of chain dynamics and polymerization was obtained by using the so called force bias Monte Carlo method, this section presents a simple molecular dynamics simulation.

The simulation uses a modified Lennard–Jones potential and the finite extendable nonlinear elastic attractive potential (FENE potential) to mimic the interaction among the monomers. Figure 7.2, as an example, shows a number of successive positions for a polymer chain.

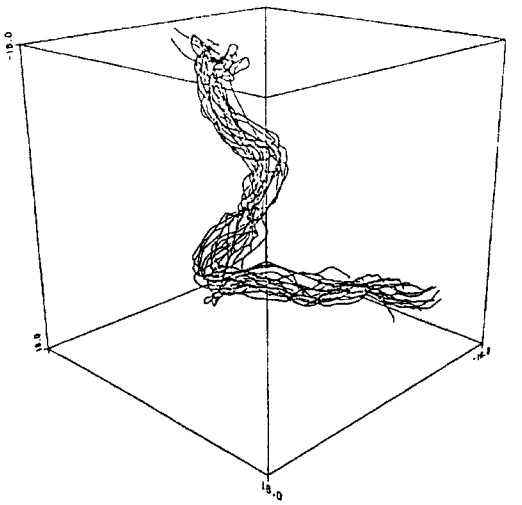

Figure 7.2: Molecular dynamics simulation showing a number of successive positions of a polymer chain (Müller-Krumbhaar 1989).

7.7.2 Simulation of Brittle Fracture

Gumbsch (1996b) has introduced a finite element – atomistic method to simulate crack tips in brittle materials. The main difficulties in dealing with the structure and the dynamic properties of crack tips arise both from the singularity of the elastic stress field, which scales inversely with the square root of the distance in the immediate vicinity of the crack tip, and from the fact that the crack tip morphology might reveal relaxations at the atomic scale. Figure 7.3 shows the basic setup of the finite element – atomistic method for the simulation of crack tips in NiAl. While the outer region is modeled using the finite element method, the crack tip is described using the relaxation of single atoms (Figure 7.4). The atomic interaction is described in terms of an embedded atom potential. The coupling between both regimes is provided by a transition layer. Similar simulations, coupling finite element and atomistic simulations, have been carried out by Tadmore, Phillips, and Ortiz (1996).

7.7.3 Simulation of Wafer Bonded Silicon Interfaces

Scheerschmidt, Conrad, and Gösele (1996) have carried out a molecular dynamics simulation of bonded wafer interfaces in silicon. The bonding of silicon wafers becomes of increasing importance for silicon applications and micromechanics.

The molecular dynamics simulation has been performed using a modified Stilling–Weber potential. The bonding has been described between cube-oriented silicon surfaces. Figure 7.5 demonstrates the gradual simulated generation of a twist boundary during a computed annealing experiment, starting from two misoriented single crystals.

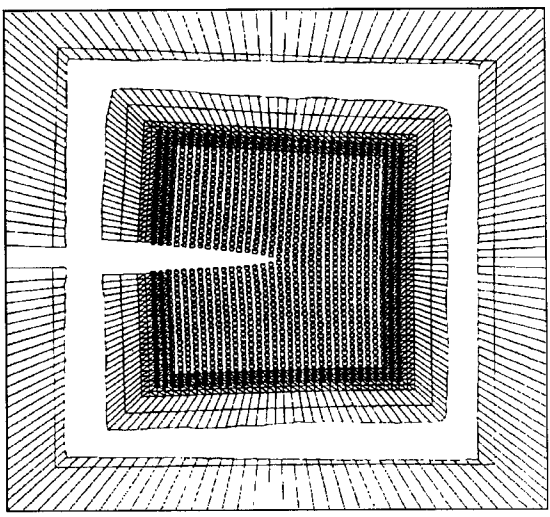

Figure 7.3: Basic setup of the finite element – atomistic method for the simulation of crack tips in NiAl (Gumbsch 1996b).

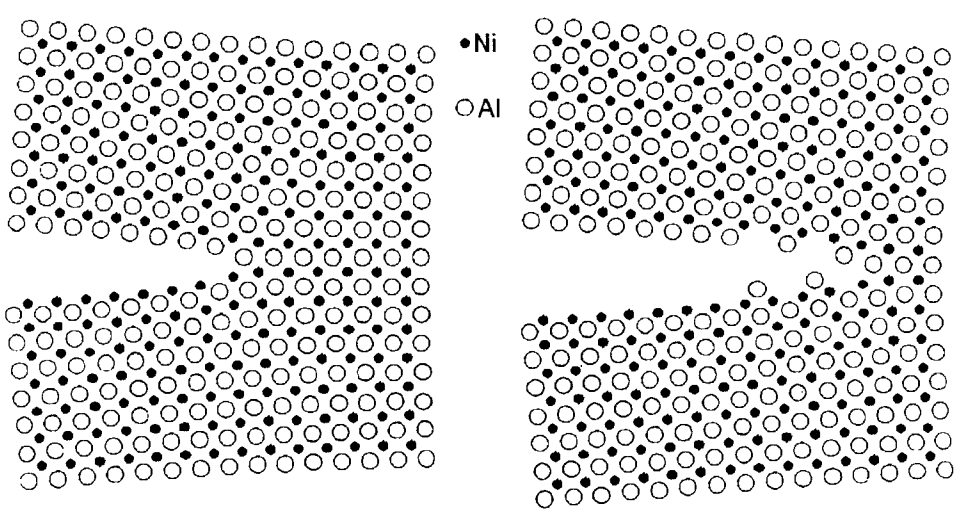

Figure 7.4: Atomic structure of a moving crack tip in NiAl (Gumbsch 1996b).

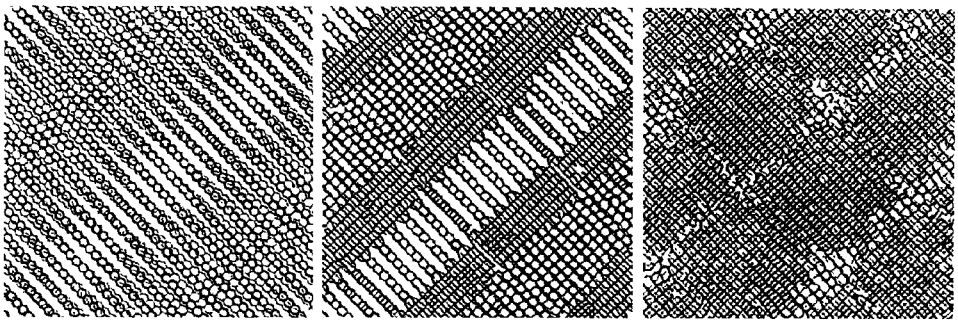

Figure 7.5: Gradual generation of a twist boundary during a simulated molecular dynamics annealing experiment, starting from two misoriented single crystals (Scheerschmidt et al. 1996).

7.7.4 Simulation of Void Formation during Thin Film Deposition

Smith and Srolovitz (1996) have performed two-dimensional non-equilibrium molecular dynamics simulations of void formation during thin film deposition. The simulations have been made using single crystalline substrates with a Lennard–Jones potential. The integration of the equations of motion was performed in a step-wise manner using a fifth-order predictor–corrector method.

Figure 7.6 presents some typical simulated microstructures for thin films grown at various substrate temperatures under a constant deposition kinetic energy. The main microstructural features to develop within these films are single vacancies and small voids. The voids tend to be slightly elongated and to be aligned in the growth direction of the film. Voids are generated as a consequence of both surface roughness and shadowing effects. The authors observed that both the void volume and the mean surface roughness of the films were decreasing functions of substrate temperature and deposition kinetic energy.

7.7.5 Simulation of Interaction of Dislocations with Grain Boundaries

Zhang and Wang (1996) have carried out two-dimensional molecular dynamics simulations of the interaction of a dislocation array from a crack tip with grain boundaries. The dislocation array was emitted from a moving crack tip under mode II loading conditions. The dislocations interacted with asymmetric tilt grain boundaries.

The boundaries revealed planar and linear matching zones and unmatching zones. All grain boundaries were observed to emit dislocations and to migrate as a result of the interaction.

The simulations have been made using a Finnis–Sinclair type second moment potential. Figure 7.7 shows a representative simulated microstructure with grain boundary segments, dislocations, and a newly formed grain.

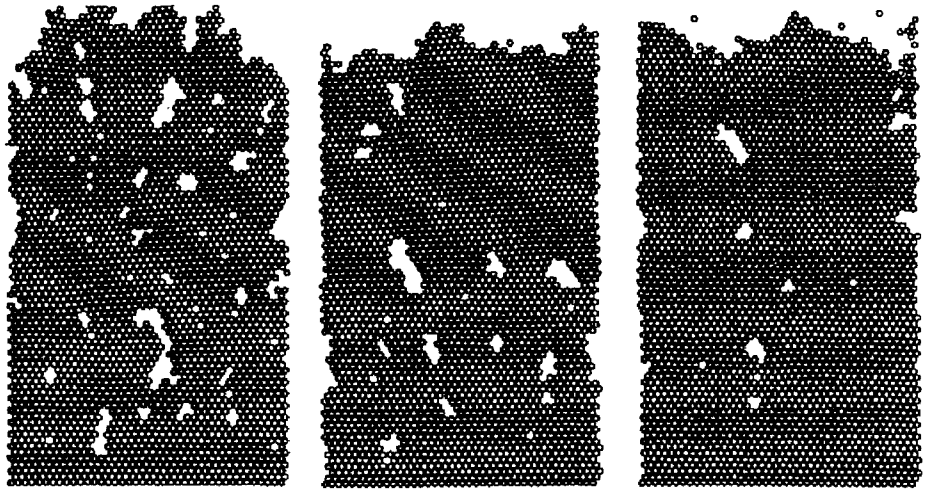

(a) (b) (c)

Figure 7.6: Simulated microstructures for thin films grown at various substrate temperatures under a constant deposition kinetic energy; (a) T=0.0 ϵ/k_B; (b) T=0.0625 ϵ/k_B; (c) T=0.125 ϵ/k_B; ϵ= 0.74 eV; (Smith and Srolovitz 1996).

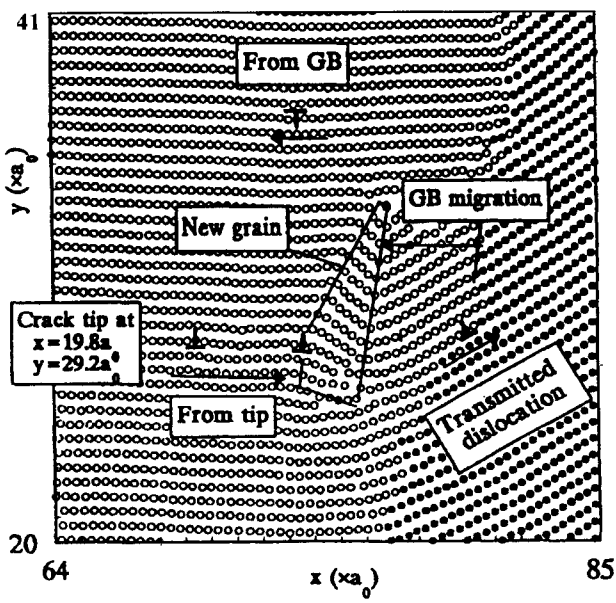

Figure 7.7: Simulated microstructure with grain boundary segments, dislocations, and a newly formed grain (Zhang and Wang 1996).

Part III

Simulation Techniques at the Microscopic–Mesoscopic Scale

Computational Materials Science: The Simulation of Materials, Microstructures and Properties By Dierk Raabe
Copyright © 1998 Wiley-VCH Verlag GmbH
ISBN: 3-527-29541-0

Chapter 8

Introduction

The quantitative investigation and prediction of microstructure evolution, and the derivation of corresponding microstructure-property relations at the micro- and mesoscale, constitute possibly the broadest and most characteristic discipline of computational materials science. Structure evolution at the microscopic–mesoscopic level is typically a thermodynamically non-equilibrium process, and thus mainly governed by kinetics. In other words, *thermodynamics* prescribes the principal *direction* of microstructure evolution while *kinetics* selects one out of many possible microstructural *paths*. This non-equilibrium character of structure evolution leads to a large variety of lattice defect structures and interactions.

Optimizing microstructure evolution at the mesoscopic scale is of fundamental importance, since it is particularly these non-equilibrium ingredients that can lead to beneficial materials properties. A thorough understanding of microstructural mechanisms thus enables one to tailor materials with certain property profiles for specific applications.

Investigating microstructural phenomena at realistic time and space scales, for predicting macroscopic properties, requires the consideration of relatively large portions of material (Table 8.1). However, due to the huge number of atoms involved ($\approx 10^{23}$ in a cubic centimeter), mesoscale simulations of microstructures can be performed neither by exactly solving the Schrödinger equation nor by using phenomenological atomistic approaches, such as molecular dynamics in conjunction with empirical potentials. This means that appropriate mesoscale simulations must be formulated which are capable of spanning a wider range of scales allowing predictions far beyond the atomic scale.

In most cases, this requires the introduction of continuum models in which averaging constitutive relations and phenomenological rate equations replace the exact or approximate solution of the equations of motion of all atoms. However, due to the large variety of mesoscale mechanisms and possible constitutive laws, there exists no *unique* method of formulating mesoscale models.

It is not the aim of this chapter to provide an exhaustive review of the large number of statistical, phenomenological, and more or less empirical models that dominate the field of mesoscopic non-space-discretized materials modeling, but to concentrate on those simulations that are discrete in both space and time, and explicitly incorporate the properties of individual lattice defects in a continuum formulation. The philosophy behind this is twofold. First, the various classical phenomenological mesoscopical modeling approaches, which are discrete in time but not in space, have already been the subject of numerous thorough studies in the past, particularly in the fields of crystal plasticity,

Computational Materials Science: The Simulation of Materials, Microstructures and Properties By Dierk Raabe
Copyright © 1998 Wiley-VCH Verlag GmbH
ISBN: 3-527-29541-0

Table 8.1: Typical scales in microstructures.

Scale [m]	Characteristic phenomenon or defect
10^{-10}–10^{-7}	point defects, atomic clusters, short-range order, structural units in glasses and interfaces, dislocation cores, crack tips, nuclei
10^{-9}–10^{-5}	spinodal decomposition, coatings, thin films, surface corrosion
10^{-9}–10^{-4}	diblock-, triblock-, and starblock-copolymers, massive and athermal transformations, interface facets, dislocation sources, pile-ups
10^{-9}–10^{-3}	particles, precipitations, dendrites, eutectics, eutectoids
10^{-8}–10^{-5}	microcracks, cracks, powder, magnetic domains, internal stresses
10^{-8}–10^{-4}	stacking faults, microbands, microtwins, dislocation channels
10^{-8}–10^{-3}	spherolites in polymers, structure domains/crystal clusters (crystalline, amorphous) in metals, ceramics, glass, and polymers
10^{-8}–10^{-2}	clusters of conformative defects in polymers
10^{-8}–10^{-1}	dislocations, dislocation walls, disclinations, magnetic walls, subgrains, high-angle grain boundaries, interfaces
10^{-7}–10^{-1}	grains, shear bands, second phases in composites
10^{-7}–10^{0}	diffusion, convection, heat transport, current transport
10^{-7}–10^{0}	microstructural percolation paths (fracture, recrystallization, interface wetting, diffusion, corrosion, current, Bloch walls)
10^{-6}–10^{1}	surfaces, sample necking, fracture surfaces

recrystallization phenomena, and phase transformation (Kocks 1966; Argon 1975; Kocks et al. 1975; Mughrabi 1980; Mecking and Kocks 1981; Mughrabi 1983; Estrin and Mecking 1984; Prinz and Argon 1984; Estrin and Kubin 1986; Gottstein and Argon 1987; Kocks 1987; Rösler and Arzt 1988a; Rösler and Arzt 1988b; Marthinsen et al. 1989; Rösler and Arzt 1990; Estrin and McCormick 1991; Kubin 1993b; Gil Sevilliano 1993; Reppich 1993). These models usually provide statistical rather than discrete solutions and can often be solved without employing time-consuming numerical methods. This is why they often serve as a physical basis for deriving phenomenological constitutive equations that can be incorporated in advanced larger-scale finite element, self-consistent, or Taylor-type simulations (Argon 1975; Gittus and Zarka 1986; Andersen et al. 1987; Kocks 1987; Nemat-Nasser and Hori 1993; Krausz and Krausz 1996). However, since such constitutive descripions only provide an *averaged* picture of the material response to changes in the external constraints, they are confined to statistical predictions and do not mimic any details of the microstructural evolution. Hence, they are beyond the scope of this book. Second, physically sound micro- and mesoscale material models that are discrete in both space and time must incorporate the statics and kinetics of *individual* lattice defects. This makes them superior to the more descriptive statistical models in that they allow simulations that are more precise in their microscopical predictions due to the smaller number of phenomenological assumptions involved.

The concept of discretizing materials-related models on the basis of the discrete properties of each individual lattice defect involved confronts one, as in molecular dynamics, with the task of formulating and solving many-body interaction phenomena[1]. The gov-

[1] "Many-body" means "many lattice defects", i.e. dislocation segments, interface segments, etc.

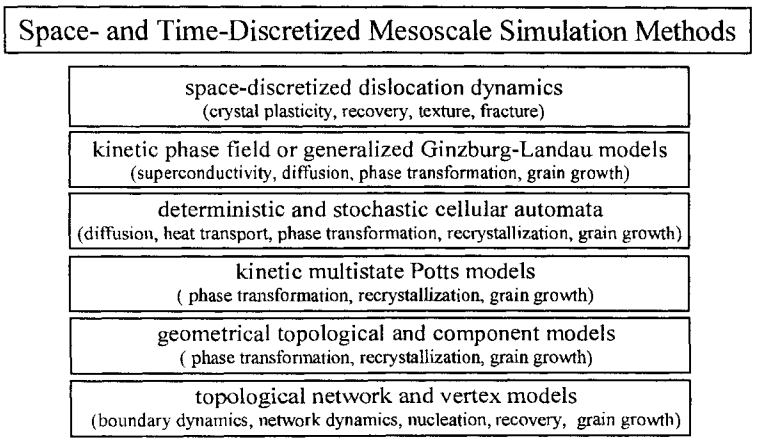

Figure 8.1: Main mesoscale simulation methods with typical fields of application.

erning equations in such approaches are usually partial differential equations that reflect the behavior of individual rather than averaged populations of lattice defects. These expressions, particularly when coupled, are typically of a nonlinear character and thus can entail self-organization on a microstructural scale (Haken 1978; Kubin 1988).

Extracting quantitative predictions from such models typically requires numerical computation. The discussion of highly discretized microstructure simulations at the meso- and microscale thus fits exactly the purpose of this book.

This chapter deals with six major groups of techniques that occur in the field of mesoscale materials simulations, namely, space-discretized dislocation dynamics (Chapter 9), kinetic phase field or generalized Ginzburg–Landau models (Chapter 10), deterministic and stochastic cellular automata (Chapter 11), multistate kinetic Potts models (Chapter 12), geometrical and component models (Chapter 13), and topological network or vertex models (Chapter 14) (Figure 8.1).

These simulation methods have in common that they do not explicitly incorporate atomic-scale dynamics, but they idealize the material as a *continuum*. This means that the lattice defects share a common homogeneous matrix medium through which their interaction is coupled. Consequently, the corresponding governing equations do not usually introduce an explicit intrinsic space or time scale. Classifying these approaches as simulation techniques at the micro–meso level is thus to a certain extent arbitrary and depends strictly on the underlying physical model. Continuum-type mesoscale models involving individual lattice defects are typically formulated in terms of phenomenological sets of partial differential rate and constitutive equations. The character of these differential equations and their coefficients and variables usually provide means of identifying appropriate temporal and spatial scaling parameters and a correct level of discretization for the finite difference, finite element, or Monte Carlo methods which are used to solve them. The state variables, e.g. atomic concentration, dislocation density, structure parameters, displacement, or lattice orientation, are in these models often assigned to the coordinates of a spatial grid and the governing differential equations are applied to them in a local or global fashion, depending on the character of the interaction (long-range, short-range). Using continuum approaches for yielding mesoscale predictions makes sense,

since phenomenological state equations and structural evolution laws are often well investigated at the mesoscale, where experimental data can be obtained more easily than at the microscale, and more detailed than at the macroscale.

Chapter 9 is concerned with the simulation of plasticity at the microscopic and mesoscopic levels using space- and time-discretized dislocation dynamics. While Potts models, cellular automata, and the various topological approaches are particularly suited for simulating interface phenomena with short-range interactions, discrete dislocation models are designed to deal with line defects problems that involve long-range interactions.

Space-discretized dislocation simulations idealize dislocations outside their cores as linear defects which are embedded within an otherwise homogeneous, isotropic or anisotropic, linear elastic medium. This applies for both straight infinite dislocations and dislocation segments. They are based on discretely simulating the dynamics of individual dislocations considering both time and the actual position of each defect as independent variables. The previous work in this field can be grouped into simulations in two dimensions (2D) and three dimensions (3D). 2D calculations are conducted either with taut dislocations that cannot leave their actual glide plane (Foreman and Makin 1966; Bacon et al. 1973; Scattergood and Bacon 1975; Altintas 1978; Rönnpagel 1987; Rönnpagel et al. 1993; Mohles and Rönnpagel 1996; Mohles 1996), or with nonflexible infinite straight dislocations which may leave their glide plane but cannot bow out (Neumann 1971; Lépinoux and Kubin 1987; Ghoniem and Amodeo 1989; Gulluoglu et al. 1989; Amodeo 1990; Gulluoglu et al. 1990; Gulluoglu and Hartley 1992; Lubarda et al. 1993; Raabe and Roters 1995; Wang and LeSar 1995; Raabe et al. 1996; Roters and Raabe 1997; Zacharopoulos et al. 1997).

3D simulations which decompose each dislocation into a sequence of piecewise straight segments with a scaling length much below the length of the complete dislocation line are independent of such geometrical constraints (Kubin et al. 1992; Demir et al. 1992; Devincre and Condat 1992; Devincre and Kubin 1994; Kubin 1993a; Rhee et al. 1994; Raabe 1995a; Raabe 1996a; Raabe 1996b; Devincre 1996; Rönnpagel 1996; Fivel et al. 1996; Raabe 1998a). The dynamics of the dislocations are usually described by assuming phenomenological viscous or viscoplastic flow laws[2] or by solving Newton's second law for each dislocation or dislocation segment, respectively. The solution of the temporal evolution of the dislocation positions is as a rule obtained by finite difference algorithms.

Chapter 9 reviews the fundamentals required for formulating and solving field equations describing two-dimensional *infinite dislocations* and interconnected three-dimensional *dislocation segments*. The displacement and stress fields for the isotropic limit are derived according to the theory of Yoffe (1960), Li (1965), de Wit (1967), Hirth and Lothe (1982), Devincre (1995), and Rönnpagel (1996) and for the general anisotropic case according to Kröner (1958), Brown (1967), Indenbom and Orlov (1968), Bacon et al. (1979), Hirth and Lothe (1982), and Raabe (1996). This framework of dislocation statics in general dyadic presentation forms the backbone of time- and space-discretized plasticity simulations. It allows one to describe the long-range elastic Peach–Koehler interaction among dislocations in arbitrary ensembles with a high spatial resolution in two and three dimensions.

Chapter 10 deals with Ginzburg–Landau and Cahn–Hilliard-type kinetic phase field models. These represent a group of very general and flexible phenomenological continuum field approaches which are capable of describing continuous and quasi-discontinuous phase separation phenomena in coherent and incoherent systems at the nanoscopic and mesoscopic level (Cahn and Hilliard 1958; Cahn 1961; Cahn 1962; Cahn and Hilliard 1965;

[2] "Viscous flow" means that the dislocation is in an overdamped state of motion so that its velocity is linearly proportional to the local net line force. Viscoplastic dynamics phenomenologically describe strain rate sensitive flow.

Khachaturyan 1968; Landau and Lifshitz 1980; Landau and Lifshitz 1981). While original versions of the Ginzburg–Landau approach addressed electromagnetic problems with non-conserved field variables, such as phase separation phenomena in Shubnikov phases, i.e. the concentration distribution of Cooper pairs, advanced metallurgical variants are capable of addressing the distribution of conserved continuous atomic concentration parameters and nonconserved quasi-discontinuous structural and/or orientational parameters in coherent and non-coherent systems[3] (Wang et al. 1996). Phase field models can be regarded as a set of Onsager kinetic equations furnished with an appropriate free energy functional that may depend on such quantities as atomic or boson concentration and long-range order. For transcribing this approach into a form that is discrete in space, these state parameters are used as field variables. The dependence of the variables on the spatial coordinates enables one to prescribe heterogeneous composition and structure fields, and allows one to simulate both the kinetics and the resulting morphology of phase separation phenomena.

Phase field approaches are generally based on the assumption that the material is homogeneous and that the chemical portion of the total free energy density functional can be expressed in a Landau form.

In those versions where only the conservative concentration field is considered (original Cahn–Hilliard theory), the phase field method is confined to describing isostructural phase transformations. The phases may then differ from each other only in concentration, but not in long-range order or crystal structure. For incorporating the latter parameters, the theory can be extended by introducing additional, nonconservative field variables (Allen–Cahn theory) and by complementing the energy density functional with corresponding terms (Khachaturyan 1983; Chen and Khachaturyan 1991a; Wang et al. 1991; Chen et al. 1992; Wang et al. 1993; Chan and Rey 1995; Johnson et al. 1994; Dreyer 1995; Chen and Wang 1996; Löchte and Gottstein 1996; Löchte et al. 1998).

Chapter 11 is concerned with cellular automata, the use of which ranges from diffusion simulations at the atomic level to the description of population evolution and traffic systems at the macroscale. In computational materials science, they are increasingly used for phase transformation simulations at the mesoscale.

The chapter addresses both deterministic and stochastic cellular automata with local transformation rules, such as are used for recrystallization simulations. While deterministic cellular automata discretely solve differential equations locally with a finite difference or finite element method, stochastic automata use random sampling techniques. The particular strength of cellular automata lies in the local or global application of practically arbitrary transformation rules which determine the value of a state variable at a site as a function of the neighboring sites (local) or of all sites (global) (Wolfram 1983). This property makes the cellular automaton approach a highly effective technique for simulating microstructur evolutions on the basis of short- and long-range interactions. Cellular automata must not be confused with ordinary finite difference or finite element methods. Their definition is much more general and flexible. For instance, cellular automata may not only use differential equations as local transformation rules and functional formulations as global transformation rules, but they may define any additional arbitrary deterministic, probabilistic, or even fuzzy-type rule to be applied to the state variables. Cellular automata have some similarity to the Potts Monte Carlo method. Both work in a discrete spatial lattice whose sites can switch according to the status of neighboring

[3]The term "quasi-discontinuous" means that the structural and chemical field variables used in Ginzburg–Landau-type approaches are generally defined as continuous spatial functions. This means that interfaces are described in terms of a more or less smooth gradient term with a non-zero spatial extension rather in terms of a sharp change in the corresponding field variable.

sites through certain transformation rules. However, except for this similarity in the spatial discretization, cellular automata are fundamentally different from the Monte Carlo method since they perform a simultaneous rather than a sequential state variable update, and can involve a huge variety of possible transformation rules.

Chapter 12 deals with kinetic Monte Carlo simulations. The original Potts Monte Carlo model (Chapter 6) was introduced to simulate ensemble averages on the basis of nearest-neighbor interactions, but with a Hamiltonian which only accounts for interactions among dissimilar neighbors (equation (6.36)). Its application in the field of mesoscale microstructure simulation was made possible through the introduction of generalized spins and kinetic measures (Potts 1952; Wu 1982; Fernandez 1989; Hu and Hsiao 1992; Bassler and Zia 1994; Chen and Hu 1994; Chen et al. 1995; Janke and Villanova 1995).

For predicting ripening phenomena, particularly grain growth, the Potts models used in computational materials science take a quasi-microscopic metallurgical view where the crystal interior consists of a number of lattice portions of equal size with a specific energy content and/or orientation. While regions with identical values of their state variables form homogeneous crystals, the grain boundaries are identified as the interfaces between different types of such regions. According to the interaction term that occurs in the delta-type Hamiltonian each interface segment has a finite energy. Interface curvature leads to increased wall energy on the convex side and thus to wall migration (Anderson et al. 1984; Srolovitz et al. 1984; Srolovitz et al. 1986; Grest et al. 1988; Srolovitz et al. 1988; Müller-Krumbhaar 1989; Rollett et al. 1989; Rollett et al. 1989; Doherty et al. 1990; Glazier et al. 1990; Tavernier and Szpunar 1991b; Tavernier and Szpunar 1991a; Rollett et al. 1992; Peczak 1995; Murch and Zhang 1995; Desplat et al. 1996; Holm et al. 1996; Mehnert and Klimanek 1998).

Chapter 13 is concerned with geometrical and component models of materials topology. These are mainly used to mimic recrystallization and grain growth phenomena. They typically construct Wigner–Seitz-type topologies for a given distribution of starting points in a spatial lattice. The starting points can be defined as nucleation sites. Geometrical models of growth topology do not include the true dynamics of lattice defects. However, they allow a fast prediction of simple recrystallization and growth textures and microstructures. For site-saturated and spatially random nucleation conditions, geometrical models predict Voronoi structures (Frost and Thompson 1987a; Frost et al. 1990; Juul Jensen 1992; Juul Jensen 1997a).

Chapter 14 deals with topological network or vertex models. These methods provide the main tools for simulating boundary dynamics, i.e. they predict the structural evolution of dislocation networks as well as subgrain and large-angle grain structures. The boundaries are approximated as straight or curved line defects. They can rearrange themselves according to the influence of external loads, interface curvature, and gradients in the stored internal energy across the interface, giving rise to forces that act perpendicularly on each portion of interface.

The resulting boundary movements are usually performed according to the resulting net force and the boundary mobility. The underlying law of motion usually consists in viscous flow rules amounting to using a linearized rate equation. The solutions are obtained by using finite difference schemes. The network models usually consider line tension equilibrium at the triple points and the preservation of line connectivity (Weaire and Kermode 1983; Scavuzzo et al. 1990; Humphreys 1992a; Humphreys 1992b; Draheim and Gottstein 1996b; Svoboda 1996a; Svoboda 1996b; Adams et al. 1997).

Chapter 9

Discrete Dislocation Statics and Dynamics

9.1 Introduction

The numerical simulation of three-dimensional internal stress fields arising from discrete dislocation arrangements is a pertinent tool in formulating advanced flow stress theory. Together with the kinetic parameters of plastic deformation and additional external and internal stress sources arising from the presence of lattice defects other than dislocations, the internal stress fields enter the kinetic law of crystal plasticity which relates the strain rate to the stress state and to microstructure (Kocks 1970; Kocks et al. 1975):

$$\dot{\gamma} = f\left(\sigma, \dot{\sigma}, T, S_1, S_2, ..., S_n\right) \tag{9.1}$$

In this scalar presentation $\dot{\gamma}$ is the strain rate accomplished by a single slip system being controlled by a single stress component σ, the rate of stress change $\dot{\sigma}$, the temperature T, and the microstructure parameters S_1, S_2, ..., S_n which define the actual state of the material. This kinetic part of the constitutive laws of crystal plasticity represents a scalar, path-independent, mechanical equation of state, i.e. its result is determined by the values of state variables. Summarizing the motion of the individual dislocations it can be expressed as a tensorial rate equation (Kocks et al. 1975; Mecking and Kocks 1981):

$$\dot{\varepsilon}_{ij} = f\left(\sigma_{ij}, \dot{\sigma}_{ij}, T, S_1, S_2, ..., S_n\right) \tag{9.2}$$

In these kinematic approaches the time acts as an independent variable and the dislocation density as a state variable. Most approximations using equation (9.2) incorporate microstructure via the Taylor state equation, which relates stress to the square root of the global dislocation density. However, the general application of this equation can lead to inaccurate stress predictions if the dislocation arrangements are neglected. For consideration of dislocation structures especially numerical simulations of dislocation stress fields using three-dimensional dislocation statics represent a helpful diagnostic means of testing, complementing, and improving analytical approaches to the kinetic law of crystal plasticity.

Computational Materials Science: The Simulation of Materials, Microstructures and Properties By Dierk Raabe
Copyright © 1998 Wiley-VCH Verlag GmbH
ISBN: 3-527-29541-0

In addition to these applications in the field of dislocation statics, the internal stresses are required for calculating dislocation structure evolution during plastic deformation. This subject falls into the domain of dislocation dynamics. It represents an essential ingredient in formulating the structural evolution law. The structural evolution law depends on the microstructural path. It is in the classical phenomenological models usually statistically described by a work-hardening term which scales with the square root of the dislocation density, and a dynamic recovery term which is proportional to the global dislocation density.

In differential form the structure change equations constitute, together with the kinetic equation of state, a set of coupled differential equations (Kocks 1966; Kocks et al. 1975; Argon 1975; Mecking and Kocks 1981; Estrin and Mecking 1984; Estrin and Kubin 1986; Kocks 1987; Blum 1993).

$$\begin{aligned} \mathrm{d}S_1 &= f_1\left(\sigma_{ij}, \dot{\sigma}_{ij}, \varepsilon, T, S_1, S_2, ..., S_n\right) \mathrm{d}t \\ \mathrm{d}S_2 &= f_2\left(\sigma_{ij}, \dot{\sigma}_{ij}, \varepsilon, T, S_1, S_2, ..., S_n\right) \mathrm{d}t \\ &\ldots \\ \mathrm{d}S_n &= f_n\left(\sigma_{ij}, \dot{\sigma}_{ij}, \varepsilon, T, S_1, S_2, ..., S_n\right) \mathrm{d}t \end{aligned} \tag{9.3}$$

While the kinematic approaches have matured to a group of models which allow one to predict the stress–strain behavior of pure and commercial polycrystalline metals on an average statistical basis by using a small number of phenomenological parameters which can be fitted from experiment, discrete dislocation simulations focus on such aspects of plasticity where the spatial arrangement of the dislocations is of particular relevance. For this reason discrete simulations of crystal plasticity consider both time and the actual position of each dislocation as independent variables.

This section reviews the basic techniques required for conducting time- and space-discretized simulations of dislocation dynamics in two and three dimensions.

The state equation in these approaches usually amounts to expressing the local stress and strain fields in terms of the local displacement gradients generated by the dislocations according to Hooke's law. Consequently, this section starts with a general introduction to isotropic and anisotropic linear elasticity theory. On this basis the field equations for infinite dislocations (two dimensions) and dislocation segments (three dimensions) will be derived.

Structure evolution, i.e. the dynamics of defect motion, is typically incorporated by using a phenomenological viscous law, strain-rate sensitive (viscoplastic) law, or Newton's law of motion for each portion of dislocation. Simulating the motion of dislocations by using a viscous law where the velocity is linearly proportional to the force reflects the belief that the dislocations are in an overdamped state of glide without inertia. Thus, the use of viscous flow laws confines corresponding dislocation simulations to regimes of high forces (Friedel 1956; Rosenfield et al. 1968; Simmons et al. 1970; Kocks et al. 1975; Weertman and Weertman 1980; Aifantis and Hirth 1983; Nadgornyi 1988; Suzuki 1991).

In contrast, the description of dislocation motion by using Newtonian dynamics, where dislocation inertia is incorporated via its effective mass, provides a more rigorous treatment of the dislocation movement (Granato and Lücke 1956; Granato et al. 1964; Gillis and Kratochvil 1970; Rönnpagel et al. 1993; Raabe 1998a).

The studies in this field can be classified into two-dimensional and three-dimensional calculations. Two-dimensional simulations can be carried out either with flexible dislocations which are constrained to lie in their glide plane (Foreman and Makin 1966; Bacon et al. 1973; Scattergood and Bacon 1975; Arsenault 1986; Rönnpagel 1987; Rönnpagel

et al. 1993; Mohles and Rönnpagel 1996; Mohles 1996), or with infinite straight dislocations which can leave their glide plane (Neumann 1971; Lépinoux and Kubin 1987; Ghoniem and Amodeo 1989; Gulluoglu et al. 1989; Amodeo 1990; Gulluoglu et al. 1990; Gulluoglu and Hartley 1992; Gulluoglu and Hartley 1993; Lubarda et al. 1993; Raabe and Roters 1995; van der Giessen and Needleman 1995; Wang and LeSar 1995; Roters and Raabe 1996; Roters et al. 1996; Raabe et al. 1996; Zacharopoulos et al. 1997). While the first approach provides a top view into the glide plane, the second one provides a lateral perspective parallel to the dislocation tangent. Three-dimensional simulations are independent of such geometrical constraints (Demir et al. 1992; Devincre and Condat 1992; Kubin et al. 1992; Kubin 1993a; Devincre and Kubin 1994; Rhee et al. 1994; Raabe 1995a; Raabe 1995b; Devincre 1996; Fivel et al. 1996; Hirth 1996; Raabe 1996a; Raabe 1996b; Rönnpagel 1996; Raabe 1998a).

9.2 Linear Elasticity Theory for Crystal Plasticity

9.2.1 Introduction

This section reviews the theoretical backbone of linear continuum elasticity theory as required in formulating dislocation field approaches. The interaction between the dislocations is transmitted by the constituent parts of the material. In this approach the material is described as an isotropic or anisotropic linear elastic unbounded homogeneous continuum in which the dislocations are embedded as elementary carriers of displacement and stress. This statement already implies some essentials associated with the mathematical treatment of dislocations, namely, that they are outside their cores simulated as line defects in the framework of linear elasticity. Large strains occurring close to the dislocation cores are naturally excluded from the elastic treatment. For this purpose an inner cut-off radius in the order of the magnitude of the Burgers vector is used.

The dislocations are generally treated as stationary defects, i.e. their displacement field does not depend on time. This implies that for all derivations the time-independent Green's function may be used.

While in the pioneering studies (Devincre and Condat 1992; Kubin 1993b; Raabe 1996a) the field equations for the isotropic elastic case were used for three-dimensional simulations, this chapter presents the general anisotropic field approach (Raabe 1996b; Raabe 1998a). For this reason the following sections recapitulate the elementary concepts of isotropic and anisotropic linear elastic theory. On this basis the field equations for both infinite dislocations (two-dimensional) and finite dislocation segments (three-dimensional) will be developed in Section 9.3.

In what follows the notation x_1, x_2, x_3 will be used in place of x, y, z for the Cartesian coordinate system. This notation has the particular advantage that in combination with Einstein's summation convention it permits general results to be expressed and manipulated in a concise manner. The summation convention states that any term in which the same Latin suffix occurs twice stands for the sum of all the terms obtained by giving this suffix each of its possible values. For instance, the trace of the strain tensor can be written as ε_{ii} and interpreted as

$$\varepsilon_{ii} \equiv \sum_{i=1}^{3} \varepsilon_{ii} = \varepsilon_{11} + \varepsilon_{22} + \varepsilon_{33} \tag{9.4}$$

For the trace of the displacement gradient tensor the same applies:

$$\frac{\partial u_i}{\partial x_i} \equiv \sum_{i=1}^{3} \frac{\partial u_i}{\partial x_i} = \frac{\partial u_1}{\partial x_1} + \frac{\partial u_2}{\partial x_2} + \frac{\partial u_3}{\partial x_3} \tag{9.5}$$

On the other hand, certain results are more conveniently expressed in vector notation (bold symbols, e.g. $\boldsymbol{u}$) or as components (suffices $1, 2, 3$, e.g. u_1, u_2, u_3). In lengthy terms, partial spatial derivatives will be expressed by the abbreviation $v_{1,2}$ instead of $\partial v_1/\partial x_2$.

9.2.2 General Concepts of Elasticity Theory

9.2.2.1 The Displacement Field

In a solid unstrained body the position of each infinitesimal volume element[1] can be described by three Cartesian coordinates x_1, x_2 and x_3. In a strained condition the position of the volume element considered will shift to a new site described by $x_1 + u_1$, $x_2 + u_2$, $x_3 + u_3$, where the triple u_1, u_2, u_3 is referred to as displacement parallel to the x_1, x_2, and x_3 axis, respectively.

The displacement field corresponds to the values of u_1, u_2 and u_3 at every coordinate x_1, x_2, x_3 within the material. In general, the displacement is a vector field which depends on all three spatial variables. It maps every point of the body from its position in the undeformed to its position in the deformed state. For instance, translations represent trivial examples of displacement, namely, that of a rigid-body motion where u_1, u_2, and u_3 are constants (Love 1892; Volterra 1907; Sokolnikoff 1956; Kröner 1958b; Kröner 1965; Eschenauer and Schnell 1993).

9.2.2.2 The Strain Field

Let the corners of a volume element which is much larger than the atomic volume be given by the coordinates (x_1, x_2, x_3), $(x_1 + \Delta x_1, x_2, x_3)$, $(x_1, x_2 + \Delta x_2, x_3)$ and so on. During straining, the displacement of the corner with the coordinates (x_1, x_2, x_3) will amount to (u_1, u_2, u_3). Since the displacement is a function of space it can be different for each corner. Using a Taylor expansion the displacements can be described by

$$\begin{pmatrix} u_1 + \frac{\partial u_1}{\partial x_1}\,\delta x_1 + \frac{\partial u_1}{\partial x_2}\,\delta x_2 + \frac{\partial u_1}{\partial x_3}\,\delta x_3 \\ u_2 + \frac{\partial u_2}{\partial x_1}\,\delta x_1 + \frac{\partial u_2}{\partial x_2}\,\delta x_2 + \frac{\partial u_2}{\partial x_3}\,\delta x_3 \\ u_3 + \frac{\partial u_3}{\partial x_1}\,\delta x_1 + \frac{\partial u_3}{\partial x_2}\,\delta x_2 + \frac{\partial u_3}{\partial x_3}\,\delta x_3 \end{pmatrix} \tag{9.6}$$

Using concise suffix notation equation (9.6) can be rewritten

$$(\, u_1 + u_{1,j}\,\delta x_j, \quad u_2 + u_{2,j}\,\delta x_j, \quad u_3 + u_{3,j}\,\delta x_j\,) \tag{9.7}$$

where the summation convention is implied. The abbreviation $u_{1,2}$ refers to the spatial derivative $\partial u_1/\partial x_2$. These partial derivatives represent the components of the displacement gradient tensor $\partial u_i/\partial x_j = u_{i,j}$. In linear elasticity theory only situations in which

[1] Since for small displacements the elastic bulk modulus is proportional to the spatial derivative of the interatomic forces, any cluster of lattice atoms can be chosen as an infinitesimal volume element.

the derivatives $\partial u_i/\partial x_j$ are small compared with 1 are treated. If the extension of the considered volume element Δx_1, Δx_2, Δx_3 is sufficiently small, the displacement described by equation (9.6) can be written

$$\begin{pmatrix} u_1 + \frac{\partial u_1}{\partial x_1}\Delta x_1 + \frac{\partial u_1}{\partial x_2}\Delta x_2 + \frac{\partial u_1}{\partial x_3}\Delta x_3 \\ u_2 + \frac{\partial u_2}{\partial x_1}\Delta x_1 + \frac{\partial u_2}{\partial x_2}\Delta x_2 + \frac{\partial u_2}{\partial x_3}\Delta x_3 \\ u_3 + \frac{\partial u_3}{\partial x_1}\Delta x_1 + \frac{\partial u_3}{\partial x_2}\Delta x_2 + \frac{\partial u_3}{\partial x_3}\Delta x_3 \end{pmatrix} \tag{9.8}$$

Using suffix notation equation (9.8) is found to be

$$(\, u_1 + u_{1,j}\,\Delta x_j \;,\quad u_2 + u_{2,j}\,\Delta x_j \;,\quad u_3 + u_{3,j}\,\Delta x_j\,) \tag{9.9}$$

For the corner of the volume element with the coordinates $(x_1, x_2 + \Delta x_2, x_3 + \Delta x_3)$ equation (9.8) reduces to

$$\begin{aligned}(u_1 + \frac{\partial u_1}{\partial x_2}\Delta x_2 + \frac{\partial u_1}{\partial x_3}\Delta x_3\,,\; u_2 + \frac{\partial u_2}{\partial x_2}\Delta x_2 + \frac{\partial u_2}{\partial x_3}\Delta x_3\,,& \\ u_3 + \frac{\partial u_3}{\partial x_2}\Delta x_2 + \frac{\partial u_3}{\partial x_3}\Delta x_3)&\end{aligned} \tag{9.10}$$

Similar displacement expressions can be obtained for the other corners of the volume element being considered.

For situations where all of the derivatives except those denoted by $\partial u_1/\partial x_1$, $\partial u_2/\partial x_2$, and $\partial u_3/\partial x_3$ are equal to zero it is straightforward to see that a rectangular volume element preserves its shape. In such a case the considered portion of material merely undergoes positive or negative elongation parallel to its edges. For the x_1 direction the elongation amounts to $(\partial u_1/\partial x_1)\,\Delta x_1$. Hence, the elongation per unit length amounts to $(\partial u_1/\partial x_1)\cdot(\Delta x_1)/(\Delta x_1) = \partial u_1/\partial x_1$. This expression is referred to as strain in the x_1 direction and is indicated by ε_{11}. Positive values are defined as tensile strains and negative ones as compressive strains. The sum of these strains parallel to x_1, x_2, and x_3 defines the dilatation, which equals the change in volume per unit volume associated with a given strain field, i.e. $\varepsilon_{ii} = \varepsilon_{11} + \varepsilon_{22} + \varepsilon_{33} = \operatorname{div} \boldsymbol{u}$, where div is the operator $\partial/\partial x_1 + \partial/\partial x_2 + \partial/\partial x_3$. In case of a nonzero dilatation the strain components describe the change in both shape and size. The situation is different when each of the derivatives denoted by $\partial u_1/\partial x_1$, $\partial u_2/\partial x_2$, $\partial u_3/\partial x_3$ is zero, but the others are not. In such cases the considered initial rectangular volume element is no longer preserved but can both rotate and assume a rhombic shape. A single component of the displacement gradient tensor, for instance $\partial u_2/\partial x_1$, denotes the angle by which a line originally in the x_1 direction rotates towards the x_2 axis during deformation. However, the rotation of an arbitrary boundary line of a small volume element does not necessarily imply that the material is deformed. One could rotate the boundary line simply by rotating the other boundaries accordingly. Such an operation would leave the body undeformed and is therefore referred to as rigid-body rotation. However, if different boundary lines rotate by different angles the volume element undergoes both deformation and rigid-body rotation. By subtracting the rotation components from the displacement gradients one obtains the elements which describe the shape changes. These components are denoted as shear strains $\frac{1}{2}\,(\partial u_1/\partial x_2 + \partial u_2/\partial x_1)$, $\frac{1}{2}\,(\partial u_1/\partial x_3 + \partial u_3/\partial x_1)$, and $\frac{1}{2}\,(\partial u_2/\partial x_3 + \partial u_3/\partial x_2)$. They describe half the angular change between mutually orthogonal lines which were initially parallel to each other. In engineering terms one often encounters the so-called technical strain γ_{ij} which is defined

by $\gamma_{ij} = 2\,\varepsilon_{ij}$. However, this quantity does not represent a tensor component and will not be used in what follows.

From the above, it becomes clear that a deformation state is entirely characterized by the displacement vector field u_i. However, this quantity is an inconvenient representation of deformation since it does not naturally separate shape changes from rigid-body rotations or volume changes. For this purpose the displacement gradient tensor $u_{i,j}$, which in the general case still contains the strain tensor ε_{ij} (tensile/compressive and shear components) and the rigid-body rotation ω_{ij}, seems more appropriate if adequately dismantled. Simple geometrical considerations show that the former portion corresponds to the symmetric part of the displacement gradient tensor and the latter one to its antisymmetric (skew symmetric) part:

$$\begin{pmatrix} u_{1,1} & u_{1,2} & u_{1,3} \\ u_{2,1} & u_{2,2} & u_{2,3} \\ u_{3,1} & u_{3,2} & u_{3,3} \end{pmatrix} = \frac{1}{2}\begin{pmatrix} 2\,u_{1,1} & u_{1,2}+u_{2,1} & u_{1,3}+u_{3,1} \\ u_{2,1}+u_{1,2} & 2\,u_{2,2} & u_{2,3}+u_{3,2} \\ u_{3,1}+u_{1,3} & u_{3,2}+u_{2,3} & 2\,u_{3,3} \end{pmatrix}$$

$$+\frac{1}{2}\begin{pmatrix} 0 & u_{1,2}-u_{2,1} & u_{1,3}-u_{3,1} \\ u_{2,1}-u_{1,2} & 0 & u_{2,3}-u_{3,2} \\ u_{3,1}-u_{1,3} & u_{3,2}-u_{2,3} & 0 \end{pmatrix} \tag{9.11}$$

Using suffix notation this can be concisely rewritten as

$$u_{i,j} = \varepsilon_{ij} + \omega_{ij} = \frac{1}{2}\left(\frac{\partial u_i}{\partial x_j} + \frac{\partial u_j}{\partial x_i}\right) + \frac{1}{2}\left(\frac{\partial u_i}{\partial x_j} - \frac{\partial u_j}{\partial x_i}\right) \tag{9.12}$$

From the linear decomposition of the displacement gradient tensor it is evident that the equivalences $\varepsilon_{ij} = \varepsilon_{ji}$ and $\omega_{ij} = -\omega_{ji}$ apply.

Since the trace elements of the antisymmetric part of the displacement gradient tensor are by definition equal to zero, only three independent components remain. These represent small positive rotations about the axes perpendicular to the displacements from which they are derived, i.e. $\omega_{23} = \omega_{x_1}$ denotes a rotation about the x_1 axis, $\omega_{13} = \omega_{x_2}$ about the x_2 axis, and $\omega_{12} = \omega_{x_3}$ about the x_3 axis. By using the totally antisymmetric Levi–Civita operator ϵ_{ijk}, the components of which are defined to be 1 if the suffices are in cyclic order, -1 if they are in reverse cyclic order and 0 if any two suffices are the same, the three rotations can be compactly written as

$$\omega_{x_k} = \frac{1}{2}\left(\epsilon_{ijk}\,\frac{\partial u_i}{\partial x_j}\right) \tag{9.13}$$

Summarizing the three rotation components as a vector one obtains

$$\boldsymbol{\omega} = \frac{1}{2}\,\mathrm{curl}\,\boldsymbol{u} = \frac{1}{2}\,\boldsymbol{\nabla} \times \boldsymbol{u} \tag{9.14}$$

where $\boldsymbol{\nabla}$ denotes the operator $(\frac{\partial}{\partial x_1}, \frac{\partial}{\partial x_2}, \frac{\partial}{\partial x_3})$ and $\times$ the vector product.

9.2.2.3 The Stress Field

The introduction of the traction vector serves as a starting point for deriving the stress tensor. The traction is defined by

$$\boldsymbol{T} = \lim_{\Delta A \to 0}\left(\frac{\Delta \boldsymbol{F}}{\Delta A}\right) = \frac{\mathrm{d}\boldsymbol{F}}{\mathrm{d}A} \tag{9.15}$$

where $\boldsymbol{T}$ denotes the traction vector, A the area, and $\boldsymbol{F}$ the externally imposed force vector. In suffix notation the traction can be written

$$T_i = \lim_{\Delta A \to 0} \left(\frac{\Delta F_i}{\Delta A} \right) = \frac{\mathrm{d}F_i}{\mathrm{d}A} \tag{9.16}$$

Since the traction vector depends on the inclination of the area element considered, it is pertinent to look for a more general form to describe the effect of external forces on the material. Such a description can be found by considering the traction vectors of three orthogonal sections, the unit normal vectors of which are denoted by n_1, n_2, n_3:

$$T_j = \sigma_{ij}\, n_i \tag{9.17}$$

Thus, by definition of equation (9.17), the stress σ_{ij} is a tensor field which connects $\boldsymbol{T}$ to $\boldsymbol{n}$ at any point within the material. Equation (9.17) is referred to as the Cauchy stress formula.

The components σ_{ij} with $i = j$ give the respective force component along the positive x_j axis acting through the area element having its normal along the same direction. They are referred to as normal stresses. The components σ_{ij} with $i \neq j$ give the corresponding two orthogonal force components acting in the same area element along the two respective positive x_j axes, where $i \neq j$. They are referred to as shear stresses. Considering momentum equilibrium under static conditions one obtains $\sigma_{ij} = \sigma_{ji}$. By solving the eigenvalue problem

$$| \sigma_{ij} - \delta_{ij}\sigma | = \sigma^3 - I_1\, \sigma^2 + I_2\, \sigma - I_3 = 0 \tag{9.18}$$

where δ_{ij} is the Kronecker symbol, and I_1, I_2, I_3 the invariants of the stress state, one obtains the principal stresses $\sigma = \sigma_1, \sigma_2, \sigma_3$. The principal axes are the eigenvectors associated with this stress tensor. The invariants amount to

$$\begin{aligned}
I_1 &= \sigma_{ii} = \sigma_{11} + \sigma_{22} + \sigma_{33} \\
&= \sigma_1 + \sigma_2 + \sigma_3 \\
I_2 &= \frac{1}{2}\left(\sigma_{ii}\sigma_{jj} - \sigma_{ij}\sigma_{ij}\right) = \sigma_{11}\sigma_{22} - \sigma_{12}^2 + \sigma_{22}\sigma_{33} - \sigma_{23}^2 + \sigma_{11}\sigma_{33} - \sigma_{13}^2 \\
&= \sigma_1\,\sigma_2 + \sigma_1\,\sigma_3 + \sigma_2\,\sigma_3 = \begin{vmatrix} \sigma_{11} & \sigma_{12} \\ \sigma_{12} & \sigma_{22} \end{vmatrix} + \begin{vmatrix} \sigma_{22} & \sigma_{23} \\ \sigma_{23} & \sigma_{33} \end{vmatrix} + \begin{vmatrix} \sigma_{11} & \sigma_{13} \\ \sigma_{13} & \sigma_{33} \end{vmatrix} \\
I_3 &= \det\left(\sigma_{ij}\right) = \sigma_{11}\sigma_{22}\sigma_{33} + 2\,\sigma_{12}\sigma_{13}\sigma_{23} - \sigma_{11}\sigma_{23}^2 - \sigma_{22}\sigma_{13}^2 - \sigma_{33}\sigma_{12}^2 \\
&= \sigma_1\,\sigma_2\,\sigma_3 = \begin{vmatrix} \sigma_{11} & \sigma_{12} & \sigma_{13} \\ \sigma_{12} & \sigma_{22} & \sigma_{23} \\ \sigma_{13} & \sigma_{23} & \sigma_{33} \end{vmatrix}
\end{aligned} \tag{9.19}$$

Since conservative dislocation motion is practically unaffected by the hydrostatic stress, it is pertinent to dismantle a given static stress state into its deviatoric and its hydrostatic portions. The latter contribution is given by

$$\sigma^{\mathrm{h}} = \frac{1}{3}\,\sigma_{ii} = \frac{1}{3}\,\left(\sigma_{11} + \sigma_{22} + \sigma_{33}\right) = \frac{1}{3}\,I_1 \tag{9.20}$$

The deviatoric stress tensor can then be written

$$\sigma_{ij}^{\mathrm{d}} = \sigma_{ij} - \delta_{ij}\,\sigma^{\mathrm{h}} = \begin{pmatrix} \sigma_{11} - \sigma^{\mathrm{h}} & \sigma_{12} & \sigma_{13} \\ \sigma_{21} & \sigma_{22} - \sigma^{\mathrm{h}} & \sigma_{23} \\ \sigma_{31} & \sigma_{32} & \sigma_{33} - \sigma^{\mathrm{h}} \end{pmatrix} = S_{ij}$$

$$= \begin{pmatrix} S_{11} & S_{12} & S_{13} \\ S_{21} & S_{22} & S_{23} \\ S_{31} & S_{32} & S_{33} \end{pmatrix} = \begin{pmatrix} S_{11} & \sigma_{12} & \sigma_{13} \\ \sigma_{21} & S_{22} & \sigma_{23} \\ \sigma_{31} & \sigma_{32} & S_{33} \end{pmatrix} \tag{9.21}$$

The operation of adding or subtracting hydrostatic contributions to or from the deviator corresponds to a shift of the Mohr circle parallel to the abscissa or to the generation of a closed stress surface which is a hypersurface in stress space. Since the first invariant of the stress deviator is equal to zero, the characteristic polynom reduces to

$$|\,\sigma_{ij} - \sigma^{\mathrm{h}} - \delta_{ij}\,\sigma\,| = \sigma^3 + J_2\,\sigma_d - J_3 = 0 \tag{9.22}$$

where J_2 and J_3 are the remaining two invariants of the deviator and $\sigma = S_1, S_2, S_3$ the corresponding principal stresses (von Mises 1913; Westergaard 1920; von Mises 1928; Reuss 1930; Sokolnikoff 1956). The invariants of the stress deviator are

$$\begin{aligned} J_1 &= S_{ii} = 0 \\ J_2 &= \frac{1}{2}\left(S_{ij}\,S_{ij}\right) = \frac{1}{2}\left(S_{11}^2 + S_{22}^2 + S_{33}^2\right) + \sigma_{12}^2 + \sigma_{23}^2 + \sigma_{13}^2 \\ &= \frac{1}{2}\left(S_1^2\,S_2^2\,S_3^2\right) = \frac{1}{6}\left[(\sigma_{11} - \sigma_{22})^2 + (\sigma_{22} - \sigma_{33})^2 + (\sigma_{33} - \sigma_{11})^2\right] + \sigma_{12}^2 + \sigma_{23}^2 + \sigma_{13}^2 \\ J_3 &= \det\left(S_{ij}\right) = \frac{1}{3}\,S_{ij}\,S_{jk}\,S_{ki} = S_1 + S_2 + S_3 = \begin{vmatrix} S_{11} & S_{12} & S_{13} \\ S_{12} & S_{22} & S_{23} \\ S_{13} & S_{23} & S_{33} \end{vmatrix} = \begin{vmatrix} S_{11} & \sigma_{12} & \sigma_{13} \\ \sigma_{12} & S_{22} & \sigma_{23} \\ \sigma_{13} & \sigma_{23} & S_{33} \end{vmatrix} \end{aligned} \tag{9.23}$$

where S_{ij} are the components and S_1, S_1, and S_3 the principal stresses of the deviator.

9.2.3 Equilibrium Equations

For deriving the differential equations of equilibrium one has to apply Newton's second law to a small rectangular volume element, $\delta x_1 \delta x_2 \delta x_3$, under externally imposed forces $\boldsymbol{F}$ and body forces $\boldsymbol{P}$ acting on it[2]. It is assumed that the external forces may vary with position so that they can be dissimilar on opposite faces of the volume element. Using a Taylor expansion for the variation of stress as a function of position and Newton's second law gives the dynamic equations of equilibrium

$$\begin{aligned} m\,\frac{\partial^2 u_1}{\partial t^2} = &\left(\sigma_{11} + \frac{\partial \sigma_{11}}{\partial x_1}\delta x_1 - \sigma_{11}\right)\delta x_2 \delta x_3 + \left(\sigma_{12} + \frac{\partial \sigma_{12}}{\partial x_2}\delta x_2 - \sigma_{12}\right)\delta x_1 \delta x_3 \\ &+ \left(\sigma_{13} + \frac{\partial \sigma_{13}}{\partial x_3}\delta x_3 - \sigma_{13}\right)\delta x_1 \delta x_2 + P_1\,\delta x_1 \delta x_2 \delta x_3 \end{aligned}$$

[2] A body force is one that acts directly on every particle of the body, rather than being applied by tractions at its boundaries and transmitted through the various particles by means of internal stresses. Common examples of body forces are forces due to gravity and centrifugal forces.

$$m\,\frac{\partial^2 u_2}{\partial t^2} = \left(\sigma_{22} + \frac{\partial \sigma_{22}}{\partial x_2}\delta x_2 - \sigma_{22}\right)\delta x_1 \delta x_3 + \left(\sigma_{21} + \frac{\partial \sigma_{21}}{\partial x_1}\delta x_1 - \sigma_{21}\right)\delta x_2 \delta x_3 + \left(\sigma_{23} + \frac{\partial \sigma_{23}}{\partial x_3}\delta x_3 - \sigma_{23}\right)\delta x_2 \delta x_1 + P_2\,\delta x_1 \delta x_2 \delta x_3$$

$$m\,\frac{\partial^2 u_3}{\partial t^2} = \left(\sigma_{33} + \frac{\partial \sigma_{33}}{\partial x_3}\delta x_3 - \sigma_{33}\right)\delta x_1 \delta x_2 + \left(\sigma_{31} + \frac{\partial \sigma_{31}}{\partial x_1}\delta x_1 - \sigma_{31}\right)\delta x_3 \delta x_2 + \left(\sigma_{32} + \frac{\partial \sigma_{32}}{\partial x_2}\delta x_2 - \sigma_{32}\right)\delta x_3 \delta x_1 + P_3\,\delta x_1 \delta x_2 \delta x_3 \quad (9.24)$$

where $\boldsymbol{u}$ is the displacement vector, t the time, $\boldsymbol{P}$ the body force vector, $\partial^2 \boldsymbol{u}/\partial t^2$ the acceleration, and m the mass. Hence, dividing by $(\delta x_1 \delta x_2 \delta x_3)$ and proceeding to the limit where these infinitesimals tend to zero, one obtains for the static equilibrium

$$\begin{aligned} \frac{\partial \sigma_{11}}{\partial x_1} + \frac{\partial \sigma_{12}}{\partial x_2} + \frac{\partial \sigma_{13}}{\partial x_3} + P_1 &= 0 \\ \frac{\partial \sigma_{22}}{\partial x_2} + \frac{\partial \sigma_{21}}{\partial x_1} + \frac{\partial \sigma_{23}}{\partial x_3} + P_2 &= 0 \\ \frac{\partial \sigma_{33}}{\partial x_3} + \frac{\partial \sigma_{31}}{\partial x_1} + \frac{\partial \sigma_{32}}{\partial x_2} + P_1 &= 0 \end{aligned} \quad (9.25)$$

Using the Einstein convention, equation (9.25) can be written

$$\frac{\partial \sigma_{ij}}{\partial x_j} + P_i = \sigma_{ij,j} + P_i = 0 \quad (9.26)$$

Equation (9.26) represents the basic field equation to be satisfied for any stress field in a volume element in static equilibrium. In other words the divergence of the stress tensor $\mathrm{div}(\sigma_{ij})$ must vanish in the absence of body forces. This equation is sometimes referred to as the condition for translational equilibrium whilst the expression $\sigma_{ij} = \sigma_{ji}$ denotes rotational equilibrium.

9.2.4 Compatibility Equations

Strict compatibility is achieved when the strains can be expressed in terms of a single-valued, continuously differentiable displacement. This condition implies that any integration of strain (displacement gradient) around an infinitesimal closed loop is equal to zero and independent of the path so that gaps and overlaps are avoided. To put the matter formally, one may write

$$\oint \frac{\partial \boldsymbol{u}}{\partial S}\,\mathrm{d}S = 0 \quad (9.27)$$

It should be mentioned that this condition is not fulfilled in the case of dislocated elastic media (see Section 9.2.7).

The definition of strain as expressed by equation (9.12) can be regarded as a set of six independent differential equations for the displacement components u_i. Although there exist only three independent displacement components, an arbitrary choice of the strains does not, in general, allow the strain–displacement relations expressed by equation (9.12)

to be integrated. A single-valued, continuously differentiable displacement vector is only obtained when the strains satisfy the six independent compatibility conditions,

$$\epsilon_{pmk}\,\epsilon_{qnj}\;\varepsilon_{kj,nm} = 0 \tag{9.28}$$

9.2.5 Hooke's Law — the Linear Relationship between Stress and Strain

For small imposed forces the time-independent reversible response of the material which is quantified by the displacement field can be linearly related to the force. The strains expressed by the symmetric part of the displacement gradient tensor then describe a linear elastic shape change which is proportional to the stress (equation (9.29)). This relation is referred to as Hooke's law. Experience substantiates its validity for a broad class of materials and stress–strain regimes of practical relevance:

$$\varepsilon_{ij} = S_{ijkl}\;\sigma_{kl} \qquad\qquad \sigma_{ij} = C_{ijkl}\;\varepsilon_{kl} \tag{9.29}$$

These expressions hold for the general anisotropic elastic case, where a component of the strain tensor (stress tensor) can depend on each of the stress components (strain components). The proportionality or elastic constants then consist of the four-rank tensors S_{ijkl}, or C_{ijkl}. The former quantities are referred to as elastic compliances and the latter ones as elastic stiffnesses. For uniaxial tensile deformation the stiffness represents the stress that is required to yield an elastic elongation of 100%, which of course is not realistic because of plastic deformation or material failure. The general form of Hooke's law accounts for the anisotropy imposed by the interatomic bond and the crystalline nature of matter. Although the values of S_{ijkl} and C_{ijkl} can depend slightly on the experimental conditions (adiabatic or isothermal), they are used as constants throughout this study[3]. The stiffnesses and compliances are related by

$$C_{ijmn}\,S_{mnpq} = \frac{1}{2}\left(\delta_{ip}\delta_{jq} + \delta_{iq}\delta_{jp}\right) \tag{9.30}$$

Exploiting the symmetries $\varepsilon_{ij} = \varepsilon_{ji}$ and $\sigma_{ij} = \sigma_{ji}$ allows one to reduce the number of independent elastic constants from 81 to 36.

$$\begin{aligned} C_{ijkl} &= C_{ijlk} \qquad & C_{ijkl} &= C_{jikl} \\ S_{ijkl} &= S_{ijlk} \qquad & S_{ijkl} &= S_{jikl} \end{aligned} \tag{9.31}$$

Since classical elasticity is based on the assumption of reversible displacements, the only work done is due to elastic deformation. This fact defines additional thermodynamic constraints on the elastic constants:

$$\sigma_{ij} = C_{ijkl}\,\varepsilon_{kl} = \frac{\partial W}{\partial \varepsilon_{ij}} \tag{9.32}$$

which implies

$$C_{ijkl} = \frac{\partial^2 W}{\partial \varepsilon_{ij}\,\partial \varepsilon_{kl}} \tag{9.33}$$

[3]However, the temperature dependence of the elastic constants *is* considered in the dislocation simulations.

where W is the Helmholtz free energy density, which is a path-independent state function. From this condition it follows that

$$C_{ijkl} = C_{klij} \tag{9.34}$$

These additional relations make it possible to reduce the number of independent elastic constants from 36 to 21. For materials obeying Hooke's law these symmetry conditions allow one to express equations (9.24)–(9.26) for the dynamic case more conveniently as

$$C_{ijkl}\, u_{k,lj} + P_i = \rho\, \frac{\partial^2 u_i}{\partial t^2} \tag{9.35}$$

where ρ is the mass density, and for the static case as

$$C_{ijkl}\, u_{k,lj} + P_i = 0 \tag{9.36}$$

Accordingly, the stresses are given by

$$\sigma_{ij} = C_{ijkl}\, u_{k,l} \tag{9.37}$$

For simplifying the complicated tensor notation, which requires up to four indices, Voigt (1910) suggested the so-called matrix notation. This notation is a transformation rule by which index pairs ij are mapped into a single index m according to the following scheme:

$$\begin{array}{cccccccccc} ij & 11 & 22 & 33 & 23 & 32 & 13 & 31 & 12 & 21 \\ m & 1 & 2 & 3 & 4 & 4 & 5 & 5 & 6 & 6 \end{array} \tag{9.38}$$

By employing this transformation convention one can define the symmetric 6×6 matrices C'_{mn} and S'_{mn}. However, the following rules must be considered.

$$\begin{aligned} C'_{mn} &= C_{ijkl} \text{ for } 1 \le m, n \le 6 \\ S'_{mn} &= \begin{cases} S_{ijkl} & : \text{ if both } m \text{ and } n = 1,2,3 \\ 2\,S_{ijkl} & : \text{ if either } m \text{ or } n \text{ but not both } = 1,2,3 \\ 4\,S_{ijkl} & : \text{ if both } m \text{ and } n = 4,5,6 \end{cases} \end{aligned} \tag{9.39}$$

When using the matrix notation C_{mn} and S_{mn} it must be considered that for coordinate transformation or invariant determination it is more useful to use the stiffnesses and compliances in their original tensorial form C_{ijkl} and S_{ijkl}. However, for conducting matrix inversions it is easier to use the notation suggested as equation (9.38) (Steeds 1973; Bacon et al. 1979a). For cubic crystal symmetry the reference coordinate system is chosen to coincide with the crystal cube axes [100], [010], [001]. The stiffness tensor then reduces to the simplest possible form:

$$C^{\text{cub}}_{ijkl} = \begin{pmatrix} C_{1111} & C_{1122} & C_{1122} & 0 & 0 & 0 \\ C_{1122} & C_{1111} & C_{1122} & 0 & 0 & 0 \\ C_{1122} & C_{1122} & C_{1111} & 0 & 0 & 0 \\ 0 & 0 & 0 & C_{2323} & 0 & 0 \\ 0 & 0 & 0 & 0 & C_{2323} & 0 \\ 0 & 0 & 0 & 0 & 0 & C_{2323} \end{pmatrix} \tag{9.40}$$

In matrix notation this can be rewritten

$$C_{mn}^{\text{cub}} = \begin{pmatrix} C_{11} & C_{12} & C_{12} & 0 & 0 & 0 \\ C_{12} & C_{11} & C_{12} & 0 & 0 & 0 \\ C_{12} & C_{12} & C_{11} & 0 & 0 & 0 \\ 0 & 0 & 0 & C_{44} & 0 & 0 \\ 0 & 0 & 0 & 0 & C_{44} & 0 \\ 0 & 0 & 0 & 0 & 0 & C_{44} \end{pmatrix} \tag{9.41}$$

For hexagonal materials the stiffness tensor is referred to two axes in the basal plane and a third one normal to it. Hexagonal metals are isotropic in their basal plane, so that the stiffness tensor is invariant with respect to the orientation of the coordinate basis vectors in the basal plane (Steeds 1973):

$$C_{ijkl}^{\text{hex}} = \begin{pmatrix} C_{1111} & C_{1122} & C_{1133} & 0 & 0 & 0 \\ C_{1122} & C_{1111} & C_{1133} & 0 & 0 & 0 \\ C_{1133} & C_{1133} & C_{3333} & 0 & 0 & 0 \\ 0 & 0 & 0 & C_{2323} & 0 & 0 \\ 0 & 0 & 0 & 0 & C_{2323} & 0 \\ 0 & 0 & 0 & 0 & 0 & \frac{1}{2}(C_{1111} - C_{1122}) \end{pmatrix} \tag{9.42}$$

In matrix notation it can be rewritten

$$C_{mn}^{\text{hex}} = \begin{pmatrix} C_{11} & C_{12} & C_{13} & 0 & 0 & 0 \\ C_{12} & C_{11} & C_{13} & 0 & 0 & 0 \\ C_{13} & C_{13} & C_{33} & 0 & 0 & 0 \\ 0 & 0 & 0 & C_{44} & 0 & 0 \\ 0 & 0 & 0 & 0 & C_{44} & 0 \\ 0 & 0 & 0 & 0 & 0 & \frac{1}{2}(C_{11} - C_{12}) \end{pmatrix} \tag{9.43}$$

Whilst in cubic crystals hence only three independent elastic constants remain, i.e. C_{11}, C_{12}, and C_{44}, in the hexagonal lattice five constants C_{11}, C_{12}, C_{13}, C_{33}, and C_{44} must be considered. A more detailed overview on the elastic constants required for the various crystal symmetries was given by Steeds (1973) and Bacon et al. (1979). In the case of cubic symmetry, the inversion of the stiffnesses to the compliances and vice versa leads to the relations

$$\begin{aligned} C_{11} &= \frac{(S_{11} + S_{12})}{(S_{11} - S_{12})\,(S_{11} + 2\,S_{12})} \\ C_{12} &= \frac{-\,S_{12}}{(S_{11} - S_{12})\,(S_{11} + 2\,S_{12})} \\ C_{44} &= \frac{1}{S_{44}} \end{aligned} \tag{9.44}$$

$$\begin{aligned} S_{11} &= \frac{(C_{11} + C_{12})}{(C_{11} - C_{12})\,(C_{11} + 2\,C_{12})} \\ S_{12} &= \frac{-C_{12}}{(C_{11} - C_{12})\,(C_{11} + 2\,C_{12})} \\ S_{44} &= \frac{1}{C_{44}} \end{aligned} \tag{9.45}$$

Table 9.1: Elastic stiffness constants for some cubic metals.

Element	Structure	C_{1111} [GPa]	C_{1122} [GPa]	C_{2323} [GPa]	A^z	ν
Ag	fcc	12.40	9.34	4.61	3.013	0.43
Al	fcc	10.82	6.13	2.85	1.215	0.36
Au	fcc	18.60	15.70	4.20	2.987	0.46
Cr	bcc	35.00	5.78	10.10	0.691	0.14
Cu	fcc	16.84	12.14	7.54	3.209	0.42
Fe	bcc	24.20	14.65	11.20	2.346	0.38
Li	bcc	1.48	1.25	1.08	9.391	0.46

Before using general anisotropic elastic field equations in three-dimensional numerical simulations of plasticity, it is useful to test the predictions in the isotropic limit. A material is defined as elastically isotropic if the elastic properties are completely independent of direction. In the case of cubic crystal symmetry this is realized when $C_{44} = (C_{11} - C_{12})\,/\,2$. The deviation from isotropy can in the cubic lattice be quantified by the so-called Zener anisotropy ratio A^z (Hirth and Lothe 1968):

$$A^z = \frac{2\,C_{44}}{C_{11} - C_{12}} \tag{9.46}$$

Indeed, most metals deviate considerably from the isotropic limit. Tungsten has the smallest deviation with a Zener ratio of $A^z = 1$ and lithium the largest one with a ratio of $A^z = 9.39$ (Table 9.1). Detailed values of the elastic constants and Zener ratios of many materials were given by Steeds (1973) and Bacon et al. (1979). The two elastic constants of isotropic materials are often expressed in terms of μ and ν, which are defined by

$$\mu = C_{44} = C_{2323} = \frac{1}{2}(C_{11} - C_{12}) \tag{9.47}$$

and

$$\nu = \frac{C_{12}}{C_{11} + C_{12}} = \frac{C_{1122}}{C_{1111} + C_{1122}} = -\frac{S_{12}}{S_{11}} = -\frac{S_{1122}}{S_{1111}} \tag{9.48}$$

where μ is often referred to as the shear modulus or modulus of rigidity and ν as Poisson's ratio. The elastic modulus E, which relates elastic stress and strain in the case of tensile deformation, can be expressed in terms of μ and ν:

$$E = 2\,\mu\,(1 + \nu)\,. \tag{9.49}$$

For relating the mean hydrostatic stress to dilatation one additionally defines the bulk modulus B^{el} (Hirth and Lothe 1968).

$$B^{\mathrm{el}} = \left(\frac{1}{3}\right)\frac{\sigma_{kk}}{\varepsilon_{ii}} = \lambda + \frac{2}{3}\,\mu = \frac{E}{3(1 - 2\,\nu)} \tag{9.50}$$

In addition to these constants the Lamé constants μ (see definition above) and λ are common as well:

$$\lambda = \frac{2\,\mu\,\nu}{1 - 2\,\nu} \tag{9.51}$$

In terms of Lamé's constants the elastic modulus is given by

$$E = \frac{\mu\,(3\,\lambda + 2\,\mu)}{\mu + \lambda} \tag{9.52}$$

The use of Lamé's constants allows one to give a compact tensorial expression of the elastic constants and thus of Hooke's law in the isotropic limit:

$$C_{ijkl} = \lambda\,\delta_{ij}\delta_{kl} + \mu\,(\delta_{ik}\delta_{jl} + \delta_{il}\delta_{jk}) \tag{9.53}$$

$$\sigma_{ij} = \lambda\,\varepsilon_{kk}\,\delta_{ij} + 2\,\mu\,\varepsilon_{ij} \tag{9.54}$$

The inverse form can be written

$$\varepsilon_{ij} = \frac{1}{2\,\mu}\,\sigma_{ij} - \frac{\lambda}{2\,\mu\,(3\,\lambda + 2\,\mu)}\,\sigma_{kk}\,\delta_{ij} \tag{9.55}$$

For presenting strains and stresses associated with dislocations in the isotropic limit, the constant ν is often used instead of λ. The elastic constants are then given by

$$C_{ijkl} = \mu\left(\delta_{ik}\delta_{jl} + \frac{2\,\nu}{1 - 2\,\nu}\,\delta_{ij}\delta_{kl}\right) \tag{9.56}$$

Accordingly the compliances can be written

$$S_{lnpq} = \frac{1}{2\,\mu}\left(\delta_{lp}\delta_{nq} - \frac{\nu}{1 + \nu}\,\delta_{ln}\delta_{pq}\right) \tag{9.57}$$

Using equations (9.56) and (9.57) Hooke's law can be written

$$\sigma_{ij} = 2\,\mu\left(\varepsilon_{ij} + \frac{\nu}{1 - 2\,\nu}\,\delta_{ij}\,\varepsilon_{kk}\right) \tag{9.58}$$

or in its inverse form

$$\varepsilon_{ij} = \frac{1}{2\,\mu}\left(\sigma_{ij} - \frac{\nu}{1 + \nu}\,\delta_{ij}\,\sigma_{kk}\right) \tag{9.59}$$

The equations of equilibrium can also be expressed in a compact form by using μ and ν:

$$\epsilon_{ikp}\,\epsilon_{jmq}\,\sigma_{pq,km} - \frac{\nu}{1 + \nu}\,(\delta_{ij}\,\sigma_{pp,kk} - \sigma_{pp,ij}) = 0 \tag{9.60}$$

Some general restrictions for the values of the elastic constants are imposed by the positive definiteness of the strain energy density function W, namely,

$$C_{44} > 0 \qquad C_{11} > |\,C_{12}\,| \qquad C_{11} + 2\,C_{12} > 0 \tag{9.61}$$

From these conditions it follows that

$$\lambda > 0 \qquad \text{and} \qquad -1 < \nu < \frac{1}{2} \tag{9.62}$$

9.2.6 Elastic Energy

Tractions and body forces that act on the surface and interior of a small volume element can give rise to an incremental displacement $\delta \boldsymbol{u}$. Under the assumption of quasi-static conditions, which allows equilibrium of the acting forces, the work done on the considered volume element is given by

$$\delta W = \oiint_S \sigma_{ij}\, \delta u_j \, \mathrm{d}S_i + \oiiint_V P_j\, \delta u_j \, \mathrm{d}V \tag{9.63}$$

where $\boldsymbol{P}$ is the body force and S the surface enclosing the volume element V (Steeds 1973; Bacon et al. 1979a; Mura 1987). By employing Gauss' divergence theorem one can convert surface integrals into volume integrals

$$\oiiint_V A_{ij,k} \, \mathrm{d}V = \oiint_S A_{ij} \, \mathrm{d}S_k \tag{9.64}$$

where A_{ij} is a tensor field of arbitrary rank (here of rank 2). Equation (9.63) can then be rewritten

$$\delta W = \oiiint_V (P_j\, \delta u_j + \sigma_{ij,i}\, \delta u_j + \sigma_{ij}\, \delta\, u_{j,i}\,) \, \mathrm{d}V \tag{9.65}$$

By exploiting the conditions for static equilibrium, equation (9.26), one obtains

$$\delta W = \oiiint_V \sigma_{ij}\, \delta u_{j,i} \, \mathrm{d}V \tag{9.66}$$

This equation substantiates the fact that rigid-body rotations do not contribute to the elastic work. Owing to the symmetry of the stress tensor, $\sigma_{ij} = \sigma_{ji}$, and the antisymmetry of the components of the displacement gradient tensor which describe the rigid-body rotation, $\omega_{ij} = -\omega_{ji}$, the corresponding sum of these products will always balance. Considering an infinitesimal volume element, the work per volume can be written

$$\delta W = \sigma_{ij}\, \delta \varepsilon_{ij} \tag{9.67}$$

With the relation between stress and strain restricted to a linear one, the elastic potential, i.e. the elastic strain energy per volume, can be derived by inserting Hooke's law:

$$W = \frac{1}{2}\, \sigma_{ij}\, \varepsilon_{ij} = \frac{1}{2}\, C_{ijkl}\, \varepsilon_{ij}\, \varepsilon_{kl} \tag{9.68}$$

9.2.7 Green's Tensor Function in Elasticity Theory

Green's functions represent a group of useful tools in solving partial differential equations. However, they can also be employed in solving ordinary differential equations. This can be briefly demonstrated by the following example. The differential equation

$$\frac{\mathrm{d}^2 x}{\mathrm{d}t^2} + \omega^2 x = f(t) \qquad \text{with} \qquad x_0 = x_0' = 0 \tag{9.69}$$

describes the oscillation of a point mass suspended by a spring which is characterized by some given force function $f(t)$. This force function can be dismantled into a whole sequence of single impulses.

$$f(t) = \int_0^\infty f(t')\,\delta\left(t'-t\right)\,\mathrm{d}t' \tag{9.70}$$

where $\delta(t'-t)$ is the Dirac delta function describing an infinitesimally narrow function localized at t', the integral of which is 1. In the next step, one solves equation (9.69), but with the original force function $f(t)$ replaced by the delta function $\delta(t'-t)$; that is, one obtains the response $G(t,t')$ of the system to a unit impulse at t'. Equation (9.69) can then be rewritten

$$\frac{\mathrm{d}^2 G(t,t')}{\mathrm{d}t^2} + \omega^2\,G(t,t') = \delta\left(t'-t\right) \tag{9.71}$$

Finally, one obtains a solution of the original differential equation by adding up the responses of many such small unit impulses.

$$x(t) = \int_0^\infty G(t,t')\,f(t')\,\mathrm{d}t' \tag{9.72}$$

This example demonstrates that the use of the Green's function often makes it possible to find a solution of a nonhomogeneous differential equation by solving the system for a delta function on the right-hand side.

In dislocation theory the time-independent Green's tensor function $G_{ij}(\boldsymbol{x},\boldsymbol{x}')$ is used for the integration of the differential equations of elasticity, equation (9.35). The tensor field $G_{ij}(\boldsymbol{x},\boldsymbol{x}')$ gives the displacement along the $x\,\boldsymbol{e}_i$ axis at $\boldsymbol{x}$ in response to a delta-type unit point force exerted parallel to the $x\,\boldsymbol{e}_j$ axis at $\boldsymbol{x}'$. This approach is valid for an infinite body with homogeneous elastic properties in static equilibrium. In the present case the Green's tensor satisfies the conditions of translational invariance, centrosymmetry, and reciprocity (Bacon et al. 1979).

$$G_{ij}(\boldsymbol{x},\boldsymbol{x}') = G_{ij}(\boldsymbol{x}-\boldsymbol{x}') = G_{ji}(\boldsymbol{x}-\boldsymbol{x}') = G_{ij}(\boldsymbol{x}'-\boldsymbol{x}) \tag{9.73}$$

For the derivatives similar relations follow:

$$G_{ij,s}(\boldsymbol{x}-\boldsymbol{x}') = -G_{ji,s'}(\boldsymbol{x}-\boldsymbol{x}') = G_{ij,s}(\boldsymbol{x}'-\boldsymbol{x}) \tag{9.74}$$

where primed subscripts denote derivatives with respect to $\boldsymbol{x}'$ and unprimed subscripts those to $\boldsymbol{x}$. The same notation is used for the second derivatives,

$$G_{ij,sk}(\boldsymbol{x}-\boldsymbol{x}') = -G_{ji,s'k'}(\boldsymbol{x}-\boldsymbol{x}') = G_{ij,sk}(\boldsymbol{x}'-\boldsymbol{x}) \tag{9.75}$$

Provided that the dislocation motion is uniform, the time-independent Green's tensor may be used for dislocation dynamics as well. In the case of non-uniform motion the time-dependent Green's tensor must be employed (Barnett 1996).

The Green's tensor field and its derivatives required in dislocation theory must, for the general anisotropic case, be evaluated by numerical techniques. However, in the isotropic limit it can be derived analytically (de Wit 1960; Hirth and Lothe 1982; Indenbom and Lothe 1992; Rönnpagel 1996):

$$G_{ij}(\boldsymbol{x}-\boldsymbol{x}') = \frac{1}{16\,\pi\,\mu\,(1-\nu)}\,\frac{1}{\mid \boldsymbol{x}-\boldsymbol{x}' \mid}\left[(3-4\,\nu)\,\delta_{ij} + \frac{(x_i-x_i')\,(x_j-x_j')}{(\boldsymbol{x}-\boldsymbol{x}')^2}\right] \tag{9.76}$$

As will be shown below not the Green's tensor function itself but its spatial derivatives are required to solve dislocation field equations. For the general anisotropic case the Nth derivative of equation (9.76) is given by

$$G_{ij,s_1,s_2,\ldots,s_N}(\boldsymbol{x}-\boldsymbol{x}') = \frac{1}{8\pi^2}\oint_{|\boldsymbol{z}|=1} (\boldsymbol{zz})^{-1}_{ij}\,\delta_{s_1,s_2,\ldots,s_N}[\boldsymbol{z}(\boldsymbol{x}-\boldsymbol{x}')]\,\mathrm{d}S$$
$$= \frac{1}{8\pi^2|\,\boldsymbol{x}-\boldsymbol{x}'\,|^{N+1}}\oint_{|\boldsymbol{z}|=1} (\boldsymbol{z})^{-1}_{ij}\,z_{s_1}z_{s_1}\ldots z_{s_N}\times\delta^{(N)}(\boldsymbol{z}\boldsymbol{T})\,\mathrm{d}S \quad (9.77)$$

where $\boldsymbol{T}$ is defined by $\boldsymbol{x}-\boldsymbol{x}' = \boldsymbol{T}\;|\,\boldsymbol{x}-\boldsymbol{x}'\,|$. $\boldsymbol{z}$ is the integration variable lying in the plane $\boldsymbol{T}\,\boldsymbol{z}=0$. The second-rank symmetric matrix integrand $(\boldsymbol{zz})^{-1}_{ij}$ is the inverse of the Christoffel stiffness matrix $(\boldsymbol{zz})_{ij}$ (Barnett et al. 1972). This operator with the general form $(\boldsymbol{ab})_{jk}$ is defined by

$$(\boldsymbol{ab})_{jk} = a_i\,C_{ijkl}\,b_l \quad (9.78)$$

The inverse of the symmetric stiffness matrix with the general form $(\boldsymbol{aa})^{-1}_{ij}$ is given by

$$(\boldsymbol{aa})^{-1}_{ij} = \frac{\epsilon_{ism}\,\epsilon_{jrw}\,(\boldsymbol{nn})_{mw}\,(\boldsymbol{nn})_{sr}}{2\,\epsilon_{pgn}\,(\boldsymbol{nn})_{1p}\,(\boldsymbol{nn})_{2g}\,(\boldsymbol{nn})_{3n}} \quad (9.79)$$

Details of the derivation of the Green's tensor function will be outlined in more detail in Sections 9.3.4 and 9.3.5 when deriving the three-dimensional field equations for dislocation segments on the basis of Brown's theorem.

Using the above relations and the definition for $G_{ij}(\boldsymbol{x}-\boldsymbol{x}')$, the displacement due to a point force $\boldsymbol{F}$ can be expressed by

$$u_i(\boldsymbol{x}) = G_{ij}(\boldsymbol{x}-\boldsymbol{x}')\,F_j \quad (9.80)$$

The first derivative can then be written

$$u_{i,m}(\boldsymbol{x}) = G_{ij,m}(\boldsymbol{x}-\boldsymbol{x}')\,F_j \quad (9.81)$$

Following Hooke's law and the symmetry relations, equations (9.31) and (9.34), the resulting stress can then be written

$$\sigma_{kp} = C_{kpim}\,u_{i,m} = C_{kpim}\,G_{ij,m}(\boldsymbol{x}-\boldsymbol{x}')\,F_j \quad (9.82)$$

Using the static equilibrium condition the governing equation for the Green's tensor can be derived:

$$C_{kpim}\,G_{ij,mp}(\boldsymbol{x}-\boldsymbol{x}') + \delta_{kj}\,\delta(\boldsymbol{x}-\boldsymbol{x}') = 0 \quad (9.83)$$

The general solution for the displacements expressed in terms of the Green's function is

$$u_j(\boldsymbol{x}) = \oiiint_V G_{jk}(\boldsymbol{x}-\boldsymbol{x}')f_k(\boldsymbol{x}')\,\mathrm{d}V' + \oiint_S C_{kpim}u_{i,m'}(\boldsymbol{x}')G_{kj}(\boldsymbol{x}-\boldsymbol{x}')\,\mathrm{d}S'_p$$
$$- \oiint_S C_{kpim}u_k(\boldsymbol{x}')G_{ij,m'}(\boldsymbol{x}-\boldsymbol{x}')\,\mathrm{d}S'_p \quad (9.84)$$

where $f_k(\boldsymbol{x}')$ is the body force density. Equations (9.80)–(9.84) are generally valid in anisotropic linear elastic media and are not confined to dislocation problems.

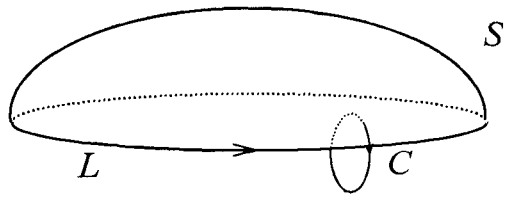

Figure 9.1: A closed dislocation loop L and integration circuit C used for the Burgers vector determination, equation (9.85). S is an arbitrary surface bounded by the dislocation line L (Volterra 1907; Mura 1963; Bacon et al. 1979).

A special solution for the displacement due to a dislocation is obtained by considering the appropriate displacement boundary conditions. By definition, L is a dislocation if for any closed circuit C the following equation applies (see Figure 9.1):

$$\oint_C u_{j,k}(\boldsymbol{x})\,\mathrm{d}x_k = \begin{cases} b_j \text{ if } C \text{ irreducibly encloses } L \\ 0 \text{ otherwise} \end{cases} \tag{9.85}$$

Since the dislocation is defined by displacement boundary conditions one may set the body force density equal to zero, so that equation (9.84) simplifies to

$$u_j(\boldsymbol{x}) = -C_{kpim}\, b_k \oiint_S G_{ij,m'}(\boldsymbol{x}-\boldsymbol{x}')\,\mathrm{d}S'_p \tag{9.86}$$

This equation is referred to as Volterra's displacement formula (1907). The surface S can be any surface bounded by L. The distortion field can be derived by differentiating equation (9.86) with respect to $\boldsymbol{x}$:

$$u_{j,s}(\boldsymbol{x}) = -C_{kpim}\, b_k \oiint_S G_{ij,m's'}(\boldsymbol{x}-\boldsymbol{x}')\,\mathrm{d}S'_p \tag{9.87}$$

After the application of Stokes theorem, by which a surface integral can be rendered into a line integral, equation (9.87) reads:

$$u_{j,s}(\boldsymbol{x}) = -C_{kpim}\, b_k\, \epsilon_{qps} \oint_L G_{ij,m}(\boldsymbol{x}-\boldsymbol{x}')\,\mathrm{d}x'_q \tag{9.88}$$

This expression is commonly referred to as Mura's equation (Mura 1963).

9.2.8 Airy's Scalar Stress Function in Elasticity Theory

In field theories it can be pertinent to express vector quantities in terms of gradients of a scalar potential (Love 1892; Sokolnikoff 1956; Schmutzer 1988; Eschenauer and Schnell 1993; Honerkamp and Römer 1993). In some theories these scalar potentials have an obvious physical significance, for instance in gravitation theory. In elasticity theory an equivalent method can be used, although endowed with less physical significance. This approach allows one to express stress and displacement fields in terms of spatial derivatives of scalar potentials. The latter are referred to as stress or displacement functions (Eschenauer and Schnell 1993). In two-dimensional problems of elasticity the following

form of expressing stresses as derivatives of a potential was suggested by G.B. Airy in 1862 and is therefore referred to as the Airy stress function:

$$\sigma_{11} = \frac{\partial^2 \phi}{\partial x_2^2} \qquad \sigma_{22} = \frac{\partial^2 \phi}{\partial x_1^2} \qquad \sigma_{12} = -\frac{\partial^2 \phi}{\partial x_2 \, \partial x_1} \tag{9.89}$$

For tackling three-dimensional problems a different notation is often used, namely

$$\sigma_{11} = \frac{\partial^2 \psi}{\partial x_1^2} \qquad \sigma_{22} = \frac{\partial^2 \psi}{\partial x_2^2} \qquad \sigma_{12} = \frac{\partial^2 \psi}{\partial x_1 \, \partial x_2} \tag{9.90}$$

Equation (9.89) transforms as a Cartesian tensor. As was outlined in the preceding sections, stress and strain fields must satisfy the equations of equilibrium and compatibility if they are to describe permissible states of elastic bodies. This condition imposes certain constraints on the selection of stress functions. In general these constraints are expressed by requiring that the stress functions are solutions of certain partial differential equations. This stipulation is readily demonstrated by substituting equation (9.89) into the equilibrium equations (9.26), assuming plane strain conditions and the absence of body forces:

$$\begin{aligned} \sigma_{11,1} + \sigma_{12,2} &= \frac{\partial^3 \phi}{\partial x_2^2 \, \partial x_1} + \frac{\partial^3 \phi}{\partial x_1 \, \partial x_2^2} = 0 \\ \sigma_{21,1} + \sigma_{22,2} &= \frac{\partial^3 \phi}{\partial x_1^2 \, \partial x_2} + \frac{\partial^3 \phi}{\partial x_2 \, \partial x_1^2} = 0 \end{aligned} \tag{9.91}$$

Thus, the Airy stress function automatically satisfies the equilibrium equations, provided the body forces are equal to zero. If the body forces are not zero, they must be expressed as conservative forces, i.e. as negative gradients of a scalar potential, so that equation (9.89) can be cast into a generalized form. However, the constraints imposed by compatibility must be included as well. By using Hooke's law, equation (9.54), the compatibility equations (9.28), and the Airy stress function, equation (9.89), one obtains the biharmonic equation for plane strain conditions:

$$\frac{\partial^4 \phi}{\partial x_1^4} + 2 \, \frac{\partial^4 \phi}{\partial x_1^2 \, \partial x_2^2} + \frac{\partial^4 \phi}{\partial x_2^4} = \left(\frac{\partial^2}{\partial x_1^2} + \frac{\partial^2}{\partial x_2^2} \right)^2 \phi = 0 \tag{9.92}$$

Except for some well-investigated cases, the analytical solution of the biharmonic equation is an intricate task. Thus, most modern approaches to solving it are based on representing the underlying stress function in terms of analytic functions of the complex variable and subsequent numerical solution.

9.3 Dislocation Statics

9.3.1 Introduction

In the preceding sections the fundamentals of linear isotropic and anisotropic elasticity theory that are required in dislocation theory have been reviewed. In this section the basic field equations for displacement, strain, and stress associated with infinite dislocations and finite dislocation segments will be derived. These equations form the basis for conducting space- and time-discretized numerical simulations of dislocation dynamics.

Two stages of dislocation field equations will be discussed. First, the field description of infinite dislocations in two dimensions will be derived exploiting anti-plane strain conditions for the screw dislocation and plane strain conditions for the edge dislocation. Second, compact tensorial three-dimensional field equations will be derived for arbitrary finite dislocation segments.

The latter field equations make it possible to dismantle three-dimensional dislocations into sequentially arranged, piecewise straight, dislocation segments. This approach enables one to calculate the statics and dynamics associated with arbitrary three-dimensional dislocation arrangements which are not amenable to closed analytical approaches.

For solving the various dislocation field problems one can use the equilibrium equations (9.26), combined with the compatibility equations (9.28), or the Green's function method, equation (9.84). While the first two equation systems are used in the sextic approach (Stroh 1958), the latter method is commonly referred to as the integral formalism (Bacon et al. 1979a). Which of these methods will be used in the following depends on the required field quantities and on existing symmetries. All field quantities are given for both the isotropic and the general anisotropic case.

9.3.2 2D Field Equations for Infinite Dislocations in an Isotropic Linear Elastic Medium

9.3.2.1 Edge Dislocation

The two-dimensional field equation for edge dislocations with an infinite extension of their dislocation line can be derived by solving the compatibility equations (9.28) for plane strain conditions under consideration of the equilibrium equations (9.26). The plane strain state describes a situation where all particles of a body are displaced parallel to an arbitrary plane, and the displacements are independent of their coordinate parallel to the plane normal. For an infinite edge dislocation with its Burgers vector parallel to say x_1 and tangent vector parallel to say x_3, only one displacement component, namely that parallel to the dislocation line, u_3, is equal to zero. The two remaining displacements are not equal to zero. However, they are independent of x_3 (Hirth and Lothe 1968). To express this matter formally, one can write

$$u_1 = f(x_1, x_2) \qquad u_2 = g(x_1, x_2) \qquad u_3 = 0 \qquad \frac{\partial u_1}{\partial x_3} = 0 \qquad \frac{\partial u_2}{\partial x_3} = 0 \tag{9.93}$$

As opposed to the derivation in Section 9.3.2.2, where the stresses of the screw dislocation are immediately expressed in terms of its quite simple displacement field, this method is less tractable in the case of the edge dislocation. Since the direct determination of the displacement field of the latter defect is too complicated, the prescribed plane strain state advocates the use of the Airy stress function, equations (9.89)–(9.91). By using the substitution

$$(\sigma_{11} + \sigma_{22}) = \nabla\phi \tag{9.94}$$

the biharmonic equation (9.91) can be transformed into the harmonic Laplace equation. A detailed description of the solution of the harmonic equation is given by Hirth and Lothe (1968). The result for the stress function ϕ amounts to

$$\phi = -\frac{\mu\, b\, x_2}{4\,\pi\,(1-\nu)}\, \ln\left(x_1^2 + x_2^2\right) \tag{9.95}$$

The stress field of the infinite edge dislocation parallel to x_3 is then obtained by employing equation (9.89):

$$\begin{aligned}
\sigma_{11} &= -\frac{\mu b}{2\pi(1-\nu)}\,\frac{x_2(3x_1^2+x_2^2)}{(x_1^2+x_2^2)^2} \\
\sigma_{22} &= \frac{\mu b}{2\pi(1-\nu)}\,\frac{x_2(x_1^2-x_2^2)}{(x_1^2+x_2^2)^2} \\
\sigma_{12} &= \frac{\mu b}{2\pi(1-\nu)}\,\frac{x_1(x_1^2-x_2^2)}{(x_1^2+x_2^2)^2} \\
\sigma_{33} &= \nu(\sigma_{11}+\sigma_{22}) = -\frac{\mu b \nu}{\pi(1-\nu)}\,\frac{x_2}{x_1^2+x_2^2}
\end{aligned} \tag{9.96}$$

The strain field is readily obtained by using Hooke's law, equation (9.54).

9.3.2.2 Screw Dislocation

The two-dimensional field equation for screw dislocations with an infinite extension of their dislocation line can be derived by solving the equilibrium equations (9.26) under anti-plane strain conditions. The anti-plane strain state describes a situation where all particles of a body are displaced in a direction normal to an arbitrary plane, and the displacements are independent of this direction. For an infinite screw dislocation with its Burgers vector and tangent vector parallel to say x_3, only one component, i.e. u_3, which is parallel to the Burgers vector and independent of x_3, appears in the displacement field (Hirth and Lothe 1968):

$$u_1 = 0 \qquad u_2 = 0 \qquad u_3 = f(x_1, x_2) \qquad \frac{\partial u_3}{\partial x_3} = 0 \tag{9.97}$$

For the infinite homogeneous linear elastic body, Hooke's law in the isotropic limit is given by the expression

$$\sigma_{ij} = \lambda\,\varepsilon_{kk}\,\delta_{ij} + 2\,\mu\,\varepsilon_{ij} \tag{9.98}$$

Since all displacements except u_3 are zero and u_3 is independent of x_3, the dilatation of bodies in an anti-plane strain state must always be equal to zero, i.e. $\varepsilon_{kk} = 0$. Hooke's law then reduces to

$$\sigma_{ij} = 2\,\mu\,\varepsilon_{ij} \tag{9.99}$$

Inserting the above equation into the equilibrium equation in the absence of body forces, $\sigma_{ij,j} = 0$, leads to

$$\varepsilon_{ij,j} = \frac{1}{2}\,\frac{\partial}{\partial x_j}\left(\frac{\partial u_i}{\partial x_j} + \frac{\partial u_j}{\partial x_i}\right) = 0 \tag{9.100}$$

For the infinite screw dislocation this expression reduces to the harmonic equation

$$\frac{\partial^2 u_3}{\partial x_1^2} + \frac{\partial^2 u_3}{\partial x_2^2} = 0 \tag{9.101}$$

The solution of this expression is readily obtained by considering that the displacement u_3 increases from zero to b by traversing a closed circuit about the dislocation line vector. As a reasonable approach for expressing u_3 as a function of the angle θ about the dislocation line one can use

$$u_3 = b\left(\frac{\theta}{2\pi}\right) \quad \text{with} \quad \theta = \arctan\left(\frac{x_2}{x_1}\right) \tag{9.102}$$

which is indeed a solution of the harmonic equation. By differentiating u_3 with respect to x_1 and x_2 one obtains the strain field and by inserting the result into equation (9.99) one obtains the stress field of an infinite screw dislocation with its line vector being tangent to x_3:

$$\begin{aligned} \sigma_{13} = \sigma_{31} &= -\frac{\mu b}{2\pi}\frac{x_2}{x_1^2 + x_2^2} \\ \sigma_{23} = \sigma_{32} &= \frac{\mu b}{2\pi}\frac{x_1}{x_1^2 + x_2^2} \end{aligned} \tag{9.103}$$

9.3.3 2D Field Equations for Infinite Dislocations in an Anisotropic Linear Elastic Medium

9.3.3.1 Introduction

Explicit analytical expressions for the stress field equations in the anisotropic case can be obtained by using the sextic approach. A detailed description of this mathematical procedure, which is based on solving the equilibrium equations (9.26) combined with the compatibility equations (9.28), was given by Stroh (1958), Steeds (1973), Bacon, Barnett, and Scattergood (1979a), Mura (1987), and Indenbom and Lothe (1992).

The basic task in this eigenvalue problem is to find the roots of a sextic equation. Relatively simple analytical solutions are available for certain cases of high symmetry, namely, when the dislocation line is either parallel or perpendicular to a twofold or sixfold axis. A large number of possible solutions for real crystals were derived and thoroughly discussed by Steeds (1973). This section presents the general field solution for the simplest possible case, viz., for twofold symmetry.

9.3.3.2 Edge Dislocation

The coordinate system is defined in such a manner that the dislocation line points in the negative x_3 direction. Assuming that one of the axes perpendicular to the dislocation line $(-x_3)$ is parallel to a twofold axis, and using the matrix notation given in equation (9.38), the stiffness tensor can be written in the dislocation coordinate system:

$$\boldsymbol{C} = \begin{pmatrix} C_{11} & C_{12} & C_{13} & 0 & 0 & 0 \\ C_{12} & C_{22} & C_{23} & 0 & 0 & 0 \\ C_{13} & C_{23} & C_{33} & 0 & 0 & 0 \\ 0 & 0 & 0 & C_{44} & 0 & 0 \\ 0 & 0 & 0 & 0 & C_{55} & 0 \\ 0 & 0 & 0 & 0 & 0 & C_{66} \end{pmatrix} \tag{9.104}$$

For further calculations it is pertinent to introduce some abbreviations, namely,

$$\bar{C} = (C_{11}\, C_{22})^{1/2} \qquad \lambda = \left(\frac{C_{11}}{C_{22}}\right)^{1/4} \qquad \phi = \frac{1}{2}\arccos\left(\frac{C_{12}^2 + 2\,C_{12}\,C_{66} - \bar{C}_{11}^2}{2\,\bar{C}_{11}\,C_{66}}\right) \tag{9.105}$$

Furthermore, the solutions are confined to the case

$$2\,C_{66} + C_{12} - \bar{C}_{11} > 0 \tag{9.106}$$

so that ϕ gives a real value. Finally, it is useful to define

$$q^2 = x_1^2 + 2\,x_1\,x_2\,\lambda\cos\phi + x_2^2\lambda^2 \qquad t^2 = x_1^2 - 2\,x_1\,x_2\,\lambda\cos\phi + x_2^2\lambda^2 \tag{9.107}$$

Using these constraints, the equations for the displacement and stress field can then be compactly written

$$\begin{aligned} u_1 = -\frac{b_1}{4\pi}\Bigg[&\arctan\left(\frac{2\,x_1\,x_2\,\lambda\,\sin\phi}{x_1^2 - (\lambda\,x_2)^2}\right) + \frac{\bar{C}_{11}^2 - C_{12}^2}{2\,\bar{C}_{11}^2\sin(2\phi)}\ln\left(\frac{q}{t}\right)\Bigg] \\ &- \frac{b_2}{4\pi\,\lambda\,\bar{C}_{11}\,\sin(2\phi)}\Bigg[(\bar{C}_{11} - C_{12})\cos\phi\,\ln(qt) \\ &- (\bar{C}_{11} + C_{12})\sin\phi\,\arctan\left(\frac{x_1^2\sin(2\phi)}{(\lambda\,x_2)^2 - x_1^2\cos(2\phi)}\right)\Bigg] \end{aligned} \tag{9.108}$$

$$\begin{aligned} u_2 = \frac{\lambda\,b_1}{4\pi\bar{C}_{11}\sin(2\phi)}\Bigg[&(\bar{C}_{11} - C_{12})\cos\phi\,\ln(qt) \\ &- (\bar{C}_{11} + C_{12})\sin\phi\,\arctan\left(\frac{(\lambda\,x_2)^2\sin(2\phi)}{x_1^2 - (\lambda\,x_2)^2\cos(2\phi)}\right)\Bigg] \\ &- \frac{b_2}{4\pi}\left[\arctan\left(\frac{2\,x_1\,x_2\,\lambda\,\sin\phi}{x_1^2 - (\lambda\,x_2)^2}\right) - \frac{\bar{C}_{11}^2 - C_{12}^2}{2\,\bar{C}_{11}^2\sin(2\phi)}\ln\left(\frac{q}{t}\right)\right] \end{aligned} \tag{9.109}$$

Switching partly to the fourth-rank tensorial form of the stiffness tensor, the stress field associated with the infinite edge dislocation can compactly be written in tensorial notation

$$\begin{aligned} \sigma_{ij} = &-\frac{b_1\,\lambda\,(C_{12} - \bar{C}_{11})}{4\pi(q\,t)^2\,\bar{C}_{11}\,C_{66}\,\sin\phi}\,\cdot \\ &\Big\{C_{ij11}\left[(\bar{C}_{11} + C_{12} + C_{66})\,{x_1}^2 x_2 + \lambda^2 C_{66} {x_2}^3\right] - C_{ij12}(C_{12} + \bar{C}_{11})\,x_1(x_1^2 - (\lambda\,x_2)^2) \\ &\quad - \frac{C_{ij22}}{C_{22}}\left[(C_{12}^2 + \bar{C}_{11}\,C_{12} + 2\,C_{12}\,C_{66} + \bar{C}_{11}\,C_{66})\,x_1^2 x_2 - \bar{C}_{11}\,C_{66}\,\lambda^2\,x_2^3\right]\Big\} \\ &+ \frac{b_2\,\lambda\,(C_{12} - \bar{C}_{11})}{4\pi(q\,t)^2\,\bar{C}_{11}\,C_{66}\,\sin\phi}\,\cdot \\ &\Big\{C_{ij22}\left[(\bar{C}_{11} + C_{12} + C_{66})(\lambda\,x_2)^2\,x_1 + C_{66}\,x_1^3\right] - C_{ij12}(C_{12} + \bar{C}_{11})\,x_2(x_1^2 - (\lambda x_2)^2) \\ &\quad - \frac{C_{ij11}}{C_{11}}\left[(C_{12}^2 + \bar{C}_{11}\,C_{12} + 2\,C_{12}\,C_{66} + \bar{C}_{11}\,C_{66})\,(\lambda\,x_2)^2\,x_1 - \bar{C}_{11}\,C_{66}\,x_1^3\right]\Big\} \end{aligned} \tag{9.110}$$

9.3.3.3 Screw Dislocation

For infinite screw dislocations the corresponding expressions are, for the displacement field,

$$u_3 = -\frac{b_3}{2\pi} \arctan \left[\frac{(C_{44}\, C_{55} - C_{45}^2)^{1/2}\, x_2}{C_{44}\, x_1 - C_{45}^2\, x_2} \right] \tag{9.111}$$

and for the stress field,

$$\begin{aligned} \sigma_{13} &= -\frac{b_3}{2\pi} \left(C_{44}\, C_{55} - C_{45}^2\right)^{1/2} \left(\frac{C_{45}\, x_1 - C_{55}\, x_2}{C_{44}\, x_1^2 - 2\, C_{45}\, x_1\, x_2 + C_{55}\, x_2^2} \right) \\ \sigma_{23} &= -\frac{b_3}{2\pi} \left(C_{44}\, C_{55} - C_{45}^2\right)^{1/2} \left(\frac{C_{44}\, x_1 - C_{45}\, x_2}{C_{44}\, x_1^2 - 2\, C_{45}\, x_1\, x_2 + C_{55}\, x_2^2} \right) \end{aligned} \tag{9.112}$$

9.3.4 3D Field Equations for Dislocation Segments in an Isotropic Linear Elastic Medium

Analytical calculations of displacement, strain, and stress fields associated with dislocation arrays of low symmetry lead to very complicated expressions. For complex dislocation structures a closed analytical treatment is thus no longer possible.

For nonetheless calculating arbitrary dislocation arrays, it is hence straightforward to approximate real dislocation arrangements by sequences of piecewise straight segments which are much shorter as compared with the entire dislocation.

The local field quantities can then be computed by a summation of the contributions of all individual segments assembled in the array. The summation is possible since the line integrals that occur in Mura's expression for the calculation of the displacement field, equation (9.88), transform like vectors for each dislocation line segment (Hirth and Lothe 1982; Mura 1987). Consequently, all tensor quantities obtained for the individual segments can be transformed to a common coordinate system.

Owing to the fact that dislocation lines must not end within an otherwise perfect region of crystal, it is clear that the segmentation of dislocation lines is only allowed if the segments are interconnected or terminate at free surfaces under consideration of image forces.

However, the fundamental problem remains, of how the occurrence of connected isolated segments can be *physically* interpreted. An elegant justification is given in Figure 9.2, which shows how a curved dislocation line can be approximated by combining dislocation loops with identical Burgers vectors but alternating line vectors. While the parallel portions of these loops align to form a continuous dislocation line, the anti-parallel portions can be arranged in a manner to allow mutual annihilation. This construction also substantiates the fact that a segmented dislocation cannot terminate within an otherwise perfect crystal region. At the end points of the dislocation which consists of the parallel segments, the underlying loops do not simply vanish but continue in the crystal. This shows that the introduction of a geometrical cut-off at these end points would entail an error which amounts to the stresses contributed by the remaining semi-infinite loop portions. This error vanishes if the segmented loop approximation is closed. A more detailed discussion of such constructions has been published by Brown (1967) and Bacon, Barnett, and Scattergood (1979a).

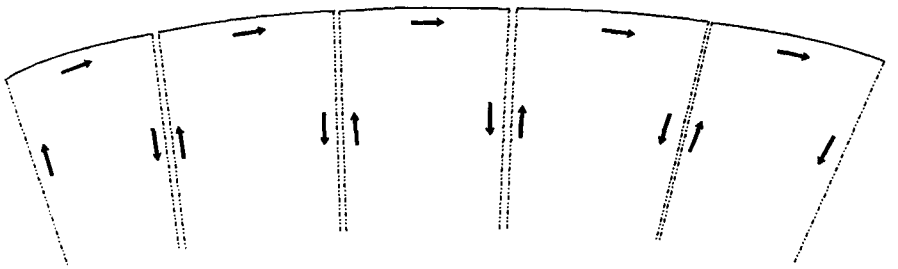

Figure 9.2: Approximation of a curved dislocation line by combining dislocation loops with identical Burgers vectors but alternating line vectors (arrows).

Pioneering contributions on the discretization of three-dimensional dislocation lines into sequences of piecewise straight segments and the subsequent calculation of field quantities arising from all these segments were published by de Wit (1960), Brown (1967), Indenbom and Orlov (1967), Asaro and Barnett (1974), Bacon, Barnett, and Scattergood (1979a), Hirth and Lothe (1982), Mura (1987), Devincre (1995), and Mohles and Rönnpagel (1996). For the derivation of the corresponding strain and stress tensors the authors employed either the sextic theory of Stroh or the integral theory using Green's tensor function method.

As a starting point for presenting three-dimensional field expressions for piecewise straight dislocation segments it is convenient to follow the derivation of Hirth and Lothe (1982). The stresses are first derived in rectangular coordinates x_1, x_2, x_3. The vector $\boldsymbol{R}$ indicates the spacing between the coordinates that are fixed on the dislocation line, $\boldsymbol{r}'^{\mathrm{T}} = (x_1', x_2', x_3')$, and the field coordinates under inspection, $\boldsymbol{r}^{\mathrm{T}} = (x_1, x_2, x_3)$, so that

$$\begin{aligned} \boldsymbol{R} &= \boldsymbol{r} - \boldsymbol{r}' \\ R &= \sqrt{(x_1 - x_1')^2 + (x_2 - x_2')^2 + (x_3 - x_3')^2} \end{aligned} \tag{9.113}$$

applies. It is assumed that the dislocation line vector is parallel to x_3. For simplicity, the dislocation line passes through the origin, so that $x_1' = 0$ and $x_2' = 0$. The above expression then reduces to

$$R = \sqrt{(x_1)^2 + (x_2)^2 + (x_3 - x_3')^2} \tag{9.114}$$

By combining the expressions for the stress, equations (9.29) or (9.37), rendered into the isotropic limit, equation (9.58), with the Green's function for the isotropic case, equation (9.76), and the formula for the displacement gradient after applying Stokes' theorem, equation (9.76), one obtains a convenient line integral expression for the stress,

$$\begin{aligned} \sigma_{11} &= \frac{\mu}{4\pi(1-\nu)} \int b_m \epsilon_{imz} \left(\frac{\partial^3 R}{\partial x_i \partial x_1^2} - \frac{\partial}{\partial x_i} \nabla^2 R \right) \mathrm{d}x_3' \\ &= \frac{\mu}{4\pi(1-\nu)} \int \left[b_1 \left(-\frac{\partial^3 R}{\partial x_2 \partial x_1^2} + \frac{\partial}{\partial x_2} \nabla^2 R \right) + b_2 \left(\frac{\partial^3 R}{\partial x_1^3} + \frac{\partial}{\partial x_1} \nabla^2 R \right) \right] \mathrm{d}x_3' \end{aligned} \tag{9.115}$$

where μ is the bulk shear modulus, ν Poisson's ratio, $\boldsymbol{b}^{\mathrm{T}} = (b_1, b_2, b_3)$ the Burgers vector, and ϵ_{ijk} the totally antisymmetric Levi–Civita operator, the components of which are

defined to be 1 if the suffixes are in cyclic order, -1 if they are in reverse cyclic order and 0 if any two suffixes are the same. The spatial variables $x_1' = 0$ and $x_2' = 0$ were set equal to zero. It must be noted that the partial derivatives $\partial/\partial x_i$ are equal to $-\partial/\partial x_i'$. A more detailed derivation of this expression is given by Hirth and Lothe (1982).

Dropping the terms that are independent of x_3' the line integrals in equation (9.115) can be solved according to

$$\int \frac{\partial}{\partial x_2} \nabla^2 R \, \mathrm{d}x_3' = \int \frac{\partial}{\partial x_2} \frac{2}{R} \mathrm{d}x_3' = -\int \frac{2\,x_2}{R^3} \mathrm{d}x_3' = \\ -\frac{2\,x_2\,(x_3' - x_3)}{(x_1^2 + x_2^2)\,R} = -\frac{2\,x_2\,(x_3' - x_3)}{R\left[R^2 - (x_3' - x_3)^2\right]} \,. \tag{9.116}$$

Proceeding in this manner for all the stress components ($x_1' = 0, x_2' = 0$) leads to

$$\sigma_{11}' = b_1 \frac{x_2}{R(R+\lambda)} \left[1 + \frac{x_1^2}{R^2} + \frac{x_1^2}{R(R+\lambda)}\right] + \\ b_2 \frac{x_1}{R(R+\lambda)} \left[1 - \frac{x_1^2}{R^2} - \frac{x_1^2}{R(R+\lambda)}\right] \tag{9.117}$$

$$\sigma_{22}' = -b_1 \frac{x_2}{R(R+\lambda)} \left[1 - \frac{x_2^2}{R^2} - \frac{x_2^2}{R(R+\lambda)}\right] - \\ b_2 \frac{x_1}{R(R+\lambda)} \left[1 + \frac{x_2^2}{R^2} + \frac{x_2^2}{R(R+\lambda)}\right] \tag{9.118}$$

$$\sigma_{33}' = b_1 \left[\frac{2\,\nu\,x_2}{(R+\lambda)} + \frac{x_2\,\lambda}{R^3}\right] + b_2 \left[-\frac{2\,\nu\,x_1}{(R+\lambda)} - \frac{x_1\,\lambda}{R^3}\right] \tag{9.119}$$

$$\sigma_{12}' = -b_1 \frac{x_1}{R(R+\lambda)} \left[1 - \frac{x_2^2}{R^2} - \frac{x_2^2}{R(R+\lambda)}\right] + \\ b_2 \frac{x_2}{R(R+\lambda)} \left[1 - \frac{x_1^2}{R^2} - \frac{x_1^2}{R(R+\lambda)}\right] \tag{9.120}$$

$$\sigma_{13}' = -b_1 \frac{x_1 x_2}{R^3} + b_2 \left(-\frac{\nu}{R} + \frac{x_1^2}{R^3}\right) + b_3 \frac{x_2\,(1-\nu)}{R(R+\lambda)} \tag{9.121}$$

$$\sigma_{23}' = b_1 \left(\frac{\nu}{R} - \frac{x_2^2}{R^3}\right) + b_2 \frac{x_1 x_2}{R^3} - b_3 \frac{x_1\,(1-\nu)}{R(R+\lambda)} \tag{9.122}$$

where $\sigma_{ij}' = \sigma_{ij} 4\pi(1-\nu)/\mu$ and $\lambda = x_3' - x_3$. The stress at $\boldsymbol{r}$ from a straight segment which lies between $x_3'(\boldsymbol{A})$ and $x_3'(\boldsymbol{B})$ then amounts to

$$\sigma_{ij}^{\boldsymbol{A}\to\boldsymbol{B}}(\boldsymbol{r}) = [\sigma_{ij}(\boldsymbol{r})]_{\boldsymbol{r}'=\boldsymbol{B}} - [\sigma_{ij}(\boldsymbol{r})]_{\boldsymbol{r}'=\boldsymbol{A}} \tag{9.123}$$

The above sets of equations are limited in their applicability in that they depend on the coordinate system employed. Furthermore, they are only formulated for situations

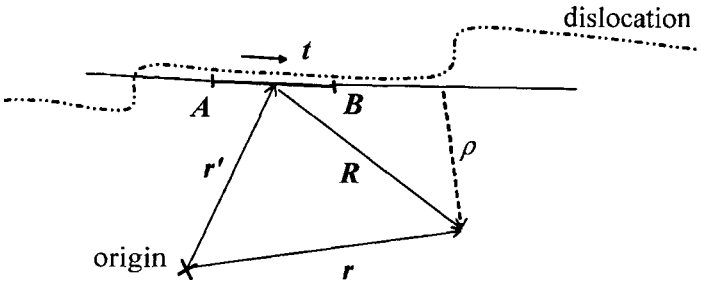

Figure 9.3: Schematic diagram of the vector geometry used for deriving the field equations (9.126) for infinite straight dislocations.

where straight segments cut through the origin. Therefore, in the following text they are transformed into a dyadic form which is more convenient for numerical purposes.

Following de Wit (1960) and Devincre (1995), the starting point of the derivation is the expression for the stress field associated with an infinite straight dislocation line at a point $\boldsymbol{r}$ in an unbounded, isotropic, linear, homogeneous, elastic medium:

$$\sigma_{ij}(\boldsymbol{r}) = \frac{\mu\, b_n}{8\pi}\Big[\, q_{,mqq}\left(\epsilon_{jmn}\, t_i + \epsilon_{imn}\, t_j\right) + \frac{2}{(1-\nu)}\, \epsilon_{kmn}\left(q_{,mij} - q_{,mqq}\delta_{ij}\right) t_k \Big] \tag{9.124}$$

where $\boldsymbol{t}$ is the unit vector tangent to the dislocation line, $\boldsymbol{b}$ the Burgers vector, and q the indefinite line integral along the dislocation line (de Wit 1967). Symbols following the commas refer to spatial derivatives[4]. After deriving the spatial derivatives of q and introducing the tensor operator

$$[\,\boldsymbol{a}\,\boldsymbol{b}\,\boldsymbol{c}\,]_{ij} = \frac{1}{2}\,[(\boldsymbol{a}\times\boldsymbol{b})_i\, c_j + (\boldsymbol{a}\times\boldsymbol{b})_j\, c_i] \tag{9.125}$$

one obtains for the stress field (Devincre 1995)

$$\begin{aligned}\sigma_{ij}(\boldsymbol{r}) = \frac{\mu}{\pi Y^2}\Big\{&[\,\boldsymbol{b}\,\boldsymbol{Y}\,\boldsymbol{t}\,]_{ij} - \frac{1}{(1-\nu)}[\,\boldsymbol{b}\,\boldsymbol{t}\,\boldsymbol{Y}\,]_{ij} \\ &- \frac{(\boldsymbol{b},\boldsymbol{Y},\boldsymbol{t})}{2(1-\nu)}\Big[\delta_{ij} + t_i\, t_j + \frac{2}{Y^2}\big(\rho_i Y_j + \rho_j Y_i + \frac{L}{|\,\boldsymbol{R}\,|} Y_i\, Y_j\big)\Big]\Big\}\end{aligned} \tag{9.126}$$

where $(\boldsymbol{b},\boldsymbol{Y},\boldsymbol{t})$ is the mixed product of the vectors involved. The vectors and scalars that enter the above field equation are

$$\begin{gathered}\boldsymbol{R} = \boldsymbol{r} - \boldsymbol{r}' \qquad L = \boldsymbol{R}\cdot\boldsymbol{t} \qquad \boldsymbol{\rho} = \boldsymbol{R} - L\boldsymbol{t} \\ \boldsymbol{Y} = \boldsymbol{R} + |\boldsymbol{R}|\boldsymbol{t} = (\,L + |\boldsymbol{R}|)\,\boldsymbol{t} + \boldsymbol{\rho}\end{gathered} \tag{9.127}$$

where $\boldsymbol{R}$ is the spacing between the point in the middle of the segment, $\boldsymbol{r}'$, and the considered field point, $\boldsymbol{r}$, and $\boldsymbol{\rho}$ is the portion of $\boldsymbol{R}$ normal to the dislocation line $\boldsymbol{t}$. These various vectors and scalars are shown in Figure 9.3. The stress of the segment between $\boldsymbol{A}$ and $\boldsymbol{B}$ is then computed by

$$\sigma_{ij}^{A\to B}(\boldsymbol{r}) = [\sigma_{ij}(\boldsymbol{r})]_{\boldsymbol{r}'=\boldsymbol{B}} - [\sigma_{ij}(\boldsymbol{r})]_{\boldsymbol{r}'=\boldsymbol{A}} \tag{9.128}$$

[4]The tedious calculation of the derivatives $q_{,ijk}$ was reviewed by de Wit (1967) and Devincre (1995).

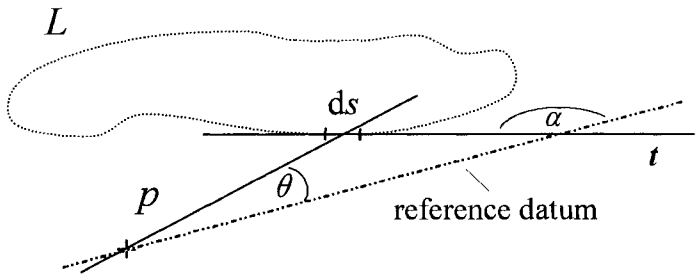

Figure 9.4: Geometry for the definition of the stress field at the field point $\boldsymbol{P}$ due to an arbitrary planar dislocation.

9.3.5 3D Field Equations for Dislocation Segments in an Anisotropic Linear Elastic Medium

In the present approach the dislocation segments are outside their cores (inner cut-off at $\approx |\boldsymbol{b}|$ where $\boldsymbol{b}$ is the Burgers vector) described as linear defects which are embedded within an otherwise homogeneous, linear elastic, anisotropic medium in static equilibrium having an arbitrary direction in a three-dimensional space. As in the case of linear elasticity, each dislocation consists of piecewise straight segments with a scaling length much smaller than the length of the original dislocation line to be described (scaling length of the segments $\approx |\boldsymbol{b}|$). The stress field associated with a polygonal dislocation loop is obtained by summing over the stress contributions of all segments (Bacon et al. 1979a). The mathematical problem of describing stress fields of arbitrarily shaped three-dimensional dislocations is thus reduced to the determination of the three-dimensional stress field of a single dislocation segment.

The fundamental theorem, from which to start, relates the field of an arbitrary planar dislocation to that of an infinite straight dislocation line. Figure 9.4 shows a planar dislocation loop L containing a field point P. The angles α and θ are measured anticlockwise from a fixed co-planar reference datum to the unit vector $\boldsymbol{t}$ which is tangential to an elemental arc ds on the dislocation loop L and to the vector $\boldsymbol{x}$ which points from the arc to the field point P, respectively (Brown 1967; Bacon et al. 1979b). The stress field at P is given by

$$\sigma_{ij} = \frac{1}{2}\oint_L \frac{1}{r^2}\left[\Sigma_{ij} + \frac{\mathrm{d}^2\Sigma_{ij}}{\mathrm{d}\theta^2}\right]\sin(\theta-\alpha)\mathrm{d}s \tag{9.129}$$

where Σ_{ij} is the angular stress factor and r the distance between the arc segment and the field point. This tensor expresses the angular dependence in the field which is associated with an infinite, straight dislocation line with the same Burgers vector as the loop L. It must be emphasized that, according to Brown (1967), its dislocation line points from the considered arc to the field point, i.e. it is tangent to $\boldsymbol{x}$ rather than to the loop portion ds. Equation (9.129), which is referred to as Brown's theorem, holds for the displacement field as well. Its use reduces the solution for a finite dislocation arc ds to the calculation of the field of an infinite straight dislocation which is characterized by Σ_{ij}.

Integration of equation (9.129) between points A and B gives the stress field contribution of a straight dislocation segment as a function of its Euclidean distance d from the field point (equation (9.130); Figure 9.5). The angular stress factors and their angular

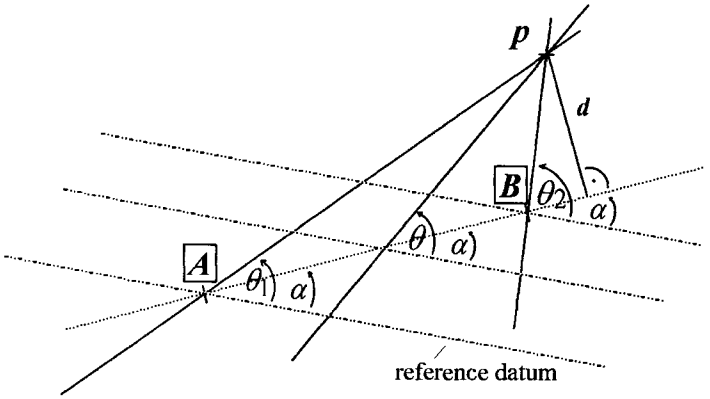

Figure 9.5: Definition of a straight dislocation segment $\boldsymbol{A} \rightarrow \boldsymbol{B}$.

derivatives in equation (9.130) then refer to the two infinite straight dislocations which point from the start and the end of the segment towards the field coordinate (Figure 9.5).

$$\sigma_{ij} = \frac{1}{2d}\left[-\Sigma_{ij}\,\cos(\theta-\alpha) + \frac{\mathrm{d}\Sigma_{ij}}{\mathrm{d}\theta}\,\sin(\theta-\alpha)\right]_{\theta_1}^{\theta_2} \tag{9.130}$$

Since the two auxiliary dislocation lines which limit the segment are infinite and intersect at the field point, they construct two segments rather than one, the second being generated from the first through a point-mirror operation.

Using equation (9.130) as a starting point, Asaro and Barnett (1974) have proposed a method to transform the three-dimensional calculation of the segment field contributions to a set of piecewise planar problems. Each planar field calculation can then be carried out by applying the integral formalism (Mura 1963; Barnett 1972; Bacon et al. 1979a; Indenbom and Lothe 1992) or the sextic approach (Eshelby et al. 1953; Stroh 1958). The former method involves the integration of the Green's function of anisotropic elasticity. The latter approach is based on solving the equilibrium equations under appropriate boundary conditions, which leads to a six-dimensional characteristic equation of which the eigenvalues are complex and occur in conjugate pairs.

In this study the stress fields of the infinite dislocations are derived by integration of the time-independent Green's tensor field $G_{ij}(\boldsymbol{x}, \boldsymbol{x}')$ which gives the displacement along the x_i axis at $\boldsymbol{x}$ in response to a delta-type unit point force exerted parallel to the x_j axis at $\boldsymbol{x}'$. This approach is valid for an infinite body with homogeneous elastic properties in static equilibrium. In the present case the Green's tensor satisfies the conditions of translational invariance, centrosymmetry, and reciprocity (Bacon et al. 1979a), equation (9.73). Provided that the dislocation motion is uniform, the time-independent Green's tensor may be used for dislocation dynamics as well. In the case of non-uniform motion the time-dependent Green's tensor must be employed. The integral approach provides two advantages as compared with the sextic method. First, it is directly applicable to crystal defects other than dislocations. Second, the integral solutions pass into the isotropic limit where the Zener ratio is equal to 1, i.e. $C_{2323} = \frac{1}{2}(C_{1111} - C_{1122})$ for arbitrary values of Poisson's ratio, $C_{1122}/(C_{1111} + C_{1122})$. The main shortcoming of this method is the required numerical integration of the Green's tensor, which is more time-consuming than

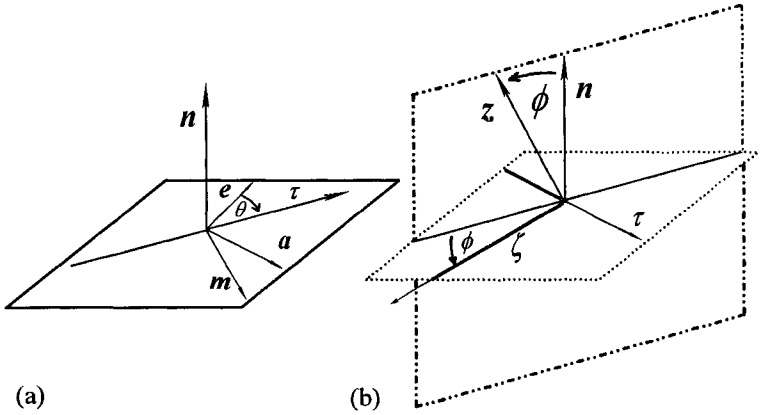

Figure 9.6: (a) Dislocation coordinate system. (b) Integration variables and their relation to the dislocation coordinate system (Asaro and Barnett 1974).

the solution of the eigenvalue problem in the sextic approach (Barnett 1996)[5]. Following Asaro and Barnett (1974), one first has to define the local coordinate system of the infinite dislocations, Figure 9.6. The normal $\boldsymbol{n}$ to the plane which contains the infinite dislocations, the segment line, and the field point can be expressed as the outer product of any pair of the vectors involved. The unit vector parallel to the infinite dislocation line $\boldsymbol{t}$ is described by two unit vectors $\boldsymbol{e}$ and $\boldsymbol{a}$ normal to $\boldsymbol{n}$. The unit vector $\boldsymbol{m}$ is the angular derivative of $\boldsymbol{t}$ (Asaro et al. 1973; Asaro and Barnett 1974).

$$\boldsymbol{t} = \boldsymbol{e}\cos(\theta) + \boldsymbol{a}\sin(\theta) \qquad \boldsymbol{m} = \frac{\mathrm{d}\boldsymbol{t}}{\mathrm{d}\theta} = -\boldsymbol{e}\sin(\theta) + \boldsymbol{a}\cos(\theta) \tag{9.131}$$

Since $\boldsymbol{m}$ is a unit vector and located in the same plane as the infinite dislocation line, it can be computed as the vector product of $\boldsymbol{n}$ and $\boldsymbol{t}$. Employing the Radon transform for the development of the single line integral solution for $G_{ij}(\boldsymbol{x}-\boldsymbol{x}')$ leads to the compact tensorial expression:

$$G_{ij}(\boldsymbol{x}-\boldsymbol{x}') = \frac{1}{8\pi^2 \mid \boldsymbol{x}-\boldsymbol{x}' \mid} \oint_{|z|=1} (\boldsymbol{zz})^{-1}_{ij} \mathrm{d}s \tag{9.132}$$

The variable $\boldsymbol{z}$ is a unit vector normal to $\boldsymbol{t}$, Figure 9.6, defined by

$$\boldsymbol{z} = \boldsymbol{n}\cos(\phi) - \boldsymbol{m}\sin(\phi) \tag{9.133}$$

The normal to the plane described by the unit integration contour, $\mid \boldsymbol{z} \mid = 1$, equation (9.132), is thus parallel to $\boldsymbol{t}$. The second-rank symmetric matrix integrand $(\boldsymbol{zz})^{-1}_{ij}$ is the inverse of the Christoffel stiffness matrix $(\boldsymbol{zz})_{ij}$ (Barnett et al. 1972). The latter operator is for the general nonsymmetric case, $(\boldsymbol{ab})_{jk}$, defined by equation (9.78). The inverse of the symmetric stiffness matrix with the form $(\boldsymbol{aa})^{-1}_{ij}$ is given by equation (9.79). The Einstein summation convention is used throughout the calculations. For skipping redundant integrations the symmetries of equations (9.78) and (9.79) should be

[5]Numerical integrations that appear in large vector loops, especially, degrade the speed of dislocation calculations considerably.

exploited. For media with cubic lattice symmetry one can use simplified expressions for the inverse stiffness matrix (Barnett et al. 1972) :

$$(\boldsymbol{aa})_{11}^{-1} = \frac{e\,(e+f) - e\,f\,a_1^2 + (f^2-1)(a_2a_3)^2}{(C_{1122}+C_{2323})\,\Delta} \tag{9.134}$$

$$(\boldsymbol{aa})_{12}^{-1} = -\frac{(a_1a_2)\,\left[(f-1)a_3^2+e\right]}{(C_{1122}+C_{2323})\,\Delta} \tag{9.135}$$

$$\Delta = e^2(e+f) + e(f^2-1)\left[(a_1a_2)^2+(a_1a_3)^2+(a_2a_3)^2\right] + (f-1)^2(f+2)(a_1a_2a_3)^2 \tag{9.136}$$

$$e = \frac{C_{2323}}{C_{1122}+C_{2323}} \qquad f = \frac{C_{1111}-C_{2323}}{C_{1122}+C_{2323}} \tag{9.137}$$

The remaining elements $(\boldsymbol{aa})_{ij}^{-1}$ are derived by cyclic permutation of the indices of $\boldsymbol{a}$. The two matrices, equations (9.78) and (9.79), are related through

$$(\boldsymbol{aa})_{ij}^{-1}\,(\boldsymbol{aa})_{jk} = \delta_{ik} \tag{9.138}$$

where δ_{ik} is the Kronecker symbol. The elements of the fourth-ranked tensor of the elastic constants C_{ijkl} are throughout expressed in crystal coordinates. The orientation-dependent part of the Green's tensor, equation (9.132), is given by Q_{ij},

$$Q_{ij} = -\frac{1}{2\pi}\int_0^{2\pi}(\boldsymbol{zz})_{ij}^{-1}\mathrm{d}\phi \tag{9.139}$$

Equation (9.132) can then be written

$$G_{ij}(\boldsymbol{x}-\boldsymbol{x}') = -\frac{1}{4\pi\mid \boldsymbol{x}-\boldsymbol{x}'\mid}\,Q_{ij} \tag{9.140}$$

Additionally, one requires the nonsymmetric transposed matrix S_{ij}^{T}, which is defined by

$$S_{ij}^{\mathrm{T}} = \frac{1}{2\pi}\int_0^{2\pi}\left[(\boldsymbol{\zeta z})\,(\boldsymbol{zz})^{-1}\right]_{ij}\,\mathrm{d}\phi \tag{9.141}$$

The integration variable $\boldsymbol{\zeta}$ is the angular derivative of $\boldsymbol{z}$ (Figure 9.6).

$$\boldsymbol{\zeta} = \frac{\mathrm{d}\boldsymbol{z}}{\mathrm{d}\theta} = -\boldsymbol{n}\,\sin(\phi) - \boldsymbol{m}\,\cos(\phi) \tag{9.142}$$

The Christoffel stiffness matrix associated with the unit vectors $\boldsymbol{\zeta}$ and $\boldsymbol{z}$ can be derived as shown in equation (9.78).

However, the integrals Q_{ij} and S_{ij}^{T} are not independent of each other. Instead of using equation (9.141) the matrix S_{ij}^{T} can be computed algebraically if Q_{ij} is known also, and vice versa. Kirchner and Lothe (1986) showed that

$$V_s\,X_{st} = d_t \tag{9.143}$$

with

$$X_{st} = \epsilon_{ilt}[\epsilon_{ijs}\, Q^{-1}_{jk}\, (\boldsymbol{nn})^{-1}_{kl} + (\boldsymbol{nn})^{-1}_{ij}\, Q^{-1}_{jk}\, \epsilon_{ijs}] \tag{9.144}$$

and

$$d_t = [(\boldsymbol{nn})^{-1} \cdot (\boldsymbol{nm}) \cdot \boldsymbol{Q} - \boldsymbol{Q} \cdot (\boldsymbol{mn}) \cdot (\boldsymbol{nn})^{-1}]_{il}\, \epsilon_{ilt} \tag{9.145}$$

After solving equation (9.143) the matrix $\boldsymbol{S}$ and its transposed $\boldsymbol{S}^{\mathrm{T}}$ are obtained by using

$$(\boldsymbol{SQ})_{ij} = \epsilon_{ijs} V_s \qquad \text{and} \qquad \boldsymbol{S} = (\boldsymbol{SQ})\, \boldsymbol{Q}^{-1} \tag{9.146}$$

In the examples given later in this Chapter, Q_{ij} is mostly computed by integration, equation (9.139), and S^{T}_{ij} algebraically by equations (9.143)–(9.146) because it has a more complicated integrand than Q_{ij}. Finally, the angular stress factor of the infinite dislocation can be calculated according to

$$\Sigma_{gh} = r\, C_{ghip}\, u_{i,p} \tag{9.147}$$

where $u_{i,p}$ is the displacement gradient tensor.

$$\Sigma_{gh} = -\frac{1}{2\pi}\, \epsilon_{pjw} C_{ghip} C_{mwrs} b_m t_j \Big(m_s Q_{ir} + n_s \Big\{ -(\boldsymbol{nn})^{-1}_{il} S^T_{lr} - [(\boldsymbol{nn})^{-1}(\boldsymbol{nm})]_{il} Q_{lr} \Big\} \Big) \tag{9.148}$$

The angular derivative of the stress factor is given by

$$\frac{\mathrm{d}\Sigma_{gh}}{\mathrm{d}\theta} = -\frac{1}{2\pi}\, \epsilon_{pjw}\, C_{ghip}\, C_{mwrs}\, b_m \left(m_j F_{sir} + t_j \frac{\mathrm{d}F_{sir}}{\mathrm{d}\theta} \right) \tag{9.149}$$

where

$$F_{sir} = m_s Q_{ir} - n_s (\boldsymbol{nn})^{-1}_{il} S^T_{lr} - n_s\, [(\boldsymbol{nn})^{-1}(\boldsymbol{nm})]_{il}\, Q_{lr} \tag{9.150}$$

$$\frac{\mathrm{d}F_{sir}}{\mathrm{d}\theta} = m_s \frac{\mathrm{d}Q_{ir}}{\mathrm{d}\theta} - t_s Q_{ir} - n_s (\boldsymbol{nn})^{-1}_{il} \frac{\mathrm{d}S^T_{lr}}{\mathrm{d}\theta} + n_s \Big\{ [(\boldsymbol{nn})^{-1}(\boldsymbol{nt})]_{il}\, Q_{lr} - n_s\, [(\boldsymbol{nn})^{-1}(\boldsymbol{nm})]_{il} \frac{\mathrm{d}Q_{lr}}{\mathrm{d}\theta} \Big\} \tag{9.151}$$

The angular derivatives of Q_{ij} and S^{T}_{ij} are given by

$$\frac{\mathrm{d}Q_{ij}}{\mathrm{d}\theta} = -\frac{1}{2\pi} \int_0^{2\pi} (\boldsymbol{zz})_{is}\, [(\boldsymbol{\eta z}) + (\boldsymbol{z\eta})]_{sr}\, (\boldsymbol{zz})^{-1}_{rj}\, \mathrm{d}\phi \tag{9.152}$$

$$\frac{\mathrm{d}S^{\mathrm{T}}_{ij}}{\mathrm{d}\theta} = \frac{1}{2\pi} \int_0^{2\pi} \Big\{ [(\boldsymbol{\beta z}) + (\boldsymbol{\zeta\eta})]_{is}\, (\boldsymbol{zz})^{-1}_{sj} + [(\boldsymbol{\zeta z})(\boldsymbol{zz})^{-1}]_{is}\, [(\boldsymbol{\eta z}) + (\boldsymbol{z\eta})]_{sr}\, (\boldsymbol{zz})^{-1}_{rj} \Big\}\, \mathrm{d}\phi \tag{9.153}$$

The integrands contain the unit vectors $\boldsymbol{\eta}$ and $\boldsymbol{\beta}$ which are defined by

$$\boldsymbol{\eta} = \boldsymbol{t}\,\sin(\phi) = \frac{\mathrm{d}\boldsymbol{z}}{\mathrm{d}\theta} \qquad \boldsymbol{\beta} = \boldsymbol{t}\,\cos(\phi) = \frac{\mathrm{d}\boldsymbol{\zeta}}{\mathrm{d}\theta} \tag{9.154}$$

For closed-loop or infinite-line dislocation configurations the contribution of the first angular derivative $\mathrm{d}\Sigma_{ij}/\mathrm{d}\theta$ to the stress field may be dropped (Bacon et al. 1979b) so that equation (9.130) can be reduced to

$$\sigma_{ij} = \frac{1}{2d}\left[-\Sigma_{ij}\,\cos(\theta-\alpha)\right]_{\theta_1}^{\theta_2} \tag{9.155}$$

For computing dislocation fields in cubic media, the following relations among the elastic constants (equations (9.31) and (9.34)) apply,

$$C_{2222} = C_{3333} = C_{1111} \qquad C_{1212} = C_{1313} = C_{2323} \qquad C_{1122} = C_{1133} = C_{2233}$$

$$C_{ijkl} = C_{jikl} = C_{ijlk} = C_{klij} \tag{9.156}$$

with all remaining elements being equal to zero.

9.4 Dislocation Dynamics

9.4.1 Introduction

The earliest phenomenological models to describe the dynamics of dislocations in crystals date back to the pioneering work of Orowan (1934), Polanyi (1934), and Taylor (1934) in which the motion of dislocations was already understood as an intrinsic defect property. Orowan (1934) stated that dislocation glide consists in the movement of dislocations across their respective glide planes. Polanyi (1934) complemented this view by adding that dislocation glide across glide planes should take place at stresses much below the value predicted by the theoretical strength which is required to slide one lattice plane rigidly across the other. Taylor (1934) studied the atomic positions in the core of what is today referred to as edge dislocation, and the respective positions change during dislocation motion. Common to all these early contributions was the belief that dislocations should have a high mobility, at least in closely packed crystal structures.

The next generation of researchers elaborated these concepts in more detail by identifying two relevant scaling quantities of plasticity, namely, the maximum intrinsic lattice resistance to dislocation motion which is referred to as Peierls[6] stress σ^{P} (Peierls 1940; Nabarro 1947a) and the "relativistic" increase in the dislocation energy in the vicinity of the speed of sound (Eshelby 1949a; Frank 1949).

In the next step a number of contributions addressed the highly dissipative character of dislocation motion by identifying various drag forces which act proportionally to the dislocation velocity (Eshelby 1949b; Leibfried 1950; Nabarro 1951; Rosenfield et al. 1968). At the same time, the theory of dislocation motion was complemented by considering inertia effects (Granato and Lücke 1956; Granato et al. 1964; Gillis and Kratochvil 1970) and by the advent of the concept of thermal activation (Seeger 1954; Friedel 1956; Leibfried 1957; Seeger et al. 1957; Seeger 1957; Kröner 1965).

[6] In all that follows, σ is used as the symbol for stresses instead of τ. The introduction of τ to indicate shear stresses is not necessary since this can be expressed through σ_{ij} where $i \neq j$.

The integrands contain the unit vectors $\boldsymbol{\eta}$ and $\boldsymbol{\beta}$ which are defined by

$$\boldsymbol{\eta} = \boldsymbol{t}\,\sin(\phi) = \frac{\mathrm{d}\boldsymbol{z}}{\mathrm{d}\theta} \qquad \boldsymbol{\beta} = \boldsymbol{t}\,\cos(\phi) = \frac{\mathrm{d}\boldsymbol{\zeta}}{\mathrm{d}\theta} \tag{9.154}$$

For closed-loop or infinite-line dislocation configurations the contribution of the first angular derivative $\mathrm{d}\Sigma_{ij}/\mathrm{d}\theta$ to the stress field may be dropped (Bacon et al. 1979b) so that equation (9.130) can be reduced to

$$\sigma_{ij} = \frac{1}{2d}\left[-\Sigma_{ij}\,\cos(\theta-\alpha)\right]_{\theta_1}^{\theta_2} \tag{9.155}$$

For computing dislocation fields in cubic media, the following relations among the elastic constants (equations (9.31) and (9.34)) apply,

$$C_{2222} = C_{3333} = C_{1111} \qquad C_{1212} = C_{1313} = C_{2323} \qquad C_{1122} = C_{1133} = C_{2233}$$

$$C_{ijkl} = C_{jikl} = C_{ijlk} = C_{klij} \tag{9.156}$$

with all remaining elements being equal to zero.

9.4 Dislocation Dynamics

9.4.1 Introduction

The earliest phenomenological models to describe the dynamics of dislocations in crystals date back to the pioneering work of Orowan (1934), Polanyi (1934), and Taylor (1934) in which the motion of dislocations was already understood as an intrinsic defect property. Orowan (1934) stated that dislocation glide consists in the movement of dislocations across their respective glide planes. Polanyi (1934) complemented this view by adding that dislocation glide across glide planes should take place at stresses much below the value predicted by the theoretical strength which is required to slide one lattice plane rigidly across the other. Taylor (1934) studied the atomic positions in the core of what is today referred to as edge dislocation, and the respective positions change during dislocation motion. Common to all these early contributions was the belief that dislocations should have a high mobility, at least in closely packed crystal structures.

The next generation of researchers elaborated these concepts in more detail by identifying two relevant scaling quantities of plasticity, namely, the maximum intrinsic lattice resistance to dislocation motion which is referred to as Peierls[6] stress σ^{P} (Peierls 1940; Nabarro 1947a) and the "relativistic" increase in the dislocation energy in the vicinity of the speed of sound (Eshelby 1949a; Frank 1949).

In the next step a number of contributions addressed the highly dissipative character of dislocation motion by identifying various drag forces which act proportionally to the dislocation velocity (Eshelby 1949b; Leibfried 1950; Nabarro 1951; Rosenfield et al. 1968). At the same time, the theory of dislocation motion was complemented by considering inertia effects (Granato and Lücke 1956; Granato et al. 1964; Gillis and Kratochvil 1970) and by the advent of the concept of thermal activation (Seeger 1954; Friedel 1956; Leibfried 1957; Seeger et al. 1957; Seeger 1957; Kröner 1965).

[6] In all that follows, σ is used as the symbol for stresses instead of τ. The introduction of τ to indicate shear stresses is not necessary since this can be expressed through σ_{ij} where $i \neq j$.

Computational Materials Science: The Simulation of Materials, Microstructures and Properties By Dierk Raabe
Copyright © 1998 Wiley-VCH Verlag GmbH
ISBN: 3-527-29541-0

Detailed contributions to these various fundamental aspects associated with the kinetics and thermodynamics of crystal dislocations and to the historical background were published by Friedel (1956), Cottrell (1964), Hirth and Lothe (1968), Rosenfield, Hahn, Bement, and Jaffee (1968), Kocks, Argon, and Ashby (1975), Ashby, Bullough, Hartley, and Hirth (1980), Schöck (1980), Nadgornyi (1988), Suzuki (1991), and Mughrabi (1993).

Following the large body of fundamental studies on dislocations it may be assumed that the most general approach to the prediction of the dynamics of lattice dislocations consists in solving Newton's equation of motion discretely in time and space for each dislocation portion, with consideration of all internal and external forces. This concept can be realized either through the use of molecular dynamics at the atomic scale or space-discretized continuum dislocation dynamics at the micro- and mesoscale.

This section is concerned with an introduction to the latter technique, i.e. to continuum dislocation dynamics. It presents the basic conceptual ingredients required in describing the dynamics associated with two- and three-dimensional dislocation arrays in a space- and time-discretized fashion. The section is organized in such a way that it presents at first a general three-dimensional Newtonian concept for the description of dislocation dynamics and subsequently simpler, more phenomenological viscous and viscoplastic two- and three-dimensional derivatives of that concept.

9.4.2 Newtonian Dislocation Dynamics

9.4.2.1 Introduction

The general approach outlined in this section idealizes the crystal as a canonical ensemble in the quasi-harmonic approximation (Kramers 1940; Schöck 1980; Rönnpagel et al. 1993). This allows one to consider anharmonic effects such as the temperature and pressure dependence of the elastic constants and at the same time to treat the crystal in the continuum approach using a linear relation between stress and strain. The dislocations, outside their cores, can then be approximated as line defects which are embedded in a homogeneous, unbounded, linear, anisotropic, elastic medium (Volterra 1907; Eshelby et al. 1953; Mura 1963; Steeds 1973; Bacon et al. 1979a; Hirth and Lothe 1982; Teodosiu 1982; Mura 1987).

The dislocations are regarded as the elementary carriers of velocity fields from the gradients of which both the strain rate and the spin can be calculated. Each dislocation is described as a line defect which consists of a sequence of piecewise straight segments. The displacement and stress fields associated with these segments can be generally formulated to consider elastic anisotropy and arbitrary crystal symmetry using Brown's theorem and the integral formalism in the version of Asaro and Barnett (Section 9.3.5). The stress field of each dislocation line is computed through a linear superposition of the stress contributions of all segments.

Time t and space x_i are independent variables. The atomic concentration of the vacancies c and the displacement field u_i from which the displacement gradient tensor $u_{i,j}$ can be calculated are used as space- and time-dependent state variables [7]. Hooke's law of anisotropic elasticity and the chemical potential of the vacancies act as equations of state. Newton's law of motion and Fick's modified second law of diffusion are used as structural evolution equations assuming local mechanical equilibrium at each segment.

[7] Tensor quantities of all orders are indicated by bold symbols or indices. Partial derivatives are abbreviated using a comma, e.g. $u_{i,j} = \partial u_i / \partial x_j$.

The differential equations of motion of the individual portions belonging to the same dislocation are coupled through the line tension which is considered discretely by calculating the self-interaction force among the segments according to the concept of Brown (1967). The chemical back-driving force associated with nonconservative dislocation motion is introduced by considering the osmotic pressure that arises from emitting or adsorbing point defects in the climbing segment.

The temperature acts as a state variable which is dependent on time but independent of space, i.e. it remains constant throughout the simulation box during each strain increment. This approach reflects the fact that the crystal is regarded as a canonical ensemble where each dislocation segment is embedded in an infinite heat reservoir (Rönnpagel et al. 1993). The dissipation of heat due to friction is assumed to be much faster than the glide velocity of the dislocation. This postulation is justified because the dissipation rate of heat is determined by the velocity of the electrons at the Fermi level while the glide velocity can only assume values below the speed of sound. In the equation of motion the temperature is included through a stochastic Langevin force as proposed by Leibfried (1957) and Rönnpagel, Streit, and Pretorius (1993).

Further forces such as phonon drag, electron drag, and the elastic Peach–Koehler interaction among dislocations are considered following earlier classical work (Rosenfield et al. 1968; Simmons et al. 1970; Nadgornyi 1988; Nabarro 1989; Suzuki 1991).

This discrete approach can be referred to as a hybrid model, since it considers both the dynamics of the dislocations and the kinetics of the point defects that are generated by nonconservative dislocation motion. Simulations in this framework involve the solution of a set of coupled stochastic, nonlinear, second-order, partial differential equations for each single dislocation line discretely in space and time by using finite difference or finite element algorithms.

9.4.2.2 Segmentation of Dislocations

Fundamentals Each dislocation line can be approximated by a sequence of interconnected piecewise straight dislocation segments in three dimensions (Yoffe 1960; Hokanson 1963; Li 1965). Owing to the fact that dislocation lines must not end within an otherwise perfect region of crystal, their segmentation is only allowed if the segments stick together to form closed loops, are semi-infinite, or terminate at a free surface with consideration of image forces, a reaction product, a grain boundary, or some other lattice defect, where stress equilibrium is preserved. This means in the general three-dimensional case each dislocation line consists of j sequentially arranged segments defined by $j + 1$ vectors.

Bacon, Barnett, and Scattergood (1979a) elegantly justified the concept of decomposing dislocations into segments. They showed that a curvilinear dislocation line can be approximated through a seamless combination of angular dislocation loops with identical Burgers vectors and piecewise alternating tangential vectors. While the non-antiparallel portions of these loops align to form a continuous dislocation line, the antiparallel portions can be arranged in a manner to mutually annihilate each other (Figure 9.2).

This construction shows that a segmented dislocation cannot terminate within a perfect crystal portion because the underlying loops, the non-antiparallel parts of which generate the dislocation under consideration, continue in the crystal. It is thus obvious that the introduction of a geometrical cut-off at the end points of a dislocation entails an error which amounts to the stress field imposed by the remaining semi-infinite loop portions. This error vanishes if the loop approximation is closed or if image forces are considered (Yoffe 1960; Hokanson 1963; Li 1965; Brown 1967; Indenbom and Lothe 1992).

Orientation of Segments Two approaches are conceivable to arranging the segment tangential vector with respect to the crystal lattice. In the method suggested by Kubin, Canova, Condat, Devincre, Pontikis, and Bréchet (1992), the individual dislocation portions are aligned parallel to potential valleys with a low crystal index so as to either assume pure edge- or pure screw-type character. This technique maps the abrupt- or hard-kink model, where the influence of the Peierls force on the dislocation shape exceeds that of the self-interaction force. In the method suggested by Bacon, Kocks, and Scattergood (1973), Hirth (1996), Mohles and Rönnpagel (1996), and Raabe (1998a), the dislocation portions can have arbitrary orientation and mixed character. This approach reflects the smooth-kink model, which implies that the Peierls force is of less influence on the dislocation shape than the self-interaction force. While the abrupt-kink model is in accord with experimental observations and theoretical predictions for crystals with covalent or ionic bonding, the smooth-kink approximation applies for crystals with metallic bonding (Nadgornyi 1988; Suzuki 1991).

Length of Segments Discrete dislocation dynamics simulations which are based on the linear elastic line approximation are at first sight not intrinsically scaled as, for instance, is apparent in molecular dynamics. However, some physical arguments can be identified, resulting essentially from dynamic aspects, which allow one to define an adequate length scale for such simulations. These are the reaction/interaction, the stress fluctuation, the bow-out, the linear elastic-limit, and the cutting criteria.

The reaction/interaction criterion means that the time that elapses during one simulation step is confined to a value prescribed by the condition that dislocation segments must not pass each other without being given a possibility to interact or react. For a given law of motion, say viscous glide, $v \propto \tau$, the half-minimum segment spacing $\Delta\lambda_{\min}^{\text{seg}}$ and the local stress τ dynamically determine the real time that is mapped by one calculation step according to $\Delta t^{\text{step}} \propto \Delta\lambda_{\min}^{\text{seg}}/2\,\tau$. Choosing this approach for the determination of the real time increment ensures that neighboring dislocation segments cannot pass each other within one time step without an interaction or reaction. After the determination of the time increment, all dislocations are moved according to their respective local velocity.

The stress fluctuation criterion considers that changes in the local force acting on a given straight segment should not exceed a critical value that would entail significantly different velocities of neighboring segment portions. Fulfilling this condition seems difficult, at least from a continuous point of view. It is obvious that it is nearly impossible to avoid a velocity gradient on one segment within a complex dislocation array, once the friction force is reached. Thus, it is necessary to transform this continuum problem into a discrete one. This can be attained by conducting the simulation in such a way that the stress fluctuations on single segments do not lead to different velocities within a chosen discrete velocity or respectively stress spectrum.

The bow-out criterion means that the discretization of space should permit simulation of the activation of a Frank–Read source or of the Orowan mechanism on a realistic scale. Typical data are available from the literature (Mughrabi 1993).

The linear elastic-limit principle means that the elastic distortions should be sufficiently low to justify solutions in the framework of Hooke's law. For instance, scaling values below the magnitude of the Burgers vector would spoil the validity of approximate solutions derived in the framework of linear elasticity.

The cutting criterion means that intersecting segments mutually increase their total dislocation length by exactly one Burgers vector. In simulations where cutting represents a prevailing mechanism, the scaling parameter should thus amount to one Burgers vector.

Further physical scaling limits can be found from experimental data about kink pair width, double-kink pair extension, jog height, and single-kink width. Owing to these constraints three-dimensional simulations involving dislocation segments are usually scaled by values of one to ten Burgers vectors or lattice parameters, respectively. In order to avoid scaling parameters that are too small, the introduction of a dynamical segment length is conceivable.

9.4.2.3 The Mechanical Equation of State

The basic problem encountered in space-discretized dislocation statics consists in calculating the local displacement gradient tensor $u_{i,j}(\boldsymbol{x})$ for a given spatial distribution of dislocations. Discretizing such arrays into sequentially arranged segments reduces the problem to the determination of the displacement gradient field associated with an individual straight portion of dislocation. From this quantity the local stress field can be derived using Hooke's law.

Calculating the stresses in dyadic form allows one to rotate the contributions of all segments to a common reference lattice and to derive the net field quantity through a linear superposition (Li 1965). The derivation of the required field equations was outlined previously for the isotropic (Section 9.3.4) and for the anisotropic case (Section 9.3.5).

9.4.2.4 The Chemical Equation of State

Besides the purely mechanical state equation which allows one to calculate the stress distribution from a given displacement field, one requires a second path-independent equation which quantifies any departure from chemical equilibrium. Neglecting the influence of foreign atoms, this chemical state equation amounts to the chemical potential of intrinsic point defects.

Any nonconservative motion of edge dislocation segments leads to the emission or adsorption of point defects. If not instantly equilibrated by local short-circuit diffusion processes, such a defect production term entails a local change in the chemical potential of the respective type of point defect. This local deviation from the thermal equilibrium leads to a chemical back-driving force which is referred to as osmotic force (Nabarro 1947b; Herring 1950; Weertman 1965; Lothe and Hirth 1967; Balluffi and Granato 1979; Hirth and Lothe 1982).

The chemical potential μ can be described as a change in the Gibbs free enthalpy G of the system on modifying the atomic concentration of intrinsic point defects from a reference concentration c_0 to an actual local concentration $c(\boldsymbol{r})$.

$$\mu(c) = \left(\frac{\partial G}{\partial n}\right)_{p,\,T} = k_{\mathrm{B}} T \ln\left(\frac{c(\boldsymbol{r})}{c_0}\right) \tag{9.157}$$

where k_{B} is the Boltzmann constant and T the temperature. The reference concentration c_0 is the concentration of the respective type of point defect in local equilibrium with the surface and the local hydrostatic pressure (Burke and Nix 1978; Rauh and Simon 1978; Hirth and Lothe 1982). As will be addressed in Section 9.4.2.6 the calculation of a local concentration of point defects c under consideration of climb requires the space- and time-discretized solution of the modified continuity equation and Fick's first law of diffusion, turning the model into a hybrid approach.

Following the concept of Hirth and Lothe (1982) for the case of a crystal exposed to both external and internal stress, the reference concentration amounts to

$$c_0 = \exp\left(-\frac{G_0 + (\sigma^{\mathrm{h}} + p)\Delta V}{k_{\mathrm{B}}\,T}\right) \tag{9.158}$$

where G_0 is the Gibbs free enthalpy of formation of the considered point defect in a stress-free crystal, σ^{h} the external hydrostatic stress component, p the space-dependent internal hydrostatic stress component, and ΔV the externally measured volume change.

Concerning the magnitude and sign of the internal stress, two aspects are worth emphasizing. First, it must be noted that in dislocation simulations the magnitude of the internal hydrostatic stress component can considerably exceed that of the externally imposed stress field. This applies particularly for the stresses close to the segment core. Second, the sign of the hydrostatic stress component changes in the glide plane, with a compression field above it and a dilatation field below it.

If the reference state is given by consideration of thermal equilibrium with the free crystal surface c_0', an additional term W_{e} must be introduced, namely,

$$c_0' = c_0 \exp\left(-\frac{W_{\mathrm{e}}}{k_{\mathrm{B}}\,T}\right) = \exp\left(-\frac{G_0 + (\sigma^{\mathrm{h}} + p)\Delta V \pm \sigma^{\mathrm{h}}\,\Omega}{k_{\mathrm{B}}\,T}\right) \tag{9.159}$$

where $+\sigma^{\mathrm{h}}\,\Omega$ applies for the formation of vacancies and $-\sigma^{\mathrm{h}}\,\Omega$ for the formation of interstitials. This work has to be done on the crystal for removing or adding the atomic volume Ω from or to the surface, respectively (Schöck 1980; Hirth and Lothe 1982).

9.4.2.5 The Mechanical Structure Evolution Equation

The Equation of Motion A general concept for the dynamics of dislocations can be formulated by assuming dynamic equilibrium of the forces at each time and portion along the dislocation line and by solving a modified form of Newton's equation of motion for each such dislocation segment. This approach, which was introduced by Rönnpagel (1987) for the two-dimensional case, can in principle be extended to three-dimensional problems (Raabe 1998a).

$$\sum_i \boldsymbol{F}^i\,(t, \boldsymbol{x}, \dot{\boldsymbol{x}}, \ddot{\boldsymbol{x}}) = 0 \tag{9.160}$$

where $\boldsymbol{x}$ and t are the independent variables, $\dot{\boldsymbol{x}}$ the velocity, $\ddot{\boldsymbol{x}}$ the acceleration, and $\boldsymbol{F}^i$ the various line forces that act on each portion of dislocation. The forces that enter equation (9.160) can be described as a function of the independent variables and their partial derivatives. The most important contributions in three-dimensional simulations are the Peierls force, $\boldsymbol{F}^{\mathrm{P}}$, the dislocation–dislocation force, $\boldsymbol{F}^{\mathrm{disl}}$, the self force, $\boldsymbol{F}^{\mathrm{self}}$, the external force, $\boldsymbol{F}^{\mathrm{ext}}$, the obstacle force, $\boldsymbol{F}^{\mathrm{obs}}$, the image force, $\boldsymbol{F}^{\mathrm{ima}}$, the osmotic force, $\boldsymbol{F}^{\mathrm{osm}}$, the phonon drag force, $\boldsymbol{F}^{\mathrm{Pdrag}}$, the electron drag force, $\boldsymbol{F}^{\mathrm{Edrag}}$, the inertia force, $\boldsymbol{F}^{\mathrm{iner}}$, the cross-slip drag force, $\boldsymbol{F}^{\mathrm{cross}}$, and the thermal force, $\boldsymbol{F}^{\mathrm{therm}}$.

The Peierls Force The Peierls force $\boldsymbol{F}^{\mathrm{P}}$ is a constant for the slip system being considered and represents the maximum intrinsic resistance to dislocation motion at 0 K. While the Peierls potential is very small in face-centered cubic metals, it can be of substantial relevance in body-centered metals, semiconductors, covalent, and ionic materials.

The use of the Peierls concept in the case of three-dimensional dislocation dynamics is somewhat diffuse because it originally denotes the force to bring an infinite rather than a finite dislocation from one potential valley to the next.

The Dislocation–Dislocation Force The dislocation–dislocation term $\boldsymbol{F}^{\text{disl}}$ represents the sum of all Peach–Koehler forces between the segment considered and *all* other dislocation portions in the ensemble. However, it must be underlined that this term does thus *not* include any interactions with dislocation segments that belong to the *same* dislocation. The spacing between the inspected portion of dislocation and the segments that belong to other dislocations usually exceeds the inner cut-off radius by one order of magnitude, except for dislocation reactions. Thus, this value enters the differential equation of motion at each time step as a constant. Since the character of the interactions is long-range in nature, the predictions obtained by dislocation dynamics simulations are highly sensitive to the introduction of an outer cut-off radius. A recent paper substantiated the fact that the use of an insufficiently small outer cut-off radius can entail incorrect predictions of the internal stress fields (Raabe 1996a). For obtaining reliable results it is thus necessary to impose periodic boundary conditions or to account for all dislocation segments in the array under consideration of the respective image forces imposed by the free surface. It is clear that the latter method leads to substantial difficulties in terms of data storage. Recent efforts therefore aim at the introduction of multipole techniques and parallel codes (Wang and LeSar 1995; Hirth 1996; Zacharopoulos et al. 1997).

The Self Force The self force $\boldsymbol{F}^{\text{self}}$ comprises those contributions to the total force that arise from the elastic Peach–Koehler interaction between the inspected line segment and all other dislocation portions that belong to the *same* dislocation. Although the physical nature of this line force is exactly identical to the aforementioned dislocation–dislocation force, their main difference lies in the fact that the self force *directly* enters the differential equation of motion as a variable rather than as a constant. The self force vanishes for infinite straight dislocations. However, for curved dislocation lines its contribution has substantial influence on the dynamics.

For sufficiently small dislocation curvatures, the self force can be expressed in terms of the curvature-dependent portion of the line tension. In this concept the dislocation is regarded as a taut elastic string (Cottrell 1953; Stroh 1954; de Wit and Koehler 1959). The line tension mimics the back-driving force of the dislocation in reducing the core and elastic energy that arises from any increase in dislocation length in the bowed-out state as compared with the straight state. An analytical treatment of the line tension predicts a back driving force that depends on the increase in the core energy and on the local curvature. However, this classical concept neglects the dependence of the dislocation energy on the dislocation arrangement (Hirth and Lothe 1982). For large curvatures this simple analytical approximation of the line tension is no longer valid and must be replaced by more detailed energy calculations which account for the overlap of the displacement fields of neighboring portions of the same dislocation. In a thorough analysis Brown (1967) showed the consistency between the generalized line tension and the self force, which can be computed through the Peach–Koehler interaction among sequentially arranged segments belonging to the same defect.

The introduction of the self force turns equation (9.160) into a nonlinear differential equation. Furthermore, the hyperbolic long-range force acts as a coupling term between the partial differential equations that describe the motion of the individual segments.

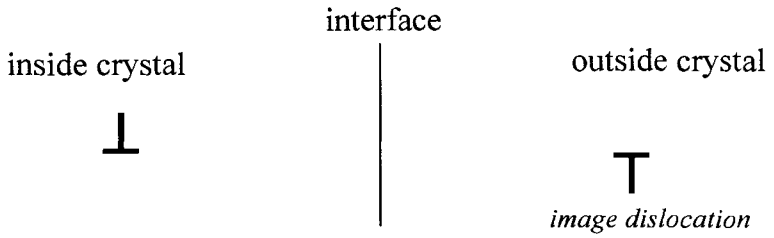

Figure 9.7: Construction for the calculation of the image force in two dimensions in a simple case where the infinite dislocation line is parallel and the Burgers vector perpendicular to the interface.

The External and the Obstacle Force The externally imposed force $\boldsymbol{F}^{\text{ext}}$ enters the solution of the differential equation as a constant Peach–Koehler force on each portion of all dislocations in the array. Further Peach–Koehler-type contributions can arise from lattice defects other than dislocations. Among these, particularly the contributions from obstacles $\boldsymbol{F}^{\text{obs}}$ are relevant. Obstacles give rise to elastic interactions, such as are imposed by coherent precipitations or foreign atoms with a parelastic and dielastic matrix coupling (Eshelby 1957; Mura 1987). Details of the incorporation of obstacles in time- and space-discretized dislocation simulations have been thoroughly investigated by Rönnpagel (1987), Mohles (1996), and Mohles and Rönnpagel (1996).

The Image Force Another term arises from stress relaxation in the vicinity of a free surface or internal interface. Such contributions are referred to as surface or image forces $\boldsymbol{F}^{\text{ima}}$. They result from the necessity that a free surface must be in the stress-free state. Image effects are modeled by including surface stresses that exactly compensate the stresses imposed by lattice defects in the interface. Thus, they generate surface forces that act attractively on each portion of dislocation (Hirth and Lothe 1968).

The incorporation of image forces is straightforward in two-dimensional systems, involving only screw dislocations or simple edge dislocation arrangements. In these cases a surface stress compensation is achieved by appropriate mirror operations carried out on each infinite dislocation line with the surface acting as a mirror plane (Figure 9.7). In three dimensions geometrical difficulties in treating these forces arise from the fact that the individual dislocation portions are in most cases no longer straight, infinite, or parallel to the free surface.

According to van der Giessen and Needleman (1995) this three-dimensional boundary-value problem can be solved by using a finite element approach. On the other hand, Gosling and Willis (1994) have suggested an analytical method to compensate surface stresses. Recently, Fivel, Gosling, and Canova (1996) compared the approach of Gosling and Willis (1994) with that of Boussinesq (1985) and found a good accord between both techniques.

The Osmotic Force Dislocation dynamics shows a fundamental difference from molecular dynamics. While in the latter approach one deals with a conservative system and can thus describe the local force as a negative gradient of the potential, dislocation motion is highly dissipative and reveals a strong anisotropy in its kinetic modes, i.e. the existence of glide and climb. In contrast to two-dimensional simulations, which are confined

to one slip plane, the extension of discrete dislocation simulations to three dimensions implies the occurrence of climb (Raabe 1998a). However, nonconservative motion of edge dislocation segments generally occurs by the generation of intrinsic point defects. This leads to an under- or oversaturation of such defects, i.e. to a deviation from chemical equilibrium. The force that results from the tendency of the system to return to thermal equilibrium is quantified in terms of an osmotic force $\boldsymbol{F}^{\mathrm{osm}}$ (Section 9.4.2.6). Following the original concept of Nabarro (1947b), Herring (1950), Bardeen and Herring (1952), Weertman (1965), Lothe and Hirth (1967), Wiedersich and Herschbach (1972), and Balluffi and Granato (1979), this contribution can enter the equation of motion through an expression of the form

$$\boldsymbol{F}^{\mathrm{osm}} = -\frac{\mu}{\Omega}\frac{(\boldsymbol{b}\times\boldsymbol{t})}{|\boldsymbol{b}\times\boldsymbol{t}|} = -\frac{k_{\mathrm{B}}\,T}{\Omega}\frac{(\boldsymbol{b}\times\boldsymbol{t})}{|\boldsymbol{b}\times\boldsymbol{t}|}\ln\left(\frac{c(\boldsymbol{r})}{c_0}\right) \tag{9.161}$$

where $\boldsymbol{t}$ is the dislocation tangential vector and μ the chemical potential. This term couples the equation of motion with diffusion.

The Phonon Drag Force It is a characteristic feature of dislocations that they dissipate energy during their motion. This is due to the velocity-dependent electron and phonon drag (Eshelby 1949b; Leibfried 1950; Nabarro 1951; Rosenfield et al. 1968). The dominant contribution to friction arises from phonon–dislocation interactions $\boldsymbol{F}^{\mathrm{Pdrag}}$. In this context two mechanisms have been discussed, namely, the nonlinearity mechanism which is imposed by the anharmonicity of the potential (Seeger and Engelke 1968; Brailsford 1972) and the fluttering mechanism (Ninomiya 1970) which is due to inelastic scattering between the dislocation and a phonon. A comparison of both approaches which provide very similar predictions except at very low temperatures was given by Suzuki (1991). Following the approach of Ninomiya (1970), i.e. assuming a fluttering mechanism, the temperature-dependent portion of the friction force can be written

$$\begin{aligned}\boldsymbol{F}^{\mathrm{Pdrag}}(T) &= B_{\mathrm{p}}(T)\,\dot{\boldsymbol{x}} = \frac{k_{\mathrm{B}}\,T\,\omega_{\mathrm{D}}^2}{\pi^2\,c_i^3}\,\dot{\boldsymbol{x}} \qquad \text{at } T > 0.5\,\Theta\\ \boldsymbol{F}^{\mathrm{Pdrag}}(T) &= B_{\mathrm{p}}(T)\,\dot{\boldsymbol{x}} = \frac{14.4\;k_{\mathrm{B}}\,T\,\omega_{\mathrm{D}}^2}{\pi^2\,c_i^3}\left(\frac{T}{\Theta}\right)^2\dot{\boldsymbol{x}} \qquad \text{at } T < 0.5\,\Theta\end{aligned} \tag{9.162}$$

where $B_{\mathrm{p}}(T)$ is the temperature-dependent friction coefficient, Θ the Debye temperature, ω_{D} the Debye frequency, and c_i the transverse or longitudinal velocity of sound, respectively.

The Electron Drag Force The frictional force due to conduction electrons with the coefficient B_{e} was assessed by Tittmann and Bömmel (1966) using standard perturbation theory, and by Kravchenko (1966) and Brailsford (1969) using the Boltzmann equation. According to the analysis of these papers given by Suzuki (1991) the contribution of electrons to friction is practically independent of the temperature. For edge-type segments the electronic portion of the friction amounts to

$$\boldsymbol{F}^{\mathrm{Edrag}} = B_{\mathrm{e}}\,\dot{\boldsymbol{x}} = \left(\frac{1-2\nu}{1-\nu}\right)^2\frac{n_0\,m_{\mathrm{e}}\,v_{\mathrm{F}}\,b^2\,q_{\mathrm{D}}}{96}\,\frac{1}{2}\left(\frac{1}{1+\left(\frac{q_{\mathrm{D}}}{q_{\mathrm{TF}}}\right)^2}+\left(\frac{q_{\mathrm{TF}}}{q_{\mathrm{D}}}\right)\tan^{-1}\left(\frac{q_{\mathrm{D}}}{q_{\mathrm{TF}}}\right)\right)\dot{\boldsymbol{x}} \tag{9.163}$$

where ν is Poisson's ration, n_0 the equilibrium value of the electron density, m_e the mass of the quasi-free electron, v_F the Fermi velocity, q_D the radius of a Debye sphere, and q_{TF} the reciprocal of the Thomas–Fermi screening length. For screw dislocations the electronic frictional force is negligible.

The Inertia Force When the dislocation movement does not take place in the overdamped regime, i.e. at very high applied forces, inertial effects $\boldsymbol{F}^{\text{iner}}$ must be taken into consideration. This contribution renders the equation of motion into a second-order differential equation. The effective mass m_{eff} per length of a dislocation can be calculated according to

$$m_{\text{eff}} = m'_{\text{eff}} \frac{1}{\sqrt{1 - \left(\frac{\dot{x}}{c_i}\right)^2}} \qquad m'_{\text{eff}} = \frac{\mu b^2}{2\, c_i{}^2} \tag{9.164}$$

where μ is the shear modulus, c_i the velocity of sound, and m'_{eff} the rest mass of the dislocation. The mass point assigned to a dislocation segment of length $L = |\boldsymbol{r}'_A - \boldsymbol{r}'_B|$ then amounts to $\Delta m = m_{\text{eff}} L$.

The Cross-Slip Force While edge dislocations generally have a well-defined slip plane, this is not the case for screw dislocations. A particular glide plane for screw dislocations can only be defined in terms of the present maximum orientation factor which would force an ideal screw dislocation into a certain plane, or through the occurrence of dissociation of the original complete dislocation into partial dislocations. The tendency to dissociate is inversely weighted by the stacking fault energy of the particular material. Thus, dislocation cross-slip is obstructed by the enthalpy that is required to recombine the dissociated portions of the dislocation. This gives rise to a cross-slip drag force $\boldsymbol{F}^{\text{cross}}$.

The Thermal Force The contributions discussed above represent relevant line forces that must be considered for simulating athermal dislocation dynamics. However, in order to allow simulations at temperatures other than 0 K, thermal forces $\boldsymbol{F}^{\text{therm}}$ must be included in the model. This concept is particularly important for simulating thermal activation processes (Leibfried 1957; Rönnpagel et al. 1993; Mohles and Rönnpagel 1996; Mohles 1996).

From a thermodynamic point of view dislocations in thermodynamic equilibrium with the crystal can be regarded as a canonical ensemble, the energy of which fluctuates in time. Thermal fluctuations, which are also referred to as thermal noise, represent a formal term by which to express the unpredictable influence of many uncorrelated tiny perturbances, each of which changes the state variables of the system in a small but random fashion (Haken 1978; Schuss 1980; Freedman 1982; Haken 1983; Risken 1984; Gardiner 1985). Irrespective of the thermal fluctuations, the macroscopic mean value of the energy is a well-defined function of temperature, which is prescribed by the heat bath, i.e. by the temperature of the crystal.

Due to the drag force terms, the moving dislocation continuously dissipates energy as a function of its velocity. Since the dislocation is assumed to be in thermodynamic equilibrium with the crystal, the energy lost through dissipation must be compensated by applying thermal pulses. These pulses can be described in terms of a Langevin force in case of the Brownian motion (Kramers 1940; Chandrasekhar 1943; Rönnpagel et al.

1993). It is assumed that the average of this force over the ensemble should vanish, i.e.

$$\langle \boldsymbol{F}^{\text{therm}}(t) \rangle = 0 \tag{9.165}$$

since the equation of motion of the average velocity $\langle \dot{\boldsymbol{x}} \rangle$ does not contain any probabilistic term. When multiplying the Langevin force term at two different times t and t', one further assumes that the resulting average value vanishes if the time step $(t' - t)$ exceeds the duration time τ^{c} of a collision of the considered particle with the atoms:

$$\langle \boldsymbol{F}^{\text{therm}}(t), \boldsymbol{F}^{\text{therm}}(t') \rangle = 0 \qquad \text{where} \qquad |t - t'| \geq \tau^{\text{c}} \tag{9.166}$$

This amounts to stating that the Langevin force changes randomly in size and sign without correlation. This assumption is reasonable since it is likely that the collisions of the atoms with the small particle are approximately independent[8].

Usually, the collision time τ^{c} is much smaller than the relaxation time of the velocity of the small particle, which amounts to $\tau^{\text{r}} = 1/B(T)$ where $B(T)$ is the friction coefficient. Thus, the approximation $\tau^{\text{c}} \to 0$ appears reasonable. This leads to the form

$$\langle \boldsymbol{F}^{\text{therm}}(t), \boldsymbol{F}^{\text{therm}}(t') \rangle = q\,\delta(t - t') \qquad \text{where} \qquad \tau^{\text{c}} \to 0 \tag{9.167}$$

The Dirac delta function appears in this equation because otherwise the energy of the particle considered cannot be finite as it should be in accord with equipartition law. According to Rönnpagel, Streit, and Pretorius (1993), the strength of the thermal noise term is given by

$$q = \frac{2\,B(T)\,k_{\text{B}}\,T}{m_{\text{eff}}^2} \tag{9.168}$$

where m_{eff} is the effective mass per length. Combining equations (9.168) and (9.162) substantiates the fact that the strength of the Langevin force is not simply linearly proportional to the temperature but also temperature-dependent through the phonon-dependent part of $B(T)$. In order to produce such thermal pulses, one must provide Gaussian-distributed random vectors $\boldsymbol{\Lambda}(i,j)$ for each segment i at position $\boldsymbol{x}(i)$ and time step j:

$$f(\Lambda_k) = \frac{1}{\sqrt{2\pi}} \exp\left(-\frac{{\Lambda_k}^2}{2}\right) . \tag{9.169}$$

where Λ_k is the kth component of the vector $\boldsymbol{\Lambda}$. The thermal force $\boldsymbol{F}^{\text{therm}}(\boldsymbol{x}(i), t_j \leq t < t_j + \Delta t_j)$ imposed in the time between t_j and $t_j + \Delta t_j$ then amounts to

$$\boldsymbol{F}^{\text{therm}}(\boldsymbol{x}(i), t_j \leq t < t_j + \Delta t_j) = \boldsymbol{\Lambda}(i,j)\,|\boldsymbol{b}| \sqrt{\frac{2\,B(T)\,k_{\text{B}}\,T}{\Delta l(i)\,\Delta t_j\,b^2}} \tag{9.170}$$

where $\Delta l(i)$ is the length of the segment i (Rönnpagel et al. 1993). The portions of $\boldsymbol{\Lambda}(i,j)$ that are parallel to the segment tangential vector can be neglected (Mohles 1996).

Local heating of the slip plane is usually not considered. In metals it is generally assumed that the dissipation of heat due to friction is much faster as compared with the glide velocity of the dislocation. After each deformation step the temperature increase of the heat bath can be calculated from the disspiated power.

[8] It is not necessarily straightforward that this applies also to the interaction with moving dislocations. Furthermore, the phonon spectrum of crystals might be relevant in this context.

Solution of the Equation of Motion Incorporating all the above-mentioned contributions in equation (9.160) results, for *each* dislocation consisting of j sequentially arranged segments defined by $j+1$ vectors, in a set of $3 \cdot j$ coupled, nonlinear, stochastic, partial differential equations of second order (Rönnpagel 1993; Raabe 1997). Such a set of equations must be solved for appropriate initial-value conditions, i.e. for given initial positions $\boldsymbol{x}_0^j$ and initial velocities $\dot{\boldsymbol{x}}_0^j$ by using finite difference techniques, e.g. a higher-order Runge–Kutta or predictor–corrector method (see methods in Chapter 3).

9.4.2.6 The Chemical Structure Evolution Equation

Each edge dislocation portion in the state of nonconservative motion acts as a sink or source of intrinsic point defects. Their production entails a concentration change and thus a shift of the chemical potential (Section 9.4.2.4). This can exert a substantial influence on the dynamics of the dislocations in terms of an osmotic force that obstructs further climb.

As will be sketched out here the kinetics of these intrinsic defects must be treated separately from the kinetics of the dislocations. This can be achieved by using a continuum diffusion model, i.e. Fick's first law and the continuity equation. The concept of using Newton's law of motion for the dislocations and the diffusion law for the point defects causes the outlined simulation to approach a hybrid model. The separate treatment of dislocation dynamics and point defect diffusion becomes necessary since a fundamental three-dimensional space- and time-discretized description of dislocation dynamics cannot be attained by simply stipulating instant equilibration of the newly generated point defects. The immediate restoration of the thermal equilibrium concentration of the point defects is not obstructed by thermodynamics but by kinetics.

This becomes evident from a simple example: let us consider a small crystal volume element at a temperature near absolute zero which contains a single positive edge dislocation. If one now imposes a sufficiently large tensile stress σ parallel to the Burgers vector b so that σb^3 becomes similar to the energy of the vacancy formation, the dislocation will show negative climb. Such nonconservative motion thus occurs by mechanical rather than thermal generation of vacancies. Once produced, the mobility of these point defects would at $T \gtrapprox 0$ K practically amount to zero, entailing a drastic increase in the osmotic force on the climbing dislocation. On the other hand it is obvious that if the experiment were repeated at $T \lessapprox T_{\mathrm{melt}}$ no chemical effects would occur due to the instant equilibration of the newly formed point defects.

In the simulation, for each climbing segment with a length of one Burgers vector, the number of point defects generated can be tracked directly during each time step. The local point defect production rate in a volume element can be expressed in terms of the respective adsorption or emission rate of such defects $\partial n_s / \partial t$ at the segments that act as sink or source in that portion of volume. The production rate can thus be calculated from the nonconservative component of the velocity vector of the considered dislocation portion $\dot{x}_s^{\perp}(\boldsymbol{r}, t)$,

$$\frac{\partial c_{\mathrm{s}}(\boldsymbol{r}, t)}{\partial t} = \frac{1}{N^{\mathrm{vol}}} \frac{\varrho N_{\mathrm{L}}}{M} \frac{\partial n_{\mathrm{s}}^{\mathrm{vol}}(\boldsymbol{r}, t)}{\partial t} = f(1/|\boldsymbol{b}|) \frac{\varrho N_{\mathrm{L}}}{M} \frac{\partial x_{\mathrm{s}}^{\perp}(\boldsymbol{r}, t)}{\partial t} \tag{9.171}$$

where N^{vol} is the number of lattice sites in the considered volume element, $\dot{n}_{\mathrm{s}}^{\mathrm{vol}}$ the production rate in that volume element, ϱ the density of the material, M its molar mass, N_{L} the Loschmidt number, and $\dot{c}_{\mathrm{s}}$ the change in the volume concentration due to climb. The latter expression is hereafter referred to as the source term. The function $f(1/|\boldsymbol{b}|)$ is

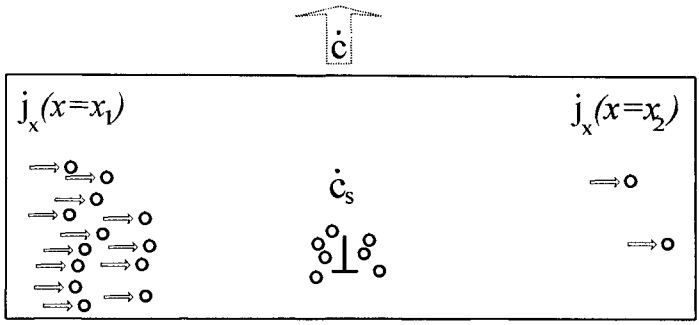

Figure 9.8: Schematic representation of the modified continuity equation for point defect production at a climbing dislocation considering a source term $\dot{c}_s$ (equation (9.172)).

a step function that introduces a normalization by $|\boldsymbol{b}|$, indicating that a point defect is only generated when the climb step amounts to at least one Burgers vector.

For a small crystal volume element the original continuity equation (10.16) must then be complemented by the source term derived above,

$$\frac{\partial c(\boldsymbol{r},t)}{\partial t} = -\nabla j + \frac{\partial c_s(\boldsymbol{r},t)}{\partial t} \tag{9.172}$$

where c is the volume concentration of point defects, $\nabla j = \mathrm{div} j$ their flux density divergence, and $\dot{c}_s$ the source term (Figure 9.8).

Although the continuity equation was originally meant to describe the conservation of mass rather than of vacancies its use in the present context is reasonable, since equation (9.172) expresses the fact that both the spatial divergence in the flux density and local source terms must entail a temporal concentration change in the volume element considered. Combining the modified continuity equation with Fick's first law

$$j = -D\,\nabla \mathrm{c} \tag{9.173}$$

where D is the bulk self-diffusion coefficient, leads to an expression similar to Fick's second law of diffusion,

$$\frac{\partial c(\boldsymbol{r},t)}{\partial t} = D\,\Delta c + \frac{\partial c_s(\boldsymbol{r},t)}{\partial t} = D\,\Delta c + f(1/|\boldsymbol{b}|)\,\frac{\varrho N_L}{M}\,\frac{\partial x_s^{\perp}(\boldsymbol{r},t)}{\partial t} \tag{9.174}$$

where $\Delta = \mathrm{div}\,\mathrm{grad}$ is the Laplace operator. The diffusion coefficient is assumed to be dependent on the local hydrostatic stress state but independent of the concentration of the point defects. Since the free enthalpy for the formation of intrinsic interstitials considerably exceeds that for the formation of vacancies, it is reasonable to neglect them in the calculation. That means one generally deals with a vacancy source term with either a negative or positive sign according to the actual direction of climb.

In its present form equation (9.174) provides a statistical description of self-diffusion by consideration of source terms. In a more generalized version this equation can be rewritten

$$\frac{\partial c(\boldsymbol{r},t)}{\partial t} = \tilde{M}\,\Delta\left(\frac{\delta g^{\mathrm{chem}}}{\delta c(\boldsymbol{r},t)} + \frac{\delta g^{\mathrm{elast}}}{\delta c(\boldsymbol{r},t)}\right) + \frac{\partial c_s(\boldsymbol{r},t)}{\partial t} \tag{9.175}$$

where $\tilde{M}$ is the mobility, g^{chem} the chemical and g^{elast} the elastic contribution to the Gibbs enthalpy density. While the chemical interaction among the vacancies is negligible in that it merely consists in the local change of the electron density, the additional influence of their elastic interaction must be regarded as a relevant term. While it is conceivable that this elastic vacancy–vacancy interaction term can enter the Landau free enthalpy form in a closed analytical fashion, the incorporation of the elastic interaction between the vacancies and the dislocations is less straightforward.

While the space-discretized simulation of dislocation dynamics which is based on solving Newton's equation of motion, equation (9.160), requires a finite difference solution only at those coordinates where dislocation portions are actually located, the *simultaneous* solution of the diffusion problem sketched above must be carried out continuously for the entire volume under consideration. Thus, any such dislocation dynamics simulation must be accompanied by a finite difference simulation to solve the modified diffusion equation, equation (9.174). A reasonable approach to implementing the proposed model might be to combine a modified Cahn–Hilliard code for the simulation of isostructural spinodal phase transformation phenomena with the mechanics outlined above. It should be noted that even without the presence of source terms in equation (9.175), substantial vacancy diffusion can nonetheless occur due to the inhomogeneity of stress. If in neighboring finite difference cells different dislocation densities and arrangements impose unequal displacement fields, net diffusion fluxes can occur due to the dependence of the free enthalpy functional on that stress.

9.4.3 Viscous and Viscoplastic Dislocation Dynamics

9.4.3.1 Introduction

When dislocation simulations are conducted to mimic dynamics in the overdamped high-stress regime, the differential equations that were presented in the preceding section can be simplified. For instance, by dropping the inertia term in equation (9.160) the system can be turned into a set of first-order differential equations which is easier and faster to solve. In a second step, the treatment of thermal activation can be simplified by using a statistical exponential expression (Kocks et al. 1975; Weertman and Weertman 1980; Nadgornyi 1988) in conjunction with one single Monte Carlo step instead of a Langevin term. Furthermore, the discrete consideration of self-interaction can be replaced by a discrete line tension approximation (Fivel et al. 1996).

Most phenomenological simulations have been conducted in two dimensions with infinite straight edge dislocations (Neumann 1971; Lépinoux and Kubin 1987; Ghoniem and Amodeo 1989; Gulluoglu et al. 1989; Amodeo 1990; Gulluoglu et al. 1990; Gulluoglu and Hartley 1992; Gulluoglu and Hartley 1993; Lubarda et al. 1993; Raabe and Roters 1995; van der Giessen and Needleman 1995; Wang and LeSar 1995; Roters and Raabe 1996; Roters et al. 1996; Raabe et al. 1996; Zacharopoulos et al. 1997). Edge dislocation glide is typically modeled in such approaches as successive periods of resting in front of obstacles and viscous glide between them.

Accounting for both effects, the dislocation velocity component in the direction of glide can be expressed according to

$$\dot{x}_{\text{glide}} = \frac{\lambda}{t_{\text{w}} + t_{\text{g}}} \tag{9.176}$$

where λ is the obstacle spacing, t_{w} the waiting time *in front of* obstacles and t_{g} the time for glide *between* obstacles. When no particles or precipitates are considered, the

obstacle spacing λ is determined exclusively by the forest dislocation density. In cases where additional obstacles such as precipitates are included, the effective obstacle spacing can be computed according to

$$\frac{1}{\lambda} = \sum_i \frac{1}{\lambda_i} \tag{9.177}$$

where λ_i is the respective spacing of lattice defects i that interact with moving dislocations. If only forest dislocations are considered with a density proportional to the total dislocation density, one can write

$$\lambda \propto \frac{1}{\sqrt{\varrho}} \tag{9.178}$$

where ϱ is the total dislocation density. Cutting of forest dislocations is a thermally activated process. Therefore, the cutting frequency ν_{cut} can be expressed in the following manner:

$$\nu_{\text{cut}} = 2\,\nu_0 \exp\left(-\frac{Q}{k_{\text{B}}\,T}\right) \sinh\left(\frac{\sigma\,V}{k_{\text{B}}\,T}\right) = 2\,\nu_0 \exp\left(-\frac{Q}{k_{\text{B}}\,T}\right) \sinh\left(\frac{F_{\text{glide}}\,A}{k_{\text{B}}\,T}\right) \tag{9.179}$$

where Q is the activation energy, $\sigma\,V = F_{\text{glide}}\,A$ the mechanical work that results from the net local stress, and ν_0 the attack frequency. It is typically assumed that the activation area A is proportional to the spacing of the forest dislocations. The sinh function results from the consideration of both forward and backward jumps.

The time spent resting in front of an obstacle is then simply given by

$$t_{\text{w}} = \frac{1}{\nu_{\text{cut}}} \tag{9.180}$$

Between the obstacles viscous glide is assumed. Hence, the *local* glide velocity for unimpeded motion, $\dot{x}^{\text{u}}_{\text{glide}}$, is proportional to the force F_{glide}, so that t_{g} can be calculated as

$$t_{\text{g}} = \frac{\lambda}{\dot{x}^{\text{u}}_{\text{glide}}} = \frac{\lambda}{c\,F_{glide}} \tag{9.181}$$

where c is a constant. From equations (9.176)–(9.181) the net velocity in the direction of glide can be derived:

$$\dot{x}_{\text{glide}} = \frac{\lambda}{t_{\text{w}} + t_{\text{g}}} = \frac{2\,\nu_0\,c\,\lambda\,F_{\text{glide}} \sinh\left(\frac{F_{\text{glide}}\,A}{k_{\text{B}}\,T}\right)}{c\,F_{\text{glide}} \exp\left(\frac{Q}{k_{\text{B}}\,T}\right) + 2\,\nu_0 \sinh\left(\frac{F_{\text{glide}}\,A}{k_{\text{B}}\,T}\right)} \tag{9.182}$$

In contrast to this glide law, the nonconservative climb process is controlled by diffusion. The velocity of dislocation climb $\dot{x}_{\text{climb}}$ is thus directly proportional to the respective force component with the diffusion coefficient D as constant, viz.

$$\dot{x}_{\text{climb}} = B\,F_{\text{climb}} = \frac{D}{k_{\text{B}}\,T}\,F_{\text{climb}} = \frac{F_{\text{climb}}}{k_{\text{B}}\,T}\,D_0 \exp\left(-\frac{H}{k_{\text{B}}\,T}\right) \tag{9.183}$$

where H is the activation enthalpy for vacancy formation and migration.

Once the dislocation velocities are determined in accord with the respective local stress fields, it has to be ensured that possible resulting dislocation reactions are considered by the simulation prior to the movement of the dislocations. Therefore, the time increment of each simulation step is chosen dynamically. For this purpose the minimum spacing between two dislocations is determined. The distance traveled by the fastest dislocation can then be limited to half this value. After the time increment has been determined, all dislocations are then moved according to their individual velocities.

It is clear that two-dimensional simulations of edge dislocation dynamics do not account for dislocation multiplication. This shortcoming is due to the fact that all dislocations are parallel. This means that new dislocations have to be introduced by some artificial argument. This can be done by inserting a new mobile dislocation into the system whenever a dislocation is immobilized, or by explicitly relating the production rate to the glide activity in each glide system.

Phenomenological dislocation dynamics simulations are also possible in three dimensions (Devincre and Condat 1992; Raabe 1995a; Devincre 1996; Fivel et al. 1996). In these approaches the dislocation lines are typically subdivided into piecewise straight, sequentially arranged segments of either pure screw- or edge-type character (Kubin et al. 1992). Thus, in contrast to the two-dimensional simulations, in three dimensions the mobility of the two different segment types must be distinguished.

Following the above concept, the glide velocity of an edge segment in kink motion, $\dot{x}_{\mathrm{kink}}$, can be written

$$\dot{x}_{\mathrm{kink}} = \frac{C_{\mathrm{k}}\,\omega_0\,\Lambda\,F_{\mathrm{kink}}\,\sinh\left(\frac{F_{\mathrm{kink}}\,A}{k_{\mathrm{B}}\,T}\right)}{\frac{F_{\mathrm{kink}}}{B_{\mathrm{k}}}\,\exp\left(\frac{Q_{\mathrm{k}}}{k_{\mathrm{B}}\,T}\right) + C_{\mathrm{k}}\,\Gamma_0\,\sinh\left(\frac{F_{\mathrm{kink}}\,A}{k_{\mathrm{B}}\,T}\right)} \tag{9.184}$$

where ω_0 is the Debye frequency, Λ the local flight path of the segment, F_{kink} the net glide force acting on the kink segment, Q_{k} the activation energy, C_{k} a constant, and B_{k} the drag coefficient. For situations where either the waiting or the flying time dominates, simpler phenomenological laws can be used, namely,

$$\dot{x}_{\mathrm{kink}} = \tilde{C}_{\mathrm{k}}\left(\frac{\tau}{\tau_0}\right)^m \exp\left(-\frac{Q_{\mathrm{k}}}{k_{\mathrm{B}}\,T}\right) \tag{9.185}$$

for the former, and

$$\dot{x}_{\mathrm{kink}} = \frac{\tau\,b}{\tilde{B}_{\mathrm{k}}} \tag{9.186}$$

for the latter case, where $\tilde{C}_{\mathrm{k}}$ and $\tilde{B}_{\mathrm{k}}$ are constants, τ_0 the reference shear stress[9], and m a variable which quantifies the stress dependence of the kink velocity.

For the screw portions similar glide expressions apply, although furnished with somewhat different constants, which reflect the influence of the dislocation core on the segment mobility. However, screw dislocations in three-dimensional simulations can also leave their actual glide plane. For describing this cross-slip probability p in discrete calculations, Fivel, Gosling, and Canova (1996) suggested using an expression of the form

$$p \propto \exp\left(\frac{(\tau_{\mathrm{f}} - \tau_{\mathrm{III}})V}{k_{\mathrm{B}}\,T}\right) \tag{9.187}$$

[9]The reference shear stress is not identical to the critical resolved shear stress.

where τ_f represents the effective friction stress, τ_{III} the stage-III stress, and V the activation volume of the process. The nonconservative movement of jogs is climb-controlled and can be described in accord with equation (9.183)

$$\dot{x}_{\text{climb}} = B\,F_{\text{climb}} = \frac{D}{k_B\,T}\,F_{\text{climb}} = \frac{F_{\text{climb}}}{k_B\,T}\,D_0\,\exp\left(-\frac{H}{k_B\,T}\right) \tag{9.188}$$

where H is the activation enthalpy of self-diffusion in the bulk material. For considering the influence of the local stress on the jog climb rate, equation (9.188) can be rewritten

$$\begin{aligned}\dot{x}'_{\text{climb}} &= \frac{F_{\text{climb}}}{k_B\,T}\,D_0\,\exp\left(-\frac{H}{k_B\,T}\right) = \frac{F_{\text{climb}}}{k_B\,T}\,D_0\,\exp\left(-\frac{(H^f + H^m)}{k_B\,T}\right)\\ &= \frac{F_{\text{climb}}}{k_B\,T}\,D_0\,\exp\left(-\frac{H^m}{k_B\,T}\right)\exp\left(-\frac{(H^f - \sigma^h\,\Omega)}{k_B\,T}\right)\end{aligned} \tag{9.189}$$

where Ω is the atomic volume which can be approximated by $|\boldsymbol{b}|^3$, σ^h the local hydrostatic stress component, H^f the enthalpy of formation of vacancies, and H^m their enthalpy of migration (Friedel 1964; Hirth and Lothe 1968; Suzuki 1991).

The influence of osmotic forces (Section 9.4.2.5) which can gradually oppose jog climb is usually neglected in phenomenological dislocation dynamics simulations. The omission of such chemical effects is often justified by the assumption that jog drag-stimulated vacancy fluxes mutually compensate each other by short-range diffusional processes among jogs with opposite sign. The self-interaction of such phenomenological dislocation simulations is typically considered by including the analytical line tension approximation or some numerical criteria derived therefrom (Devincre and Condat 1992).

9.5 Kinematics of Discrete Dislocation Dynamics

Dislocation dynamics can be used for the calculation of stress–strain curves and lattice reorientations. By tracing all distances traveled by the individual dislocations during each time step it is straightforward to use the Orowan equation for the calculation of the shear rate during a particular time step $\dot{\gamma}$ according to

$$\dot{\gamma} = \varrho_m\,b\,\bar{\dot{x}}_{\text{glide}} \tag{9.190}$$

where ϱ_m is the density of mobile dislocations, b the magnitude of their Burgers vector, and $\bar{\dot{x}}_{\text{glide}}$ their average glide velocity.

In the case where N individual dislocations are considered in a two-dimensional simulation, the right-hand side of equation (9.190) can be substituted by a sum over all dislocations. The shear rate in the x_1-direction can then be calculated by

$$\dot{\gamma}_{x_1} = \frac{1}{A}\sum_i^N b^i_{x_1}\,\dot{x}^i_{x_1} \tag{9.191}$$

where $b^i_{x_1}$ is the x_1-component of the Burgers vector of the ith dislocation and $\dot{x}^i_{x_1}$ its velocity in the x_1-direction during the considered time interval. A is the area of the simulation cell. The shear rate in the x_2-direction can be calculated analogously, i.e.

$$\dot{\gamma}_{x_2} = \frac{1}{A}\sum_i^N b^i_{x_2}\,\dot{x}^i_{x_2} \tag{9.192}$$

The shear rate $\dot{\varepsilon}_{x_1 x_2}$ can be calculated according to

$$\dot{\varepsilon}_{x_1 x_2} = \frac{1}{2}\left(\dot{\gamma}_{x_1} + \dot{\gamma}_{x_2}\right) \tag{9.193}$$

This leads to a strain increment per simulation step Δt which amounts to $\Delta\varepsilon_{x_1 x_2} = \dot{\varepsilon}_{x_1 x_2}\,\Delta t$.

In three dimensions the strain rate tensor during a numerical experiment can be calculated by applying Orowan's equation to *all* segments in the array. Following equation (9.191) the shear rate in the three spatial directions can be calculated by

$$\dot{\gamma}_{x_1} = \frac{1}{V}\sum_i^N b_{x_1}^i\,\dot{x}_{x_1}^i\,\Delta s \qquad \dot{\gamma}_{x_2} = \frac{1}{V}\sum_i^N b_{x_2}^i\,\dot{x}_{x_2}^i\,\Delta s \qquad \dot{\gamma}_{x_3} = \frac{1}{V}\sum_i^N b_{x_3}^i\,\dot{x}_{x_3}^i\,\Delta s \tag{9.194}$$

where Δs the segment length and V the volume of the simulation box. The normal components of the strain rate tensor are then determined by

$$\dot{\varepsilon}_{x_1 x_1} = \dot{\gamma}_{x_1} \qquad \dot{\varepsilon}_{x_2 x_2} = \dot{\gamma}_{x_2} \qquad \dot{\varepsilon}_{x_3 x_3} = \dot{\gamma}_{x_3} \tag{9.195}$$

and its shear components by

$$\dot{\varepsilon}_{x_1 x_2} = \frac{1}{2}\left(\dot{\gamma}_{x_1} + \dot{\gamma}_{x_2}\right) \qquad \dot{\varepsilon}_{x_1 x_3} = \frac{1}{2}\left(\dot{\gamma}_{x_1} + \dot{\gamma}_{x_3}\right) \qquad \dot{\varepsilon}_{x_2 x_3} = \frac{1}{2}\left(\dot{\gamma}_{x_2} + \dot{\gamma}_{x_3}\right) \tag{9.196}$$

The strain increments per simulation step Δt amount to

$$\Delta\varepsilon_{x_1 x_1} = \dot{\gamma}_{x_1}\,\Delta t \qquad \Delta\varepsilon_{x_2 x_2} = \dot{\gamma}_{x_2}\,\Delta t \qquad \Delta\varepsilon_{x_3 x_3} = \dot{\gamma}_{x_3}\,\Delta t \tag{9.197}$$

and its shear components to

$$\Delta\varepsilon_{x_1 x_2} = \frac{\Delta t}{2}\left(\dot{\gamma}_{x_1} + \dot{\gamma}_{x_2}\right) \quad \Delta\varepsilon_{x_1 x_3} = \frac{\Delta t}{2}\left(\dot{\gamma}_{x_1} + \dot{\gamma}_{x_3}\right) \quad \Delta\varepsilon_{x_2 x_3} = \frac{\Delta t}{2}\left(\dot{\gamma}_{x_2} + \dot{\gamma}_{x_3}\right) \tag{9.198}$$

The rotation rate of the lattice affected, $\dot{\omega}_{x_i x_j}^{\text{latt}}$, which results from the shears on the individual slip systems, can be computed from the rigid-body rotation rate, i.e. from the skew symmetric portion of the discretized crystallographic velocity gradient tensor, $\dot{\omega}_{x_i x_j}^{\text{spin}}$, and from the antisymmetric part, $\dot{u}_{x_i,x_j}^{\text{anti}}$, of the externally imposed macroscopic velocity gradient tensor, $\dot{u}_{x_i,x_j}^{\text{ext}}$:

$$\dot{\omega}_{x_i x_j}^{\text{latt}} = \dot{u}_{x_i,x_j}^{\text{anti}} - \dot{\omega}_{x_i x_j}^{\text{spin}} = \frac{1}{2}\left(\dot{u}_{x_i,x_j}^{\text{ext}} - \dot{u}_{x_j,x_i}^{\text{ext}}\right) - \frac{1}{2}\left(\dot{\gamma}_{x_i} - \dot{\gamma}_{x_j}\right) \tag{9.199}$$

9.6 Dislocation Reactions and Annihilation

In the preceding chapters it was mainly long-range interactions between the dislocation segments that were addressed. However, strain hardening and dynamic recovery are essentially determined by short-range interactions, i.e. by dislocation reactions and by annihilation, respectively.

Using a phenomenological approach which can be included in continuum-type simulations, one can differentiate between three major groups of short-range hardening dislocation reactions (Franciosi et al. 1980): the strongest influence on strain hardening is

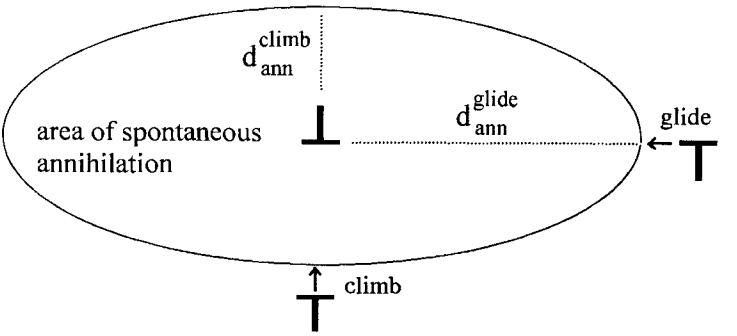

Figure 9.9: Annihilation ellipse in 2D dislocation dynamics. It is constructed by the values for the spontaneous annihilation spacing of dislocations that approach by glide and by climb.

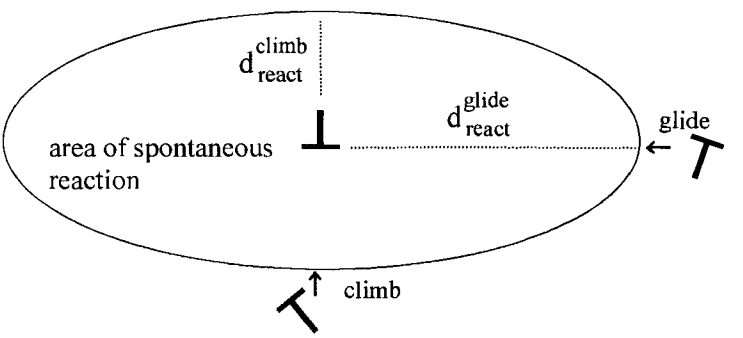

Figure 9.10: Reaction ellipse in 2D dislocation dynamics. It is constructed by the values for the spontaneous reaction spacing of dislocations that approach by glide and by climb.

exerted by sessile reaction products such as Lomer–Cottrell locks. The second strongest interaction type is the formation of mobile junctions. The weakest influence is naturally found for the case in which junctions are formed.

Two-dimensional dislocation dynamics simulations usually account for annihilation and the formation of sessile locks. Mobile junctions and the Peach–Koehler interaction occur naturally among parallel dislocations. The annihilation rule is straightforward. If two dislocations on identical glide systems but with opposite Burgers vectors approach more closely than a certain minimum allowed spacing, they spontaneously annihilate and are removed from the simulation. Current two-dimensional simulations (Roters et al. 1996) use different minimum distances in the direction of glide ($d^{\mathrm{g}}_{\mathrm{ann}} \approx 20|\boldsymbol{b}|$) and climb ($d^{\mathrm{c}}_{\mathrm{ann}} \approx 5|\boldsymbol{b}|$), respectively (Essmann and Mughrabi 1979) (Figure 9.9).

Lock formation takes place when two dislocations on different glide systems react to form a new dislocation with a resulting Burgers vector which is no longer a translation vector of an activated slip system. In the two-dimensional simulation this process can be realized by the immobilization of dislocations on different glide systems when they approach each other too closely (Figure 9.10). The resulting stress fields of the sessile reaction products are usually approximated by a linear superposition of the displacement fields of the original dislocations before the reaction.

Dislocation reactions and the resulting products can also be included in three-dimensional simulations. Due to the larger number of possible reactions, two aspects require special consideration, namely, the magnitude and sign of the latent heat that is associated with a particular reaction, and the kinematic properties and the stress field of the reaction product.

The first point addressed can be solved without using additional analytical equations. For investigating whether a particular reaction between two neighboring segments will take place or not, one subtracts the total elastic and core energy of all initial segments that participate in the reaction from that of the corresponding configuration after the reaction. If the latent heat is negative, the reaction takes place. Otherwise, the segments pass each other without reaction. In face-centered cubic materials two dislocations can undergo 24 different types of reactions. From this number only 12 entail sessile reaction products. Assuming simple configurations, i.e. only a small number of reacting segments, the corresponding latent heat data can be included in the form of a reference table.

The short-range back-driving forces that arise from cutting processes are calculated from the corresponding increase in line energy. For either of the cutting defects, the increase in dislocation line amounts to the Burgers vector of the intersecting dislocation. Although this short-range interaction does not impose the same immediate hardening effect as a Lomer–Cottrell lock, it subsequently gives rise to the so-called jog drag effect, which is of the utmost relevance to the mobility of the dislocations affected.

The treatment of annihilation is also straightforward. If two segments have a spacing below the critical annihilation distance (Essmann and Mughrabi 1979) the reaction takes place spontaneously. However, the subsequent reorganization of the dislocation segment vectors is not simple and must be treated with care.

The stress and mobility of glissile dislocation junctions can be simulated by using a simple superposition of the segments involved. Unfortunately, this technique does not adequately reflect the behavior of Lomer–Cottrell locks. Such sessile junctions must therefore be artificially rendered immobile.

9.7 Application of Dislocation Statics and Dynamics in Materials Science

The literature on discrete dislocation dynamics can be grouped essentially into simulations in two dimensions and in three dimensions. Two-dimensional (2D) calculations can be carried out either with flexible dislocations which are constrained to lie in their glide plane or with nonflexible infinite straight dislocations which can leave their glide plane. While the first type of 2D simulation provides a view normal to the glide plane, the second one provides a lateral perspective parallel to the dislocation tangent. Three-dimensional (3D) simulations are independent of such geometrical constraints.

Field of application	Reference
two-dimensional, straight dislocations	Neumann (1971)
	Lépinoux and Kubin (1987)
	Ghoniem and Amodeo (1989)
	Gulluoglu, Srolovitz, LeSar, and Lomdahl (1989)
	Amodeo (1990)
	Gulluoglu, LeSar, Srolovitz, and Lomdahl (1990)

	Gulluoglu and Hartley (1992)
	Gulluoglu and Hartley (1993)
	Lubarda, Blume, and Needleman (1993)
	Raabe and Roters (1995)
	van der Giessen and Needleman (1995)
	Wang and LeSar (1995)
	Raabe, Roters, and Marx (1996)
	Roters and Raabe (1996)
	Roters, Raabe, and Gottstein (1996)
	Roters and Raabe (1997)
	Zacharopoulos, Srolovitz, and LeSar (1997)
two-dimensional, curved dislocations	Foreman and Makin (1966)
	Bacon, Kocks, and Scattergood (1973)
	Scattergood and Bacon (1975)
	Rönnpagel (1987)
	Rönnpagel, Streit, and Pretorius (1993)
	Mohles and Rönnpagel (1996)
	Mohles (1996)
three-dimensional	Devincre and Condat (1992)
	Demir, Hirth, and Zbib (1992)
	Kubin, Canova, Condat, Devincre, Pontikis, and Bréchet (1992)
	Kubin (1993a)
	Kubin (1993b)
	Devincre and Kubin (1994)
	Rhee, Hirth, and Zbib (1994)
	Devincre (1995)
	Raabe (1995a)
	Raabe (1995b)
	Raabe (1996a)
	Raabe (1996b)
	Devincre (1996)
	Raabe (1998a)

9.8 Examples of Dislocation Dynamics Simulations in Materials Science

9.8.1 Two-Dimensional Dynamics

Two-dimensional dislocation dynamics simulations are pertinent tools in understanding the origin of structure formation and dislocation patterning. This is obvious from Figures 9.11 and 9.12, which were calculated by some of the pioneers in this domain (Ghoniem and Amodeo 1989; Amodeo 1990; Gulluoglu and Hartley 1992). Both examples show the formation of dislocation patterns, i.e. of areas with a high dislocation density and with a low dislocation density. Figure 9.13 shows a dislocation cell structure together with the local microtexture. The misorientation distribution was calculated from the spatial distribution of the antisymmetric portion of the displacement gradient tensor (Roters and Raabe 1997).

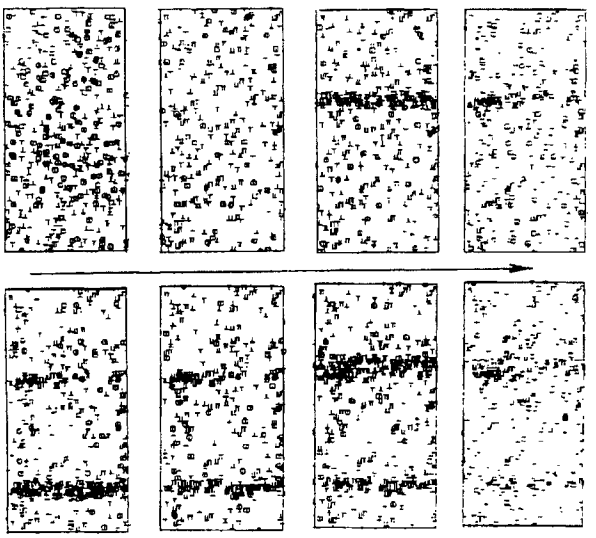

Figure 9.11: Gradual generation of shear-type dislocation bands in a 2D dislocation dynamics simulation (Ghoniem and Amodeo 1989).

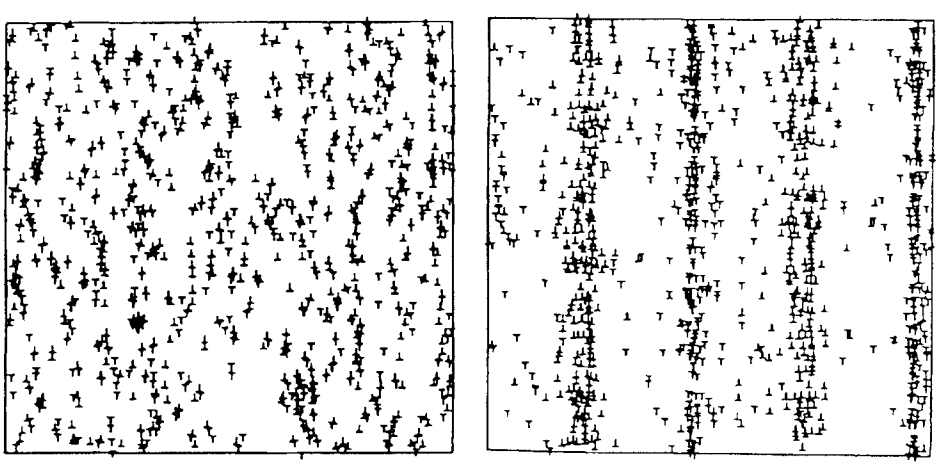

Figure 9.12: Gradual generation of dense dislocation walls in a 2D dislocation dynamics simulation (Gulluoglu 1992).

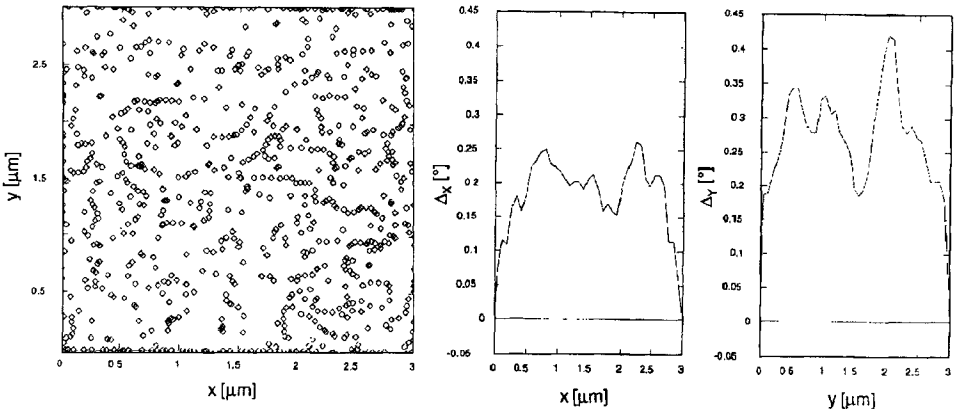

Figure 9.13: 2D Dislocation cell structure together with the local microtexture in x and y direction. The misorientation distribution was calculated from the spatial distribution of the antisymmetric portion of the displacement gradient tensor (Roters and Raabe 1997).

Mohles and Rönnpagel (1996) have conducted two-dimensional dislocation dynamics calculations using a model where the dislocations are regarded as taut elastic defects that cannot leave their actual glide plane. The simulations presented were conducted with periodic boundary conditions. The model was used for the prediction of the interaction between solute atoms and moving flexible dislocations (Figure 9.14).

9.8.2 Three-Dimensional Dynamics

Two-dimensional dislocation dynamics simulations suffer from the disadvantage that they do not allow the dislocations to cross-slip, climb, and multiply in a straightforward manner. However, these kinetic aspects can be of relevance in the prediction of dislocation patterning phenomena.

Figures 9.15 and 9.16 show an example of the pioneering simulations of Kubin (1993a) in this field. The dislocation lines are subdivided into piecewise straight sequentially arranged segments. The calculations have been conducted for an fcc crystal with a multislip orientation. The individual dislocation portions are aligned parallel to potential valleys with a low crystal index so as to either assume pure edge or pure screw character. This technique maps the abrupt- or hard-kink model, where the influence of the Peierls force on the dislocation shape exceeds that of the self-interaction force. The results can give some ideas of the early stages of dislocation cell formation.

Similar calculations have been carried out by Raabe (1995a). The simulations presented consider thermally activated climb (Figures 9.17, 9.18). The scaling length of these simulations is much below that of the calculations shown above. However, they therefore involve fewer dislocation lines. The individual dislocation segments can have arbitrary orientation and mixed character. This approach reflects the smooth-kink model. The dynamics of the dislocations are computed by solving Newton's law of motion for each segment assuming local stress equilibrium.

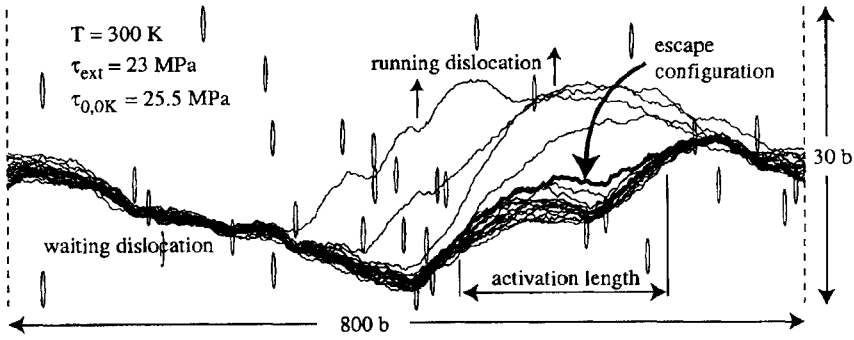

Dislocation in a field of statistically arranged obstacles

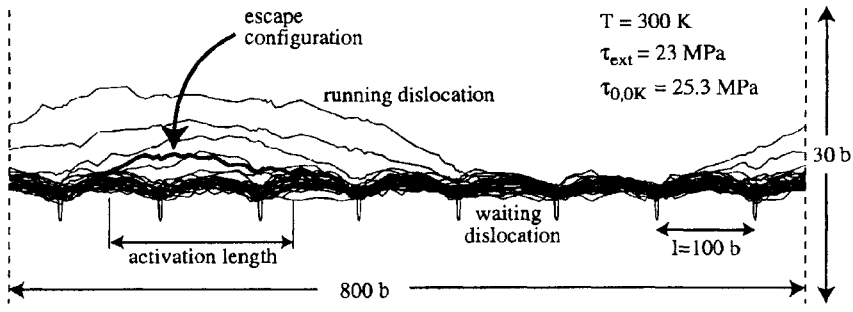

Dislocation at a row of attractive obstacle

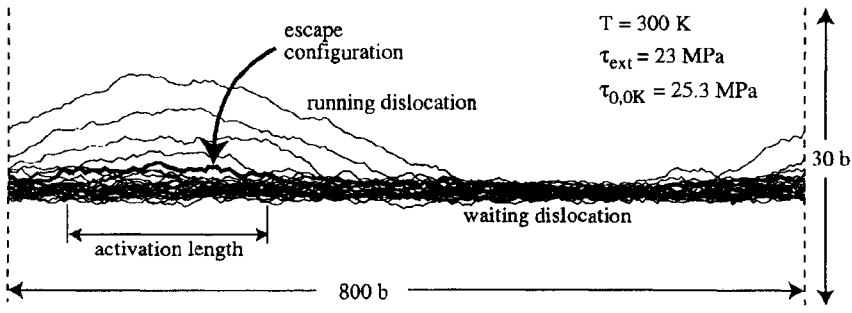

Dislocation at attractive obstacle wall

Figure 9.14: 2D dislocation dynamics calculations where the dislocations are regarded as taut elastic defects that cannot leave their actual glide plane (Mohles and Rönnpagel 1996).

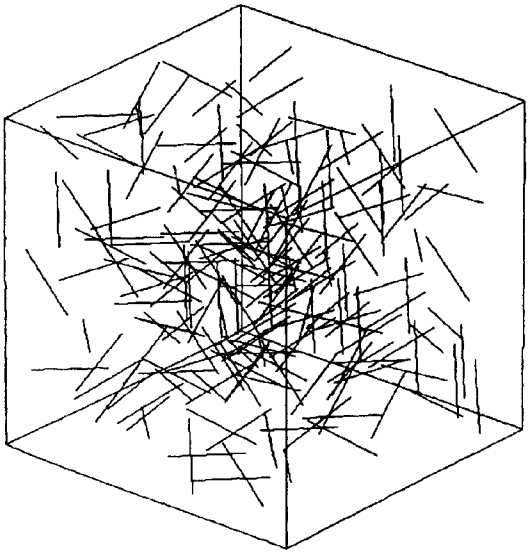

Figure 9.15: Initial 3D dislocation configuration in an fcc single crystal (Kubin 1993).

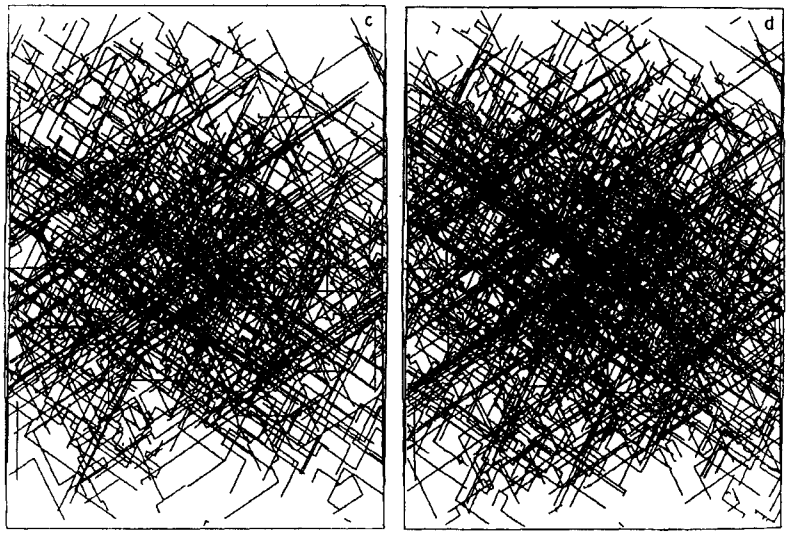

Figure 9.16: 3D dislocation configuration after a strain of about 10^{-4} and 10^{-3} (Kubin 1993).

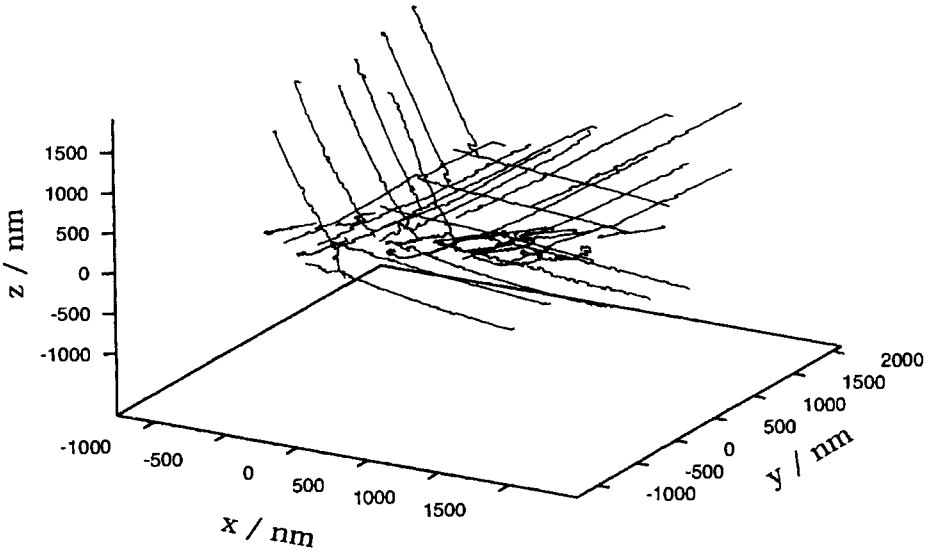

Figure 9.17: 3D dislocation dynamics simulation considering climb; structure after a total strain of about 10^{-4} (Raabe 1995).

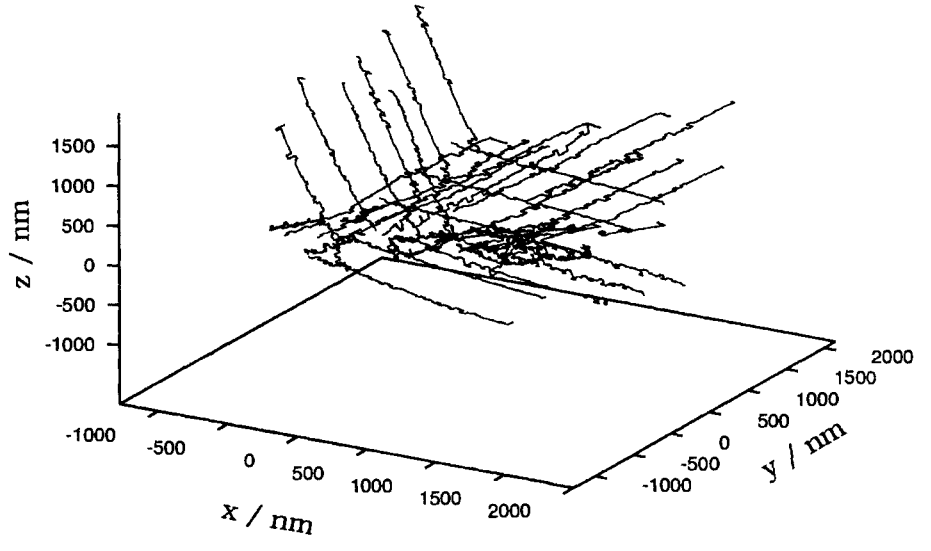

Figure 9.18: 3D dislocation dynamics simulation considering climb; structure after a total strain of about 10^{-3} (Raabe 1995).

Chapter 10

Ginzburg–Landau-Type Phase Field Kinetic Models

10.1 Introduction

The capability of predicting equilibrium and non-equilibrium phase transformation phenomena, particularly of the liquid–solid and solid–solid types, at a microstructural scale, is among the most challenging topics in modern materials science. This is due to the fact that a detailed knowledge of the structural, topological, morphological, and chemical characteristics of microstructures that arise from such transformations forms the basis of most, if not all, advanced microstructure–property models. For instance, to predict such important characteristics of engineering materials as strength, electrical conductivity, or toughness requires a rather detailed consideration of features like the type, shape, and distribution of second phases, the grain size, or the solute concentration of certain atoms. Introducing methods to predict such microstructure characteristics of materials can thus be regarded as an opportunity to open the door to the microstructural tailoring of materials, i.e. to the design of specific microstructures with regard to beneficial material property profiles (Brout 1965; Stanley 1971; Warlimont 1974; Christian 1975; Gunton et al. 1983; Khachaturyan 1983; Ratke and Thieringer 1985; Ratke 1987; Haasen 1991; Porter and Easterling 1992; Johnson et al. 1994).

It is clear, that models which aim to predict not only final thermodynamic equilibrium states but also realistic microstructures must consider both the various chemical, elastic, electromagnetic, and thermal contributions to the thermodynamic potential functions and the kinetics of the lattice defects involved. While the thermodynamics of phase transformation phenomena only prescribes the general ***direction*** of microstructure evolution, with the final tendency to eliminate all non-equilibrium lattice defects[1], the kinetics of the lattice defects determines the actual microstructural ***path***. For instance, the rate and the path of microstructural changes such as diffusional decomposition in a supersaturated substitutional alloy, nonconservative motion of edge dislocations, or migration of heavily curved homophase interfaces, are not only governed by the decrease in the free energy

[1] According to Haasen (1984) only certain point defects can be regarded as equilibrium lattice defects, since their entropy contribution compensates their enthalpy of formation or solution, respectively.

Computational Materials Science: The Simulation of Materials, Microstructures and Properties By Dierk Raabe
Copyright © 1998 Wiley-VCH Verlag GmbH
ISBN: 3-527-29541-0

of the system, but also by the temperature-dependent mobility of the various defects involved. The dominance of kinetics in structure evolution of technical alloys has the effect that the path towards equilibrium often leads the system through a series of competing non-equilibrium microstructural states.

In this context, it is an essential fact that it is not those microstructures that are close to equilibrium, but those that are in a highly non-equilibrium state, that provide advantageous materials properties. In that sense microstructure optimization at the mesoscopic level has to concentrate on the control and prediction of kinetics.

In past decades the exploitation of non-equilibrium effects associated with phase transformations for the optimization of materials properties and manufacturing processes was mostly confined to the use of empirical methods.

Only recently has the advent of powerful computer facilities made it possible for the first time to render fundamental theoretical state variable approaches, that in parts have been known for a long time, into numerical codes for tackling solid- and liquid-state phase transformation kinetics in a discretized fashion, considering both spatial and temporal changes in the chemical, crystallographic, and structural fields. These state variables appear frequently as so-called phase field variables and give this chapter its title.

Among the most versatile approaches in this domain are the Cahn–Hilliard and Allen–Cahn kinetic phase field models, which can be regarded as metallurgical derivaties of the theories of Onsager and Ginzburg–Landau. These models represent a class of very general and flexible phenomenological continuum field approaches which are capable of describing continuous and quasi-discontinuous phase separation phenomena in coherent and non-coherent systems. The term quasi-discontinuous means that the structural and/or chemical field variables in these models are generally defined as continuous spatial functions which change smoothly rather than sharply across internal interfaces.

While the Cahn–Hilliard model originally describes the kinetics of transformation phenomena with conserved field variables (e.g. chemical concentration), the Allen–Cahn model describes transformations with nonconserved variables (e.g. crystal orientation, long-range order, crystal structure).

While the original Ginzburg–Landau approach was directed at calculating electromagnetic second-order phase transition phenomena, advanced metallurgical variants are capable of addressing a variety of transformations in metals, ceramics, and polymers, such as spinodal decomposition, competitive particle ripening, non-isostructural precipitation and growth phenomena, grain growth, solidification, and dendrite formation in terms of corresponding chemical and structural phase field variables (Cahn and Hilliard 1958; Cahn 1961; Cahn 1962; Cahn and Hilliard 1965; Khachaturyan 1968; Morral and Cahn 1971; Langer et al. 1975; Khachaturyan 1983; Gurtin 1989; Chen and Khachaturyan 1991a; Chen and Khachaturyan 1991b; Chen and Khachaturyan 1991c; Wang et al. 1991; Gurtin 1996; Chen et al. 1992; Takenaka and Hashimoto 1993; Wang et al. 1993; Cahn and Taylor 1994; Johnson et al. 1994; Chan and Rey 1995; Dreyer 1995; Chen and Wang 1996; Löchte and Gottstein 1996).

This chapter has the following strategy. First, some analytical fundamentals will be reviewed, which are of relevance in the modeling of diffusive phase transformations in solids, viz., Fick's second law, which describes the kinetics of concentration profile changes, the Gibbs–Thomson equation, which relates the chemical potential to the surface-to-volume ratio $\partial A/\partial V$, and the Lifshitz–Slyozov–Wagner (LSW) theory, which provides an analytical approach to describe particle coarsening. Subsequently, advanced approaches to the space- and time-discretized description of diffusive phase transformations will be reviewed, focusing on the continuum and microscopic phase field kinetic concepts.

10.2 Diffusional Phase Transformation

10.2.1 The Phenomenological Laws of Diffusion

An equilibrium between any set of phases α, β, γ, ... in an isobaric–isothermal system is not described by the absence of concentration gradients in the sense of Fick's first law, but by the condition that the chemical potential μ of any component A, B, C, ... is the same in every phase (Ludwig 1979; Atkins 1986).

$$\begin{aligned} \mu_{\mathrm{A}}^{\alpha} &= \mu_{\mathrm{A}}^{\beta} = \mu_{\mathrm{A}}^{\gamma} = \ldots \\ \mu_{\mathrm{B}}^{\alpha} &= \mu_{\mathrm{B}}^{\beta} = \mu_{\mathrm{B}}^{\gamma} = \ldots \\ \mu_{\mathrm{C}}^{\alpha} &= \mu_{\mathrm{C}}^{\beta} = \mu_{\mathrm{C}}^{\gamma} = \ldots \\ &\ldots \end{aligned} \tag{10.1}$$

For a one-dimensional binary isothermal system with components A and B containing vacancies V, the flux densities j_i of the respective particles i, i.e. the net number that passes through a plane of unit area in time, is given by

$$\begin{aligned} j_{\mathrm{A}} &= -M_{\mathrm{AA}} \frac{\partial \mu_{\mathrm{A}}}{\partial x} - M_{\mathrm{AB}} \frac{\partial \mu_{\mathrm{B}}}{\partial x} - M_{\mathrm{AV}} \frac{\partial \mu_{\mathrm{V}}}{\partial x} \\ j_{\mathrm{B}} &= -M_{\mathrm{BA}} \frac{\partial \mu_{\mathrm{A}}}{\partial x} - M_{\mathrm{BB}} \frac{\partial \mu_{\mathrm{B}}}{\partial x} - M_{\mathrm{BV}} \frac{\partial \mu_{\mathrm{V}}}{\partial x} \\ j_{\mathrm{V}} &= -M_{\mathrm{VA}} \frac{\partial \mu_{\mathrm{A}}}{\partial x} - M_{\mathrm{VB}} \frac{\partial \mu_{\mathrm{B}}}{\partial x} - M_{\mathrm{VV}} \frac{\partial \mu_{\mathrm{V}}}{\partial x} \end{aligned} \tag{10.2}$$

where the coefficients M_{ij}, which are often referred to as mobilities, are connected by a number of relations (Shewmon 1963; Crank 1967; Haasen 1984).

Provided sinks and sources of the particles A, B, and vacancies V, are absent, the following flux density balance equation holds:

$$\sum_i j_i = j_{\mathrm{A}} + j_{\mathrm{B}} + j_{\mathrm{V}} = 0 \tag{10.3}$$

For the general case it must be considered that *real* microstructures are often not free from sinks and sources. For instance, while solute atoms can be stored temporarily at other lattice defects such as grain boundaries and dislocations, short-range vacancy diffusion cycles are typical of nonconservative dislocation motion. However, these effects will be neglected in the following. The coefficients M_{ij} are related by

$$\begin{aligned} \sum_i M_{\mathrm{A}i} &= M_{\mathrm{AA}} + M_{\mathrm{AB}} + M_{\mathrm{AV}} = 0 \\ \sum_i M_{\mathrm{B}i} &= M_{\mathrm{BA}} + M_{\mathrm{BB}} + M_{\mathrm{BV}} = 0 \\ \sum_i M_{\mathrm{V}i} &= M_{\mathrm{VA}} + M_{\mathrm{VB}} + M_{\mathrm{VV}} = 0 \end{aligned} \tag{10.4}$$

From the Onsager relations of reciprocity (1931a) it follows that the matrix of the mobility coefficients is always symmetric (Shewmon 1963; Crank 1967)

$$M_{ij} = M_{ji} \tag{10.5}$$

Equations (10.2) can then be written

$$\begin{aligned} j_{\mathrm{A}} &= -M_{\mathrm{AA}}\,\frac{\partial}{\partial x}(\mu_{\mathrm{A}}-\mu_{\mathrm{V}}) - M_{\mathrm{AB}}\,\frac{\partial}{\partial x}(\mu_{\mathrm{B}}-\mu_{\mathrm{V}}) \\ j_{\mathrm{B}} &= -M_{\mathrm{AB}}\,\frac{\partial}{\partial x}(\mu_{\mathrm{A}}-\mu_{\mathrm{V}}) - M_{\mathrm{BB}}\,\frac{\partial}{\partial x}(\mu_{\mathrm{B}}-\mu_{\mathrm{V}}) \end{aligned} \tag{10.6}$$

If the vacancies are everywhere in equilibrium, i.e. $\partial\mu_{\mathrm{V}}/\partial x = 0$, equations (10.6) reduce to

$$\begin{aligned} j_{\mathrm{A}} &= -M_{\mathrm{AA}}\,\frac{\partial\mu_{\mathrm{A}}}{\partial x} - M_{\mathrm{AB}}\,\frac{\partial\mu_{\mathrm{B}}}{\partial x} \\ j_{\mathrm{B}} &= -M_{\mathrm{AB}}\,\frac{\partial\mu_{\mathrm{A}}}{\partial x} - M_{\mathrm{BB}}\,\frac{\partial\mu_{\mathrm{B}}}{\partial x} \end{aligned} \tag{10.7}$$

Anticipating that the nondiagonal terms of the mobility matrix M_{ij} are negligible, one obtains an expression for the phenomenological first law of Fick:

$$\begin{aligned} j_{\mathrm{A}} &= -M_{\mathrm{AA}}\,\frac{\partial\mu_{\mathrm{A}}}{\partial x} = -M_{\mathrm{AA}}\,k_{\mathrm{B}}T\,\frac{\partial\ln a_{\mathrm{A}}}{\partial x} \\ j_{\mathrm{B}} &= -M_{\mathrm{BB}}\,\frac{\partial\mu_{\mathrm{B}}}{\partial x} = -M_{\mathrm{BB}}\,k_{\mathrm{B}}T\,\frac{\partial\ln a_{\mathrm{B}}}{\partial x} \end{aligned} \tag{10.8}$$

where $\mu = \mu_0 + k_{\mathrm{B}}T\ln a$ and a is the chemical activity. These expressions reproduce the well-known form of Fick's law

$$\begin{aligned} j_{\mathrm{A}} &= -\widetilde{D}_{\mathrm{A}}\,\frac{\partial c_{\mathrm{A}}}{\partial x} \\ j_{\mathrm{B}} &= -\widetilde{D}_{\mathrm{B}}\,\frac{\partial c_{\mathrm{B}}}{\partial x} \end{aligned} \tag{10.9}$$

where $\widetilde{D}_i$ is the chemical diffusion coefficient, i.e.

$$\widetilde{D}_i = D_i\left(1+\frac{\mathrm{d}\ln\gamma_i}{\mathrm{d}\ln\nu_i}\right) \tag{10.10}$$

where γ_i is the activity coefficient of the component i and $\nu_i = c_i/c$. Using the Gibbs–Duhem equation $\sum_i(n_i\,\mathrm{d}\mu_i) = 0$, the net flux density $j = j_{\mathrm{B}} - j_{\mathrm{A}}$ can be written

$$j = -M\frac{\partial}{\partial x}\,(\mu_{\mathrm{B}}-\mu_{\mathrm{A}}) \tag{10.11}$$

If the nondiagonal terms are not neglected M amounts to

$$M = \frac{1}{2}\left[(1-c)(M_{\mathrm{BB}}-M_{\mathrm{AB}}) + c(M_{\mathrm{AA}}-M_{\mathrm{AB}})\right] \tag{10.12}$$

where $c = c_{\mathrm{B}}$. Expressing the Helmholtz free energy density f in terms of the chemical potential and using the Gibbs–Duhem relation leads to

$$\frac{\partial f}{\partial c} = \mu_{\mathrm{B}} - \mu_{\mathrm{A}} \tag{10.13}$$

The free energy F is obtained by integration over the volume,

$$F = \int_V f(c(\boldsymbol{r}))\,\mathrm{d}V \tag{10.14}$$

where $dV = dx_1\, dx_2\, dx_3$. Fick's first law can then be written in a modified form:

$$j = -M \frac{\partial}{\partial x} \frac{\partial f}{\partial c} = -M \frac{\partial^2 f}{\partial x \partial c} \frac{\partial c}{\partial c} = -M \frac{\partial^2 f}{\partial c^2} \frac{\partial c}{\partial x} \tag{10.15}$$

The derivation of Fick's second law makes use of the continuity equation which states that any spatial divergence in the flux density must entail a temporal concentration change. To express this matter formally, one may write for a one-dimensional system

$$\frac{\partial c}{\partial t} + \frac{\partial j}{\partial x} = 0 \tag{10.16}$$

Fick's second law can then be written

$$\frac{\partial c}{\partial t} = \frac{\partial}{\partial x} \left(M \frac{\partial}{\partial x} \frac{\partial f}{\partial c} \right) = \frac{\partial}{\partial x} \left(M \frac{\partial^2 f}{\partial c^2} \frac{\partial c}{\partial x} \right) \tag{10.17}$$

This type of kinetic equation can be interpreted as a diffusional form of the more general Onsager or Ginzburg–Landau equation (Onsager 1931a; Onsager 1931b):

$$\frac{\partial \psi_i}{\partial t} = -\hat{M}_{ij} \frac{\delta \widetilde{F}}{\delta \psi_j} \tag{10.18}$$

where $\widetilde{F}$ is the free energy functional of the various functions ψ_j, $\delta\widetilde{F}/\delta\psi_j$ the thermodynamic driving force, t the time, $\hat{M}_{ij}$ the symmetric Onsager kinetic operator matrix, and $i = 1, 2, ..., \vartheta$ the variable of the ϑ dynamic fields. The Einstein summation is implied. Expressions according to equation (10.18) provide a fundamental means of describing the kinetic equations of dynamic fields as a function of the thermodynamic driving force. It should be noted that although equation (10.18) is linear with respect to the driving force, it can be highly nonlinear with respect to the fields ψ_i. It is well known that such nonlinear coupled partial differential equations have solutions that depend in a very sensitive manner on the starting conditions.

10.2.2 Ostwald Ripening and Gibbs–Thomson Equation

As early as 1900 the chemist W. Ostwald carried out the first systematic work on ripening. In his study he investigated the dissolution of HgO particles[2] in water. The experiments showed that small HgO particles had a larger solubility, i.e. a larger tendency to dissolve in water, than large particles. He interpreted this observation correctly in terms of the dependence of the chemical potential on the respective particle surface curvature as predicted by the Gibbs–Thomson equation (Ostwald 1900). In its original meaning the term "Ostwald ripening" is confined to a coarsening reaction where the second-phase particles act as the only sinks and sources of solute atoms. In the present chapter this narrow definition is dropped and Ostwald ripening is used as a general synonym for competitive coarsening phenomena among polydispersed precipitates.

Ripening phenomena are of the utmost importance in the manufacturing and long-term use of all precipitation-hardened alloys, especially technical aluminum alloys and superalloys. While the former materials represent main structural compounds in aerospace applications, the latter ones, as blades, are essential parts in high-temperature turbines.

[2]The notion "particle" in materials science is often reserved for indicating ceramic bonding. However, in this chapter the terms particle, precipitate, and precipitation will be used synonymously.

In these systems Ostwald ripening starts beyond the nucleation stage from a quenched supersaturated state under isothermal conditions. It determines the dynamic evolution of the size distribution of the precipitation microstructure by linking the diffusion profiles near the surface of the precipitates, $c^{\mathrm{M}}(R)$, through the respective average concentration of the matrix $\bar{c} = c(R^*)$. Coarsening phenomena are observed in conjunction with many first- and second-order phase transitions, such as precipitation of supersaturated alloys, eutectic, peritectic, eutectoid, and peritectoid phase transitions, isothermal primary and secondary dendrite growth, late stages of spinodal decomposition, and in liquids (Warlimont 1974; Garrido 1980; Voorhees and Glicksman 1984; Ratke and Thieringer 1985; Khachaturyan et al. 1988; Haasen 1991; Wagner and Kampmann 1991).

For deriving the Gibbs–Thomson equation as a basis to understand growth and shrink phenomena, it is useful to dismantle the Gibbs free enthalpy G according to

$$G = G_{\mathrm{S}} + G_0 \tag{10.19}$$

where G_0 is the free enthalpy contribution that is independent, and G_{S} the contribution that is not independent of the interface area. The latter portion may depend on the orientation if at least one of the interacting phases is ordered, e.g. crystalline. For isotropic interface energy equation (10.19) can be written

$$G = \sigma_{\mathrm{MP}}\, A_{\mathrm{MP}} + G_0 \tag{10.20}$$

where σ_{MP} is the specific isotropic interface energy and and A_{MP} the interface area between the spherical precipitate P and the matrix M.

The chemical potential of atom type A in the precipitate P amounts to

$$\mu_{\mathrm{A}}^{\mathrm{P}} = \left(\frac{\partial G}{\partial N_{\mathrm{A}}}\right)_{T,p} = \mu_{\mathrm{A}_0} + \sigma_{\mathrm{MP}}\,\frac{\partial A}{\partial N_{\mathrm{A}}} \tag{10.21}$$

where μ_{A_0} is the interface-independent portion of the chemical potential and N_{A} the number of atoms in the precipitation. With the precipitation volume V and the average atomic volume $\Omega = \partial V/\partial N_{\mathrm{A}}$ equation (10.21) can be written

$$\mu_{\mathrm{A}}^{\mathrm{M}} = \mu_{\mathrm{A}_0} + \Omega\,\frac{\partial A}{\partial V} \tag{10.22}$$

Considering only spherical precipitates with radius R, the term $\partial A/\partial V$ can be written $\mathrm{d}A/\mathrm{d}V$, which is equal to the curvature $2/R$. Equation (10.22) then reduces to

$$\mu_{\mathrm{M}}^{\mathrm{P}} = \mu_{\mathrm{A}_0} + \frac{2\,\Omega\,\sigma_{\mathrm{MP}}}{R} \tag{10.23}$$

When assuming an ideal solution, the chemical potential of atoms A in the matrix can be written

$$\mu_{\mathrm{A}}^{\mathrm{M}} = \mu_{\mathrm{A}}^{\mathrm{M},0} + k_{\mathrm{B}}T\,\ln\left(c^{\mathrm{M}}\right) \tag{10.24}$$

where $\mu_{\mathrm{A}}^{\mathrm{M},0}$ is the concentration-independent part of the chemical potential of atoms A in the matrix. In thermodynamic equilibrium the chemical potential of atoms A must be the same in all phases, i.e.

$$\mu_{\mathrm{A}}^{\mathrm{P}} = \mu_{\mathrm{A}}^{\mathrm{M}} \tag{10.25}$$

Combining equations (10.23)–(10.25) leads to

$$k_B T \ln\left(c^M\right) = \frac{2\,\Omega\,\sigma_{MP}}{R} + \mu_{A_0} - \mu_A^{M,0} \tag{10.26}$$

If the curvature $1/R$ is very small, i.e. $R \to \infty$, equation (10.26) can be written

$$k_B T \ln\left(c^M\,(R \to \infty)\right) = k_B T \ln\left(c_\infty^M\right) = \mu_{A_0} - \mu_A^{M,0} \tag{10.27}$$

where the value of c_∞^M corresponds to the equilibrium concentration of atoms A in the matrix as given by the solubility curve in the phase diagram. By inserting equation (10.27) into equation (10.26) one obtains the well-known Gibbs–Thomson equation[3],

$$c^M(R) = c_\infty^M \exp\left(\frac{2\,\sigma_{MP}\,\Omega}{k_B\,T}\,\frac{1}{R}\right) \tag{10.28}$$

which reflects that the equilibrium concentration of atoms A near the surface of a precipitation depends in an exponentially inverse manner on its actual radius R. If the argument in the exponential function is very small, i.e. $(2\,\sigma_{MP}\,\Omega/(k_B T\,R)) \ll 1$, equation (10.28) may be linearized:

$$c^M(R) \cong c_\infty^M\left(1 + \frac{2\,\sigma_{MP}\,\Omega}{k_B T}\,\frac{1}{R}\right) \tag{10.29}$$

While the concentration directly near the surface of each precipitation is prescribed by equation (10.29), the average matrix concentration at a sufficiently large distance from the particle amounts to $\bar{c}$. As will be discussed later, this assumption is only valid for an infinitely small precipitated volume fraction. The average matrix concentration $\bar{c}$ corresponds to the equilibrium concentration near the surface of a precipitation with critical radius R^*. Its relation to the actual particle radius determines the local growth rate. Figure 10.1 shows that the particle radius or, more precisely, its surface-to-volume ratio decides whether it will shrink ($c^M(R) > \bar{c}$), grow ($c^M(R) < \bar{c}$), or remain unchanged ($c^M(R^*) = \bar{c}$).

The average matrix concentration must therefore be a function of time and can be calculated by

$$c(R^*) = \bar{c} = \frac{\int_0^\infty c(R) f(R,t)\,\mathrm{d}R}{\int_0^\infty f(R,t)\,\mathrm{d}R} \tag{10.30}$$

where $f(R,t)$ is the distribution of the spherical precipitates in space and time and $f(R,t)\,\mathrm{d}R$ the number of precipitations with a radius within the range R to $R+\mathrm{d}R$. Combining equation (10.30) and equation (10.29) gives a simple expression for the critical radius R^*:

$$c(R^*) = \bar{c} = \frac{\int_0^\infty c(R) f(R,t)\,\mathrm{d}R}{\int_0^\infty f(R,t)\,\mathrm{d}R} = c_\infty^M\left(1 + \frac{2\,\sigma_{MP}\,\Omega}{k_B T}\,\frac{1}{R^*}\right) \tag{10.31}$$

which leads to

$$R^* = \frac{2\,\sigma_{MP}\,\Omega}{k_B T}\,\frac{1}{\ln\left(\frac{\bar{c}}{c_\infty^M}\right)} \tag{10.32}$$

[3] All functions that express the chemical potential or the concentration as a function of the incremental change of surface per volume (curvature in the case of spherical precipitates) are typically referred to as Gibbs–Thomson equations.

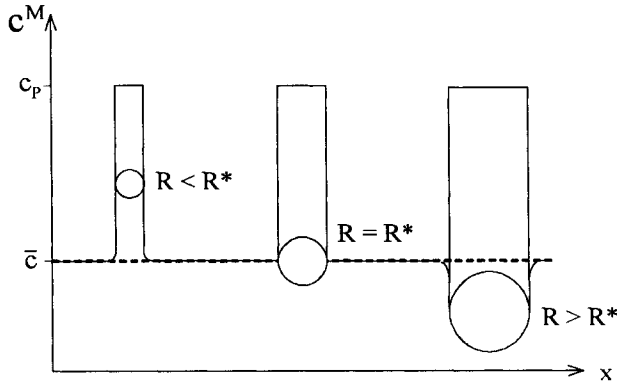

Figure 10.1: Schematic illustration of the concentration profiles near the surfaces of various precipitations. R indicates the particle radius and R^* the critical radius. c_p is the equilibrium concentration inside the particle and $\bar{c}$ the average matrix concentration which corresponds to the equilibrium concentration near the surface of a precipitation with critical radius R^*.

A more detailed derivation of equation (10.32) requires the consideration of chemical diffusion (Martin and Doherty 1976). Due to Ostwald ripening the average precipitate number density changes from $\approx 10^{25}\mathrm{m}^{-3}$ to less than $\approx 10^{19}\mathrm{m}^{-3}$ in typical two-phase alloys (Wagner and Kampmann 1991).

10.2.3 Lifshitz–Slyozov–Wagner Theory

The classical analytical description of isothermal competitive ripening phenomena of polydispersed precipitates is provided by the LSW theory (Lifshitz and Slyozov 1961; Wagner 1961) The basic assumptions that are made in the analytical derivation of the LSW theory are that the volume fraction of the precipitate phase is (close to) zero, no relative movement of matrix and precipitate occurs, the matrix is infinite, the precipitates are equiaxial, no elastic stresses occur, and stationary conditions exist.

For the derivation of the LSW theory it is more convenient to use the general operators ∇ and Δ instead of Cartesian derivatives. The volume change during ripening of a particle is proportional to the diffusion flux that penetrates its surface. The flux counts positive when the atoms diffuse from the precipitation into the matrix. To express this matter formally, for isotropic diffusion through the interface one can write

$$\frac{\mathrm{d}V}{\mathrm{d}t} = 4\pi R^2 \frac{\mathrm{d}R}{\mathrm{d}t} = -j\,\Omega\,4\pi\,R^2 \tag{10.33}$$

where j is the flux density, Ω the atomic volume, and R the radius of a spherical particle. The above formulation implies the absence of a relative movement of precipitation and matrix (Ratke and Thieringer 1985; Wan and Sahm 1990a; Wan and Sahm 1990b). Neglecting the concentration dependence of the diffusion coefficient, the flux density can be calculated using Fick's first law, equation (10.8), in its conventional form,

$$j = -D\,\nabla c \tag{10.34}$$

where D is the diffusion constant of A atoms near the surface of the precipitate. The neglect of chemical diffusion is admissible in this context since the LSW theory generally stipulates $c \to 0$. Using the stationary form ($\partial c/\partial t = 0$) of Fick's second law (Laplace equation) without consideration of chemical diffusion

$$\nabla (D \nabla c(r)) = D \nabla^2 c(r) = \nabla^2 c(r) = \Delta c(r) = 0 \tag{10.35}$$

where the nabla operator ∇ refers to the first and the Laplace operator Δ to the second spatial derivative, under the border conditions

$$\begin{aligned} c(r = R) &\equiv c_R \\ c(r \to \infty) &= \bar{c} \end{aligned} \tag{10.36}$$

one obtains the concentration gradient at the surface of the precipitate:

$$\nabla c \,|_R = \frac{\bar{c} - c_R}{R} \tag{10.37}$$

The growth rate of the particle amounts to

$$\frac{\mathrm{d}R}{\mathrm{d}t} = \Omega D \frac{\bar{c} - c_R}{R} \tag{10.38}$$

Combining equation (10.38) with

$$c_R = c_\infty + \frac{\lambda}{R} \qquad \text{and} \qquad \bar{c} = c_\infty + \frac{\lambda}{R^*} \tag{10.39}$$

where $\lambda = 2\,\sigma_{\mathrm{MP}}\,\Omega\, c_\infty/(k_{\mathrm{B}}T)$, leads to

$$\frac{\mathrm{d}R}{\mathrm{d}t} = \frac{\lambda\,\Omega\,D}{R^2}\left(\frac{R}{R^*(t)} - 1\right) \tag{10.40}$$

(Greenwood 1956). During the ripening process the large precipitates grow at the expense of the small ones. This leads to a shift in the average particle size and thus to a different average matrix concentration $\bar{c}$. Thus, the critical particle radius $R^*(t)$ will gradually increase as a function of time.

The corresponding evolution of the distribution function of the spherical precipitates $f(R,t)$ satisfies the continuity equation (Lifshitz and Slyozov 1961; Wagner 1961):

$$\frac{\partial f(R,t)}{\partial t} + \frac{\partial}{\partial R}\left(f(R,t)\,\frac{\partial R}{\partial t}\right) = 0 \tag{10.41}$$

This nonlinear partial differential equation can be rewritten by introducing the dimensionless parameters

$$\rho = R/R^* \qquad \text{and} \qquad \tau = \ln\left(\frac{R^*}{R_0^*}\right)^3 \tag{10.42}$$

where R_0^* is the critical particle radius at time t_0. As was shown by Lifshitz and Slyozov (1961) and Wagner (1961) for the asymptotic case, $t \to \infty$, the dimensionless distribution function $f(\rho,\tau)$ reveals a stationary state where it may be separated according to

$$f(\rho,\tau) = g(\tau)\cdot h(\rho) \tag{10.43}$$

By using this separation ansatz the dimensionless distribution function can be solved. The first function $g(\tau)$ describes the temporal evolution of the critical radius R^*:

$$g(\tau) = g_0 \exp(-\beta\,\tau) \tag{10.44}$$

where $\tau = \tau(R^*)$ (equation (10.42)). The second function $h(\rho)$ describes the particle size distribution:

$$h(\rho) = \frac{81}{2^{5/3}} \frac{\rho^2}{(3/2-\rho)^{11/3}} \frac{1}{(3+\rho)^{7/3}} \exp\left(-\frac{\rho}{3/2-\rho}\right) \tag{10.45}$$

It must be considered that this solution obtained through separation is valid only for $t \to \infty$, i.e. it applies to the late stages of ripening. Finally, LSW predicts a temporal evolution of the critical radius R^* according to

$$R^{*3} - R_0^{*3} = \nu\,\varepsilon(t-t_0) = C_{\mathrm{LSW}}(t-t_0) \tag{10.46}$$

where ε and C_{LSW} are material-dependent constants and ν a material-independent constant ($\nu_{\mathrm{LSW}} = 4/9$).

Based on the original LSW theory a number of refined analytical mean field approaches, considering for example nonzero precipitate volume fractions, were suggested. These theories typically predict a flattened particle size distribution and an identical time dependence for the evolution of the critical radius, namely, $R^* \propto t^{1/3}$.

10.3 Continuum Phase Field Kinetic Models

10.3.1 Cahn–Hilliard and Allen–Cahn Model

When a homogeneous, single-phase, binary solution is rapidly quenched from a sufficiently elevated homologous temperature to a temperature below its upper critical solution temperature, gradual phase separation may occur. However, phase transition will only happen if the quench brings the solution into the two-phase coexistence region and if the temperature suffices for diffusion.

Phase separation may proceed through the discontinuous process of nucleation and growth in the metastable region, or by the continuous process of spinodal decomposition in the unstable region (Cahn and Hilliard 1971; Christian 1975; Gunton et al. 1983; Ratke 1987; Wagner and Kampmann 1991). While small concentration fluctuations in the metastable region increase the total free energy of the system in terms of the nucleation energy, a sufficiently large but finite concentration (concentration in the precipitate) perturbation can degrade it. This renders the entire solid solution unstable and leads to phase separation by discontinuous nucleation and subsequent growth.

In contrast, continuous phase separation, as described by spinodal decomposition, gradually degrades the free energy right from the beginning of phase transition, i.e. it is a non-activated process and does not reveal any threshold energy. Such coherent, i.e. isostructural, decomposition phenomena are theoretically described by the Cahn–Hilliard model (1958), which combines the generalized law of diffusion (equations (10.17) and (10.18)) with a Landau energy term (Section 10.3.2). The extension of the original Cahn–Hilliard model to non-coherent phase transformations, i.e. transitions which change the long-range order, the crystal orientation, or the crystal structure, is provided by the Allen–Cahn model (1979) and its generalized derivatives.

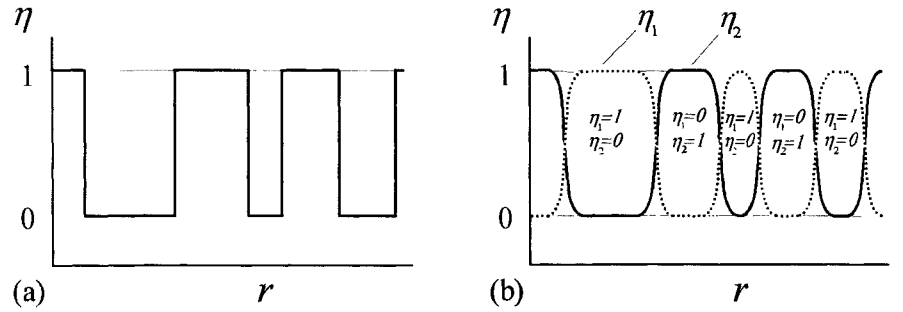

Figure 10.2: Schematic one-dimensional representation of a sharp (a) and of a diffuse (b) interface. Grain boundaries are in the phase field models not sharp but realized in terms of gradients between 0 and 1 in the orientational field variable.

While the Cahn–Hilliard model describes the kinetics of transformation phenomena with conserved field variables (e.g. chemical concentration), the Allen–Cahn model describes transformations with nonconserved variables (e.g. long-range order).

Both the Cahn–Hilliard model and the Allen–Cahn model can in certain cases be solved analytically. However, in advanced computational materials science applications, the approaches are transcribed into a form that is discrete in space, i.e. the time-dependent variables are defined as spatial field variables, which requires the employment of numerical solution methods (Khachaturyan 1983; Chen and Khachaturyan 1991a; Chen et al. 1992; Johnson et al. 1994; Chan and Rey 1995; Chen and Wang 1996; Wang et al. 1996). The dependence of the variables on the spatial coordinates enables one to prescribe heterogeneous composition and structure phase fields, and allows one to simulate both the kinetics and the resulting morphology associated with phase separation. Since spatial gradients in the various conserved and nonconserved field variables (concentration, structure, orientation, long-range order) represent diffuse, i.e. non-sharp, interfaces between phases, the underlying models are sometimes also referred to as "phase field kinetic models" or "diffuse phase field kinetic models" (Figure 10.2).

The generalized phase field methods are based on furnishing a set of Ginzburg–Landau or Onsager kinetic equations, equation (10.18), with an appropriate well-fitted Landau- or Redlich–Kister-type free energy density functional that may depend on both conserved and nonconserved field variables.

$$\begin{aligned}
\frac{\partial c(\boldsymbol{r},t)}{\partial t} &= M\,\nabla^2 \frac{\delta \widetilde{F}}{\delta c(\boldsymbol{r},t)} \\
\frac{\partial \eta_1(\boldsymbol{r},t)}{\partial t} &= -\hat{L}_{1j}\,\frac{\delta \widetilde{F}}{\delta \eta_j(\boldsymbol{r},t)} \\
&\cdots \\
\frac{\partial \eta_\vartheta(\boldsymbol{r},t)}{\partial t} &= -\hat{L}_{\vartheta j}\,\frac{\delta \widetilde{F}}{\delta \eta_j(\boldsymbol{r},t)}
\end{aligned} \tag{10.47}$$

where $c(\boldsymbol{r},t)$ is the concentration field variable, which is defined here as the solvent volume fraction, $\eta_i(\boldsymbol{r},t)$ are the i different structure field variables with $i = 1, ..., \vartheta$, $\widetilde{F}$ is the free energy functional, t the time, $\boldsymbol{r}$ the spatial coordinate, $\hat{L}_{ij}$ the symmetric matrix of the

kinetic structure operators, M the kinetic coefficient of diffusion (mobility), and ϑ the number of dynamic structure fields. It is stipulated that the coefficients M and $\hat{L}_{ij}$ are independent of the structure parameters and of the concentration. The local value of the chemical potential is given by the common derivative

$$\left(\frac{\delta\widetilde{F}}{\delta\chi_i(\boldsymbol{r},t)}\right)_{T,j\neq i} = \mu_i(\boldsymbol{r}) \tag{10.48}$$

where $\chi_i(\boldsymbol{r},t)$ is the generalized field form of the original functions $c(\boldsymbol{r},t)$ and $\eta_j(\boldsymbol{r},t)$. If the effect of the structural parameters on the chemical potential is neglected, the derivative $\delta\widetilde{F}/\delta c(\boldsymbol{r},t)$ corresponds to the local value of the chemical potential $\mu(\boldsymbol{r})$.

If M becomes a function of concentration, for instance in the case of large concentrations, the first Onsager relation in equations (10.47) must be written in the form

$$\frac{\partial c(\boldsymbol{r},t)}{\partial t} = \nabla\left(M\,\nabla\frac{\delta\widetilde{F}}{\delta c(\boldsymbol{r},t)}\right) \tag{10.49}$$

The Cahn–Hilliard model is based on the first expression in equations (10.47) and the assumption that a concentration field exists, which characterizes the phase of the system at each point in space and time, and that the total free energy of an inhomogeneous binary solution can be expressed through its energy density as a functional of that concentration field and its gradients in the form

$$\widetilde{F} = \int_V f_t\left(c(\boldsymbol{r},t)\right)\,\mathrm{d}V \equiv \int_V \left(f(c(\boldsymbol{r},t)) + \kappa\left(\nabla c(\boldsymbol{r},t)\right)^2\right)\mathrm{d}V \tag{10.50}$$

where V is the volume occupied by the system, $f_t(c(\boldsymbol{r},t))$ the total density of the free energy, $f(c(\boldsymbol{r},t))$ the homogeneous portion of $f_t(c(\boldsymbol{r},t))$, i.e. the free energy density of the homogeneous phase with no gradients, and $\kappa(\nabla c(\boldsymbol{r},t))^2$ a gradient term for the description of additional free energy in inhomogeneous systems, for instance interfacial energy. The constant κ is positive and related to the respective interfacial constants. It can be regarded as the weighting constant in the interfacial "penalty" term, quantifying the system's tendency to reduce the total interfacial area. Since the term $\kappa(\nabla c(\boldsymbol{r},t))^2$ amounts to a non-sharp description of interfaces, its application is straightforward for the identification of interfaces arising from concentration changes, but less obvious for the treatment of boundaries arising solely from structure changes, such as grain boundaries. The homogeneous portion $f(c(\boldsymbol{r},t))$ in the free energy density term is in the case of spinodal problems usually assumed to have a "double-well" form (Figure 10.3). It should be noted in this context that for the realistic simulation of continuous phase separation this homogeneous portion in the free energy must be fitted to describe a typical spinodal free energy curve including convex and concave sections. A classical chemical approach for the approximation of $f(c(\boldsymbol{r},t))$ is

$$f(c(\boldsymbol{r},t)) = f_0(c(\boldsymbol{r},t)) + f_{\mathrm{loc}}(c(\boldsymbol{r},t)) - Ts(c(\boldsymbol{r},t)) \tag{10.51}$$

where $f_0(c(\boldsymbol{r},t))$ is the equilibrium free energy density function of an ideal two-phase solution, $f_{\mathrm{loc}}(c(\boldsymbol{r},t))$ the local energy density, and $s(c(\boldsymbol{r},t))$ the molar entropy. In isostructural systems with fluctuations only in the chemical field the local energy density is identical to the chemical mixing energy density. For an ideal mixture $f_0(c(\boldsymbol{r},t))$ depends on the

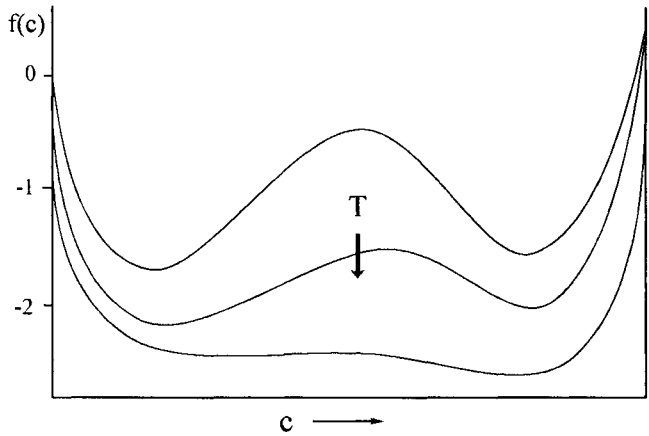

Figure 10.3: Typical "double-well" form of the homogeneous portion in the free energy density term $f(c(\boldsymbol{r},t))$ in the case of a binary solid solution for describing spinodal systems. The arrow indicates the increase in temperature.

chemical potential of the pure constituents, say A and B, weighted linearly as a function of the concentration:

$$f_0(c(\boldsymbol{r},t)) = c(\boldsymbol{r},t)\,\mu_0^{\mathrm{A}} + (1 - c(\boldsymbol{r},t))\,\mu_0^{\mathrm{B}} \tag{10.52}$$

According to the Redlich–Kister approach, the local or mixing energy of a solid solution containing A and B atoms can be approximated by

$$f_{\mathrm{loc}}^{\mathrm{R}}(c(\boldsymbol{r},t)) = c(\boldsymbol{r},t)\,(\,1 - c(\boldsymbol{r},t)\,)\sum_i C_{\mathrm{A}\leftrightarrow\mathrm{B}}^i(T)\,[\,(\,1 - c(\boldsymbol{r},t)\,) - c(\boldsymbol{r},t)]^i \tag{10.53}$$

where $C_{\mathrm{A}\leftrightarrow\mathrm{B}}^i(T)$ is a set of phenomenological coefficients, which in part is dependent on the temperature, and must be extracted from experiments or determined theoretically. The entropy contribution, which ensures that the slope of $f(c(\boldsymbol{r},t))$ goes to infinity as c goes to 0 or 1, can be written

$$s = -R\,[\,c(\boldsymbol{r},t)\,\ln c(\boldsymbol{r},t) + (\,1 - c(\boldsymbol{r},t)\,)\,\ln(\,1 - c(\boldsymbol{r},t)\,)\,]\,/\,\Omega_m \tag{10.54}$$

where Ω_m is the molar volume and $R = k_{\mathrm{B}}\,N_{\mathrm{L}}$.

The total free energy of an inhomogeneous binary isostructural solution, consisting of A and B, can then be calculated according to

$$\begin{aligned}\widetilde{F} = \int_V \Big(\, & c(\boldsymbol{r},t)\,\mu_0^{\mathrm{A}} + (1 - c(\boldsymbol{r},t))\,\mu_0^{\mathrm{B}} \\ & + c(\boldsymbol{r},t)\,(\,1 - c(\boldsymbol{r},t)\,)\sum_i C_{\mathrm{A}\leftrightarrow\mathrm{B}}^i(T)\,(\,(\,1 - c(\boldsymbol{r},t)\,) - c(\boldsymbol{r},t))^i \\ & + RT\,(\,c(\boldsymbol{r},t)\,\ln c(\boldsymbol{r},t) + (\,1 - c(\boldsymbol{r},t)\,)\,\ln(\,1 - c(\boldsymbol{r},t)\,))^i\,/\Omega_m + \kappa\,(\nabla c(\boldsymbol{r},t))^2\,\Big)\,\mathrm{d}V\end{aligned} \tag{10.55}$$

A second often encountered approach for the description of the free energy density is the Landau form

$$\begin{aligned} f(c(\boldsymbol{r},t)) &= f_0(c(\boldsymbol{r},t)) + f_{\text{loc}}^{\text{Land}}(c(\boldsymbol{r},t)) - Ts(c(\boldsymbol{r},t)) \\ &= f_0(c(\boldsymbol{r},t)) + \frac{C_1}{2}\left(c(\boldsymbol{r},t) - c_{\text{crit}}\right)^2 + \frac{C_2}{4}\left(c(\boldsymbol{r},t) - c_{\text{crit}}\right)^4 - Ts(c(\boldsymbol{r},t)) \end{aligned} \tag{10.56}$$

where C_1, C_2, and c_{crit} are phenomenological constants which must be fitted from theory or experiment. The Landau energy density function will be discussed more detailed in the next section.

The Cahn–Hilliard equation uses field variables for the description of the concentration array. The concentration field is a conservative field since any change must happen in accord with the continuity equation, equation (10.16). This approach is consequently only capable of describing isostructural phase transformations, where different phases differ from each other only in concentration, but not in long-range order, crystal orientation, elastic strain, or crystal structure. The latter aspects, however, are often of relevance in phase transformations that occur in engineering materials. To extend the use of diffuse Ginzburg–Landau-type kinetic phase field models to the prediction of non-isostructural phase transformation phenomena one has to additionally consider nonconservative fields, e.g. structure and phase fields. The influence of such structure and order phase fields on the kinetics and morphology of phase separation can be considered by using the remaining differential expressions in equation (10.47) together with a modified free energy form which does not only depend on the chemical concentration but also on one or more structure variables $\eta_i(\boldsymbol{r},t)$ with $i = 1, ..., \vartheta$.

For systems with only one structure variable, say a long-range order field variable $\eta(\boldsymbol{r},t)$, the local contribution to the free energy density can be written

$$\begin{aligned} f_{\text{loc}}(c(\boldsymbol{r},t),\eta(\boldsymbol{r},t)) = \frac{C_3}{2}\left(c(\boldsymbol{r},t) - c_{\text{crit1}}\right)^2 + \frac{C_4}{4}\left(c_{\text{crit2}} - c(\boldsymbol{r},t)\right)\eta(\boldsymbol{r},t)^2 \\ - \frac{C_5}{4}\eta(\boldsymbol{r},t)^4 + \frac{C_6}{6}\eta(\boldsymbol{r},t)^6 \end{aligned} \tag{10.57}$$

where C_3, C_4, C_5, C_6, c_{crit1}, and c_{crit2} are phenomenological constants which must be fitted from theory or experiment.

More complex functionals for the total free energy density to consider a larger number of variables, say a number of ϑ orientational, i.e. texture variable fields, in addition to the β chemical concentration fields, follow the general form

$$\begin{aligned} f_t\left(c_1(\boldsymbol{r},t), c_2(\boldsymbol{r},t), ..., c_\beta(\boldsymbol{r},t), \eta_1(\boldsymbol{r},t), \eta_2(\boldsymbol{r},t), ..., \eta_\vartheta(\boldsymbol{r},t)\right) \\ = f_0\left(c_1(\boldsymbol{r},t), c_2(\boldsymbol{r},t), ..., c_\beta(\boldsymbol{r},t), \eta_1(\boldsymbol{r},t), \eta_2(\boldsymbol{r},t), ..., \eta_\vartheta(\boldsymbol{r},t)\right) \\ + f_{\text{loc}}\left(c_1(\boldsymbol{r},t), c_2(\boldsymbol{r},t), ..., c_\beta(\boldsymbol{r},t), \eta_1(\boldsymbol{r},t), \eta_2(\boldsymbol{r},t), ..., \eta_\vartheta(\boldsymbol{r},t)\right) \\ - Ts\left(c_1(\boldsymbol{r},t), c_2(\boldsymbol{r},t), ..., c_\beta(\boldsymbol{r},t), \eta_1(\boldsymbol{r},t), \eta_2(\boldsymbol{r},t), ..., \eta_\vartheta(\boldsymbol{r},t)\right) \\ + \frac{1}{2}\sum_{q=1}^{\beta}\kappa_q^c\left(\nabla c_q(\boldsymbol{r},t)\right)^2 + \frac{1}{2}\sum_{p=1}^{\vartheta}\kappa_p^s\left(\nabla \eta_p(\boldsymbol{r},t)\right)^2 \end{aligned} \tag{10.58}$$

where κ_q^c are the interface energy coefficients for chemical gradients and κ_q^s the interface energy coefficients for orientational gradients (grain boundaries) (Cahn and Hilliard 1958; Chen and Wang 1996). The influence of elastic stresses on the total free energy (see Section 10.5) must be included in a variational form similar to Eshelby's inclusion formulation (Khachaturyan 1983; Dreyer 1995; Löchte et al. 1998).

10.3.2 Thermal Fluctuation

Except for the initial chemical and structural spatial state of the system, which is often randomly chosen, the simulations according to equations (10.47) are entirely deterministic. Although they can adequately describe growth and coarsening, they do not cover nucleation (Wang et al. 1996). For overcoming this handicap they can be complemented by adding a stochastic Langevin type force term $\xi(x,t)$ to the right-hand parts of each equation (Landau and Lifshitz 1980; Landau and Lifshitz 1981; Wang et al. 1996) that transforms equations (10.47) into

$$\begin{aligned}
\frac{\partial c(\boldsymbol{r},t)}{\partial t} &= M\,\nabla^2 \frac{\delta \widetilde{F}}{\delta c(\boldsymbol{r},t)} + \xi(\boldsymbol{r},t) \\
\frac{\partial \eta_1(\boldsymbol{r},t)}{\partial t} &= -\hat{L}_{1j}\,\frac{\delta \widetilde{F}}{\delta \eta_j(\boldsymbol{r},t)} + \xi_1(\boldsymbol{r},t) \\
&\cdots \\
\frac{\partial \eta_\vartheta(\boldsymbol{r},t)}{\partial t} &= -\hat{L}_{\vartheta j}\,\frac{\delta \widetilde{F}}{\delta \eta_j(\boldsymbol{r},t)} + \xi_\vartheta(\boldsymbol{r},t)
\end{aligned}$$

The noise functions $\xi_\vartheta(\boldsymbol{r},t)$ and $\xi(\boldsymbol{r},t)$ are Gaussian-distributed and have to satisfy the requirements of the fluctuation-dissipation theorem (Landau and Lifshitz 1980; Wang et al. 1996).

Considering a Langevin-type noise term amounts to recasting the statistical expression into a microscopic form. The incorporation of such random pulses reflects the influence of Brownian particle motion, i.e. of thermal fluctuation, assuming that the average of this force over the ensemble should vanish (Kramers 1940; Chandrasekhar 1943; Risken 1984). That means the Langevin force changes randomly in size and sign without correlation.

Solutions of the above field are typically obtained by using fast Fourier transforms which are available in common FORTRAN and C libraries. Convenient overviews of the solution algorithms in reciprocal space have been published by Küpper and Masbaum (1994), Chan and Rey (1995), and Copetti and Elliott (1996).

10.3.3 Landau Energy Density Functional

One of the most straightforward and widely used methods to formulate thermodynamic potentials near critical points was suggested by Landau for magnetic systems (Landau 1937a; Landau 1937b). It is based on the assumption that one can expand the thermodynamic potential in a power series about the critical point. A simple physical derivation of the quadratic Landau form can also be made by expressing the free energy in terms of all the nearest-neighbor binding enthalpies and their configurational entropy.

This section presents the combination of a Landau-type potential, formulated for a concentration field, with a kinetic equation (Cahn and Hilliard 1958).

The starting point is the Onsager or Ginzburg–Landau diffusion equation (equation (10.18)). Furnished with a Landau potential and a gradient interface term of the type described by equation (10.50), one obtains the classical Cahn–Hilliard equation (Cahn 1961).

$$\frac{\partial c(\boldsymbol{r},t)}{\partial t} = M\,\nabla^2 \left[\left(\frac{\partial F}{\partial c(\boldsymbol{r},t)} \right)_T - k\nabla^2 c(\boldsymbol{r},t) \right] \tag{10.59}$$

Close to the critical coordinates T_c and c_{crit} the following Taylor series approach for the local free energy density can be used in accord with Landau's magnetic theory:

$$f(c(\boldsymbol{r},t)) = f_0 + \frac{A}{2}\left(c(\boldsymbol{r},t) - c_{\text{crit}}\right)^2 + \frac{B}{4}\left(c(\boldsymbol{r},t) - c_{\text{crit}}\right)^4 + \frac{C}{6}\left(c(\boldsymbol{r},t) - c_{\text{crit}}\right)^6 + \ldots \tag{10.60}$$

The derivative of this expression is

$$\left(\frac{\partial f(c(\boldsymbol{r},t))}{\partial c(\boldsymbol{r},t)}\right)_T = A\left(c(\boldsymbol{r},t) - c_{\text{crit}}\right) + B\left(c(\boldsymbol{r},t) - c_{\text{crit}}\right)^3 + C\left(c(\boldsymbol{r},t) - c_{\text{crit}}\right)^5 + \ldots \tag{10.61}$$

where $c(\boldsymbol{r},t) \equiv c_B$, and $A < 0, B > 0$ if T is below the critical temperature T_c. Since the above series expansion depends on the small quantity $c(\boldsymbol{r},t) - c_{\text{crit}}$ it can be rewritten

$$\left(\frac{\partial f(c(\boldsymbol{r},t))}{\partial c(\boldsymbol{r},t)}\right)_T \cong A\left(c(\boldsymbol{r},t) - c_{\text{crit}}\right) + B\left(c(\boldsymbol{r},t) - c_{\text{crit}}\right)^3 \tag{10.62}$$

By combining equation (10.59) and equation (10.62) one obtains the classical Ginzburg–Landau equation for describing phase transition phenomena in magnetic media (Gunton et al. 1983):

$$\frac{\partial}{\partial t}\left(c(\boldsymbol{r},t) - c_{\text{crit}}\right) = M\nabla^2\left[A\left(c(\boldsymbol{r},t) - c_{\text{crit}}\right) + B\left(c(\boldsymbol{r},t) - c_{\text{crit}}\right)^3 - k\nabla^2\left(c(\boldsymbol{r},t) - c_{\text{crit}}\right)\right] \tag{10.63}$$

10.3.4 Solution of the Linearized CHGL theory

Estimations of the incipient stages of spinodal precipitation can be made under the assumption that the concentration fluctuations are small. This allows one to drop terms that are not linear in the concentration on the right-hand side of equation (10.59). Furthermore, it is stipulated that the phase separation is isostructural. That means the field is a conservative one and no additional phase field needs to be considered.

Assuming a constant mobility M the Cahn–Hilliard equation, equation (10.59), can be linearized according to

$$\frac{\partial c}{\partial t} = M\left(\left.\frac{\partial^2 F}{\partial c^2}\right|_{c_0}\nabla^2 c - 2\kappa\nabla^4 c\right) \tag{10.64}$$

where c_0 is the initial average concentration. In the unstable region and for relatively large diffusion distances, the diffusion coefficient $\widetilde{D}$ becomes negative, which means that existing concentration fluctuations will be sharpened rather than removed.

$$\widetilde{D} \cong M\left.\frac{\partial^2 F}{\partial c^2}\right|_{c_0} \tag{10.65}$$

The change of the sign of $\widetilde{D}$ from positive to negative describes the phenomenon of up-hill diffusion and is a characteristic feature of spinodal decomposition (Cahn 1961).

An analytical solution of equation (10.64) is obtained by using Fourier transforms (Cahn and Hilliard 1958). The general solution amounts to

$$c - c_0 = \sum_k \left[A(k)\cos(\boldsymbol{k}\,\boldsymbol{r}) + B(k)\sin(\boldsymbol{k}\,\boldsymbol{r})\right]\mathrm{e}^{R(k)\,t} \tag{10.66}$$

where $R(k)$ is the amplification factor, $k_i = 2\pi/\lambda_i$, and λ_i the wavelength for fluctuation i. $R(k)$ amounts to

$$R(k) = -Mk^2 \left(\left. \frac{\partial^2 F}{\partial c^2} \right|_{c_0} + 2\,\kappa\, k^2 \right) \tag{10.67}$$

The amplification factor determines the thermodynamic direction of the phase separation. Equations (10.66) and (10.67) substantiate the fact that concentration fluctuations will only grow if $\partial^2 F/\partial c^2|_{c_0} < 0$ and $\left|\partial^2 F/\partial c^2|_{c_0}\right| > \left|2\kappa\, k^2\right|$, i.e. $R(k)$ is positive in the unstable region so that existing fluctuations $c - c_0$ will be promoted. The fastest-growing wavelength $\lambda_{\max}$, which can be obtained from equation (10.67), amounts to

$$\lambda_{\max} = \sqrt{8\pi^2} \left[\left(-\frac{1}{2\,\kappa} \right) \left. \frac{\partial^2 F}{\partial c^2} \right|_{c_0} \right]^{-\frac{1}{2}} \tag{10.68}$$

The morphology that results for the initial stages of spinodal phase separation is then a superposition of periodic concentration modulations of a fixed wavelength, but random in amplitude.

10.4 Microscopic Phase Field Kinetic Model

While the deterministic phase field variants of the Ginzburg–Landau model correctly predicts the main microstructural path of phase transition from a more statistical point of view, it cannot generally deal with structural events at the atomic level (Khachaturyan 1968; Wang et al. 1996).

Thus, Khachaturyan (1968) suggested an extension of the Ginzburg–Landau-type continuum field kinetic models for the simulation of phase separation phenomena, namely, the microscopic lattice diffusion theory. Chen (1995) employed a similar microscopic approach to simulate grain growth.

The microscopic approach of Khachaturyan simultaneously describes the diffusion kinetics of ordering and decomposition in a spatially inhomogeneous alloy where the composition and long-range order parameter are coupled through a non-equilibrium free energy functional. The main contrast of this approach with its continuum type counterpart is that the macroscopic kinetic coefficients that occur in the underlying set of Ginzburg–Landau or Onsager equations can be computed at a microscopic level. For this purpose Khachaturyan suggested introduction of a microscopic field for the description of displacive transformations caused by the elementary diffusional jumps of atoms over crystal lattice sites that result in atomic ordering, antiphase domain boundary movement, concentration delamination, and Ostwald ripening phenomena of polydispersed precipitates in terms of a temporal evolution of composition and long-range order profiles. Thus, the microscopic field kinetic approach is formulated in terms of the crystal lattice site diffusion in a non-ideal solid solution, which is actually a random walk-type problem for a system of interacting atoms (Chen and Khachaturyan 1991a). The resulting kinetic equations are nonlinear finite difference differential equations which can be solved only numerically.

The microscopic field representing the atomic structure and alloy morphologies is described by the single-site occupation probability function $\chi(\boldsymbol{r}, t)$, which is actually an average of the occupation number $c(\boldsymbol{r})$ over the time-dependent ensemble $\chi(\boldsymbol{r}, t) = \langle c(\boldsymbol{r}) \rangle$, where $\langle ... \rangle$ denotes averaging. This means that the values of this real-space function

represent the probability of observing a solute atom at lattice site $\boldsymbol{r}$ and time t. The values of the occupation number are described by

$$c(\boldsymbol{r}) = \begin{cases} 1, \text{ if a site } \boldsymbol{r} \text{ is occupied by a solute atom} \\ 0, \text{ otherwise} \end{cases} \tag{10.69}$$

The dynamic evolution of this microscopic field is described by a Ginzburg–Landau or Onsager-type kinetic equation (10.18),

$$\frac{\partial \chi(\boldsymbol{r},t)}{\partial t} = \sum_{\boldsymbol{r}'} L\left(\boldsymbol{r}-\boldsymbol{r}'\right) \frac{\delta \widetilde{F}}{\delta \chi(\boldsymbol{r}',t)} \tag{10.70}$$

where $\widetilde{F}$ is the free energy functional of the functions $\chi(\boldsymbol{r}',t)$, $\delta\widetilde{F}/\delta\chi(\boldsymbol{r}',t)$ the thermodynamic driving force, t the time, and $L(\boldsymbol{r}-\boldsymbol{r}')$ the symmetric microscopic kinetic matrix. The coefficients in this kinetic matrix are inversely proportional to the average diffusion time required for the number of elementary jumps from lattice site $\boldsymbol{r}$ to lattice site $\boldsymbol{r}'$. This concept for deriving of the kinetic coefficient matrix establishes the main progress of the microscopic lattice diffusion theory as compared with the conventional continuum field kinetic approach, page (Khachaturyan 1968; Khachaturyan et al. 1988; Wang et al. 1996). The numerical solution of equations (10.47) with a Landau-type potential containing the gradient term $(\nabla c(\boldsymbol{r}))^2$, equation (10.50), only considers the influence of the nearest neighborhood. In contrast, the microscopic approach, equation (10.70), considers the entire concentration field in each time step.

The occupation probability for solute atoms meets the conservation condition

$$N_s = \sum_{\boldsymbol{r}} \chi\left(\boldsymbol{r}',t\right) \tag{10.71}$$

where N_s is the number of solute atoms in the system. Since the presence of sources or sinks other than precipitations are excluded, the following equation holds as well:

$$\frac{\mathrm{d}N_s}{\mathrm{d}t} = 0 \tag{10.72}$$

Combining equations (10.72) and (10.70) then leads to

$$\frac{\mathrm{d}N_s}{\mathrm{d}t} = \left(\sum_{\boldsymbol{r}} L(\boldsymbol{r})\right) \left(\sum_{\boldsymbol{r}'} \frac{\delta \widetilde{F}}{\delta \chi(\boldsymbol{r}',t)}\right) = 0 \tag{10.73}$$

Since it cannot be assured that the sum of the elementary thermodynamic driving forces $\delta\widetilde{F}/\delta\chi(\boldsymbol{r}',t)$ is equal to zero, the first multiplier should therefore be zero, i.e.

$$\sum_{\boldsymbol{r}} L(\boldsymbol{r}) = 0 \tag{10.74}$$

The Fourier transform of equation (10.70) gives the reciprocal space representation and can be written

$$\frac{\partial \check{\chi}(\boldsymbol{k},t)}{\partial t} = \sum_{\boldsymbol{r}'} \check{L}(\boldsymbol{k}) \left[\frac{\delta \widetilde{F}}{\delta \chi(\boldsymbol{r},t)}\right]_{\boldsymbol{k}} \tag{10.75}$$

where $[\delta\widetilde{F}/\delta\chi(\boldsymbol{k},t)]_{\boldsymbol{k}}$, $\check{\chi}(\boldsymbol{k},t)$, and $\check{L}(\boldsymbol{k})$ are the discrete Fourier transforms of the corresponding functions in real space, $\delta\widetilde{F}/\delta\chi(\boldsymbol{r},t)$, $\chi(\boldsymbol{r},t)$, and $L(\boldsymbol{r})$. They are given by

$$\begin{aligned}\check{\chi}(\boldsymbol{k},t) &= \sum_{\boldsymbol{r}} \chi(\boldsymbol{k},t)\,\mathrm{e}^{-\mathrm{i}\,\boldsymbol{k}\boldsymbol{r}} \\ \check{L}(\boldsymbol{k}) &= \sum_{\boldsymbol{r}} L(\boldsymbol{k})\,\mathrm{e}^{-\mathrm{i}\,\boldsymbol{k}\boldsymbol{r}}\end{aligned} \tag{10.76}$$

For phase separation without structure change the characteristic wavelength of the mesoscopic inhomogeneity d_s is typically much larger than the lattice spacing a. In that case $\check{\chi}(\boldsymbol{k},t)$ is only significant around $\boldsymbol{k}=0$, with $|\boldsymbol{k}|$ being of the order of $2\pi/d_s$. The function $\check{\chi}(\boldsymbol{k},t)$ is then a Fourier transform of the mesoscopic concentration field $c(\boldsymbol{r})$. Similar considerations apply for the form of $\check{\chi}(\boldsymbol{q},t)$ where $|\boldsymbol{q}|=|\boldsymbol{k}-\boldsymbol{k}_0|$. The function $\check{\chi}(\boldsymbol{q},t)$ is the Fourier transform of the long-range parameter field $\chi(\boldsymbol{r})$. The Fourier transform of $L(\boldsymbol{r})$ is given by

$$\check{L}(\boldsymbol{k}) \approx -M_{ij}k_ik_j \tag{10.77}$$

with the expansion coefficients tensor

$$M_{ij} = \left(\frac{\partial^2\check{L}(\boldsymbol{k})}{\partial k_i\partial k_j}\right) \tag{10.78}$$

Re-substituting these coefficients into the Fourier transform of the Onsager equation, equation (10.75), leads to

$$\frac{\partial\check{\chi}(\boldsymbol{k},t)}{\partial t} = -M_{ij}k_ik_j\left[\frac{\delta\widetilde{F}}{\delta\chi(\boldsymbol{r},t)}\right]_{\boldsymbol{k}} \tag{10.79}$$

and the Fourier back-transform amounts to

$$\frac{\partial c(\boldsymbol{r},t)}{\partial t} = M_{ij}\nabla_i\nabla_j\left(\frac{\delta\widetilde{F}}{\delta\chi(\boldsymbol{r},t)}\right) \tag{10.80}$$

which corresponds to the Cahn–Hilliard equation. From this transition of the microscopic approach to the mesoscopic phenomenological kinetic equation one finds that the macroscopic kinetic coefficients can be computed from elementary diffusion jumps. Further details of this method were given by Chen and Khachaturyan (1991a), Chen and Wang (1996), and Wang, Chen, and Khachaturyan (1996).

10.5 Consideration of Elastic Stresses

The incorporation of elastic terms in addition to the interfacial contribution and the Landau-type chemical portion into the free energy functional can be realized following the work of Eshelby (1957) and Khachaturyan (1983). A derivation of the classical Eshelby inclusion formulas is also given in Chapter 17.

The derivation of the elastic term is based on the assumption of continuum homogeneity with respect to the elastic properties, i.e. the elastic constants are independent of the atomic concentration. The elastic fields which are described in terms of pairwise interactions of strain sources can be calculated by superposition.

According to Khachaturyan (1983) the derivation can be made in five steps. First, the volume is divided into s identical subunits, each having a homogeneous concentration. These small units are described by the form-function

$$\vartheta_p(\boldsymbol{r}) \begin{cases} 1 & \text{in the volume unit } \Omega_p \\ 0 & \text{outside the volume unit } \Omega_p \end{cases} \tag{10.81}$$

where the total volume is $\Omega = \sum_{p=1}^{s} \Omega_p$.

In the second step, one removes a volume unit of interest, Ω_p^0, from the homogeneous matrix, so that it is free of external stresses, and subjects it to an internal change of state, for instance a concentration change, which may entail an eigenstrain $\varepsilon_{ij}^0(p)$. This strain transforms the affected volume into Ω_p^{ex}.

It has to be noted that the first two steps do not change the elastic energy, since the first step did not create a true surface and the second step did not expand or shrink the affected volume unit against any external stress state.

In the third step, one imposes a stress state on the volume Ω_p^{ex} in such a way as to restore the original shape of the volume Ω_p^0. Using Hooke's linear law of anisotropic elasticity, equation (9.29), the mechanical portion of work required to deform the volume, equations (9.63)–(9.68), can be calculated according to

$$\begin{aligned} F_1^{\text{el}} &= \frac{1}{2} \sum_{p=1}^{s} \int_\Omega \vartheta_p(\boldsymbol{r})\, \sigma_{ij}^0(p)\, \left(-\varepsilon_{ij}^0(p)\right) \mathrm{d}\boldsymbol{r}^3 \\ &= \frac{1}{2} \sum_{p=1}^{s} \int_\Omega \vartheta_p(\boldsymbol{r})\, C_{ijkl}\, \left(-\varepsilon_{ij}^0(p)\right) \left(-\varepsilon_{kl}^0(p)\right) \mathrm{d}\boldsymbol{r}^3 \end{aligned} \tag{10.82}$$

where the Einstein summation rule applies.

As indicated by the expressions $\sigma_{ij}^0(p)$ and $\varepsilon_{ij}^0(p)$, the stress and strain state may be different in each of the subvolumes. C_{ijkl} is the fourth-order tensor of the elastic stiffness constants (see Chapter 9, Table 9.1).

In the forth step, the strained volume element Ω_p^0 is repositioned into the original matrix, exactly at its original location. Since no elastic interaction with the matrix is considered at this stage, there is no elastic energy contribution arising from this step.

The last step considers the elastic interaction between the volume element Ω_p^0 and the surrounding matrix, which occurs by the relaxation of the stress $\sigma_{ij}^0(p)$ that was imposed on that piece of volume. The relaxation leads to a mechanical equilibrium which depends on the values of the variabes, e.g. on the atomic concentration or the values of possible structure variables in case of a non-isostructural transformation, that characterize the state of Ω_p^0.

Using $\sigma_{ij}(p)$ and $\varepsilon_{ij}(p)$ to indicate the true stress and strain fields that are present in the material after relaxation, one can express the contribution of the relaxation to the elastic energy by

$$F_2^{\text{el}} = \frac{1}{2} \sum_{p,q=1}^{s} \int_\Omega \left(\int_\Omega \vartheta_p(\boldsymbol{r})\, \left(-\varepsilon_{ij}(p)\right) \widetilde{A}_{ijkl}(|\boldsymbol{r}-\boldsymbol{r}'|)\, \left(-\varepsilon_{kl}(q)\right) \vartheta_q(\boldsymbol{r})\, \mathrm{d}\boldsymbol{r}'^3 \right) \mathrm{d}\boldsymbol{r}^3 \tag{10.83}$$

where the fourth-order interaction tensor $\widetilde{A}_{ijkl}$ connects the pairwise elastic interactions between the various volume elements. The factor $\frac{1}{2}$ comes from the fact that the interactions must not be counted twice.

For a binary alloy an analytical solution for the total elastic contribution to the free energy was given as a function of the concentration field by Gitt (1997).

$$F^{\mathrm{el}}(c) = F_1^{\mathrm{el}}(c) + F_2^{\mathrm{el}}(c) = \frac{1}{2} \int_{\mathrm{Fo}} \left(\widetilde{A}(\boldsymbol{k}) - \widetilde{A}_{\mathrm{min}} \right) |\widetilde{c}(\boldsymbol{k})|^2 \, \frac{\mathrm{d}\boldsymbol{k}^3}{(2\,\pi)^3} \tag{10.84}$$

where Fo indicates integration in Fourier space and $\widetilde{c}(\boldsymbol{k})$ the Fourier transform of the concentration field $c(\boldsymbol{r})$ in Fourier space

$$\widetilde{c}(\boldsymbol{k}) = \int_{\Omega} \frac{\mathrm{d}\boldsymbol{k}^3}{(2\,\pi)^3} \, c(\boldsymbol{r}) \, \mathrm{e}^{-\mathrm{i}\,\boldsymbol{k}\,\boldsymbol{r}} \tag{10.85}$$

The interaction tensor is a complicated function of the elastic constants (Khachaturyan 1983; Dreyer 1995; Gitt 1997). The constant $\widetilde{A}_{\mathrm{min}}$ indicates the minimum value of $\widetilde{A}(\boldsymbol{k})$.

Adding this term to the Landau functional form allows one to rewrite the Cahn–Hilliard equation for isostructural transformation phenomena, equation (10.49), in a more general fashion:

$$\frac{\partial c(\boldsymbol{r},t)}{\partial t} = \nabla \left(M \, \nabla \left(\frac{\delta F^{\mathrm{chem}}}{\delta c(\boldsymbol{r},t)} + \frac{\delta F^{\mathrm{el}}}{\delta c(\boldsymbol{r},t)} \right) \right) \tag{10.86}$$

10.6 Application of Phase Field Kinetic Models in Materials Science

This section gives a number of classical or recently published references on applications of phase field kinetic simulations related to various domains of materials science. The list can by no means be complete but may serve as a bibliography for getting better acquainted with some examples of the recent original literature in this field.

Field of application	Reference
classics and fundamentals	Onsager (1931a)
	Onsager (1931b)
	Landau (1937a)
	Landau (1937b)
	Cahn and Hilliard (1958)
	Cahn (1961)
	Cahn (1962)
	Cahn and Hilliard (1965)
	Landau (1965)
	Khachaturyan (1968)
	Chan (1977)
	Khachaturyan (1983)
	Allen and Cahn (1979)
	Gurtin (1989)
	Penrose and Fife (1990)
	Chen and Khachaturyan (1991a)
	Chan and Rey (1995)
	Gurtin (1996)

isostructural spinodal decomposition	Khachaturyan (1967)
	Khachaturyan and Shatalov (1969)
	Morral and Cahn (1971)
	Langer, Bar-On, and Miller (1975)
	Hohenberg and Halperin (1977)
	Rogers, Elder, and Desai (1988)
	Onuki (1989)
	Rogers (1989)
	Chen and Khachaturyan (1991b)
	Chen and Khachaturyan (1991c)
	Wang, Chen, and Khachaturyan (1991)
	Wang, Chen, and Khachaturyan (1992)
	Takenaka and Hashimoto (1993)
	Wang, Chen, and Khachaturyan (1993)
	Dreyer (1995)
	Löchte and Gottstein (1996)
	Eliott and Garcke (1996)
	Löchte, Gitt, and Gottstein (1998)
non-isostructural transformation, ordering phenomena	Johnson, Howe, Laughlin, and Soffa (1994)
	Kobayashi (1994)
	Wang and Khachaturyan (1995a)
	Wang and Khachaturyan (1995b)
	Fan and Chen (1995)
	Chen, Wang, and Khachaturyan (1992)
	Wang, Chen, and Khachaturyan (1996)
	Chen and Wang (1996)
solidification and dendrite growth	Caginalp and Fife (1986)
	Caginalp (1989)
	Caginalp and Socolowski (1991)
	Wheeler, Boettinger, and McFaden (1992)
	Kobayashi (1993)
	Wheeler, Murray, and Schaefer (1993)
	Caginalp and Xie (1993)
	Wheeler, Boettinger, and McFaden (1993)
	Warren and Boettinger (1995)
homophase and heterophase grain growth	Chen and Yang (1994)
	Chen (1995)
	Chen and Wang (1996)
	Chen and Fan (1996)
	Fan and Chen (1997)
	Fan, Geng, and Chen (1997)
numerical and computational aspects	Küpper and Masbaum (1994)
	Copetti and Elliott (1996)

10.7 Examples of Phase Field Simulations in Materials Science

10.7.1 Simulation of Spinodal Decomposition

This section presents a two-dimensional continuum Cahn–Hilliard field kinetic simulation of a spinodal decomposition and competitive isostructural ripening process in the system aluminum–copper. The simulation considers the influence of internal ansiotropic elastic stresses among the particles.

Light alloys based on the aluminum–copper system were the first ones in which the process of spinodal decomposition and the resultant hardening was discovered and thoroughly studied. As a classical group of light and hardenable alloys, they are indispensable, particularly in the field of aerospace engineering.

The simulations presented in Figure 10.4 were conducted by Löchte (1997). The two-dimensional approach (Figure 10.4) considers the chemical, elastic, and interfacial contributions to the free energy density. The calculations were performed using an initial solute matrix concentration of 0.050 at% copper, a temperature of 423 K, and a value of 0.07^{-10} J/m for the gradient energy coefficient. The plots reveal the kinetics and the microstructural path at an early and at the later stage of ripening by projecting the copper concentration after various annealing times.

The solutions were obtained using a finite difference scheme. The maximum admissible grid size is related to the width of the diffuse heterophase interface, i.e. it is of an atomic order of magnitude.

10.7.2 Simulation of Grain Growth

A number of mechanical and also many electromagnetic properties of polycrystalline materials depend on the microstructure arising from grain growth phenomena. This applies in particular to the grain shapes, the grain size distribution, and the crystallographic texture.

Because of the complexity of the various processes involved there is no closed analytical treatment which allows one to predict all the topological and crystallographic aspects associated with grain growth phenomena in sufficient detail. This section therefore presents an application of the diffuse phase field model to grain growth.

Figure 10.5 shows the application of a diffuse field Ginzburg–Landau type of calculation for predicting two-dimensional grain growth by Fan and Chen (1997). The extension of the classical Cahn–Hilliard model to non-coherent phase transformations, i.e. transitions which change the long-range order, the crystal structure, or, as in this case, the crystal orientation, is provided by a modified Ginzburg–Landau or Allen–Cahn model. While the original Cahn–Hilliard approach describes the kinetics of transformation phenomena with conserved field variables (e.g. chemical concentration), the generalized Ginzburg–Landau or Allen–Cahn model can mimic transformations with nonconserved variables (e.g. long-range order or crystallographic texture). The free energy density must then be a function of all orientation or texture components η_i that appear in the simulation and of the corresponding gradient "penalty" terms. The variable field of each texture component is described in terms of values between 0 and 1 (Figure 10.2).

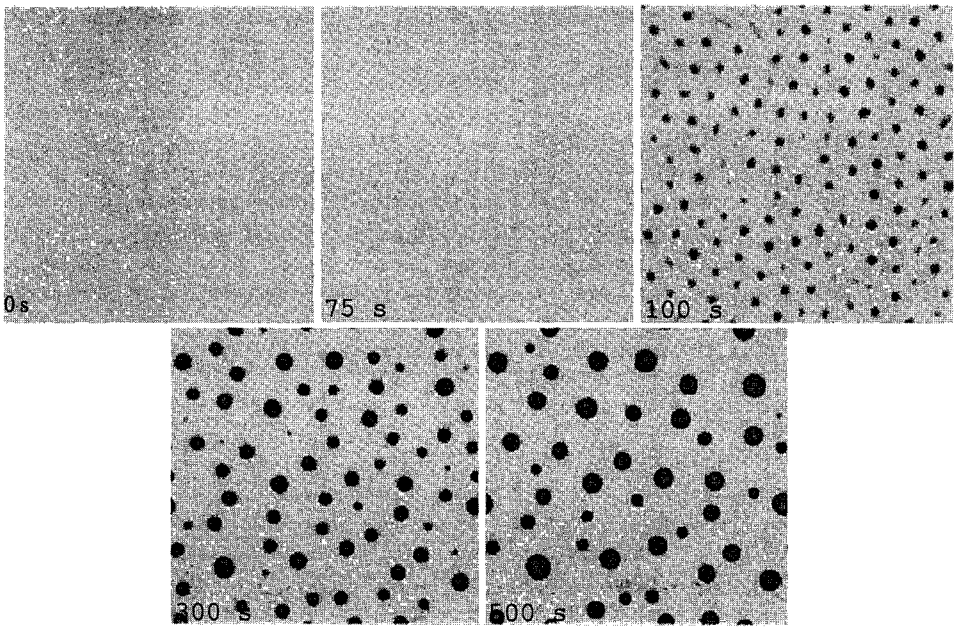

Figure 10.4: 2D simulation of spinodal decomposition and ripening in the system copper–aluminum at an early stage; projection of the copper concentration, T = 423 K, t=0 s, 75 s, 100 s, 300 s and 500 s (Löchte, unpublished results 1997).

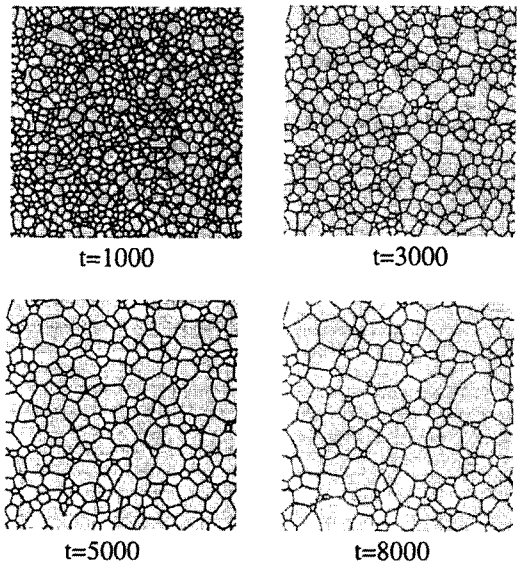

Figure 10.5: 2D simulation of grain growth using a diffuse field Ginzburg–Landau approach (Fan et al. 1997).

Chapter 11

Cellular Automata

11.1 Introduction and Fundamentals

Cellular automata are algorithms that describe the discrete spatial and/or temporal evolution of complex systems by applying local or global deterministic or probabilistic transformation rules to the sites of a lattice[1]. The space variable can stand for real space, momentum space, or wave vector space. The lattice is defined in terms of a fixed number of points. These can be regarded as the nodes of a finite difference field. The lattice is typically regular and its dimensions can be arbitrary. It maps the elementary system entities that are regarded as relevant to the model under consideration. These can be arbitrarily sized continuum-type volume units, atomic particles, lattice defects, or animals and so forth. The system entities are quantified in terms of generalized state variables, such as dimensionless numbers, particle density, lattice defect density, particle velocity, color, blood pressure, or animal species. The actual values of these state variables are defined at each of the individual lattice sites. Each node must assume one of a finite set of possible discrete states.

The evolution of the automaton takes place through the application of certain transformation rules that act on the state of each node. These rules determine the state of a site as a function of its previous state and the state of the neighboring sites (local rules) or the state of all sites (global rules). Most classical cellular automata use local transformation rules.

Deviations from the regular lattice structure are conceivable. This applies especially to heterogeneous media, where the use of a smaller spacing can be pertinent in the vicinity of relevant lattice regions. However, an adequate correction and renormalization of the transformation rate must then be considered.

A cellular automaton evolves in discrete time steps. After each time interval the values of the state variables are simultaneously updated for all nodes.

In recent years the concept of classical (CCA) cellular automata as defined by Wolfram (1986) has been slightly extended to a class of more generalized (CGA) cellular automata. The latter variant of the cellular automaton method is more flexible than the original one, particlularly with respect to specific applications in computational materials science.

[1] Conventional cellular automata use local rules. Some modern variants consider intermediate or long-range interactions also.

Computational Materials Science: The Simulation of Materials, Microstructures and Properties By Dierk Raabe
Copyright © 1998 Wiley-VCH Verlag GmbH
ISBN: 3-527-29541-0

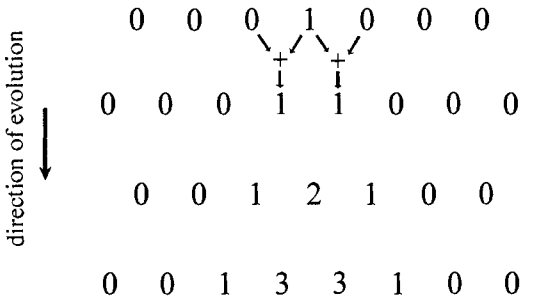

Figure 11.1: The Pascal triangle can be regarded as a one dimensional cellular automaton. The transformation rule is indicated by the arrows.

Generalized microstructure cellular automata can use a discrete spatial grid of cells or sites, where space can be real space, momentum space, or wave vector space. Space is usually homogeneous, i.e. all sites are identical and are arranged in a regular lattice, where the transformation rules are the same everywhere. Like conventional automata, they must assume one out of a finite number of possible states and the update of the cell states is made in synchrony. In contrast to conventional automata, the transformation of sites can follow deterministic or probabilistic laws. Generalized microstructure cellular automata therefore increasingly gain momentum in computational materials science.

Owing to these features, the cellular automaton method provides a direct means of simulating the evolution of dynamic systems which contain large numbers of similar components on the basis of their mutual short- or long-range interactions (Schulman and Seiden 1978; Wolfram 1983; Vichniac 1984; Wolfram 1986; Stauffer 1991). For simple physical systems this amounts to discretely mapping approximate finite difference solutions to a set of more or less complicated partial differential equations where one of the independent variables is the time.

However, it must be underlined that cellular automata do not have any restrictions in the type of elementary entities or transformation rules employed. They can map such different situations as the distribution of the values of state variables in a simple finite difference simulation, the colors in a blending algorithm, the health state of children in a school building, the elements of fuzzy sets (see Appendix C.2) which can be subject to arbitrary transformations, or elementary growth and decay processes of cells[2].

For instance, the Pascal triangle, which can be used to calculate higher-order binominal coefficients or the Fibonaccy numbers, can be regarded as a one-dimensional cellular automaton, where the value that is assigned to each site of a regular triangular lattice is calculated through the summation of the two numbers above it (Figure 11.1). In this case the entities of the automaton are dimensionless integer numbers and the transformation law is the summation rule.

Another automaton might consist of a cubic lattice where each point has a certain color which can switch according to such simple transformation rules as "if more than 50% of the neighboring sites have the color blue, then the point considered switches from its present color to red" or "if more than 75% of the neighboring sites have the color red, then the point considered also switches to red." For describing the mutual infection of

[2]For instance in Conway's game of life.

children in a school building, one could define a cellular automaton through the trivial rule "if more than 50% of the children in one room are ill, all other children in that room are infected". In order to render such simple phenomenological models more plausible and realistic, further transformation rules may be added. The above example could be complemented by the rules "infected children recover after a certain number of time steps" or "children can only be infected once", and so forth.

In the field of computational materials science, the transformation rules of cellular automata typically consist in the finite difference, finite element, or even Monte Carlo approximation of an underlying set of coupled partial differential equations which depend on time and two or three independent spatial coordinates. While local transformation rules describe short-range interactions among neighboring sites, global transformation rules can consider long-range interactions. The states of the sites are usually characterized in terms of the values of the respective dependent variables, which are referred to as state variables.

These introductory examples show that the cellular automaton concept is not simply identical to conventional simulation approaches such as the various finite difference, finite element, Ising, or Potts methods, but is defined in a much more general and versatile manner. Cellular automata can even be regarded as a generalization of discrete calculation methods. This flexibility is due to the fact that, besides the use of crisp mathematical expressions as variables and transformation rules, automata can incorporate practically any kind of element or rule that is assumed to be relevant.

For instance, in materials science, it may sometimes make sense to complement conventional finite difference calculations, such as are encountered in the field of plasticity, fracture mechanics, or grain growth, by a number of "if–then" rules. Such additions can provide a simple and efficient way to deal with mathematical singularities, i.e. with critical or spontaneous effects within an otherwise smooth function behavior. Indeed, such rules occur frequently in microstructure simulations. For example, discrete dislocation dynamics simulations often contain a rule of the type "if two antiparallel screw dislocations approach closer than say, 5 Burgers vectors, they will undergo spontaneous annihilation." In fracture mechanics or spring models one often includes rules of the type "if the crack velocity assumes a certain value, the sample will fail spontaneously". In recrystallization simulations one often encounters the rule "if a certain local value of the crystal misorientation is reached, the site fulfills the kinetic instability criterion of nucleation" or "if a certain local value of the stored elastic energy is reached, the site fulfills the thermodynamic instability criterion of nucleation".

Complementing the governing differential equations with such sets of "if–then" transformation rules enables one to mimic the dynamic behavior of complex systems, often entirely on the basis of the local interactions among the particles considered.

Cellular automata were introduced by von Neumann and Ulam for the simulation of self-reproducing Turing automata and population evolution. In their original work they denoted them at first as cellular spaces. Other authors used notions like tessellation automata, homogeneous structures, tessellation structures, or iterative arrays. Later applications were particularly in the field of describing nonlinear dynamic behavior of fluids and reaction–diffusion systems (Grosbas 1988; Mareschal and Lemarchand 1996).

Only recently, cellular automata also became important as a technique for the prediction of microstructure evolution. In this domain a number of different aspects were addressed, namely, primary static recrystallization (Hesselbarth and Göbel 1991; Pezzee and Dunand 1994; Marx and Raabe 1995; Marx et al. 1995; Marx et al. 1996; Sheldon and Dunand 1996), recovery (Raabe et al. 1996), formation of dendritic grain structures

in solidification processes (Brown et al. 1994; Gandin and Rappaz 1994), dislocation kink formation (Lépinoux 1996), sintering (Pimienta et al. 1992), and radial growth of two-phase grain structures (Spittle and Brown 1994).

Cellular automata reveal a certain similarity to kinetic Monte Carlo integration approaches (Chapters 6 and 12). While the latter methods generally represent probabilistic approaches to predict microstructures, cellular automata were originally designed as deterministic models. However, stochastic automata with probabilistic transformation rules increasingly gain importance (Grassberger et al. 1984; Kinzel 1985; Raabe 1998b). The original intention of introducing cellular automata into microstructure simulation was the same as for the introduction of Potts-type Monte Carlo models, namely, the direct mapping and simulation of microstructure evolution on the basis of *local* interactions. For this purpose large numbers of deterministic (cellular automata) or stochastic (Monte Carlo, probabilistic cellular automata) calculation steps are carried out in ensembles with microscopically (Monte Carlo), mesoscopically (Potts Monte Carlo), or arbitrarily scaled elementary units (cellular automata). Depending on the underlying physical model, the results are then evaluated in the framework of statistical mechanics (Monte Carlo) or by extracting microstructural parameters (Potts Monte Carlo, cellular automata).

Although cellular automaton simulations are typically carried out at an elementary level (e.g. atoms, clusters of atoms, dislocation segments, subgrains), it should be emphasized that particularly those variants that discretize and map in a continuuum space are not intrinsically calibrated by a characteristic physical length or time scale (Wolfram 1983). This means that a cellular automaton simulation of continuum systems requires the definition of elementary units and transformation rules that adequately reflect the system behavior at the level addressed. This explains why cellular automata approaches are presented in this chapter on mesoscopic–microscopic approaches rather than together with Monte Carlo (Chapter 6) or molecular dynamics simulations (Chapter 7). While the latter techniques represent real microscopic models in a physical sense, the use of cellular automata is not restricted to any particular regime but scalable to arbitrary systems. Deriving thermodynamic quantities of equilibrium ensembles with cellular automata has thus less foundation in physics than deriving them with Monte Carlo methods (Binder and Stauffer 1987; Binder 1991a; Mareschal and Lemarchand 1996). For this reason it is important to examine whether the elementary simulation units adequately reflect the behavior of the underlying physical entities before performing a cellular automaton computer experiment. Since the use of cellular automata is not confined to the microscopic regime, it provides a convenient numerical means for bridging various space and time scales in microstructure simulation.

11.2 Versatility of Cellular Automata in Materials Science

The particular versatility of the cellular automaton approach for the simulation of microstructures arising from recrystallization, grain growth, and phase transition phenomena is mainly due to its flexibility in the consideration of a large variety of possible spatial state variables and transformation laws.

For instance, in the field of recrystallization and grain growth, cellular automata can incorporate the local crystallographic texture and deformation in a discrete manner. For describing these features, one typically uses the local crystal orientation g, the stroed

elastic energy, i.e. some approximate measure such as the dislocation density ϱ or the local Taylor factor M, and the temperature T as state variables. These variables are dependent variables, i.e. they depend on the independent variables that quantify space and time, x_1, x_2, x_3, t.

The state quantities so defined enter the various local structural evolution laws such as are required for the description of the particular phenomenon under investigation. This concept allows a reasonable phenomenological description of individual mechanisms such as recovery, nucleation, and the growth of nuclei on the basis of local data and transformation rules.

By mapping the state variables on a two- or three-dimensional spatial grid, cellular automaton simulations are capable of accounting for microstructural inhomogeneities such as second phases, microbands, shear bands, transition bands, heterophase interfaces, grain boundaries, or twins. These local defect structures can be described in terms of corresponding values of the state variables or their gradients. Shear bands are characterized by high dislocation densities and large local lattice curvatures. The mobility m of grain boundaries can be described[3] for a given impurity content in terms of the local misorientation between adjacent grains, $\Delta g = \Delta g(\varphi_1, \phi, \varphi_2)$, and the spatial orientation of the grain boundary normal $\boldsymbol{n}$, i.e. $m = m(\varphi_1, \phi, \varphi_2, \boldsymbol{n})$.

11.3 Formal Description of Cellular Automata

The local interaction of neighboring sites in a cellular automaton is specified through a set of deterministic or stochastic transformation rules. The value of an arbitrary state variable ξ assigned to a particular site at a time $(t_0 + \Delta t)$ is determined by its present state (t_0) (or its last few states t_0, $t_0 - \Delta t$, etc.) and the state of its neighbors. Considering the last two time steps for the evolution of a one-dimensional cellular automaton, this can be put formally by writing

$$\xi_j^{t_0+\Delta t} = f\left(\xi_{j-1}^{t_0-\Delta t}, \xi_j^{t_0-\Delta t}, \xi_{j+1}^{t_0-\Delta t}, \xi_{j-1}^{t_0}, \xi_j^{t_0}, \xi_{j+1}^{t_0}\right) \tag{11.1}$$

where $\xi_j^{t_0}$ indicates the value of the variable at a time t_0 at the node j. The positions $j+1$ and $j-1$ indicate the nodes in the immediate neighborhood of position j. The function f specifies the set of transformation rules, such as provided by standard finite difference algorithms.

If the state of the node depends only on its nearest neighbors (NN) the array is referred to as von Neumann neighboring, equation (11.1). If both the NN and the next-nearest neighbors (NNN) determine the ensuing state of the node, the array is called Moore neighboring (Figure 11.2). In this context it must be underlined that, due to the discretization of space, the type of neighboring affects the local transformation rates. For instance, in the case of a higher-dimensional cellular automaton simulation, say with three independent spatial variables described by rectangular coordinates, Moore neighboring, and cubic cells, is carried out in a homogeneous medium, the predictions become dependent on the shape of the cells. When the physical rules that determine the interactions among the

[3]For completely describing the character of a grain boundary as many as 8 independent parameters are required, namely, three for the orientation, two for the (normalized) grain boundary plane, and three for the components of the local relaxation vector, which is referred to as translation. Since the latter three degrees of freedom are only accessible by molecular dynamics simulations, they are neglected in the present context.

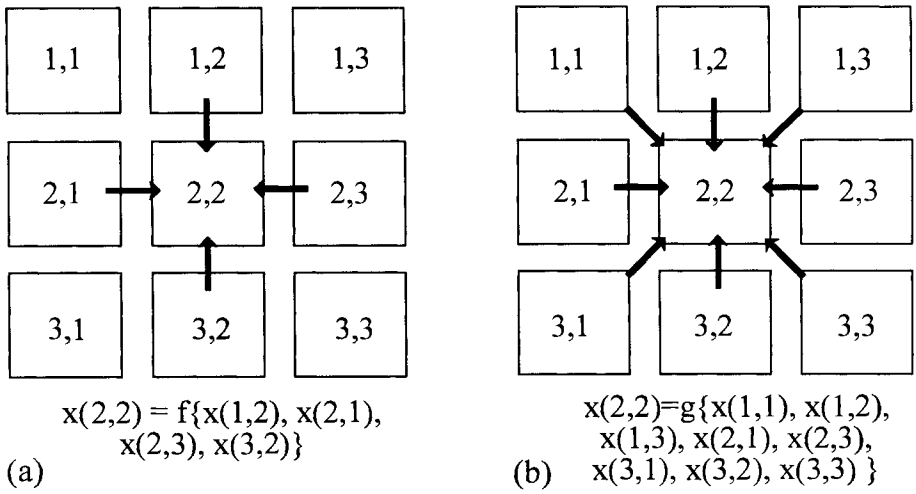

Figure 11.2: (a) Example of a two-dimensional von Neumann configuration considering nearest neighbors. (b) Example of two-dimensional Moore configuration considering both nearest and next-nearest neighbors.

sites are isotropic the transformation rate predicted parallel to $\langle 110 \rangle$ must be normalized by $\sqrt{2}$ and that parallel to $\langle 111 \rangle$ by $\sqrt{3}$.

Transforming these somewhat abstract rules and properties associated with general automata into a materials-related simulation concept consists in mapping the values of relevant state variables onto the cells of a cellular automaton grid which reflects the independent spatial coordinates, and using the approximate local finite difference solutions of the underlying partial differential equations of the model addressed as local transformation rules.

For the Moore configuration, which allows one to introduce a certain medium-range interaction among the sites, equation (11.1) can be rewritten as

$$\xi_j^{t_0+\Delta t} = f\left(\xi_{j-2}^{t_0-\Delta t}, \xi_{j-1}^{t_0-\Delta t}, \xi_j^{t_0-\Delta t}, \xi_{j+1}^{t_0-\Delta t}, \xi_{j+2}^{t_0-\Delta t}, \xi_{j-2}^{t_0}, \xi_{j-1}^{t_0}, \xi_j^{t_0}, \xi_{j+1}^{t_0}, \xi_{j+2}^{t_0}\right) \tag{11.2}$$

The above examples show that the state of a cellular automaton is completely specified by the transformation rules and by the values of the state variables at each site. The transformation rules used in general automata may indeed be very simple, for example: "if three of the neighboring sites are in state X the site addressed switches to Z". However, in deterministic microstructure simulations where the site interactions are described in accord with the physical nature of the interaction, the transformation rules essentially amount to obtaining approximate discretized finite difference solutions to locally acting partial differential equations.

Even for very simple automata there exists an enormous variety of possible transformation rules. For a one-dimensional binary cellular automaton with von Neumann neighboring, each node must assume one of two possible states, say $\xi_j = 1$ or $\xi_j = 0$. For such a scenario equation (11.1) assumes the form

$$\xi_j^{t_0+\Delta t} = f\left(\xi_{j-1}^{t_0}, \xi_j^{t_0}, \xi_{j+1}^{t_0}\right) \tag{11.3}$$

This simple configuration already allows one to define 2^8 possible deterministic or probabilistic transformation rules f. One of them is

$$\begin{array}{lcl}
(\xi_{j-1}^{t_0}=1,\xi_j^{t_0}=1,\xi_{j+1}^{t_0}=1) & \rightarrow & \xi_j^{t_0+\Delta t}=0\\
(\xi_{j-1}^{t_0}=1,\xi_j^{t_0}=1,\xi_{j+1}^{t_0}=0) & \rightarrow & \xi_j^{t_0+\Delta t}=1\\
(\xi_{j-1}^{t_0}=1,\xi_j^{t_0}=0,\xi_{j+1}^{t_0}=1) & \rightarrow & \xi_j^{t_0+\Delta t}=0\\
(\xi_{j-1}^{t_0}=1,\xi_j^{t_0}=0,\xi_{j+1}^{t_0}=0) & \rightarrow & \xi_j^{t_0+\Delta t}=1\\
(\xi_{j-1}^{t_0}=0,\xi_j^{t_0}=1,\xi_{j+1}^{t_0}=1) & \rightarrow & \xi_j^{t_0+\Delta t}=1\\
(\xi_{j-1}^{t_0}=0,\xi_j^{t_0}=1,\xi_{j+1}^{t_0}=0) & \rightarrow & \xi_j^{t_0+\Delta t}=0\\
(\xi_{j-1}^{t_0}=0,\xi_j^{t_0}=0,\xi_{j+1}^{t_0}=1) & \rightarrow & \xi_j^{t_0+\Delta t}=1\\
(\xi_{j-1}^{t_0}=0,\xi_j^{t_0}=0,\xi_{j+1}^{t_0}=0) & \rightarrow & \xi_j^{t_0+\Delta t}=0
\end{array}$$

In abbreviated form this scheme can be rewritten

$$\begin{array}{lcl}
(1,1,1) & \rightarrow & 0\\
(1,1,0) & \rightarrow & 1\\
(1,0,1) & \rightarrow & 0\\
(1,0,0) & \rightarrow & 1\\
(0,1,1) & \rightarrow & 1\\
(0,1,0) & \rightarrow & 0\\
(0,0,1) & \rightarrow & 1\\
(0,0,0) & \rightarrow & 0
\end{array}$$

This rule is encoded by 01011010_2. Such a digital description of the transformation scheme is of course only valid for a particular order of the corresponding basis. This order is commonly chosen as a decimal row with decreasing value, i.e. $(1,1,1) = 111$, $(1,1,0) = 110$, and so on. Transforming the binary code into decimal numbers using

2^7	2^6	2^5	2^4	2^3	2^2	2^1	2^0
0	1	0	1	1	0	1	0

leads to the decimal code number 90_{10}. The digital coding system is commonly used for compactly describing relevant transformation rules for cellular automata (Schulman and Seiden 1978; Vichniac 1984).

If the state of a node is simply determined by the sum of the values taken by the variables of the neighboring sites, the model is referred to as totalistic cellular automaton. If the state of a node has a separate dependence on the state itself and on the sum of the values taken by the variables of the neighbors, the model is referred to as outer totalistic cellular automaton (Wolfram 1986).

As in the exemple shown above, the value of a variable at a node is derived from the state of the neighbors through the employment of transformation rules. These rules are identical at each node. It might seem useful to allow deviations from this condition in the case of nonhomogeneous media. However, such materials are more easily simulated by assigning corresponding properties to the state of the nodes and exploiting the huge variety of possible switching rules rather than by changing the transformation laws locally. The simulation of microstructure evolution with consideration of stochastic processes can be achieved by rendering deterministic into probabilistic transformation rules (Grassberger et al. 1984; Kinzel 1985; Raabe 1998b). If some of the transformation rules refer to different real time scales (e.g. recrystallization and recovery, bulk diffusion and grain boundary diffusion) it is essential to achieve a correct common scaling of the entire system.

The requirement for an artificial adjustment of time scaling among various rules is due to the fact that the transformation behavior is often determined by noncoupled Boolean routines rather than by the exact local solutions to coupled differential equations. The scaling problem becomes essential in the simulation of nonlinear systems. During the simulation it can be useful to refine or coarsen the scale according to the kinetics (time re-scaling) and spatial resolution (space re-scaling).

11.4 Probabilistic Cellular Automata

In order to avoid confusion when discussing nondeterministic cellular automata, one must clearly indicate the stochastic element that appears in the algorithm. There are essentially two possibile ways to transform a deterministic cellular automaton into a nondeterministic one. The first approach consists in selecting the investigated lattice sites randomly, rather than systematically in sequential order, but using a deterministic transformation law. The second approach consists in using a probabilistic instead of a deterministic transformation, but with a systematic investigation of all lattice sites. The first type of automaton is in its basic setup similar to the Potts model[4]. In this section we are exclusively concerned with the latter approach and refer to it as probabilistic or stochastic cellular automaton.

Probabilistic cellular automata are in their elementary setup very similar to conventional cellular automata, except for the fact that the transition rules are stochastic rather than deterministic (Grassberger et al. 1984; Kinzel 1985; Raabe 1998b).

The principle of probabilistic cellular automata is readily explained by considering a one-dimensional chain of N lattice sites, each of which can assume one of k possible states $S_\nu = 0, 1, 2, ..., k-1$. Thus the whole chain can assume k^N different configurations. In the following, a given lattice state described by $(S_1, S_2, ...S_N)$ is labeled by the integer number

$$i = \sum_{\nu=1}^{N} S_\nu \, k^{\nu-1} \tag{11.4}$$

In a probabilistic cellular automaton it is now assumed that each state i occurs with the probability P_i. This probability is a function of time, i.e $P_i(t)$, and develops in discrete time steps $t = 0, 1, 2, ...$ according to some transition probabilities T_{ij}. If only the last time step $(t-1)$ is considered, this rule can be expressed formally by

$$P_i(t) = \sum_{j=0}^{(k^N-1)} T_{ij} \, P_j(t-1) \tag{11.5}$$

Thus, the transfer matrix T_{ij} reflects the probability of obtaining a chain configuration i if the system is in state j at the preceding time step.

Due to the underlying discrete cellular automaton technique, the transfer matrix T_{ij} is defined by local rules, i.e.

$$T_{ij} = \prod_{\nu=1}^{N} p\left(S^j_{\nu-1}, S^j_\nu \, , \, S^j_{\nu+1} \,\middle|\, S^i_\nu \right) \tag{11.6}$$

[4]The Potts model uses both the random sequential selection of lattice sites and a probabilistic transformation algorithm (Monte Carlo method).

where S_ν^j and S_ν^i are the site variables of states j and i, respectively. Thus, the transition of the variable S_ν^j depends only on the state of its nearest neighbors and on its own state. The generalization of this concept from von Neumann to Moore neighboring is straightforward. The time evolution is entirely defined by the matrix p of rank k^3 by k.

Probabilistic cellular automata can use both totalistic and discrete transformation rules. Although probabilistic cellular automata reveal a certain resemblance to the Metropolis Monte Carlo algorithm, two main differences occur. First, in contrast to the Monte Carlo method where only one site is updated per time step, probabilistic cellular automata are, like most automata, updated simultaneously. Second, they are generally not calibrated by any intrinsic length or time scale.

Albeit most cellular automata and especially their probabilistic variants are typically employed to mimic problems at the microscopic level, their scaling parameters are principally determined by the underlying physical model rather than by the cellular automaton algorithm.

11.5 Lattice Gas Cellular Automata

The basic definition of the lattice gas spin model was together with the corresponding Hamiltonian introduced in Chapter 6. The use of lattice gas cellular automata generally allows space- and time-discretized simulations of reaction–diffusion-type phenomena with consideration of stochastic fluctuations.

Although these stochastic automata are typically employed for simulations in the microscopic regime, their use, like that of all automaton-type models, is not necessarily restricted to applications at the microscopic level. They can be used as well to mimic mesoscopic or macroscopic systems, provided that adequate cellular automaton transformation rules can be identified[5].

When used at the microscopic level, lattice gas cellular automaton simulations essentially provide information about the topological evolution of reaction–diffusion systems, but with much less computational effort than is required, by molecular dynamics for instance.

Lattice gas cellular automata were originally suggested by Hardy et al. (1976) for the simulation of time correlation functions and long-term behavior of complex reaction–diffusion systems. In microstructure simulation the use of lattice gas cellular automata has gained momentum, especially for the prediction of diffusion coefficients (Lemarchand and Mareschal 1996) and the solution of Navier–Stokes-type problems (Wolfram 1986; Rothman and Zaleski 1994; Mareschal and Lemarchand 1996).

Lattice gas automata have a number of properties in common with conventional automata, namely, they are discrete in both space and time, they use a discrete lattice, and they are able to mimic complex dynamic system behavior at the macroscopic and mesoscopic level also on the basis of simple local next-neighbor transformation, reaction, and diffusion rules.

The lattice gas cellular automaton grid consists of a regular array of nodes which are connected with their nearest neighbors. The grid can have cubic or hexagonal symmetry. The connections between the sites are often referred to as bonds.

[5]The absence of intrinsic physical scales justifies the presentation of lattice gas cellular automata in this chapter on meso- and microscale approaches rather than together with Monte Carlo (Chapter 6) or molecular dynamics simulations (Chapter 7).

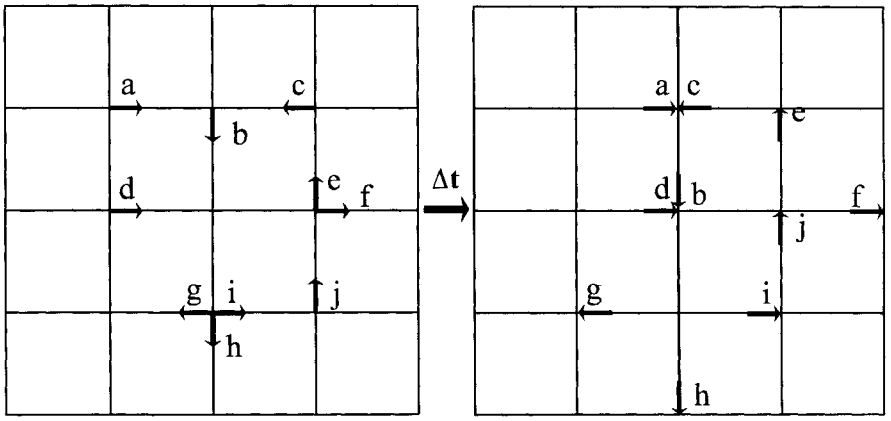

Figure 11.3: Two-dimensional lattice gas cellular automaton with a cubic grid. The diagram shows two consecutive particle arrangements without collisions. The momentum (magnitude of particle velocities), the flight directions, and the mass (particle number) are preserved. In the next step, collisions must be carried out in accord with a set of fixed collision rules. Collisions will occur for particle pairs (a,c) and (b,d).

Typically, the transformation and reaction rules are attached to the nodes rather than to the bonds. In classical cellular automata the lattice sites are assigned by the values of state variables that can assume one out of a certain set of admissible states. In lattice gas automata these state variables are replaced by a discrete set of particles. These have usually a certain velocity, zero mass, and zero interaction energy. The number of particles is conserved during the simulation reflecting the conservation of mass. The state of the nodes in a lattice gas automaton is thus characterized by local particle densities rather than by field variables. The set of particles is referred to as lattice gas.

In a simple two-dimensional lattice gas cellular automaton with cubic grid symmetry, each node can be occupied by at most four particles. These can have four velocities, all equal in absolute value, but pointing in the four possible directions (Figure 11.3). In a grid with a planar hexagonal symmetry each node can be occupied by up to six particles which can have six different velocity vectors (Figure 11.4). In either case configurations are excluded in which more than one particle occupies a given state. This means that no two particles may have the same grid position and direction of their velocity vector. This rule must not be confused with the Pauli principle, but is simply introduced to improve computational efficiency (Mareschal and Lemarchand 1996).

The dynamic evolution of lattice gas cellular automata is as follows. At discrete time intervals Δt, particles are moved from the sites they occupy to the sites, to which they are pointing. At the node, elastic collisions are performed which conserve the mass (number) and momentum (magnitude of the velocity) of the incoming configuration. Figures 11.3 and 11.4 show such consecutive situations, but before the actual collisions. Depending on the configuration of the incoming particles, several post-collision configurations are conceivable. The final node state is then usually randomly chosen among them or selected in accord with a fixed deterministic set of collision rules. Following the pioneering work of Frisch, Hasslacher, and Pomeau (1986), such collision rules are often referred to as FHP collision rules. Figure 11.5 gives some examples of such rules. In the case of inert

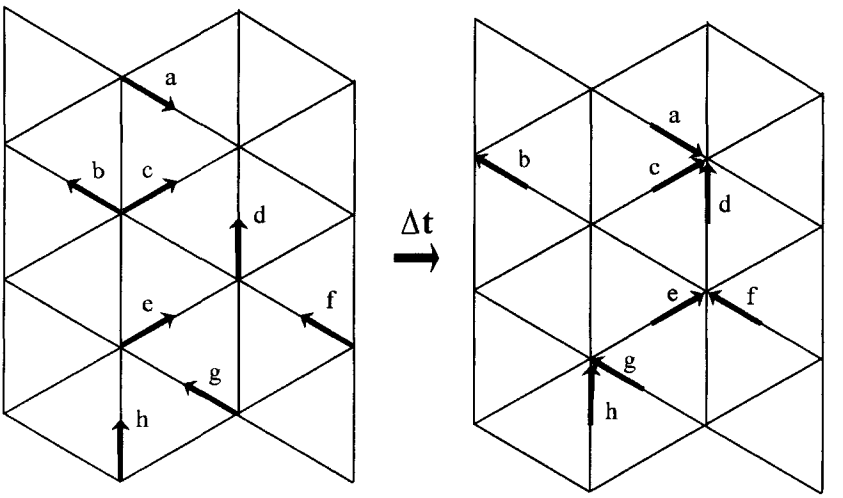

Figure 11.4: Two-dimensional lattice gas cellular automaton with a hexagonal grid. The diagram shows two consecutive particle arrangements without collisions. The momentum (magnitude of particle velocities), the flight directions, and the mass (particle number) are preserved. In the next step, collisions must be carried out in accord with a set of fixed collision rules. Collisions will occur for particle clusters (a,c,d), (e,f), and (g,h).

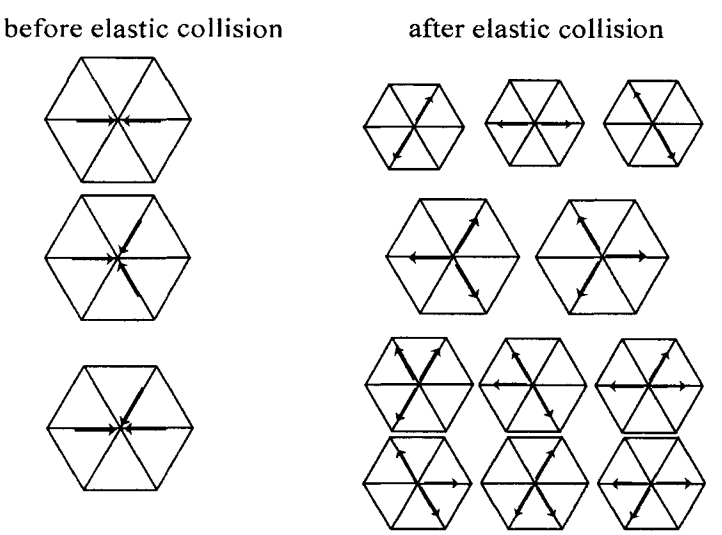

Figure 11.5: Two-dimensional lattice gas cellular automaton with a hexagonal grid. The plots show some possible pre-collision configurations at a node together with some collision rules. The rules represent possible consecutive particle arrangements after elastic collision. Some lattice gas automata select these configurations randomly rather than from a fixed list. During the collision, the momentum (magnitude of particle velocities) and the mass (particle number) are conserved. The flight directions are usually changed.

particles, only collisions are considered. Modified chemical versions of lattice gas cellular automata also consider reactions, where the colliding species may lead to new reaction products with different properties.

The post-collision products and configurations arising from all possible different two-, three-, four-, five-, or even six-particle collisions, including those between ordinary particles and reaction products, are usually recorded in a database before the simulation. The information in this list thus reflects the underlying microscopical physical and chemical characteristics of the particle interactions.

In recent years various modified lattice gas cellular automaton approaches have been suggested, such as the lattice–Boltzmann method, the temperature-dependent lattice gas automaton using a variety of velocity amplitudes, and the various multi-phase models which consider the character of the neighboring particles before the move (Wolfram 1983; Mareschal and Lemarchand 1996).

11.6 Mesh Types for Cellular Automaton Simulations

Most cellular automata used in computational materials science map the state variable distribution on a simple cubic two- or three-dimensional grid using periodic boundary conditions. The neighboring shells considered in the transformation and the symmetry of the mesh can be of substantial influence on the topological evolution of the system. For instance, simple and face-centered cubic lattices which consider only the first and second nearest-neighbor shells artificially inhibit grain growth phenomena, where the driving force is typically computed by using a discrete form of the Gibbs–Thomson equation.

Many two-dimensional cellular automaton simulations dealing with interface phenomena use a mesh with hexagonal symmetry in order to allow the formation artificially of equilibrium angles at triple points (see Section 12.2).

Cellular automata generally do not have an intrinsic scaling length. This value must be derived by some physical argument associated with the phenomenon to be described.

11.7 Optimization of Cellular Automata with Respect to Storage Limitation

In order to reduce the computer memory required by cellular automata, one can in some cases make use of the fact that the information stored in the cells inside an expanding volume is often of no relevance to the further course of the calculation. This applies particularly for the simulation of primary, secondary, and tertiary recrystallization phenomena, solidification, and thin film deposition.

In these cases it is possible to separate the necessary information into two groups. For example, in the case of primary static recrystallization, the first group contains the data of the non-recrystallized cells with a high information density, for instance the local dislocation density and the crystal orientation. The second group contains the data of the recrystallized cells with a relatively low information density necessary to describe the homogeneous interior of the newly formed grains. This approach allows one to store the properties of the deformed microstructure on a hard disk, a low-price storage medium with relatively slow access time, using the entire resolution of the grid. This information can be

Table 11.1: Comparison of the Metropolis Monte Carlo algorithm (Potts lattice model) and the cellular automaton algorithm.

Monte Carlo (Potts model)	Cellular automaton
sequential update	simultaneous update
microscopic length scale	arbitrary length scale
probabilistic	deterministic, probabilistic
applicable to statistical mechanics	not suited for statistical mechanics
applicable to microstructure simulation	applicable to microstructure simulation

retrieved into the main memory during the running time of the program with only a minor increase in computation time. During the whole simulation this information has to be stored on disk only once, namely, when the growth front passes the cell being considered. In contrast, the surface of the growing grains, i.e. the recrystallization front, needs to be constantly monitored during the entire recrystallization process. For this reason, the positions of the grain surfaces must be kept in the comparatively fast and expensive main memory. However, since surface rather than volume data are stored the required capacity in random access computer memory (RAM) depends only on the square of the grid dimension as opposed to a cubic dependence in a conventional three-dimensional model. Therefore, it is possible to simulate larger structures with less computer memory.

For n cubic grains in a grid containing a^3 cells, the number of cells in the surface of these grains N is given by

$$N \leq 6 \sqrt[3]{n}\, a^2 \tag{11.7}$$

For example, assuming a cubic grid with a base length of $a = 500$ cells and considering a number of $n = 100$ grains, one has to consider only $7 \cdot 10^6$ cells as compared with $500^3 = 125 \cdot 10^6$ cells in a conventional model. The latter represents the maximum number of cells and would only be reached if the lattice were filled with grains that just do not impinge upon each other (Marx 1998).

11.8 Cellular Automata and Monte Carlo

Cellular automata are often confused with the Potts Monte Carlo spin model. However, there are fundamental differences between both methods. First, the cellular automaton method is not intrinsically calibrated to the microscopic regime. Provided that adequate elementary units and appropriate algebraic, differential, or integral equations with suitable field variables can be identified, cellular automaton models can be used with arbitrary length and time scales. This is not the case for the Monte Carlo model, which is intrinsically scaled to the microscopic regime. Second, while in all Metropolis and Potts Monte Carlo methods the sites of the generalized spins are examined sequentially by stochastic sampling, cellular automata are updated simultaneously. Third, cellular automata provide a much larger variety of possible deterministic or probabilistic transformation rules than the multistate Potts model. The main similarities and differences between the Potts-type Metropolis Monte Carlo and the cellular automaton algorithm are listed in Table 11.1.

11.9 Simulation of Non-Equilibrium Phenomena

11.9.1 Thermodynamic Aspects

During the thermomechanical processing of metals one encounters a number of non-equilibrium transformation phenomena and microstructure transients such as recyrstallization, continuous grain growth, discontinuous grain growth, tertiary recyrstallization, and discontinuous precipitation. From a microstructural point of view, these transformations have in common that they occur by the motion of high-angle grain boundaries. The movement of homophase interfaces can be described phenomenologically in terms of the transition of atoms or groups of atoms from one grain into a neighboring one, due to a gradient of the Gibbs free enthalpy. The net driving pressure p can be written

$$p = \frac{\mathrm{d}G}{\mathrm{d}V} \tag{11.8}$$

where G is the Gibbs free enthalpy and V the volume affected. In real materials various contributions affect the value of the local free enthalpy.

In cold-worked metals the elastic energy that is stored due to the increased dislocation-density ϱ contributes the largest portion to the driving pressure. Using a classical statistical state variable approach, this contribution $p(\varrho)$ can be written

$$p(\varrho) \approx \frac{1}{2}\,\Delta\varrho\,\mu\,b^2 \tag{11.9}$$

In this equation $\Delta\varrho$ is the difference in dislocation density across the internal interface, μ the bulk shear modulus in the isotropic limit, and b the magnitude of the Burgers vector. Sometimes the contribution of the dislocations that are stored in the cell walls ϱ_{w} and inside the cells ϱ_{i} are expressed separately. While the latter value enters the formula directly, the former one can be expressed in terms of the subgrain size D and the interfacial energy of the subgrain walls γ_{sub}:

$$p(\varrho_{\mathrm{i}}, \varrho_{\mathrm{w}}) \approx \frac{1}{2}\,\Delta\varrho_{\mathrm{i}}\,\mu\,b^2 + \frac{\alpha\,\gamma_{\mathrm{sub}}}{D} \tag{11.10}$$

where α is a constant. Using the Read–Shockley equation, the contribution of the subgrain walls can be calculated as a function of the misorientation angle. Although this approach is somewhat more detailed than that in equation (11.9) it nonetheless neglects the contribution of internal long-range stresses.

A second contribution generally arises from the Laplace or capillary pressure that acts on each crystal. This arises from the tendency to decrease the total interfacial area and can be expressed for spherical grain shapes in terms of the local curvature of the interface. One may assume for a conventional grain size distribution and spherical grain shapes that

$$p(\gamma) = \frac{\alpha\,\gamma}{R} \tag{11.11}$$

where α is a constant of the order 2–3, γ the interfacial energy, and $1/R$ the curvature.

In thin films an additional driving force stems from the gradient in surface energy,

$$p(\gamma_s) = \frac{2\,(\gamma_1 - \gamma_2)\,B\,\mathrm{d}x}{h\,B\,\mathrm{d}x} = \frac{2\,\Delta\gamma\,B}{h} \tag{11.12}$$

where B is the film width, h the film thickness, and $\Delta\gamma$ the change in surface energy.

A chemical contribution to the driving pressure arises in the oversaturated state. The corresponding transformation is referred to as discontinuous precipitation. For small concentrations this chemical driving force amounts to

$$p(c) \approx \frac{k_B}{\Omega} (T_0 - T_1)\, c_0 \ln c_0 \tag{11.13}$$

where k_B is the Boltzmann constant, Ω the atomic volume, T_1 the real temperature during the (numerical) experiment, T_0 the equilibrium temperature which corresponds to the oversaturated concentration at T_1, and c_0 the concentration. A similar contribution can enter the total driving pressure due to the loss of long-range order in a cold-worked or quenched intermetallic material. Further terms, which are of minor relevance in a practical context, are due to gradients of the magnetic, elastic, or temperature field. Possible back driving forces are due to impurity drag (Lücke and Detert 1957; Lücke and Stüwe 1963), particle drag (Hu et al. 1966; Haeßner 1978; Gottstein 1984; Doherty et al. 1990), and the generation of domains behind the moving high-angle grain boundary in ordered alloys (Humphreys and Hatherly 1995).

11.9.2 Kinetic Aspects

For the onset of primary recrystallization a thermodynamic, mechanic, and kinetic instability is required (Cahn 1966; Haeßner 1978; Gottstein 1984; Humphreys and Hatherly 1995). The first type of instability is referred to as nucleation, the second one as net driving force, and the third one as motion of high-angle grain boundaries.

Nucleation during primary recrystallization cannot take place as a homogeneous process in a thermodynamic sense. This means that the gain in free enthalpy that is obtained by locally reducing the elastic energy does *not* effectively compensate the surface energy required to produce the new high-angle grain boundary that surrounds the nucleus. Thus, it is straightforward that heterogeneous nucleation prevails during recrystallization. Potential nucleation sites are areas with very high dislocation densities or small subgrain sizes, respectively, and large local lattice misorientations, such as shear bands, microbands, transition bands, existing high-angle grain boundaries, and deformation zones in the vicinity of precipitates (Himmel 1963; Cahn 1966; Hansen et al. 1995).

During primary recrystallization the criterion of a net driving pressure component normal to the newly formed boundary is usually satisfied. In cases in which smaller driving forces are being considered, such as are encountered in secondary and ternary recrystallization or grain growth, the driving pressure inherent to these processes can be compensated by back driving forces such as those caused by impurities and precipitates.

In the early stages of primary recrystallization, nuclei with high-angle grain boundaries are formed which have the kinematic freedom to sweep as incoherent interfaces through the deformed matrix. In a simple physical picture the motion of high-angle grain boundaries can be described in terms of the diffusion of atoms or atomic clusters through the interface under one or more of the aforementioned driving forces. A symmetric rate equation, which describes interface motion in terms of an isotropic single-atom diffusion process perpendicularly through a homogeneous grain boundary, can be written

$$\dot{\mathrm{x}} = \nu_{\mathrm{D}}\, \lambda_{\mathrm{gb}}\, \boldsymbol{n}\, c \left\{ \exp\left(-\frac{\Delta G - \Delta G_{\mathrm{t}}/2)}{k_{\mathrm{B}}\, T} \right) - \exp\left(-\frac{\Delta G + \Delta G_{\mathrm{t}}/2}{k_{\mathrm{B}}\, T} \right) \right\} \tag{11.14}$$

where $\dot{\mathrm{x}}$ is the velocity of the interface, ν_{D} the Debye frequency, λ_{gb} the jump width through the interface, c the intrinsic concentration of in-plane self-diffusion carrier defects

(e.g. grain boundary vacancies or shuffle sources), $\boldsymbol{n}$ the normal of the grain boundary segment, ΔG the Gibbs enthalpy of motion through in the interface, ΔG_t the Gibbs enthalpy associated with the transformation, k_B the Boltzmann constant, and T the absolute temperature. Bold symbols indicate vector quantities. The Debye frequency is of the order of 10^{13}–10^{14} s^{-1} and the jump width of the order of the magnitude of the Burgers vector. Inserting the enthalpy, the entropy, and the driving pressure, equation (11.14) can be rewritten

$$\dot{x} = \nu_D \lambda_{gb} \boldsymbol{n} \exp\left(\frac{\Delta S^f}{k_B}\right) \exp\left(-\frac{\Delta H^f}{k_B T}\right) \cdot \left\{\exp\left(-\frac{\Delta H^m - T\Delta S^m - (p/2)\Omega)}{k_B T}\right) - \exp\left(-\frac{\Delta H^m - T\Delta S^m + (p/2)\Omega)}{k_B T}\right)\right\} \tag{11.15}$$

where p the driving force (e.g. stored elastic energy or interface curvature), Ω the atomic volume, ΔS^f the entropy of formation, ΔH^f the enthalpy of formation, ΔS^m the entropy of motion, and ΔH^m the enthalpy of motion. The atomic volume is of the order of b^3, where b is the Burgers vector. While ΔS^f mainly quantifies the vibrational entropy, ΔS^m contains both configurational and vibrational contributions. By summarizing these terms, equation (11.15) can be written

$$\dot{x} = \nu_D b \boldsymbol{n} \exp\left(\frac{\Delta S^f + \Delta S^m}{k_B}\right) \sinh\left(\frac{p\Omega}{k_B T}\right) \exp\left(-\frac{\Delta H^f + \Delta H^m}{k_B T}\right) \tag{11.16}$$

Due to the small argument in the sinh, equation (11.16) can be linearized,

$$\dot{x} \approx \nu_D b \boldsymbol{n} \exp\left(\frac{\Delta S^f + \Delta S^m}{k_B}\right) \left(\frac{p\Omega}{k_B T}\right) \exp\left(-\frac{\Delta H^f + \Delta H^m}{k_B T}\right) \tag{11.17}$$

This approximation can be compared with the well-known phenomenological expression which is used for the Arrhenius analysis of experimental grain boundary mobility data,

$$\dot{x} = \boldsymbol{n} m p = \boldsymbol{n} m_0 \exp\left(-\frac{Q_{gb}}{k_B T}\right) p \tag{11.18}$$

where m is the mobility and Q_{gb} the activation energy of grain boundary motion. Comparing the coefficients in equations (11.17) and (11.18) yields

$$m_0 = \frac{\nu_D b \Omega}{k_B T} \exp\left(\frac{\Delta S^f + \Delta S^m}{k_B}\right) \quad \text{and} \quad Q_{gb} = \Delta H^f + \Delta H^m \tag{11.19}$$

equations (11.14)–(11.19) provide a classical kinetic picture of grain boundary motion.

During annealing, primary recrystallization in its advanced state competes to a certain extent with recovery. In the incipient stages of primary recrystallization, local recovery processes promote the formation of nuclei. However, in the latter stages, the continuous degradation of the stored energy due to dislocation annihilation and rearrangements can substantially degrade the local driving force so that recrystallization is slowed down. Assuming that the rate of recovery $\dot{\varrho}$ is proportional to the stored dislocation density ϱ, a simple exponential law can be derived, namely,

$$\varrho(t) = \varrho_0 \exp\left(-\frac{t}{\tau}\right) \tag{11.20}$$

where $\varrho(t)$ is the dislocation density as a function of time t, ϱ_0 the dislocation density after deformation, and τ the relaxation time.

11.9.3 Deterministic Cellular Automaton Solution

This section presents a deterministic cellular automaton approach for simulating primary recrystallization of cold-worked metals. It is assumed that the driving force for both nucleation and growth of newly recrystallized grains is the gradient of the local dislocation density. Growth terminates upon impingement. The cellular automaton method allows one to introduce arbitrary conditions for recovery and nucleation (Reher 1998).

The start data contain information on the geometry of the grid and the values of the state variables, e.g. temperature, nucleation probabilities, grain boundary mobilities, dislocation density, and crystal orientation. These data must be provided in the form of a three-dimensional matrix, i.e. they map the major features of the initial microstructure as a function of space. To reduce the computer memory required, the grains can be numbered and only this number can then be stored for each cell.

The arrays that are held in the main memory of the computer are the so-called grain list and the surface list. The first of these contains information on the crystallographic orientation of the grains. Its entries comprise the number of a grain and the three Euler angles describing its orientation. The second describes only those cells which belong to the surface of a grain. To minimize further the amount of required memory only two indispensable data sets should be stored in this list, namely, the coordinates of the cells and the number of the grain to which this cell belongs.

The main loop of a cellular automaton for simulating primary static recrystallization starts at time t_0. It follows the physical process of primary recrystallization and can be subdivided into three major routines which can be called sequentially during each timestep t_i, viz., recovery, nucleation, and growth of nuclei.

In the recovery step the dislocation density, which is related to the driving force and potentially to the nucleation rate, can be reduced according to the kinetics outlined in equation (11.20). In a simple finite difference formulation a factor $f < 1$ can be calculated which depends on the relaxation time τ, the temperature T, and the time t_i. The dislocation density at time t_i then amounts to

$$\varrho(x_1, x_2, x_3, t_i, T, \tau, \varphi_1, \phi, \varphi_2) = f_\varrho(T, \tau, t_i)\ \varrho(x_1, x_2, x_3, t_0, T, \tau, \varphi_1, \phi, \varphi_2) \qquad (11.21)$$

In a more sophisticated approach the function f might also depend on the local orientation, $\varphi_1, \phi, \varphi_2$, rendering ordinary recovery into orientation dependent recovery.

In the nucleation step individual cells or cell clusters must be switched from the deformed into the recrystallized state.

In the grid this can be described geometrically by an arrangement of spheres with a given radius in the bulk of the sample being modeled. Various deterministic or stochastic nucleation criteria are conceivable. In the simplest possible approach, one can use a site-saturated statistical spatial arrangement of nucleus grains in the deformation matrix without referring to particular criteria. Depending on the underlying model, the orientation of a nucleus could be identical to, similar to ($\Delta \boldsymbol{g} \leq 15°$), or different from that of the surrounding deformation matrix ($\Delta \boldsymbol{g} > 15°$). Nuclei with identical or similar orientation can only grow when they are located on existing high-angle grain boundaries, where they can grow into neighboring grains with a sufficiently different orientation. In a somewhat more physical approach one could select only those cells as nucleation sites that reveal a maximum in the stored energy and/or a maximum local misorientation in the deformation matrix. Combining these criteria which are characteristic features of the considered grain orientation with the rule of producing nuclei with a similar orientation to the surrounding host matrix amounts to assuming oriented nucleation. The decision about the nucleation

event could be made by applying a deterministic rule or a Monte Carlo step. Introducing the latter transformation rule would change the deterministic cellular automaton into a hybrid automaton with a probabilistic nucleation and a deterministic growth and recovery module.

After the nucleation step, the nucleus grain can be added to the grain list. It is usually assumed to be of spherical shape. All cells which belong to the surface of this sphere should be appended to the surface list. Cells in the interior of the sphere are marked as recrystallized. Usage of spheres is necessary to suppress the strong influence of the grid geometry on the shape of the developing grains. The nucleation condition determines the number of nuclei N_i that are created at time t_i. Different nucleation conditions such as site-saturation and constant nucleation rate can be easily implemented.

In the growth step a loop can be executed for each nucleus over all the cells that belong to the surface of the grain considered. During this loop the difference in crystallographic orientation between a surface cell and its non-recrystallized neighbor cells is determined. The grain boundary mobility is a function of this misorientation $\Delta \boldsymbol{g}$ and the temperature T. Its value can be extracted from a simple reference table. For Read–Shockley type small angle boundaries and twin boundaries with a low coincidence value, such as $\Sigma = 3$ or $\Sigma = 9$, the mobility is usually set equal to zero.

In the case of primary recrystallization the local driving force depends on the actual dislocation density ϱ of the non-recrystallized cell. The velocity of the moving boundary, i.e. the growth step (in units of cell diameters) in a single time increment, is the product of driving force and mobility. As a result the surface cell considered is displaced laterally into its environment by the calculated number of cells in the direction of its neighbor cell. This movement can be performed by means of Bresenham's algorithm adapted for a three-dimensional environment. All cells encountered during this displacement are marked as recrystallized. Growth ceases when the recrystallized cells impinge upon each other (Hesselbarth and Göbel 1991; Pezzee and Dunand 1994; Marx and Raabe 1995; Raabe et al. 1996; Marx et al. 1996).

11.9.4 Probabilistic Cellular Automaton Solution

Differential equations of the type given in equations (11.17) or (11.18) can be directly used as transformation rules in a mesoscale kinetic cellular automaton. In contrast to the deterministic approach described above, the probabilistic cellular automaton method consists in replacing the deterministic integration by a stochastic one using a weighted random sampling scheme. For this purpose equation (11.17) or (11.18) must be separated into a deterministic part, $\dot{\mathrm{x}}_0$, and a probabilistic part, w,

$$\dot{\mathrm{x}} = \dot{\mathrm{x}}_0\, w = \boldsymbol{n}\, \frac{k_\mathrm{B}\, T m_0}{\Omega}\, \frac{p\,\Omega}{k_\mathrm{B}\, T}\, \exp\left(-\frac{Q_\mathrm{gb}}{k_\mathrm{B}\, T}\right) \tag{11.22}$$

where $\dot{\mathrm{x}}$ is the velocity of the boundary and

$$\dot{\mathrm{x}}_0 = \boldsymbol{n}\, \frac{k_\mathrm{B}\, T m_0}{\Omega} \qquad \text{and} \qquad w = \frac{p\,\Omega}{k_\mathrm{B}\, T}\, \exp\left(-\frac{Q_\mathrm{gb}}{k_\mathrm{B}\, T}\right) \tag{11.23}$$

The simulations are to be conducted on a spatial mesh, the given scale of which, λ_m, is much above the atomic scale (λ_m can relate to the dislocation cell size or some similar more or less arbitrary quantity). If a transformation event takes place, the grain thus

grows (or shrinks) by λ_m^3 rather than b^3. For correcting the scaling, equation (11.22) must therefore be rewritten

$$\dot{\mathbf{x}} = \dot{\mathbf{x}}_0\, w = \boldsymbol{n}\,(\lambda_m\,\nu)\; w \qquad \text{with} \qquad \nu = \frac{k_B\, T m_0}{\Omega\,\lambda_m} \tag{11.24}$$

However, depending on the value of λ_m, the time scale, $(1/\nu)$, imposed by such a frequency might be not appropriate for stochastic integration. It is therefore helpful to normalize the above equation by an attack frequency ν_0, so that

$$\dot{\mathbf{x}} = \dot{\mathbf{x}}_0\, w = \boldsymbol{n}\,\lambda_m\,\nu_0 \left(\frac{\nu}{\nu_0}\right) w = \hat{\dot{\mathbf{x}}}_0 \left(\frac{\nu}{\nu_0}\right) w = \hat{\dot{\mathbf{x}}}_0\, \widehat{w} \tag{11.25}$$

where

$$\hat{\dot{\mathbf{x}}}_0 = \boldsymbol{n}\,\lambda_m\,\nu_0 \qquad \text{and} \qquad \widehat{w} = \left(\frac{\nu}{\nu_0}\right) \frac{p\,\Omega}{k_B\, T} \exp\left(-\frac{Q_{gb}}{k_B\, T}\right) = \frac{m_0\, p}{\lambda_m\,\nu_0} \exp\left(-\frac{Q_{gb}}{k_B\, T}\right) \tag{11.26}$$

While $\hat{\dot{\mathbf{x}}}_0$ is determined by the mesh size and the chosen attack frequency, $\widehat{w}$ is determined by the temperature and experimental input data. For instance, the grain boundary characteristics involved can depend on the misorientation and plane inclination, and the driving forces on the stored elastic energy and local curvature. Coupled sets of differential equations of the type given by equation (11.25) can be integrated stochastically.

11.10 Application of Cellular Automata in Materials Science

This section gives a number of classical or recently published references on applications of cellular automata simulations related to various domains of materials science. The list can by no means be complete but it may serve as a bibliography for getting better acquainted with some examples of the recent original literature in this field. Materials-related applications of cellular automaton simulations are particularly in the field of transformation phenomena, such as those encountered during solidification and recrystallization. A second major portion of the publications is concerned with reaction–diffusion systems and lattice gas automata.

Field of application	Reference
fundamentals, mathematical properties	Schulman and Seiden (1978)
	Wolfram (1983)
	Vichniac (1984)
	Packard and Wolfram (1985)
	Wolfram (1985)
	Wolfram (1986)
	Stauffer (1991)
	Mahnke (1996)
primary static recrystallization	Hesselbarth and Göbel (1991)
	Pezzee and Dunand (1994)
	Marx and Raabe (1995)

	Marx, Raabe, and Gottstein (1995)
	Marx, Raabe, and Gottstein (1996)
	Sheldon and Dunand (1996)
	Raabe (1998b)
	Reher (1998)
reaction–diffusion and lattice gas automata	Frisch, Hasslacher, and Pomeau (1986)
	Berryman and Franceschetti (1989)
	Gerhardt and Schuster (1989)
	Dab, Lawniczak, and Boon (1990)
	Kong and Cohen (1991)
	Mai and von Niessen (1991)
	van der Hoef and Frenkel (1991)
	Sahimi (1993)
	Chopard, Luthi, and Croz (1994)
	Cheng, Chan, and Chau (1995)
	Cohen and Wang (1995)
	Wang and Cohen (1995)
	Lemarchand and Mareschal (1996)
	Mareschal and Lemarchand (1996)
crystal dislocation recovery	Raabe, Roters, and Marx (1996)
fracture mechanics	Ossadnik (1993)
	Henderson, Main, and Norman (1994)
dendrites and crystal solidification	Packard (1986)
	Cortie (1993b)
	Gandin and Rappaz (1994)
	Brown, Williams, and Spittle (1994)
	Spittle and Brown (1995)
	Rezende, Ludwig, and Sahm (1996)
	Gandin and Rappaz (1997)
dislocation patterning and kink formation	Hesselbarth and Steck (1992)
	Nummelin (1994)
	Lépinoux (1996)
sintering	Pimienta, Garboczi, and Carter (1992)
phase transition phenomena	Alexander, Edrei, and Garrido (1992)
	Karapiperis (1995)
	Bussemaker, Deutsch, and Geigant (1997)
	Petersen and Alstrom (1997)
crystal and domain growth	Langer (1980)
	Kessler, Levine, and Koplik (1984)
	Willson (1984)
	Ben-Jakob, Goldenfeld, Langer, and Schon (1985)
	Takahashi and Suzuki (1990)
	Kohyama (1991)
	Willson (1992)
	Braga, Cattaneo, and Vogliatti (1995)
	Liu, Baudin, and Penelle (1996)
	Davies (1997b)
two-phase grain structures	Spittle and Brown (1994)

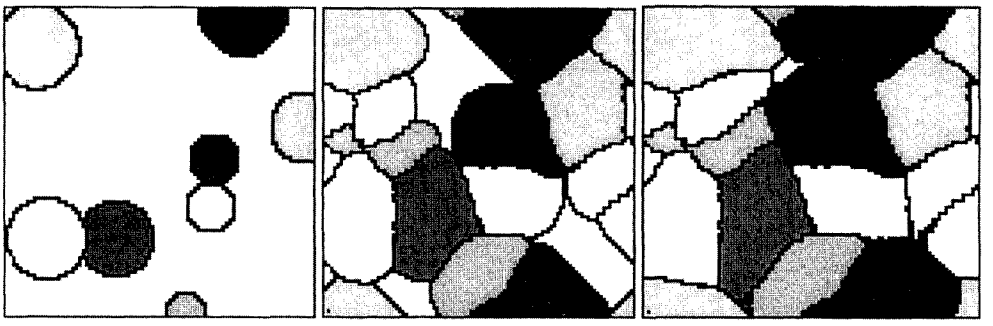

Figure 11.6: Consecutive sections of a recrystallizing sample. Deterministic 3D cellular automaton simulation. The grid size amounts to 200 × 200 × 200 points (Reher 1997).

11.11 Examples of Cellular Automaton Simulations in Materials Science

11.11.1 Simulation of Recrystallization by Use of a CA with Deterministic Transformation Rules

This section presents a deterministic three-dimensional cellular automaton simulation. The method has been developed to simulate primary recrystallization of strongly cold-worked metals (Marx and Raabe 1995; Marx et al. 1995; Gottstein 1996; Reher 1998).

The driving force for the nucleation and growth of recrystallized grains is the dislocation density of the deformed matrix. Growth terminates upon impingement. The model allows one to introduce different conditions for recovery, nucleation and grain growth. The model is capable of simulating kinetics, microstructure and texture development during recrystallization. Figure 11.6 shows some consecutive sections of a recrystallizing sample. Figure (11.7) shows three sections through the center of a simulated recrystallization microstructure. The simulation used a grid of 200 × 200 × 200 points in real space. Figure (11.8) shows two sections of a simulated recrystallization microstructure. The simulations were conducted with different nucleation rates.

11.11.2 Simulation of Recrystallization and Coarsening by Use of a CA with Stochastic Transformation Rules

This section gives an example of an application of a discrete kinetic three-dimensional stochastic cellular automaton. The local transformation rule of the automaton consists in solving a probabilistic analogue of a classical linear symmetric rate equation for grain boundary segment motion at each site of a three-dimensional lattice (Raabe 1998b). The rate equation is turned into a form which makes it usable at the mesoscopic scale. The time integration of the underlying differential equations is achieved through a weighted Monte Carlo scheme[6]. The stochastic cellular automaton allows one the spatial, kinetic,

[6]The use of a probabilistic transformation rule that acts on each site synchronously must not be confused with the Potts model, where the sites are picked randomly, and where the update is sequential.

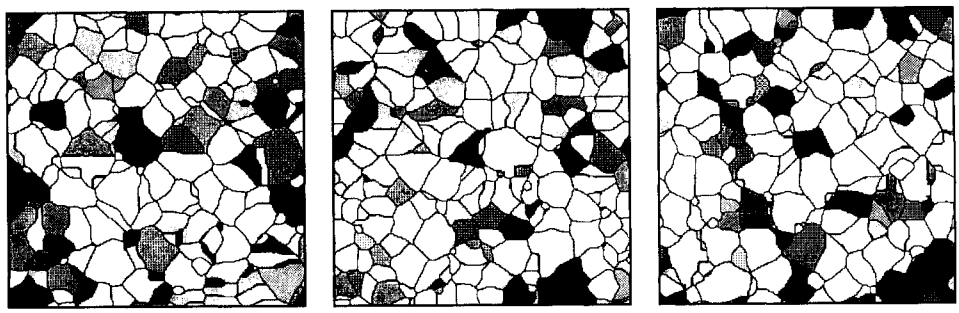

Figure 11.7: Three perpendicular sections from a deterministic 3D cellular automaton simulation. The grid size amounts to 200 × 200 × 200 points (Reher 1997).

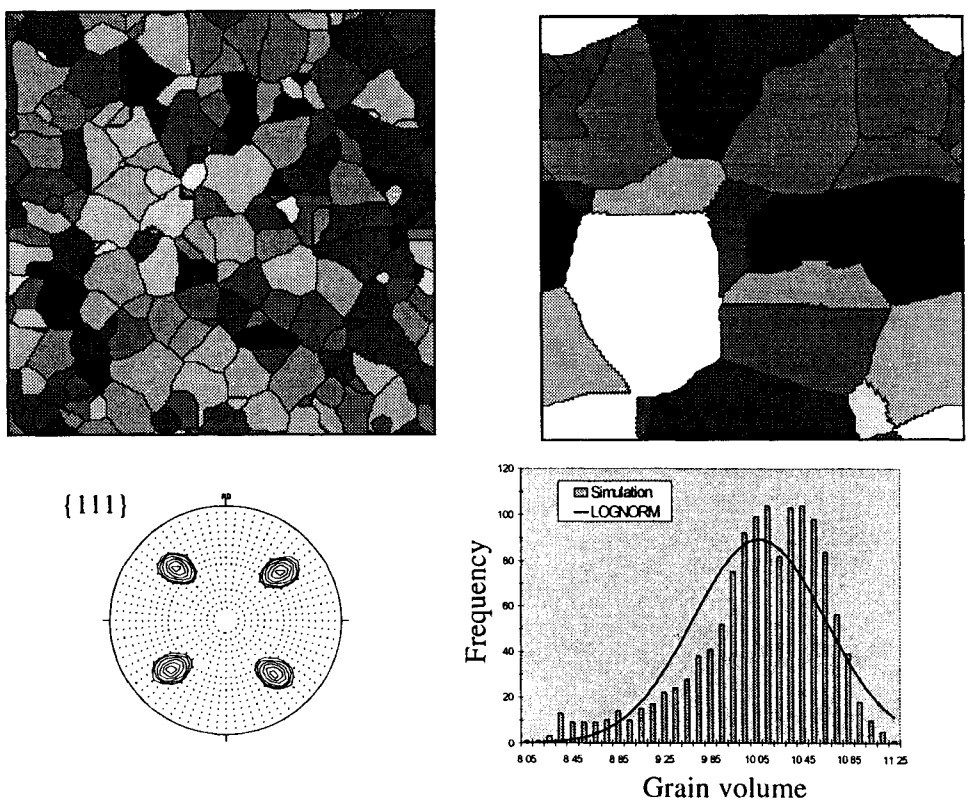

Figure 11.8: 2D sections from a deterministic 3D cellular automaton simulation on the basis of deformation data incorporated from a preceding finite element simulation. Simulation in areas with a high and a low nucleation rate. The diagram also shows the final texture and the grain size distrubution (Reher 1997).

and crystallographic simulation of mesoscale transformation phenomena that involve non-conserved orientational field variables and the motion of sharp interfaces. The automaton is discrete in time, real space, and orientation space. The approach works without empirical quantities and allows one to incorporate theoretical or experimental texture, mobility, and grain boundary energy data.

Figure 11.9 shows a two-dimensional recrystallization simulation of a heavily deformed aluminum single crystal with a uniform near-cube orientation and an initial dislocation density of 10^{15} m^{-2}. The driving force is due to the stored elastic energy. Crystal recovery and the back driving force arising from boundary curvature are not considered.

The simulation uses site-saturated nucleation conditions with a statistical distribution of the nuclei in real and orientation space. It considers three classes of grain boundaries.

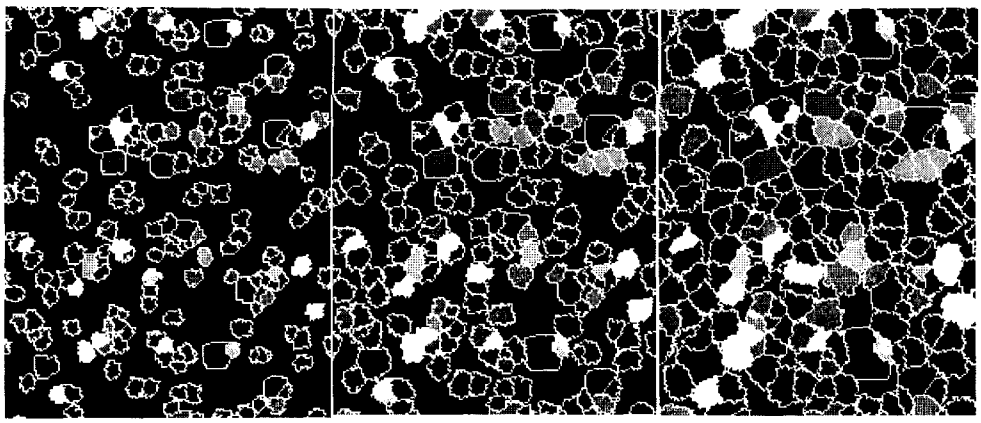

Figure 11.9: 2D recrystallization of an aluminum single crystal, $T = 800$ K, 30%, 51%, and 82% recrystallized, square length 20 μm. Probabilistic 3D cellular automaton simulation (Raabe 1998).

The near 35° $\langle 112 \rangle$ special boundaries are characterized by $Q_1 = 1.58$ eV and $\ln m_{01}/\gamma = 16.4$ μm^2/s, the near 40° $\langle 111 \rangle$ special boundaries by $Q_2 = 1.56$ eV and $\ln m_{02}/\gamma = 16.8$ μm^2/s, and average boundaries by $Q_a = 1.60$ eV and $\ln m_{0a}/\gamma = 16.0$ μm^2/s. Q is the activation energy of the mobility, m_0 the temperature-independent part of the mobility, and γ the grain boundary energy. The ratio m_0/γ is referred to as reduced mobility. γ is assumed as 0.7 J/m^2. The boundary planes can have arbitrary inclination.

Figure 11.10 shows some consecutive two-dimensional sections from a three-dimensional grain growth simulation of a recrystallized aluminum single crystal. This automaton works on a three-dimensional cubic lattice considering the first, second, and third neighbor shell for the calculation of the local Laplace driving pressure that acts through the boundary curvature on each portion of the interface. All equations of motion are simultaneously integrated using a weighted stochastic sampling integration scheme. The presented simulations were carried out for a temperature of $T = 800$ K with a grid length of 30 μm. The sections were taken after 0 s, 75 s, 755 s, and 1510 s.

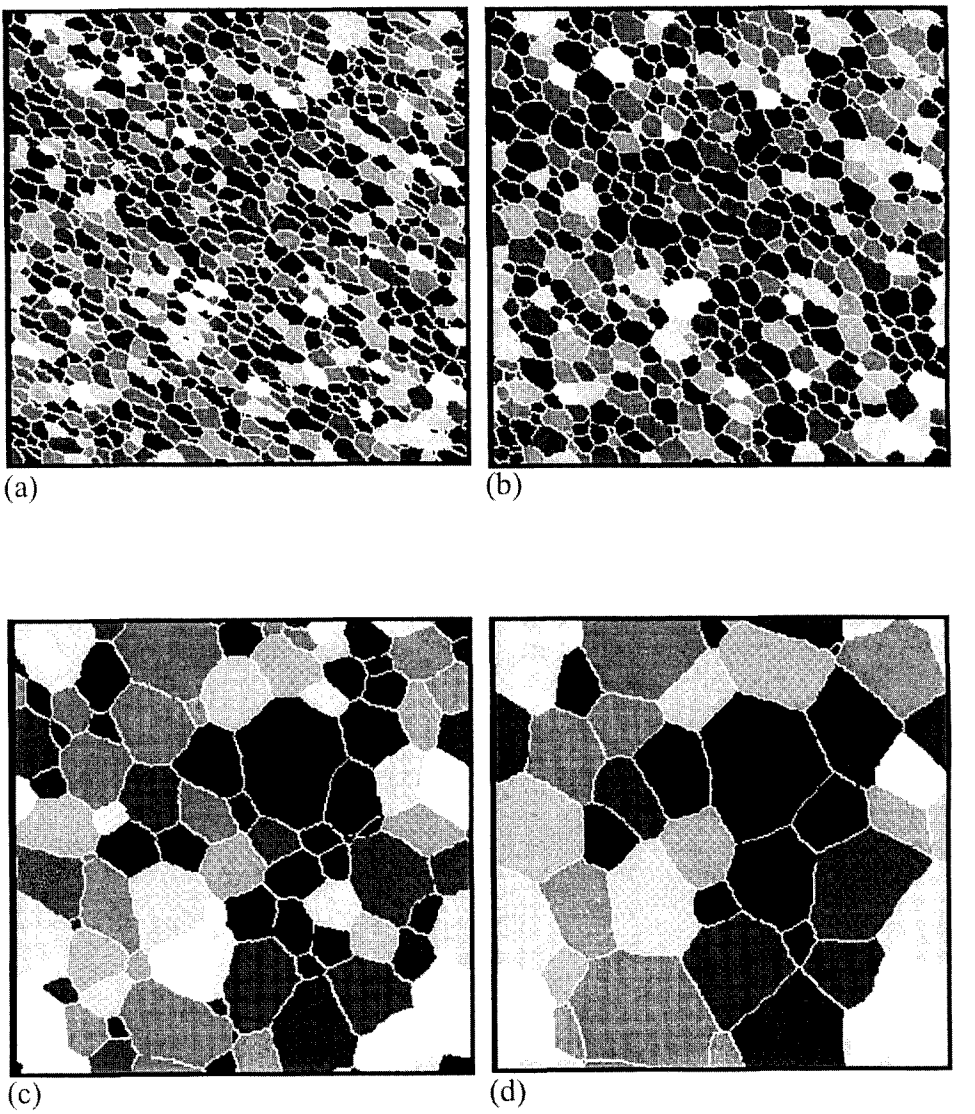

Figure 11.10: Some consecutive 2D sections from a 3D grain growth simulation of a recrystallized aluminum single crystal, $T = 800$ K, section length $30\,\mu m$, (a) 0 s, (b) 75 s, (c) 755 s, (d) 1510 s. Probabilistic 3D cellular automaton simulation (Raabe 1998).

Chapter 12

Mesoscale Kinetic Monte Carlo and Potts Models

12.1 Introduction and Fundamentals

The application of the Metropolis Monte Carlo method (Chapter 6) in microstructure simulation has gained momentum particularly through the extension of the Ising lattice model for modeling magnetic spin systems to the kinetic multistate Potts lattice model (Potts 1952; Wu 1982).

The original Ising model is in the form of a $\frac{1}{2}$ spin lattice model where the internal energy of a magnetic system is calculated as the sum of pair-interaction energies between the atoms or molecules, which are attached to the nodes of a regular lattice (Huang 1963; Binder 1984; Koonin 1986; Binder 1991a; Yeomans 1992). The Hamiltonian is defined in equation (6.31). In its original version the Ising spin model takes a quasi-thermodynamic view of the local magnetic interactions without quantifying time (Chapter 6).

The Potts model deviates from the Ising model by generalizing the spin and by using a different Hamiltonian. It replaces the boolean spin variable where only two states are admissible ("spin up", "spin down") by a generalized variable S_i which can assume one out of a discrete set of q possible states, and accounts only for the interaction between dissimilar neighbors as defined by equation (6.36) (Potts 1952; Wu 1982; Fernandez 1989; Hu and Hsiao 1992; Bassler and Zia 1994; Chen and Hu 1994; Chen et al. 1995; Janke and Villanova 1995; Eichorn and Binder 1996).

The introduction of such a discrete spectrum of possible spins enables one to represent domains by regions of identical spin or better state. For instance, in microstructure simulation such domains can be interpreted as areas of similarly oriented crystal material. Each of these spin orientation variables can then be equipped with a set of characteristic state variable values quantifying for instance the lattice energy, the surface energy, the dislocation density, the Taylor factor, or any other structure- or orientation-dependent constitutive quantity of interest. Lattice regions which consist of domains with identical spin or state can be interpreted as crystal grains (Figure 12.1). The values of the state variable enter the Hamiltonian of the Potts model. The most characteristic property of this energy operator is that it defines the interaction energy between nodes with like spins to be zero, and between nodes with unlike spins to be one (equation (12.4)). This rule

Computational Materials Science: The Simulation of Materials, Microstructures and Properties By Dierk Raabe
Copyright © 1998 Wiley-VCH Verlag GmbH
ISBN: 3-527-29541-0

14	14	14	14	14	14	9	9	15	15	1	4	4	4	4
3	3	14	14	14	10	10	15	15	15	4	4	4	4	4
3	3	16	16	10	10	10	10	15	15	7	7	4	4	4
3	3	16	16	10	10	11	11	7	7	7	7	5	5	3
3	3	3	16	8	8	11	11	7	7	7	7	5	5	3
3	3	3	8	8	11	11	11	7	7	7	5	5	5	3
9	9	9	8	8	8	11	11	7	7	7	5	5	5	9
9	9	9	8	8	11	11	11	7	7	5	5	12	9	9
9	9	9	9	10	10	11	11	9	7	5	5	5	12	9
9	9	9	10	10	10	9	9	9	4	5	5	5	12	9
9	7	7	7	10	10	9	9	9	4	4	4	4	4	7
7	7	7	7	1	10	9	9	9	4	4	4	4	7	7
7	7	7	7	1	1	1	9	9	14	4	4	4	9	7
7	1	1	1	1	1	1	9	14	14	14	14	9	9	7
7	1	1	1	1	1	1	14	14	14	14	14	14	9	9

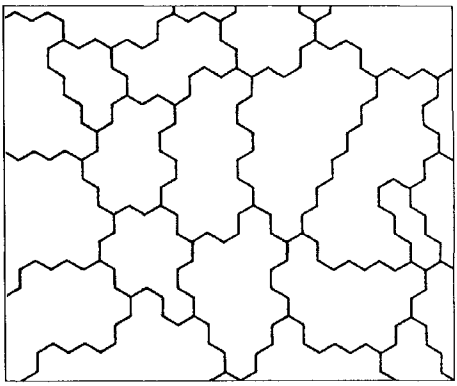

Figure 12.1: Mapping of generalized spin numbers to sites in a Potts lattice model. This approach allows one to represent domains discretely by regions of identical spin. Such areas can be interpreted as crystal grains. Each lattice site is then assigned a certain energy content, reflecting for instance the stored elastic energy arising from plastic deformation (Tavernier and Szpunar 1991).

allows the identification of interfaces and the quantification of the interfacial energies for each boundary segment as a function of the abutting domains.

This property of the Potts model makes it very versatile for describing coarsening phenomena. In this field it takes a quasi-microscopic metallurgical view of grain growth or ripening, where the crystal interior is composed of lattice points (e.g. atom clusters) with identical energy (e.g. orientation) and the grain boundaries are the interfaces between different types of such domains. As in a real ripening scenario, interface curvature leads to increased wall energy on the convex side and thus to wall migration (Figure 12.2) (Srolovitz et al. 1984; Grest et al. 1988; Glazier et al. 1990; Holm et al. 1996). The discrete simulation steps in the Potts model, by which the progress of the system towards thermodynamic equilibrium, i.e. the kinetic evolution, takes place, are typically calculated by randomly switching lattice sites and weighting the resulting interfacial energy changes in terms of Metropolis Monte Carlo sampling. In pure coarsening simulations the switching of sites that are inside domains without any connection to existing interfaces is of no relevance and can be regarded as fluctuation. In Potts simulations which also include a state-variable measure for the orientation-dependent stored elastic energy, fluctuation inside grains can be interpreted as nucleation events of primary recrystallization.

Switching events that are relevant for coarsening can only take place by orientation changes of sites close to interfaces. This means that, if the new total configurational energy after switching two interface domains A and B, is *smaller* than the preceding one, the move would bring the system to a state of lower total interfacial energy. Hence, the move is accepted and the switched domains remain in their respective new positions. However, if the new energy *exceeds* the preceding one, i.e. if the configurational change ΔE has a positive value, the move is accepted only with a certain probability, namely

$$p_{\mathrm{A}\to\mathrm{B}} \propto \exp\left(-\frac{\Delta E}{k_{\mathrm{B}}T}\right) \tag{12.1}$$

One now generates a pseudo-random number ξ between 0 and 1 and determines the new

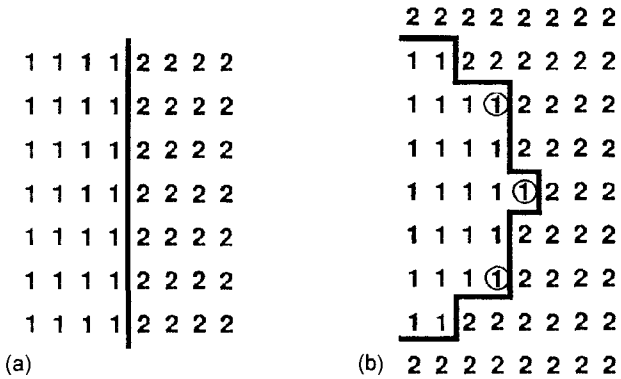

Figure 12.2: Characterization of a grain boundary in the Potts model. (a) Flat interface; interaction among nearest (NN) and next-nearest neighbors (NNN); all spins assigned to the boundary segments i have an energy of γ^i. Single flips to change the topology through bulging entail an energy increase from three to five "interaction" pairs. Neglecting geometrical corrections, i.e. different weighting functions for NN and NNN, the energy of the bulging cell would increase from $3\,\gamma$ to $5\,\gamma$. (b) Convex interface; interaction among NN and NNN; boundary cells i have an energy of γ^i. The circled spins reduce energy by flipping ($5\,\gamma \rightarrow 3\,\gamma$). The grain with spins 2 will grow at the expense of grain 1 (Srolovitz et al. 1984; Glazier et al. 1990).

interface configuration according to the rule:

$$\xi \begin{cases} \leq \exp\left(-\frac{\Delta E}{k_B T}\right) & : \text{ the switch is accepted} \\ > \exp\left(-\frac{\Delta E}{k_B T}\right) & : \text{ the switch is not accepted} \end{cases} \tag{12.2}$$

If the new configuration is rejected, one counts the original position as a new one and repeats the process by switching two other arbitrarily chosen neighboring interface domains.

Although multistate Potts models thus correctly describe grain coarsening phenomena in terms of the weighted change of crystal orientations across boundaries, and typically reveal a distinct topological transient evolution, originally they did not provide a clear kinetic measure of these changes.

This disadvantage was to a certain extent surmounted by the introduction of the kinetic multistate Potts models. Like all Monte Carlo methods, they sample the N sites in the array in a random fashion. N such trial rearrangements are then defined as one Monte Carlo step (Anderson et al. 1984; Rollett et al. 1989). This method of introducing a kinetic unit into the model amounts to interpreting these N reorientation attempts as one single *simultaneous* sampling step rather than a number of N *successive* sampling steps. The number of such Monte Carlo steps is then used as a unit proportional to time. The microstructural evolution is reflected by the temporal mesoscopic development of the domain size and shape. While the classical Monte Carlo approach is confined to time-independent predictions of state function values, through the advent of the kinetic Potts model it becomes a convenient means in simulating microstructure evolution (Srolovitz et al. 1984).

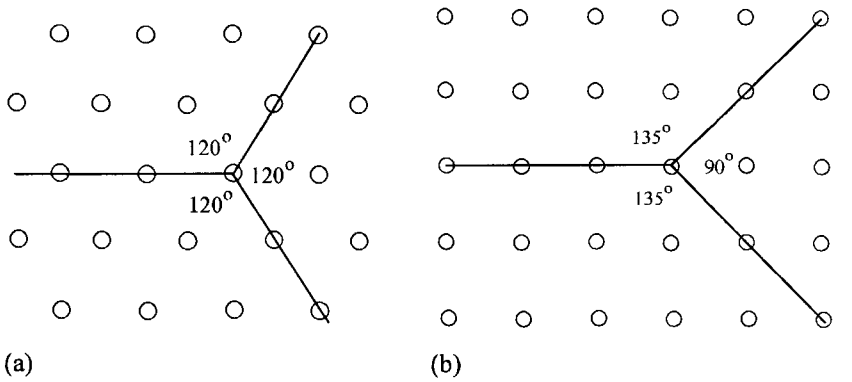

Figure 12.3: Influence of lattice symmetry on the angles at triple points in two-dimensions. The use of hexagonal planar grids supports the evolution of the 120° angles at boundary triple points (a). The use of a simple square lattice with consideration of the first and second nearest-neighbor shells leads to the formation of 135° and 90° angles at boundary triple points (b).

Materials-related Potts-type simulations have been devoted to nucleation (Tavernier and Szpunar 1991b), static primary recrystallization (Srolovitz et al. 1986; Srolovitz et al. 1988; Rollett et al. 1989; Tavernier and Szpunar 1991a; Holm et al. 1996), normal grain growth (Anderson et al. 1984; Srolovitz et al. 1984), secondary recrystallization (Rollett et al. 1989; Holm et al. 1996), dynamic recrystallization (Rollett et al. 1992; Peczak 1995; Holm et al. 1996), recrystallization in the presence of particles (Doherty et al. 1990; Holm et al. 1996), and solidification (Müller-Krumbhaar 1989).

12.2 Influence of Grid Size and Symmetry

According to Glazier, Anderson, and Grest (1990), reliable simulations on the basis of the Potts model are obtained if the lattice has at least 1000 spins per lattice side. The Potts model can be used both with von Neumann neighboring (nearest-neighbor interaction) and with Moore neighboring (first, second, and third nearest-neighbor interaction (three-dimensional)) (Chapter 11, Figure 11.2).

Most of the early Potts simulations used a hexagonal planar grid. This symmetry artificially supports the evolution of the 120° angles at boundary triple points. This angle maps the equilibrium topology of grain boundaries in two-dimensional structures when all the interface energies are identical. In contrast, the use of a simple square lattice with consideration of the first and second nearest-neighbor shells leads to the formation of 135° and 90° angles at boundary triple points (Figure 12.3). In most recent simulations, particularly in the three-dimensional versions, simple cubic lattices are preferred.

Both the symmetry and the considered neighboring have a substantial influence on the energetics and thus on the topological evolution of the system. For instance, simple and face-centered cubic lattices which consider only the first and second nearest-neighbor shells artificially inhibit grain growth. However, when used with consideration of the first, second, and third nearest-neighbor shells, simple cubic lattices do not inhibit grain growth.

12.3 Application of Multistate and Kinetic Potts Models in Materials Science

This section gives some references on examples of applications of Potts simulations related to materials science. The list can by no means be complete but may serve as a bibliography for getting better acquainted with the original literature in this field. Materials-related applications of the Potts model have been devoted to nucleation, static primary recrystallization, normal grain growth, secondary recrystallization, dynamic recrystallization, recrystallization in the presence of particles, solidification, and diffusion.

Field of application	Reference
classics, fundamentals	Potts (1952)
	Wu (1982)
	Binder (1984)
	Binder (1991c)
nucleation	Tavernier and Szpunar (1991b)
primary recrystallization	Srolovitz, Grest, and Anderson (1986)
	Srolovitz, Grest, Anderson, and Rollett (1988)
	Rollett, Srolovitz, Doherty, and Anderson (1989)
	Tavernier and Szpunar (1991a)
	Holm, Rollett, and Srolovitz (1996)
normal grain growth	Anderson, Srolovitz, Grest, and Sahni (1984)
	Srolovitz, Anderson, Sahni, and Grest (1984)
	Mehnert and Klimanek (1998)
secondary recrystallization	Rollett, Srolovitz, and Anderson (1989)
	Holm, Rollett, and Srolovitz (1996)
dynamic recrystallization	Rollett, Luton, and Srolovitz (1992)
	Peczak (1995)
	Holm, Rollett, and Srolovitz (1996)
grain growth with particles	Doherty, Li, Anderson, Rollett, and Srolovitz (1990)
solidification	Müller-Krumbhaar (1989)

12.4 Examples of Potts Simulations in Materials Science

12.4.1 Grain Coarsening Phenomena

In the basic variant of the Potts model (1952) the interaction energy between nodes with like spins is defined to be zero, and between nodes with unlike spins to be one. The corresponding Hamiltonian thus contains sums of the components of the Kronecker symbol, multiplied by the exchange interaction energy J between nearest neighbors (NN) (Binder 1984). For the case of the multistate Potts model, which is based on using a set of q generalized spin numbers, the Hamiltonian for the two-dimensional case can be written

$$\mathcal{H}_{\text{Potts}} = -J \sum_{\langle i,j \rangle} \left(\delta_{s_i\, s_j} - 1 \right) \qquad s_i = 1, 2, ..., q \tag{12.3}$$

where q is the number of possible states, and $\langle i, j \rangle$ the sum over nearest-neighbor pairs in the lattice.

In microstructure simulation the above energy operator can be extended to allow the identification of internal interfaces because it defines a nonvanishing interaction energy between lattice points with unlike generalized spin, and zero energy between points of identical spin. Following Rollett, Srolovitz, Doherty, Anderson, and Grest (1990) a Potts-type operator for the simulation of orientation-dependent problems can be formulated according to

$$\mathcal{H}_{gg} = -\frac{J}{2} \sum_{i}^{N} \sum_{j}^{nn} \left(\delta_{s_i s_j} - 1\right) \qquad s_i = 1, 2, ..., q \tag{12.4}$$

where q is the number of texture components considered, s_k the corresponding spin number of each lattice site representing a particular crystal orientation g_k in which the site is embedded, $\sum_i^N$ the sum over all lattice sites, and $\sum_j^{nn}$ the sum over all nearest neighbors. Lattice sites s_i that are adjacent to sites having different grain orientations $s_{j \neq i}$ are defined as being separated by a high-angle grain boundary (Figure 12.1). Lattice sites which are surrounded by sites with the same orientation are located in the grain interior. Thus, equation (12.4) yields an energy value J for each unlike pair of sites which amounts to identifying a grain boundary.

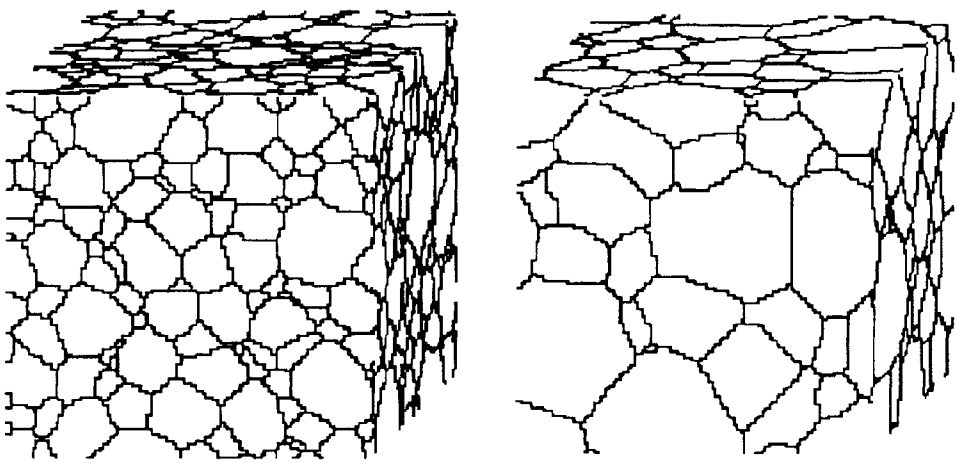

Figure 12.4: Three-dimensional grain growth simulation using a kinetic Potts Monte Carlo model (Mehnert 1998).

In a more generalized q-state Potts model the exact value of the interface energy J could even vary depending on the respective values of the energy or respectively of the orientation variables that are assigned to the considered neighboring lattice sites. Such a general approach may be referred to as a microscopic multistate interface model.

A grain growth simulation that is based on this approach is shown in Figure 12.4. Figure 12.5 shows a similar grain growth simulation, but with additional consideration of particles.

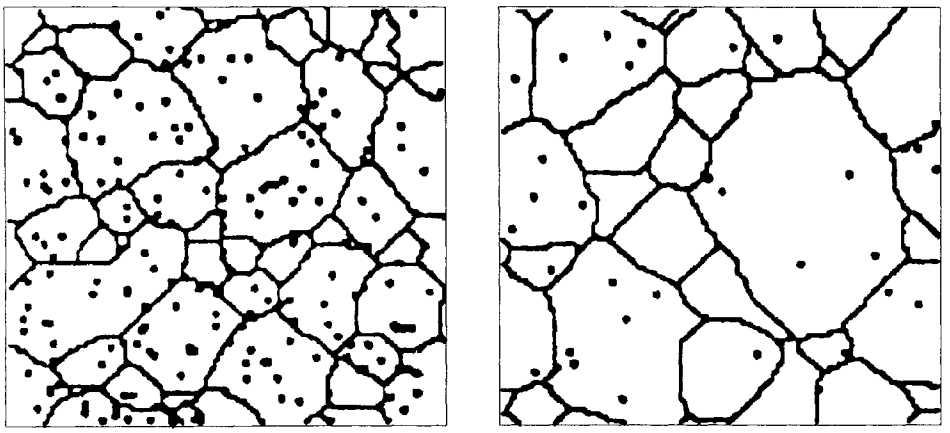

Figure 12.5: Two-dimensional grain growth simulation using a kinetic Potts Monte Carlo model with particles (Doherty et al. 1990).

12.4.2 Recrystallization

The approach outlined in the preceding section is designed to predict grain coarsening phenomena by using a classical Potts-type Hamiltonian, equation (12.4). For extending this concept to the simulation of recrystallization *and* grain growth phenomena at the same time, a modified operator can be formulated which additionally accounts for the energy that is accumulated during plastic deformation (Srolovitz et al. 1986, Rollett et al. 1990), namely

$$\mathcal{H}_{rx} = \sum_{i}^{N} \left(E\, f(s_i) + \frac{J}{2} \sum_{j}^{nn} \left(\delta_{s_i s_j} - 1 \right) \right) \qquad s_i = 1, 2, ..., q \tag{12.5}$$

where q is the number of texture components, s_k the spin number of each lattice site with a particular orientation g_k, $f(s_i)$ a step function which amounts to unity for unrecrystallized and zero for recrystallized sites, E the stored elastic energy per site accumulated during the preceding plastic deformation, $\sum_i^N$ the sum over all lattice sites, and $\sum_j^{nn}$ the sum over all nearest neighbors. The influence of nucleation rates and sites were discussed in some detail by Rollett, Srolovitz, Doherty, Anderson, and Grest (1990).

A recrystallization simulation by Srolovitz, Grest, and Anderson (1986) based on the above operator is shown in Figure 12.6. From equation (12.5) it is obvious that, since recrystallization and ordinary grain coarsening take place simultaneously, the kinetics and the topological evolution depend on the ratio of the stored elastic energy to the interfacial energy E/J. In metallic systems, the energy contribution of the dislocations typically exceeds that of the grain boundaries by up to one order of magnitude. Figure 12.6 shows a partially recrystallized microstructure which exhibits a bimodal grain size distribution. The two-dimensional calculation was conducted with an E/J ratio of 3 and with site-saturated nucleation conditions using 10 nuclei on 40 000 lattice sites. Figure 12.7 shows the Avrami kinetics as predicted by two-dimensional simulations with a different number of nuclei.

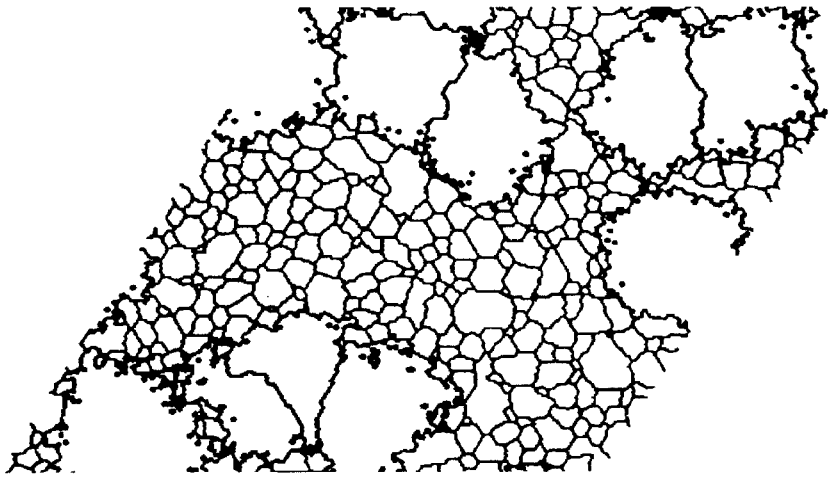

Figure 12.6: Partially recrystallized microstructure with a bimodal grain size distribution (Srolovitz et al. 1986). The 2D calculation was conducted with an E/J ratio of 3 and with site-saturated nucleation conditions using 10 nuclei on 40 000 lattice sites.

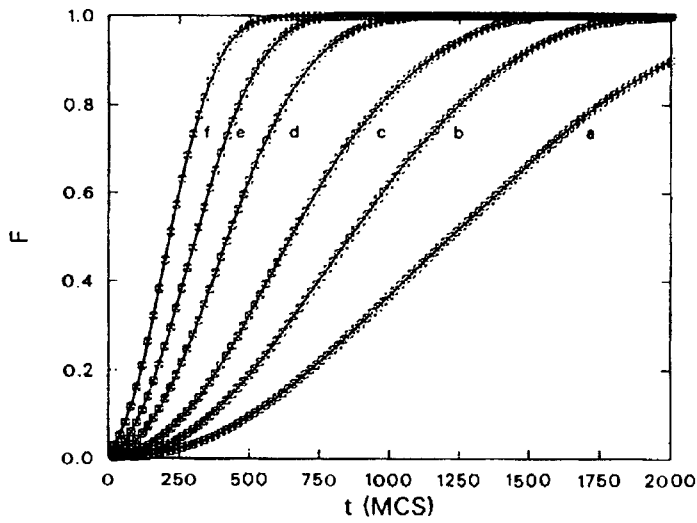

Figure 12.7: Avrami curves for 2D simulations with a different number of nuclei (Srolovitz et al. 1986). F is the recrystallized area fraction and t the number of MC units. The calculations used an E/J ratio of 3 and with site-saturated nucleation conditions. The grid had 40 000 lattice sites. Curves a-f correspond to 5, 10, 20, 50, 100, 200 nuclei.

Chapter 13

Geometrical and Component Models

13.1 Introduction

This section presents two groups of models which are based on geometrical considerations for the simulation of recrystallization and grain growth problems. The first approach is the geometrical or topological model of Mahin, Hanson, and Morris Jr. (1980) and Frost, Whang, and Thompson (1986) which is mainly based on incorporating the elementary geometry of nucleation, growth and impingement. It was employed mainly to mimic topologies of thin films. The second model is the more versatile component approach of Juul Jensen (1992). While the first model is particularly useful for predicting the dependence of grain topology and grain size distribution on the nucleation conditions, the second approach complements conventional analytical growth expressions with spatial aspects of nucleation, impingement, and texture.

13.2 Geometrical Model

Geometrical models, like all mesoscale recrystallization and grain growth models, represent continuum approaches. They consist basically of three major steps: nucleation, crystal growth to impingement, and, in some cases, subsequent grain coarsening. The last of these steps will be discussed in Chapter 14.

As in most related models, the nuclei are either initially distributed in a site-saturated fashion or constantly added to the non-recrystallized volume fraction as a linear or decreasing function of time. After their generation, it is assumed that all nuclei grow isotropically in space at a constant growth rate. This means that all existing nuclei expand equally to spheres until they impinge upon each other.

For site-saturated nucleation conditions the final grain topology can be constructed by employing straightforward geometrical considerations (Frost et al. 1986; Frost and Thompson 1987a; Frost et al. 1990). If two neighboring grains nucleate at the same time, and expand in radius at the same constant growth rate, the final interface between them will be a straight line. This boundary is identical to the perpendicular bisector of the

Computational Materials Science: The Simulation of Materials, Microstructures and Properties By Dierk Raabe
Copyright © 1998 Wiley-VCH Verlag GmbH
ISBN: 3-527-29541-0

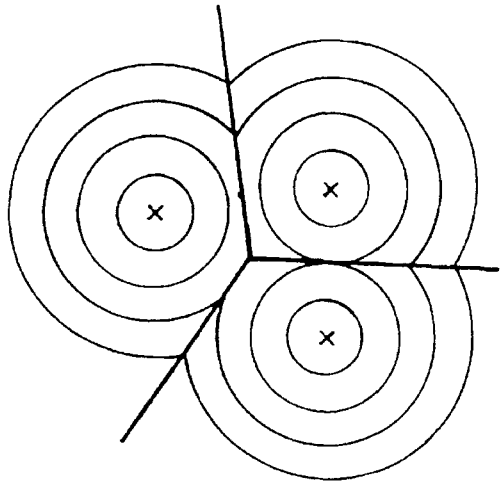

Figure 13.1: Development of straight interfaces between three crystals formed at the same time, under isotropic and constant growth rate conditions.

line joining the two initial nucleation sites. This simple geometrical result is identical to the construction rule of Wigner–Seitz cells. When three neighboring crystals grow under the same conditions, the resulting topology will be a triple point, which is the meeting coordinate of the three perpendicular bisectors of the edges of the triangle formed by the nucleation sites (Figure 13.1). If the three nuclei are generated at different times, but grow at the same rate, they will impinge upon another along an interface line with hyperbolic shape (Figure 13.2). The final position of the triple point can be specified by

$$r_1 + G\,t_1 = r_2 + G\,t_2 = r_3 + G\,t_3 \tag{13.1}$$

where r_i is the distance from the nucleation site of grain i to the triple point, G the isotropic growth rate, and t_i the nucleation time for grain i. Using this algorithm with site-saturated nucleation conditions will generate the well-known Voronoi structure, which is identical to a Wigner–Seitz construction on the basis of random lattice points in space (Figure 13.3). Voronoi topologies are sometimes also referred to as Dirichlet or Theissen structure. Similar structures, which are often called Johnson–Mehl topologies, arise from such geometrical models equipped with a constant nucleation rate (Figure 13.4).

13.3 Component Model

An extended version of the geometrical model was introduced by Juul Jensen (1992) as a simulation method for the prediction of recrystallization. This approach, which is referred to as the component model, complements conventional analytical growth expressions with advanced spatial aspects of texture, growth, and impingement (Juul Jensen 1997b). The simulations are conducted on a three-dimensional spatial cubic grid, which is referred to as a "computer sample" (Figure 13.5). The grid size is determined by the number of grains in the simulation and the density of the nuclei. The input data required to perform

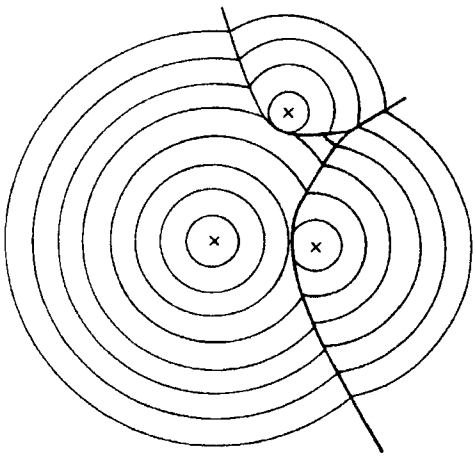

Figure 13.2: Development of hyperbolic interfaces between three crystals, formed at different times, under isotropic and constant growth rate conditions.

a simulation are the number of grains N, the number of different texture components i, the total nucleation density, the size of the nuclei $r(i)$, the nucleation rate $\dot{n}(t,i)$, the spatial distribution of the nuclei, which also may depend on the orientation (i), the grain shape as a function of i, and the growth rate $G(i,t)$.

The simulation proceeds as follows. At first, the N nuclei are distributed according to the nucleation information, after which each nucleus has a position (x_1, x_2, x_3) and a nucleation time t_0. Subsequently, one calculates for each non-recrystallized point in the finite difference grid the time when each of the N nuclei would arrive at that point. From this information one registers that particular grain which arrives first at the coordinate inspected, together with its time of arrival. This method amounts to excluding the possibility that the newly formed grains can overlap, i.e. they generally stop when they impinge upon each other. However, further growth of impinging grains in all the other non-recrystallized directions is not impeded.

From this geometrical rule, which is systematically applied to all points in the lattice, one obtains the entire topology and texture of the partially and completely recrystallized material. The particular versatility of the component or multicomponent method lies in its ability to include experimental information, for instance on particular nucleation conditions and/or starting textures.

13.4 Application of Geometrical and Component Models in Materials Science

This section lists some classical and recent publications on applications of geometrical and component simulations related to various domains of materials science. The list can by no means be complete but may serve as a bibliography for getting better acquainted with the recent original literature in this field. Geometrical and component models are usually

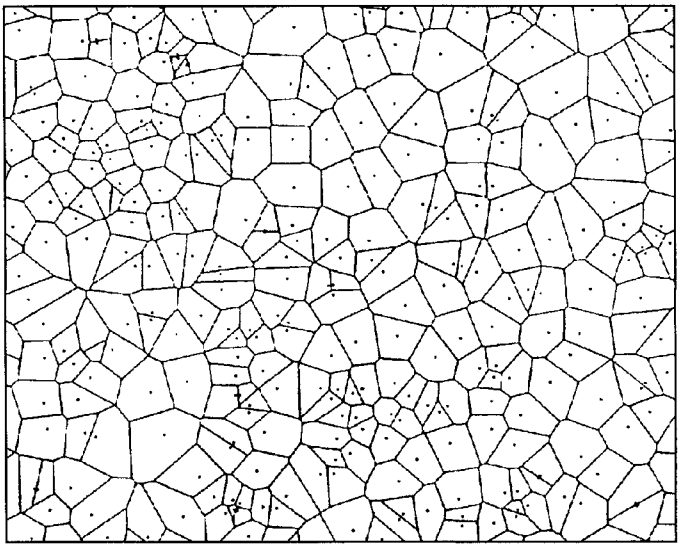

Figure 13.3: 2D Voronoi or Dirichlet crystal topology generated through a Wigner–Seitz cell construction on random points. The metallurgical analog to this is a nucleation–growth process with site-saturated nucleation followed by isotropic and constant growth. Under such conditions only straight interfaces can develop (Frost et al. 1986).

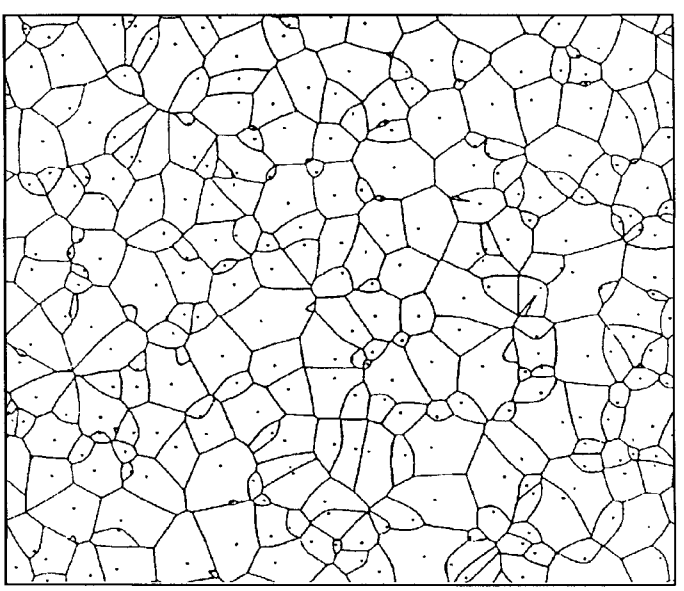

Figure 13.4: 2D Johnson–Mehl crystal topology generated through a nucleation–growth process with constant nucleation rate and isotropic and constant growth. Under such conditions both straight and hyperbolic interfaces can develop (Frost et al. 1986).

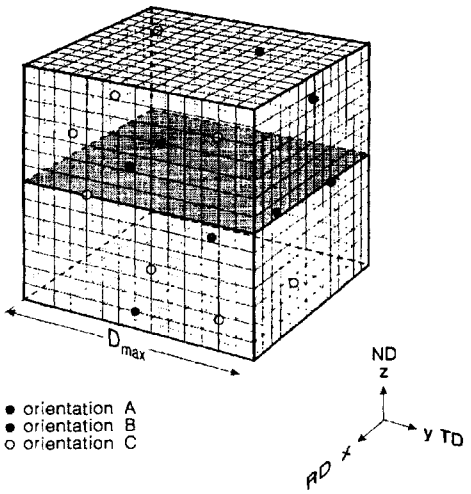

Figure 13.5: Presentation of the 3D calculation grid as used in the component model of Juul Jensen (1992). The lattice contains nuclei with three different initial crystal orientations. The shaded plane indicates how 2D slices are extracted for statistical analysis.

employed for the fast computation of microstructures and crystallographic textures with consideration of various nucleation and growth conditions. Advanced versions allow the incorporation of the initial texture.

Field of application	Reference
classics about geometrical modeling	Getis and Boots (1979)
	Mahin, Hanson, and Morris Jr. (1980)
	Frost, Whang, and Thompson (1986)
	Frost and Thompson (1987a)
	Frost and Thompson (1987b)
	Frost, Thompson, and Walton (1990)
component or multicomponent model	Juul Jensen (1992)
	Juul Jensen (1997b)

13.5 Examples of Geometrical and Component Simulations in Materials Science

Following equation (13.1), the deviation of the interface shape from a straight line in geometrical models can be determined either by the nucleation time or by the growth rate (Frost and Thompson 1987a). Figure 13.6 shows two 2D crystal structures produced by continuous nucleation with different exclusion zones around them. Figure 13.7 shows two 2D sections extracted from a 3D component simulation of primary static recrystallization at two different times (Juul Jensen 1992; Juul Jensen 1997b). The different gray scales indicate the various texture components.

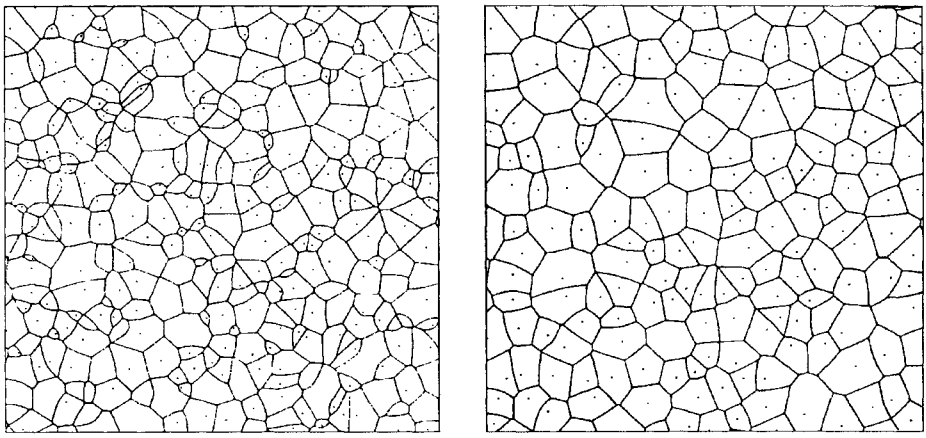

Figure 13.6: Two 2D crystal topologies computed by Frost and Thomson (1987) by continuous nucleation with different exclusion zones.

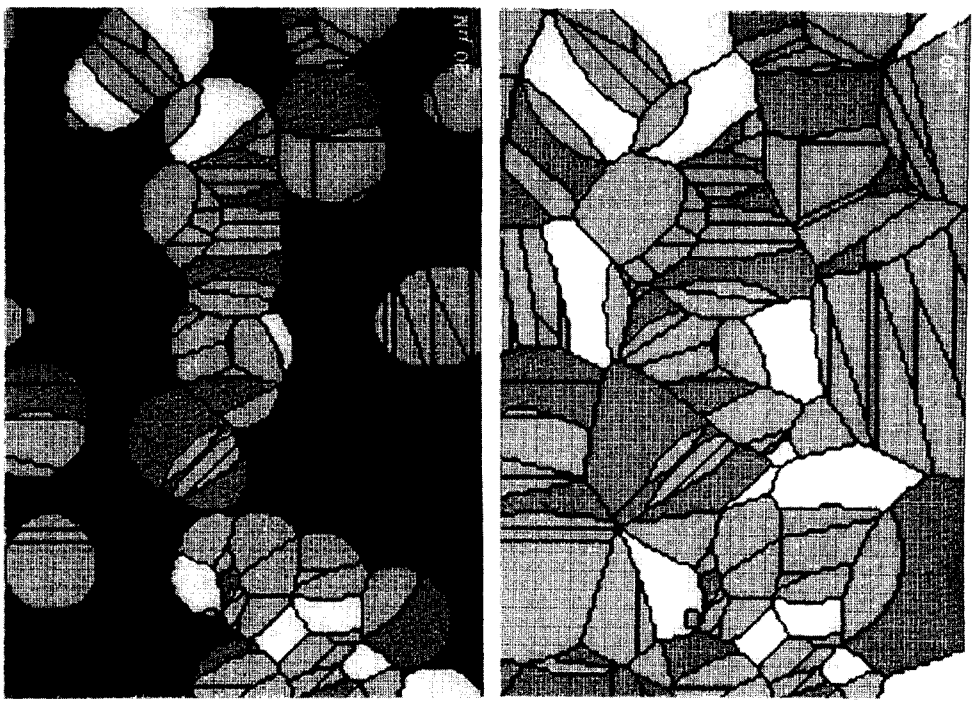

Figure 13.7: Recrystallization simulation of Juul Jensen (1997) according to the component model.

Chapter 14

Topological Network and Vertex Models

14.1 Introduction and Fundamentals

Topological network and vertex models idealize solid materials or soap-like structures as homogeneous continua which contain interconnected boundary segments that meet at vertices, i.e. boundary junctions. Depending on whether the system dynamics lies in the motion of the junctions or of the boundary segments, they are sometimes also referred to as boundary dynamics models. The grain boundaries appear as lines or line segments in two-dimensional and as planes or plane segments in three-dimensional simulations. The dynamics of these coupled interfaces or interface portions and of the vertices determine the evolution of the entire network. The motion of the boundaries and sometimes that of the vertices also can be described either in terms of a Newtonian equation of motion which contains a frictional portion (equation (9.160)) or in terms of a linearized first-order rate equation (equations (11.14)-(11.18)).

Depending on the physical model behind such a simulation, the boundary segments and vertices can have different types of equations of motion, considering for instance aspects such as an effective mass, frictional terms, or, in a rate context, characteristic activation enthalpies.

Using the frictional form of the classical equation of motion with a strong damping term results in a steady-state motion where the velocity of the defect depends only on the local force but not on its previous velocity. The overdamped steady-state description is similar to choosing a linearized rate equation, where the defect velocity is described in terms of a temperature-dependent mobility term and the local driving pressure.

The calculation of the local forces in most vertex models is based on equilibrating the line energies of subgrain walls and high-angle grain boundaries at the interface junctions according to Herring's equation. The enforcement of local mechanical equilibrium at these nodes, i.e. triple points, is for obvious topological reasons usually only possible by allowing the abutting interfaces to curve. These curvatures in turn act through their capillary force, which is directed towards the center of curvature, on the junctions; in sum this may lead to their displacement (Figure 14.1). In order to avoid the artificial enforcement of a constant boundary curvature between two neighboring nodes, the interfaces are usually

Computational Materials Science: The Simulation of Materials, Microstructures and Properties By Dierk Raabe
Copyright © 1998 Wiley-VCH Verlag GmbH
ISBN: 3-527-29541-0

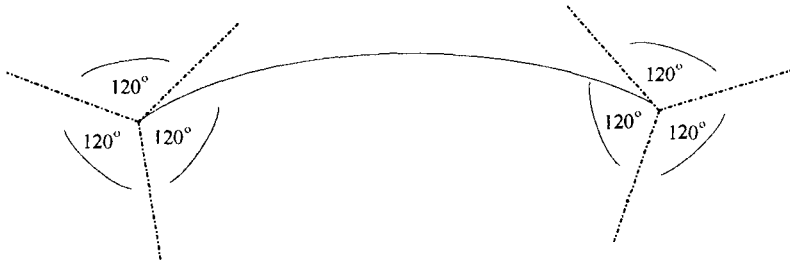

Figure 14.1: Constant boundary curvature induced by the enforcement of local mechanical equilibrium at the junctions. All grain boundaries have the same energy.

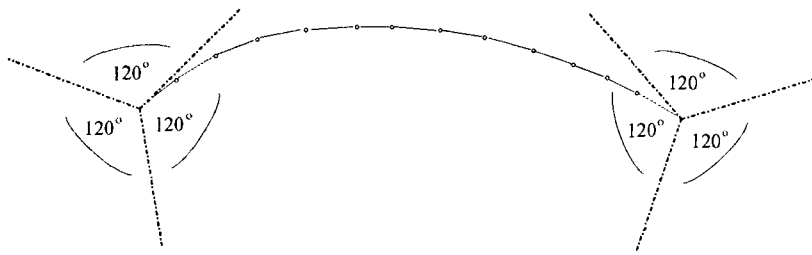

Figure 14.2: Nonconstant boundary curvature induced by the enforcement of local mechanical equilibrium at the junctions. All grain boundaries have the same energy.

decomposed into sequences of piecewise straight boundary segments (Figure 14.2). Some currently used versions of topological models formulate and integrate the equations of motion successively for each segment and/or node through the entire network. This method of decoupling the originally coupled differential equations of motion can lead to inaccurate predictions, because it renders the simulation dependent on the order in which the differential equations are solved. More sophisticated codes thus solve all the coupled equations of motion simultaneously.

Most vertex and network models use switching rules which describe the topological recombination of approaching vertices. This is an analogy to the use of phenomenological annihilation and lock-formation rules that appear in dislocation dynamics. As in all continuum models, the consideration of such more or less artificial recombination laws replaces the exact atomistic treatment which requires molecular dynamics methods. According to the Mullins–von Neumann law for two-dimensional cell structures, crystals with less than six sides will be prone to shrink. Figure 14.3 shows some possible recombination reactions which take place when neighboring vertices are closer than some critical spontaneous recombination spacing. It is worth noting in this context that the recombination rules, particularly the various critical recombination spacings, can substantially affect the topological results of a simulation. Depending on the underlying constitutive continuum description, vertex simulations can consider crystal orientation and therefore misorientations across the boundaries, interface mobility, and the difference in elastic energy between adjacent grains. Due to the stereological complexity of grain boundary arrays and the large number of degrees of freedom encountered in such approaches, most network simulations are currently confined to the two-dimensional regime (Figure 14.4).

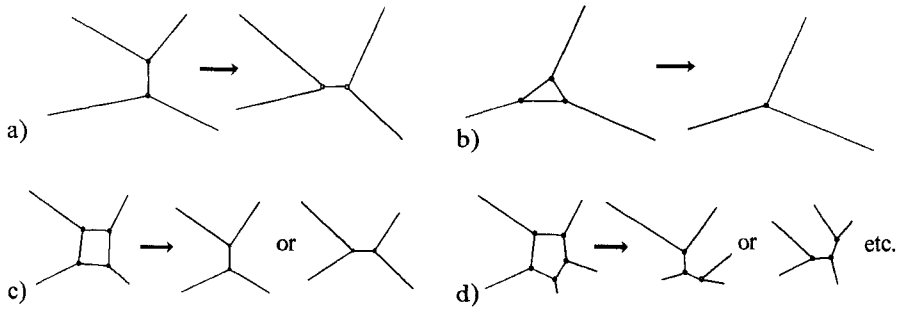

Figure 14.3: Some switching or recombination rules to describe the topological rearrangement of approaching vertices in boundary networks. The recombination of cells with more than three sides (c,d) can be reduced to binary (a) and triangular recombinations (b). (a) Flip of two vertices. (b) Collapse of a triangular cell. (c) Collapse of a cell with four sides. (d) Collapse of a cell with five sides.

Depending on which lattice defect is assumed to determine the dynamical evolution of the system, one sometimes speaks of pure vertex models, where only the motion of the junctions is considered, or of pure network models, where only the motion of the boundary segments is considered. Since they are not intrinsically scaled, vertex and network models are a convenient means of simulating the kinetics and the resulting topological rearrangements of interface ensembles at the mesoscopic scale.

Topological interface or boundary dynamics simulations, together with dislocation dynamics simulations, can be classified as continuum dynamical methods since they proceed by calculating the dynamics of each individual continuum defect entity (dislocation segment, interface segment, vertex) instead of minimizing the total system energy. In contrast, molecular dynamics simulations can be regarded as atomistic dynamical systems since they proceed by calculating the dynamics of individual atoms.

Topological boundary dynamics models are different from kinetic Potts models in that they are not based on minimizing the total energy but directly calculate the motion of the lattice defects, usually on the basis of capillary and elastic forces. They are also different from phase field Ginzburg–Landau type-interface models in that they use sharp rather than diffuse boundaries.

14.2 Application of Topological and Vertex Models in Materials Science

This section presents a list of some classical and recently published references on applications of topological network and vertex simulations related to various domains of materials science. The list can by no means be complete but may serve as a bibliography for getting better acquainted with some examples of the recent original literature in this field. Vertex and topological network models are typically used to mimic crystal recovery and nucleation by subgrain growth, continuous recrystallization, incipient stages of discontinuous recrystallization, bulging phenomena, continuous and discontinuous grain growth, low-cycle fatigue, and superplastic deformation.

Application	Authors
topological and dynamic fundamentals	Weaire and Kermode (1983)
	Weaire and Kermode (1984)
	Ceppi and Nasello (1986)
	Scavuzzo, Ré, and Ceppi (1990)
ordinary high-angle boundary grain growth	Weaire and Kermode (1983)
	Frost and Thompson (1988)
	Kawasaki (1989)
	Pan and Cocks (1993)
subgrain growth, nucleation	Humphreys (1992b)
	Humphreys (1992a)
	Humphreys (1993)
	Svoboda (1996a)
low-cycle fatigue	Draheim (1995)
	Draheim and Gottstein (1996b)

14.3 Examples of Topological and Vertex Simulations in Materials Science

14.3.1 Vertex Model for Recovery and Recrystallization

In two-dimensional vertex approaches for the simulation of recovery and the early stages of recrystallization, the interfaces are idealized as line defects. Their mobility and energy are typically related to the misorientation angle, for instance using the Read–Shockley equation. The boundaries can rearrange according to their local curvature and the stored energy. The resulting movements of the junctions occur with preservation of connectivity according to the resulting net forces and boundary mobilities.

Most analytical recrystallization models (Marthinsen et al. 1989; Furu and Nes 1990; Marthinsen et al. 1990; Vandermeer and Rath 1990; Vandermeer et al. 1991) and numerical simulations (Srolovitz et al. 1986; Srolovitz et al. 1988; Rollett et al. 1989; Hesselbarth and Göbel 1991; Tavernier and Szpunar 1991a; Rollett et al. 1992; Pezzee and Dunand 1994; Marx and Raabe 1995; Marx et al. 1995; Holm et al. 1996; Raabe et al. 1996; Sheldon and Dunand 1996; Reher 1998) describe the growth and impingement of *given* nuclei rather than the incipient transformation stages that rearrange the subgrain structure and thus can *lead to* nucleation.

For the simulation of such subgrain coarsening nucleation events, Humphreys (1992a) introduced a vertex model to simulate the early, rather than the late, stages of recrystallization and recovery. The physical picture behind this type of model is that the nucleation process can be simulated by the inhomogeneity of subgrain growth, which can lead to cells of a critical size through an accumulation of local misorientations that were introduced during deformation. This means that the model regards the subgrain as an elementary nucleation unit for recrystallization phenomena (Humphreys 1992b). This concept is in line with the classical picture of subgrain coalescence (Hu 1962; Hu 1963). Consequently, the vertex simulation treats the subgrain walls as underlying elementary lattice defects which determine the formation of nuclei through their respective mobilities. The consideration of subgrain growth as a major nucleation mechanism of primary static

recrystallization is in good accord with numerous microstructural observations of growth kinetics of dislocation cell structures in aluminum (Doherty 1978; Gottstein 1984; Juul Jensen et al. 1985; Lan et al. 1990; Ananthan et al. 1991; Rosen et al. 1995) and various body-centered cubic alloys (Swann and Nutting 1961; Dillamore and Roberts 1965; Dillamore et al. 1972). However, it is less obvious for materials with low stacking fault energy, such as austenitic stainless steels or brass (Haeßner 1978), and materials with inhomogeneous microstructures, such as many intermetallic alloys. The vertex model

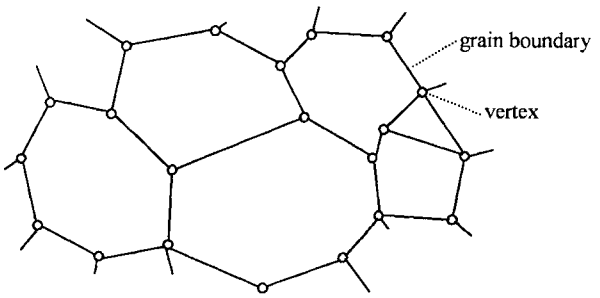

Figure 14.4: Basic setup of the subgrain network model.

suggested by Humphreys (1992a) represents the microstructure as an array of subgrains. The cell coordinates are given by their respective node points (Figure 14.4). This technique requires much less random access memory compared with Potts-type Metropolis Monte Carlo or deterministic cellular automaton methods, where the entire volume must be discretized. The initial subgrain network can be constructed as a regular or Voronoi array[1]. As shown in Figure 14.4, each subgrain is then assigned a certain orientation.

For obtaining subgrain growth, the cell walls must be mobile under the influence of a driving force. The velocity of the interfaces v is described in the model of Humphreys (1992a) by a viscous flow rule which mimics steady-state overdamped boundary motion,

$$v = m \frac{\mathrm{d}G}{\mathrm{d}V} \tag{14.1}$$

where G is the Gibbs free enthalpy, V the volume, and m the interface mobility. The free enthalpy change can be expressed through the interface curvature:

$$\frac{\mathrm{d}G}{\mathrm{d}V} = \frac{2\gamma^{\mathrm{c}}(g)}{R^{\mathrm{c}}} \tag{14.2}$$

where $1/R^{\mathrm{c}}$ is the cell wall curvature, and $\gamma^{\mathrm{c}}(g)$ the specific interface energy as a function of the boundary misorientation $\boldsymbol{g}$. The curvature of the subgrain walls is obtained by equilibrating the total force at each node, which follows the well-known relation

$$\begin{aligned}\frac{\gamma_{23}}{(1+\epsilon_2\epsilon_3)\sin\Psi_1 + (\epsilon_3-\epsilon_1)\cos\Psi_1} &= \frac{\gamma_{13}}{(1+\epsilon_1\epsilon_3)\sin\Psi_2 + (\epsilon_1-\epsilon_2)\cos\Psi_2} \\ &= \frac{\gamma_{12}}{(1+\epsilon_1\epsilon_2)\sin\Psi_3 + (\epsilon_2-\epsilon_3)\cos\Psi_3}\end{aligned} \tag{14.3}$$

[1] A Voronoi array corresponds to a Dirichlet tesselation. It is constructed according to the Wigner–Seitz method but with randomly distributed starting points.

where γ_{ij} is the specific boundary energy that separates grain i from grain j, and $\epsilon_i = \partial \ln \gamma^{(hkl)}/\partial \Psi_i$ the dependence of the energy on the spatial orientation of the boundary plane Ψ. If the subgrain energy is independent of Ψ, equation (14.3) can be written

$$\frac{\gamma_{ij}}{\Psi_k} = \text{constant} \tag{14.4}$$

It should be noted that the local curvature must not be confused with the grain size. Both values can differ by orders of magnitude.

In three dimensions the subgrain misorientation can be described in terms of Euler angles, $\boldsymbol{g} = \boldsymbol{g}(\varphi_1, \phi, \varphi_2)$, or Rodrigues vectors, $\boldsymbol{q} = \boldsymbol{n} \tan(\Theta/2)$, i.e. by using three independent parameters. In two-dimensional simulations one parameter, viz. the misorientation angle Θ, suffices because the rotation axis is generally perpendicular to the grain boundary normal. Since in network models the orientations of adjacent subgrains are known, the local misorientation is known as well. For misorientation angles below 15° the Read–Shockley (RS) equation can be used. Since the cell walls being considered are not treated at the dislocation level, the conventional version of the RS equation applies, implying that only one group of dislocations contributes to the misorientation:

$$\begin{gathered} \gamma^{c}_{2D}(\Theta) \cong \Theta\,[A_c - B_c \ln(\Theta)] \\ A_c = \frac{E_d}{b} - B_c \ln \alpha_d \qquad \text{and} \qquad B_c = \frac{\mu b}{4\pi(1-\nu)} \end{gathered} \tag{14.5}$$

where Θ is the misorientation angle between two neighboring subgrains in two dimensions, E_d the energy of the dislocation core, b the magnitude of the Burgers vector, μ the shear modulus, ν Poisson's ratio, and α_d the inner cut-off radius around the dislocation core expressed in units of $|\boldsymbol{b}|$ (Hirth and Lothe 1968).

The forces of the individual subgrain boundaries that meet at a junction are summed to give the total driving force on the node considered. The resulting velocity of the junction is then determined by assuming viscous flow, equation (14.1). The mobility of the node is determined from the misorientation-dependent mobilities of the boundaries in the direction of the driving force, which in turn is obtained from an average of the mobilities of the moving boundaries, weighted by the boundary lengths resolved perpendicular to the direction of motion (Humphreys 1992a). The node is then shifted a small distance according to its actual velocity (Figure 14.5). The determination or theoretical prediction of the low-angle grain boundary mobilities as a function of misorientation is less straightforward than assessing their energy. In various studies Humphreys (1992a) tested different mobility laws; in all of them, mobilities increased with misorientation up to 15°, where they remained constant.

14.3.2 Toplogical Network Model for Grain Growth

Figures 14.6, 14.7, and 14.8 show a two-dimensional network simulation of homogeneous grain coarsening according to the method of Svoboda (1996a). This approach is based on the assumption of mechanical equilibrium of the grain boundary line forces at the triple junctions. The corresponding tangent angles of the boundaries at the triple points determine the curvature of the boundaries. The interfaces consists of a number of individual sequentially arranged piecewise straight segments. The capillary force imposed by them is summed, and determines the resulting shift of the junction. The simulation uses viscous flow rules.

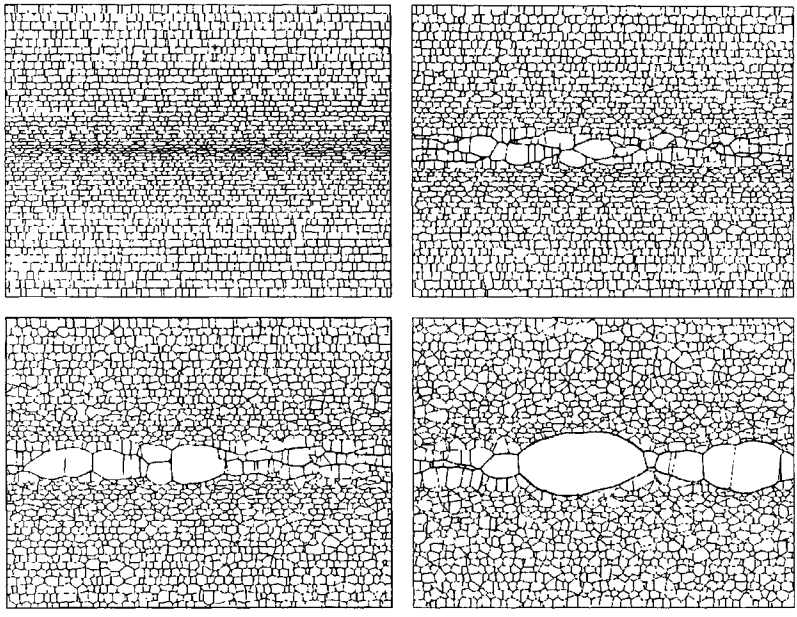

Figure 14.5: Example of the incipient stages of nucleation described by subgrain coarsening in the network model (Humphreys 1992).

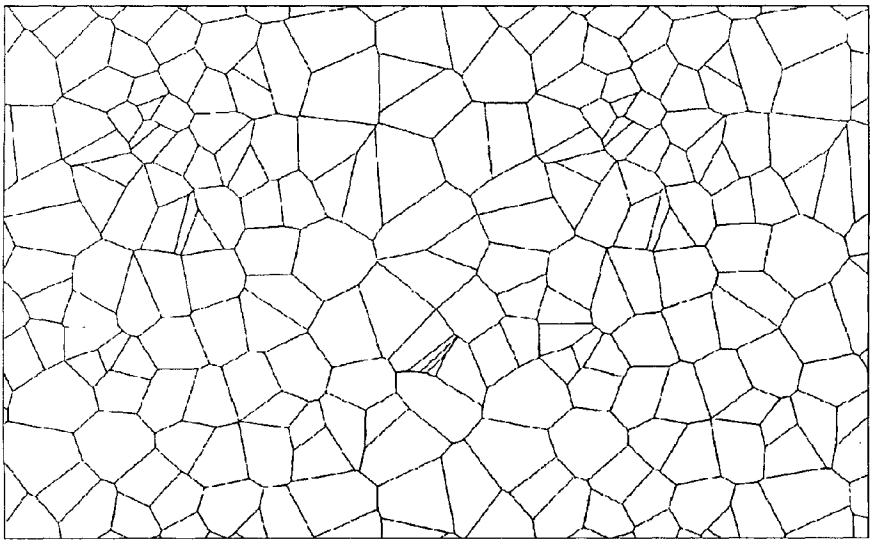

Figure 14.6: Initial microstructure of a network model (Svoboda 1996).

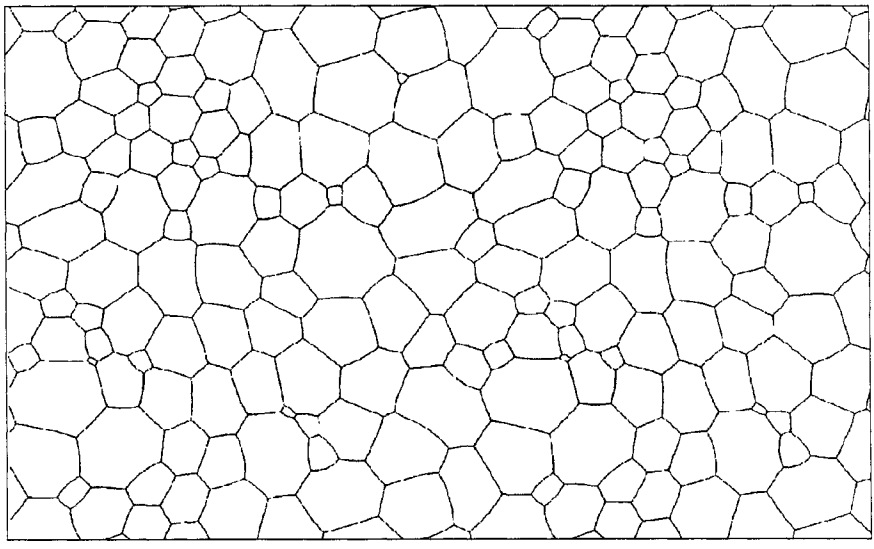

Figure 14.7: Intermediate microstructure of an annealed network; model of Svoboda (1996).

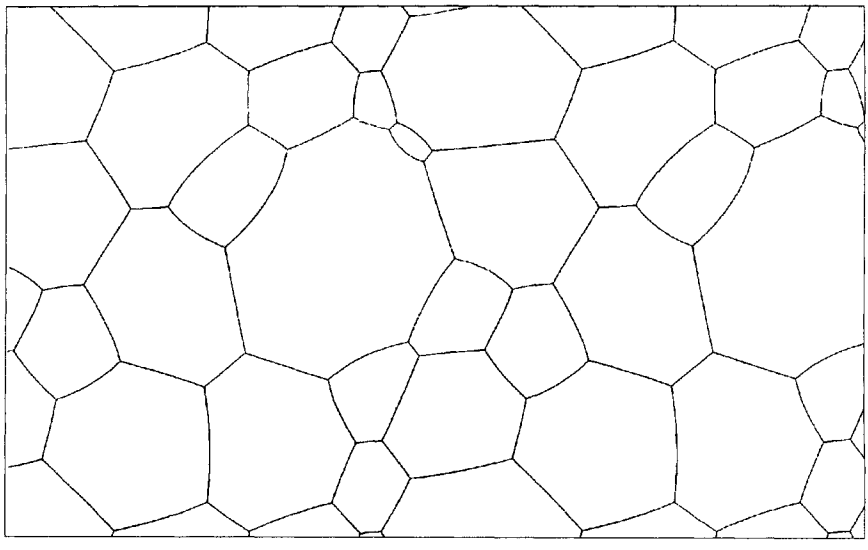

Figure 14.8: Final microstructure of an annealed and coarsened network; model of Svoboda (1996).

Part IV

Simulation Techniques at the Mesoscopic–Macroscopic Scale

Computational Materials Science: The Simulation of Materials, Microstructures and Properties By Dierk Raabe
Copyright © 1998 Wiley-VCH Verlag GmbH
ISBN: 3-527-29541-0

Chapter 15

Introduction

This Part deals with the simulation of materials properties and microstructures at the mesoscopic (grain and subgrain scale) and macroscopic (entire specimen) levels. Of course, a strict subdivision of the numerous methods that exist in computational materials science according to the length scales that they address is to a certain extent arbitrary and depends on the aspect under investigation.

The following chapters provide an introduction to the macroscale application of the finite element, the finite difference, and various polycrystal elasticity and plasticity methods. While the finite element method is discussed with particular respect to applications in the field of plasticity, the finite difference method is applied to the macroscale solution of the heat and diffusion equation. The polycrystal models are discussed with particular respect to the homogenization assumptions on which they are based.

Selecting these particular simulation techniques for an overview on meso- and macroscale materials simulations deserves some justification.

The finite element method is a versatile numerical means of obtaining approximate solutions to boundary and initial-value problems. Its approach consists in subdividing the sample of interest into a number of subdomains and by using polynomial functions to approximate the true course of a state function in a piecewise fashion over each subdomain (Courant 1943; Zienkiewicz and Morgan 1983). Hence, finite element methods are *not* intrinsically calibrated to some specific physical length or time scale. The mathematical foundations of the finite element method have already been presented in a more general chapter about differential equations and their numerical solution (Chapter 3). However, it is well known that the application of the finite element method in materials science lies particularly in the field of macro- and mesoscale simulations where averaging empirical or phenomenological constitutive laws can be incorporated. Emphasis is often placed on computational mechanics, particularly when the considered shapes are complicated, the material response is nonlinear, or the applied forces are dynamic (Rowe et al. 1991; Nemat-Nasser and Hori 1993). All three features are typically encountered in the calculation of large scale structures and plastic deformation. The extension of classical computational solid mechanics to microstructure mechanics or computational micromechanics requires a scale-dependent physical formulation of the underlying constitutive behavior that is admissible at the level addressed, and a detailed incorporation of microstructure (Gittus and Zarka 1986; Andersen et al. 1994; Krausz and Krausz 1996; Schmauder and Weichert 1996; Schmauder and Raabe 1996).

Computational Materials Science: The Simulation of Materials, Microstructures and Properties By Dierk Raabe
Copyright © 1998 Wiley-VCH Verlag GmbH
ISBN: 3-527-29541-0

This task reveals a certain resemblance to molecular dynamics, where the equations of motion are solved for a large number of interacting particles. These calculations require some approximate formulation of the interatomic potential. It is clear that the accuracy of the underlying potential determines the reliability of the predictions. Similar arguments apply for the use of computational solid mechanics in materials science. The validity of the constitutive laws and the level at which the microstructure is incorporated in the finite element grid determine the predictive relevance of the simulation. As a rule the accuracy of solid mechanics calculations can be increased by decreasing the level at which the required microstructural and constitutive data are incorporated. Advanced finite element methods have recently also been used on a much finer microstructural scale for the prediction of diffusion and transformation phenomena.

In addition to the above-mentioned field of solid states mechanics and its treatment with finite element methods, many materials problems exist, which must be formulated as initial-value rather than as boundary-value problems. Such time dependent simulations are characterized by the presence of time derivatives in the governing differential equations and the prescription of initial conditions at the time origin. Methods to numerically integrate equations which involve time derivatives are provided by the various finite difference approaches (Forsythe and Wasow 1960; Richtmyer and Morton 1967; Dettman 1969; Marsal 1976; DeVries 1994; Bellomo and Preziosi 1995). Finite difference methods comprise a number of general numerical means for solving initial-value problems. Typical examples in materials science are the solution of the diffusion or heat equation, of the atomic equations of motion in molecular dynamics, or of the equations of motion in dislocation dynamics. As is apparent from these examples, the use of finite difference algorithms is also *not* confined to any particular scale. The fundamentals of the finite difference methods have therefore already been discussed in Chapter 3. The present chapter is devoted exclusively to discussing the potential of the finite difference method at the meso- and macroscale.

Numerical methods to solve initial- and boundary-value problems have in common the discretization of the independent variables, which are usually time and space, and the transformation of the continuous derivatives into finite difference quotients. Performing these discretizations amounts to recasting the continuous problem expressed by differential equations with an infinite number of unknowns, i.e. function values, into an algebraic one with a finite number of unknown parameters which can be calculated in an approximate fashion. Although both the finite difference and the finite element method can essentially be used to solve boundary- and initial-value problems, the latter technique represents the more general approach since it uses polynomial shape functions and a minimalization procedure. According to Zienkiewicz and Morgan (1983), the finite difference techniques can thus be regarded as a subset of the finite element approximation.

In contrast to these rather scale-independent techniques, polycrystal models represent classical homogenization approaches to the simulation of the elastic and plastic response of polycrystalline and multiphase materials at the macro- and mesoscale with particular consideration of crystallographic textures. As examples of polycrystal elasticity and plasticity simulations Voigt, Reuss, Hashin–Shtrikman, Taylor–Bishop–Hill, relaxed constraints Taylor-type, advanced grain interaction models, inclusion, and self-consistent approaches will be discussed.

Part IV

Simulation Techniques at the Mesoscopic–Macroscopic Scale

Computational Materials Science: The Simulation of Materials, Microstructures and Properties By Dierk Raabe
Copyright © 1998 Wiley-VCH Verlag GmbH
ISBN: 3-527-29541-0

Chapter 15

Introduction

This Part deals with the simulation of materials properties and microstructures at the mesoscopic (grain and subgrain scale) and macroscopic (entire specimen) levels. Of course, a strict subdivision of the numerous methods that exist in computational materials science according to the length scales that they address is to a certain extent arbitrary and depends on the aspect under investigation.

The following chapters provide an introduction to the macroscale application of the finite element, the finite difference, and various polycrystal elasticity and plasticity methods. While the finite element method is discussed with particular respect to applications in the field of plasticity, the finite difference method is applied to the macroscale solution of the heat and diffusion equation. The polycrystal models are discussed with particular respect to the homogenization assumptions on which they are based.

Selecting these particular simulation techniques for an overview on meso- and macroscale materials simulations deserves some justification.

The finite element method is a versatile numerical means of obtaining approximate solutions to boundary and initial-value problems. Its approach consists in subdividing the sample of interest into a number of subdomains and by using polynomial functions to approximate the true course of a state function in a piecewise fashion over each subdomain (Courant 1943; Zienkiewicz and Morgan 1983). Hence, finite element methods are *not* intrinsically calibrated to some specific physical length or time scale. The mathematical foundations of the finite element method have already been presented in a more general chapter about differential equations and their numerical solution (Chapter 3). However, it is well known that the application of the finite element method in materials science lies particularly in the field of macro- and mesoscale simulations where averaging empirical or phenomenological constitutive laws can be incorporated. Emphasis is often placed on computational mechanics, particularly when the considered shapes are complicated, the material response is nonlinear, or the applied forces are dynamic (Rowe et al. 1991; Nemat-Nasser and Hori 1993). All three features are typically encountered in the calculation of large scale structures and plastic deformation. The extension of classical computational solid mechanics to microstructure mechanics or computational micromechanics requires a scale-dependent physical formulation of the underlying constitutive behavior that is admissible at the level addressed, and a detailed incorporation of microstructure (Gittus and Zarka 1986; Andersen et al. 1994; Krausz and Krausz 1996; Schmauder and Weichert 1996; Schmauder and Raabe 1996).

Computational Materials Science: The Simulation of Materials, Microstructures and Properties By Dierk Raabe
Copyright © 1998 Wiley-VCH Verlag GmbH
ISBN: 3-527-29541-0

This task reveals a certain resemblance to molecular dynamics, where the equations of motion are solved for a large number of interacting particles. These calculations require some approximate formulation of the interatomic potential. It is clear that the accuracy of the underlying potential determines the reliability of the predictions. Similar arguments apply for the use of computational solid mechanics in materials science. The validity of the constitutive laws and the level at which the microstructure is incorporated in the finite element grid determine the predictive relevance of the simulation. As a rule the accuracy of solid mechanics calculations can be increased by decreasing the level at which the required microstructural and constitutive data are incorporated. Advanced finite element methods have recently also been used on a much finer microstructural scale for the prediction of diffusion and transformation phenomena.

In addition to the above-mentioned field of solid states mechanics and its treatment with finite element methods, many materials problems exist, which must be formulated as initial-value rather than as boundary-value problems. Such time dependent simulations are characterized by the presence of time derivatives in the governing differential equations and the prescription of initial conditions at the time origin. Methods to numerically integrate equations which involve time derivatives are provided by the various finite difference approaches (Forsythe and Wasow 1960; Richtmyer and Morton 1967; Dettman 1969; Marsal 1976; DeVries 1994; Bellomo and Preziosi 1995). Finite difference methods comprise a number of general numerical means for solving initial-value problems. Typical examples in materials science are the solution of the diffusion or heat equation, of the atomic equations of motion in molecular dynamics, or of the equations of motion in dislocation dynamics. As is apparent from these examples, the use of finite difference algorithms is also *not* confined to any particular scale. The fundamentals of the finite difference methods have therefore already been discussed in Chapter 3. The present chapter is devoted exclusively to discussing the potential of the finite difference method at the meso- and macroscale.

Numerical methods to solve initial- and boundary-value problems have in common the discretization of the independent variables, which are usually time and space, and the transformation of the continuous derivatives into finite difference quotients. Performing these discretizations amounts to recasting the continuous problem expressed by differential equations with an infinite number of unknowns, i.e. function values, into an algebraic one with a finite number of unknown parameters which can be calculated in an approximate fashion. Although both the finite difference and the finite element method can essentially be used to solve boundary- and initial-value problems, the latter technique represents the more general approach since it uses polynomial shape functions and a minimalization procedure. According to Zienkiewicz and Morgan (1983), the finite difference techniques can thus be regarded as a subset of the finite element approximation.

In contrast to these rather scale-independent techniques, polycrystal models represent classical homogenization approaches to the simulation of the elastic and plastic response of polycrystalline and multiphase materials at the macro- and mesoscale with particular consideration of crystallographic textures. As examples of polycrystal elasticity and plasticity simulations Voigt, Reuss, Hashin–Shtrikman, Taylor–Bishop–Hill, relaxed constraints Taylor-type, advanced grain interaction models, inclusion, and self-consistent approaches will be discussed.

Chapter 17

Polycrystal Elasticity and Plasticity Models

17.1 Introduction and Fundamentals

Polycrystal models are classical averaging methods to predict the elastic and plastic response of polycrystalline and multiphase materials at the meso- and macroscale without immediate incorporation of the dynamics of the lattice and its defects[1]. Real materials tend to have highly complex microstructures which can substantially influence their overall response to external loads. However, meso- and macroscale models must use methods to level out these fine details of the microstructure. This must be done by replacing the microstructure by an appropriate constitutive description and by including certain assumptions about material homogeneity. The main differences among the various polycrystal models therefore arise from their particular approach to tackling these two tasks.

Consequently, this chapter reviews first some aspects of homogenization in polycrystalline aggregates and some fundamentals of their constitutive description. Subsequently the Voigt, Reuss, Hashin–Shtrikman, Taylor-Bishop-Hill, relaxed constraints Taylor type, advanced grain interaction models, and self-consistent approaches are presented.

Most of the ensuing sections focus on materials mechanics. It might be helpful to insert here a brief remark on notation, because in most books which take a mechanics perspective the expressions for tensor operations differ from those in books with a materials science background. The following expressions for Hooke's law are all equivalent:

$$\begin{aligned} \sigma_{ij} &= C_{ijkl}\,\varepsilon_{kl} \\ \boldsymbol{\sigma} &= \boldsymbol{C}\,\boldsymbol{\varepsilon} \\ \boldsymbol{\sigma} &= \boldsymbol{C} : \boldsymbol{\varepsilon} \end{aligned} \tag{17.1}$$

Expressions of the first and second type will be used in the following text.

[1]Some recent polycrystal plasticity simulations consider mesoscopic microstructural aspects. For instance, the mutual blocking of dislocations on different slip systems is sometimes phenomenologically described in terms of unequal coefficients of the hardening matrix.

Computational Materials Science: The Simulation of Materials, Microstructures and Properties By Dierk Raabe
Copyright © 1998 Wiley-VCH Verlag GmbH
ISBN: 3-527-29541-0

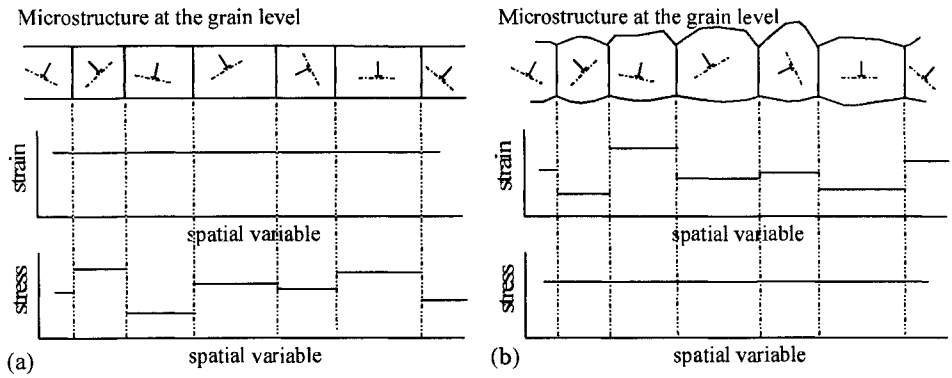

Figure 17.1: In mesoscopically heterogeneous microstructures (grain-scale heterogeneity) neither the strain nor the stress can be homogeneous throughout the sample. The dislocation symbols indicate the heterogeneity. (a) Voigt (elastic) or Taylor full-constraints (plastic) model of strain homogeneity. Constant strain everywhere in the sample violates stress equilibrium. (b) Reuss (elastic) or Sachs (plastic) model of stress homogeneity. Constant stress everywhere in the sample violates strain compatibility.

17.2 Homogenization Models for Polycrystals

Single-phase polycrystals are materials that usually consist of a large number of grains (m_g), each having a different crystallographic orientation. The distribution of the grain orientations in such aggregates is referred to as crystallographic texture. It can be described in terms of a set of Gauss-type scattering texture component functions (Lücke et al. 1981) or in terms of the orientation distribution function which is based on spherical harmonics (Bunge 1982). Since both the elastic and the plastic responses to external mechanical loads or electromagnetic fields are typically highly anisotropic within each of these individual crystals, it is an intricate task to predict the total response of the entire sample when all the grains are mutually misoriented. For instance, the elastic anisotropy[2] of matter is evident from the components of the elastic tensor and the plastic anisotropy from the geometry of dislocation slip, crack propagation, and athermal mechanisms such as twinning or martensite transformation.

The problem of material heterogeneity becomes even more pronounced when dealing with polyphase polycrystals, where not only the orientation but also the intrinsic elastic and plastic responses of each material portion can vary from point to point.

Due to this heterogeneity imposed by microstructure at the meso- or grain-scale it is obvious that neither the strain nor the stress will be homogeneous throughout mechanically loaded samples (Figure 17.1). However, meso- and macroscale polycrystal simulations are explicitly designed to deal somehow with these subtleties of microstructure and to find sufficiently precise solutions for the material's response by introducing an appropriate homogenization of stress and/or strain.

According to Aernoudt, van Houtte, and Leffers (1993) and van Houtte (1996b), a straightforward mechanical approach to solve this problem of stress and strain heterogeneity might consist in formulating and solving the equations of force equilibrium and

[2]Tungsten is the only elastically isotropic material. Its Zener ratio is equal to one.

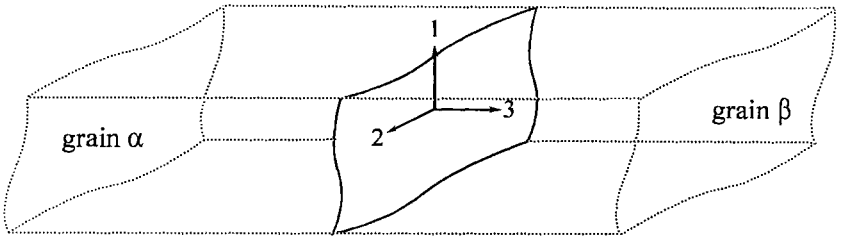

Figure 17.2: Force equilibrium and strain rate compatibility at a grain boundary according to van Houtte (1993, 1996).

strain rate compatibility at each grain or phase boundary that exists within a polyphase polycrystalline aggregate. For instance, let us consider equilibrium and compatibility at a grain boundary as shown in Figure 17.2. At such a flat and infinite grain interface with the normal x_3 which separates grain α from grain β, the following equations must be satisfied expressing static equilibrium of the stresses:

$$\sigma_{33}^{\alpha} = \sigma_{33}^{\beta} \qquad \sigma_{13}^{\alpha} = \sigma_{13}^{\beta} \qquad \sigma_{23}^{\alpha} = \sigma_{23}^{\beta} \tag{17.2}$$

and compatibility of the strain rates at that boundary:

$$\dot{\varepsilon}_{11}^{\alpha} = \dot{\varepsilon}_{11}^{\beta} \qquad \dot{\varepsilon}_{22}^{\alpha} = \dot{\varepsilon}_{22}^{\beta} \qquad \dot{\varepsilon}_{12}^{\alpha} = \dot{\varepsilon}_{12}^{\beta} \tag{17.3}$$

Identical considerations apply for the remaining boundaries. Unfortunately, up to now neither elastic nor plastic models exist that satisfy these constraints for real microstructures, i.e. for polycrystals consisting of grains with arbitrary morphology and orientation with consideration of stress and strain homogeneity inside the crystals (Aernoudt et al. 1993). However, this shortcoming of existing theoretical approaches of micromechanics is not due to a lack in physical understanding but to an insufficient incorporation of microstructural details.

This is made clear by the following simple estimation. Consider a microstructure with as many as m_g grains. The strain and stress may be homogeneous within each individual crystal. The number of unknowns in such a material amounts to $6\,m_g$ for the components of the stress tensor and $6\,m_g$ for the components of the strain tensor. This set of unknowns can be reduced from $12\,m_g$ to $6\,m_g$ through the use of a stress–strain relation.

On the other hand, the system would have to satisfy certain boundary conditions. For the macroscopic stress state $\boldsymbol{\sigma}^{\text{macro}}$ and the macroscopic strain state $\boldsymbol{\varepsilon}^{\text{macro}}$ the boundary conditions amount to

$$\boldsymbol{\sigma}^{\text{macro}} = \frac{1}{V}\int \boldsymbol{\sigma}^{\text{grain}}\,\mathrm{d}V \qquad \boldsymbol{\varepsilon}^{\text{macro}} = \frac{1}{V}\int \boldsymbol{\varepsilon}^{\text{grain}}\,\mathrm{d}V \tag{17.4}$$

which leads to 12 equations, 6 for the components of the macroscopic stress and 6 for the components of the macroscopic strain. Using a stress–strain relation, this number can be reduced from 12 to 6. Now assume that the number of grain boundaries where stress equilibrium and strain compatibility must be preserved according to equations (17.2) and (17.3) amounts to m_b. These m_b interfaces separate the m_g grains. One could then formulate as many as $6\,m_b$ additional equations for the polycrystal, namely $3\,m_b$ equations for strain compatibility and $3\,m_b$ equations for stress equilibrium. Together with the

boundary conditions, one can thus identify at least $6 + 6\,m_b$ equations for the $6\,m_g$ unknowns. For the case of simplicity let us assume that the grains have an orthorhombic symmetry and hence 6 boundaries each[3]. Thus, one can formulate $6 + 36/2\,m_g$ equations[4]. This means that there is no unambigious solution to this problem since there are too many equations for a limited number of unknowns.

Physically, the ambiguity arises from the fact that the strain and stress are presumably not homogeneous but heterogeneous within each of the crystals. In other words, each grain typically contains further lattice defects apart from conventional high-angle grain boundaries, which influence the course of stress and strain. For instance, even well-annealed polycrystalline samples can contain relatively stable dislocation substructures, which can give rise to long- or short-range internal stress and strain fields.

The simplest possible approaches to approximate the true course of the unknown stress and strain functions in the material by homogenization are the strain homogeneity approaches of Voigt for the elastic case and Taylor for the plastic case, and the stress homogeneity approaches of Reuss for the elastic case and Sachs for the plastic case (Figure 17.1). While the assumption of stress homogeneity violates the compatibility of strain, the assumption of strain homogeneity violates the equilibrium of stress.

Further details of the mechanical anisotropy of crystalline matter and the treatment of homogenization of mesoscopically heterogeneous materials can be found in the works of Hill (1950), Nye (1967), Mura (1987), van Houtte (1992), Nemat-Nasser and Hori (1993), and Stouffer and Dame (1996).

17.3 Constitutive Models for Polycrystals

The constitutive model for the linear elastic material response of solid matter is Hooke's law in tensorial notation, equation (9.29). Hooke's law means that for small external or internal forces the time-independent reversible response of the material which is quantified by the displacement field can be linearly related to that force. The strains, expressed by the symmetric part of the displacement gradient tensor, then describe a linear elastic shape change which is proportional to the stress.

In the field of low-temperature crystal plasticity and in many areas of elasticity and pseudo-elasticity of noncrystalline materials nonlinear relations between strain and stress prevail. The phenomenological methods of describing such constitutional behavior at the macroscale are often grouped into rate-independent or yield surface approaches and rate-dependent or viscoplastic approaches.

The rate-independent or yield surface description can be formulated in stress space and in strain space. It is sometimes also referred to as the elastic–plastic description. Usually, these approaches are used for plastically incompressibles materials, approximating the typical plastic response of many metals and alloys. The construction of a yield surface in stress space for a rate-insensitively deforming material is based on the assumption that irriversible deformation starts when a certain critical shear stress σ_{crit} is reached. The tensorial expression that defines this critical stress in stress space as a function of the applied stress tensor describes the yield surface (Westergaard 1920; von Mises 1928). It is referred to as the yield criterion and can be written

$$f(\boldsymbol{\sigma}) = \sigma_{\text{crit}} \tag{17.5}$$

[3]On average, real grains have about 14 interface planes, at least from a mesoscopic viewpoint.
[4]Each grain boundary in the bulk belongs to 2 grains.

Figure 17.3 shows sections of two classical yield criteria in the principal or Haigh–Westergard stress space, namely the Tresca and the von Mises critera. While the Tresca criterion represents a maximum shear stress criterion, the von Mises approach takes an energetic view by formulating the yield surface as a potential function which can be derived from the distorsion energy. For a general stress state, the von Mises yield function can be written

$$\frac{1}{2}\left[(\sigma_{11}-\sigma_{22})^2+(\sigma_{22}-\sigma_{33})^2+(\sigma_{33}-\sigma_{11})^2+6\,\sigma_{12}^2+6\,\sigma_{23}^2+6\,\sigma_{13}^2\right]=\sigma_{\text{crit}}^2 \tag{17.6}$$

When transformed to the principal stresses $\sigma_1, \sigma_2, \sigma_3$ (Chapter 9), it can then be rewritten

$$\frac{1}{2}\left[(\sigma_1-\sigma_2)^2+(\sigma_2-\sigma_3)^2+(\sigma_3-\sigma_1)^2\right]=\sigma_{\text{crit}}^2 \tag{17.7}$$

When expressed in deviatoric stress space, the von Mises yield function can be written

$$3\,J_2=\frac{3}{2}\,S_{ij}\,S_{ij}=\sigma_{\text{crit}}^2 \tag{17.8}$$

where J_2 is the second invariant of the stress deviator, and S_{ij} are the deviatoric stress components (see Chapter 9). According to equation (17.8), plasticity theories which are based on the von Mises yield function, are often referred to as J_2 flow theories, i.e. they are independent on the hydrostatic stress.

Yield surfaces of the kind presented in Figure 17.3 have some important features. Stress states outside the yield surface cannot occur. At stress states below the yield surface the material is only elastically deformed. Any imposed stress tensor that describes a stress state on the yield surface gives rise to irreversible deformation. That means all admissible stress states for plastic flow must lie on the yield surface (Mendelson 1968; Kocks 1970; Rice 1975; Gittus and Zarka 1986; Besseling and van der Giessen 1993; Krausz and Krausz 1996; Stouffer and Dame 1996). The symmetry of the Tresca and von Mises yield surfaces reflects the assumption that the flow stress under compression is equal to that under tension. This flow law is violated for materials which show a so-called Bauschinger effect. The classical yield criteria determine the begin of irriversible nonlinear flow for a material with plastically isotropic behavior which is exposed to a general three-dimensional stress state. Real polycrystalline materials, however, often show an anisotropic yield surface (Kocks et al. 1983; Canova et al. 1984; Lequeu et al. 1987; Lequeu and Jonas 1988; van Houtte 1992; Bacroix and Gilormini 1995; Maudlin and Schiferl 1996). This anisotropy can be attributed to the crystallographic nature of plasticity which occurs by the activation of discrete slip, twinning, and martensite systems, and to the formation of preferred crystallographic orientations during processing. The largest plastic anisotropy is consequently found for single crystals (see Section 17.10). It is worth noting that anisotropic yield surfaces cannot be presented in the principal or Haigh–Westergard stress space. Hill (1950) suggested a quadratic yield function for describing the anisotropy at the onset of plastic flow. For a three-dimensional stress state the Hill yield function can be written

$$\frac{1}{2}\left[F\,(\sigma_{22}-\sigma_{33})^2+G\,(\sigma_{33}-\sigma_{11})^2+H\,(\sigma_{11}-\sigma_{22})^2 + 2\,N\,\sigma_{12}^2+2\,M\,\sigma_{13}^2+2\,L\,\sigma_{23}^2\right]=\sigma_{\text{crit}}^2 \tag{17.9}$$

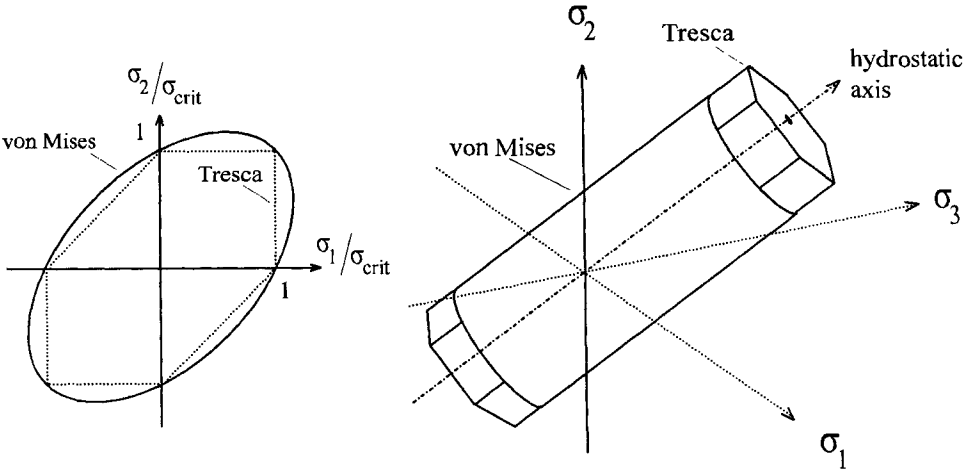

Figure 17.3: Sections of two classical yield criteria in the principal or Haigh–Westergard stress space: Tresca and von Mises yield criteria.

In the deviatoric stress space, the Hill function can be written

$$\frac{1}{2}\left[\,(G+H)^2\,S_{11}^2 + (F+H)^2\,S_{22}^2 + (F+G)^2\,S_{33}^2 - 2\,H\,S_{11}\,S_{22} - 2\,G\,S_{11}\,S_{33} - 2\,F\,S_{22}\,S_{33} + 2\,N\,S_{12}^2 + 2\,M\,S_{13}^2 + 2\,L\,S_{23}^2\right] = \sigma_{\text{crit}}^2 \tag{17.10}$$

In index notation this can be rewritten more compactly as

$$\frac{1}{2}\,\alpha_{ijkl}\,S_{kl}\,S_{ij} = \sigma_{\text{crit}}^2 \tag{17.11}$$

where the components of the symmetrical matrix $\boldsymbol{\alpha}$ amount to

$$\begin{aligned}
&\alpha_{1111} = G+H \qquad \alpha_{2222} = F+H \qquad \alpha_{3333} = F+G\\
&\alpha_{1122} = \alpha_{2211} = -H \qquad \alpha_{1133} = \alpha_{3311} = -G \qquad \alpha_{2233} = \alpha_{3322} = -F\\
&\alpha_{1212} = \alpha_{2121} = \alpha_{1221} = \alpha_{2112} = \frac{1}{2}N\\
&\alpha_{1313} = \alpha_{3131} = \alpha_{1331} = \alpha_{3113} = \frac{1}{2}M\\
&\alpha_{2323} = \alpha_{3232} = \alpha_{2332} = \alpha_{3223} = \frac{1}{2}L
\end{aligned} \tag{17.12}$$

These equations of Hill can be used for empirically describing the texture-dependent evolution of yield surface anisotropy, i.e. of the yield surface shape. However, yield surfaces do not only change their shape but can also expand in stress space due to work-hardening. Figure 17.4 shows two typical cases of hardening as used frequently in the conventional isotropic rate-independent J_2 approach. The rate-dependent or viscoplastic approaches assume that the flow stress is related to the actual strain rate of the material. The incorporation of a rate-dependent constitutive law into polycrystal models is outlined in Section 17.14.

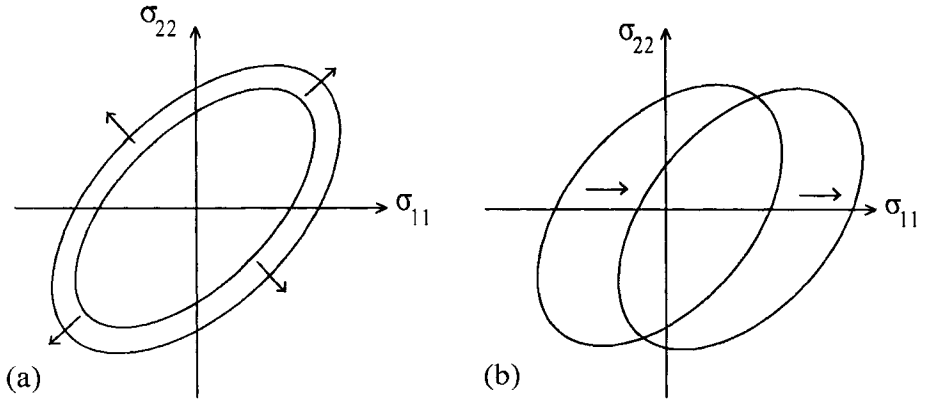

Figure 17.4: Two examples of material hardening in the rate-independent constitutive approach. (a) Isotropic work hardening; the yield surface expands isotropically in stress space; (b) Kinematic hardening; the yield surface is shifted without changing its shape. The diagrams show only two-dimensional sections of the six-dimensional yield surfaces in general stress space.

By applying the theory of plastic potentials and by introducing a constitutive law that relates the flow stress to both the strain and the strain rate it can be shown that the rate-independent or yield surface concept is only a limiting case for a series of equipotential flow surfaces when the strain-rate sensitivity approaches zero (Hill 1987; van Houtte 1994; van Houtte 1996b) (Figure 17.5). A crystallographic interpretation of the rate-insensitive yield surface is given in Section 17.10.

17.4 Voigt Model of Homogeneous Elastic Strain

An early homogenization approach for elastic loading was suggested by Voigt (1910), who assumed that in the case of a macroscopically prescribed strain state $\boldsymbol{\varepsilon}^{\text{macro}}$

each material portion $\mathrm{d}V_i$ is in the same strain state as the entire sample $\boldsymbol{\varepsilon}_i^{\text{micro}}(\boldsymbol{x})$, irrespective of its spatial position in the specimen,

$$\boldsymbol{\varepsilon}^{\text{macro}} = \boldsymbol{\varepsilon}^{\text{micro}}(\boldsymbol{x}) \tag{17.13}$$

The strain would then be homogeneous throughout the sample.

However, for instance in a polycrystalline sample, the elastic response typically varies from grain to grain, due to the spatially changing crystal orientation. The elastic stiffness tensor components C_{ijkl} are usually given in crystal rather than in sample coordinates (Chapter 9, Table 9.1). To use them in sample coordinates for the calculation of the macroscale polycrystal elasticity, they can be rotated parallel to the sample coordinates according to

$$C_{ijkl}^{\text{sample}} = a_{mi}\, a_{nj}\, a_{ok}\, a_{pl}\, C_{mnop}^{\text{crystal}} \tag{17.14}$$

where a_{mi}, a_{nj}, a_{ok}, and a_{pl} are the elements of the transformation matrix between the sample and the crystal reference system.

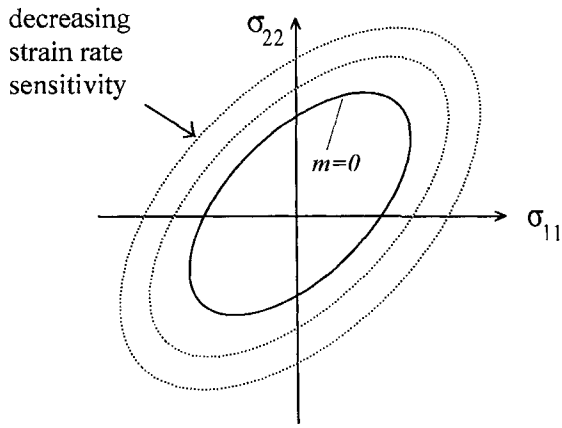

Figure 17.5: The theory of plastic potentials shows that by applying a constitutive law which relates the flow stress to the strain and its actual rate, the yield surface can be regarded as a limiting surface for a series of equipotential flow surfaces when the strain-rate sensitivity approaches zero (van Houtte 1994, 1996). The diagram shows only a two-dimensional section of the six-dimensional yield surface.

This transformation shows that the local elastic properties of the sample will differ from grain to grain, according to the local crystallographic texture (Figure 17.1). The example can easily be generalized for polyphase materials. Since in the Voigt model the prescribed strain is the same everywhere in the sample, the stress must vary according to

$$\sigma_{ij}^{\text{crystal}}(\boldsymbol{g},\boldsymbol{x}) = C_{ijkl}^{\text{crystal}}(\boldsymbol{g},\boldsymbol{x})\,\varepsilon_{kl}^{\text{crystal}}(\boldsymbol{g},\boldsymbol{x}) = C_{ijkl}^{\text{crystal}}(\boldsymbol{g},\boldsymbol{x})\,\varepsilon_{kl}^{\text{sample}} \tag{17.15}$$

where $\boldsymbol{g}$ is the local orientation of the crystal. The prescribed strain $\varepsilon_{kl}^{\text{sample}}$ corresponds to $\varepsilon_{kl}^{\text{macro}}$ in equation (17.13).

The Voigt limit for the elastic response of a polycrystalline sample can be calculated by weighting the tensor of the elastic stiffness as a function of orientation with the orientation distribution function.

17.5 Reuss Model of Homogeneous Elastic Stress

A different approach to treating the homogenization problem in an elastically loaded polycrystalline sample was suggested by Reuss (1930). He suggested that in the case of a macroscopically prescribed stress state $\boldsymbol{\sigma}^{\text{macro}}$ each material portion $\mathrm{d}V_i$ is in the same stress state $\boldsymbol{\sigma}_i^{\text{micro}}(\boldsymbol{x})$, irrespective of its spatial position in the specimen,

$$\boldsymbol{\sigma}^{\text{macro}} = \boldsymbol{\sigma}^{\text{micro}}(\boldsymbol{x}) \tag{17.16}$$

The stress would then be homogeneous throughout the specimen.

As was outlined above for the stiffness tensor, in a polycrystal the elastic response may vary from grain to grain, in accord with the local orientation of the crystal. Prior to using the components of the compliance tensor in the coordinates of the sample, they

must be rotated parallel to the sample coordinates according to

$$S_{ijkl}^{\text{sample}} = a_{mi}\, a_{nj} a_{ok}\, a_{pl}\, S_{mnop}^{\text{crystal}} \tag{17.17}$$

where a_{mi}, a_{nj}, a_{ok}, and a_{pl} are the elements of the transformation matrix between the sample and the crystal reference system. The compliance will thus differ from grain to grain, according to the local grain orientation (Figure 17.1).

Since in the Reuss model the prescribed external stress is constant throughout the specimen, the strain must vary according to

$$\varepsilon_{ij}^{\text{crystal}}(\boldsymbol{g}, \boldsymbol{x}) = S_{ijkl}^{\text{crystal}}(\boldsymbol{g}, \boldsymbol{x})\, \sigma_{kl}^{\text{crystal}}(\boldsymbol{g}, \boldsymbol{x}) = S_{ijkl}^{\text{crystal}}(\boldsymbol{g}, \boldsymbol{x})\, \sigma_{kl}^{\text{sample}} \tag{17.18}$$

where the stress $\sigma_{kl}^{\text{sample}}$ corresponds to $\sigma_{kl}^{\text{macro}}$ in equation (17.16).

The elastic Reuss limit can be calculated for a polycrystal by weighting the tensor of the elastic compliance as a function of orientation with the orientation distribution function.

Since neither the Voigt nor the Reuss method provides reliable approximations to the elastic modulus of a polycrystal, Hill defined an average modulus which consists of the equally weighted results of both above models.

17.6 Hashin–Shtrikman Homogenization for Polycrystal Elasticity

The basic idea of the Hashin–Shtrikman homogenization approach for elastic (polycrystalline) materials consists in replacing a microstructurally heterogeneous material by a homogeneous volume element with a different homogeneous modulus (Hashin and Shtrikman 1962a). The solution is found by using a variational principle.

The derivation starts by considering a representative volume element with the stiffness tensor $\boldsymbol{C}$ and the compliance tensor $\boldsymbol{S}$, and n linearly elastic inclusions Ω_i with $i = 1, 2, ..., n$ which have the stiffness tensor $\boldsymbol{C}^{\text{i}}$ and the compliance tensor $\boldsymbol{S}^{\text{i}}$. It is convenient to introduce the variables $\boldsymbol{C}'$ and $\boldsymbol{S}'$ which assume the values $\boldsymbol{C}$ and $\boldsymbol{S}$ inside the matrix and $\boldsymbol{C}^{\text{i}}$ and $\boldsymbol{S}^{\text{i}}$ inside the inclusion.

Now one considers that the representative volume element is subjected to a uniform macroscopic stress $\boldsymbol{\sigma}^0$. This stress is used to define an overall compliance tensor according to

$$\boldsymbol{\varepsilon} \equiv \widetilde{\boldsymbol{S}}\, \boldsymbol{\sigma}^0 \tag{17.19}$$

In the next step one considers an equivalent homogeneous volume v of material which has an identical geometry to that of the representative volume element, and introduces the eigenstrain field for the homogenization. It is assumed that the newly introduced material exhibits everywhere a constant stiffness tensor $\boldsymbol{C}^{\text{v}}$ and compliance tensor $\boldsymbol{S}^{\text{v}}$. These tensors are associated with an arbitrary homogeneous linear elastic comparison material which replaces the former heterogeneous representative volume element. They do not represent field variables but are constant.

Now one introduces the eigenstrain field $\boldsymbol{\varepsilon}^{\text{e}}(\boldsymbol{x})$ such that the comparison material has the same stress and strain fields as the original heterogeneous representative volume element. This leads to the consistency conditions

$$\begin{aligned} \boldsymbol{\sigma}(\boldsymbol{x}) &= \boldsymbol{C}'(\boldsymbol{x})\, \boldsymbol{\varepsilon}(\boldsymbol{x}) = \boldsymbol{C}^{\text{v}}\, [\boldsymbol{\varepsilon}(\boldsymbol{x}) - \boldsymbol{\varepsilon}^{\text{e}}(\boldsymbol{x})] \\ \boldsymbol{\varepsilon}(\boldsymbol{x}) &= \boldsymbol{S}'(\boldsymbol{x})\, \boldsymbol{\sigma}(\boldsymbol{x}) = \boldsymbol{S}^{\text{v}}\, \boldsymbol{\sigma}(\boldsymbol{x}) + \boldsymbol{\varepsilon}^{\text{e}}(\boldsymbol{x}) \end{aligned} \tag{17.20}$$

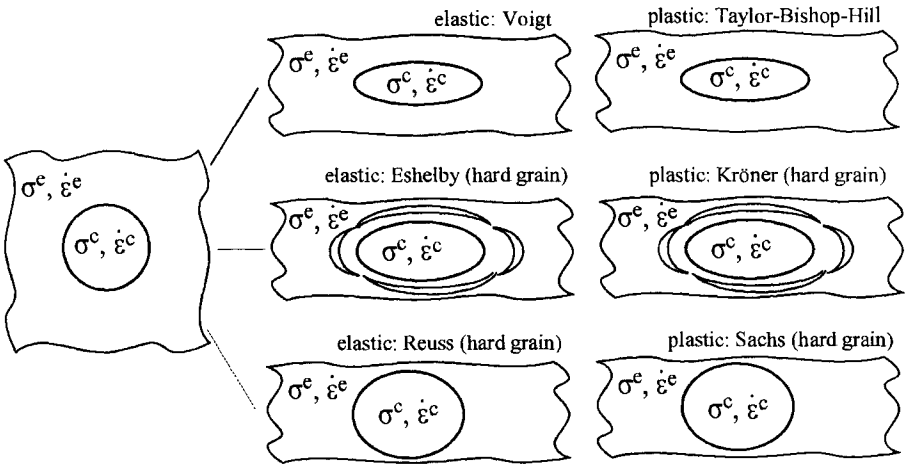

Figure 17.6: Schematic representation of various homogenization approaches.

After that the eigenstrain $\boldsymbol{\varepsilon}^{\mathrm{e}}(\boldsymbol{x})$ can be used to determine the stress in the homogeneous comparison material which is equivalent to the stress field in the original representative volume element:

$$\boldsymbol{\sigma}(\boldsymbol{x}) = \left[\boldsymbol{S}'(\boldsymbol{x}) - \boldsymbol{S}^{\mathrm{v}}\right] \boldsymbol{\varepsilon}^{\mathrm{e}}(\boldsymbol{x}) \tag{17.21}$$

By assuming that the volume is subjected to uniform boundary tractions one can now define the perturbation stress $\boldsymbol{\sigma}^{\mathrm{p}}(\boldsymbol{x})$. This stress field can be regarded as a measure for the deviation of the stress field in the homogeneous comparison material $\boldsymbol{\sigma}(\boldsymbol{x})$ from $\boldsymbol{\sigma}^{0}$, equation (17.19).

$$\boldsymbol{\sigma}^{\mathrm{p}}(\boldsymbol{x}) \equiv \boldsymbol{\sigma}(\boldsymbol{x}) - \boldsymbol{\sigma}^{0} \tag{17.22}$$

The so-defined perturbation stress field is in general a functional of the distributed eigenstrains. The solution of this variational problem using tensor integral operators which include an appropriate Green's function leads to the Hashin–Shtrikman formulation. Details of the solution technique can be found in the works of Hashin and Shtrikman (1962b), Hill (1963), Kröner (1977), Willis (1977), and Nemat-Nasser and Hori (1993).

17.7 Eshelby's Inclusion Approach

The Voigt model of homogeneous internal strain under an externally imposed elastic strain and the Reuss model for homogeneous internal stress under an externally imposed elastic load can be regarded as the upper (Voigt) and lower (Reuss) bounds of the overall modulus of elastically heterogeneous materials. From a mechanical standpoint both approaches are unsatisfactory since they violate either elastic stress equilibrium (Voigt) or elastic strain compatibility (Reuss) (Figure 17.6).

Eshelby (1957) formulated an improved elastic homogenization approach which is based on inserting a linear elastic inclusion of spherical or ellipsoidal shape into an infinite matrix medium. The strain and stress distributions are obtained after relaxing this

compound. A similar approach which was used by Khachaturyan (1983) for deriving the elastic contribution to the free enthalpy functional in phase field models is discussed in Chapter 10.

In contrast to the Voigt and Reuss descriptions, the inclusion in the Eshelby model does not simply experience a strain or stress state identical to the sample without any consideration of the surrounding matrix, but as a rule generates an elastic response in the inclusion and in the matrix. In the classical inclusion model the matrix is homogeneous and has isotropic elastic properties.

The first part of the derivation consists in formulating and solving the so-called transformation problem. This amounts to finding a solution for an embedded inclusion which has the same linear elastic properties as the matrix but undergoes a shape change due to transformation.

The transformation problem can be separated into a number of subsequent calculation steps. First, one removes a volume unit from the homogeneous matrix, so that it be free of external stresses, and subjects it to a shape change.

This transformation can be due to changes in temperature or electrical field, or a consequence of martensite formation. The physical reason for this transformation is without relevance for the further derivation. Since the volume affected is not connected to the matrix, it undergoes a shape change which is in accord with the transformation or eigenstrain $\boldsymbol{\varepsilon}^{\mathrm{e}}$. The elastic energy remains unchanged during this step since it does not expand or shrink the affected volume unit in response to an external stress state.

In the next step, one imposes a stress on the transformed unit volume in order to restore exactly its original shape prior to transformation and fit it back into the rigid matrix. As a rule a stress $\boldsymbol{\sigma}^{\mathrm{i}}$ will be generated in the inclusion which is proportional to the deviation of the transformed from the original shape,

$$\boldsymbol{\sigma}^{\mathrm{i}} = \boldsymbol{C}\,[\boldsymbol{\varepsilon}^{\mathrm{c}} - \boldsymbol{\varepsilon}^{\mathrm{e}}] \tag{17.23}$$

where $\boldsymbol{\varepsilon}^{\mathrm{c}}$ is the strain that is imposed on the inclusion to fit it back into the matrix.

Eshelby found an analytical solution for this problem by consideration of Hooke's law, stress equilibrium, and strain compatibility. The macroscopic stress and strain in the matrix at an infinite distance from the inclusion were assumed to be zero. The distributions of stress and strain were homogeneous in the spherical or ellipsoidal inclusion and heterogeneous in the matrix.

According to Eshelby (1957), Mura (1987), Indenbom and Lothe (1992) and van Houtte (1992) the solution can be written in the general form

$$\boldsymbol{\varepsilon}^{\mathrm{c}} = \boldsymbol{D}\,\boldsymbol{\varepsilon}^{\mathrm{e}} \qquad \text{or} \qquad \varepsilon^{\mathrm{c}}_{ij} = D_{ijkl}\,\varepsilon^{\mathrm{e}}_{kl} \tag{17.24}$$

where $\boldsymbol{D}$ is a fourth-rank elastic tensor, the components of which amount to α and β. They are defined by

$$\begin{aligned} \varepsilon^{\mathrm{c\,hyd}} &= \alpha\,\varepsilon^{\mathrm{e\,hyd}} \\ \varepsilon^{\mathrm{c\,dev}}_{ij} &= \beta\,\varepsilon^{\mathrm{e\,dev}}_{ij} \end{aligned} \tag{17.25}$$

where $\varepsilon^{\mathrm{c\,hyd}}$ and $\varepsilon^{\mathrm{e\,hyd}}$ are the scalar hydrostatic strain portions

$$\begin{aligned} \varepsilon^{\mathrm{c\,hyd}} &= \frac{1}{3}\,\varepsilon^{\mathrm{c}}_{ii} \\ \varepsilon^{\mathrm{e\,hyd}} &= \frac{1}{3}\,\varepsilon^{\mathrm{e}}_{ii} \end{aligned} \tag{17.26}$$

and $\varepsilon_{ij}^{c\,dev}$ and $\varepsilon_{ij}^{e\,dev}$ the deviatoric strain components

$$\begin{aligned} \varepsilon_{ij}^{c\,dev} &= \varepsilon_{ij}^{c} - \varepsilon^{c\,hyd}\,\delta_{ij} \\ \varepsilon_{ij}^{e\,dev} &= \varepsilon_{ij}^{e} - \varepsilon^{e\,hyd}\,\delta_{ij}\,. \end{aligned} \tag{17.27}$$

The values of α and β amount to

$$\begin{aligned} \alpha &= \left(\frac{1}{3}\right)\left(\frac{1+\nu}{1-\nu}\right) \\ \beta &= \left(\frac{2}{15}\right)\left(\frac{4-5\nu}{1-\nu}\right) \end{aligned} \tag{17.28}$$

Based on this classical solution the second part of the derivation consists in solving the so-called inhomogeneity problem. It changes the conditions with respect to the transformation problem by allowing dissimilar linear elastic properties of the matrix and the inclusion and by assuming a nonzero matrix stress $\boldsymbol{\sigma}^{M}$ and strain $\boldsymbol{\varepsilon}^{M}$ at infinite distance from the inclusion, i.e. by loading the entire material. Eshelby solved this problem by reducing it to the transformation problem. He showed that the body consisting of matrix and inhomogeneous inclusion can be replaced by an unbounded matrix and a transformed inclusion with the same elastic constants as the matrix.

First, one has to derive the transformation eigenstrain $\boldsymbol{\varepsilon}^{e}$ of the inclusion, which makes it equivalent to an inhomogeneous inclusion:

$$\boldsymbol{\varepsilon}^{e} = \boldsymbol{D}'\,\boldsymbol{\varepsilon}^{M} \qquad \text{or} \qquad \varepsilon_{ij}^{e} = D'_{ijkl}\,\varepsilon_{kl}^{M} \tag{17.29}$$

where $\boldsymbol{D}'$ is a fourth-rank elastic tensor, the components of which amount to α' and β'. They are defined by

$$\begin{aligned} \varepsilon^{e\,hyd} &= \alpha'\,\varepsilon^{M\,hyd} \\ \varepsilon_{ij}^{e\,dev} &= \beta'\,\varepsilon_{ij}^{M\,dev} \end{aligned} \tag{17.30}$$

where $\varepsilon^{e\,hyd}$ and $\varepsilon^{M\,hyd}$ are the scalar hydrostatic portions of the eigenstrain and of the matrix strain tensor, respectively

$$\begin{aligned} \varepsilon^{e\,hyd} &= \frac{1}{3}\,\varepsilon_{ii}^{e} \\ \varepsilon^{M\,hyd} &= \frac{1}{3}\,\varepsilon_{ii}^{M} \end{aligned} \tag{17.31}$$

and $\varepsilon_{ij}^{e\,dev}$ and $\varepsilon_{ij}^{M\,dev}$ the corresponding deviatoric strain components

$$\begin{aligned} \varepsilon_{ij}^{e\,dev} &= \varepsilon_{ij}^{e} - \varepsilon^{e\,hyd}\,\delta_{ij} \\ \varepsilon_{ij}^{M\,dev} &= \varepsilon_{ij}^{M} - \varepsilon^{M\,hyd}\,\delta_{ij} \end{aligned} \tag{17.32}$$

The values for α' and β' are

$$\begin{aligned} \alpha' &= \frac{\kappa^{i} - \kappa^{M}}{(\kappa^{M} - \kappa^{i})\,\alpha - \kappa^{M}} \\ \beta' &= \frac{\mu^{i} - \mu^{M}}{(\mu^{M} - \mu^{i})\,\beta - \mu^{M}} \end{aligned} \tag{17.33}$$

where μ^{i} is the Lamé constant of the inclusion, μ^{m} the Lamé constant of the matrix, κ^{i} the bulk modulus of the inclusion, and κ^{m} that of the matrix; α and β are the same as in equation (17.28).

After the calculation of the eigenstrain $\boldsymbol{\varepsilon}^{\mathrm{e}}$ of this so called inhomogeneous inclusion, one can further proceed by inserting this result into equation (17.24) for the calculation of the true inclusion strain $\boldsymbol{\varepsilon}^{\mathrm{c}}$.

By combining the elastic tensor coefficients from equations (17.24) and (17.29) one can rewrite compactly the relationship between the true inclusion strain and the macroscopic strain in the unbounded matrix at infinity

$$\boldsymbol{\varepsilon}^{\mathrm{c}} = \boldsymbol{D}^{*}\,\boldsymbol{\varepsilon}^{\mathrm{M}} \qquad \text{or} \qquad \varepsilon^{\mathrm{c}}_{ij} = D^{*}_{ijkl}\,\varepsilon^{\mathrm{M}}_{kl} \tag{17.34}$$

The above results now make it possible to establish a relation between the true strain $\boldsymbol{\varepsilon}^{\mathrm{c}}$ and the stress $\boldsymbol{\sigma}^{\mathrm{i}}$ in the inclusion. Such a relation can be derived by use of some of the above formulas under the assumption that the stress and strain in the matrix go to zero at an infinite distance from the inclusion. From

$$\boldsymbol{\varepsilon}^{\mathrm{e}} = \boldsymbol{D}^{-1}\,\boldsymbol{\varepsilon}^{\mathrm{c}} \tag{17.35}$$

and

$$\boldsymbol{\sigma}^{\mathrm{i}} = \boldsymbol{C}\,[\boldsymbol{\varepsilon}^{\mathrm{c}} - \boldsymbol{\varepsilon}^{\mathrm{e}}] \tag{17.36}$$

one obtains

$$\boldsymbol{\sigma}^{\mathrm{i}} = \boldsymbol{C}\,\left[\boldsymbol{\varepsilon}^{\mathrm{c}} - \boldsymbol{D}^{-1}\,\boldsymbol{\varepsilon}^{\mathrm{c}}\right] = \boldsymbol{C}\,\left[\boldsymbol{I} - \boldsymbol{D}^{-1}\right]\,\boldsymbol{\varepsilon}^{\mathrm{c}} \tag{17.37}$$

This formulation has the advantage that it establishes a relation between the true strain and the stress in the inclusion *without* the use of the transformation strain.

For a system where the macroscopic stress and strain decay to zero at infinity it is often written in a somewhat more compact form, namely

$$\boldsymbol{\sigma}^{\mathrm{i}} = -\boldsymbol{L}^{*}\,\boldsymbol{\varepsilon}^{\mathrm{i}} \tag{17.38}$$

where $\boldsymbol{\varepsilon}^{\mathrm{i}}$ is equal to $\boldsymbol{\varepsilon}^{\mathrm{c}}$. The fourth-rank elastic tensor $\boldsymbol{L}^{*}$, which is usually referred to as the interaction tensor amounts to

$$\boldsymbol{L}^{*} = -\boldsymbol{C}\,\left[\boldsymbol{I} - \boldsymbol{D}^{-1}\right] \tag{17.39}$$

The unit tensor $\boldsymbol{I}$ can be written

$$I_{ijkl} = \frac{1}{2}\,(\,\delta_{ik}\,\delta_{jl} + \delta_{il}\,\delta_{jk}\,) \tag{17.40}$$

Under a nonvanishing stress and strain field in the matrix, $\boldsymbol{\sigma}^{\mathrm{M}}$ and $\boldsymbol{\varepsilon}^{\mathrm{M}}$, the interaction formula becomes

$$\left[\boldsymbol{\sigma}^{\mathrm{i}} - \boldsymbol{\sigma}^{\mathrm{M}}\right] = -\boldsymbol{L}^{*}\,\left[\boldsymbol{\varepsilon}^{\mathrm{i}} - \boldsymbol{\varepsilon}^{\mathrm{M}}\right] \tag{17.41}$$

This result shows that a hard grain which carries less strain as compared with the entire sample, has a higher stress.

17.8 Kröner's Self-Consistent Approach

The self-consistent approach of Kröner (1958a) is based on equation (17.41). It treats each crystal as a spherical inclusion in a linear elastic unbounded matrix. The matrix consists of all the other crystals (Kröner 1961).

By replacing the stress in the inclusion $\boldsymbol{\sigma}^{\mathrm{i}}$ by the local elastic tensor as a function of grain orientation $\boldsymbol{c}(\boldsymbol{g})$ and the strain in the inclusion $\boldsymbol{\varepsilon}^{\mathrm{i}}$ and replacing the stress in the matrix $\boldsymbol{\sigma}^{\mathrm{M}}$ by the elastic tensor of the entire polycrystalline sample $\boldsymbol{C}$ and the strain in the matrix $\boldsymbol{\varepsilon}^{\mathrm{M}}$, one can rewrite equation (17.41)

$$\left[\boldsymbol{c}(\boldsymbol{g})\,\boldsymbol{\varepsilon}^{\mathrm{i}}\right] - \left[\boldsymbol{C}\,\boldsymbol{\varepsilon}^{\mathrm{M}}\right] = \boldsymbol{L}^{*}\left[\boldsymbol{\varepsilon}^{\mathrm{i}} - \boldsymbol{\varepsilon}^{\mathrm{M}}\right] \tag{17.42}$$

This expression can be transformed into

$$\boldsymbol{\sigma}^{\mathrm{i}} = \boldsymbol{c}(\boldsymbol{g})\,[\boldsymbol{c}(\boldsymbol{g}) + \boldsymbol{L}^{*}]^{-1}\,[\boldsymbol{C} + \boldsymbol{L}^{*}]\,\boldsymbol{\varepsilon}^{\mathrm{M}} \tag{17.43}$$

This equation can be averaged over all crystals in the sample. Integrating the right-hand side of the equation over the orientation distribution function $f(\boldsymbol{g})$ of the considered sample yields an averaged elastic matrix stress. This matrix stress can be written as a function of all crystal orientations

$$\boldsymbol{\sigma}^{\mathrm{M}} = \left\{\int \boldsymbol{c}(\boldsymbol{g})\,[\boldsymbol{c}(\boldsymbol{g}) + \boldsymbol{L}^{*}]^{-1}\,[\boldsymbol{C} + \boldsymbol{L}^{*}]\,f(\boldsymbol{g})\,\mathrm{d}\boldsymbol{g}\right\}\boldsymbol{\varepsilon}^{\mathrm{M}} \tag{17.44}$$

By comparison of the coefficients one obtains an integral equation for the polycrystal modulus $\boldsymbol{C}$:

$$\boldsymbol{C} = \int \boldsymbol{c}(\boldsymbol{g})\,[\boldsymbol{c}(\boldsymbol{g}) + \boldsymbol{L}^{*}(\boldsymbol{C})]^{-1}\,[\boldsymbol{C} + \boldsymbol{L}^{*}(\boldsymbol{C})]\;f(\boldsymbol{g})\,\mathrm{d}\boldsymbol{g} \tag{17.45}$$

Since this equation is an implicit form, i.e. its integrand contains $\boldsymbol{C}$ itself, it must be solved by iteration. Polycrystal methods based on such a formulation are referred to as self-consistent models.

17.9 Taylor Full-Constraints Model for Homogeneous Plastic Strain in Polycrystals

Taylor (1938) suggested in his pioneering work that strain (rate) compatibility among the grains assembled in a polycrystal is necessarily preserved if all crystals undergo the same shape change as the entire sample (Figure 17.6). The original Taylor model, which is referred to as the full-constraints model, thus considers strain compatibility throughout the sample but neglects stress equilibrium at the grain boundaries.

For fulfilling a prescribed plastic strain state, crystals must use slip or twinning systems, i.e. they do not behave like a homogeneous isotropic continuum which can follow any arbitrary shape change. Due to their different crystal orientations, different grains in a polycrystalline aggregate will as a rule employ different combinations of slip systems to attain an externally imposed velocity gradient state.

In this context the Taylor full-constraints model makes two main assumptions. First, it stipulates that an approach which is based on the strict fulfillment of strain rate compatibility reflects polycrystal plasticity better than a model that is based on the mere

fulfillment of strict stress equilibrium[5]. Second, it assumes that large strain deformation of metals is not adequately described from a physical point of view by an isotropic homogeneous constitutive law, but requires the incorporation of the crystallographic character of plasticity.

The original Taylor full-constraints model assumes that the external macroscopic strain corresponds to the internal microscopic strain, and that a prescribed deformation must be accomplished by crystallographic slip, twinning, or martensitic transformation (Taylor 1938). Following the work of Bunge (1970), Kocks (1970), Gil Sevilliano, van Houtte, and Aernoudt (1980), van Houtte (1985), van Houtte (1988), and Aernoudt, van Houtte, and Leffers (1993), the classical Taylor theory can be formulated in a somewhat generalized fashion.

In the full-constraints approach the externally imposed macroscopic velocity gradient tensor serves as an input quantity. The fields of the velocity gradient, rotation, stress, strain, and strain rate are supposed to be homogeneous within each grain. For preserving compatibility, the external velocity gradient tensor is prescribed for each crystal. The distortion of each grain is accomplished by crystal slip and/or twinning in such a manner that the local velocity gradient assumes the prescribed external value. In most cases this requires multiple slip. The mathematical treatment of this model will be discussed now in more detail.

The activation of a slip system t takes place if the shear stress τ^t on that system reaches the value of the *critical* resolved shear stress τ^t_{crit} for this family of slip systems. The actual shear stress on the glide system t can be calculated from a given stress state σ_{ij} by using

$$\tau^t = \sigma_{ij}\, m^t_{ij} \tag{17.46}$$

where the Einstein summation rule applies. The matrix with the components m^t_{ij} is a crystallographic transformation matrix which describes the orientation of the slip system t with respect to the crystal coordinate system. For the case of single slip in a single crystal under pure tension m^t_{ij} degenerates into the Schmid factor. This means that the expressions

$$\tau^t_{\text{crit}} = \sigma_{ij}\, m^t_{ij} \qquad \text{and} \qquad -\tau^t_{\text{crit}} = \sigma_{ij}\, m^t_{ij} \tag{17.47}$$

describe the yield locus or yield function for a single crystal.

Written in index notation, the transformation matrix $\boldsymbol{m}^t$ of the coefficients m^t_{ij} is given by

$$m^t_{ij} = b^t_i\, n^t_j \tag{17.48}$$

where $b^t_i n^t_j$ is the dyadic product of the normalized Burgers vector $\boldsymbol{b}^t$ and normalized glide plane normal $\boldsymbol{n}^t$ of the slip system t. In matrix notation, equation (17.48) can be rewritten

$$\boldsymbol{m}^t = \boldsymbol{b}^t \odot \boldsymbol{n}^t \tag{17.49}$$

[5]Self-consistent and coupled finite element/Taylor models of crystal plasticity consider both stress equilibrium and strain compatibility, at least in an approximate fashion. The main approximation of self-consistent schemes lies in the averaging of the surroundings as an effective medium and that of finite element codes in the use of interpolation functions instead of the real displacements.

where $\boldsymbol{b}^t \odot \boldsymbol{n}^t = b_i^t n_j^t$ is the dyadic product written in matrix form. The symmetric part $\boldsymbol{M}^t$ of the transformation matrix $\boldsymbol{m}^t$ is given by[6]

$$M_{ij}^t = \frac{1}{2}\left(m_{ij}^t + m_{ji}^t\right) = \frac{1}{2}\left(b_i^t\, n_j^t + b_j^t\, n_i^t\right) \tag{17.50}$$

Using a detailed notation, equation (17.50) can be rewritten for the slip system t:

$$\begin{aligned}\begin{pmatrix} M_{11}^t & M_{12}^t & M_{13}^t \\ M_{21}^t & M_{22}^t & M_{23}^t \\ M_{31}^t & M_{32}^t & M_{33}^t \end{pmatrix} &= \frac{1}{2}\begin{pmatrix} m_{11}^t & m_{12}^t & m_{13}^t \\ m_{21}^t & m_{22}^t & m_{23}^t \\ m_{31}^t & m_{32}^t & m_{33}^t \end{pmatrix} + \frac{1}{2}\begin{pmatrix} m_{11}^t & m_{21}^t & m_{31}^t \\ m_{12}^t & m_{22}^t & m_{32}^t \\ m_{13}^t & m_{23}^t & m_{33}^t \end{pmatrix} \\ &= \frac{1}{2}\begin{pmatrix} b_1^t n_1^t & b_1^t n_2^t & b_1^t n_3^t \\ b_2^t n_1^t & b_2^t n_2^t & b_2^t n_3^t \\ b_3^t n_1^t & b_3^t n_2^t & b_3^t n_3^t \end{pmatrix} + \frac{1}{2}\begin{pmatrix} b_1^t n_1^t & b_2^t n_1^t & b_3^t n_1^t \\ b_1^t n_2^t & b_2^t n_2^t & b_3^t n_2^t \\ b_1^t n_3^t & b_2^t n_3^t & b_3^t n_3^t \end{pmatrix}\end{aligned} \tag{17.51}$$

The antisymmetric part $\boldsymbol{Y}^t$ of $\boldsymbol{m}^t$ is given by

$$Y_{ij}^t = \frac{1}{2}\left(m_{ij}^t - m_{ji}^t\right) = \frac{1}{2}\left(b_i^t\, n_j^t - b_j^t\, n_i^t\right) \tag{17.52}$$

Using a detailed notation, equation (17.52) can be rewritten

$$\begin{aligned}\begin{pmatrix} Y_{11}^t & Y_{12}^t & Y_{13}^t \\ Y_{21}^t & Y_{22}^t & Y_{23}^t \\ Y_{31}^t & Y_{32}^t & Y_{33}^t \end{pmatrix} &= \frac{1}{2}\begin{pmatrix} m_{11}^t & m_{12}^t & m_{13}^t \\ m_{21}^t & m_{22}^t & m_{23}^t \\ m_{31}^t & m_{32}^t & m_{33}^t \end{pmatrix} - \frac{1}{2}\begin{pmatrix} m_{11}^t & m_{21}^t & m_{31}^t \\ m_{12}^t & m_{22}^t & m_{32}^t \\ m_{13}^t & m_{23}^t & m_{33}^t \end{pmatrix} \\ &= \frac{1}{2}\begin{pmatrix} b_1^t n_1^t & b_1^t n_2^t & b_1^t n_3^t \\ b_2^t n_1^t & b_2^t n_2^t & b_2^t n_3^t \\ b_3^t n_1^t & b_3^t n_2^t & b_3^t n_3^t \end{pmatrix} - \frac{1}{2}\begin{pmatrix} b_1^t n_1^t & b_2^t n_1^t & b_3^t n_1^t \\ b_1^t n_2^t & b_2^t n_2^t & b_3^t n_2^t \\ b_1^t n_3^t & b_2^t n_3^t & b_3^t n_3^t \end{pmatrix}\end{aligned} \tag{17.53}$$

The transformation coefficients m_{ij}^t and therefore also M_{ij}^t and Y_{ij}^t depend on the crystal orientation when expressed in the external reference system. However, they are independent of the crystal orientation when written in crystal coordinates. For instance, if one assumes a rolling stress state according to Tucker (1964)[7], a single active slip system t = (101)[10$\bar{1}$] in a (001)[100] oriented crystal, and a sample coordinate system defined by x_1 || rolling direction, x_2 || transverse direction, and x_3 || normal direction, one obtains for the shear stress on the slip system (101)[10$\bar{1}$]: $\tau^t = \sigma_{11} = -\sigma_{33}$. In the example the coefficients m_{ij}^t are the *same* in the crystal and in the sample coordinate system. For arbitrary orientations, the transformations of $\boldsymbol{m}$, $\boldsymbol{M}$, and $\boldsymbol{Y}$ can be calculated using

$$m_{kl}^t = a_{ki}\, a_{lj}\, m_{ij}^t \tag{17.54}$$

where the transformation operators a_{ki} and a_{lj} are related to the rotation matrix $\boldsymbol{g}$ which transforms the specimen coordinate system into the crystal coordinate system. The rotation matrix contains the normalized components h', k', l' corresponding to the crystal direction parallel to the sheet normal x_3, q', r', s' to that parallel to the transverse direction x_2, and u', v', w' to that parallel to the rolling direction x_1,

$$\boldsymbol{g} = \begin{pmatrix} u' & q' & h' \\ v' & r' & k' \\ w' & sk' & l' \end{pmatrix} \tag{17.55}$$

[6] no summation over t.

[7] According to Tucker, the stress deviator during rolling can be dismantled into a compressive stress parallel to the sheet normal ($\sigma_{33} = -\sigma_{11}$) and a tensile stress parallel to the rolling direction (σ_{11}).

However, these various considerations about the calculation of resolved shear stresses and their relation to crystal slip are at first of minor importance since in the Taylor theory only the strain rate is prescribed whilst the stress is initially unknown. The above equations therefore cannot be used to determine the active slip systems and the resulting grain rotations, as for instance in the Sachs approach.

Instead, one has to start with the deformation gradient tensor $\boldsymbol{F}$ and the displacement gradient tensor $\boldsymbol{H}$. According to their respective definitions given in Chapter 16, equations (16.16) and (16.17), $\boldsymbol{F}$ can be expressed in terms of $\boldsymbol{H}$

$$\boldsymbol{F} = \boldsymbol{I} + \boldsymbol{H} \tag{17.56}$$

where $\boldsymbol{I}$ is the unit matrix. In vector gradient notation the above equation amounts to

$$\frac{\partial r_i}{\partial x_j} = \frac{\partial x_i}{\partial x_j} + \frac{\partial u_i}{\partial x_j} \tag{17.57}$$

where $\boldsymbol{x}$ is a vector that combines two physical points in the crystal and $\boldsymbol{r}$ a vector that combines the same points after an infinitesimal deformation step, equation (16.15). Thus one can express $\boldsymbol{r}$ in terms of $\boldsymbol{F}$ or $\boldsymbol{H}$, respectively:

$$\boldsymbol{r} = \boldsymbol{F}\,\boldsymbol{x} = (\boldsymbol{H} + \boldsymbol{I})\,\boldsymbol{x} \tag{17.58}$$

Both tensors $\boldsymbol{H}$ and $\boldsymbol{F}$ can be dismantled to distinguish strain from rotation. For instance, one uses a linear decomposition of the deformation gradient tensor $\boldsymbol{F}$ into a symmetric portion $\boldsymbol{U}$ or $\boldsymbol{W}$, and an orthogonal normalized antisymmetric (skew symmetric) portion $\boldsymbol{F}_{\mathrm{a}}$:

$$\boldsymbol{F} = \boldsymbol{F}_{\mathrm{a}}\boldsymbol{U} = \boldsymbol{W}\boldsymbol{F}_{\mathrm{a}} \tag{17.59}$$

It must be emphasized that the tensors $\boldsymbol{W}$ and $\boldsymbol{U}$ are not necessarily identical to each other, but depend on the deformation path. However, for sufficiently small strains one may assume that both symmetric tensors are very similar, so that the above equation can be rewritten

$$\boldsymbol{F} = \boldsymbol{F}_{\mathrm{a}}\boldsymbol{U} = \boldsymbol{W}\boldsymbol{F}_{\mathrm{a}} \approx \boldsymbol{F}_{\mathrm{a}}\boldsymbol{F}_{\mathrm{s}} \tag{17.60}$$

where $\boldsymbol{F}_{\mathrm{s}}$ is the approximate symmetric portion of $\boldsymbol{F}$. The linear decomposition of the displacement gradient tensor, written in crystal coordinates, can then by obtained from equation (17.56):

$$\boldsymbol{F} \approx \boldsymbol{F}_{\mathrm{a}}\boldsymbol{F}_{\mathrm{s}} = \boldsymbol{I} + \boldsymbol{H} = (\boldsymbol{I} + \boldsymbol{H}_{\mathrm{a}})(\boldsymbol{I} + \boldsymbol{H}_{\mathrm{s}}) = \boldsymbol{I} + \boldsymbol{H}_{\mathrm{a}} + \boldsymbol{H}_{\mathrm{s}} + \boldsymbol{H}_{\mathrm{a}}\boldsymbol{H}_{\mathrm{s}} \tag{17.61}$$

where $\boldsymbol{H}_{\mathrm{s}}$ is the symmetric portion of $\boldsymbol{H}$ which represents shape changes, and $\boldsymbol{H}_{\mathrm{a}}$ its antisymmetric portion which describes a rigid body rotation of the continuum. For incremental strains the above equation simplifies to

$$\boldsymbol{H} \approx \boldsymbol{H}_{\mathrm{a}} + \boldsymbol{H}_{\mathrm{s}} \tag{17.62}$$

The symmetric and antisymmetric components of $\boldsymbol{H}$ can be found by

$$\begin{aligned} \boldsymbol{H}_{\mathrm{s}} &= \frac{1}{2}\left(\boldsymbol{H} + \boldsymbol{H}^{\mathrm{T}}\right) \\ \boldsymbol{H}_{\mathrm{a}} &= \frac{1}{2}\left(\boldsymbol{H} - \boldsymbol{H}^{\mathrm{T}}\right) \end{aligned} \tag{17.63}$$

where $\boldsymbol{H}^{\mathrm{T}}$ is the transpose of $\boldsymbol{H}$. However, it must be underlined, that in the generalized Taylor theory not the *displacement* gradient, but the macroscopic *velocity* gradient tensor, as prescribed by the deformation process, serves as input quantity. The latter tensor corresponds to the displacement gradient rate tensor. This can be expressed formally by writing

$$\begin{aligned} \dot{\boldsymbol{H}}_{\mathrm{s}} &= \frac{1}{2}\left(\dot{\boldsymbol{H}} + \dot{\boldsymbol{H}}^{\mathrm{T}}\right) \\ \dot{\boldsymbol{H}}_{\mathrm{a}} &= \frac{1}{2}\left(\dot{\boldsymbol{H}} - \dot{\boldsymbol{H}}^{\mathrm{T}}\right) \end{aligned} \tag{17.64}$$

Details of the derivation of the Green–Lagrange form of the strain rate tensor and related quantities are presented in Chapter 16.

Now one has to consider a crystal with f different slip systems. The shear rate on slip system t is described by $\dot{\gamma}^t$. Using the normalized slip plane normal $\boldsymbol{n}^t$ and the normalized shear direction $\boldsymbol{b}^t$, $\dot{\gamma}^t$ can be linearly dismantled into its symmetric and its antisymmetric parts according to equations (17.51) and (17.53):

$$\begin{aligned} \dot{\gamma}^t \boldsymbol{M}^t &= \dot{\gamma}^t \frac{1}{2}\left(\boldsymbol{b}^t \odot \boldsymbol{n}^t + \boldsymbol{n}^t \odot \boldsymbol{b}^t\right) \\ \dot{\gamma}^t \boldsymbol{Y}^t &= \dot{\gamma}^t \frac{1}{2}\left(\boldsymbol{b}^t \odot \boldsymbol{n}^t - \boldsymbol{n}^t \odot \boldsymbol{b}^t\right) \end{aligned} \tag{17.65}$$

where $\boldsymbol{b}^t \odot \boldsymbol{n}^t = b_i^t n_j^t$ is the dyadic product according to equation (17.51). These contributions must be summed over all active slip systems $t = 1, ..., f$; this defines the symmetric tensor $\dot{\boldsymbol{\Gamma}}_{\mathrm{s}}$ and its antisymmetric counterpart $\dot{\boldsymbol{\Gamma}}_{\mathrm{a}}$.

$$\begin{aligned} \dot{\boldsymbol{\Gamma}}_{\mathrm{s}} &= \sum_{t=1}^{f} \dot{\gamma}^t \boldsymbol{M}^t \\ \dot{\boldsymbol{\Gamma}}_{\mathrm{a}} &= \sum_{t=1}^{f} \dot{\gamma}^t \boldsymbol{Y}^t \end{aligned} \tag{17.66}$$

Before deriving the orientation change of the grain it must be considered that in general an extra spin $\boldsymbol{\Omega}$ will be required in order to respond to the geometrical constraints imposed by the macroscopic deformation process (van Houtte and Aernoudt 1975; Kocks and Chandra 1982). This extra spin determines the rate of the orientation change of the crystal. Thus, the sum of the tensors $\dot{\boldsymbol{\Gamma}}_{\mathrm{s}}$, $\dot{\boldsymbol{\Gamma}}_{\mathrm{a}}$, and $\boldsymbol{\Omega}_{\mathrm{s}}$ must be equal to the externally imposed velocity gradient tensor $\dot{\boldsymbol{H}}$ written in lattice coordinates:

$$\dot{\boldsymbol{H}} = \dot{\boldsymbol{\Gamma}}_{\mathrm{s}} + \dot{\boldsymbol{\Gamma}}_{\mathrm{a}} + \boldsymbol{\Omega} \tag{17.67}$$

Again, this expression can be dismantled into its symmetric and its antisymmetric portion.

$$\begin{aligned} \dot{\boldsymbol{H}}_{\mathrm{s}} &= \dot{\boldsymbol{\Gamma}}_{\mathrm{s}} \\ \dot{\boldsymbol{H}}_{\mathrm{a}} &= \dot{\boldsymbol{\Gamma}}_{\mathrm{a}} + \boldsymbol{\Omega} \end{aligned} \tag{17.68}$$

According to the generalized full-constraints Taylor theory, the strain rate of the neighboring crystals should be identical. Hence, the symmetric part of equation (17.67) is now solved to identify the unknown shear rates $\dot{\gamma}^t$ for the f active systems out of $\dot{\boldsymbol{H}}_{\mathrm{s}}$, which is known since $\dot{\boldsymbol{H}}$ and thus also $\dot{\boldsymbol{H}}^{\mathrm{T}}$ are prescribed by the deformation process. Once the

$\dot{\gamma}^t$ are found, the antisymmetric tensor $\dot{\mathbf{\Gamma}}_a$ can be calculated. The lattice rotation $\mathbf{\Omega}$ is finally obtained by solving $\mathbf{\Omega} = \dot{\boldsymbol{H}}_a - \dot{\mathbf{\Gamma}}_a$.

At this point it is worth emphasizing that under certain relaxed-constraints conditions the method outlined above for the calculation of the lattice rotation is not generally unambiguous. This is readily shown by expressing the rotation for crystals subjected to a uniaxial compression test both in terms of the rigid-body rotation and the antisymmetric contribution of the active slip systems, equation (17.68), and in terms of the conservation of the compression plane. The expressions yield a different result in one of the antisymmetric matrix component pairs and thus show different properties with respect to symmetry operations that should leave them invariant. However, for plane-strain rolling which consists of thickness reduction (invariant rolling plane) and an equivalent elongation (invariant rolling direction), both results are exactly identical.

If several combinations of slip systems fulfill the imposed strain tensor, the solution with the minimum plastic work rate per unit volume that is dissipated along the glide planes will be selected:

$$P = \tau_{\text{crit}} \sum_{t=1}^{f=5} \left|\dot{\gamma}^t\right| \;\rightarrow\; \min \tag{17.69}$$

where $\tau_{\text{crit}} = \tau^t_{\text{crit}}$ is the critical resolved shear stress which is assumed here to be identical on all $t = 1, ..., f$ active slip systems.

This rule is referred to as the first-order plastic criterion. If k different families of slip systems with different critical resolved shear stresses $\tau^{t_k}_{\text{crit}}$ are considered, the above equation must be rewritten

$$P = \sum_{t_1=1}^{f_1} \tau^{t_1}_{\text{crit}} \left|\dot{\gamma}^{t_1}\right| + ... + \sum_{t_k=1}^{f_k} \tau^{t_k}_{\text{crit}} \left|\dot{\gamma}^{t_k}\right| \;\rightarrow\; \min \tag{17.70}$$

The consideration of k different types of slip systems is of fundamental importance in describing polycrystal plasticity of body-centered cubic alloys, intermetallic compounds, and face-centered cubic alloys at elevated temperatures.

If the first-order plastic criterion does not yield an unambiguous result, the selection procedure must be complemented by a second criterion. Renouard and Wintenberger (1980) suggested such a second-order plastic criterion which selects from a given set of possible solutions the combination that leads to a minimum energy of the rotated grain. However, Kocks (1994) pointed out that this criterion is inadequate from a physical point of view, since it stipulates that the final orientation of the grain is already known before deformation.

An alternative method of selecting an active set of slip systems on a physically sound basis is the consideration of small fluctuations of the local critical resolved shear stress. However, the local intrinsic work or latent hardening matrix $h_{\alpha\beta}$, which quantifies the change of flow stress $\tau^{\alpha}_{\text{crit}}$ on slip system α due to a shear increment γ^{β} on slip system β is usually unknown. Therefore, small stress oscillations must be introduced in a random fashion. This corresponds to assuming a random selection criterion.

The second-order plastic criterion can have a noticeable influence on the predicted crystallographic texture. This was investigated by comparing Taylor simulations using either the criterion of Renouard and Wintenberger (1980) or random choice with viscoplastic Taylor simulations[8]. It was observed that predictions obtained for body-centered cubic

[8] Viscoplastic Taylor codes do not have to use a second-order plastic criterion (Section 17.14).

metals were less sensitive with respect to the selection method employed than those obtained for face-centered cubic materials and some intermetallic compounds. However, in all cases it was revealed that the simulation results were very sensitive to the slip system families involved and their respective critical shear stresses. Further relevant Taylor simulation parameters are the number of different grain orientations and their scatter width. The set of initial orientations that enters a Taylor simulation is usually identified by decomposing the measured starting texture into a number of 800-3000 Gauss-type scattering model components. The final orientation distribution function is then determined from a set of predicted orientations by using the Gauss method of Lücke, Pospiech, Virnich, and Jura (1981). The scatter width employed should be in accord with local texture measurements (Raabe 1994; Raabe and Boeslau 1994).

17.10 Bishop–Hill Polycrystal Model

The theory of Bishop and Hill (1951) is essentially equivalent to Taylor's full-constraints model (Kocks 1970; Aernoudt et al. 1993). Similarly to Taylor's approach, the Bishop–Hill theory assumes strain rate compatibility among the grains. According to the generalized Schmid law the activation of a slip system t is governed by

$$-\tau^t_{\text{crit}} \leq \tau^t \leq \tau^t_{\text{crit}} \tag{17.71}$$

where τ^t_{crit} is the critical resolved shear stress on the slip system t. Combining this equation for τ_t with equation (17.46) defines two hyperplanes in the six-dimensional stress space (Westergaard 1920; von Mises 1928).

These planes are used to determine the elastic limit for a general three-dimensional stress state (Section 17.3). Stress states outside this surface are not admissible. If the actual stress is *below* these hyperplanes, no slip occurs. The coordinates *on* the planes represent stress states which give rise to slip activity. The combination of the hyperplanes of all possible slip systems creates a hypersurface which contains all possible stress states for plastic flow. The coordinates of the entire hypersurface in stress space can be derived by adding hydrostatic stresses to the actual stress tensor. This method implicitly postulates isotropy and plastic incompressibility. The deviatoric stress vector which then determines the elastic limit is generally normal to the hydrostatic stress line which is generated in stress space by gradually changing the hydrostatic portion. The hydrostatic line is the axis of the yield surface and the plane normal to it is referred to as π plane. This six-dimensional surface of the elastic limit is referred to as the yield locus, yield function, or yield surface for the single crystal considered and has the form of a hyperprism (Mendelson 1968; Kocks 1970; Gittus and Zarka 1986; van Houtte et al. 1989; Krausz and Krausz 1996; Stouffer and Dame 1996).

If the yield locus is determined, the maximum work principle can be used for the determination of the unknown plastic stress state that corresponds to the known plastic strain rate (Hill 1950; Kocks 1970; Kocks et al. 1983). The plastic stress is located on or below the yield surface and satisfies the condition

$$P = \sigma_{ij}\,\dot{\varepsilon}_{ij} \;\rightarrow\; \max \tag{17.72}$$

which means that the dissipated plastic work rate per unit volume should be maximized. van Houtte (1988) has suggested a convenient tensor–vector conversion which allows one to express a given strain rate as a vector in stress space. Except for some special cases,

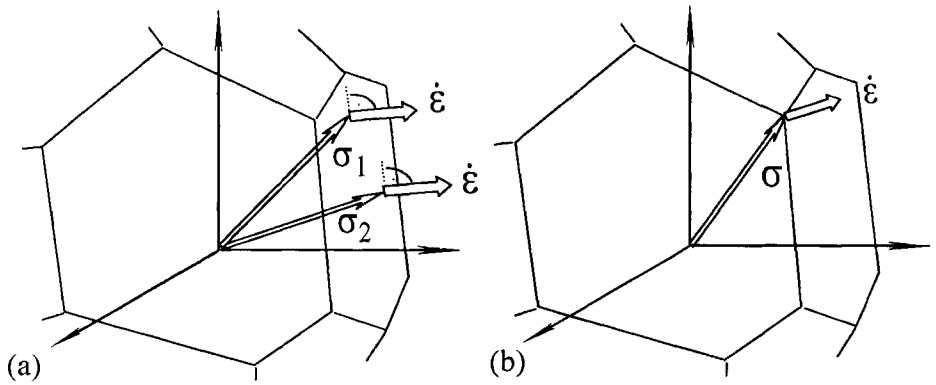

Figure 17.7: Section of the single crystal yield locus in stress space. (a) The strain rate vector $\dot{\varepsilon}$ is normal to the facet of the yield locus. All stresses σ_i that belong to this facet satisfy the maximum work principle (single slip). (b) The strain rate vector $\dot{\varepsilon}$ is *not* normal to any facet or edge of the yield locus. Therefore only one particular stress state σ_i satisfies the maximum work principle (multiple slip), van Houtte (1988).

this strain rate vector will not be normal to a single facet (single slip) or to an edge of the yield surface (double slip) (Aernoudt et al. 1993). In the usual case equation (17.72) will thus be satisfied for a stress state which corresponds to a vertex of the yield locus (multiple slip) (Figure 17.7). The identification of the *active* yield vertex makes it possible to find the active set of slip systems. As was discussed by Kocks (1970) and Aernoudt et al. (1993), the Taylor and the Bishop–Hill theories lead to identical predictions of active slip systems, provided that identical first- and second-order plastic criteria are used. Hence, the Taylor full-constraints approach is often synonymously denoted as the Taylor–Bishop–Hill theory.

17.11 Taylor Relaxed-Constraints Models

In the full-constraints (FC) Taylor model the externally imposed strain rate is entirely transferred into each grain where it has to be achieved by crystallographic slip, mechanical twinning, or martensitic transformation. This concept implies the possibility of avoiding incompatibilities between neighboring grains.

In the relaxed-constraints (RC) Taylor-type models some of the shear rate components imposed need not be fulfilled, i.e. they are relaxed (Honneff and Mecking 1978; van Houtte 1981; Kocks and Chandra 1982; Wenk 1985; van Houtte 1988). This assumption allows for local incompatibilities between neighboring grains. The basic approach of all RC models is the relaxation of strain compatibility in favor of improved stress homogeneity. If one of the imposed strain rate components is dropped, only four instead of the original five equations (FC) need to be solved. Consequently, strain relaxation leads to the reduction of the number of slip systems employed and hence to a lower deformation energy (Taylor energy) as compared with the FC model. Since for each prescribed strain rate component that is relaxed the corresponding compatibility equation is neglected, the number of strain

rate equations to be solved reflects the number of active slip systems. For simulating cold-rolling textures, various strain rate relaxation schemes have been used (Honneff and Mecking 1981; Kocks and Chandra 1982; Raphanel and van Houtte 1985; Hirsch et al. 1987; Hirsch and Lücke 1988a; Raabe 1992; Raabe 1995c; Tóth et al. 1997). In these approaches the gradual strain relaxation was justified by the changing grain shape. It is clear that for an equiaxed grain morphology, large interactions with the neighboring crystals arise when the strain constraints are dropped. In contrast, when the grains are very flat, for instance after large-strain cold reduction, the interaction with grains in the rolling or transverse direction seems to be less relevant.

For low thickness reductions one can assume an equiaxed grain shape[9]. Therefore, it is reasonable to start Taylor simulations at low strains by imposing full strain constraints (FC model) (Raabe 1995c). At intermediate thickness reductions the grain shape is elongated and flattened but retains its original width. According to Honneff (1980), Honneff and Mecking (1981), and van Houtte (1982) one can therefore allow for strain incompatibility in the rolling direction and relax the corresponding shear strain rate constraint. This approach is referred to as the lath model (van Houtte 1982). Using a coordinate system with $x_1 \parallel$ rolling direction, $x_2 \parallel$ transverse direction, and $x_3 \parallel$ normal direction, the lath model corresponds to a relaxation of the $\dot{\varepsilon}_{13}$ strain rate constraint (Figure 17.8).

Lath-type Taylor simulations only require four rather than five slip systems to achieve a relaxed prescribed external shape change. At large rolling strains the grain shape is usually very flat and equiaxed in the rolling plane. Such morphology is assumed to allow for strain rate incompatibility in both the rolling and transverse directions. In the simulation, two shear strain rate constraints are then dropped, namely $\dot{\varepsilon}_{13}$ and $\dot{\varepsilon}_{23}$. On account of the flat grain shape this approach is referred to as the pancake model (Honneff and Mecking 1981; van Houtte 1982) (Figure 17.8). Pancake-type Taylor simulations only require three rather than five slip systems to achieve a relaxed prescribed external shape change in the crystals being considered. Especially combined full- and relaxed-constraints models with gradual lath and pancake relaxation have been successfully used for the description of texture formation during large-strain rolling reduction of body-centered cubic (bcc) alloys (Raphanel and van Houtte 1985; Raabe 1995d). In face-centered cubic alloys (fcc) with a low stacking fault energy the third possible strain rate relaxation, which is referred to as the brass shear relaxation (relaxation of $\dot{\varepsilon}_{12}$), has also been discussed. It is clear that even for the flat grain limit this relaxation mode gives rise to a larger interaction among neighboring grains than the lath or pancake case. However, it is conceivable that the interaction could be lowered when positive and negative brass shears of neighboring crystals mutually compensate (Duggan et al. 1990; Lee and Duggan 1993). Such behavior was indeed observed in experiments (Köhlhoff 1988).

17.12 Sachs Model for Homogeneous Plastic Stress in Polycrystals

The early model of Sachs (1928) describes the simplest case of crystal deformation. It assumes that plastic strain is obtained by activation of the slip system(s) with the highest resolved shear stress according to the externally imposed stress. When used for the

[9]The assumption of equiaxed grain shapes at the beginning of cold rolling is no longer justified for certain technical iron–chromium, iron–silicon, and aluminum alloys. Depending on the strain and temperature distribution during hot rolling, recovery instead of recrystallization can prevail. This leads to elongated rather then equiaxed grain shapes, especially in the center layers of the hot-rolled sheets.

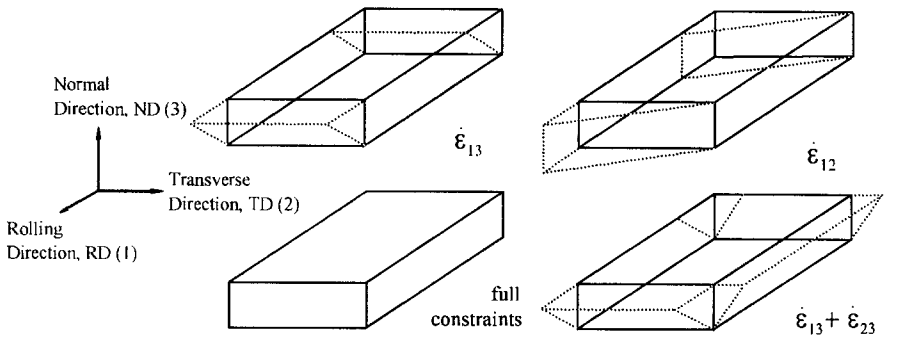

Figure 17.8: Schematic representation of the strain rate relaxation modes used for the simulation of polycrystal plasticity at intermediate strains (classical lath model, relaxation of $\dot{\varepsilon}_{13}$; modified lath-type model, relaxation of $\dot{\varepsilon}_{12}$) and large strains (pancake model, relaxation of $\dot{\varepsilon}_{13}$ and $\dot{\varepsilon}_{23}$).

description of polycrystal plasticity, the Sachs model thus considers stress equilibrium but neglects strain compatibility. For this reason its employment was originally confined to the description of single crystal rather than polycrystal plasticity. However, modified Sachs models have also been used successfully to describe polycrystal deformation (Leffers 1968; Pedersen and Leffers 1987). When the resolved shear stress reaches the critical resolved shear stress, the Sachs model predicts for face-centered cubic crystals under tensile or compression conditions the activation of one slip system in the case of a less symmetric orientation, e.g. {134}, and up to eight slip systems in the case of a symmetric orientation, e.g. {001}.

17.13 Statistical Grain Interaction Model

The use of the full-constraints (FC) Taylor model requires the activation of five slip systems[10] for fulfilling a prescribed plastic strain state in the crystals being considered. The use of relaxed-constraints (RC) simulations reduces the required number of active slip systems from five to four (lath model) or even three (pancake model). This relaxation reduces strain rate homogeneity and increases stress homogeneity. This leads to the reduction of the deformation energy (Taylor energy) as compared with the FC model, equation (17.69).

In a new Taylor-type approach by Schmitter (1991b) the imposed shear strain components are not entirely ignored but only partially relaxed according to the gain in the Taylor deformation energy (van Houtte 1996a). The latter quantity depends on the grain orientation. In Schmitter's model the shear-dependent degradation of the Taylor energy is expressed in terms of a so-called shear capacity, Γ. This value is defined as the maximum slope of the plane combining the deformation energy predicted by the FC model with that computed by the RC model. The shear capacity is thus dependent on the orientation of

[10]The activation of five slip systems does not generally imply that all five systems contribute identical amounts of shear. Depending on the second-order plastic criterion, even in the Taylor full-constraints model certain grain orientations can reveal one, two or even three slip systems with a shear contribution much below that of the dominant systems.

the grain $\boldsymbol{g}$ and is a measure of the gain in energy that is achieved when a certain shear component is relaxed. The shear capacities are calculated independently for the three shear rate components, $\dot{\Gamma}_{12}(\boldsymbol{g})$, $\dot{\Gamma}_{13}(\boldsymbol{g})$, $\dot{\Gamma}_{23}(\boldsymbol{g})$, and the broadening component of the strain rate tensor, $\dot{\Gamma}_{22}(\boldsymbol{g})$. Each orientation-dependent shear capacity is then normalized by the highest occurring value for the corresponding shear rate component, $\dot{\Gamma}_{12}^{\max}$, $\dot{\Gamma}_{13}^{\max}$, $\dot{\Gamma}_{23}^{\max}$, and $\dot{\Gamma}_{22}^{\max}$. The respective shear rate of the considered crystal is then calculated from the shear rate predicted by the relaxed-constraints (RC) model weighted by the normalized shear capacity according to

$$\begin{aligned}
\hat{\dot{\varepsilon}}_{12}(\boldsymbol{g}) &= \left(\frac{\dot{\Gamma}_{12}(\boldsymbol{g})}{\dot{\Gamma}_{12}^{\max}}\right) \dot{\varepsilon}_{12}^{\mathrm{RC}}(\boldsymbol{g}) \\
\hat{\dot{\varepsilon}}_{13}(\boldsymbol{g}) &= \left(\frac{\dot{\Gamma}_{13}(\boldsymbol{g})}{\dot{\Gamma}_{13}^{\max}}\right) \dot{\varepsilon}_{13}^{\mathrm{RC}}(\boldsymbol{g}) \\
\hat{\dot{\varepsilon}}_{23}(\boldsymbol{g}) &= \left(\frac{\dot{\Gamma}_{23}(\boldsymbol{g})}{\dot{\Gamma}_{23}^{\max}}\right) \dot{\varepsilon}_{23}^{\mathrm{RC}}(\boldsymbol{g}) \\
\hat{\dot{\varepsilon}}_{22}(\boldsymbol{g}) &= \left(\frac{\dot{\Gamma}_{22}(\boldsymbol{g})}{\dot{\Gamma}_{22}^{\max}}\right) \dot{\varepsilon}_{22}^{\mathrm{RC}}(\boldsymbol{g})
\end{aligned} \tag{17.73}$$

In other words the shear capacity quantifies the larger tendency of certain grains to neglect local strain rate constraints at the expense of compatibility than others. By including this approach, the original Taylor model was modified in a way which renders it more physically plausible and at the same time in better agreement with experiments (Schmitter 1991b; Raabe 1995e).

17.14 Viscoplastic Polycrystal Modeling

The numerical solution of Taylor–Bishop–Hill-type polycrystal models can be elegantly obtained by using linear programming techniques (van Houtte and Aernoudt 1975). However, these models require a second-order plastic criterion for interpreting the multiple-solution problem.

An alternative concept in dealing with secondary effects was suggested by the nonlinear strain rate sensitivity polycrystal models (Canova et al. 1984; Asaro and Needleman 1985; Canova 1988; Tóth et al. 1988; Engler et al. 1993; Tóth et al. 1997). These approaches, which are typically referred to as viscoplastic models, assume that during plastic deformation crystallographic slip and/or twinning are not confined to those few systems which fulfill the Taylor–Bishop–Hill criterion. In contrast, it is suggested that glide takes place on nearly all existing slip systems, even if their respective resolved shear stress, as calculated from the external stress, is small. This concept is put formally by expressing the critical resolved shear stress τ_{crit}^{t} on a particular glide system t as a function of the shear rate $\dot{\gamma}^{t}$ on this system:

$$\tau_{\mathrm{crit}}^{t} = \tau_0 \operatorname{sgn}\left[\dot{\gamma}^{t}\right] \left|\frac{\dot{\gamma}^{t}}{\dot{\gamma}_0}\right|^{\mathrm{m}} = \tau_0 \left(\frac{\dot{\gamma}^{t}}{\dot{\gamma}_0}\right) \left|\frac{\dot{\gamma}^{t}}{\dot{\gamma}_0}\right|^{\mathrm{m}-1} \tag{17.74}$$

where τ_0 is the reference shear stress (*not* the critical resolved shear stress), $\dot{\gamma}_0$ the shear rate associated with the reference stress τ_0, m the strain rate sensitivity, and $\operatorname{sgn}\left[\dot{\gamma}^{t}\right]$ the

sign of $\dot{\gamma}^t$. The reference stress τ_0 and the reference strain rate $\dot{\gamma}_0$ must have equal signs. The dependence of the shear rate on system t on the critical resolved shear stress τ^t_{crit} can then be written

$$\dot{\gamma}^t = \dot{\gamma}_0 \operatorname{sgn}\left[\tau^t_{\text{crit}}\right] \left|\frac{\tau^t_{\text{crit}}}{\tau_0}\right|^{1/\text{m}} \tag{17.75}$$

For simulating cold deformation, low m values of about $\frac{1}{100}$–$\frac{1}{20}$ are typically used (Canova 1988; Engler et al. 1993; Molinari and Tóth 1994; Tóth et al. 1997).

The viscoplastic flow law given by equation (17.74) can be combined with the crystallographic form of the yield surface function (equation 17.47)

$$\tau^t_{\text{crit}} = \sigma_{ij}\, m^t_{ij} \tag{17.76}$$

where σ_{ij} is the stress and m^t_{ij} the orientation matrix which describes the geometry of the slip systems with respect to the crystal coordinate system[11], and with the externally prescribed strain rate tensor (equations 17.50, 17.66, and 17.68)

$$\dot{H}_{s_{ij}} = \sum_{t=1}^{f} \dot{\gamma}^t\, M^t_{ij} \tag{17.77}$$

to give

$$\dot{H}_{s_{ij}} = \frac{1}{2}\left(\frac{\dot{\gamma}_0}{\tau_0^{1/m}}\right) \sum_{t=1}^{f} \left(m^t_{ij} + m^t_{ji}\right) m^t_{kl}\, \sigma_{kl}\, \left|m^t_{pq}\, \sigma_{pq}\right|^{(1/m)-1} \tag{17.78}$$

which can be solved consistently for $\boldsymbol{\sigma}$, $\dot{\boldsymbol{H}}_s$, and γ^t by use of an iterative scheme.

17.15 Generalized Self-Consistent Polycrystal Models

The full-constraints Taylor model accounts for strain compatibility but not for stress equilibrium among the grains during plastic deformation. Relaxed-constraints Taylor-type models improve stress homogeneity at the expense of strain homogeneity on a phenomenological basis. However, from a mechanical point of view neither approach provides a convincing theoretical solution to polycrystal deformation since the requirement for either strain compatibility or stress equilibrium is violated.

As was outlined in Sections 17.7 and 17.8, self-consistent models describe the deformation of simply shaped grains embedded within a polycrystal in a mechanically more rigorous manner than Taylor approaches.

Self-consistent calculations are based on the model of a spherical or ellipsoidal material portion, for instance a crystal grain or a particle, which is embedded within infinite surroundings with homogeneous properties. The crystal or particle considered is usually referred to as an inclusion and the surrounding material as the matrix (Eshelby 1957; Eshelby 1961; Kröner 1958a; Kröner 1961). While the inclusion represents a grain characterized by its orientation or a particle characterized by its different elastic or plastic

[11] The transformation matrix $\boldsymbol{m}^t$ of the slip system t must not be confused with the strain rate sensitivity m.

behavior and ellipsoidal strain-dependent shape, the matrix reflects the average homogeneous properties of all the other crystals or of the matrix material, respectively.

The stress and strain rate distributions within the inclusion are assumed to be homogeneous. While the properties of the matrix are homogeneous, the resulting stress and strain rate fields are typically heterogeneous. The first solutions to this model satisfying both stress and strain constraints was suggested by Eshelby (1957) for the elastic case. Kröner (1958a) extended this inclusion approach to the so-called self-consistent scheme for elastic and plastic cases (Kröner 1961).

In generalizing equation (17.41) all plasticity self-consistent schemes proceed by relating the local stress to the local strain or strain rate by using a set of constitutive equations and by applying the equilibrium conditions. As a starting point one assumes a constitutive relation between stress σ_{ij} and strain rate $\dot{\varepsilon}_{kl}$, for instance

$$\sigma_{ij} = A_{ijkl}\,\dot{\varepsilon}_{kl} = A_{ijkl}\,\dot{u}_{k,l} \tag{17.79}$$

where A_{ijkl} is the fourth-rank tensor with the symmetry properties $A_{ijkl} = A_{jikl} = A_{ijlk}$ that characterize the constitutive law, $\dot{u}_k$ the velocity vector, and $\dot{u}_{k,l}$ the second-rank velocity gradient tensor. It is stipulated that A_{ijkl} is space-independent and the strain rate much below one, i.e. $\dot{\varepsilon}_{kl} \ll 1$. The equilibrium condition for the entire polycrystal is expressed by

$$\sigma_{ij,j} = 0 \tag{17.80}$$

where body forces are neglected. The expression $\sigma_{ij,j}$ denotes the derivative $\partial\sigma_{ij}/\partial x_j$, where x_j is the spatial coordinate parallel to the j direction[12]. Using the constitutive law, equation (17.79), the equilibrium equation can be rewritten

$$\sigma_{ij,j} = \left(A_{ijkl}\,\dot{u}_{k,l}\right)_{,j} = A_{ijkl}\,\dot{u}_{k,lj} = 0 \tag{17.81}$$

The tensor A_{ijkl} can be decomposed into a uniform portion A^0_{ijkl} and a space-dependent portion $\tilde{A}_{ijkl}(\boldsymbol{r})$. Following Thiem, Berveiller, and Canova (1986), and Molinari, Canova, and Ahzi (1987) the above equation can then be rewritten

$$A^0_{ijkl}\,\dot{u}_{k,lj} + f_i = 0 \tag{17.82}$$

where the hydrostatic pressure is neglected. The term f_i can be interpreted as a fictitious body force and expressed by

$$f_i = \left(\tilde{A}_{ijkl}(\boldsymbol{r})\,\dot{u}_{k,l}\right)_{,j} = \tilde{A}_{ijkl}(\boldsymbol{r})\,\dot{u}_{k,lj} \tag{17.83}$$

Body forces act directly on each particle of the body, rather than being applied by tractions at its boundaries and transmitted through the various particles by means of internal stresses.

For an infinite medium with homogeneous properties this set of partial differential equations can be solved using the Green's tensor functions $G_{km}(\boldsymbol{r}-\boldsymbol{r}')$ and Green's vector functions $H_m(\boldsymbol{r}-\boldsymbol{r}')$ satisfying the equation

$$A^0_{ijkl}\,G_{km,lj}(\boldsymbol{r}-\boldsymbol{r}') - H_{m,i}(\boldsymbol{r}-\boldsymbol{r}') + \delta_{im}\,\delta(\boldsymbol{r}-\boldsymbol{r}') = 0 \tag{17.84}$$

[12] A detailed discussion of the equilibrium equations and Hooke's law is given in Chapter 9.

where δ_{im} is the Kronecker symbol and $\delta(\boldsymbol{r}-\boldsymbol{r}')$ the Dirac delta function located at $\boldsymbol{r}'$. For a given value of m the expression $\delta_{i(m=\text{const.})}\,\delta(\boldsymbol{r}-\boldsymbol{r}')$ maps the ith component of a point force concentrated at $\boldsymbol{r}'$ and parallel to the direction m (Asaro et al. 1973; Bacon et al. 1979a; Mura 1987; Boas 1983).

The total displacement rates can then be expressed as integrals of the set of Green's tensor functions which provide solutions to delta-type portions of the underlying differential equations, equation (17.83).

$$\dot{u}_n = \bar{\dot{u}}_n + \oiiint_V G_{ni}(\boldsymbol{r}-\boldsymbol{r}')\; f_i(\boldsymbol{r}')\;\mathrm{d}V \tag{17.85}$$

The total velocity gradient field can then be derived by

$$\dot{u}_{n,m} = \bar{\dot{u}}_{n,m} + \oiiint_V \tilde{A}_{ijkl}(\boldsymbol{r}')\; G_{ni,m}(\boldsymbol{r}-\boldsymbol{r}')\; \dot{u}_{k,lj}\;\mathrm{d}V \tag{17.86}$$

where $\dot{u}$ is the local displacement rate, $\bar{\dot{u}}$ the macroscopic displacement rate, and V the volume of the inclusion. Using the convolution symbol $\otimes$ allows one to rewrite the integral according to

$$G_{ni} \otimes f_i = \oiiint_V G_{ni}(\boldsymbol{r}-\boldsymbol{r}')\, f_i(\boldsymbol{r}')\,\mathrm{d}V \tag{17.87}$$

so that the displacement rate fields can be written compactly as

$$\dot{u}_n = \bar{\dot{u}}_n + G_{ni} \otimes f_i \tag{17.88}$$

and the corresponding velocity gradient fields as

$$\dot{u}_{n,m} = \bar{\dot{u}}_{n,m} + G_{ni,mj} \otimes \tilde{A}_{ijkl}(\boldsymbol{r}')\,\dot{u}_{k,l} \tag{17.89}$$

This expression can be symmetrized and written as

$$\dot{\varepsilon}^{\mathrm{T}}_{nm} = \bar{\dot{\varepsilon}}^{\mathrm{T}}_{nm} + \Gamma_{nmij} \otimes \tilde{A}_{ijkl}(\boldsymbol{r}')\,\dot{\varepsilon}^{\mathrm{T}}_{kl} \tag{17.90}$$

where $\dot{\boldsymbol{\varepsilon}}^{\mathrm{T}}$ is the symmetric part of the local strain rate and $\bar{\dot{\boldsymbol{\varepsilon}}}^{\mathrm{T}}$ the symmetric part of the macroscopic strain rate tensor. The tensor Γ_{nmij} is defined by

$$\Gamma_{nmij} = \frac{1}{4}\left(G_{ni,mj} + G_{mi,nj} + G_{nj,mi} + G_{nj,ni}\right) \tag{17.91}$$

Equations (17.89) constitute a linear set of integral equations with respect to the unknown velocity gradients. The above expressions, equations (17.79)–(17.91), give an idea of the general method of developing plasticity self-consistent schemes.

Exact solutions to particular materials depend on the respective type of constitutive law. For instance, by using the shape-dependent Eshelby tensor E_{ijkl}, the elastic strains can be separated from the plastic strains, so that one obtains the general formula (equation 17.41)

$$\sigma^{\mathrm{i}}_{ij} - \sigma^{\mathrm{M}}_{ij} = C_{ijkl}\left(I_{klmn} - E_{klmn}\right)\left(\dot{\varepsilon}^{\mathrm{M}}_{mn} - \dot{\varepsilon}^{\mathrm{i}}_{mn}\right) \tag{17.92}$$

where C_{ijkl} is the linear elasticity tensor for general anisotropy, I_{ijkl} the identity tensor on symmetric tensors, defined by $I_{ijkl} = \frac{1}{2}\left(\delta_{ik}\delta_{jl} + \delta_{il}\delta_{jk}\right)$, $\dot{\varepsilon}^{\mathrm{M}}_{kl}$ the strain rate tensor in

the matrix, $\dot{\varepsilon}^{\mathrm{i}}_{kl}$ the strain rate tensor in the inclusion, σ^{i}_{ij} the stress in the inclusion, and σ^{M}_{ij} the macroscopic stress. In the isotropic limit the Eshelby equation can be rewritten

$$\sigma^{\mathrm{i}}_{ij} - \sigma^{\mathrm{M}}_{ij} = 2\mu\,(I_{ijkl} - E_{ijkl})\,(\dot{\varepsilon}^{\mathrm{M}}_{kl} - \dot{\varepsilon}^{\mathrm{i}}_{kl}) \tag{17.93}$$

where μ is the modulus of rigidity. As expressed by equation (17.92) it is a crucial assumption of all self-consistent models that a linear relation exists between the deviation of the local stress σ^{i}_{ij} in the inclusion from the macroscopic stress σ^{M}_{ij}, and the deviation of the local strain rate $\dot{\varepsilon}^{\mathrm{i}}_{ij}$ from the macroscopic strain rate $\dot{\varepsilon}^{\mathrm{M}}_{ij}$. For considering the grain shape of the inclusion under the assumption of homogeneous matrix properties, equation (17.92) can be rewritten

$$\sigma^{\mathrm{i}}_{ij} - \sigma^{\mathrm{M}}_{ij} = \chi\, T_{ijkl}\,(\dot{\varepsilon}^{\mathrm{M}}_{kl} - \dot{\varepsilon}^{\mathrm{i}}_{kl}) \tag{17.94}$$

where χ is the coupling factor and T_{ijkl} the fourth-rank accommodation tensor which accounts for the grain shape.

Based on this general background, various self-consistent models were developed considering different types of microstructurally relevant material features in their respective constitutive laws (Eshelby 1961; Kröner 1961; Eshelby 1970; Thiem et al. 1986; Molinari et al. 1987; Canova 1988; Lipinski and Berveiller 1989; Lipinski et al. 1992; Muller et al. 1994a; Muller et al. 1994b).

Wagner, Canova, van Houtte, and Molinari (1991), Royer, Nadari, Yala, Lipinski, Ceccaldi, Berveiller, and Penelle (1991), Aernoudt, van Houtte, and Leffers (1993), and Tóth, Molinari, and Raabe (1997) have shown that the texture predictions of self-consistent polycrystal models are very similar to those of pancake Taylor-type models.

17.16 Simulation of Local Orientation Gradients by Use of Polycrystal Theory

Grains are defined as crystalline areas with a uniform orientation that changes discontinuously at the grain boundary. The orientation distribution of all the grains in a polycrystalline aggregate is referred to as crystallographic texture. However, in contrast to the basic definition, local texture measurements substantiate the fact that as a rule deformed grains do not have a uniform orientation but contain local orientation gradients (Haeßner 1978; Gottstein 1984; Ananthan et al. 1991; Boeslau and Raabe 1994).

This section presents a Taylor-based model for the prediction of deformation microtextures, i.e. of the orientation distributions that are generated at the grain scale during plastic deformation. The introductory question is why grains in a polycrystal, which by definition should be oriented uniformly, reveal orientation gradients after deformation. Although grains in undeformed polycrystals already contain a considerable number of dislocations, only weak overall orientation gradients can be detected within each single crystal before deformation. This means that in the initial state only a small number of geometrically necessary dislocations are present (Nye 1953; Ashby 1970). Clearly, most dislocations are arranged in such a manner that long range misorientations are mutually compensated.

However, if the polycrystal is cold-deformed, local orientation gradients gradually appear. Consequently, there must be some elementary reason why a sufficiently large content of geometrically necessary dislocations is generated and accumulated during plastic deformation.

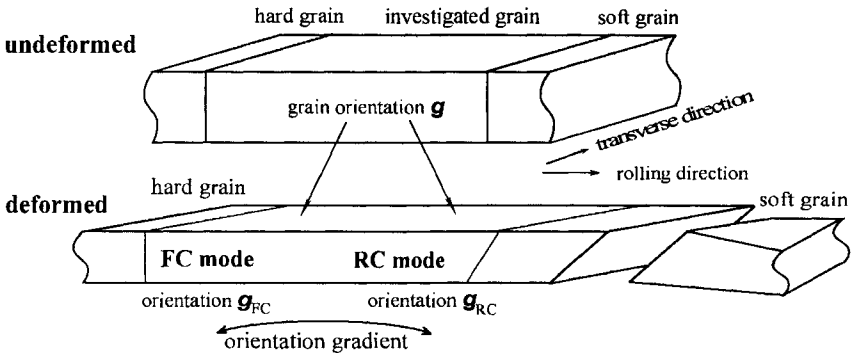

Figure 17.9: Grain with two neighboring crystals that impose unequal strain rate constraints on opposite borders (Raabe 1992).

The present model assumes that one predominant reason can be found in the requirement for strain compatibility, i.e. it stipulates that the development of local orientation gradients is due to the influence of the neighboring crystals. The model aims to give an upper-bound evaluation of this influence (Raabe 1994). As a starting point it is assumed that on opposite borders of a considered grain the respective neighboring crystals can impose different strain rate constraints. For instance, it is conceivable that either of the neighboring grains is hard, while the other one is soft. The prescription of unequal strain rate constraints on adjacent borders of the considered grain can lead to different shear rates locally, entailing different local spins[13].

Using this concept, upper-bound values of potential orientation gradients can be computed for various strains and initial orientations of the considered grain. However, the model does *not* predict any microscopic spatial details of the computed misorientations. The investigation of the evolution of microtexture within single grains is expected to allow relevant insight into the orientation-dependent deformation of grains in polycrystalline samples and thus into the formation of nuclei during primary recrystallization.

In order to simulate the upper-bound values for the evolution of local misorientations, Taylor full-constraints and Taylor relaxed-constraints can be imposed on opposite grain boundaries, respectively (Figure 17.9). It is first assumed that one boundary connects the grain to a neighboring crystal that is very hard (high Taylor factor). For that region of crystal the full-constraints (FC) Taylor model is applied. The calculation leads to the final orientation $\boldsymbol{g}_{\mathrm{FC}}(\Delta\varepsilon)$. On the opposite border where an adjacent soft grain is positioned (low Taylor factor), the simulation is repeated using either the Sachs (FC–Sachs combination model) or the relaxed-constraints (RC) Taylor model (FC–RC combination model), which leads to an orientation $\boldsymbol{g}_{\mathrm{RC}}(\Delta\varepsilon)$.

The resulting misorientation between $\boldsymbol{g}_{\mathrm{FC}}(\Delta\varepsilon)$ and $\boldsymbol{g}_{\mathrm{RC}}(\Delta\varepsilon)$ can then be regarded as an upper-bound value for the orientation gradient which can occur in the considered grain. In this simple approach it is not explicitly specified whether the neighboring pairs of grains that impose inhomogeneous constraints are positioned in the rolling, transverse, or normal direction.

[13]If the local misorientations exceed a certain value, one should no longer speak of orientation gradients but of grain fragmentation or deformation banding.

17.17 Application of Polycrystal Models in Materials Science

This section gives some classical and some recently published references on applications of polycrystal simulation methods related to various domains of materials science. The table can by no means be complete but may serve as a bibliography for getting better acquainted with some examples from the recent original literature in this field. Materials-related applications of polycrystal simulations are particularly in the field of solid-state mechanics and crystallographic textures.

Field of application	Reference
classics about homogenization and polycrystal models	Voigt (1910)
	Reuss (1930)
	Taylor (1938)
	Bishop and Hill (1951)
	Eshelby (1957)
	Kröner (1958a)
	Eshelby (1961)
	Kröner (1961)
	Hashin and Shtrikman (1962a)
	Hashin and Shtrikman (1962b)
constitutive models for polycrystals	Westergaard (1920)
	von Mises (1928)
	Hill (1950)
	Mendelson (1968)
	Rice (1971)
	Argon (1975)
	Gittus and Zarka (1986)
	Kocks (1987)
	Krausz and Krausz (1996)
	Stouffer and Dame (1996)
polycrystal modeling of creep	Brown (1970)
	Hutchinson (1976)
	Weng (1982)
	Turner and Tomé (1993)
polycrystal Taylor simulation	Chin and Mammel (1967)
	Dillamore, Smith, and Watson (1967)
	Dillamore, Butler, and Green (1968)
	Bunge (1970)
	Kocks (1970)
	Dillamore and Katoh (1974)
	van Houtte and Aernoudt (1975)
	Honneff and Mecking (1978)
	Gil Sevilliano, van Houtte, and Aernoudt (1980)
	Honneff and Mecking (1981)
	van Houtte (1981)
	Kocks and Chandra (1982)

	van Houtte (1982)
	Kocks, Canova, and Jonas (1983)
	Asaro and Needleman (1985)
	van Houtte (1985)
	Raphanel and van Houtte (1985)
	von Schlippenbach, Emren, and Lücke (1986)
	Emren, von Schlippenbach, and Lücke (1986)
	Bacroix and Jonas (1988)
	Hirsch and Lücke (1988b)
	van Houtte (1988)
	van Houtte, Mols, van Bael, and Aernoudt (1989)
	Aernoudt, van Houtte, and Leffers (1993)
	Raabe and Lücke (1993)
	Kocks and Necker (1994)
	Raabe and Lücke (1994)
	Hölscher, Raabe, and Lücke (1994)
	Raabe (1995e)
	Raabe and Mao (1995)
	Raabe (1996c)
polycrystal plasticity self-consistent	Berveiller and Zaoui (1979)
	Berveiller and Zaoui (1981)
	Thiem, Berveiller, and Canova (1986)
	Molinari, Canova, and Ahzi (1987)
	Canova (1988)
	Lipinski and Berveiller (1989)
	Tomé, Lebensohn, and Kocks (1991)
	Lipinski, Naddari, and Berveiller (1992)
	Lebensohn and Tomé (1993a)
	Lebensohn and Tomé (1993b)
	Lebensohn and Tomé (1994)
	Muller, Lemoine, and Berveiller (1994a)
	Muller, Lemoine, and Berveiller (1994b)
	Turner, Tomé, and Woo (1994)
	Molinari and Tóth (1994)
	Tóth and Molinari (1994)
	Tóth, Molinari, and Raabe (1997)

17.18 Examples of Polycrystal Simulations in Materials Science

17.18.1 Simulation of the Elastic Constants of Steels

This example (Figure 17.10) of Klinkenberg, Raabe, and Lücke (1992) shows the course of the overall elastic moduli of textured polycrystalline steels according to the Voigt, Reuss, and Hill models. The simulation clearly demonstrates the strong influence of the crystallographic orientation distribution on the elastic properties.

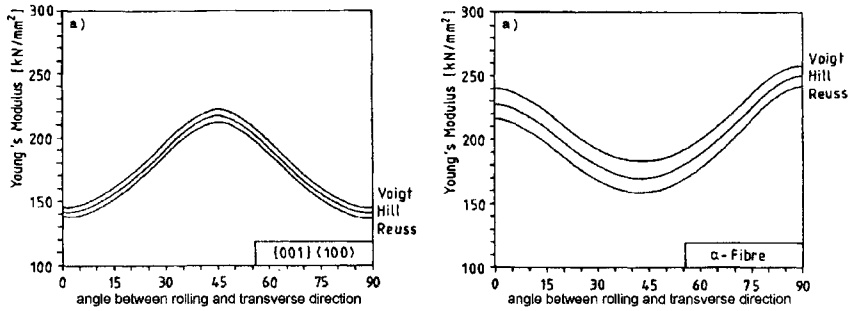

Figure 17.10: Simulated course of the elastic modulus of textured polycrystalline steels according to the Voigt, Reuss, and Hill models (Klinkenberg, Raabe, Lücke 1992).

17.18.2 Comparison of Polycrystal Homogenization Approaches

This section presents the comparison of texture simulations which were obtained from different polycrystal models (Tóth et al. 1997). The simulations were compared to experimental data of a 90% cold-rolled iron-chromium steel.

Figure 17.11 shows the ⟨100⟩ and ⟨110⟩ pole figures of a finite element tuned self-consistent viscoplastic simulation (a), of a Taylor full-constraints viscoplastic simulation (b), of a Taylor relaxed-constraints pancake viscoplastic simulation (c), and of the experimental texture (d). The texture predictions according to the viscoplastic self-consistent polycrystal model are in good accord with the Taylor relaxed-constraints viscoplastic model and with the experimental data.

17.18.3 Simulation of Textures in Iron-Aluminides

In this section the rolling texture of $B2/DO_3$ ordered polycrystalline iron-aluminides is simulated by use of a Taylor model and compared to experimental data (Raabe 1996c). In the simulations $\{110\}\langle 111\rangle$ and $\{112\}\langle 111\rangle$ slip systems are considered. The ratio of the critical resolved shear stress of the two systems, $\lambda = \tau^{\{110\}\langle 111\rangle}/\tau^{\{112\}\langle 111\rangle}$, is varied between 1 and 10. The evolution of the grain shape during rolling is considered by gradually relaxing the strain rate constraintss.

The simulations with $\lambda = 10$ (activation mainly of $\{112\}$ slip planes) yield a better agreement with experiment than the simulations with $\lambda = 1$ (activation of $\{110\}$ and $\{112\}$ slip planes). Figure 17.12 shows the simulated texture for a ratio of $\tau^{\{110\}\langle 111\rangle} = 10 \cdot \tau^{\{112\}\langle 111\rangle}$ together with the experimental results.

17.18.4 Combination of Texture and FE Simulation

Figure 17.13 shows the through-thickness gradient in the experimental hot-rolling texture of a low-carbon steel together with the corresponding texture predictions which were obtained from combined Taylor–finite element simulations (Beckers et al. 1998). The simulations proceeded by using the velocity gradient tensor, as calculated from the finite element program, as input for a Taylor simulation. The finite element simulation considered surface friction.

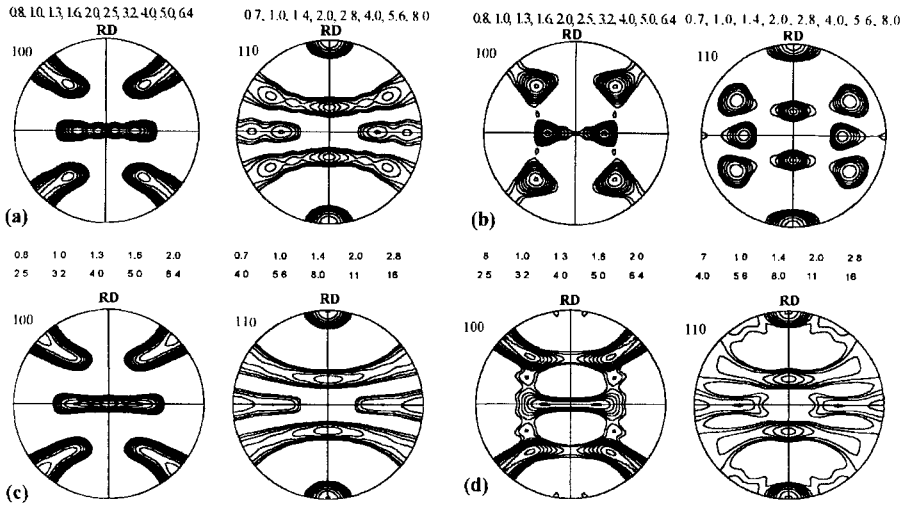

Figure 17.11: ⟨100⟩ and ⟨110⟩ pole figures of a finite element tuned self-consistent viscoplastic simulation (a), of a Taylor full-constraints viscoplastic simulation (b), of a Taylor relaxed-constraints pancake viscoplastic simulation (c), and of the experimental texture (d). (Tóth, Molinari, and Raabe 1997).

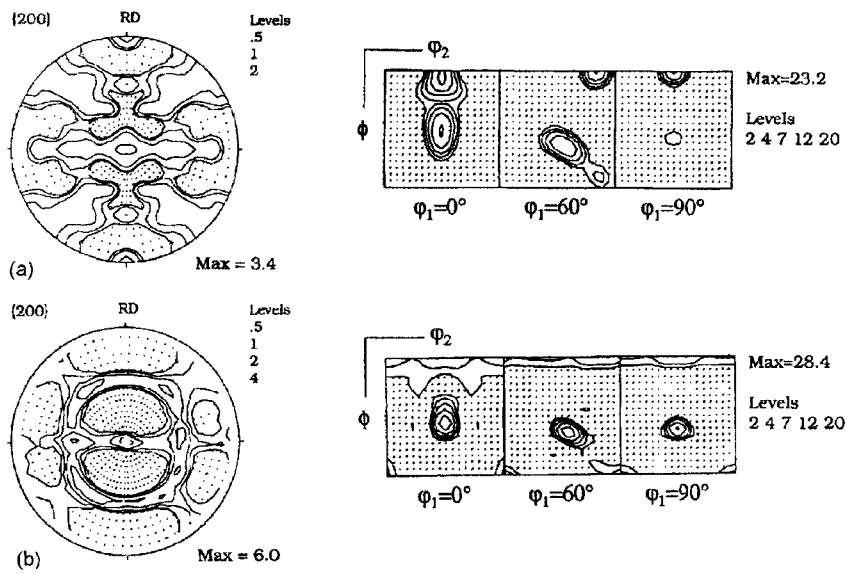

Figure 17.12: Texture of 80% warm-rolled ordered iron-aluminide; (a) simulated texture, $\{110\}\langle 111\rangle$ and $\{112\}\langle 111\rangle$ slip, $\tau^{\{110\}\langle 111\rangle} = 10 \cdot \tau^{\{112\}\langle 111\rangle}$, gradual strain rate relaxation; (b) experimental textures in the center layer (T_{roll} = 800-830 K) (Raabe 1996)

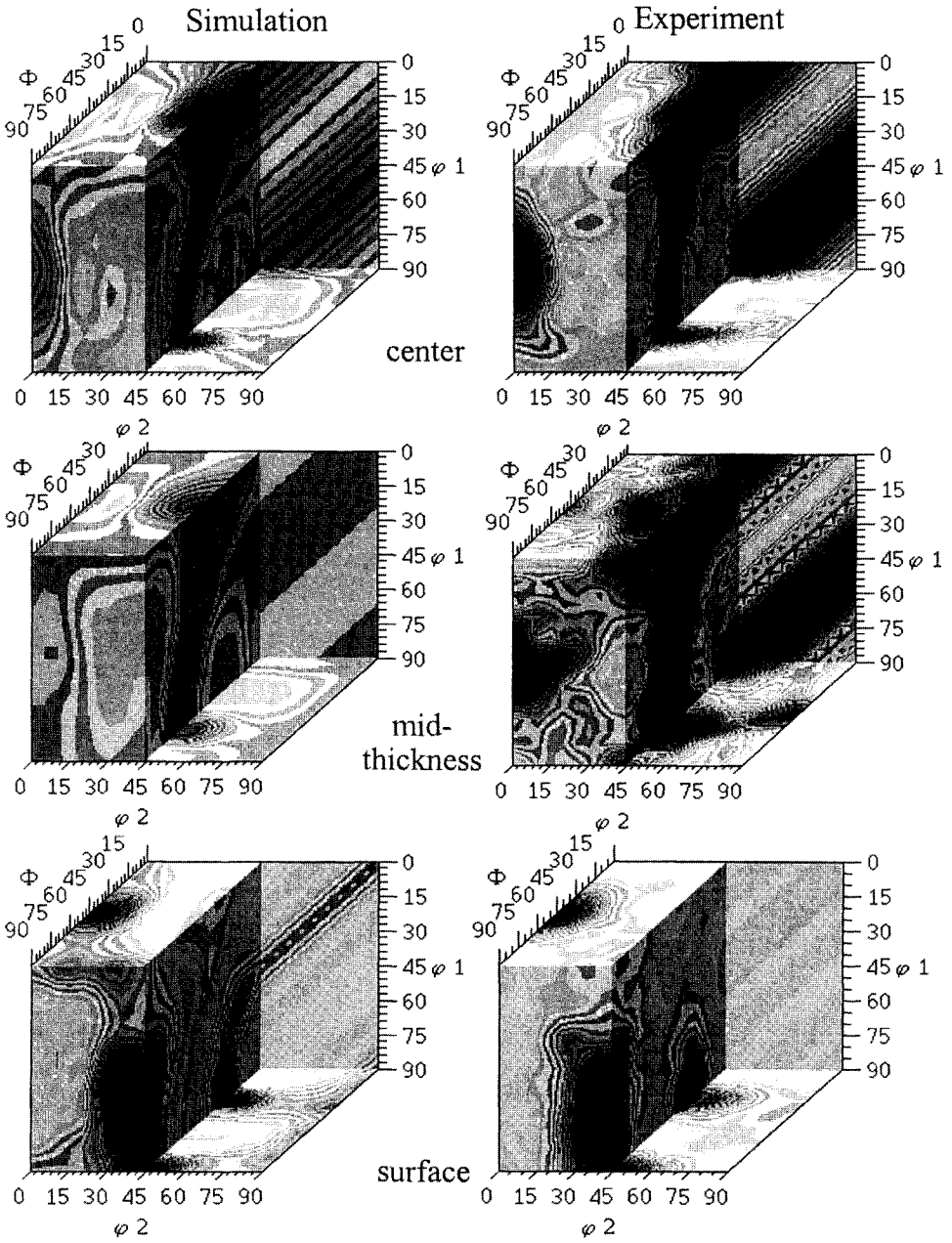

Figure 17.13: Through-thickness gradient in the experimental hot-rolling texture of a low-carbon steel and texture predictions obtained from combined Taylor–finite element simulations (Beckers, Sebald, Gottstein 1998).

Part V

Integrated Modeling and Simulation

Computational Materials Science: The Simulation of Materials, Microstructures and Properties By Dierk Raabe
Copyright © 1998 Wiley-VCH Verlag GmbH
ISBN: 3-527-29541-0

Chapter 18

Fundamentals

The behavior of materials is determined by thermodynamics and kinetics. The thermodynamic forces prescribe the general evolution direction of the microstructures according to their average chemistry, temperature, pressure, and so forth. The kinetic features of those lattice defects that are involved in microstructure evolution select one out of the many possible evolution paths. It is thus mainly the kinetics which determines the actual microstructural path of materials. It is hence obvious that any microstructure simulation effort has to place special emphasis on the incorporation of microstructure kinetics.

However, the kinetic details associated with the various microstructural ingredients depend on the scale and the lattice defects addressed. For instance, a macroscale finite element simulation of a hot-rolling process does usually not consider the fine details associated with the dynamics of dislocations or transformation phenonena at the mesoscale (Figure 18.1. However, the predictive character of microstructure simulations depends on the level at which kinetics is incorporated. The evolution of materials microstructures is characterized by the production, annihilation, transformation, and accumulation of lattice defects at a scale that can range from the atomic spacing to the specimen size. This means that microstructures can evolve in parallel at entirely different space and time levels (King et al. 1995; Bréchet and Kubin 1996; Gottstein 1996; Campbell et al. 1997; Cleveringa et al. 1997; Shenoy et al. 1998). Due to the nonlinear character of microstructure evolution it is often a critical task to assess which kinetic details are relevant for predicting microstructures and which may be neglected.

Based on this experience, microstructure simulations typically address three salient points: first, they aim at improving our insight into the underlying physical principles that govern the nature of microstructure evolution at the various scales. This task falls into the domain of elaborating physically plausible structural evolution laws. Second, they provide quantitative microstructure–property relations. This point can be regarded as a contribution to identifying appropriate microstructural equations of state. Third, they allow us to investigate both of the aforementioned aspects at levels that are not amenable to experimentation or under conditions that have not yet been studied. The latter aspect is particularly important for introducing simulations in industry.

For meeting these aims it is important to identify those defects and levels that are of relevance for solving a particular problem. The large spread of scales often encountered advocates introduction of the concept of integrated modeling and simulation (Gottstein 1996). This notion describes the coupling of computer codes with the aim to *bridge* the

Computational Materials Science: The Simulation of Materials, Microstructures and Properties By Dierk Raabe
Copyright © 1998 Wiley-VCH Verlag GmbH
ISBN: 3-527-29541-0

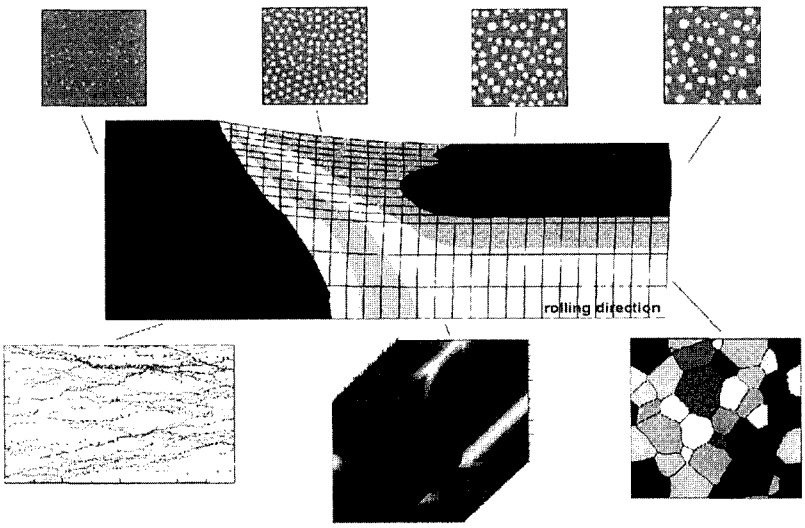

Figure 18.1: Large-scale finite element simulation of a hot-rolling process with some mesoscopic and microscopic details indicated, such as grain growth, transformation, ripening, crystallographic texture, and dislocation dynamics.

scale gaps among different simulation levels. This can be achieved by simultaneous (synchronous, direct) integration or sequential integration. The first term means that various interacting simulation levels are simultaneously considered in one computer experiment. The second notion describes the simpler method of an adequate parameter transfer among simulations that are used sequentially.

Some aspects associated with the integration of different levels have been addressed in the literature. Ashby (1992) quantified the problem of scale coupling in materials modeling in terms of four different levels of complexity, namely, structure evolution, multiple mechanisms, linked processes, and spatial variation. Bréchet and Kubin (1996) gave a detailed overview of the characteristic microstructural length scales, time scales, and driving forces that represent underlying scaling parameters of simulations. Goryachev (1996) discussed the connection of the basic conservation and flow laws among different simulation levels. Gottstein (1996) and Campbell, Huang, King, Lassila, Nikkel, dias de la Rubia, Shu, Foiles, Hughes, and Smyshyaev (1997) have started ambitious materials simulation initiatives in which both sequentially and simultaneously integrated approaches are extensively used. This Part is concerned with reviewing some fundamentals of simultaneously and sequentially integrated modeling and simulation under consideration of various space and time scales, with the aim of identifying the characteristic scales of microstructure evolution and identifying upper and lower bounds that limit the application of the various modeling and simulation methods. This information can serve as a platform to decide whether a simulation should be nanoscopic, microscopic, mesoscopic, or macroscopic, i.e. whether the underlying lattice defects are treated individually, collectively, or in an averaging continuum approach. Furthermore, it makes it possible to estimate whether the chosen scale-dependent simulation should be complemented by integrated concepts.

Chapter 19

Space and Time Scales in Microstructure Simulation

Tables 1.1–1.3 and Figures 1.1–1.2 (Chapter 1) showed the main space and time levels encountered in engineering materials. These scales introduce a certain hierarchy into microstructure simulation, at least from a spatial and temporal point of view. However, it should be emphasized that this hierarchy of scales or levels does not necessarily reflect a hierarchy of relevance. For instance, the strength or the electrical conductivity of a specimen can be substantially influenced by solute atoms, i.e. by lattice defects that act at the microscopic–nanoscopic scale. In contrast, it is conceivable that mesoscopic and macroscopic defects such as the surface or internal interfaces can be of much less relevance in the investigation of a macroscopic problem.

It is the task of this chapter to identify the physically relevant scaling parameters in the various models that are used in computational materials science and to give an estimation of whether they impose certain upper- or lower-bound constraints on the corresponding simulation approaches (Table 19.1). This point is of relevance to both the performance and the reliability of computer simulations since they generally depend on an adequate discretization of space and time.

The upper-bound parameters of a simulation should cover all relevant features of the system addressed. They should be small enough to reduce computation time and large enough to catch the physically relevant characteristics of the microstructural problem in a statistical fashion. The latter point means that simulations should provide sufficient data so that the results may be interpreted with a certain statistical reliability. The lower-bound parameters of a simulation should capture the main physics of the underlying lattice defects.

If the underlying minimum length scales and time increments used in a simulation are too large compared with those that are physically admissible, the calculations will lead to incorrect predictions. From a mathematical point of view these minimum characteristic length and time scales are related to the maximum increments that may be used in numerically solving the underlying discretized differential equations without introducing artifacts. However, if the chosen resolution of the simulation is too high the performance of the calculation is unnecessarily degraded. The gap between the upper and the lower scaling parameters, which define the spatial and temporal spread of the

Computational Materials Science: The Simulation of Materials, Microstructures and Properties By Dierk Raabe
Copyright © 1998 Wiley-VCH Verlag GmbH
ISBN: 3-527-29541-0

Table 19.1: Characteristic scaling lengths at the nanoscopic, microscopic, mesoscopic, and macroscopic level.

Length scale [m]	Physical origin (upper bound)	Physical origin (lower bound)	Simulation method
10^0–10^{-3}	external load	cross sectional reduction, critical regions	finite elements, finite difference
10^0–10^{-7}	external load	grain size, dislocation cell size, crack size, particle size	advanced microstructure finite element models (microstructure mechanics)
10^0–10^{-7}	external load	grain shape	Taylor–Bishop–Hill models
10^0–10^{-8}	external load	grain shape, inclusion shape, cell size	self consistent models
10^0–10^{-9}	system size	atom	percolation models
10^0–10^{-9}	system size	atomic clusters	cellular automata (deterministic or probabilistic)
10^{-3}–10^{-7}	grain clusters	dislocation cell size, microband	boundary dynamics, topological network models, vertex models
10^{-4}–10^{-9}	grain clusters	Burgers vector, annihilation spacing	dislocation dynamics
10^{-5}–10^{-9}	grain clusters	atom clusters	continuum field kinetic theory
10^{-5}–10^{-9}	grain clusters	structural interface unit, atom clusters	Potts model
10^{-5}–10^{-9}	grain	Burgers vector, annihilation spacing	dislocation segment dynamics
10^{-6}–10^{-9}	grain	atom clusters	microscopic field kinetic theory
10^{-7}–10^{-10}	system size	atom clusters	cluster variation method
10^{-7}–10^{-10}	system size	atom clusters	molecular field approximation
10^{-7}–10^{-10}	system size	atom	Metropolis Monte Carlo
10^{-6}–10^{-10}	cell size	atom	molecular dynamics (pair potentials, embedded atom potentials)
10^{-8}–10^{-12}	atom clusters	ion, electron	ab initio molecular dynamics (tight binding potentials, local density functional theory)

simulation, should at least amount to one or two orders of magnitude. This value allows bridging of at least one microstructural level. This means that microstructure simulations at the atomic level should provide some insight at the lattice defect level (e.g. dislocation, grain boundary), calculations at the lattice defect level should allow predictions at the grain level (e.g. second order stresses, particle distribution), and simulations at the grain level should produce reliable results at the specimen level.

The main spatial scaling parameters and some upper and lower bounds are shown in Table 19.1 for the nanoscopic–microscopic, the microscopic–mesoscopic level, and for the mesoscopic–macroscopic level.

The difference in scale that exists between the upper and lower bounds usually determines the storage and performance capabilities required in microstructure simulations. For instance, the number of elements used in a finite element simulation directly determines the rank of the system stiffness matrix. The upper-bound parameters that typically define the size of microscopic–mesoscopic simulations are prescribed by the grain size or some similar value such as particle spacing or phase spacing. Calculations in this regime often bridge the scale between elementary lattice defects or ensembles of lattice defects and the grain size. In cases where samples are sufficiently small at least in one or two dimensions (foil, wire), microscopic–mesoscopic simulations can even yield predictions at the specimen level. Dislocation dynamics represents a simulation technique that is related to molecular dynamics. Its main differences from atomistic modeling lies in the coarser discretization of time and space and in the fact that it is not intrinsically scaled by the Debye frequency and the atomic spacing, as is the molecular dynamics method, but scaled by the jump frequency of the atoms and some spatial value that lies between the Burgers vector and the minimum dislocation spacing. In contrast to molecular dynamics, dislocation dynamics can bridge scaling gaps between the microscopic and mesoscopic regime.

Appendices

Computational Materials Science: The Simulation of Materials, Microstructures and Properties By Dierk Raabe
Copyright © 1998 Wiley-VCH Verlag GmbH
ISBN: 3-527-29541-0

Appendix A

General Reading

Overviews

R. J. Arsenault, J. R. Beeler, J. A. Simmons *Computer Simulation for Materials Applications* **1976** National Bureau of Standards

T. Ericson *Computers in Materials Technology* **1981** Pergamon Press

R. J. Arsenault, J. R. Beeler, D. M. Esterling *Computer Simulation in Materials Science* **1986** ASM International

J. E. Mark, M. E. Glicksman, S. P. Marsh *Computational Methods in Materials Science* **1992** MRS

J. Q. Broughton, P. Bristowe, J. Newsam *Materials Theory and Modeling* **1993** MRS

H. O. Kirchner, L. P. Kubin, V. Pontikis *Proceedings of NATO ASI on Computer Simulation in Materials Science, Nano/Meso/Macroscopic Space and Time Scales* **1996** NATO Advanced Science Institutes Series

P. Klimanek and W. Pantleon *Simulationstechniken in der Materialwissenschaft* (in German) **1996** Technische Universität Freiberg

D. Raabe *Microstructure Simulation in Materials Science* **1997** Shaker

J. Hirsch *Simulation, Modellierung, Informationssysteme* (in German) **1997** DGM

R. LeSar and D. Clarke *Computer Simulation: A Textbook for Materials Scientists and Engineers* (in preparation) **1998**

Mathematical Modeling and Scientific Computation

J. von Neumann *Collected Works of J. von Neumann* **1963** Pergamon Press

I. G. Andrews, R. R. McLone *Mathematical Modeling* **1976** Butterworths

E. A. Bender *An Introduction to Mathematical Modeling* **1978** John Wiley & Sons

---

The complete references for the listed titles are given in the References at the end of the book.

C. L. Dym and E. S. Ivay *Principles of Mathematical Modeling* **1980** Academic Press

X. J. R. Avula, R. E. Kalman, A. I. Liapis, E. Y. Rodin *Mathematical Modeling in Science and Technology* **1983** Pergamon Press

H. P. Williams *Model Building in Mathematical Programming* **1985** John Wiley & Sons

S. E. Koonin *Computational Physics* **1986** The Benjamin/Cummings Publishing Company, Inc.

J. M. Smith *Mathematical Modeling and Digital Simulation for Engineers and Scientists* **1987** John Wiley & Sons

F. Neelamkavil *Computer Simulation and Modeling* **1987** John Wiley & Sons

W. Cheney and D. Kincaid *Numerical Mathematics and Computing* **1994** Brooks/Cole Publishing Company

N. Bellomo, L. Preziosi *Modeling Mathematical Methods and Scientific Computation* **1995** CRC Press

Monte Carlo and Molecular Dynamics

J. M. Hammersley, D. C. Handscomb *Monte Carlo Methods* **1964** Methuen's and Co./John Wiley & Sons

I. M. Torrens *Interatomic Potentials* **1972** Academic Press

W. Bruns, I. Motoc, K. O'Driscol *Monte Carlo Applications in Polymer Science* **1981** Springer Verlag

R. W. Hockney, J. W. Eastwood *Computer Simulation using Particles* **1981** McGraw-Hill

K. Binder *Applications of the Monte Carlo Method in Statistical Physics* **1984** Springer–Verlag

D. W. Heermann *Computer Simulation Methods in Theoretical Physics* **1986** Springer-Verlag

W. G. Hoover *Molecular Dynamics* **1986** Springer-Verlag

K. Binder, D. Stauffer *A Simple Introduction to Monte Carlo Simulation* **1987** Springer-Verlag

G. Ciccotti, D. Frenkel, I. R. McDonald *Simulation of Liquids and Solids — Molecular Dynamics and Monte Carlo Methods in Statistical Mechanics* **1987** North-Holland

M. P. Allen, D. J. Tildesley *Computer Simulation of Liquids* **1989** Clarendon Press

M. Meyer, V. Pontikis *Proceedings of NATO ASI on Computer Simulation in Materials Science, Interatomic Potentials, Simulation Techniques and Applications* **1989** Kluwer Academic Publishers and NATO Science Division

J. Tersoff, D. Vanderbilt, V. Vitek *Atomic Scale Calculations in Materials Science* **1989** MRS

V. Vitek, D. J. Srolovitz *Atomistic Simulation of Materials: Beyond Pair Potentials* **1989** Plenum Press

M. P. Allen, D. J. Tildesley *Proceedings of NATO ASI on Computer Simulation in Chemical Physics* **1992** Kluwer Academic Publishers/NATO Science Division

D. Wolf, S. Yip *Materials Interfaces* **1992** Chapman and Hall

A. F. Voter *Interatomic Potentials for Atomistic Simulations* **1996** *MRS Bulletin*

Cellular Automata

S. Wolfram *Theory and Applications of Cellular Automata* **1986** World Scientific Publishing

Simulation of Microstructure and Transformation

L. Kaufman, H. Bernstein *Computer Calculation of Phase Diagrams* **1970** Academic Press

H. E. Stanley *Introduction to Phase Transitions and Critical Phenomena* **1971** Clarendon Press

M. F. Ashby, R. Bullough, C. S. Hartley, J. P. Hirth *Dislocation Modeling of Physical Systems* **1980** Pergamon Press

A. G. Khachaturyan *Theory of Structural Transformations in Solids* **1983** John Wiley & Sons

L. H. Bennett *Computer Modeling of Phase Diagrams* **1986** The Metallurgical Society of AIME

D. J. Srolovitz *Computer Simulation of Microstructural Evolution* **1986** Metallurgical Society of AIME

L. P. Kubin, G. Martin *Non-Linear Phenomena in Materials Science I, II* **1988, 1992** Trans Tech Publication

M. P. Anderson, A. D. Rollett *Simulation and Theory of Evolving Microstructures* **1990** TMS Publication

F. J. Humphreys, M. Hatherly *Recrystallization and Related Annealing Phenomena* **1995** Pergamon Press

Industrial Modeling

R. S. Andersen, F. R. de Hoog *The Application of Mathematics in Industry* **1976** Butterworths

P. R. Sahm, P. N. Hansen *Numerical Simulation and Modeling of Casting and Solidification Processes for Foundry and Cast-House* **1984** International Commercial Foundry Association, New York

M. Predeleanu *Computational Techniques for the Prediction of Materials Processes and Defects* **1987** Elsevier Science

J. Szekely, W. E. Wahnsiedler *Mathematical Modeling Strategies in Materials Processing* **1988** John Wiley & Sons

J. L. Chenot, E. Onate *Modeling of Metal Forming Processes* **1988** Kluwer

J. W. Evans, J. Brimacombe *Mathematical and Physical Modeling of Metals Processing* **1989** John Wiley & Sons

S. Yue *Proceedings of the International Symposium on Mathematical Modeling of Hot Rolling of Steel* **1990** TMS

J. H. Beynon, P. Ingham, H. Teichert, K. Waterson *Proceedings of the First and Second International Conference on Modeling of Metal Rolling Processes* **1993, 1996** The Institute of Materials

R. Tomellini *Proceedings of an ECSC Workshop on Modeling of Steel Microstructural Evolution during Thermomechanical Treatment* **1997** European Commision

Microstructure Mechanics and Textures

J. Gittus, J. Zarka *Modeling Small Deformations of Polycrystals* **1986** Elsevier Applied Science

T. Mura *Micromechanics of Defects in Solids* **1987** Martinus Nijhoff Publishers

P. Hartley, I. Pillinger, C. E. N. Sturgess *Modeling of Material Deformation Processes* **1992** Springer Verlag

S. Schmauder, D. Weichert, D. Raabe, A. Cornec *Proceedings 3rd–6th International Workshops on the Computational Modeling of the Mechanical Behaviour of Materials* **1994, 1996, 1996, 1997** Elsevier Science

S. Nemat-Nasser, M. Hori *Micromechanics: Overall Properties of Heterogeneous Materials* **1993** North-Holland

D. Raabe, H. J. Bunge *Proceedings of the Symposium Computer Simulation and Modeling in Texture Research* **1997** Gordon and Breach Science

Finite Element and Finite Difference Methods

G. E. Forsythe, W. R. Wasow *Finite Difference Methods for Partial Differential Equations* **1960** John Wiley & Sons

M. J. O. Carroll, A. W. Bush, M. Cross, R. D. Gibson, T. S. Wilkinson *Modeling and Simulation in Practice* **1980** Emjoc Press

O. C. Zienkiewicz and K. Morgan *Finite Elements and Approximation* **1983** John Wiley & Sons

O. C. Zienkiewicz, R. L. Taylor *The Finite Element Method, 4th Edition, Vols. 1, 2* **1989, 1991** McGraw-Hill

A. Curnier *Computational Methods in Solid Mechanics* **1994** Kluwer

S. S. Rao *The Finite Element Method in Engineering* **1989** Pergamon Press

G. W. Rowe, C. E. N. Sturgess, P. Hartley, and I. Pillinger *Finite Element Plasticity and Metal Forming Analysis* **1991** Cambridge University Press

Journals on Materials Modeling and Simulation

Modeling and Simulation in Materials Science and Engineering, Institute of Physics

Computational Materials Science, Elsevier

Computers and Structures, Pergamon Press

Computers in Physics, American Institute of Physics,

Simulation and Computation, M. Dekker

Molecular Simulation, Gordon and Breach

Appendix B

Computer Classification

As far as computational materials science is concerned, progress in computer technology can be quantified in terms of speed, information storage, infrastructure, technical reliability, and investment costs.

The performance of a computer is essentially determined by three factors, namely, by the physical properties of its ingredients (e.g. thermionic valves or complementary field-effect transistors), by the chip design (e.g. processors with a complex or reduced instruction set), and by its architecture (e.g. von Neumann architecture or massively parallel architecture). The speed of a computer can be measured in units of floating point operations per second (FLOP/s)[1]. While this value only provides a measure for the numerical performance of the processor, the average speed of a memory-processor system is better quantified in terms of million instructions per second (MIPS) or cycles per instruction (CPI) (Kästner 1978).

However, for estimating the performance of a simulation code on a particular computer, the number of FLOP/s or MIPS is insufficient information, since these quantities do not account for further limiting factors such as the cache, bus, and swapping speed. For analyzing mixed requirements, benchmark tests represent a more appropriate means of assessing the system performance with respect to particular simulation applications. Benchmark tests are programs that test the characteristics of a computer such as its numerical power (CPU benchmarks[2]) or its general performance, considering the co-operation of the various hardware components (system benchmarks).

Technically, the chip performance is determined by the quality and arrangement of its key elements. These elements are devices, gates, and lines. Typical devices are transistors and capacitors. Gates perform functions and are typically made up, on average, of three or four devices. Lines link together blocks of gates. There are two typical integrated circuit (IC) designs, which differ in the type of gate integration technology. The first one is the complementary metal oxide semiconductor (CMOS) and the second one is referred to as emitter coupled logic (ECL).

Physically, the performance of a processor chip is determined by the gate delay or, more precisely, by the speed of a signal between two subsequent gatter entrances. While the early thermionic valves ($\approx$ 1950) provided switching times of 1 μs, the first germanium

[1] Larger units in use are Mega, Giga and Tera FLOP/s (MFLOP/s, GFLOP/s, TFLOP/s).
[2] CPU = central processor unit.

Table B.1: Progressive technology of integrated circuits.

Date	Integration level	Number of transistors	Equivalent gates	Typical functions or systems
1950	SSI	1–40	1–10	single circuit
Late 1960s	MSI	40–400	10–100	functional network
Late 1970s	LSI	40–4500	100–1000	hand calculator
Mid 1980s	VLSI	4500–300000	1000–80000	microprocessor
Present	ULSI	> 300000	> 80000	computer on a chip

SSI, small-scale integration; MSI, mid-scale integration; LSI, large-scale integration; VLSI, very large-scale integration; ULSI, ultra large-scale integration.

based transistors required only $0.3\,\mu s$ ($\approx$ 1960). The first ICs had switching times of $10\,ns$ ($\approx$ 1965). Modern very large-scale integrated (VLSI) and ultra large-scale integrated (ULSI) chips have switching times of less then $1\,ns$ (Table B.1). It is clear that enhanced integration, i.e. reduced transistor size will further degrade this value (e.g. Giga-scale integration, GSI) (Tietze and Schenk 1980; Size 1981). For semiconductor transistors this construction principle of large-scale integration is naturally limited when the source and drain geometry reach the level of mono-atomic layers.

However, the switching speed is constrained not only by the gatter spacing, but also by the mean free path of the electrons and holes. The mean free path of the charge carriers can be increased by using gallium arsenide or aluminum gallium arsenide instead of silicon (Seeger 1982). This concept is realized by using metal semiconductor field-effect transistors (MESFETs) instead of conventional metal oxide field-effect transistors (MOSFETs) or complementary metal oxide field effect transistors (CMOSFETs).

Even beyond the scale predetermined by the mean free path of the charge carriers, the switching speed of a transistor can be further increased. This is attained when the mean free electron path is in the order of the channel length. When the electron penetrates the channel without inelastic scattering, it is referred to as a ballistic electron. The ballistic speed of a charge carrier is much larger than its drift velocity. Further substantial improvement can be expected from the exploitation of quantum effects (Tietze and Schenk 1980; Size 1981; Seeger 1982). Owing to these various technical improvements, development in processor speed has in the recent decades described an exponential increase. As a rule, in a five-year period the maximum attainable speed (counted in FLOP/s) increases by a factor of ten (Lau 1994; Märtin 1994).

Besides these physical parameters the chip speed is also affected by its architecture. Since about 1985 an increasing number of VLSI and ULSI processors were designed as reduced instruction set computers (RISCs) rather than as conventional complex instruction set computers (CISCs). RISCs have a smaller number of instructions than CISCs. Thus, in most cases RISCs require a larger number of single instructions than CISCs. However, in modern processor architectures this intrinsic disadvantage is over-compensated by increasing the number of internal registers, which reduces the memory access, and by the efficient use of hardware pipelines (Märtin 1994). Furthermore, traditional large-scale integration chip concepts are increasingly complemented by application-specific integrated circuits (ASICs). In recent decades the costs for buying, operating, and maintaining computers have been tremendously reduced. This progress was essentially due to the transi-

tion from bipolar to silicon-based MOSFET and CMOSFET technology, the large-scale integration of transistors, and the mass production of these ingredients. The production of MOSFET and double-metal CMOSFET chips is nowadays characterized by the use of more than 10 active mask layers and requires about 50 major process steps. However, it is less expensive than that of bipolar components, which are therefore increasingly confined to applications where high current densities are required. When expressed in terms of floating point operations, computing costs have been decreased by a factor of about 10^6 since 1955.

In 1946 John von Neumann suggested a basic theoretical architecture as a universal approach for computers. This concept was first realized in the so-called Princeton computer (Flynn 1972; Märtin 1994). The von Neumann computer contains five structural ingredients which establish its logical and spatial subdivision. These are the computer memory unit, the arithmetic logic unit, the control unit, the input/output unit, and the unit communication network (system bus).

The memory unit stores program codes and data. It contains a register for data and addresses. The memory is decomposed into memory cells, each having a width of w bits. The use of a memory unit allows each scientific task to be represented by a particular computer program and loaded from an external source. The arithmetic logic unit carries out arithmetic, logic, and shift operations. For this purpose an accumulator unit, a combination unit, and at least one further register (multiplication register) is required. The control unit contains an instruction register, an instruction counter, a decoding unit, and a control unit for instruction execution. The input/output unit makes it possible to communicate data and programs from/to external data sources. The system bus represents the communication network unit among the above-mentioned parts and makes possible the transfer of data packages with a respective word length of w bits. This basic structure of the von Neumann architecture is typical of many computers until now. However, for attaining further substantial power enhancement, departure from this concept and introduction of competitive architectures such as may be realized in multiprocessor machines gain momentum.

According to the scheme of Flynn (1966), computers can be classified into four categories depending on their respective instruction and data stream organization, namely, single instruction stream–single data stream (SISD), single instruction stream–multiple data stream (SIMD), multiple instruction stream–single data stream (MISD), and multiple instruction stream–multiple data stream (MIMD) architectures (Table B.2.

Among these four groups SISD represents the traditional von Neumann concept. In SISD computers only one instruction is carried out using one particular information unit per time step. For running a program, one control unit produces a single instruction stream which is gradually executed by the arithmetic logic unit. The required data and the results are exchanged between the central memory unit and one single arithmetic logic unit. The personal computers with processor types 8088, i286, i386, and i486, the VAX 11/780, and the IBM 360/91 represent typical examples of SISD architectures.

In the ideal SIMD computer one instruction considers multiple data per time step. For running a program, one single control unit produces a single instruction stream at the same time parallel in various processing elements. This technique must not be confused with parallel computing, where the various arithmetic logic units can work entirely independently with different data *and* different instructions. The parallel distribution of the relevant information arranged in the instruction to the various processing elements is referred to as instruction broadcasting. Vector computers are often assorted to the SIMD architecture. However, the pipeline technique does not represent a pure SIMD concept,

Table B.2: Computer classification according to Flynn

Category	Instruction stream–data stream	Examples
SISD	single instruction stream–single data stream	von Neumann architecture, e.g. personal computer
SIMD	single instruction stream–multiple data stream	pipeline architecture, e.g. vector computer
MISD	multiple instruction stream–single data stream	-
MIMD MIMD	multiple instruction stream–multiple data stream	multi-processor architecture, e.g. parallel computer

since the data are subsequently tackled by the single processing units. The ILLIAC IV field computer and the Goodyear STARAN computer represent typical examples of SIMD architectures. The S6000 and most RISC workstations contain massive pipeline architectures. The MISD architecture is a theoretical concept without practical relevance. In the Flynn scheme it is only included forsymmetry reasons.

MIMD computers are referred to as parallel or multiple processor machines, where a processor represents a component with its own control unit and various processing elements. The components, especially the processors of an MIMD computer, are interconnected to each other. This means that a MIMD computer contains numerous processors which can independently execute individual instruction streams using individual data streams. MIMD computers were developed along two main directions. In the first type all processors share a common memory unit. These architectures are referred to as shared memory MIMD concepts. In the second type the memory is not globally accessible but distributed among the processors. This approach is thus referred to as the distributed memory MIMD concept. The latter class of MIMD computer is typically denoted as a massively parallel processor (MPP) computer. The Cray machines C98, T3D, and J916, the IBM SP2, the Intel XP/S140, the Fujiutsu VPP500, and the Parsitec GC/192 and GC/128 are typical examples of MIMD computers. Among these, the Fujiutsu VPP500 computer of the Japanese National Aerospace Laboratory, which is equipped with 140 individual processors and distributed memory, is at present (1997) regarded as the fastest running machine. It realizes 170 GFLOP/s. Current technology forecasts in that field even predict an MMP computer with as much as 1 TFLOP/s by the year 2000. The classification of Flynn (1966) was refined by Shore (1973) who uses six different classes.

Appendix C

Advanced Empirical Methods

C.1 Artificial Neural Networks

Modern artificial neural networks are adaptive systems in the form of computer programs which are typically based on the implementation of nonlinear mathematical models on parallel architectures and/or large-scale integrated circuits. However, the basic installation of neural networks does not necessarily require massively parallel architectures but can be simulated by computer programs.

The main philosophy behind artificial neural networks is their ability to learn by example, or if expressed more technically, to modify input data systematically and map them on output data (Rumpelhart and McCelland 1986; Ritter et al. 1991; Schmitter 1991a; Nauck et al. 1994; Wassermann 1994; Mukherjee et al. 1995; Schmitter 1995).

The principle of artificial neural networks was adapted from the neurophysiology of the human brain, which represents a genetic, morphological, functional network of interconnected neuron cells (Pschyrembel 1990). The average human brain can contain as many as 10^{11} neurons which are connected to each other by as many as 10^{15} interconnections (Figure C.1).

The biological neuron cells contain two types of interconnections, namely, the axons and the dendrites. Axons are usually much longer and also thicker than dendrites, which transmit electrochemical signals from other neuron cells to the cell to which they belong. The axon carries the signal from the neuron of which it is a part to various other neuron cells. These can be located in the immediate neighborhood or very far away from the emitting neuron. Accordingly, axons can have a length of the order of micrometers or in the meter range.

The basic mathematical principle of learning by experience in artificial neural networks corresponds to a nonlinear procedure that maps an input vector to an output vector by using free parameters that are referred to as weights. The learning process is then realized by comparing correct standard patterns or data with results obtained from analyzing modified training data in an iterative fashion. Depending on the deviation between output and standard, the weighting functions between the neurons are gradually adapted (Figures C.2 and C.3).

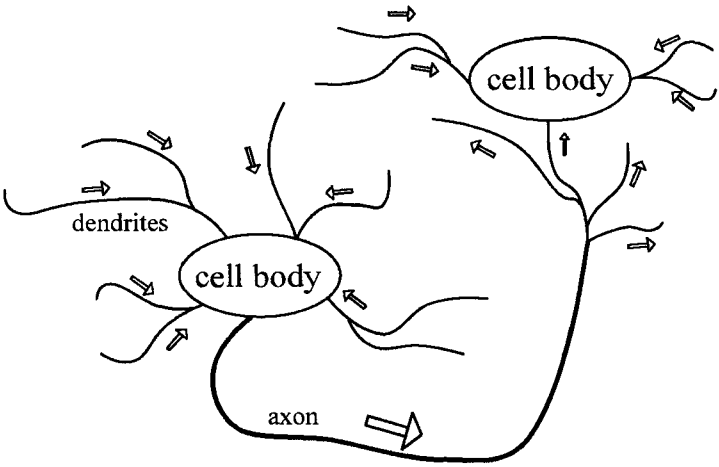

Figure C.1: Schematic illustration of two biological neurons. The arrows indicate the direction of the transmitted electrochemical signal.

The development of artificial neural networks is based on the pioneering work of W. S. McCulloch and W. H. Pitts in 1943 on neurons as elementary logical units of adaptive systems. All neural network models are essentially designed to mimic the basic principle of information transfer among biological neurons. This is achieved by connecting the information content provided by a number of input data and mapping them to a set of output data with variable intensity in an adaptive manner.

The first neural network systems were based on a one-neuron architecture. These early attempts, which were rooted in the work of F. Rosenblatt and B. Widrow, were termed adaptive linear elements and already had the ability to identify letters irrespective to their orientation. Current advanced approaches to artificial neural networks can be roughly classified in three groups, namely, multilayer feedforward nets, self-organizing maps, and learning vector quantizers.

Multilayer perceptron-type networks belong to the group of multilayer feedforward nets. They consist of one or more neuron layers connected in forward direction. The input layer is usually not connected. The layers between input and output layer are not directly accessible and are therefore termed hidden layers. Figure C.2 shows a typical example of a multilayer perceptron neural network and the corresponding type of sigmoidal weighting function. The supervised training of multilayer perceptrons is performed by the backpropagation algorithm with respect to the summed squared difference of the actual and desired output data set.

Self-organizing maps are usually characterized by a one- or two-dimensional array of output neurons. The neurons in self-organizing maps compute their activation by using a so-called distance measure that quantifies the discrepancy between input and output vectors. Their weighting function is usually bell-shaped. The learning process proceeds by identifying the neuron with the smallest deviation between input and output and by adapting the weighting functions of the neighboring neurons accordingly. Thus, a self-organizing neural network generates topological clusters of similarly weighted neurons (Figure C.3).

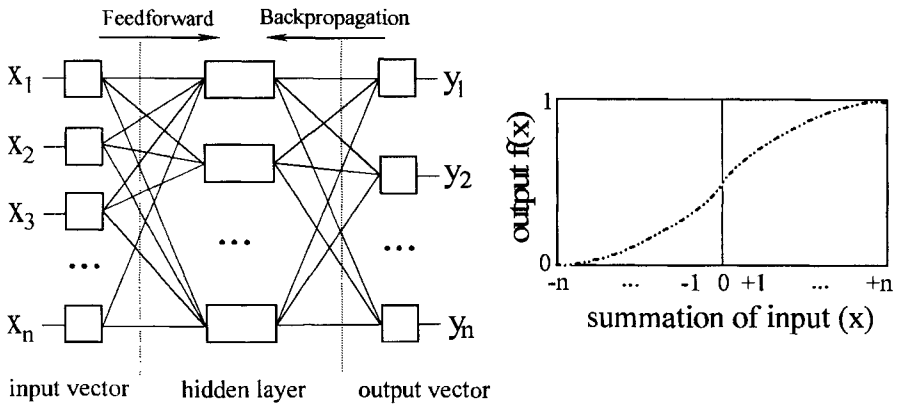

Figure C.2: Schematic illustration of the basic structure of a multilayer perceptron neural network.

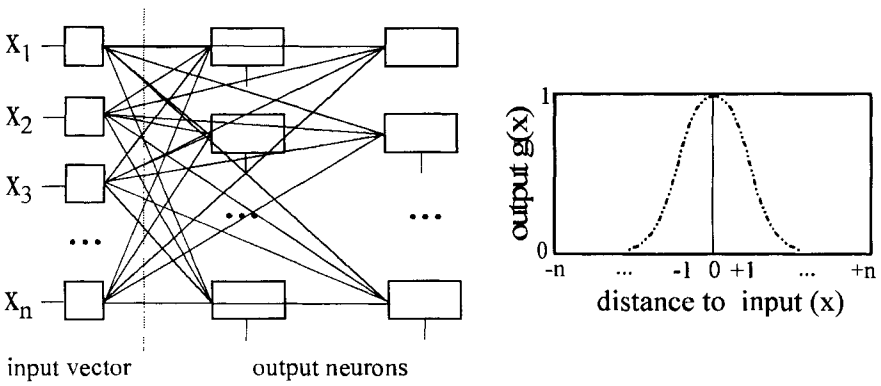

Figure C.3: Schematic illustration of the basic structure of a self-organizing map (Kohonen net).

C.2 Fuzzy Set Theory

Scientific concepts are characterized by a crisp and often deterministic description of the problems addressed. Solutions are usually obtained numerically or analytically under well-defined boundary- and initial-value conditions. This means that answers which are obtained through scientific computing are given in a quantitative fashion, or if Boolean aspects are concerned, in a dichotomous manner, in terms of *true* or *false*. These concepts make sense when the model under investigation is formulated quantitatively by using state variables, state equations, evolution equations, and independent variables, as well as boundary- and initial-value conditions. The solutions obtained can then be interpreted in the framework of the underlying formal model.

However, our everyday experience in the observation of *real* situations discloses three major problems which together can make it difficult to render real events into conventional formal scientific models. First, real situations are often not precisely defined and

not entirely deterministic in nature, at least not in the average phenomenological human perception. Second, real systems tend to be highly complex. This means that a comprehensive deterministic description of real situations typically requires a large variety of dependent and independent variables as well as detailed boundary and initial data. For instance, one main aspect of classical scientific modeling consists in extracting from a real system those variables that are assumed to be of particular relevance in the context addressed, rather than using all available data. Finally, one must admit that there are a number of possible input data to a model which are not accessible to measurements. Third, a discrepancy exists between real languages and exact formal languages which are in the incipient stages employed to formulate models. Thus the problem arises in transfering a human thought into a formal mathematical framework without losing some aspects because of deficiencies and discrepancies in syntax and semantics.

As the name implies, fuzzy set approaches define a theory of graded concepts (Zadeh 1968; Zadeh et al. 1974; Zadeh 1978; Zimmermann 1978; Nauck et al. 1994; Bothe 1995). This is a theory in which neither classical probabilistic nor bivalent logic concepts prevail, but in which decisions are a matter of degree. In other words, every aspect in fuzzy logic is elastic[1] rather than stiff.

Some basic definitions of fuzzy sets will be reviewed below in a more detailed manner. In a classical set of objects $\langle \boldsymbol{C} \rangle$, for each individual element $c_i \in \langle \boldsymbol{C} \rangle$ it can be clearly defined whether it belongs to a defined subset $\langle \boldsymbol{A} \rangle$ of $\langle \boldsymbol{C} \rangle$, i.e. $c_i \in \langle \boldsymbol{A} \rangle \subseteqq \langle \boldsymbol{C} \rangle$, or not, i.e. $c_i \notin \langle \boldsymbol{A} \rangle \subseteqq \langle \boldsymbol{C} \rangle$. The decision about the assignment of the object is made in a dichotomous fashion, i.e. it is answered in terms of "true" or "false". In a classical set one can enumerate the individual elements that belong to a particular set $\langle \boldsymbol{A} \rangle$,

$$c_1, c_2, ..., c_n \in \langle \boldsymbol{A} \rangle \tag{C.1}$$

and describe the set analytically,

$$c_i = x_i^2 \ , \quad x_i \in \langle \boldsymbol{X} \rangle \ , \quad c_i \in \langle \boldsymbol{A} \rangle \tag{C.2}$$

by setting boundary conditions, such as

$$\langle \boldsymbol{A} \rangle = \{c | c \leq N\} \ , \qquad N = \text{constant} \tag{C.3}$$

or by using a delta-type characteristic equation. This equation sets a Boolean variable b equal to 1 if the object belongs to the set and equal to 0 if it does not belong to the set.

In contrast to such classical sets, fuzzy sets allow one to define the membership of an element of a set in terms of a non-Boolean variable. This means that the characteristic function allows various degrees of membership $b \neq 1$ and $b \neq 0$ for the objects of a given set. In other words, if $\langle \boldsymbol{C} \rangle$ is a set of elements denoted generically by c then a fuzzy set $\langle \widetilde{\boldsymbol{A}} \rangle$ in $\langle \boldsymbol{C} \rangle$ is a set of ordered pairs according to

$$\langle \widetilde{\boldsymbol{A}} \rangle = \left\{ \left(\mathrm{c}, \vartheta_{\langle \widetilde{\boldsymbol{A}} \rangle}(c) \right) \middle| \mathrm{c} \in \langle \boldsymbol{C} \rangle \right\} \tag{C.4}$$

where $\vartheta_{\langle \widetilde{\boldsymbol{A}} \rangle}(c)$ is referred to as the membership function, grade of membership, degree of compatibility, or degree of truth of c in $\langle \widetilde{\boldsymbol{A}} \rangle$ which maps $\langle \boldsymbol{C} \rangle$ into the memberspace $\langle \boldsymbol{M} \rangle$.

[1] The terms "elastic" and "stiff" are used here in a figurative sense.

In simple cases fuzzy sets can thus be described as an ordered set of object pairs, where the first one denotes the element and the second one the degree of membership or the degree of correspondence, e.g.

$$\langle \widetilde{A} \rangle = \Big\{ (\text{light green}, 0.1),\ (\text{green}, 0.2),\ (\text{dark green}, 0.5),\ (\text{blue}, 1.0),$$
$$(\text{dark red}, 0.5),\ (\text{red}, 0.2),\ (\text{light red}, 0.1) \Big\} \quad \text{(C.5)}$$

In this fuzzy set, the element named "blue" has obviously the closest compatibility with an addressed object. $\langle \widetilde{A} \rangle$ could be named the fuzzy set "best compatibility in color". Another fuzzy set could describe "real numbers close to zero", i.e.

$$\langle \widetilde{A} \rangle = \left\{ \left(c,\ \vartheta_{\langle \widetilde{A} \rangle}(c) \right) \middle| \vartheta_{\langle \widetilde{A} \rangle}(c) = \frac{1}{\sqrt{2}} \exp\left(- \left(\frac{c}{\sqrt{2}} \right)^2 \right) \right\} \quad \text{(C.6)}$$

According to these examples a fuzzy set can be defined as a generalized set and the corresponding membership function can be referred to as a generalization of the characteristic equation (Zadeh 1968; Zimmermann 1991).

The support set $S\left(\langle \widetilde{A} \rangle\right)$ of a given fuzzy set $\langle \widetilde{A} \rangle$ is the crisp set of all $c_i \in \langle C \rangle$ with the property $\vartheta_{\langle \widetilde{A} \rangle}(c) > 0$. In the context of equation (C.5) one can state that the elements light green, green, dark green, blue, dark red, red, and light red, which all yielded positive membership values, are part of the support of $\langle \widetilde{A} \rangle$ while other colors such as yellow and brown clearly do not have a compatibility ≥ 0.

Formulating this concept in a more general fashion, one defines a set of elements that belong to the fuzzy set $\langle \widetilde{A} \rangle$ at least to the degree α. Such a subset is referred to as an α-level set and can be written

$$\langle \widetilde{A}_\alpha \rangle = \left\{ c \in \langle C \rangle \middle| \vartheta_{\langle \widetilde{A} \rangle}(c) \geq \alpha \right\} \quad \text{(C.7)}$$

or, as a so-called strong α-level set, defined by

$$\langle \widetilde{A}_\alpha \rangle = \left\{ c \in \langle C \rangle \middle| \vartheta_{\langle \widetilde{A} \rangle}(c) \alpha \right\} \quad \text{(C.8)}$$

A further point of relevance in fuzzy set theory is the convexity of a set. As opposed to conventional set theory, convexity of a fuzzy set is defined with reference to the membership function $\vartheta_{\langle \widetilde{A} \rangle}$ rather than through the support of a fuzzy set. A fuzzy set $\langle \widetilde{A} \rangle$ is referred to as convex if

$$\vartheta_{\langle \widetilde{A} \rangle}\left(\lambda c_1 + (1-\lambda) c_2\right) \geq \min\left(\vartheta_{\langle \widetilde{A} \rangle}(c_1), \vartheta_{\langle \widetilde{A} \rangle}(c_2) \right), \quad c_1, c_2 \in \langle C \rangle, \quad \lambda \in [0,1] \quad \text{(C.9)}$$

Accordingly, a fuzzy set is convex when all its α-level subsets are convex. For a fuzzy set $\langle \widetilde{A} \rangle$ the so-called cardinality $\left| \langle \widetilde{A} \rangle \right|$ is defined by

$$\left| \langle \widetilde{A} \rangle \right| = \sum_{c \in \langle C \rangle,} \vartheta_{\langle \widetilde{A} \rangle}(c) \quad \text{(C.10)}$$

and the relative cardinality $\left\|\langle\widetilde{A}\rangle\right\|$ by

$$\left\|\langle\widetilde{A}\rangle\right\| = \frac{\left|\langle\widetilde{A}\rangle\right|}{|\langle C\rangle|} \tag{C.11}$$

Above it was shown that the membership function represents the main difference between classical and fuzzy sets. While for conventional sets Boolean membership functions are defined, for fuzzy sets non-Boolean membership functions prevail. The main operations among fuzzy sets are thus defined in terms of operations on the corresponding membership functions (Zadeh 1968).

The membership function $\vartheta_{\langle\widetilde{A}\rangle\cap\langle\widetilde{B}\rangle}(c)$ of the intersection $\langle\widetilde{A}\rangle \cap \langle\widetilde{B}\rangle$ is defined pointwise by

$$\vartheta_{\langle\widetilde{A}\rangle\cap\langle\widetilde{B}\rangle}(c) = \min\left\{\vartheta_{\langle\widetilde{A}\rangle}(c),\, \vartheta_{\langle\widetilde{B}\rangle}(c)\right\}, \qquad c \in \langle C\rangle \tag{C.12}$$

The membership function $\vartheta_{\langle\widetilde{A}\rangle\cup\langle\widetilde{B}\rangle}(c)$ of the union $\widetilde{\langle A\rangle} \cup \widetilde{\langle B\rangle}$ is defined pointwise by

$$\vartheta_{\langle\widetilde{A}\rangle\cup\langle\widetilde{B}\rangle)}(c) = \max\left\{\vartheta_{\langle\widetilde{A}\rangle}(c),\, \vartheta_{\langle\widetilde{B}\rangle}(c)\right\}, \qquad c \in \langle C\rangle \tag{C.13}$$

The membership function $\vartheta_{\mathfrak{C}\langle\widetilde{A}\rangle}(c)$ of the complement of a fuzzy set $\langle\widetilde{A}\rangle$ is defined by

$$\vartheta_{\mathfrak{C}\langle\widetilde{A}\rangle}(c) = 1 - \vartheta_{\langle\widetilde{A}\rangle}(c), \qquad c \in \langle C\rangle \tag{C.14}$$

Further fuzzy set operations are discussed in detail by Zadeh (1968) and Zimmermann (1978).

Appendix D

Percolation Theory

D.1 Fundamentals

Percolation theory investigates whether a system which consists of elementary or microscopic states that are defined at the nodes of a given lattice is macroscopically connected or not (Binder 1984; Stauffer 1991; Stauffer and Aharony 1992; Sahimi 1994; Stauffer and Aharony 1995). In other words, percolation theory examines whether a given ensemble with microscopic states $A, B, \ldots$ can be penetrated along a certain path defined by neighboring sites of identical state. This requires that from the start to the end of the path each site with, say, state A has a neighboring site within the same state. A trivial solution emerges if all sites are in the same state.

Thus, if the rules that determine the respective state of the microscopic sites at a given time are put aside (e.g. spin up or spin down), percolation theory addresses a purely geometrical problem. In this view percolation models provide information about the topology of sites that share a common property.

The underlying spatial lattices can be regular or irregular, e.g. Voronoi tessellations are admissible. Figure 6.10 showed some typical lattices that are frequently used in Monte Carlo, cellular automaton, and percolation simulations. Obvious macroscopic tasks of percolation theory are the prediction of forest fire propagation and the estimation of the connectivity of oil resources. In materials research, percolation is of considerable relevance in simulating current paths, microplastic behavior, diffusion, fracture mechanics, or properties of porous media (Stauffer and Aharony 1992; Kuo and Gupta 1995). Although percolation simulations are often used for predicting structure evolution at the microscopic level, they are not intrinsically calibrated and can therefore be applied to arbitrary regimes of space and time.

D.2 Bond, Site, and Bootstrap Percolation

Percolation models follow two separate objectives. First, they determine the states of the lattice nodes by using an algorithm which reflects the physical situation to be described. For instance, this can be done by using a numerical sampling procedure. Second, they examine the topological data of the system, such as the cluster size and distribution, or macroscopic connectivity.

Percolation processes can be simulated on regular or random networks. Classical percolation approaches concentrate on two main aspects, namely, the bond percolation problem and the site percolation problem.

In the bond percolation problem the connections between neighboring nodes are either occupied, i.e. the elementary junctions establish connectivity (conducting elements) or vacant, i.e. the microscopic junctions are closed and interrupt connectivity (insulating elements). The bonds are occupied randomly and independently of each other with probability p. Thus, a junction is vacant with probability $1-p$.

Two sites are connected if there exists at least one path between them consisting solely of occupied bonds. The state of being connected does not give any information about the length of the path between the considered nodes. An array of connected positions which is entirely surrounded by vacant bonds is denoted as a cluster. If p is much below 1 the clusters are typically much smaller than the network. It is clear that the relation between cluster size and network size depends on the network size itself (Sahimi 1994; Stauffer and Aharony 1995). However, if p is close to 1 the network should be entirely connected. At some well-defined probability value p, a topological transition of the random network from a macroscopically disconnected to a connected one takes place. This value is referred to as the bond percolation threshold, p_{cb}. It represents the largest fraction of connecting elementary junctions below which there is no sample-spanning cluster of occupied bonds, i.e. no complete system penetration.

The site percolation problem is tackled accordingly. However, in this approach the nearest neighbors rather than the elementary bonds determine the connectivity. The corresponding threshold value is referred to as the site percolation threshold, p_{cs}. The analytical derivation of the percolation threshold values is only possible for the Bethe lattice and for simple two-dimensional lattices. For arbitrary grids the thresholds must be computed by using Monte Carlo methods. For the Bethe lattice it was observed that the two thresholds are related by $p_{\mathrm{cb}}^{\mathrm{Bethe}} = p_{\mathrm{cs}}^{\mathrm{Bethe}} = 1/(z-1)$, where z is the coordination number of the lattice, i.e. the number of bonds connected to the same site. Although this relation might suggest the identity of the two threshold values for other systems also, it is observed that in most investigated arrays p_{cb} is smaller than p_{cs}. The product $B_{\mathrm{c}} = z\,p_{\mathrm{cb}}$ can be regarded as an invariant of a percolation network. For a system with dimension D, B_{c} amounts to $B_{\mathrm{c}} \simeq D/(D-1)$.

Bootstrap percolation models describe system evolution and connectivity under consideration of certain local termination rules (Adler 1991; Stauffer 1991).

At each time step, all sites within a certain state S_{a} that do not have at least m neighbors with a state S_{b} are transformed into a passive state, i.e. they no longer participate in the evolution of the system.

The termination rule becomes clear when applied to a two-dimensional Ising square lattice. At each time step, all sites with "spin up", that do not have at least m neighbors occupied, i.e. in a "spin up" state, after the previous time step, are rendered passive and do not change their state again. At the beginning of the simulation, a fraction p of all sites is randomly occupied ("occupied" means "spin up"). The case $m = 0$ corresponds to ordinary random percolation. The case $m = 1$ leads to the elimination of all isolated occupied sites. For $m = 2$ all loose strings are removed and only clusters or closed chains remain. The threshold value for these cases of bootstrap percolation is not changed compared with random percolation, since the infinite cluster that penetrates the system is preserved after this culling process. On the other hand, if m equals the number of neighbors, a single empty site will finally empty the whole lattice, like an infection.

References

Abell, G. C. (1985). *Phys. Rev. B 31*, 6184.

Aboudi, J. (1991). *Mechanics of Composite Materials.* Elsevier Science, Amsterdam.

Abramovitz, M. and I. A. Segun (1964). *Handbook of Mathematical Functions.* Dover Publications, New York.

Ackermann, H., S. Crusius, and G. Inden (1986). *Acta Metall. 34*, 2311.

Ackermann, H., G. Inden, and R. Kikuchi (1989). *Acta Metall. 37*, 1.

Ackland, G. J., M. W. Finnis, and V. Vitek (1988). *J. Phys. F 18*, L153.

Adams, B. L., D. Kinderlehrer, W. W. Mullins, A. D. Rollett, and T. S. Ta'asan (1997). *Scr. Metall. Submitted.*

Adler, J. (1991). *Physica A 171*, 453.

Aernoudt, E., P. van Houtte, and T. Leffers (1993). Chapter 3: *Deformation and Textures of Metals at Large Strains*, Volume 6; Vol. ed.: H. Mughrabi: Plastic Deformation and Fracture of Materials of *Materials Science and Technology — A Comprehensive Treatment,* Ser. eds.: R. W. Cahn, P. Haasen, and E. J. Krämer. VCH, Weinheim.

Aifantis, E. C. and J. P. Hirth (1983). *Mechanics of Dislocations, Proceedings of an International Symposium, Michigan, USA.* American Society for Metals, Metals Park, Ohio.

Aktekin, N. (1996). *Physica A 232*, 397.

Alba, W. L. and K. B. Whaley (1992). *J. Chem. Phys. 97*, 3674.

Alder, B. J. and T. E. Wainwright (1959). *J. Chem. Phys. 31*, 459.

Alder, B. J. and T. E. Wainwright (1960). *J. Chem. Phys. 33*, 1439.

Alexander, F. J., I. Edrei, and P. L. Garrido (1992). *J. Stat. Phys. 68*, 497.

Allen, M. P. and D. J. Tildesley (1989). *Computer Simulation of Liquids.* Oxford Science Publication. Clarendon Press, Oxford.

Allen, M. P. and D. J. Tildesley (1992). *Proceedings of NATO ASI on Computer Simulation in Chemical Physics*, Volume 397 of *NATO Advanced Science Institute Series, Series C : Mathematical and Physical Sciences.* Kluwer Academic in cooperation with NATO Science Division.

Allen, S. M. and J. W. Cahn (1979). *Acta Metall. 27*, 1085.

Altintas, S. (1978). *Plastic Deformation of Crystals: Analytical and Computer Simulation Studies of Dislocation Glide.* Ph.D. Thesis. University of California, Berkeley.

Amodeo, R. J. (1990). *Res. Mech. 30*, 5.

Ananthan, V. S., T. Leffers, and N. Hansen (1991). *Mater. Sci. Technol. 7*, 1069.

Andersen, H. C. (1980). *J. Chem. Phys. 72*, 2384.

Andersen, R. S. and F. R. de Hoog (1976). *The Application of Mathematics in Industry.* Butterworths, London.

Andersen, S. I., J. B. Bilde-Sørensen, N. Hansen, D. Juul Jensen, T. Leffers, H. Lilholt, T. Lorentzen, O. B. Pedersen, and B. Ralph (1992). Proceedings 13th RISØ International Symposium on Materials Science. RISØ National Laboratory, Roskilde.

Computational Materials Science: The Simulation of Materials, Microstructures and Properties By Dierk Raabe

Copyright © 1998 Wiley-VCH Verlag GmbH

ISBN: 3-527-29541-0

Andersen, S. I., J. B. Bilde-Sørensen, N. Hansen, T. Leffers, H. Lilholt, O. B. Pedersen, and B. Ralph (1987). Proceedings 8th RISØ International Symposium on Materials Science. RISØ National Laboratory, Roskilde.

Andersen, S. I., J. B. Bilde-Sørensen, T. Lorentzen, O. B. Pedersen, and N. J. Sørensen (1994). Proceedings 15th RISØ International Symposium on Materials Science. RISØ National Laboratory, Roskilde.

Anderson, M. P. and A. D. Rollett (1990). *Simulation and Theory of Evolving Microstructures.* The Minerals, Metals and Materials Society, TMS Publication.

Anderson, M. P., D. J. Srolovitz, G. S. Grest, and P. S. Sahni (1984). *Acta Metall. 32*, 783.

Andersson, J. O., J. Mattsson, and P. Svedlindh (1994). *Physica B 194*, 307.

Andrews, I. G. and R. R. McLone (1976). *Mathematical Modeling.* Butterworths, London.

Andronov, A. A., E. A. Leontovich, I. I. Gordon, and A. G. Maier (1973). *Nonlinear Differential Equations.* John Wiley, New York.

Anongba, P. N. B., J. Bonneville, and J. L. Martin (1993). *Acta Metall. 41*, 2897.

Argon, A. S. (1975). *Constitutive Equations in Plasticity.* MIT Press, Cambridge.

Argon, A. S. (1986). *Modeling Small Deformations of Polycrystals,* eds.: J. Gittus and J. Zarka. Elsevier Applied Science, London.

Argon, A. S. and P. Haasen (1993). *Acta Metall. 41*, 3289.

Arrowsmith, D. K. and C. P. Place (1982). *Ordinary Differential Equations.* Chapman and Hall, London.

Arsenault, R. J. (1986). In *Computer Simulation in Materials Science,* eds.: R.J. Arsenault, J.R. Beeler, D.M. Esterling, pp. 165. ASM International, Metals Park, Ohio.

Arsenault, R. J., J. R. Beeler, and D. M. Esterling (1986). *Computer Simulation in Materials Science.* ASM International, Metals Park, Ohio.

Arsenault, R. J., J. R. Beeler, and J. A. Simmons (1976). *Computer Simulation for Materials Applications,* Volume 20, Part 1, Part 2 of *Nuclear Metallurgy.* National Bureau of Standards, Gaithersburg, Maryland.

Asaro, R. J. and D. M. Barnett (1974). *J. Phys. F, Lett. 4*, L103.

Asaro, R. J., J. P. Hirth, D. M. Barnett, and J. Lothe (1973). *Phys. Stat. Sol. (B) 60*, 261.

Asaro, R. J. and A. Needleman (1985). *Acta Metall. 33*, 923.

Ashby, M. F. (1970). *Phil. Mag. 21*, 399.

Ashby, M. F. (1992). *Mater. Sci. Technol. 8*, 102.

Ashby, M. F., R. Bullough, C. S. Hartley, and J. P. Hirth (1980). *Dislocation Modeling of Physical Systems.* Pergamon Press.

Atkins, P. W. (1986). *Physical Chemistry.* Oxford University Press.

Atlee-Jackson, E. (1982). *Finite Element Procedures in Engineering Analysis.* Prentice-Hall, Englewood Cliffs.

Ausloos, M. and A. Pekalski (1995). *Phys. Rev. B 52*, 4577.

Avrami, M. (1939). *J. Chem. Phys. 7*, 1108.

Avula, X. J. R., R. E. Kalman, A. I. Liapis, and E. Y. Rodin (1983). *Mathematical Modeling in Science and Technology.* Pergamon Press.

Bacher, P., G. Rao, and P. Wynblatt (1992). *Comput. Mater. Sci. 1*, 42.

Bacon, D. J. (1996). In *Proceedings of NATO ASI on Computer Simulation in Materials Science,* Vol. eds.: H. O. Kirchner, L. P. Kubin, and V. Pontikis, Volume 308 of *NATO Advanced Science Institutes Series, Series E : Applied Sciences*, pp. 189. Kluwer Academic in cooperation with NATO Science Division.

Bacon, D. J., D. M. Barnett, and R. O. Scattergood (1979a). *Prog. Mater. Sci. 23*, 51.

Bacon, D. J., D. M. Barnett, and R. O. Scattergood (1979b). *Phil. Mag. A 39*, 231.

Bacon, D. J., U. F. Kocks, and R. O. Scattergood (1973). *Phil. Mag. 28*, 1241.

Bacroix, B. and P. Gilormini (1995). *Mod. Sim. Mater. Sci. Eng. 3*, 1.

Bacroix, B. and J. J. Jonas (1988). *Text. Microstruct. 8–9*, 267.

Ballone, P. (1989). In *Proceedings of NATO ASI on Computer Simulation in Materials Science, Interatomic Potentials, Simulation Techniques and Applications*, Vol. eds.: M. Meyer and V. Pontikis, Volume 205 of *NATO Advanced Science Institute Series, Series E : Applied Sciences*. Kluwer Academic in cooperation with NATO Science Division.

Ballone, P., W. Andreoni, R. Car, and M. Parinello (1988). *Phys. Rev. Lett. 60*, 271.

Balluffi, R. W. and A. V. Granato (1979). Volume 4 of *Dislocations in Solids*. Elsevier Science, Amsterdam; Ser. ed.: F.R.N. Nabarro.

Bardeen, J. and C. Herring (1952). *Imperfections in Nearly Perfect Crystals*, Vol. ed.: W. Shockley . John Wiley, New York.

Barnett, D. M. (1972). *Phys. Stat. Sol. (B) 49*, 741.

Barnett, D. M. (1996). *Private communication.*

Barnett, D. M., R. J. Asaro, S. D. Gavazza, D. J. Bacon, and R. O. Scattergood (1972). *J. Phys. F 2*, 854.

Baskes, M. I. (1992). *Phys. Rev. B 46*, 2727.

Bassler, K. E. and R. K. P. Zia (1994). *Phys. Rev. E 49*, 5871.

Baumgärtner, A. (1984a). In *Applications of the Monte Carlo Method in Statistical Physics*, Vol. ed.: K. Binder, pp. 145. Springer Verlag.

Baumgärtner, A. (1984b). *Ann. Rev. Phys. Chem. 35*, 419.

Beaudoin, A. J., P. R. Dawson, K. K. Mathur, and U. F. Kocks (1995). *Int. J. Plast. 11*, 501.

Beaudoin, A. J., H. Mecking, and U. F. Kocks (1996). *Phil. Mag. A 73*, 1503.

Becker, R. (1991). *Acta Metall. 39*, 1211.

Beckers, B., R. Sebald, and G. Gottstein (1998). *Unpublished results.*

Bedford, T., M. Keane, and C. Series (1991). *Ergodic Theory, Symbolic Dynamics, and Hyperbolic Spaces*. Oxford University Press.

Bellomo, N. and L. Preziosi (1995). *Modeling Mathematical Methods and Scientific Computation*. CRC Press, 2000 Corporate Blvd., N.W., Boca Raton, Florida 33431.

Ben-Jakob, E., N. Goldenfeld, J. S. Langer, and G. Schon (1985). *Phys. Rev. Lett. 51*, 1930.

Bender, E. A. (1978). *An Introduction to Mathematical Modeling*. John Wiley, New York.

Bennett, L. H. (1986). *Computer Modeling of Phase Diagrams*. The Metallurgical Society of AIME, Warrendale, PA.

Berryman, H. S. and D. R. Franceschetti (1989). *Phys. Lett. A 136*, 348.

Bertram, A., T. Böhlke, and M. Kraska (1997). In *Proceedings 6th International Workshop on Computational Mechanics of Materials, Hamburg, 1996;* Vol. eds.: A. Cornec and S. Schmauder, Volume 9 of *Comput. Mater. Sci.*, Ser. eds.: U. Landman and R. Nieminen, pp. 158. Elsevier Science, Amsterdam.

Bertram, A. and M. Kraska (1995). *Arch. Mech. 47*, 203.

Berveiller, M. and A. Zaoui (1979). *J. Mech. Phys. Solids 26*, 325.

Berveiller, M. and A. Zaoui (1981). *Res. Mech. Lett. 1*, 119.

Besseling, J. F. and E. van der Giessen (1993). *Mathematical Modeling of Inelastic Deformation*. Applied Mathematics and Mathematical Computation. Chapman and Hall, London.

Beynon, J. H. (1990). In *Proceedings of the International Conference on Recrystallization in Metallic Materials, Recrystallization '90*, pp. 429. The Minerals, Metals and Materials Society, TMS Publication; Vol. ed.: T. Chandra.

Beynon, J. H., P. Ingham, H. Teichert, and K. Waterson (1996). *Proceedings of the Second International Conference on Modeling of Metal Rolling Processes*. The Institute of Materials.

Bichara, G. and G. Inden (1991). *Scr. Metall. 25*, 2607.

Bigger, J. R. K., D. A. McInnes, and A. P. Sutton (1992). *Phys. Rev. Lett. 69*, 2224.

Binder, K. (1984). *Applications of the Monte Carlo Method in Statistical Physics.* Springer-Verlag.

Binder, K. (1991a). *The Monte Carlo Method in Condensed Matter Physics*, Volume 71 of *Topics in Applied Physics.* Springer-Verlag.

Binder, K. (1991b). *The Monte Carlo Method in Condensed Matter Physics, Introduction, Vol. 71.* Topics in Applied Physics. Springer-Verlag.

Binder, K. (1991c). *Statistical Theories of Phase Transitions*, Volume 5; Vol. ed.: P. Haasen, Chapter: Phase Transformations in Materials of *Materials Science and Technology — A Comprehensive Treatment,* Ser. eds.: R. W. Cahn, P. Haasen, and E. J. Krämer. VCH, Weinheim.

Binder, K. and D. W. Heermann (1988). *Monte Carlo Simuation in Statistical Physics*, Volume 80 of *Springer Series in Solid-State Sciences.* Springer-Verlag.

Binder, K. and D. Stauffer (1987). *A Simple Introduction to Monte Carlo Simulation*, Volume Applications of the Monte Carlo Method in Statistical Physics, *Vol. ed.: K. Binderof Topics in Current Physics.* Springer-Verlag.

Bishop, J. F. W. and R. Hill (1951). *Phil. Mag. 42*, 414.

Blelloch, G. E. (1990). *Vector Models for Data-Parallel Computing.* MIT Press, Cambridge.

Blum, W. (1993). Chapter 8*: High Temperature Deformation and Creep of Crystalline Solids*, Volume 6; Vol. ed.: H. Mughrabi: Plastic Deformation and Fracture of Materials of *Materials Science and Technology — A Comprehensive Treatment,* Ser. eds.: R. W. Cahn, P. Haasen, and E. J. Krämer. VCH, Weinheim.

Boas, M. L. (1983). *Mathematical Methods in the Physics Sciences.* John Wiley, New York.

Boeslau, J. and D. Raabe (1994). In *Proceedings 10th International Conference on Textures of Materials (ICOTOM 10), Mater. Sci. For.*, Volume 157–162, pp. 501. Trans Tech Publications.

Boltzmann, L. (1905). *Über statistische Mechanik;* Lecture from 1904. Populäre Schriften. Barth Verlag, Leipzig.

Boltzmann, L. (1907). *Über die Unentbehrlichkeit der Atomistik in der Naturwissenschaft;* Lecture from 1897. Populäre Schriften, Wissenschaftliche Abhandlungen. Barth Verlag, Leipzig; Vol. ed.: F. Hasenöhrl.

Born, M. and J. R. Oppenheimer (1927). *Ann. Phys. 84*, 457.

Botha, J. F. and G. F. Pinder (1983). *Fundamental Concepts in the Numerical Solution of Differential Equations.* John Wiley, New York.

Bothe, H. (1995). *Fuzzy Logic — Einführung in Theorie und Anwendung.* Springer-Verlag.

Boussinesq, J. (1985). *Application des Potentiels à l'Étude de l'Équilibre et du Movement des Solides Élastiques.* Gauthier-Villars, Paris.

Braga, G., G. Cattaneo, and Q. C. Vogliatti (1995). *Th. Comput. Sci. 145*, 1.

Brailsford, A. D. (1969). *Phys. Rev. 186*, 959.

Brailsford, A. D. (1972). *J. Appl. Phys. 43*, 1380.

Bréchet, Y. J. M. and L. P. Kubin (1996). In *Proceedings of NATO ASI on Computer Simulation in Materials Science,* Vol. eds.: H. O. Kirchner, L. P. Kubin, and V. Pontikis, Volume 308 of *NATO Advanced Science Institutes Series, Series E : Applied Sciences*, pp. 3. Kluwer Academic in cooperation with NATO Science Division.

Brenner, D. W. (1990). *Phys. Rev. B 42*, 9458.

Brenner, D. W. (1993). *Phys. Rev. Lett. 70*, 2174.

Brenner, D. W. (1996). In *Interatomic Potentials for Atomistic Simulations*, Volume 21 of *MRS Bulletin,* special ed.: A.F. Voter, pp. 36. Materials Research Society.

Bronstein, I. N. and K. A. Semendjajev (1987). *Taschenbuch der Mathematik,* Vol. eds.: G. Grosche, V. Ziegler, and D. Ziegler. Verlag Harri Deutsch, Thun und Frankfurt/Main.

Broughton, J. Q. (1994). *Issues for the Nineties, Proceedings MRS meeting December 1992,* Volume 2 of *Comput. Mater. Sci., Special Edition,* Ser. eds.: U. Landman and R. Nieminen. Elsevier Science, Amsterdam.

Broughton, J. Q., P. Bristowe, and J. Newsam (1993). *Materials Theory and Modeling,* Volume 291. Mater. Res. Soc. Symp. Proc. Pittsburgh.

Brout, R. (1965). *Phase Transitions.* Benjamin Press, New York.

Brown, L. M. (1967). *Phil. Mag. 15,* 363.

Brown, L. M. (1970). *J. Mech. Phys. Solids 18,* 367.

Brown, S. G. R., T. Williams, and J. A. Spittle (1994). *Acta Metall. 42,* 2893.

Bruns, W., I. Motoc, and K. O'Driscol (1981). *Monte Carlo Applications in Polymer Science.* Springer Verlag.

Bulatov, V. V., S. Yip, and A. S. Argon (1995). *Phil. Mag. A 72,* 453.

Bunge, H. J. (1970). *Krist. Techn. 5,* 145.

Bunge, H. J. (1982). *Texture Analysis in Materials Science.* Butterworths, London.

Bunge, H. J. (1987). *Theoretical Methods of Texture Analysis.* DGM Informationsgesellschaft, Deutsche Gesellschaft für Metallkunde.

Bunge, H. J. (1991). *Proceedings 9th International Conference on Textures of Materials (ICOTOM 9),* Volume 14–18, parts I, II, III. Gordon and Breach Science.

Bunge, H. J. (1994). *Proceedings 10th International Conference on Textures of Materials (ICOTOM 10),* Volume 157–162, part I,II of *Mater. Sci. For.* Trans Tech Publications.

Bunge, H. J. (1997). In *Proceedings of the Symposium on Computer Simulation and Modeling in Texture Research, Aachen, Oct. 1995,* Vol. eds.: D. Raabe and H. J. Bunge, Volume 28 of *Text. Microstruct.,* Ser. ed.: H. J. Bunge, pp. 151. Elsevier Science, Amsterdam.

Burke, M. A. and W. D. Nix (1978). *Phil. Mag. 37,* 479.

Bussemaker, H. J., A. Deutsch, and E. Geigant (1997). *Phys. Rev. Lett. 78,* 5018.

Caginalp, G. (1989). *Phys. Rev. A 39,* 5887.

Caginalp, G. and P. C. Fife (1986). *Phys. Rev. B 33,* 7792.

Caginalp, G. and E. A. Socolowski (1991). *J. Comput. Phys. 39,* 85.

Caginalp, G. and W. Xie (1993). *Phys. Rev. E 48,* 1897.

Cahn, J. W. (1961). *Acta Metall. 9,* 795.

Cahn, J. W. (1962). *Acta Metall. 10,* 179.

Cahn, J. W. and J. E. Hilliard (1958). *J. Chem. Phys. 28,* 258.

Cahn, J. W. and J. E. Hilliard (1965). *J. Chem. Phys. 42,* 93.

Cahn, J. W. and J. E. Hilliard (1971). *Acta Metall. 19,* 151.

Cahn, J. W. and J. E. Taylor (1994). *J. Stat. Phys. 77,* 183.

Cahn, R. (1966). In *Proceedings of ASM Seminar on Recrystallization, Grain Growth and Textures,* Vol. ed.: H. Margolin, pp. 99. American Society of Metals, Metals Park, Ohio.

Callaway, J. and N. H. March (1984). *Solid State Phys. 38,* 135.

Campbell, G. H., P. Gumbsch, and W. E. King (1992). *Z. Metallk. 83,* 472.

Campbell, G. H., H. Huang, W. E. King, D. H. Lassila, D. J. Nikkel, T. dias de la Rubia, J. Shu, S. M. Foiles, D. A. Hughes, and V. P. Smyshyaev (1997). *Multi-Scale Modeling of Polycyrstal Plasticity: A Workshop Report,* Volume 97–12. Institute for Mechanics and Materials, University of California, San Diego, USA.

Canova, G. R. (1988). *Rev. Phys. Appl. 23,* 533.

Canova, G. R., U. F. Kocks, and J. J. Jonas (1984). *Acta Metall. 32,* 211.

Cao, P. L. (1994). *Phys. Rev. Lett. 73,* 2595.

Car, R. and M. Parinello (1985). *Phys. Rev. Lett. 55*, 2471.

Carriero, N. and D. Gelernter (1990). *How to Write Parallel Programs — A First Course.* MIT Press, Cambridge.

Carroll, M. J. O., A. W. Bush, M. Cross, R. D. Gibson, and T. S. Wilkinson (1980). *Modeling and Simulation in Practice.* Proceedings of the Second Annual Conference of the North East Polytechnics Mathematical Modeling and Computer Simulation Group. Emjoc Press, Nothallerton, UK.

Castan, T. and P. A. Lindgard (1989). *Phys. Rev. B 40*, 5069.

Catlow, C. R. A. and W. C. Mackroth (1982). *Computer Simulation of Solids.* Springer Verlag.

Catlow, C. R. A., S. C. Parker, and M. P. Allen (1990). *Proceedings of NATO ASI on Computer Simulation in Chemical Physics*, Volume 293 of *NATO Advanced Science Institute Series, Series C : Mathematical and Physical Sciences.* Kluwer Academic in cooperation with NATO Science Division.

Ceder, G. (1993). *Comput. Mater. Sci. 1*, 144.

Ceder, G., M. De Graef, and L. Delaey (1989). *Phys. Rev. B 39*, 381.

Ceppi, E. A. and O. B. Nasello (1986). In *Computer Simulation of Microstructural Evolution,* Vol. ed.: D.J. Srolovitz, pp. 1. The Metallurgical Society of AIME, Warrendale, PA.

Chan, P. K. and A. D. Rey (1995). *Comput. Mater. Sci. 3*, 377.

Chan, S. K. (1977). *J. Chem. Phys. 67*, 5755.

Chandrasekhar, S. (1943). *Rev. Mod. Phys. 15*, 1.

Chen, B., M. A. Gomez, and D. L. Freeman (1996). *J. Chem. Phys. 105*, 9686.

Chen, J. A. and C. K. Hu (1994). *Phys. Rev. B 50*, 6260.

Chen, L. Q. (1995). *Scr. Metall. 32*, 115.

Chen, L. Q. and D. Fan (1996). *J. Amer. Ceram. Soc. 79*, 1163.

Chen, L. Q. and A. G. Khachaturyan (1991a). *Acta Metall. 39*, 2533.

Chen, L. Q. and A. G. Khachaturyan (1991b). *Scr. Metall. 25*, 67.

Chen, L. Q. and A. G. Khachaturyan (1991c). *Scr. Metall. 25*, 61.

Chen, L. Q. and Y. Wang (1996). *JOM 48*, 13.

Chen, L. Q., Y. Wang, and A. G. Khachaturyan (1992). *Phil. Mag. Lett. 64*, 241.

Chen, L. Q. and W. Yang (1994). *Phys. Rev. B 50*, 752.

Chen, S., A. M. Ferrenberg, and D. P. Landau (1995). *Phys. Rev. E 52*, 1377.

Chen, S. P., D. J. Srolovitz, and A. F. Voter (1989). *J. Mater. Res. 4*, 62.

Chen, S. P., A. F. Voter, and R. C. Albers (1990). *J. Mater. Res. 5*, 955.

Chen, Z. and J. Ding (1996). *J. Mater. Sci. techn. 12*, 476.

Cheney, W. and D. Kincaid (1994). *Numerical Mathematics and Computing.* Brooks/Cole, Division of Wadsworth.

Cheng, K. S., T. C. Chan, and H. F. Chau (1995). *Phys. Rev. E 51*, 3045.

Cheng, V. K. W. (1993). *J. Cryst. Growth 134*, 369.

Cheng, V. K. W. and B. A. W. Coller (1992). *J. the Chem. society 88*, 2167.

Cheng, V. K. W., E. C. M. Tang, and T. B. Tang (1989). *J. Cryst. Growth 96*, 293.

Cheng, V. K. W. and C. S. Yeung (1991). *Surf. Sci. 257*, L665.

Chenot, J. L. and E. Onate (1988). *Modeling of Metal Forming Processes.* Kluwer Academic.

Chin, G. Y. and W. L. Mammel (1967). *Trans. Met. Soc. AIME 239*, 1400.

Chopard, B., P. Luthi, and M. Croz (1994). *Phys. Rev. Lett. 72*, 1384.

Christensen, R. M. (1979). *Mechanics of Composite Materials.* Wiley Interscience Publication.

Christian, J. W. (1975). *The Theory of Transformations in Metals and Alloys.* Pergamon Press.

Christian, J. W. (1983). *Metall. Trans. A 14 A*, 1237.

Chung, K. and K. Shah (1992). *Int. J. Plast. 8*, 453.

Ciccotti, G., D. Frenkel, and I. R. McDonald (1987). *Simulation of Liquids and Solids - Molecular Dynamics and Monte Carlo Methods in Statistical Mechanics.* North-Holland, Amsterdam.

Cifra, P., F. E. Karasz, and W. J. MacKnight (1992). *Macromolecules 25*, 4895.

Cleveringa, H. H. M., E. van der Giessen, and A. Needleman (1997). *Acta Mater. 45*, 3163.

Cohen, A. M. (1962). *Numerical Analysis.* McGraw-Hill, London.

Cohen, E. G. D. and F. Wang (1995). *J. Stat. Phys. 81*, 445.

Copetti, M. I. M. and C. M. Elliott (1996). *Mater. Sci. Technol. 6*, 273.

Cordero, N. A. and J. A. Alonso (1997). *Int. J. Quant. Chem. 61*, 253.

Cornec, A. and S. Schmauder (1997). *Proceedings 6th International Workshop on Computational Mechanics of Materials, Hamburg, 1996;* Vol. eds.: A. Cornec and S. Schmauder, Volume 9 of *Comput. Mater. Sci.;* Ser. eds.: U. Landman and R. Nieminen. Elsevier Science, Amsterdam.

Cortie, M. B. (1993a). *Metall. Trans. B 24*, 1045.

Cortie, M. B. (1993b). *Metall. Trans. B 24*, 1045.

Cottrell, A. H. (1953). *Dislocations and Plastic Flow in Crystal.* Oxford University Press/Clarendon Press, London.

Cottrell, A. H. (1964). *Theory of Crystal Dislocation.* Gordon and Breach, New York.

Cottrell, A. H. (1988). *Introduction to the Modern Theory of Metals.* The Institute of Metals, London.

Courant, R. (1943). *Bull. Amer. Mathemat. Soc. 49*, 1.

Cox, B. N. (1989). *Eng. Fract. Mech. 33*, 655.

Crank, J. (1967). *The Mathematics of Diffusion.* Oxford University Press/Clarendon Press, Oxford.

Crisfield, M. (1991). *Nonlinear Finite Element Analysis of Solids and Structures.* Wiley, Chichester, West Sussex.

Cyrot-Lackmann, F. (1967). *Adv. Phys. 16*, 393.

Dab, D., A. Lawniczak, and J. P. Boon (1990). *Phys. Rev. Lett. 64*, 2462.

Davies, C. H. J. (1997a). *Scr. Mater. 36*, 35.

Davies, C. H. J. (1997b). *Scr. Mater. 36*, 35.

Davison, L. (1995). *Mech. Mater. 21*, 73.

Daw, M. S. and M. I. Baskes (1983). *Phys. Rev. Lett. 50*, 1285.

Daw, M. S. and M. I. Baskes (1984). *Phys. Rev. B 29*, 6443.

Daw, M. S., S. M. Foiles, and M. I. Baskes (1993). *Mater. Sci. Rep. 9*, 251.

Dawson, I., P. D. Bristowe, and J. A. White (1996). *Phys. Rev. B 54*, 13727.

Dawson, P. R., A. J. Beaudoin, and K. K. Mathur (1994). In *Proceedings 15th RISØ International Symposium on Materials Science,* eds.: S. I. Andersen, J. B. Bilde-Sørensen, T. Lorentzen, O. B. Pedersen, and N. J. Sorensen, pp. 33. RISØ National Laboratory, Roskilde.

de Hosson, J. T. M. and V. Vitek (1990). *Phil. Mag. A 61*, 305.

de Miguel, J. J., J. Ferron, and A. Cebollada (1988). *J. Cryst. Growth 91*, 481.

de Wit, R. (1960). *Sol. St. Phys.*, 249.

de Wit, R. (1967). *Phys. Stat. Sol. 20*, 567.

de Wit, R. and J. S. Koehler (1959). *Phys. Rev. 116*, 1113.

Demir, I., J. P. Hirth, and H. M. Zbib (1992). *Mech. Res. Comm. 19*, 369.

Desplat, J., F. Bley, F. Livet, and O. Schaerpf (1996). *Acta Metall. 44*, 1849.

Dettman, J. W. (1969). *Mathematical Methods in Physics and Engineering.* John Wiley, New York.

Devincre, B. (1995). *Solid State Commun. 93*, 875.

Devincre, B. (1996). In *Proceedings of NATO ASI on Computer Simulation in Materials Science,* Vol. eds.: H. O. Kirchner, L. P. Kubin, and V. Pontikis, Volume 308 of *NATO Advanced Science Institutes Series, Series E : Applied Sciences*, pp. 309. Kluwer Academic in cooperation with NATO Science Division.

Devincre, B. and M. Condat (1992). *Acta Metall. 40*, 2629.

Devincre, B. and L. P. Kubin (1994). *Mod. Sim. Mater. Sci. Eng. 2*, 559.

DeVries, P. L. (1994). *A First Course in Computational Physics.* John Wiley, New York.

Dillamore, I. L., E. Butler, and D. Green (1968). *Met. Sci. J. 2*, 161.

Dillamore, I. L. and H. Katoh (1974). *Met. Sci. J. 8*, 21.

Dillamore, I. L., P. L. Morris, C. J. E. Smith, and W. B. Hutchinson (1972). *Proc. R. Soc. London A 329*, 405.

Dillamore, I. L. and W. T. Roberts (1965). *Met. Rev. 10*, 271.

Dillamore, I. L., C. J. E. Smith, and T. W. Watson (1967). *Met. Sci. J. 8*, 21.

Doane, D. A. and P. D. Franzon (1992). *Multichip Module Technologies and Alternatives.* Van Nostrand Reinhold, New York.

Doherty, R. D. (1978). In *Recrystallization of Metallic Materials,* Vol. ed.: F. Haeßner, pp. 23. Dr. Riederer Verlag GmbH.

Doherty, R. D., K. Li, M. P. Anderson, A. D. Rollett, and D. J. Srolovitz (1990). In *Proceedings of the International Conference on Recrystallization in Metallic Materials, Recrystallization '90, Vol. ed.: T. Chandra*, pp. 129. The Minerals, Metals and Materials Society, TMS Publication.

Draheim, K. (1995). In *Proceedings 16th RISØ International Symposium on Materials Science,* Vol. eds.: N. Hansen, D. Juul Jensen, Y.L. Liu, and B. Ralph, pp. 321. RISØ National Laboratory, Roskilde.

Draheim, K. and G. Gottstein (1996a). In *Proceedings 4th International Workshop on the Computational Modeling of the Mechanical Behaviour of Materials, Lille, 1995;* Vol. eds.: S. Schmauder and D. Weichert, Volume 5 of *Comput. Mater. Sci.,* Ser. eds.: U. Landman and R. Nieminen. Elsevier Science, Amsterdam.

Draheim, K. and G. Gottstein (1996b). In *Comput. Mater. Sci., Proceedings 5th International Workshop on the Computational Modeling of the Mechanical Behaviour of Materials, Aachen, 1996* Vol. eds.: S. Schmauder and D. Raabe, Volume 7 of *Comput. Mater. Sci.,* Ser. eds.: U. Landman and R. Nieminen, pp. 208. Elsevier Science, Amsterdam.

Dreyer, W. (1995). *Private communication and lecture at the 5. International Workshop on the Computational Modeling of the Mechanical Behaviour of Materials, Aachen, 1995.*

Duesbery, M. S. and G. Y. Richardson (1991). *Crit. Rev. Solid State Mater. Sci. 17*, 1.

Duffy, D. M., J. H. Harding, and A. M. Stoneham (1992). *Acta Metall. 40*, 11.

Duffy, D. M., J. H. Harding, and A. M. Stoneham (1993). *Phil. Mag. A 67*, 865.

Duffy, D. M., J. H. Harding, and A. M. Stoneham (1994). *J. Appl. Phys. 76*, 2791.

Duffy, D. M., J. H. Harding, and A. M. Stoneham (1995). *Acta Metall. 43*, 1559.

Duffy, D. M., J. H. Harding, and A. M. Stoneham (1996). *Acta Mater. 44*, 3293.

Duffy, P., D. P. Chong, and M. Dupuis (1995). *Phys. Rev. B 102*, 3312.

Duggan, B. J., M. Sindel, G. D. Köhlhoff, and K. Lücke (1990). *Acta Metall. 38*, 103.

Dunweg, B. and D. P. Landau (1993). *Phys. Rev. B 48*, 14182.

Dym, C. L. and E. S. Ivay (1980). *Principles of Mathematical Modeling.* Academic Press, New York.

Eichorn, K. and K. Binder (1996). *J. Phys. 8*, 5209.

Eliott, C. M. and H. Garcke (1996). *Siam. J. Mathemat. Anal. 27*, 4049.

Emren, F., U. von Schlippenbach, and K. Lücke (1986). *Acta Metall. 34*, 2105.

Engeln-Müllges, G. (1988). *Formelsammlung zur Numerischen Mathematik mit Standard-FORTRAN 77-Programmen.* BI Wissenschaftsverlag, Mannheim, Wien, Zürich.

Engler, O., P. Wagner, J. Savoie, D. Ponge, and G. Gottstein (1993). *Scr. Metall. 28*, 1317.

Ercolessi, F., E. Tosatti, and M. Parinello (1986). *Phys. Rev. Lett. 57*, 719.

Erginsoy, C., G. H. Vineyard, and A. Englert (1964). *Phys. Rev. 133 A*, 595.

Ericson, T. (1981). *Computers in Materials Technology*. Pergamon Press.

Eschenauer, H. and W. Schnell (1993). *Elastizitätstheorie*. BI-Wissenschaftsverlag, Bibliographisches Institut Mannheim Leipzig Wien Zürich.

Eshelby, J. D. (1949a). *Proc. Phys. Soc. A 62*, 307.

Eshelby, J. D. (1949b). *Proc. R. Soc. London A 197*, 396.

Eshelby, J. D. (1957). *Proc. R. Soc. London A 241*, 376.

Eshelby, J. D. (1961). *Progress in Solid Mechanics II*, Volume t.2. North Holland, Amsterdam.

Eshelby, J. D. (1970). *Proc. R. Soc. London A 319*, 247.

Eshelby, J. D., W. T. Read, and W. Shockley (1953). *Acta Metall. 1*, 251.

Essmann, U. and H. Mughrabi (1979). *Phil. Mag. A 40*, 731.

Esterling, D. M. (1986). In *Computer Simulation in Materials Science*, eds.: R.J. Arsenault, J.R. Beeler, D.M. Esterling, pp. 149. ASM International, Metals Park, Ohio.

Estrin, Y. and L. P. Kubin (1986). *Acta Metall. 34*, 2455.

Estrin, Y. and P. G. McCormick (1991). *Acta Metall. 39*, 2977.

Estrin, Y. and H. Mecking (1984). *Acta Metall. 32*, 57.

Evans, J. W. and J. Brimacombe (1989). *Mathematical and Physical Modeling of Metals Processing*. John Wiley, New York.

Fackeldey, M., A. Ludwig, and P. R. Sahm (1996). In *Proceedings 5th International Workshop on the Computational Modeling of the Mechanical Behaviour of Materials, Aachen, 1996* Vol. eds.: S. Schmauder and D. Raabe, Volume 7 of *Comput. Mater. Sci.*, Ser. eds.: U. Landman and R. Nieminen. Elsevier Science, Amsterdam.

Fan, D. and L. Q. Chen (1995). *J. Amer. Ceram. Soc. 78*, 769.

Fan, D. and L. Q. Chen (1997). *Acta Mater. 45*, 611.

Fan, D., C. Geng, and L. Q. Chen (1997). *Acta Metall. 45*, 1115.

Farlow, S. J. (1982). *Partial Differential Equations for Scientists and Engineers*. John Wiley, New York.

Farooq, M. and F. A. Khwaja (1993). *Int. J. Mod. Phys. B 7*, 1731.

Farquhar, I. E. (1964). *Ergodic Theory in Statistical Mechanics*. Wiley Interscience Publication.

Feller, S. E., Y. Zhang, and B. R. Brooks (1995). *J. Phys. Chem. 103*, 4613.

Fernandez, J. S., J. Chao, and J. M. Amo (1992). *Eng. Fract. Mech. 43*, 287.

Fernandez, L. A. (1989). *Physica A 161*, 284.

Ferrenberg, A. M. and D. P. Landau (1991). *Phys. Rev. B 44*, 5081.

Feyel, F., S. Calloch, D. Marquis, and G. Cailletaud (1997). In *Proceedings 6th International Workshop on Computational Mechanics of Materials, Hamburg, 1996;* Vol. eds.: A. Cornec and S. Schmauder, Volume 9 of *Comput. Mater. Sci.*, Ser. eds.: U. Landman and R. Nieminen, pp. 141. Elsevier Science, Amsterdam.

Fiig, T., N. H. Anderson, and P. A. Lingard (1993). *Physica C 217*, 34.

Finnis, M. W. (1996). *J. Phys. 8*, 5811.

Finnis, M. W., R. Kaschner, and M. Scheffler (1995). *J. Phys. 7*, 2001.

Finnis, M. W., C. Kruse, and U. Schönberger (1995). *Nanostruc. Mater. 6*, 145.

Finnis, M. W., A. T. Paxton, D. G. Pettifor, A. P. Sutton, and Y. Ohta (1988). *Phil. Mag. A 58*, 143.

Finnis, M. W. and M. Rühle (1993). Chapter 9*: Structures of Interfaces in Crystalline Solids*, Volume 1; Vol. ed.: V. Gerold: Structure of Solids of *Materials Science and Technology — A Comprehensive Treatment*, Ser. eds.: R. W. Cahn, P. Haasen, and E. J. Krämer. VCH, Weinheim.

Finnis, M. W. and J. E. Sinclair (1984). *Phil. Mag. A 50*, 45.

Fivel, M. C., T. J. Gosling, and G. R. Canova (1996). *Mod. Sim. Mater. Sci. Eng. 4*, 581.

Fleck, N. A., G. M. Muller, M. F. Ashby, and J. W. Hutchinson (1994). *Acta Metall. 42*, 475.

Floro, J. A., C. V. Thompson, and P. D. Bristowe (1994). *J. Mater. Res. 9*, 2411.

Flynn, M. J. (1966). *IEEE Trans. Comput. 54*, 1901.

Flynn, M. J. (1972). *IEEE Trans. Comput. C 21*, 948.

Foiles, S. M. (1989). *Acta Metall. 37*, 2815.

Foiles, S. M. (1996). In *Interatomic Potentials for Atomistic Simulations*, Volume 21 of *MRS Bulletin*, special ed.: A.F. Voter, pp. 24. Materials Research Society.

Foreman, A. J. E. and M. J. Makin (1966). *Phil. Mag. 14*, 911.

Forsythe, G. E. and W. R. Wasow (1960). *Finite Difference Methods for Partial Differential Equations*. John Wiley, New York.

Franciosi, P., M. Berveiller, and A. Zaoui (1980). *Acta Metall. 28*, 273.

Frank, F. C. (1949). *Proc. Phys. Soc. A 62*, 131.

Freedman, D. (1982). *Brownian Motion and Diffusion*. Springer-Verlag.

Friedel, J. (1952). *Phil. Mag. 43*, 153.

Friedel, J. (1956). *Les Dislocations*. Gauthier-Villars, Paris.

Friedel, J. (1964). *Dislocations*. Pergamon Press.

Frisch, U., B. Hasslacher, and Y. Pomeau (1986). *Phys. Rev. Lett. 56*, 1505.

Frontera, C., E. Vives, and A. Planes (1993). *Phys. Rev. B 48*, 9321.

Frontera, C., E. Vives, and A. Planes (1995). *Phys. Rev. B 51*, 11369.

Frost, H. J. and C. V. Thompson (1987a). *Acta Metall. 35*, 529.

Frost, H. J. and C. V. Thompson (1987b). In *Proceedings 31st Annual International Technical Symposium on Optical and Optoelectronic Applied Science and Engineering, San Diego, California, USA*. SPIE.

Frost, H. J. and C. V. Thompson (1988). *J. Elect. Mater. 17*, 447.

Frost, H. J., C. V. Thompson, and D. T. Walton (1990). *Acta Metall. 38*, 1455.

Frost, H. J., J. Whang, and C. V. Thompson (1986). In *Proceedings 7th RISØ International Symposium on Materials Science*, Vol. eds.: N. Hansen, D. Juul Jensen, T Leffers, and B. Ralph, pp. 315. RISØ National Laboratory, Roskilde.

Furu, T. and K. M. E. Nes (1990). *Mater. Sci. Technol. 6*, 1093.

Gandin, C. and M. Rappaz (1994). *Acta Metall. 42*, 2233.

Gandin, C. and M. Rappaz (1997). *Acta Mater. 45*, 2187.

Gardiner, C. W. (1985). *Handbook of Stochastic Methods*. Springer Series in Synergetics, Ser. ed.: H. Haken. Springer-Verlag.

Garrido, L. (1980). *Systems far from Equilibrium*. Springer-Verlag.

Gerhardt, M. and H. Schuster (1989). *Physica D 36*, 209.

Getis, A. and B. N. Boots (1979). *Models of Spatial Processes*. Cambridge University Press.

Ghoniem, N. M. and R. J. Amodeo (1989). *Phys. Rev. B 41*, 6958.

Gil Sevilliano, J. (1993). Chapter 2: *Flow stress and Work Hardening*, Volume 6; Vol. ed.: H. Mughrabi: Plastic Deformation and Fracture of Materials of *Materials Science and Technology — A Comprehensive Treatment*, Ser. eds.: R. W. Cahn, P. Haasen, and E. J. Krämer. VCH, Weinheim.

Gil Sevilliano, J., P. van Houtte, and E. Aernoudt (1980). *Prog. Mater. Sci. 25*, 69.

Gillis, P. P. and J. Kratochvil (1970). *Phil. Mag. 21*, 425.

Gilmer, G. H., M. H. Grabow, and A. F. Bakker (1990). *Mater. Sci. Eng. B 6*, 101.

Gitt, A. (1997). *Diplomarbeit*.

Gittus, J. and J. Zarka (1986). *Modeling Small Deformations of Polycrystals*. Elsevier Applied Science, London.

Gladyszewski, G. and L. Gladyszewski (1991). *Phys. Stat. Sol. (B) 166*, K11.

Glazier, J. A., M. P. Anderson, and G. S. Grest (1990). *Phil. Mag. B 62*, 615.

Godwin, P. D., A. P. Horsfield, and A. P. Sutton (1996). *Phys. Rev. B 54*, 15785.

Gongalez-Miranda, J., A. Labarta, and M. Puma (1994). *Phys. Rev. E 49*, 2041.

Goringe, C. M., L. J. Clark, and A. P. Sutton (1997). *J. Phys. Chem. B 101*, 1498.

Goringe, C. M. and A. P. Sutton (1996). *Mater. Sci. Eng. 37*, 150.

Goryachev, S. B. (1996). In *Proceedings of NATO ASI on Computer Simulation in Materials Science,* Vol. eds.: H. O. Kirchner, L. P. Kubin, and V. Pontikis, Volume 308 of *NATO Advanced Science Institutes Series, Series E : Applied Sciences*, pp. 17. Kluwer Academic in cooperation with NATO Science Division.

Gosling, T. J. and J. R. Willis (1994). *J. Mech. Phys. Sol. 42*, 1199.

Gotoh, M. (1978). *Int. J. Numer. Mech. Eng. 12*, 101.

Gotoh, M. (1980). *Int. J. Mech. Sci. 22*, 367.

Gotoh, M. and F. Ishise (1978). *Int. J. Mech. Sci. 20*, 423.

Gottstein, G. (1984). *Rekristallisation metallischer Werkstoffe* (in German). DGM Informationsgesellschaft, Deutsche Gesellschaft für Metallkunde.

Gottstein, G. (1996). *Arbeits- und Ergebnisbericht 94–96, Integrative Werkstoffmodellierung, SFB 370,* Deutsche Forschungsgemeinschaft (Collaborative Research Center on Integrated Modeling of Materials). Rheinisch-Westfälische Technische Hochschule Aachen, Institut für Metallkunde und Metallphysik.

Gottstein, G. and A. S. Argon (1987). *Acta Metall. 35*, 1261.

Granato, A. V. and K. Lücke (1956). *J. Appl. Phys. 27*, 583.

Granato, A. V., K. Lücke, J. Schlipf, and L. J. Teutonico (1964). *J. Appl. Phys.*, 9.

Grandjean, N., J. Massies, and M. Leroux (1996). *Phys. Rev. B 53*, 998.

Grassberger, P., F. Krause, and T. von der Twer (1984). *J. Phys. A Lett. 17*, L105.

Greenwood, G. W. (1956). *Acta Metall. 4*, 243.

Grest, G. S., M. P. Anderson, and D. J. Srolovitz (1988). *Phys. Rev. B 38*, 4752.

Grosbas, M. (1988). In *Non-Linear Phenomena in Materials Science I,* Vol. ed.: L. P. Kubin, Volume 3-4 of *Solid State Phenomena*, pp. 17. Trans Tech Publication, CH-Aedermannsdorf.

Gu, L., B. Chakraborty, and J. L. Lebowitz (1996). *Phys. Rev. B 53*, 11985.

Guan, J., M. E. Casida, and D. R. Salahub (1995). *Phys. Rev. B 52*, 2184.

Guenin, R., P. C. Clapp, and J. A. Rifkin (1996). *Mater. Sci. Eng. B 37*, 193.

Gulluoglu, A. N. and C. S. Hartley (1992). *Mod. Sim. Mater. Sci. Eng. 1*, 1.

Gulluoglu, A. N. and C. S. Hartley (1993). *Mod. Sim. Mater. Sci. Eng. 1*, 383.

Gulluoglu, A. N., R. LeSar, D. J. Srolovitz, and P. S. Lomdahl (1990). In *Simulation and Theory of Evolving Microstructures,* Vol. eds.: M.P. Anderson and A.D. Rollett, pp. 239. The Minerals, Metals and Materials Society, TMS Publication.

Gulluoglu, A. N., D. J. Srolovitz, R. LeSar, and P. S. Lomdahl (1989). *Scr. Metall. 23*, 1347.

Gumbsch, P. (1996a). In *Proceedings of NATO ASI on Computer Simulation in Materials Science,* Vol. eds.: H. O. Kirchner, L. P. Kubin, and V. Pontikis, Volume 308 of *NATO Advanced Science Institutes Series, Series E : Applied Sciences*, pp. 227. Kluwer Academic in cooperation with NATO Science Division.

Gumbsch, P. (1996b). *Z. Metallk. 96*, 341.

Gumbsch, P., M. S. Daw, and S. M. Foiles (1991). *Phys. Rev. B 43*, 13833.

Gumbsch, P., S. J. Zhou, and B. L. Holian (1997). *Phys. Rev. B 55*, 3445.

Gunton, J. D., M. San Miguel, and P. S. Sahni (1983). In *The Dynamics of First Order Phase Transitions,* Vol. eds.: C. Domb and J.L. Lebowitz, Volume 8 of *Introduction to Phase Transitions and Critical Phenomena*, pp. 267. Academic Press, New York.

Guo, X., B. Zhong, and S. Peng (1994). *Surf. Sci. 321*, L261.

Gurtin, M. E. (1989). *Quart. Appl. Mathemat. 47*, 129.

Gurtin, M. E. (1996). *Physica D 92*, 178.

Haas, F. M., R. Hilfer, and K. Binder (1995). *J. Chem. Phys. 102*, 2960.

Haasen, P. (1984). *Physikalische Metallkunde, Kap. 8.* Springer-Verlag.

Haasen, P. (1991). *Phase Transformations in Materials*, Volume 5 of *Materials Science and Technology — A Comprehensive Treatment*, Ser. eds.: R. W. Cahn, P. Haasen, and E. J. Krämer. VCH, Weinheim.

Haberlandt, R., S. Fritsche, G. Peinel, and K. Heinzinger (1995). *Molekulardynamik.* Verlag Friedrich Vieweg, Braunschweig/Wiesbaden.

Haberman, R. (1983). *Elementary Applied Partial Differential Equations.* Prentice-Hall, Englewood Cliffs.

Haeßner, F. (1978). *Recrystallization of Metallic Materials.* Dr. Riederer Verlag GmbH.

Haken, H. (1978). *Synergetics.* Springer Series in Synergetics, Ser. ed.: H. Haken. Springer-Verlag.

Haken, H. (1983). *Advanced Synergetics.* Springer Series in Synergetics, Ser. ed.: H. Haken. Springer-Verlag.

Halmos, P. R. (1955). *Lectures on Ergodic Theory.* Chelsea Publishing Co., New York.

Hamilton, J. C., M. S. Daw, and S. M. Foiles (1995). *Phys. Rev. Lett. 74*, 2760.

Hamilton, J. C. and S. M. Foiles (1995). *Phys. Rev. Lett. 75*, 882.

Hammersley, J. M. and D. C. Handscomb (1964). *Monte Carlo Methods.* Methuen's Statistical Monographs. Methuen's/John Wiley, New York.

Hammonds, K. D., I. R. McDonald, and D. J. Tildesley (1993). *Mol. Phys. 78*, 173.

Hansen, N., D. J. Jensen, Y. L. Liu, and B. Ralph (1995). In *Proceedings 16th RISØ International Symposium on Materials Science,* Vol. eds.: N. Hansen, D. Juul Jensen, Y.L. Liu, and B. Ralph. RISØ National Laboratory, Roskilde.

Hardy, J., O. de Pazzis, and Y. Pomeau (1976). *Phys. Rev. A 13*, 1949.

Harrison, J. A., R. J. Colton, and D. W. Brenner (1993). *Wear 168*, 127.

Hartley, P., I. Pillinger, and C. E. N. Sturgess (1992). *Modeling of Material Deformation Processes.* Springer Verlag.

Hartman, P. (1964). *Ordinary Differential Equations.* John Wiley, New York.

Hasenbusch, M. and K. Pinn (1994). *Physica A 203*, 189.

Hashin, Z. and S. Shtrikman (1962a). *J. Mech. Phys. Solids 10*, 335.

Hashin, Z. and S. Shtrikman (1962b). *J. Mech. Phys. Solids 10*, 343.

Havlicek, F., J. Kratochvil, M. Tokuda, and V. Lev (1990). *Int. J. Plast. 6*, 281.

Havner, K. S. (1992). *Finite Plastic Deformation of Crystalline Solids.* Cambridge University Press.

Heermann, D. W. (1986). *Computer Simulation Methods in Theoretical Physics.* Springer-Verlag.

Heermann, D. W. and A. N. Burkitt (1991). *Parallel algorithms for statistical physics problems*, Volume The Monte Carlo Method in Condensed Matter Physics, Vol. 71 of *Topics in Applied Physics.* Springer-Verlag.

Henderson, J. R., I. G. Main, and M. G. Norman (1994). *Pure and Appl. Geo. Phys. 142*, 545.

Herring, C. (1950). *J. Appl. Phys. 21*, 437.

Hesselbarth, H. W. and I. R. Göbel (1991). *Acta Metall. 39*, 2135.

Hesselbarth, H. W. and E. Steck (1992). In *Non-Linear Phenomena in Materials Science II;* Vol. eds.: G. Martin and L. P. Kubin, Volume 23–24 of *Solid State Phenomena*, pp. 445. Trans Tech Publication, CH-Aedermannsdorf.

Heuer, H. O. (1993). *J. Stat. Phys. 72*, 789.

Hill, R. (1950). *The Mathematical Theory of Plasticity.* Oxford Science Publication. Clarendon Press, Oxford.

Hill, R. (1952). *Proc. R. Soc. London A 65*, 349.

Hill, R. (1963). *J. Mech. Phys. Solids 11*, 357.

Hill, R. (1987). *J. Mech. Phys. Solids 35*, 23.

Hill, T. L. (1956). *Statistical Mechanics.* McGraw-Hill, New York.

Himmel, L. (1963). *Recovery and Recrystallization of Metals.* John Wiley, New York.

Hirsch, J. (1997). *Simulation, Modellierung, Informationssysteme* (in German). DGM Informationsgesellschaft, Deutsche Gesellschaft für Metallkunde.

Hirsch, J. and K. Lücke (1988a). *Acta Metall. 36*, 2863.

Hirsch, J. and K. Lücke (1988b). *Acta Metall. 36*, 2883.

Hirsch, J., E. Nes, and K. Lücke (1987). *Acta Metall. 35*, 427.

Hirth, J. P. (1996). *Private communication.*

Hirth, J. P. and J. Lothe (1968). *Theory of Dislocations,* 1st Edition. McGraw-Hill Series in Materials Science and Engineering.

Hirth, J. P. and J. Lothe (1982). *Theory of Dislocations,* 2nd Edition. John Wiley, New York.

Hoagland, R. G., M. S. Daw, and S. M. Foiles (1990). *J. Mater. Res. 5*, 313.

Hockney, R. W. and J. W. Eastwood (1981). *Computer Simulation using Particles.* McGraw-Hill.

Hofmann, D. and M. W. Finnis (1994). *Acta Metall. 42*, 3555.

Hohenberg, P. C. and B. I. Halperin (1977). *Rev. Mod. Phys. 49*, 435.

Hohenberg, P. C. and W. Kohn (1964). *Phys. Rev. B 136*, 864.

Hokanson, J. L. (1963). *J. Appl. Phys. 34*, 2337.

Holm, E. A., A. D. Rollett, and D. J. Srolovitz (1996). In *Proceedings of NATO ASI on Computer Simulation in Materials Science,* Vol. eds.: H. O. Kirchner, L. P. Kubin, and V. Pontikis, Volume 308 of *NATO Advanced Science Institutes Series, Series E : Applied Sciences*, pp. 373. Kluwer Academic in cooperation with NATO Science Division.

Hölscher, M., D. Raabe, and K. Lücke (1994). *Acta Metall. 42*, 879.

Holzman, L. M., J. B. Adams, and S. M. Foiles (1991). *J. Mater. Res. 6*, 298.

Honerkamp, J. and H. Römer (1993). *Klassische Theoretische Physik.* Springer-Verlag.

Hong, T., J. R. Smith, and D. J. Srolovitz (1992). *Phys. Rev. B 45*, 8775.

Hong, T., J. R. Smith, and D. J. Srolovitz (1994). *J. Adhes. Sci. Technol. 8*, 837.

Honneff, H. (1980). Dissertation. Rheinisch-Westfälische Technische Hochschule Aachen, Institut für Metallkunde und Metallphysik.

Honneff, H. and H. Mecking (1978). In *Proceedings 5th International Conference on Textures of Materials (ICOTOM 5);* Vol. eds.: G. Gottstein and K. Lücke, pp. 265. Springer-Verlag.

Honneff, H. and H. Mecking (1981). In *Proceedings 6th International Conference on Textures of Materials (ICOTOM 6);* Vol. ed.: S. Nagashima, pp. 347. Iron and Steel Institute of Japan.

Hoover, W. G. (1986). *Molecular Dynamics*, Volume 258 of *Lecture Notes in Physics.* Springer-Verlag.

Hu, C. K. and S. S. Hsiao (1992). *Physica A 184*, 192.

Hu, H. (1962). *Trans. Met. Soc. AIME 224*, 75.

Hu, H. (1963). In *Recovery and Recrystallization of Metals,* Vol. ed.: L. Himmel, pp. 311. John Wiley, New York.

Hu, H., R. S. Cline, and S. R. Goodman (1966). In *Proceedings of ASM Seminar on Recrystallization, Grain Growth and Textures,* Vol. ed.: H. Margolin, pp. 295. American Society of Metals, Metals Park, Ohio.

Huang, J., M. Meyer, and V. Pontikis (1990). *Phys. Rev. B 42*, 5495.

Huang, J., M. Meyer, and V. Pontikis (1991). *J. Physique III 1*, 867.

Huang, K. (1963). *Statistical Mechanics.* John Wiley, New York.

Humphreys, F. J. (1992a). *Mater. Sci. Technol. 8*, 135.

Humphreys, F. J. (1992b). *Scr. Metall. 27*, 1557.

Humphreys, F. J. (1993). *Mater. Sci. For. 113–115*, 329.

Humphreys, F. J. and M. Hatherly (1995). *Recrystallization and Related Annealing Phenomena.* Pergamon Press.

Hutchinson, J. W. (1970). *Proc. R. Soc. London A 319*, 247.

Hutchinson, J. W. (1976). *Proc. R. Soc. London A 384*, 101.

Inden, G. (1974). *Acta Metall. 22*, 945.

Indenbom, V. L. and J. Lothe (1992). *Elastic Strain Fields and Dislocation Mobility,* Volume 31 of *Modern Problems in Condensed Matter Sciences,* Ser. eds.: V.M. Agranovich and A.A. Maradudin. Elsevier Science, Amsterdam.

Indenbom, V. L. and S. S. Orlov (1967). *Sov. Phys. — JETP 6*, 274.

Janke, W. and R. Villanova (1995). *Phys. Lett. 209*, 179.

Jhan, R. J. and P. D. Bristowe (1990). *Scr. Metall. 24*, 1313.

Jiang, Z. and C. Ebner (1989a). *Phys. Rev. B 40*, 316.

Jiang, Z. and C. Ebner (1989b). *Phys. Rev. B 40*, 4833.

Johnson, R. W., R. K. Teng, and J. W. Balde (1992). Institute of Electrical and Electronic Engineers (IEEE) Press, New York.

Johnson, W. A. and R. F. Mehl (1939). *Trans. Met. Soc. AIME 135*, 416.

Johnson, W. C., J. M. Howe, D. E. Laughlin, and W. A. Soffa (1994). *Solid – Solid Phase Transformations.* The Minerals, Metals and Materials Society, TMS Publication.

Jokl, M. L., V. Vitek, and C. J. McMahon (1989). *Acta Metall. 37*, 87.

Jones, R. O. and O. Gunnarsson (1989). *Rev. Mod. Phys. 61*, 689.

Joos, B., Q. Ren, and M. S. Duesbery (1994). *Surf. Sci. 302*, 385.

Jordan, D. W. and P. Smith (1987). *Nonlinear Ordinary Differential Equations.* Oxford Applied Mathematics and Computing Science Series. Oxford University Press.

Justo, J. F., V. V. Bulatov, and S. Yip (1997). *Scr. Mater. 36*, 707.

Juul Jensen, D. (1992). *Scr. Metall. 27*, 1551.

Juul Jensen, D. (1997a). *Met. Mater. Trans. A 28*, 15.

Juul Jensen, D. (1997b). *Orientation Aspects of Growth during Recrystallization.* Risø-R-978 (EN), Materials Research Department, Risø National Laboratory.

Juul Jensen, D., N. Hansen, and F. J. Humphreys (1985). *Acta Metall. 33*, 2155.

Kalindindi, S. R., C. A. Bronhorst, and L. Anand (1992). *J. Mech. Phys. Solids 40*, 537.

Kalos, M. H. and P. A. Whitlock (1986). *Monte Carlo Methods.* John Wiley, New York.

Kamide, K., H. Iijima, and H. Shirataki (1994). *Polymer J. 26*, 21.

Karapiperis, T. (1995). *J. Stat. Phys. 81*, 165.

Karhausen, F. K. and R. Kopp (1992). In *Proceedings 13th RISØ International Symposium on Materials Science,* Vol. eds.: S. I. Andersen, J. B. Bilde-Sørensen, N. Hansen, T. Leffers, H. Lilholt, O. B. Pedersen and B. Ralph, pp. 291. RISØ National Laboratory, Roskilde.

Kästner, H. (1978). *Architektur und Organisation digitaler Rechenanlagen.* Teubner Verlag, Stuttgart.

Kaufman, L. and H. Bernstein (1970). *Computer Calculation of Phase Diagrams.* Academic Press, New York.

Kawasaki, K. (1989). *Phil. Mag. B 60*, 399.

Kelires, P. C. and J. Tersoff (1989). *Phys. Rev. Lett. 63*, 1164.

Kelvin, The Lord (1901). *Phil. Mag. 2*, 1.

Kessler, D., H. Levine, and J. Koplik (1984). *Phys. Rev. A 30*, 3161.

Kestin, J. and J. R. Dorfman (1971). *A Course in Statistical Thermodynamics.* Academic Press, New York.

Kew, J., M. R. Wilby, and D. D. Vvedensky (1993). *J. Cryst. Growth 127*, 508.

Khachaturyan, A. G. (1967). *Sov. Phys. — Solid State 8*, 2163.

Khachaturyan, A. G. (1968). *Sov. Phys. — Solid State 9*, 2040.

Khachaturyan, A. G. (1983). *Theory of Structural Transformations in Solids.* John Wiley, New York.

Khachaturyan, A. G., S. V. Semenovska, and J. W. Morris (1988). *Acta Metall. 36*, 1563.

Khachaturyan, A. G. and G. A. Shatalov (1969). *Sov. Phys. — Solid State 11*, 118.

Khanna, R., T. R. Welberry, and R. L. Withers (1993). *J. Phys. 5*, 4251.

Khantha, M., V. Vitek, and D. P. Pope (1992). *Mater. Sci. Eng. A 152*, 89.

Khein, A. and D. J. Singh (1995). *Phys. Rev. B 51*, 4105.

Kikuchi, R. (1974). *J. Chem. Phys. 60*, 1071.

Kinderman, A. J. and J. F. Monahan (1977). *Assoc. Comput. Machin. Trans. Mathemat. Softw. 3*, 257.

King, W. E., G. H. Campbell, T. Gonis, G. Henshall, D. Lesuer, E. Zywicz, and S. M. Foiles (1995). *Mater. Sci. Eng. A 191*, 1.

Kinzel, W. (1985). *Z. Phys. B - Condensed Matter 58*, 229.

Kirchner, H. O., L. P. Kubin, and V. Pontikis (1996). *Proceedings of NATO ASI on Computer Simulation in Materials Science, Nano/Meso/Macroscopic Space and Time Scales*, Volume 308 of *NATO Advanced Science Institutes Series, Series E : Applied Sciences.* Kluwer Academic in cooperation with NATO Scientific Division.

Kirchner, H. O. and J. Lothe (1986). *Phil. Mag. Lett. A 53*, L7.

Klimanek, P. and W. Pantleon (1996). *Freiberger Forschungsheft Reihe B, Vol. 279, Reihe Werkstoffwissenschaft, Werkstofftechnologie, Simulationstechniken in der Materialwissenschaft.* Technische Universität Freiberg, Freiberg, Sachsen.

Klinkenberg, C., D. Raabe, and K. Lücke (1992). *Steel Res. 63*, 227.

Klix, F. and K. H. Schmelowsky (1982). *Mathematische Modellbildung in Naturwissenschaft und Technik.* Akademie Verlag, Berlin.

Knuth, D. E. (1997). *The Art of Computer Programming.* Addison-Wesley, Reading.

Kobayashi, R. (1993). *Physica D 63*, 410.

Kobayashi, R. (1994). *Exper. Mathemat. 3*, 59.

Kocks, U. F. (1966). *Phil. Mag. 13*, 541.

Kocks, U. F. (1970). *Metall. Trans. 1*, 1121.

Kocks, U. F. (1985). *Metall. Trans. A 18*, 2109.

Kocks, U. F. (1987). *Unified Constitutive Equations for Creep and Plasticity;* Vol. ed.: A.K. Miller. Elsevier Science, Amsterdam.

Kocks, U. F. (1994). *Private communication.*

Kocks, U. F., A. S. Argon, and M. F. Ashby (1975). In *Prog. Mater. Sci.*, Ser. eds.: B. Chalmers, J.W. Christian, and T.B. Massalski, Volume 19. Pergamon Press.

Kocks, U. F., G. R. Canova, and J. J. Jonas (1983). *Acta Metall. 31*, 1243.

Kocks, U. F., G. R. Canova, and H. R. Wenk (1987). *Los Alamos Plasticity Code.* Los Alamos National Laboratory, Los Alamos, NM.

Kocks, U. F. and H. Chandra (1982). *Acta Metall. 30*, 695.

Kocks, U. F. and C. T. Necker (1994). In *Proceedings 15th RISØ International Symposium on Materials Science,* Vol. eds.: S. I. Andersen, J. B. Bilde-Sørensen, T. Lorentzen, O. B. Pedersen, and N. J. Sorensen, pp. 45. RISØ National Laboratory, Roskilde.

Kohan, A. F. and G. Ceder (1996). *Phys. Rev. B 54*, 805.

Köhlhoff, G. D. (1988). *Textur- und Mikrostrukturentwicklung bei Walzumformung und Rekristallisation von Einkristallen kubisch-flächenzentrierter Metalle.* Dissertation. Rheinisch-Westfälische Technische Hochschule Aachen, Institut für Metallkunde und Metallphysik.

Kohlhoff, S., P. Gumbsch, and H. F. Fischmeister (1991). *Phil. Mag. A 64*, 851.

Kohn, W. and L. J. Sham (1965). *Phys. Rev. A 140*, 1133.

Kohyama, T. (1991). *J. Stat. Phys. 63*, 637.

Kolmogorov, A. N. (1937). *Izv. Akad. Nauk. USSR Ser. Metemat 1*, 355.

Kong, X. P. and E. G. D. Cohen (1991). *J. Stat. Phys. 62*, 737.

Koonin, S. E. (1986). *Computational Physics.* Benjamin/Cummings Publishing.

Kosztin, I., B. Faber, and K. Schulten (1996). *Amer. J. Phys. 64*, 633.

Kotrla, M. and A. C. Levi (1994). *Surf. Sci. 317*, 183.

Kramers, H. A. (1940). *Physica 7*, 264.

Kraska, M. and A. Bertram (1996). *Technol. Mech. 16*, 51.

Krausz, A. S. and K. Krausz (1996). *Unified Constitutive Laws of Plastic Deformation.* Academic Press, London.

Kravchenko, V. Y. (1966). *Sov. Phys. — Solid State 8*, 740.

Krawietz, A. (1986). *Materialtheorie - Mathematische Beschreibung des phänomenologischen thermomechanischen Verhaltens.* Springer-Verlag, Berlin, Heidelberg.

Kröner, E. (1958a). *Z. Phys. 151*, 504.

Kröner, E. (1958b). *Kontinuumstheorie der Versetzungen und Eigenspannungen*, Volume 5 of *Ergebnisse der angewandten Mathematik.* Springer-Verlag, New York.

Kröner, E. (1961). *Acta Metall. 9*, 155.

Kröner, E. (1965). In *Fehlstellen, Plastizität, Strahlenschäden und Elektronentheorie,* Vol. ed.: A. Seeger, Volume 1 of *Moderne Probleme der Metallphysik.* Springer-Verlag.

Kröner, E. (1977). *J. Mech. Phys. Solids 25*, 137.

Kruse, C., M. W. Finnis, and M. J. Gillan (1996). *Phil. Mag. Lett. 73*, 377.

Kubin, L. P. (1988). *Non-Linear Phenomena in Materials Science I,*, Volume 3-4 of *Solid State Phenomena.* Trans Tech Publication, CH-Aedermannsdorf.

Kubin, L. P. (1993a). *Phys. Stat. Sol. (A) 135*, 433.

Kubin, L. P. (1993b). Chapter 4*: Dislocation Patterning*, Volume 6; Vol. ed.: H. Mughrabi: Plastic Deformation and Fracture of Materials of *Materials Science and Technology — A Comprehensive Treatment,* Ser. eds.: R. W. Cahn, P. Haasen, and E. J. Krämer. VCH, Weinheim.

Kubin, L. P. (1996). In *Proceedings of NATO ASI on Computer Simulation in Materials Science,* Vol. eds.: H. O. Kirchner, L. P. Kubin, and V, Pontikis, Volume 308 of *NATO Advanced Science Institute Series, Series E : Applied Sciences*, pp. 273. Kluwer Academic in cooperation with NATO Science Division.

Kubin, L. P., G. R. Canova, M. Condat, B. Devincre, V. Pontikis, and Y. J. M. Bréchet (1992). In *Non-Linear Phenomena in Materials Science II;* Vol. eds.: G. Martin and L. P. Kubin, Volume 23–24 of *Solid State Phenomena*, pp. 455. Trans Tech Publication, CH-Aedermannsdorf.

Kuhlmann-Wilsdorf, D. and N. Hansen (1991). *Scr. Metall. 25*, 1557.

Kuo, C. H. and P. K. Gupta (1995). *Acta Metall. 43*, 397.

Küpper, T. and N. Masbaum (1994). *Acta Metall. 42*, 1847.

Kutner, R. and W. Bogusz (1992). *Z. Phys. B 86*, 461.

Lan, Y., H. J. Klaar, and W. Dahl (1990). *Scr. Metall. 24*, 337.

Landau, L. D. (1937a). *Phys. Z. Sowjun. 11*, 26.

Landau, L. D. (1937b). *Phys. Z. Sowjun. 11*, 545.

Landau, L. D. (1965). *Collected Papers of L.D. Landau,* Vol. ed.: D. ter Haar. Gordon and Breach, New York.

Landau, L. D. and E. M. Lifshitz (1980). *Statistical Physics,* Part I. Pergamon Press, London.

Landau, L. D. and E. M. Lifshitz (1981). *Physical Kinetics.* Pergamon Press, London.

Langer, J. S. (1980). *Rev. Mod. Phys. 52*, 1.

Langer, J. S., N. Bar-On, and H. D. Miller (1975). *Phys. Rev. A 11*, 1417.

Lau, J. H. (1994). *Technologies for Multichip Modules.* Van Nostrand Reinhold, New York.

Lebensohn, R. A. and C. N. Tomé (1993a). *Phil. Mag. A 67*, 187.

Lebensohn, R. A. and C. N. Tomé (1993b). *Acta Metall. 41*, 2611.

Lebensohn, R. A. and C. N. Tomé (1994). *Mat. Sci. Eng. A 175*, 71.

Lee, C. S. and B. J. Duggan (1993). *Acta Metall. 41*, 2691.

Leffers, T. (1968). *Scr. Metall. 2*, 447.

Leffers, T. (1994). In *Proceedings 10th International Conference on Textures of Materials (ICOTOM 10), Mater. Sci. For.*, Vol. ed.: H. J. Bunge, Volume 157–162, pp. 1815. Trans Tech Publications.

Leffers, T. and R. A. Lebensohn (1996). In *Proceedings of the 11th International Conference on Textures of Materials (ICOTOM 11), Sept. 1996, Xian, China,*Vol. eds.: Z. Liang, L. Zuo, Y. Chu, Volume 1, pp. 307. International Academic, Beijing.

Lehmer, D. H. (1951). *Ann. Comput. Lab. Harvard University 26*, 141.

Leibfried, G. (1950). *Z. Phys. 127*, 344.

Leibfried, G. (1957). In *Dislocations and the Mechanical Properties of Crystals*, ed.: J.C. Fisher. John Wiley, New York.

Leiss, E. L. (1995). *Parallel and Vector Computing - A Practical Introduction.* McGraw-Hill Series on Computer Engineering. McGraw-Hill.

Lemarchand, A. and M. Mareschal (1996). In *Proceedings of NATO ASI on Computer Simulation in Materials Science,* Vol. eds.: H. O. Kirchner, L. P. Kubin, and V. Pontikis, Volume 308 of *NATO Advanced Science Institutes Series, Series E : Applied Sciences*, pp. 259. Kluwer Academic in cooperation with NATO Science Division.

Lennard-Jones, J. E. (1924). *Proc. R. Soc. London A 106*, 463.

Lépinoux, J. (1996). In *Proceedings of NATO ASI on Computer Simulation in Materials Science,* Vol. eds.: H. O. Kirchner, L. P. Kubin, and V. Pontikis, Volume 308 of *NATO Advanced Science Institutes Series, Series E : Applied Sciences*, pp. 247. Kluwer Academic in cooperation with NATO Science Division.

Lépinoux, J. and L. P. Kubin (1987). *Scr. Metall. 21*, 833.

Lequeu, P., P. Gilormini, F. Montheillet, B. Bacroix, and J. J. Jonas (1987). *Acta Metall. 35*, 439.

Lequeu, P. and J. J. Jonas (1988). *Metall. Trans. A 19*, 105.

LeSar, R. and D. Clarke (1998). *Computer Simulation: A Textbook for Materials Scientist and Engineers (in preparation).*

Leva, J. L. (1992). *Assoc. Comput. Machin. Trans. Mathemat. Softw. 18*, 449.

Li, H., L. Jun, and N. B. Ming (1991). *Solid State Commun. 80*, 311.

Li, H. and N. B. Ming (1997). *Solid State Commun. 101*, 351.

Li, H., X. D. Peng, and N. B. Ming (1995). *J. Cryst. Growth 149*, 241.

Li, J. C. M. (1965). *Acta Metall. 13*, 1097.

Lifshitz, E. M. and V. V. Slyozov (1961). *J. Phys. Chem. Sol. 19*, 35.

Limoge, Y. and J. L. Bocquet (1988). *Acta Metall. 36*, 1717.

Lipinski, P. and M. Berveiller (1989). *Int. J. Plast. 5*, 149.

Lipinski, P., A. Naddari, and M. Berveiller (1992). *Int. J. Solids Structures 29*, 1873.

Liu, C. L. and S. J. Plimpton (1995a). *Phys. Rev. B 51*, 4523.

Liu, C. L. and S. J. Plimpton (1995b). *J. Mater. Res. 10*, 1589.

Liu, J., J. M. Jin, and N. B. Ming (1989). *Solid State Commun. 70*, 763.

Liu, Y., T. Baudin, and R. Penelle (1996). *Scr. Mater. 34*, 1679.

Livesley, R. K. (1983). *Finite Elements – An Introduction for Engineers.* Cambridge University Press.

Livet, F. (1987). *Acta Metall. 35*, 2915.

Löchte, L. (1997). *Unpublished results.*

Löchte, L., A. Gitt, and G. Gottstein (1998). *In preparation.*

Löchte, L. and G. Gottstein (1996). In *Proceedings 5th International Workshop on the Computational Modeling of the Mechanical Behaviour of Materials, Aachen, 1996* Vol. eds.: S. Schmauder and D. Raabe, Volume 7 of *Comput. Mater. Sci.*, Ser. eds.: U. Landman and R. Nieminen, pp. 115. Elsevier Science, Amsterdam.

Loisel, B., J. Lapujoulade, and V. Pontikis (1991). *Surf. Sci. 256*, 242.

Lothe, J. and J. P. Hirth (1967). *J. Appl. Phys. 38*, 845.

Love, A. E. H. (1892). *Theory of Elasticity.* Cambridge University Press.

Lubarda, V. A., J. A. Blume, and A. Needleman (1993). *Acta Metall. 41*, 652.

Lücke, K. and K. Detert (1957). *Acta Metall. 5*, 628.

Lücke, K., J. Pospiech, K. H. Virnich, and J. Jura (1981). *Acta Metall. 29*, 167.

Lücke, K. and H. P. Stüwe (1963). In *Recovery and Recrystallization of Metals,* Vol. ed.: L. Himmel, pp. 171. John Wiley, New York.

Ludwig, G. (1979). *Makrosysteme, Physik und Mensch*, Volume 4 of *Einführung in die Grundlagen der Theoretischen Physik.* Verlag Friedrich Vieweg, Braunschweig/Wiesbaden.

Lundquist, S. and N. H. March (1983). *Theory of the Inhomogeneous Electron Gas.* Plenum, New York.

Lutsko, J. F., D. Wolf, and S. Yip (1988a). *Phys. Rev. B 38*, 11572.

Lutsko, J. F., D. Wolf, and S. Yip (1988b). *Phys. Rev. B 38*, 11572.

Mahin, K. W., K. Hanson, and J. W. Morris Jr. (1980). *Acta Metall. 28*, 443.

Mahnke, R. (1996). In *Simulationstechniken in der Materialwissenschaft, Freiberger Forschungsheft Reihe B,* Vol. 279, Reihe Werkstoffwissenschaft, Werkstofftechnologie, Vol. eds.: P. Klimanek and W. Pantleon, pp. 167. Technische Universität Freiberg, Freiberg, Sachsen.

Mai, J. and W. von Niessen (1991). *Phys. Rev. A 44*, 6165.

Majid, I., C. A. Counterman, and R. W. Balluffi (1994). *Acta Metall. 42*, 3331.

Majid, I., C. A. Counterman, and P. D. Bristowe (1994). *J. Phys. Chem. Solids 55*, 1007.

Mareschal, M. and A. Lemarchand (1996). In *Proceedings of NATO ASI on Computer Simulation in Materials Science,* Vol. eds.: H. O. Kirchner, L. P. Kubin, and V. Pontikis, Volume 308 of *NATO Advanced Science Institutes Series, Series E : Applied Sciences*, pp. 85. Kluwer Academic in cooperation with NATO Science Division.

Mark, J. E., M. E. Glicksman, and S. P. Marsh (1992). *Computational Methods in Materials Science*, Volume 278. Mater. Res. Soc. Symp. Proc. Pittsburgh.

Marsal, D. (1976). *Die numerische Lösung partieller Differentialgleichungen.* BI-Wissenschaftsverlag, Bibliographisches Institut Mannheim Leipzig Wien Zürich.

Marthinsen, K., T. Furu, E. Nes, and N. Ryum (1990). In *Simulation and Theory of Evolving Microstructures,* Vol. eds.: M.P. Anderson and A.D. Rollett, pp. 87. The Minerals, Metals and Materials Society, TMS Publication.

Marthinsen, K., O. Lohne, and E. Nes (1989). *Acta Metall. 37*, 135.

Märtin, C. (1994). *Rechnerarchitektur.* Hanser Studuenbücher der Informatik. Carl Hanser Verlag, München Wien.

Martin, G. and L. P. Kubin (1992). *Non-Linear Phenomena in Materials Science II,*, Volume 23–24 of *Solid State Phenomena.* Trans Tech Publication, CH-Aedermannsdorf.

Martin, J. W. and R. D. Doherty (1976). In *Stability of Microstructure in Metallic Systems*, pp. 163. Cambridge University Press.

Marx, V. (1998). *Cellular automaton simulations of recrystallization phenomena, to be publ.* Dissertation. Rheinisch-Westfälische Technische Hochschule Aachen, Institut für Metallkunde und Metallphysik.

Marx, V. and D. Raabe (1995). In *Proceedings 16th RISØ International Symposium on Materials Science,* Vol. eds.: N. Hansen, D. Juul Jensen, Y.L. Liu, and B. Ralph, pp. 461. RISØ National Laboratory, Roskilde.

Marx, V., D. Raabe, and G. Gottstein (1995). In *Proceedings of the 4th European Conference on Advanced Materials and Processes, Euromat 95, Symposium F – Materials and Processing Control*, Volume 3, pp. 395. published by Associatione Italiana di Metallurgia, Milano, Italy.

Marx, V., D. Raabe, and G. Gottstein (1996). In *Proceedings of the 11th International Conference on Textures of Materials (ICOTOM 11), Sept. 1996, Xian, China*, Vol. eds.: Z. Liang, L. Zuo, Y. Chu, Volume 1, pp. 515. International Academic, Beijing.

Mathur, K. K. and P. R. Dawson (1989). *Int. J. Plast. 8*, 67.

Mattsson, T. R., U. Engberg, and G. Wahnstrom (1993). *Phys. Rev. Lett. 71*, 2615.

Maudlin, P. J. and S. K. Schiferl (1996). *Comput. Meth. Appl. Mech. Eng. 131*, 1.

Maudlin, P. J., S. I. Wright, U. F. Kocks, and M. S. Sahota (1996). *Acta Mater. 44*, 4027.

McHugh, P. E., R. J. Asaro, and C. F. Shih (1993a). *Acta Metall. 41*, 1461.

McHugh, P. E., R. J. Asaro, and C. F. Shih (1993b). *Acta Metall. 41*, 1477.

McHugh, P. E., R. J. Asaro, and C. F. Shih (1993c). *Acta Metall. 41*, 1488.

McHugh, P. E., R. J. Asaro, and C. F. Shih (1993d). *Acta Metall. 41*, 1501.

Mecking, H. and U. F. Kocks (1981). *Acta Metall. 29*, 1865.

Mehnert, K. and P. Klimanek (1998). In *Proceedings of an International Conference on Textures, Sept. 1997, Clausthal, Germany*, eds.: R. Schwarzer and H. J. Bunge. Trans Tech Publication, CH-Aedermannsdorf.

Mendelson, A. (1968). *Plasticity: Theory and Application.* Macmillan, New York.

Menyhard, M., M. Yan, and V. Vitek (1994). *Acta Metall. 42*, 2783.

Metropolis, N., A. W. Rosenbluth, M. N. Rosenbluth, A. T. Teller, and E. Teller (1953). *J. Chem. Phys. 21*, 1087.

Meyer, M. and V. Pontikis (1989). In *Proceedings of NATO ASI on Computer Simulation in Materials Science, Interatomic Potentials, Simulation Techniques and Applications*, Vol. eds.: M. Meyer and V. Pontikis, Volume 205 of *NATO Advanced Science Institute Series, Series E : Applied Sciences.* Kluwer Academic in cooperation with NATO Science Division.

Milik, M. and A. Orszagh (1989). *Polymer 30*, 681.

Miyazaki, T., Y. Ishii, and K. Terakura (1991). *Prog. Theor. Phys., Suppl. 106*, 173.

Mohles, V. (1996). *Thermisch aktivierte Versetzungsbewegung in Kristallen auf der Grundlage von Simulationsrtechnungen.* Dissertation. Technische Universität Braunschweig, Institut für Metallphysik und Nukleare Festkörperphysik.

Mohles, V. and D. Rönnpagel (1996). In *Comput. Mater. Sci., Proceedings 5th International Workshop on the Computational Modeling of the Mechanical Behaviour of Materials, Aachen, 1996* Vol. eds.: S. Schmauder and D. Raabe, Volume 7 of *Comput. Mater. Sci.*, Ser. eds.: U. Landman and R. Nieminen, pp. 89. Elsevier Science, Amsterdam.

Molinari, A., G. R. Canova, and S. Ahzi (1987). *Acta Metall. 35*, 2983.

Molinari, A. and L. S. Tóth (1994). *Acta Metall. 42*, 2453.

Morales, J. J. and S. Toxvaerd (1992). *Comput. Phys. Com. 71*, 71.

Morhacova, E. (1995). *Cryst. Res. Technol. 30*, K9.

Moriarty, J. A. (1988). *Phys. Rev. B 38*, 3199.

Moriarty, J. A. (1994). *Phys. Rev. B 49*, 12431.

Morral, J. E. and J. W. Cahn (1971). *Acta Metall. 19*, 1037.

Morse, P. M. (1929). *Phys. Rev. 34*, 57.

Mughrabi, H. (1980). In *Proceedings of the 5th International Conference on the Strength of Metals and Alloys ICSMA 5*, Vol. eds.: P. Haasen, V. Gerold, and G. Kostorz, Volume 3, pp. 1615. Pergamon Press, Oxford.

Mughrabi, H. (1983). *Acta Metall. 31*, 1367.

Mughrabi, H. (1993). *Plastic Deformation and Fracture of Materials;* Vol. ed.: H. Mughrabi, Volume 6 of *Materials Science and Technology — A Comprehensive Treatment*, Ser. eds.: R. W. Cahn, P. Haasen, and E. J. Krämer. VCH, Weinheim.

Mughrabi, H., T. Ungár, W. Kienle, and M. Wilkens (1986). *Phil. Mag. A 53*, 793.

Mukherjee, A., S. Schmauder, and M. Rühle (1995). *Acta Metall. 43*, 4083.

Muller, D., X. Lemoine, and M. Berveiller (1994a). In *Proceedings 15th RISØ International Symposium on Materials Science,* eds.: S. I. Andersen, J. B. Bilde-Sørensen, T. Lorentzen, O. B. Pedersen, and N. J. Sorensen, pp. 75. RISØ National Laboratory, Roskilde.

Muller, D., X. Lemoine, and M. Berveiller (1994b). In *Proceedings 10th International Conference on Textures of Materials (ICOTOM 10), Mater. Sci. For.*, Volume 157–162, pp. 1821. Trans Tech Publications.

Müller, K. H. (1985). *J. Appl. Phys. 58*, 2573.

Müller-Krumbhaar, H. (1989). *Computersimulation in der Physik*, Volume 20 of *Ferienkurse der Kernforschungsanlage Jülich, Institut für Festkörperforschung.* Kernforschungsanlage Jülich.

Münster, A. (1974). *Statistical Thermodynamics*, Volume I and II. Springer-Verlag.

Mura, T. (1963). *Phil. Mag. 8*, 843.

Mura, T. (1987). *Micromechanics of Defects in Solids.* Martinus Nijhoff, Dordrecht.

Murch, G. E. and H. Zhang (1995). *Phil. Mag. A 72*, 249.

Nabarro, F. R. N. (1947a). *Proc. Phys. Soc. 59*, 256.

Nabarro, F. R. N. (1947b). *Report on the Conference on the Strength of Solids.* Dislocations in Solids. Physical Society, London.

Nabarro, F. R. N. (1951). *Proc. R. Soc. London A 209*, 278.

Nabarro, F. R. N. (1989). *Dislocations in Solids.* Elsevier Science, Amsterdam; Ser. ed.: F.R.N. Nabarro.

Nadgornyi, E. (1988). In *Prog. Mater. Sci., Pergamon Press,* Vol. eds.:J.W. Christian, P. Haasen, and T.B. Massalski, Volume 31.

Nauck, D., F. Klawonn, and R. Kruse (1994). *Neuronale Netze und Fuzzy-Systeme.* Verlag Friedrich Vieweg, Braunschweig/Wiesbaden.

Neelamkavil, F. (1987). *Computer Simulation and Modeling.* John Wiley, New York.

Nemat-Nasser, S. and M. Hori (1993). *Micromechanics: Overall Properties of Heterogeneous Materials.* North-Holland Series in Applied Mathematics and Mechanics. North-Holland, Amsterdam.

Neumann, P. D. (1971). *Acta Metall. 19*, 1233.

Ninomiya, T. (1970). *Fundamental Aspects of Dislocation Theory,* Vol. eds.: J.A. Simmons, R. de Wit, and R. Bullough *1*, 315.

Norskov, J. K. and N. D. Lang (1980). *Phys. Rev. B 21*, 2131.

Nosé, S. (1984a). *J. Chem. Phys. 81*, 511.

Nosé, S. (1984b). *Mol. Phys. 52*, 255.

Nummelin, E. (1994). *J. Stat. Phys. 75*, 879.

Nye, J. F. (1953). *Acta Metall. 1*, 153.

Nye, J. F. (1967). *Physical Properties of Crystals.* Oxford University Press.

Ochiai, S., P. W. M. Peters, and K. Schulte (1991). *J. Mater. Sci. 26*, 5433.

Oden, J. T. (1972). *Finite Elements of Nonlinear Continua.* McGraw-Hill, New York.

Onsager, L. (1931a). *Phys. Rev. 37*, 405.

Onsager, L. (1931b). *Phys. Rev. 38*, 2265.

Onuki, A. (1989). *J. Phys. Soc. Jpn. 58*, 3065.

Orowan, E. (1934). *Z. Phys. 89*, 634.

Ossadnik, P. (1993). *Int. J. Mod. Phys. 4*, 127.

Ostwald, W. (1900). *Z. Phys. Chem. 34*, 495.

Owen, D. and E. Hinton (1980). *Finite Elements in Plasticity: Theory and Practice.* Pineridge Press, Swansea, Wales.

Packard, N. and S. Wolfram (1985). *J. Stat. Phys. 38*, 90.

Packard, N. H. (1986). In *Theory and Applications of Cellular Automata,* Vol. ed.: S. Wolfram, Volume 1 of *Advanced Series on Complex Systems, selected papers 1983-1986*, pp. 305. World Scientific, Singapore.

Pan, J. and A. C. F. Cocks (1993). *Comput. Mater. Sci. 1*, 95.

Pang, T. (1997). *Computational Physics.* Cambridge University Press.

Pantelides, S. T. (1994). *Comput. Mater. Sci. 2*, 149.

Papajova, D., S. Nemeth, and M. Vesely (1995). *Thin Sol. Fil. 47*, 267.

Parinello, M. and A. Rahman (1981). *J. Appl. Phys. 52*, 7182.

Parr, R. G. and W. Yang (1989). *Density Functional Theory of Atoms and Molecules.* Oxford University Press, New York.

Paxton, A. T. and A. P. Sutton (1989). *Acta Metall. 37*, 1693.

Peczak, P. (1995). *Acta Metall. 43*, 1297.

Pedersen, O. B. and T. Leffers (1987). In *Proceedings 8th RISØ International Symposium on Materials Science,* Vol. eds.: S. I. Andersen, J. B. Bilde-Sørensen, N. Hansen, T. Leffers, H. Lilholt, O. B. Pedersen, and B. Ralph, pp. 147. RISØ National Laboratory, Roskilde.

Peierls, R. E. (1940). *Proc. Phys. Soc. 52*, 34.

Pekalski, A. and M. Ausloos (1994). *J. Chem. Phys. 100*, 3175.

Peng, G., J. U. Sommer, and A. Blumen (1996). *Phys. Rev. E 53*, 5509.

Penrose, O. and P. C. Fife (1990). *Physica D 43*, 44.

Pestman, B., J. T. M. de Hosson, and V. Vitek (1991). *Phil. Mag. A 64*, 951.

Pestman, B. J., J. T. M. de Hosson, and V. Vitek (1989). *Scr. Metall. 23*, 1431.

Petersen, N. K. and P. Alstrom (1997). *Physica A 235*, 473.

Pettifor, D. G. (1990). *J. Chem. Soc. 86*, 1209.

Pettifor, D. G. (1992). *Mater. Sci. Technol. 8*, 345.

Pettifor, D. G. (1993). Chapter 2: *Electron Theory of Crystal Structure*, Volume 1; Vol. ed.: V. Gerold: Structure of Solids of *Materials Science and Technology — A Comprehensive Treatment,* Ser. eds.: R. W. Cahn, P. Haasen, and E. J. Krämer. VCH, Weinheim.

Pettifor, D. G. and A. H. Cottrell (1992). *Electron Theory in Alloy Design.* The Institute of Materials, London.

Pezzee, C. E. and D. C. Dunand (1994). *Acta Metall. 42*, 1509.

Phillpot, S. R., J. F. Lutsko, and D. Wolf (1989a). *Phys. Rev. B 40*, 2831.

Phillpot, S. R., J. F. Lutsko, and D. Wolf (1989b). *Solid State Commun. 70*, 265.

Pieracci, A. (1997). *Fatigue Fract. Eng. Mater. 20*, 109.

Pimienta, P. J. P., E. J. Garboczi, and W. C. Carter (1992). *Comput. Mater. Sci. 1*, 63.

Pinches, M. R. S. and D. J. Tildesley (1996). *Surf. Sci. 367*, 177.

Plimpton, S. and B. Hendrickson (1996). *J. Comput. Chem. 17*, 326.

Plotz, W. M., K. Hingerl, and H. Sitter (1994). *Semiconductor Sci. techn. 9*, 2224.

Pointon, A. J. (1967). *An Introduction to Statistical Physics.* Longman, London.

Polanyi, M. (1934). *Z. Phys. 89*, 660.

Porter, D. A. and K. E. Easterling (1992). *Phase Transformations in Metals and Alloys.* Chapman and Hall, London.

Potts, R. B. (1952). *Proc. Cambridge Phil. Soc. 48*, 106.

Predeleanu, M. (1987). *Computational Techniques for the Prediction of Materials Processes and Defects.* Elsevier Science, Amsterdam.

Press, W. H. and S. A. Teukolsky (1992). *Comput. Phys. 6*, 522.

Prinz, F. B. and A. S. Argon (1984). *Acta Metall. 32*, 1021.

Procacci, P., T. Darden, and M. Marchi (1996). *J. Phys. Chem. 100*, 10464.

Pschyrembel, W. (1990). *Pschyrembel Klinisches Wörterbuch.* Verlag de Gruyter.

Qin, Z. and G. E. Murch (1993). *Phil. Mag. 67*, 381.

Quade, W., G. Hupper, and E. Scholl (1994a). *Phys. Rev. B 49*, 13408.

Quade, W., G. Hupper, and E. Scholl (1994b). *Phys. Rev. B 49*, 6748.

Raabe, D. (1992). *Texturen kubisch-raumzentrierter Übergangsmetalle.* Dissertation. Rheinisch-Westfälische Technische Hochschule Aachen, Institut für Metallkunde und Metallphysik.

Raabe, D. (1994). *Phys. Stat. Sol. (B) 181*, 291.

Raabe, D. (1995a). In *Proceedings of the 4th European Conference on Advanced Materials and Processes, Symposium F – Materials and Processing Control, F4 – Modeling of Microstructure Evolution and Processing*, pp. 187. Associatione Italiana di Metallurgia.

Raabe, D. (1995b). *Phys. Stat. Sol. (B) 192*, 23.

Raabe, D. (1995c). *Mater. Sci. Technol. 11*, 455.

Raabe, D. (1995d). *Mater. Sci. Eng. A 197*, 31.

Raabe, D. (1995e). *Acta Metall. 43*, 1023.

Raabe, D. (1996a). *Phil. Mag. A 73*, 1363.

Raabe, D. (1996b). *Z. Metallk. 87*, 493.

Raabe, D. (1996c). *Acta Metall. 44*, 937.

Raabe, D. (1997). *Microstructure Simulation in Materials Science.* Shaker Verlag, Aachen.

Raabe, D. (1998a). *Phil. Mag. A 77*, 751.

Raabe, D. (1998b). In *Proceedings of an International Conference on Textures, Sept. 1997, Clausthal, Germany*, eds.: R. Schwarzer and H. J. Bunge. Trans Tech Publication, CH-Aedermannsdorf.

Raabe, D. and J. Boeslau (1994). In *Proceedings 15th RISØ International Symposium on Materials Science*, eds.: S. I. Andersen, J. B. Bilde-Sørensen, T. Lorentzen, O. B. Pedersen, and N. J. Sorensen, pp. 481. RISØ National Laboratory, Roskilde.

Raabe, D. and H. J. Bunge (1997). *Proceedings of the Symposium on Computer Simulation and Modeling in Texture Research, Aachen, Oct. 1995*, Vol. eds.: D. Raabe and H. J. Bunge, Volume 28 of *Text. Microstruct.*, Ser. ed.: H. J. Bunge. Gordon and Breach Science.

Raabe, D. and K. Lücke (1993). *Mater. Sci. Technol. 9*, 302.

Raabe, D. and K. Lücke (1994). In *Proceedings 10th International Conference on Textures of Materials (ICOTOM 10), Mater. Sci. For.*, Vol. ed.: H. J. Bunge, Volume 157–162, pp. 1469. Trans Tech Publications.

Raabe, D. and W. Mao (1995). *Phil. Mag. A 71*, 805.

Raabe, D. and F. Roters (1995). In *Proceedings of the 4th European Conference on Advanced Materials and Processes, Euromat 95, Symposium F – Materials and Processing Control*, Volume 3, pp. 395. Associatione Italiana di Metallurgia, Milano, Italy.

Raabe, D., F. Roters, and V. Marx (1996). *Text. Microstruct. 26-27*, 611.

Radhakrishnan, B. and T. Zacharia (1995). *Met. Mater. Trans 26*, 2123.

Raeker, T. J. and A. E. DePristo (1991). *Int. Rev. Chem. Phys. 93*, 1.

Rahman, A. (1964). *Phys. Rev. 136 A*, 405.

Rao, S. S. (1989). *The Finite Element Method in Engineering.* Pergamon Press.

Raphanel, J. L. and P. van Houtte (1985). *Acta Metall. 33*, 1481.

Ratke, L. (1987). *Zur Kinetik der Vergröberung von Dispersoiden in strömenden Flüssigkeiten.* Habilitationsschrift. Max-Planck Institut für Metallforschung, Universität Stuttgart.

Ratke, L. and W. K. Thieringer (1985). *Acta Metall. 33*, 1793.

Rauh, H. and D. Simon (1978). *Phys. Stat. Sol. (A) 46*, 499.

Reher, F. (1998). *Cellular automaton simulations of recrystallization phenomena* (in German). Dissertation. Rheinisch-Westfälische Technische Hochschule Aachen, Institut für Metallkunde und Metallphysik.

Reichl, L. E. (1980). *A Modern Course in Statistical Physics.* Edward Arnold.

Reif, F. (1965). *Fundamentals of Statistical and Thermal Physics.* McGraw-Hill, New York.

Reiter, J., G. Zifferer, and O. F. Olaj (1990). *Macromolecules 23*, 224.

Renouard, M. and M. Wintenberger (1980). *Compes Rendus Academie des Science Paris B290*, 403.

Reppich, B. (1993). Chapter 7: *Particle Strengthening*, Volume 6; Vol. ed.: H. Mughrabi: Plastic Deformation and Fracture of Materials of *Materials Science and Technology — A Comprehensive Treatment*, Ser. eds.: R. W. Cahn, P. Haasen, and E. J. Krämer. VCH, Weinheim.

Reuss, A. (1930). *Mathematik und Mechanik 10*, 266.

Reynolds, A. E., D. Kaletta, and G. Ertl (1989). *Surf. Sci. 452*, 452.

Rezende, J. L. L., A. Ludwig, and P. R. Sahm (1996). In *Simulationstechniken in der Materialwissenschaft, Freiberger Forschungsheft Reihe B*, Vol. 279, Reihe Werkstoffwissenschaft, Werkstofftechnologie, Vol. eds.: P. Klimanek and W. Pantleon, pp. 193. Technische Universität Freiberg, Freiberg, Sachsen.

Rhee, M., J. P. Hirth, and H. M. Zbib (1994). *Acta Metall. 42*, 2645.

Rice, J. R. (1971). *J. Mech. Phys. Solids 19*, 433.

Rice, J. R. (1975). In *Constitutive Equations in Plasticity*, Vol. ed.: A.S. Argon, pp. 23. MIT Press, Cambridge.

Richtmyer, R. D. and K. W. Morton (1967). *Difference Methods for Initial Value Problems*. Interscience.

Risken, H. (1984). *The Fokker-Planck Equation*. Springer Series in Synergetics, Ser. ed.: H. Haken. Springer-Verlag.

Ritter, H., T. Martinetz, and K. Schulten (1991). *Neuronale Netze*. Addison-Wesley, Bonn.

Rittner, J. D., S. M. Foiles, and D. N. Seidman (1994). *Phys. Rev. B 50*, 12004.

Robertson, D. H., D. W. Brenner, and C. T. White (1995). *J. Chem. Phys. 99*, 15721.

Rogers, T. M. (1989). *Phys. Rev. B 39*, 11956.

Rogers, T. M., K. R. Elder, and R. C. Desai (1988). *Phys. Rev. B 37*, 9638.

Roland, C. and M. Grant (1989). *Phys. Rev. B 39*, 11971.

Rollett, A. D., M. J. Luton, and D. J. Srolovitz (1992). *Acta Metall. 40*, 43.

Rollett, A. D., D. J. Srolovitz, and M. P. Anderson (1989). *Acta Metall. 37*, 1227–1240.

Rollett, A. D., D. J. Srolovitz, R. D. Doherty, and M. P. Anderson (1989). *Acta Metall. 37*, 627.

Rollett, A. D., D. J. Srolovitz, R. D. Doherty, M. P. Anderson, and G. S. Grest (1990). In *Simulation and Theory of Evolving Microstructures*, Vol. eds.: M.P. Anderson and A.D. Rollett, pp. 103. The Minerals, Metals and Materials Society, TMS Publication.

Rönnpagel, D. (1987). In *Proceedings 8th RISØ International Symposium on Materials Science*, eds.: S. I. Andersen, J. B. Bilde-Sørensen, T. Lorentzen, O. B. Pedersen and N. J. Sørensen, pp. 503. RISØ National Laboratory, Roskilde.

Rönnpagel, D. (1996). *Private communication*.

Rönnpagel, D., T. Streit, and T. Pretorius (1993). *Phys. Stat. Sol. (a) 135*, 445.

Rosen, G. I., D. Juul Jensen, D. A. Hughes, and N. Hansen (1995). *Acta Metall. 43*, 2563.

Rosenblueth, A. and N. Wiener (1945). *Phil. Sci. 12*, 316.

Rosenfield, A. R., G. T. Hahn, A. L. Bement, and R. I. Jaffee (1968). *Dislocation Dynamics*. McGraw-Hill.

Rösler, J. and E. Arzt (1988a). *Acta Metall. 36*, 1043.

Rösler, J. and E. Arzt (1988b). *Acta Metall. 36*, 1053.

Rösler, J. and E. Arzt (1990). *Acta Metall. 38*, 1053.

Roters, F. and D. Raabe (1996). *Mater. Sci. Technol. 12*, 281.

Roters, F. and D. Raabe (1997). In *Proceedings of the Symposium Computer Simulation and Modeling in Texture Research, Aachen, Oct. 1995*, Vol. eds.: D. Raabe and H. J. Bunge, Volume 28 of *Text. Microstr., Ser.* Vol. ed.: H. J. Bunge, pp. 167. Gordon and Breach Science.

Roters, F., D. Raabe, and G. Gottstein (1996). In *Proceedings 5th International Workshop on the Computational Modeling of the Mechanical Behaviour of Materials, Aachen, 1996* Vol. eds.: S. Schmauder and D. Raabe, Volume 7 of *Comput. Mater. Sci.*, Ser. eds.: U. Landman and R. Nieminen, pp. 56. Elsevier Science, Amsterdam.

Rothman and Zaleski (1994). *Rev. Mod. Phys. 66*, 1417.

Rowe, G. W., C. E. N. Sturgess, P. Hartley, and I. Pillinger (1991). *Finite Element Plasticity and Metal Forming Analysis.* Cambridge University Press.

Royer, F., A. Nadari, F. Yala, P. Lipinski, D. Ceccaldi, M. Berveiller, and P. Penelle (1991). *Text. Microstruct. 14–18*, 1129.

Rumpelhart, D. E. and J. L. McCelland (1986). *Parallel Distributed Processing, Vols.1,2.* MIT Press, Cambridge.

Rupsky, I., I. Iordanova, and A. Apostolov (1990). *Phys. Stat. Sol. (A) 121*, 45.

Ryckaert, J. P., G. Ciccotti, and H. J. C. Berendsen (1977). *Comput. Phys. 23*, 327.

Sachs, G. (1928). *Z. Verein Deutsch. Ingen. 72*, 734.

Sahimi, M. (1993). *Rev. Mod. Phys. 65*, 1393.

Sahimi, M. (1994). *Applications of Percolation Theory.* Taylor and Francis.

Sahm, P. R. and P. N. Hansen (1984). *Numerical Simulation and Modeling of Casting and Solidification Processes for Foundry and Cast-House.* Interntional Commercial Foundry Association, New York.

Saito, Y. (1997). *Mater. Sci. Eng. A 223*, 125.

Saito, Y. and T. Ueta (1989). *Phys. Rev. A 40*, 3408.

Salacuse, J. J., A. R. Denton, and P. A. Egelstaff (1996). *Phys. Rev. E 53*, 2382.

Salik, J. (1985). *J. Appl. Phys. 57*, 5017.

Salomons, E. and D. de Fontaine (1990). *Phys. Rev. E 41*, 11159.

Sankey, O. F. and D. J. Niklewski (1989). *Phys. Rev. B 40*, 3979.

Sarma, G. B. and P. R. Dawson (1996). *Acta Metall. 44*, 1937.

Saul, A., G. Treglia, and B. Legrand (1994a). *Surf. Sci. 307*, 804.

Saul, A., G. Treglia, and B. Legrand (1994b). *Surf. Sci. 307*, 804.

Scattergood, R. O. and D. J. Bacon (1975). *Phil. Mag. 31*, 179.

Scavuzzo, C. M., M. A. Ré, and E. A. Ceppi (1990). *Scr. Metall. 24*, 1901.

Scheerschmidt, K., D. Conrad, and U. Gösele (1996). In *Proceedings 5th International Workshop on the Computational Modeling of the Mechanical Behaviour of Materials, Aachen, 1996* Vol. eds.: S. Schmauder and D. Raabe, Volume 7 of *Comput. Mater. Sci.*, Ser. eds.: U. Landman and R. Nieminen, pp. 40. Elsevier Science, Amsterdam.

Schlipf, J. (1992). *Acta Metall. 40*, 2075.

Schmauder, S. (1994). *Proceedings 3rd International Workshop on the Computational Modeling of the Mechanical Behaviour of Materials, Stuttgart, Germany, 1993.* Comput. Mater. Sci.; *Ser. eds.: U. Landman and R. Nieminen.* Elsevier Science, Amsterdam.

Schmauder, S. (1995). *Private communication.*

Schmauder, S. and D. Raabe (1996). *Proceedings of the 5th International Workshop on the Computational Modeling of the Mechanical Behaviour of Materials, Aachen, Germany, 1996*, Volume 7 of *Comput. Mater. Sci.;* Ser. eds.: U. Landman and R. Nieminen. Elsevier Science, Amsterdam.

Schmauder, S. and D. Weichert (1996). *Proceedings 4th International Workshop on the Computational Modeling of the Mechanical Behaviour of Materials, Lille, 1995;* Vol. eds.: S. Schmauder and D. Weichert, Volume 5 of *Comput. Mater. Sci.;* Ser. eds.: U. Landman and R. Nieminen. Elsevier Science, Amsterdam.

Schmid, F. and K. Binder (1992). *Phys. Rev. B 46*, 13565.

Schmidt, C., F. Ernst, and V. Vitek (1995). *Phys. Rev. Lett. 75*, 2160.

Schmitter, E. D. (1991a). *Neuronale Netze – eine praktische Einführung.* Hofacker Verlag, Holzkirchen.

Schmitter, E. D. (1995). *Steel Res. 66*, 444.

Schmitter, U. (1991b). *Simulation der Orientierungsänderung der Kristallite vielkristalliner Körper bei der Walzverformung und Einbeziehung der Wirkung der Kristallumgebung.* Diplomarbeit. Rheinisch-Westfälische Technische Hochschule Aachen.

Schmutzer, E. (1988). *Grundlagen der Theoretischen Physik.* BI-Wissenschaftsverlag, Bibliographisches Institut Mannheim Leipzig Wien Zürich.

Schöck, G. (1980). Chapter 10, Volume 3 of *Dislocations in Solids.* Elsevier Science, Amsterdam; Ser. ed.: F.R.N. Nabarro.

Scholten, P. D. and M. Kaufman (1997). *Phys. Rev. B 56*, 59.

Schön, C. G. and G. Inden (1996). *Scr. Metall. 34*, 1035.

Schrage, L. (1979). *Assoc. Comput. Machin. Trans. Mathemat. Softw. 5*, 132.

Schulman, L. S. and P. F. Seiden (1978). *J. Statist. Phys. 19*, 293.

Schur, L. N. and H. W. J. Blote (1997). *Phys. Rev. E 55*, 4905.

Schuss, Z. (1980). *Theory and Applications of Stochastic Differential Equations.* John Wiley, New York.

Seeger, A. (1954). *Z. Naturforsch. 9a*, 758.

Seeger, A. (1957). In *Dislocations and the Mechanical Properties of Crystals,* ed.: J.C. Fisher. John Wiley, New York.

Seeger, A., J. Diehl, S. Mader, and H. Rebstock (1957). *Phil. Mag. 2*, 323.

Seeger, A. and H. Engelke (1968). In *Dislocation Dynamics,* Vol. eds.: A.R. Rosenfield, G.T. Hahn, A.L. Bement, and R.I. Jaffee, pp. 623. McGraw-Hill.

Seeger, R. (1982). *Semiconductor Physics.* Springer-Verlag.

Seki, A., D. N. Seidman, Y. Oh, and S. M. Foiles (1991a). *Acta Metall. 39*, 3179.

Seki, A., D. N. Seidman, Y. Oh, and S. M. Foiles (1991b). *Acta Metall. 39*, 3167.

Sesták, B. and A. Seeger (1978). *Z. Metallk. 69*, 195 (H. 4), 355 (H. 6), 425 (H. 7).

Sheldon, R. K. and D. C. Dunand (1996). *Acta Mater. 44*, 4571.

Shenoy, V. B., R. Miller, E. B. Tadmore, R. Phillips, and M. Ortiz (1998). *Phys. Rev. Lett. 80*, 742.

Shewmon, P. G. (1963). *Diffusion in Solids.* McGraw-Hill.

Shimamura, S., K. Kuriyama, and Y. Kashiwagi (1990). *J. Mater. Sci. Lett. 9*, 756.

Shore, J. E. (1973). *Comput. Electr. Eng. 1*, 95.

Shreider, Y. A. (1966). *The Monte Carlo Method.* Pergamon Press, New York.

Silverman, A., A. Zunger, and J. Adler (1995a). *J. Phys. 7*, 5417.

Silverman, A., A. Zunger, and J. Adler (1995b). *J. Phys. 7*, 1167.

Simmons, J. A., R. de Wit, and R. Bullough (1970). *Fundamental Aspects of Dislocation Theory.* National Bureau of Standards, Washington, DC.

Sinnott, S. B., R. J. Colton, and D. W. Brenner (1994). *Surf. Sci. 316*, L1055.

Size, S. M. (1981). *Physics of Semiconductor Devices.* John Wiley, New York.

Smart, J. S. (1966). *Effective Field Theories of Magnetism.* W. B. Saunders, New York.

Smilauer, P., M. R. Wilby, and D. D. Vvedensky (1993). *Phys. Rev. B 48*, 4986.

Smith, G. D., T. P. Russell, and H. Kaiser (1996). *Macromolecules 29*, 4120.

Smith, G. R. and A. B. Bruce (1996). *Europhys. Lett. 34*, 91.

Smith, J. M. (1987). *Mathematical Modeling and Digital Simulation for Engineers and Scientists.* John Wiley, New York.

Smith, R. W. (1997). *J. Appl. Phys. 81*, 1196.

Smith, R. W. and D. J. Srolovitz (1996). *J. Appl. Phys. 79*, 1448.

Sokolnikoff, I. S. (1956). *Mathematical Theory of Elasticity.* McGraw-Hill, New York.

Sommer, J. U., M. Schulz, and H. L. Trautenberg (1993). *J. Chem. Phys. 98*, 7515.

Sommers, C., S. Doniach, and C. Fu (1991). *Physica B 172*, 27.

Spittle, J. A. and S. G. R. Brown (1994). *Acta Metall. 42*, 1811.

Spittle, J. A. and S. G. R. Brown (1995). *J. Mater. Sci. 30*, 3989.

Srolovitz, D. J. (1986). *Computer Simulation of Microstructural Evolution*. The Metallurgical Society of AIME, Warrendale, PA.

Srolovitz, D. J., M. P. Anderson, P. S. Sahni, and G. S. Grest (1984). *Acta Metall. 32*, 793.

Srolovitz, D. J., G. S. Grest, and M. P. Anderson (1986). *Acta Metall. 34*, 1833.

Srolovitz, D. J., G. S. Grest, M. P. Anderson, and A. D. Rollett (1988). *Acta Metall. 36*, 2115.

Srolovitz, D. J., H. Y. Wang, and R. Najafabadi (1993). *Mater. Sci. For. 126*, 23.

Stanley, H. E. (1971). *Introduction to Phase Transitions and Critical Phenomena*. Clarendon Press, Oxford.

Stauffer, D. (1991). *Percolation, Critical Phenomena in Dilute Magnets, Cellular Automata and Related Problems*, Volume The Monte Carlo Method in Condensed Matter Physics, Vol. 71 of *Topics in Applied Physics*. Springer-Verlag.

Stauffer, D. and A. Aharony (1992). *Introduction to Percolation Theory*. Taylor and Francis.

Stauffer, D. and A. Aharony (1995). *Perkolationstheorie — Eine Einführung*. VCH, Weinheim.

Steeds, J. W. (1973). *Introduction to Anisotropic Elasticity Theory of Dislocations*. Oxford University Press/Clarendon Press, Oxford.

Stoneham, A. M., J. H. Harding, and T. Harker (1996). In *Interatomic Potentials for Atomistic Simulations*, Volume 21 of *MRS Bulletin*, special ed.: A.F. Voter, pp. 29. Materials Research Society.

Stoneham, A. M., M. M. D. Ramos, and A. P. Sutton (1993). *Phil. Mag. A 67*, 797.

Stouffer, D. C. and L. T. Dame (1996). *Inelastic Deformation of Metals*. John Wiley, New York.

Stroh, A. N. (1954). *Proc. R. Soc. London A 67*, 427.

Stroh, A. N. (1958). *Phil. Mag. 3*, 625.

Struble, R. A. (1962). *Nonlinear Differential Equations*. McGraw-Hill, New York.

Sutton, A. P. (1996). In *Proceedings of NATO ASI on Computer Simulation in Materials Science*, Vol. eds.: H. O. Kirchner, L. P. Kubin, and V. Pontikis, Volume 308 of *NATO Advanced Science Institutes Series, Series E : Applied Sciences*, pp. 163. Kluwer Academic in cooperation with NATO Science Division.

Sutton, A. P. and R. W. Balluffi (1995). *Interfaces in Crystalline Materials*. Monographs on the Physics and Chemistry of Materials. Oxford University Press/Clarendon Press, Oxford.

Suzuki, M. (1987). *Quantum Monte Carlo Methods in Equilibrium and Non-Equilibrium Systems*, Volume 74 of *Springer Series in Solid State Sciences*. Springer-Verlag.

Suzuki, T. (1991). *Dislocation Dynamics and Plasticity*, Volume 12 of *Springer Series in Materials Science*. Springer-Verlag.

Svoboda, J. (1996a). *Scr. Metall. 28*, 1589.

Svoboda, J. (1996b). *Unpublished results*.

Swaerengen, J. C. and J. C. Holbrook (1985). *Res. Mech. 13*, 93.

Swann, P. and J. Nutting (1961). *J. Inst. Met. 90*, 133.

Szekely, J. and W. E. Wahnsiedler (1988). *Mathematical Modeling Strategies in Materials Processing*. John Wiley, New York.

Tabet, N. and M. Ledra (1996). *Mater. Sci. Eng. B 42*, 181.

Tadaki, T., T. Kinoshita, and Y. Hirotsu (1997). *Z. Phys. D 40*, 493.

Tadmore, E. B., M. Ortiz, and R. Phillips (1996). *Phil. Mag. A 73*, 1529.

Tadmore, E. B., R. Phillips, and M. Ortiz (1996). *Langmuir - ASC J. Surf. Collo. 12*, 4529.

Tagwerker, M., W. M. Plotz, and H. Sitter (1995). *J. Cryst. Growth 146*, 220.

Takahashi, H., H. Motohashi, M. Tokuda, and T. Abe (1994). *Int. J. Plast. 10*, 63.

Takahashi, I. and T. Suzuki (1990). *Mater. Sci. For. 56*, 125.
Takenaka, M. and T. Hashimoto (1993). *Phys. Rev. E 48*, 647.
Tanatar, B. (1992). *Phys. Rev. B 46*, 1347.
Tavernier, P. and J. A. Szpunar (1991a). *Acta Metall. 39*, 549.
Tavernier, P. and J. A. Szpunar (1991b). *Acta Metall. 39*, 557.
Taylor, B. (1715). *Methodus Incrementorum Directa et Inversa.*
Taylor, G. I. (1934). *Proc. R. Soc. London A 145*, 362.
Taylor, G. I. (1938). *J. Inst. Met. 62*, 307.
Teodosiu, C. (1982). *Elastic Models of Crystal Defects.* Springer-Verlag, Berlin.
Tersoff, J. (1986). *Phys. Rev. Lett. 56*, 632.
Tersoff, J., D. Vanderbilt, and V. Vitek (1989). *Atomic Scale Calculations in Materials Science*, Volume 141. Mater. Res. Soc. Symp. Proc. Pittsburgh.
Tetot, R., A. Finel, and F. Ducastelle (1991). *J. Stat. Phys. 61*, 121.
Thiem, S., M. Berveiller, and G. R. Canova (1986). *Acta Metall. 34*, 2139.
Tietze, U. and C. Schenk (1980). *Halbleiter-Schaltungstechnik.* Springer-Verlag.
Tittmann, B. R. and H. E. Bömmel (1966). *Phys. Rev. 151*, 178.
Tomé, C. N., R. A. Lebensohn, and U. F. Kocks (1991). *Acta Metall. 39*, 2667.
Tomellini, R. (1997). *Proceedings of an ECSC Workshop on Modeling of Steel Microstructural Evolution during Thermomechanical Treatment.* Directorate-General Science, Reserach and Development, Office for Official Publications of the European Communities, European Commission.
Toral, R. and A. Chakrabarti (1993). *Phys. Rev. E 47*, 4240.
Torrens, I. M. (1972). *Interatomic Potentials.* Academic Press, New York.
Tóth, L. S., P. Gilormini, and J. J. Jonas (1988). *Acta Metall. 36*, 3077.
Tóth, L. S. and A. Molinari (1994). *Acta Metall. 42*, 2459.
Tóth, L. S., A. Molinari, and D. Raabe (1997). *Metall. Trans. A 28*, 2343.
Trautwein, A. X., J. Antony, and M. Grodzicki (1997). *J. Chem. Phys. 101*, 2692.
Trohidou, K. N. and J. A. Blackman (1990). *Phys. Rev. B 41*, 9345.
Tucker, G. E. G. (1964). *Acta Metall. 12*, 1093.
Turner, P. A. and C. N. Tomé (1993). *J. Mech. Phys. Solids 41*, 1191.
Turner, P. A., C. N. Tomé, and C. H. Woo (1994). *Phil. Mag. A 70*, 689.
Übing, C. and R. Gomer (1991a). *J. Chem. Phys. 95*, 7648.
Übing, C. and R. Gomer (1991b). *J. Chem. Phys. 95*, 7636.
Übing, C. and R. Gomer (1991c). *J. Chem. Phys. 95*, 7626.
Udler, D. and D. N. Seidman (1993). *Mater. Sci. For. 126-128*, 169.
Vaidehi, N. and A. Jain (1996). *J. Phys. Chem. 100*, 10508.
Valderrama, E., E. V. Ludena, and J. Hinze (1997). *J. Chem. Phys. 106*, 9227.
van der Giessen, E. and A. Needleman (1995). *Mod. Sim. Mater. Sci. Eng. 3*, 689.
van der Hoef, M. A. and D. Frenkel (1991). *Physica D 47*, 191.
van Houtte, P. (1981). In *Proceedings 6th International Conference on Textures of Materials (ICOTOM 6);* Vol. ed.: S. Nagashima, pp. 428. Iron and Steel Institute of Japan.
van Houtte, P. (1982). *Mater. Sci. Eng. 55*, 69.
van Houtte, P. (1985). In *Preferred Orientations in Deformed Metals and Rocks. An Introduction of Modern Texture Analysis,* Vol. ed.: H.-R. Wenk. Academic Press, New York.
van Houtte, P. (1988). *Text. Microstruct. 8-9*, 313.
van Houtte, P. (1992). In *Modeling of Material Deformation Processes*, pp. 84. Springer Verlag.
van Houtte, P. (1994). *Int. J. Plast. 10*, 719.

van Houtte, P. (1996a). In *Proceedings of the 11th International Conference on Textures of Materials (ICOTOM 11), Sept. 1996, Xian, China*, Vol.eds.: Z. Liang, L. Zuo, Y. Chu, Volume 1, pp. 236. International Academic, Beijing.

van Houtte, P. (1996b). *Unpublished notes from lectures on Micromechanics of Polycrystalline Materials at Katholike Universiteit Leuven.*

van Houtte, P. and E. Aernoudt (1975). *Z. Metallk. 66*, 202.

van Houtte, P., K. Mols, A. van Bael, and E. Aernoudt (1989). *Text. Microstruct. 11*, 23.

Vandermeer, R. A., R. A. Musumura, and B. B. Rath (1991). *Acta Metall. 39*, 383.

Vandermeer, R. A. and B. B. Rath (1989). *Metall. Trans. A 20*, 391.

Vandermeer, R. A. and B. B. Rath (1990). In *Simulation and Theory of Evolving Microstructures*, Vol. eds.: M.P. Anderson and A.D. Rollett, pp. 119. The Minerals, Metals and Materials Society, TMS Publication.

Vashishta, P., R. K. Kalia, S. W. de Leeuw, D. L. Greenwell, A. Nakano, W. Jin, J. Yu, L. Bi, and W. Li (1994). *Comput. Mater. Sci. 2*, 180.

Verlet, L. (1967). *Phys. Rev. 159*, 98.

Verlet, L. (1968). *Phys. Rev. 165*, 201.

Vianney, J. M. and A. Koelman (1990). *Phys. Rev. Lett. 64*, 1915.

Vichniac, G. Y. (1984). *Physica D 10*, 96.

Vitek, V. (1968). *Phil. Mag. 18*, 773.

Vitek, V. (1974). *Cryst. Latt. Defec. 5*, 1.

Vitek, V. (1976). *Proc. R. Soc. London A 352*, 109.

Vitek, V. (1992). *Prog. Mater. Sci. 36*, 1.

Vitek, V. (1996). In *Interatomic Potentials for Atomistic Simulations*, Volume 21 of *MRS Bulletin*, special ed.: A.F. Voter, pp. 20. Materials Research Society.

Vitek, V., G. Gutekunst, and M. Rühle (1995). *Phil. Mag. A 71*, 1219.

Vitek, V. and M. Igarashi (1991). *Phil. Mag. A 63*, 1059.

Vitek, V. and D. J. Srolovitz (1989). *Atomistic Simulation of Materials: Beyond Pair Potentials.* Plenum Press, New York.

Vitek, V., G. J. Wang, and J. L. Bassani (1994). *J. Phys. Chem. Solids 55*, 1147.

Voigt, W. (1910). *Lehrbuch der Kristallphysik.* Teubner Verlag, Berlin.

Volterra, D. (1907). *Ann. Ecole Norm. Sup. (3) XXIV*, 400.

von Boehm, J. and R. M. Nieminen (1996). *Phys. Rev. B 53*, 8956.

von Mises, R. (1913). *Mechanik der festen Körper im plastisch-deformablen Zustand.* Nachrichten von der Königlichen Gesellschaft der Wissenschaften.

von Mises, R. (1928). *Z. Angew. Mathemat. Mech. 8*, 161.

von Neumann, J. (1963). *Collected works of J. von Neumann;* Vol. ed.: A. W. Burks, Volume 5. Pergamon Press, New York.

von Schlippenbach, U., F. Emren, and K. Lücke (1986). *Acta Metall. 34*, 1289.

Voorhees, P. W. and M. E. Glicksman (1984). *Acta Metall. 32*, 2001.

Voter, A. F. (1996). *Interatomic Potentials for Atomistic Simulations*, Volume 21 of *MRS Bulletin.* Materials Research Society.

Wagner, C. (1961). *Z. Elektrochem. 65*, 581.

Wagner, F., G. R. Canova, P. van Houtte, and A. Molinari (1991). *Text. Microstruct. 14–18*, 1135.

Wagner, P. (1995). *Zusammenhänge zwischen Mikro- und Makroskopischen Verformungsinhomogenitäten und der Textur.* Dissertation. Rheinisch-Westfälische Technische Hochschule Aachen, Institut für Metallkunde und Metallphysik.

Wagner, R. and R. Kampmann (1991). Chapter 9*: Homogeneous Second Phase Precipitations*, Volume 5; Vol. ed.: P. Haasen: Phase Transformations in Materials of *Materials Science and Technology — A Comprehensive Treatment*, Ser. eds.: R. W. Cahn, P. Haasen, and E. J. Krämer. VCH, Weinheim.

Wan, G. and P. R. Sahm (1990a). *Acta Metall. 38*, 967.

Wan, G. and P. R. Sahm (1990b). *Acta Metall. 38*, 2367.

Wang, F. and E. G. D. Cohen (1995). *J. Stat. Phys. 81*, 467.

Wang, H. Y. and R. LeSar (1995). *Phil. Mag. A 71*, 149.

Wang, H. Y., R. Najafabadi, and D. J. Srolovitz (1993). *Acta Metall. 41*, 2533.

Wang, J. and A. P. Young (1993). *J. Phys. A 26*, 1063.

Wang, N., F. R. Hall, I. Pillinger, P. Hartley, C. E. N. Sturgess, P. De Wever, A. van Bael, J. Winters, and P. van Houtte (1994). In *Proceedings 10th International Conference on Textures of Materials (ICOTOM 10), Mater. Sci. For.*, Vol. ed.: H. J. Bunge, Volume 157–162, pp. 1901. Trans Tech Publications.

Wang, Y., L. Chen, and A. G. Khachaturyan (1996). In *Proceedings of NATO ASI on Computer Simulation in Materials Science*, Vol. eds.: H. O. Kirchner, L. P. Kubin, and V. Pontikis, Volume 308 of *NATO Advanced Science Institutes Series, Series E : Applied Sciences*, pp. 325. Kluwer Academic in cooperation with NATO Science Division.

Wang, Y., L. Q. Chen, and A. G. Khachaturyan (1991). *Scr. Metall. 25*, 1387.

Wang, Y., L. Q. Chen, and A. G. Khachaturyan (1992). *Phys. Rev. B 41*, 11194.

Wang, Y., L. Q. Chen, and A. G. Khachaturyan (1993). *Scr. Metall. 25*, 1993.

Wang, Y. and A. G. Khachaturyan (1995a). *Scr. Metall. 31*, 1425.

Wang, Y. and A. G. Khachaturyan (1995b). *Phil. Mag. A 72*, 1161.

Wang, Y., B. Wang, and Z. Wu (1997). *Solid State Commun. 103*, 55.

Wang, Y. F., J. M. Rickman, and Y. T. Chou (1996). *Acta Mater. 44*, 2505.

Wannier, G. H. (1966). *Statistical Physics.* John Wiley, New York.

Wansleben, S. and D. P. Landau (1991). *Phys. Rev. B 43*, 6006.

Warlimont, H. (1974). *Order–Disorder Transformations in Alloys*, Volume 24 of *Reine und angewandte Metallkunde in Einzeldarstellungen,* Ser. ed.: W. Köster. Springer-Verlag.

Warren, J. A. and W. J. Boettinger (1995). *Acta Metall. 43*, 689.

Wassermann, P. D. (1994). *Advanced Methods in Neural Computing.* Van Nostrand Reinhold, New York.

Weaire, D. and J. P. Kermode (1983). *Phil. Mag. B 48*, 245.

Weaire, D. and J. P. Kermode (1984). *Phil. Mag. B 50*, 379.

Weertman, J. (1965). *Phil. Mag. 11*, 1217.

Weertman, J. and J. R. Weertman (1980). Chapters 8, 9, Volume 3 of *Dislocations in Solids.* Elsevier Science, Amsterdam; Ser. ed.: F.R.N. Nabarro.

Weinberg, J. D., M. Shamsuzzoha, and P. A. Deymier (1992). *Ultramicroscopy 40*, 240.

Weng, G. J. (1982). *J. Appl. Mech. 49*, 728.

Wenk, H. R. (1985). *Preferred Orientations of Metals und Rocks.* Academic Press.

Westergaard, H. M. (1920). *On the Resistance of Ductile Materials to Combined Stresses*, Volume 189 of *J. Franklin Inst.*

Wheeler, A. A., W. J. Boettinger, and G. B. McFaden (1992). *Phys. Rev. A 45*, 7424.

Wheeler, A. A., W. J. Boettinger, and G. B. McFaden (1993). *Phys. Rev. E 45*, 1893.

Wheeler, A. A., B. T. Murray, and R. J. Schaefer (1993). *Physica D 66*, 243.

Wiedersich, H. and K. Herschbach (1972). *Scr. Metall. 6*, 453.

Williams, H. P. (1985). *Model Building in Mathematical Programming.* John Wiley, New York.

Willis, J. R. (1977). *J. Mech. Phys. Solids 25*, 185.

Willson, S. (1984). *Physica D 10*, 69.

Willson, S. J. (1992). *Discr. Appl. Mathemat. 35*, 47.

Wingert, D. and D. Stauffer (1995). *Physica A 219*, 135.

Wolf, D. and S. Yip (1992). Volume Materials Interfaces. Chapman and Hall.

Wolf, U., S. M. Foiles, and H. F. Fischmeister (1991). *Acta Metall. 39*, 373.

Wolfram, S. (1983). *Rev. Mod. Phys. 55*, 601.

Wolfram, S. (1985). *Phys. Rev. Lett. 54*, 735.

Wolfram, S. (1986). *Theory and Applications of Cellular Automata*, Volume 1 of *Advanced Series on Complex Systems, selected papers 1983-1986*. World Scientific, Singapore.

Wu, F. Y. (1982). *Rev. Mod. Phys. 55*, 235.

Wulf, J., S. Schmauder, and H. F. Fischmeister (1993). *Comput. Mater. Sci. 1*, 297.

Wulf, J., T. Steinkopff, and H. F. Fischmeister (1996). *Acta Metall. 44*, 1765.

Xu, W. and J. A. Moriarty (1997). *Phys. Rev. B In press.*

Yan, M., F. Ernst, and S. P. Chen (1996). *Acta Mater. 44*, 4351.

Yeomans, J. M. (1992). *Statistical Mechanics of Phase Transition.* Clarendon Press/Oxford University Press, New York.

Yoffe, E. H. (1960). *Phil. Mag. 5*, 161.

Yue, S. (1990). *Proceedings of the International Symposium on Mathematical Modeling of Hot Rolling of Steel, Hamilton, Canada, Vol. ed.: T. Chandra.* The Minerals, Metals and Materials Society, TMS Publication.

Zacharopoulos, N., D. J. Srolovitz, and R. LeSar (1997). *Acta Mater. 45*, 3745.

Zadeh, L. A. (1968). *J. Mathem., Anal. and Appl. 23*, 421.

Zadeh, L. A. (1978). *Fuzzy Sets Syst. 1*, 3.

Zadeh, L. A., K. S. Fu, K. Tannaka, and M. Shimura (1974). *Fuzzy Sets and their Application to Cognitive and Decision Processes.* Academic Press, Boston.

Zamkova, N. G. and V. I. Zinenko (1994). *J. Phys. 6*, 9043.

Zehetbauer, M. and V. Seumer (1993). *Acta Metall. 41*, 577.

Zhang, G. M. and C. Z. Yang (1993). *Phys. Stat. Sol. B 175*, 459.

Zhang, Y. W. and T. C. Wang (1996). *Mod. Sim. Mater. Sci. Eng. 4*, 231.

Zhang, Y. W., T. C. Wang, and Q. H. Tang (1995). *J. Appl. Phys. 77*, 2393.

Zhang, Z., J. Detch, and H. Metiu (1993). *Phys. Rev. B 48*, 4972.

Zhou, R. and B. Berne (1995). *J. Phys. Chem. 103*, 9444.

Zhu, P. and R. W. Smith (1992a). *Acta Metall. 40*, 3369.

Zhu, P. and R. W. Smith (1992b). *Acta Metall. 40*, 683.

Zienkiewicz, O. C. and K. Morgan (1983). *Finite Elements and Approximation.* John Wiley, New York.

Zienkiewicz, O. C. and R. L. Taylor (1989). *The Finite Element Method*, Volume 1. McGraw-Hill, London.

Zienkiewicz, O. C. and R. L. Taylor (1991). *The Finite Element Method*, Volume 2. McGraw-Hill, London.

Zimmermann, H. (1978). *Fuzzy Sets Syst. 1*, 45.

Zimmermann, H. (1991). *Fuzzy Set Theory and its Applications.* Kluwer Academic.

Index

- A -

ab-initio
- approach, 14, 26 f, 90, 95, 97 ff
- molecular dynamics, 9, 97 ff

abstraction, 13
acceleration
- of a dislocation, 127
- of an atom, 102

accumulator unit, 317
activation energy, 18
- grain boundary motion, 18

adaptive linear element, 320
adiabatic Born–Oppenheimer approximation, 27, 87 f
adjustable parameter, 91
Airy's scalar stress function, 136 ff
algebraic expression, 18
Allen–Cahn model, 177 ff
aluminum, 91, 199
aluminum gallium arsenide, 316
amorphous, 114
analytical
- expression, 6
- result, 35
- solution, 12, 20

Andersen scheme, 100 ff
angular momentum, 95
anisotropic, 120
- elastic field, 118, 131
- elasticity, 92, 131 ff

annealed network, 244
annihilation, 168
ansatz
- function, 41, 46, 255
- polynomial, 251

antibonding state, 95 ff
antisymmetric part
- displacement gradient tensor, 124, 260
- velocity gradient tensor, 260

application, 81
- Cahn–Hilliard, 197 ff
- cellular automata, 219 ff
- component model, 235 ff
- dislocation dynamics, 170 ff
- finite difference model, 263 ff
- finite element model, 263 ff
- geometrical model, 235 ff
- molecular dynamics, 104 ff
- Monte Carlo, 81 ff
- network model, 241 ff
- phase field kinetic model, 197 ff
- polycrystal model, 296 ff
- Potts model, 229 ff
- self-consistent model, 296 ff
- specific integrated circuit, 317
- Taylor model, 296 ff
- vertex model, 241 ff

appropriate simulation technique, 12
approximate solution, 34, 41, 89, 251
arithmetic logic unit, 317
artificial
- microscopic system element, 23
- neural network, 27, 319 ff
- perturbation, 103

athermal dislocation dynamics, 160
atomic
- acceleration, 22
- basis function, 95
- bomb, 64
- charge density, 96
- cluster, 114
- displacement, 95
- function, 95
- non quantum gas, 55 ff
- nuclei, 50
- orbital, 95
- position, 22
- scale, 5, 9 ff, 49
  - simulation, 11, 51 ff
- spacing, 88
- velocity, 22

atomistic, 23, 249
- simulation, 51
- dynamics, 53
- model, 24, 26
- process, 88
- simulation, 71 f, 79, 87 ff, 98, 103

attractive interatomic force, 88, 94
average, 16
- constitutive law, 9
- description, 250
- ensemble, 55, 87

Computational Materials Science: The Simulation of Materials, Microstructures and Properties By Dierk Raabe

Copyright © 1998 Wiley-VCH Verlag GmbH

ISBN: 3-527-29541-0

- model, 250
- particle data, 55
- phenomenological law, 115
- time, 55

- B -

backstress, 257 ff
ballistic speed, 316
band
- energy, 96
- gap, 92

basis function, 95
benchmark, 315
- system, 315
- test, 315

binding
- energy, 94
- type, 89

biological neuron, 319
Bishop-Hill model, 286 ff
bits, 65
bivalent logic concept, 322
Boltzmann equation, 35, 64
bond, 89 ff
- anisotropy, 93
- charge density, 96
- chemical, 94
- covalent, 89, 93 f
- directional, 93
- directionality, 92 f
- individual, 93
- interatomic, 89
- ionic, 89, 93 f
- length, 93
- metallic, 89
- order, 94
- percolation, 325
- strength, 93
- theory, 89
- van der Waals, 89, 91

bond order potential, 9, 94 ff
bonding
- chemistry, 89
- state, 95 f

Boolean, 321
bootstrap percolation, 325
border condition, 103
Born–Mayer potential, 89, 94
Born–Oppenheimer approximation, 27, 50 ff, 87, 89
boson, 16
boundary, 52
- dynamics, 9, 25, 115
- elements, 9
- heterophase, 104
- homophase, 104
- mobility, 118
- plane, 18
- segment, 239

boundary condition, 6, 12, 20, 30, 103
- antiperiodic Möbius, 103
- atomistic simulation, 103
- Born–van Kármán, 103
- Cauchy, 32 ff
- Dirichlet, 32 ff
- finite elements, 103
- generalized helical periodic, 103
- Neumann, 32 ff
- periodic, 103

boundary-initial-value problem, 32
boundary-value problem, 30 ff, 41, 250 ff
bow-out criterion, 154
Bragg–Williams–Gorsky model, 9, 78
bridging of scales, 113, 303
Brillouin zone, 92
broadening, 24
bulk properties, 90
BWG model, 78

- C -

C60, 91
Cahn–Hilliard simulation, 16, 34, 177 ff, 187, 198
- aluminum–copper, 199
- application, 197 ff
- elastic stresses, 195 ff
- example, 199 ff
- internal stress, 199
- microscopic, 193 ff

calculation speed, 33
calibration
- of models, 33, 116

canonical ensemble, 51, 56 ff, 72 ff
- discrete energies, 58
- grand, 56
- macro, 56
- micro, 56

canonical partition function, 58 ff
capacitor, 315
capillary pressure, 214
Cartesian coordinates, 101
Cauchy
- boundary condition, 32 ff
- pressure, 93
- relations, 92
- stress tensor, 261

Ceccaldi, D., 28
cellular automata, 5, 9 f, 24, 115, 201 ff
- applications, 219 ff
- binary code, 207
- complex systems, 202 ff
- dendrites, 204
- deterministic, 11, 117, 201 ff, 219

- discrete evolution of complex systems, 202 ff
- discretized finite difference solution, 206
- dislocation kink formation, 204
- evolution of dynamic systems, 202
- examples, 221 ff
- formal description, 205 ff
- formation of dendritic grain structures, 204
- general rules, 202 ff
- generalized state variable, 201 f, 219
- global transformation rule, 203 f
- grain growth, 221
- growth of two phase grain structures, 204
- lattice gas, 209, 219
- local interaction, 205 f
- local transformation rule, 116, 203 ff
- macroscale, 116
- mesh types, 212 ff
- mesoscale applications, 116
- micostructure evolution, 204
- Moore neighboring, 208
- neighboring, 206
  - Moore, 206
  - von Neumann, 206
- non-totalistic, 207
- optimization, 212
- outer totalistic, 207
- partial differential equation, 206
- probabilistic, 11, 201 f, 206 f, 219
- rate equation, 204
- reaction-diffusion system, 219
- recrystallization, 219 ff
- scaling length, 212 ff
- sintering, 204
- solidification, 204, 219
- spatial and temporal evolution of complex systems, 202 ff
- stochastic, 204, 208, 221 ff
- storage limitation, 212 ff
- totalistic, 207 f
- traffic, 116
- transformation rule, 201 ff, 219
- variable update, 118
- von Neumann neighboring, 208

central
- difference method, 33 ff
- difference quotient, 38
- interaction, 91 ff
- limit theorem of probability theory, 61
- processor unit, 315 ff

ceramics, 104, 114

channel
- dislocation, 114
- length, 316

characteristic
- equation, 323
- function, 56
- polynom, 126
- scales, 5 ff
- scaling length, 212 ff, 305 ff

charge
- carrier, 316
- density function, 96
- transfer, 89

chemical
- bond, 94
- composition, 5
- equation of state, 155 ff
- potential, 55, 73, 78, 182
- structure evolution equation, 162

chip performance, 315

CISC, 315, 317

classical
- pair potential, 90, 92
- particle, 73

classification, 5, 24
- of models, 23 ff
- of simulation techniques, 116
- physical, 5
- spatial, 5
- spatial dimension, 24 ff
- spatial discretization, 24 ff
- spatial resolution, 23 ff

cluster, 115
- model, 9
- variation method, 9, 78

CMOSFET, 316

coarsened network, 244

cohesion, 89 ff

coincidence site lattice, 103

collective behavior, 5

collison event, 66

Coloumb interaction of nuclei, 91

combination unit, 317

commercial metal, 120

compatibility, 24, 127 ff

competitive
- isostructural ripening, 197
- particle ripening, 25, 178, 198

complementary
- field-effect transistor, 315
- metal oxide field-effect transistor, 316

complex
- alloys, 9
- instruction set, 315, 317
- loading situation, 258
- systems, 201

complicated shape, 250

component model, 233 ff

composite, 114

computation time, 93

computational materials science, 9, 12 ff, 28, 249
- definitions, 13 ff
- fundamentals, 5 ff
- introduction, 5 ff
computational micromechanics, 24
computational microstructure mechanics, 24
computer
- architecture, 315 ff
- logical subdivision, 317
- MIMD, 317
- MISD, 317
- multiple instruction stream–multiple data stream, 317
- multiple instruction stream–single data stream, 317
- parallel, 315
- pipeline, 315, 317
- register, 317
- SIMD, 317
- single instruction stream–multiple data stream, 317
- single instruction stream–single data stream, 317
- SISD, 317
- vector, 315
- von Neumann, 315
- classification, 315 ff
- Flynn, 318
- Shore, 318
- von Neumann, 318
- design, 315
- experiment, 11, 61, 64, 66
- memory, 65, 317
- performance, 317
- program, 317
- simulation, 5, 9
- technology, 315
- von Neumann, 317
concentration, 16, 18
congruential method, 65
conjugate stress–strain measures, 261 ff
conservation law, 24
- probability density, 57
conservative
- force, 102
- system, 98, 99
conserved variable, 178, 187
consistency, 34
constant
- composition, 72
- pressure, 100
- temperature, 101
constitutive
- law, 9 ff, 15, 18 ff, 24, 113, 250
- empirical, 250
- phenomenological, 250
- model, 270
- polycrystal simulation, 270 ff
- rate-dependent, 270 ff
- rate-independent, 270 ff
- viscoplastic, 270 ff
- yield surface, 270 ff
- plasticity modeling, 14, 270 ff
constraints
- external, 16
- holonomic, 98
- internal, 16
- kinetic, 98
- macroscopic, 55
continuity equation, 178
continuous
- derivative, 32
- differential equation, 34
- variable, 34
continuum, 25, 270
- Cahn–Hilliard field kinetic simulation, 197
- model, 11, 13, 24, 113 ff
- polycrystal elasticity, 268 ff
- polycrystal plasticity, 268 ff
control of a simulation, 55
control unit, 317
coordinate transformation, 41
coordinates, 55
- Cartesian, 101
- generalized, 98 f
coordination number, 77, 94
copolymers, 115
- diblock, 115
- starblock, 115
- triblock, 115
copper, 199
correlation function, 53
corrosion, 5
coupled differential equations, 20
coupling of computer codes, 11, 303
covalent bond, 89, 93 f
CPI, 315
CPU, 315
crack, 104
crack tip, 103
Crank–Nicholson
- method, 39 ff
- step, 40
Cray, 318
creep, 5
cross slip force, 156, 160 ff
crystal
- orientation, 15
- plasticity, 9, 24, 119, 268 ff
- slip, 9
- structure, 90
crystal plasticity finite element simulation, 11, 15, 24, 265
crystalline, 114
crystallographic orientation, 84, 268, 270

crystallographic texture, 24, 235, 268, 270
cubic material, 92
current transport, 9
cut-off radius, 91
cutting criterion, 154
CVM model, 78
cycles per instruction, 315

- D -

decohesion, 92
decomposition, 197, 199
definite integral, 68
definition
- atomistic, 24
- computational materials science, 13 ff
- continuum, 24
- modeling and simulation, 13 ff
deformation gradient tensor, 261
degree of discretization, 23
degrees of freedom, 55
delocalized state, 96
delta function, 134
delta-type Hamiltonian, 78
density
- functional theory, 26 f, 90, 95, 97 ff
- homogeneous, 92
- matrix, 96
- of neighboring atoms, 88
dependent variable, 9 ff, 30 f, 120, 322
deterministic, 51 f, 321 f
- cellular automata, 11, 25
- model, 26 ff
- simulation, 87, 104
- trajectory, 52, 55
- transformation rule, 203
device, 315
diagonalization, 96
difference
- equation, 33, 34
- quotient, 34
differential equation, 9, 29 ff, 43, 116, 134, 250
- continuous, 34
- coupled, 20, 250
- diffusion, 32
- discretization, 32 ff
- elliptic, 32 f
- equilibrium, 126
- fundamentals, 29 ff
- hyperbolic, 32 ff
- introduction, 30 ff
- Laplace, 32 ff
- linear, 30
- non-stationary, 32 ff
- nonhomogeneous, 134
- nonlinear, 30
- numerical solution, 32 ff
- parabolic, 32 ff
- partial, 30 ff, 250
- Poisson, 32 ff
- set of equations, 250
- stationary, 32
- substitution, 29
- superposition principle, 29
- wave, 32 ff
differential expression, 18
differential quotient, 34
differentiation error, 20
diffuse phase field kinetic model, 187 ff
diffusion, 9, 66, 179 ff, 249 f
- coefficient, 18, 32
  - scalar, 18
  - tensor, 18
- equation, 17, 32 ff, 249 ff
- phase transformation, 179 ff
- random walk, 64, 66, 84
- simulation, 66
- vacancy, 66
dimension, 23
direct integration, 11, 303 ff
directional bond, 92 f, 95
Dirichlet boundary condition, 32 ff
Dirichlet variational principle, 251 f
discrete
- differential equation, 34
- dislocation dynamics, 12
- domain, 250
- evolution of complex systems, 201
- model, 24
- spatial lattice, 117
- variable, 34
discretization, 23, 32 ff
- degree, 23
- error, 20
- Euler method, 36 ff
- in finite element simulations, 253 ff
- of independent variable, 33 ff
- spatial, 23
- temporal, 23
- time, 34 ff
discretization and interpolation in finite element simulation, 253 ff
discretized finite difference solution, 206
discretized microstructure simulation, 115
dislocation, 15, 22, 84, 115, 121, 178
- annihilation, 168
- channel, 114
- core, 104, 118
- density, 16 f, 119
  - cell interiors, 17
  - cell walls, 17
- finite, 137

- flexible, 168, 170
- glide plane, 168, 170
- grain boundary, 104
- infinite, 118, 137
- Lomer–Cottrell lock, 168
- misfit, 104
- mobile junction, 168
- mobility, 170
- motion, 29
- segment, 15, 22, 118 ff, 137, 153 ff
- segment dynamics, 115 ff
- simulation, 118
  - 2D, 118
  - 3D, 118
- straight, 118
- stress field, 119

dislocation dynamics, 5, 9 f, 17, 115 f, 119 ff, 151 ff, 250
- 2D, 5, 24, 162, 164, 167 f, 170
- 3D, 5, 24, 162, 164, 167 f, 170
- application, 170 ff
- athermal, 160
- backdriving force, 170
- bow out, 154
- canonical ensemble, 152
- chemical equation of state, 155 ff
- chemical structure evolution equation, 162 ff
- climb, 162
- constriction force, 156
- cross slip force, 156, 160 ff
- cutting, 170
- cutting criterion, 154
- discrete, 12, 164, 167
- dislocation reaction, 168 ff
- dislocation–dislocation force, 157 ff
- dynamic equilibrium, 156
- electron drag force, 156, 159 ff
- equilibrium, 156
- external force, 156 ff
- force equilibrium, 156
- forces, 156 ff
- hybrid model, 162
- image force, 156, 158 ff
- inertia, 160 ff
- kinematics, 167 ff
- Langevin force, 156
- line tension, 156
- linear elastic-limit criterion, 154
- local equilibrium, 156
- Lomer–Cottrell lock, 170
- long-range interactions, 168
- mechanical equation of state, 155
- mobility, 170
- Newton's equation of motion, 156
- Newtonian, 152 ff
- nonconservative motion, 162 ff
- obstacle force, 156 ff
- Orowan's equation, 168
- osmotic force, 156 ff, 162
- overdamped high stress regime, 164
- Peach–Koehler force, 157 ff
- Peierls force, 156 ff
- phenomenological, 164 ff
- phonon drag force, 156, 159 ff
- pressure dependence, 152
- quasi-harmonic approximation, 152
- segmentation, 154 ff
- self force, 157 ff
- short-range interactions, 164 ff
- solution of the equation of motion, 162 ff
- strain rate tensor, 168
- stress fluctuation criterion, 154
- temperature dependence, 152
- thermal, 160
- thermal activation, 160, 164
- thermal force, 156, 160 ff
- viscoplastic, 164 ff
- viscous, 164 ff

dislocation statics, 116, 119 ff, 137 ff
- 2D, 138 ff
  - anisotropic, 140 ff
  - isotropic, 138 ff
- 3D
  - anisotropic, 146 ff
  - field equation, 142 ff
  - field equations, 146 ff
  - isotropic, 142 ff
- infinite dislocation, 138 ff
- isotropic, 142 ff

dislocation substructure, 270
dislocation–dislocation force, 156 ff
displacement field, 16, 122
displacement gradient tensor, 16, 124
- antisymmetric part, 124
- skew symmetric part, 16
- symmetric part, 124

DNA-helix, 89
domain, 41, 52
- Potts model, 227 ff
- shape, 227
- size, 227

double precision, 35
drift velocity, 316
driving force, 214, 304
dynamic
- equilibrium, 156
- recovery, 120, 168
- response, 20

dynamics
- atom, 51
- dislocation, 115
- dislocation segment, 115
- electron, 51
- nanoscale, 87

- E -

EAM, 91
edge dislocation, 138 ff
effective medium model, 9, 92 f
eigenvalue problem, 50, 96
eigenvector, 96
elastic
- anisotropy, 268
- constants, 90, 92, 131 ff
- energy, 133 ff
  - orientation dependence, 226
- internal stress, 199
- modulus
  - polycrystal, 250, 267, 297
  - Reuss, 250, 267, 274 ff, 297
  - Voigt, 250, 267, 273 ff, 297
elasticity, 11
- constants, 18
- tensor, 18
- theory, 122 ff, 136 f
electrical conductivity, 50
electromagnetic field, 268
electron, 50, 87, 90, 92
- d, 92
- delocalization, 89
- density, 92
- drag force, 156 ff
- energy band calculation, 51
- free, 92
- quasi-free, 92
- s–p, 92
- system, 50
- transfer, 89
- valence, 94
electrostatic repulsion, 92
element, 251
embedded atom model, 9, 84, 90 ff
emitter coupled logic, 315
empirical
- constitutive equation, 24
- interatomic force, 92
- interatomic potential, 88
- many-body potential, 92 f
- method, 178
- model, 12, 14, 27, 114
- pair potential, 9, 90 ff
- potential, 92 f, 95
energetically conjugate, 261
energy, 95
- band, 96
- band calculation, 51
- kinetic, 98
- potential, 98
engineering materials, 5
ensemble, 55 f, 88
- average, 55, 87
- canonical, 51, 73
- constant chemical composition, 73
- equilibrium, 57
- isobaric–isothermal, 56
- isothermal-isobaric, 73
- microcanonical, 73
- stationary, 55
- variable chemical composition, 73
entropy, 56, 60
equation
- diffusion, 32
- heat, 32
- Helmholtz, 32
- Poisson, 32
- wave, 32
equation of motion, 23, 29, 38, 52, 87 f, 98 f, 252, 258
- classical, 98
- for atoms, 98
- molecular dynamics, 38
- Newton, 99, 252
equation of state, 6, 14, 17, 303
equilibrium, 24, 156
- ensemble, 57
- equation, 126 ff
- equation in finite element simulations, 253 ff
- phase transformation, 177
- rotational, 127
- statistical mechanics, 53, 55
- thermodynamics, 53, 87
- translational, 127
equipotential flow surface, 272 ff
ergoden theory, 55
ergodic
- error, 20
- system, 52
ergodicity, 51, 87
error
- differentiation, 20
- discretization, 20
- ergodic, 20
- integration, 20
- numerical, 34 ff
- programing, 20
- round-off, 34
- series expansion, 20
- statistical, 20
- truncation, 20, 34 ff
Eshelby inclusion model, 25, 195, 276 ff
Euler
- finite element method, 258
- kinematics, 258 ff
- method, 33, 36 ff
  - backward, 37 ff
  - explicit, 37 ff
  - forward, 37 ff
  - implicit, 37 ff
  - modified, 40
- representation, 258 ff
Euler–Lagrange function, 43, 100

- for hydrostatic pressure, 100
evolution
- equation, 6, 14, 17 ff
- of complex systems, 201 ff
- of dynamic systems, 202 ff
- of micostructure, 204
- path, 5
experiment, 6, 9, 52, 55, 91
- computer, 66
- numerical, 66
experimental
- process, 16
- texture, 298
exponential function, 18, 94
extensive variable, 28
external force, 156
extrinsic point defect, 114

- F -

false, 321
fatigue, 9
FD, 5
FEM, 5
Fermi level, 92
fiber texture, 84
Fick's laws, 178
field
- equation, 131, 137
- kinetic model, 187 ff
- kinetic simulation
  - application, 197 ff
  - elastic stresses, 195 ff
- kinetic theory, 9
- magnetic, 76
- variable
  - conserved, 178, 187
  - nonconserved, 178, 187
field-effect transistor, 315 f
finite deformation kinematics, 258
finite difference method, 9, 33 ff, 38, 88, 116 f, 206, 249 ff, 261 ff
- round-off error, 34 ff
- stability, 34 ff
- application, 263 ff
- backward Euler method, 37 ff
- central difference method, 38
- central difference quotient, 38
- consistency, 34 ff
- convergent, 34 ff
- Crank–Nicholson method, 39 ff
- diffusion equation, 261
- discretization of space, 34
- discretization of time, 34
- efficiency, 37 ff
- equation of motion, 38
- error, 34 ff
  - round-off, 34
  - truncation, 34 ff
- Euler method, 36 ff
- explicit Euler method, 37 ff
- first order, 38
- forward Euler method, 37 ff
- fundamentals, 34 ff
- heat conduction, 261
- implicit Euler method, 37 ff
- large scale problems, 261
- leap-frog method, 38 ff
- matrix form, 263
- molecular dynamics, 38
- order, 40
- predictor–corrector method, 38 ff
- round-off error, 35 ff
- Runge–Kutta method, 40 ff
- scaling, 33
- second-order, 40
- space discretized, 34
- time interval, 35 ff
- truncation error, 34 ff, 38
- Verlet algorithm, 38
finite difference quotient, 32, 33 ff, 34
finite element method, 9, 11 f, 15 f, 23, 25, 33, 41 ff, 249 ff
- application, 263 ff
- basic procedure, 41 ff
- boundary, 42
- crystal plasticity, 265 ff
- discretization, 41 ff, 253
- domain, 42 ff
- equation of motion, 258
- Euler representation, 258 ff
- examples, 265 ff
- finite deformation kinematics, 258
- form function, 41
- fundamentals, 41 ff
- in solid mechanics, 43
- integral expression, 44
- interpolation, 253
- interpolation function, 255 ff
- isoparametric element, 41, 255 ff
- Lagrange representation, 258 ff
- material response, 253
- mechanical energy, 253
- mesh, 41
- minimum mechanical energy, 253
- node, 41 ff
- nonlinear, 43
- polynomial form function, 41, 43
- Ritz method, 44 ff
- scaling, 33
- shape function, 41 ff, 255 ff
- solid-state kinematics, 258 ff
- solution, 41
- stable equilibrium, 253
- subdomain, 42 ff
- trial function, 43

- tuned self-consistent viscoplastic model, 298
- variational problem, 44
- virtual displacement principle, 43
- weak form of the virtual work principle, 253

Finnis–Sinclair model, 92 f
first-principles model, 12, 26 f
fissile material, 64, 66
fitting, 90
flexible dislocation, 168, 170
flight direction, 66
floating point operation, 315
FLOP/s, 315 f
flow curve, 22
force
- attractive, 88
- conservative, 102
- dislocation, 120
- interatomic, 88 f, 122
- on an atom, 88, 102

form function, 41, 251, 255 ff
formal language, 322
formulation
- model, 13

fourth-rank elasticity tensor, 18
fracture, 5
fracture mechanics, 9
free electron, 92
- band, 92
- theory, 95

free energy, 60, 178
- density, 17, 181 ff
- Ginzburg–Landau model, 181 ff
- Landau form, 17, 181 ff

full-constraints model, 280 ff
fullerenes, 91
function
- atomic, 95
- basis, 95
- Euler–Lagrange, 100
- exponential, 94
- Lagrange–Euler, 98
- steep, 71

functional, 251
fuzzy
- generalized characteristic equation, 323
- logic, 321 f
- set, 322
  - Boolean, 324
  - cardinality, 324
  - compatibility, 323
  - convexity, 324
  - element, 323
  - membership, 323 f
  - operation, 324
  - theory, 321 ff
- theory, 27, 321 ff

- G -

Galerkin method, 46
gallium arsenide, 316
gate, 315
gate delay, 316
gatter spacing, 316
Gear predictor–corrector method, 33, 101
generalized
- characteristic equation, 323 ff
- coordinates, 98 f
- spin, 75 ff, 225
- state variable, 201 f
- state variable concept, 14, 18 ff
  - definition, 18

geometrical model, 115, 118, 233 ff
- application, 235 ff

geometrically necessary dislocations, 25
germanium based transistor, 316
GFLOP/s, 315
Gibbs phase space, 53 f
Gibbs–Thomson equation, 178, 181 ff
Giga-scale integration, 316
Ginzburg–Landau model, 5, 9, 16 f, 25, 177 ff, 187, 198
glide plane, 168, 170
global
- lattice defect ensemble, 23
- transformation rule, 204 ff

glue model, 92, 93
graded concept, 322
grain, 114
- boundary, 104
  - dislocation, 84, 104
  - mobility, 216 ff
  - motion, 18
  - plane, 18
  - segment, 239
- growth, 9, 178, 198, 214, 226, 233
- interaction, 25
- interaction model, 289 ff
- scale, 5, 23, 249
- size, 15

grandcanonical ensemble, 51, 56 ff
- discrete energies, 59

graphite, 89
Green's function, 121, 133 ff
- tensor, 134
- time-dependent, 134
- time-independent, 134

Green–Lagrange
- strain tensor, 261
- tensor, 260

growth, 178, 198, 233
- grain, 178, 198
- precipitation, 178, 198

GSI, 316

- H -

Hamilton operator, 49 ff, 95
- Heisenberg model, 77
- Ising model, 76, 225
- Monte Carlo model, 26
- Potts model, 11, 26, 78, 225 ff
Hamilton's least action principle, 99
hard sphere potential, 91
Hashin–Shtrikman model, 9, 267, 275 ff
heat
- capacity, 55
- equation, 17, 32, 32 ff, 249 ff
- transport, 5
Heisenberg spin model, 77 ff
helical periodic border condition, 103
Hellmann-Feynman theorem, 96
Helmholtz
- equation, 32 ff
- free energy, 56
- phase space, 53
heterophase boundary, 104
hierarchy
- relevance, 305
- scales, 305
high-angle grain boundary, 23, 25
hit-or-miss integration, 66 ff
- trial shot, 67
holonomic constraints, 98
homogeneous density, 92
homogenization, 268 ff
homophase
- boundary, 104
- interface, 178
hot-rolling texture, 298 ff
hybrid model, 162
hydrostatic stress, 126
hyperbolic partial differential equation, 32

- I -

IBM, 317
IC, 316
idea behind modeling, 14 ff
image force, 156
imitation, 13
impingement, 233
importance sampling, 63, 71 ff
inclusion , 195
inclusion model, 276 ff
independent variable, 9, 12, 14 ff, 17, 30 f, 120, 322
- discretization, 32 ff
individual
- defect, 23
- particle, 23
- particle data, 55
industrial application, 23
inertia force, 156
infinite dislocation, 118, 120 f, 137
information storage, 315
initial condition, 30
initial-value condition, 6, 12, 20
initial-value problem, 30, 32, 34, 41, 250, 252
inner cut-off radius, 91
input/output unit, 317
instruction register, 317
instruction set
- complex, 315, 317
- reduced, 315, 317
integral, 68
- definite, 68
- expression, 18
- formulation, 43
- Monte Carlo, 68 ff
integrated circuit, 315
integrated modeling and simulation, 11, 303 ff
integration, 12, 304
- direct, 11, 303 ff
- equation of motion, 88, 101 ff
- error, 20
- Giga-scale, 316
- importance sampling, 72 ff
- large-scale, 316
- method, 71
- mid-scale, 316
- Monte Carlo, 61, 71 ff
- multidimensional definite integral, 61
- numerical, 67, 72
- of models, 304 ff
- sequential, 11
- simultaneous, 11
- small-scale, 316
- stochastic, 61, 67, 71 ff
- time, 67
- ultra large-scale, 316
- Verlet, 101
- very large-scale, 316
- weighted, 72 ff
integrative simulation, 11
intensive variable, 28
interaction
- energy, 77
- lattice defects, 9
- long-range, 116
- many-body, 9, 89, 115 f
- particle, 53
- short-range, 116
interatomic
- force, 14, 88 f
  - attractive, 94
  - empirical, 92
  - repulsive, 94

- pair potential, 17
- potential, 51, 88 ff, 99, 249
  - empirical, 88
  - many-body, 89
  - pair, 90
  - radially symmetric, 17
- spacing, 100
interface, 12, 52, 84 f
- curvature, 226
- energy, 226
- migration, 178
- mobility, 216 ff
- movement, 118
- phenomena, 9
- segregation, 104
internal interface, 52, 87
internal stress, 199
interpolation function, 41, 255
intrinsic
- calibration, 116
- point defect, 114, 162
- scale, 11
- scaling, 116
ionic
- bond, 89, 93 f
- crystal, 92
- system, 91
Ising model, 51, 75 ff, 87, 225
- alloy, 77
- interaction energy, 77
- mixing energy, 77
isobaric–isothermal ensemble, 56 ff
- discrete energies, 59
isoparametric element, 41, 255 ff
isostructural ripening, 197, 199
isotropic, 120
- elastic medium, 118
- elasticity, 131 ff
- limit, 92, 131 ff
- linear elasticity, 92
- many-body potential, 90 ff

- J -

Jaumann derivative, 261

- K -

kinematic
- approach, 120
- constraints, 16 ff
- equation, 16 ff
- model, 22
- simulation, 5, 12
kinematics, 9, 258 ff
kinetic
- constraints, 98
- energy, 57, 87, 98 f
- equation, 181
- equation of state, 303
- field theory, 5
- Monte Carlo model, 225 ff
- phase field model, 25, 177 ff, 198
- Potts model, 11, 116, 229 ff
kinetics, 5, 9, 178
- microstructure, 9
- of concentration changes, 178
- phase transformation, 9
- statistical, 53 ff
Kirchhoff stress tensor, 261
Kocks–Mecking model, 16 f, 22
Kohonen net, 320 ff
Kröner's self-consistent model, 25, 118, 280 ff

- L -

Lagrange
- equation of motion, 99
- form, 99
- formalism, 99
- formulation, 98
- representation, 258 ff
Lagrange–Euler function, 98
Lamé constants, 18
Laplace
- equation, 32 ff
- operator, 32
large-scale
- integration, 316
- problem, 33
lattice, 76
- coincidence site, 103
- defects, 5, 9, 113 f, 178
  - collective behavior, 5
  - ensemble, 23
  - kinetics, 115
  - statics, 115
- dynamics, 51
- gas cellular automata, 209 ff
- gas spin model, 78 ff
- parameter, 90 ff
- rotation, 16
- site, 117
- spacing, 94
- structure, 93
law of motion
- dislocation, 120
- Newton, 120
- portion of dislocation, 120
- strain rate sensitive, 120
- viscoplastic, 120
- viscous, 120
laws of diffusion, 179 ff

LCAO, 95 ff
leap-frog method, 38 ff
learning vector quantizer, 320
least action principle, 99
length scale, 304
Lennard–Jones
- pair potential, 88, 91 ff
Levi–Civita operator, 124
Lifshitz–Slyozov–Wagner (LSW) theory, 178
light alloy, 199
limit process, 34
line, 315
- connectivity, 118
- defect, 116
- force, 118
linear
- combination of atomic orbitals, 95 ff
- continuum elasticity, 15
- defect, 118
- elastic-limit criterion, 154
- elasticity, 92, 118, 121 ff
  - anisotropic, 92
  - isotropic, 92
- iteration, 9
- method, 34
- shape function, 255
linked processes, 304
Liouville theorem, 57
liquid-state phase transformation, 178
lithium, 91
local
- density functional theory, 26 f, 90, 95, 97 ff
- driving pressure, 239
- electron density, 92
- equilibrium, 156
- magnetic moment, 77
- misorientation, 205, 294 ff
- orbital model, 94
- orientation gradient, 294 ff
- transformation rule, 116, 204, 207 ff
localized state, 96
logarithmic strain, 261
Lomer–Cottrell lock, 168
long-range interaction, 11, 116, 204
Los Alamos Plasticity (LAP) code, 28
lower-bound parameter, 307
LSW theory, 178
Lüders band, 114

- M -

macrocanonical ensemble, 56 ff
macroscale, 250 ff
- boundary-value problem, 33
- deformation, 249
macroscopic, 5, 22, 249
- average, 15
- constraints, 55
- model, 23
- parameter, 55
- scale, 9, 249 ff
- state, 55
- transport equation, 53
- variable
  - energy, 55
  - particle number, 55
  - pressure, 55
  - temperature, 55
  - volume, 55
magnesium, 91
magnetic field, 76
mainframe, 88
Manhattan project, 64
manufacturing process, 6, 16, 178
many-body
- interaction, 9, 23, 53, 87 f, 104, 115 f
  - long-range, 204
  - mesoscopic, 23
  - microscopic, 23
  - short-range, 204
- potential, 90 ff
  - empirical, 92 f
  - isotropic, 90 ff
  - semi-empirical, 92 f
many-electron system, 51
many-particle simulation, 64
Markov chain, 51 f, 73, 87
massively parallel architecture, 315
material
- chemical composition, 5
- electromagnetic properties, 5
- engineering, 5
- heterogeneity, 11, 250
- mechanical properties, 5
- plasticity, 251
- properties, 5 ff
- research, 5
- response, 18
- science and engineering, 9
- synthesis, 104
mathematical
- approximation technique, 33
- model, 14 ff
- state variable model, 18
matrix
- diagonalization, 96
- of the Markov chain, 73
- transition probability, 73
Maxwell distribution, 103
mean free path, 316
- electron, 316
- hole, 316

mechanical
- equation of state, 155 ff
- properties, 5
medium
- anisotropic elastic, 118
- isotropic elastic, 118
- linear elastic, 118
membrane equation, 32
memory–processor system, 315
MESFET, 316
mesh, 41
mesoscale, 250 f
- boundary-value problem, 33
- cellular automata, 116
- continuum model, 11, 116
- model, 11
- Potts model, 225 ff
- simulation, 11, 113 ff
  - constitutive law, 113
  - continuum, 113
  - dislocation dynamics, 116
  - line defect, 116
  - long-range interaction, 116
  - methods, 113, 115 ff
  - phenomenological, 113
  - short-range interaction, 116
mesoscopic, 5, 22, 52, 249
- average, 15
- development of domain size, 227
- many-body problem, 23
- model, 23
- scale, 249 ff
metal, 104, 114
metal oxide
- field-effect transistor, 316
- semiconductor, 315
metallic bond, 89
Metropolis Monte Carlo method, 5, 9, 11, 51, 63 f, 71 ff, 87, 90, 113
- canonical ensemble, 74 ff
- grandcanonical ensemble, 75 ff
- microcanonical ensemble, 74 ff
MFA model, 78
MFLOP/s, 315
microcanonical ensemble, 56 ff, 71
- discrete energies, 59
micromechanics, 24
microscale simulation, 113 ff
microscopic, 5, 22, 53, 249
- analysis, 55
- field kinetic theory, 9, 177 ff
- many-body problem, 23
- model, 23
- phase field kinetic model, 16 f, 25, 177 ff, 193 ff
- state, 55 ff
- variable, 55
microstructure, 5 ff, 9, 17, 177 ff
- definition, 5 ff
- dynamics, 51 f
- evolution, 5, 9, 52 f, 87, 113, 225, 249, 303
  - direction, 5
  - path, 5
  - path-dependence, 52
  - prediction, 23
  - space, 55
  - time, 55
- hierarchy, 5 ff, 305
- homogenization, 249
- kinetics, 5, 9, 113, 303
- length scales, 114 ff, 304 ff
- many-body interaction phenomena, 9
- mechanics, 9, 15, 24
- mechanisms, 113
- modeling, 5
- morphology, 9, 24
- optimization, 113
- path, 52, 113, 120
- scales, 5, 114 ff
  - definition, 5 ff
- simulation, 5, 9, 304
  - 3D, 118
  - atomistic, 53
  - conservation law, 304
  - control, 55
  - definition, 23 ff
  - deterministic, 52
  - discrete, 53
  - discretized, 115
  - flow law, 304
  - general considerations, 12 ff
  - how-to-do list, 12 ff
  - integration, 304
  - scale coupling, 304
  - statistical, 53
  - stochastic, 52
- simulation methods, 12
- tailoring, 113
- temporal evolution, 14
- topology, 24
microstructure–property relation, 303
microtexture, 9
million instructions per second, 315
MIMD, 317
minimum potential energy principle, 251
MIPS, 315
MISD, 317
misfit dislocation, 104
misorientation, 18, 205
mixing energy, 77
mobile junction, 168
mobility, 118, 178, 239
- lattice defect, 178
model, 13
- ab-initio, 6, 14, 27
- abstraction, 13

- analytical solution, 20
- atomistic, 14, 24
- beyond the atomic scale, 14
- Bishop–Hill, 286 ff
- bond order, 94 ff
- boundary dynamics, 115
- Bragg–Williams–Gorsky, 9
- Cahn–Hilliard, 11, 17
- calibration, 116
- classification, 11, 23 ff
- cluster variation, 9
- constitutive, 14, 18 ff
- continuum, 11, 13 f, 24, 114 f
- crystal plasticity finite element, 11
- definition, 13 ff
- dependent variable, 6
- descriptive character, 27 ff
- design, 20
- deterministic, 26 ff
- empirical, 12, 14, 27, 114
- Eshelby, 276 ff
- evolution equation, 6
- first-principles, 12, 26 f
- formal, 321
- formulation, 13 ff, 20
- full-constraints, 280 ff
- geometrical, 115, 118
- Ginzburg–Landau, 9 f, 181 ff
- Hashin–Shtrikman, 275 ff
- heuristic, 14
- heuristical, 6
- how to structure, 14
- inclusion, 276 ff
- independent variable, 6
- input, 20
- Ising, 76 ff, 87
- kinematics, 6
- kinetic, 28
- kinetic multistate Potts Monte Carlo, 11, 116, 229 ff
- kinetic phase field, 11
- Kocks–Mecking, 22
- Kröner, 280 ff
- localized-orbital, 94
- macroscopic, 23
- mathematical, 18, 321
- mesoscale, 11, 14, 115 f
- microscale, 14
- microscopic phase field kinetic, 178
- microstructure, 23
- molecular field approximation, 9
- Monte Carlo, 61
- multistate Potts, 11, 225 ff
- nanoscale, 14
- network, 9, 115
- non-space discretized, 114
- overview, 5 ff
- pair-functional, 93
- path-dependence, 28
- phase field, 9, 11, 34, 177 ff, 187 ff
- phenomenological, 6, 11 ff, 27, 114
- physical mechanism, 14
- polycrystal plasticity, 291
- Potts, 9, 87, 115 f, 225 ff
- predictive power, 11, 23
- pseudopotential, 94
- relaxed-constraints, 287 ff
- Reuss, 274 ff
- Sachs, 288 ff
- scale, 23
- scaling, 116
- self-consistent, 9, 280 ff, 291, 298
- self-consistent viscoplastic, 298
- shell, 93 ff
- space-discretized, 114
- spring, 9
- state equation, 6
- state variable, 6
- static, 28
- statistical, 26 ff, 114 ff
- statistical kinematical, 12
- statistical plasticity, 17
- stochastic, 26 ff
- structure, 13
- Taylor, 280 ff
- theoretical, 14
- tight-binding, 95 ff
- topological network, 11, 115 ff
- vertex, 9, 11, 115, 118
- Voigt, 273 ff

modeling and simulation, 6, 13, 20 ff
- basic idea, 14 ff
- basic steps, 6
- definition, 6, 13 ff, 18, 23 ff
- distinction from simulation, 22
- how to do, 14
- integrated, 11, 303
- numerical, 13, 20
- principle, 13
- theory, 13 ff

Mohr circle, 126

molecular dynamics, 5, 11, 17, 22, 26 f, 33, 38, 51 f, 79, 87 ff, 94, 98, 100 ff, 113, 249
- ab-initio, 9, 97 ff
- Andersen scheme, 100 ff
- application, 104 ff
- attractive terms in potentials, 91
- boundary conditions, 103
- Coloumb interaction of nuclei, 91
- constant pressure, 100 ff
- constant temperature, 101 ff
- empirical pair potential, 90 ff
- equations of motion, 100
- finite difference method, 38
- introduction, 87 ff
- Lennard–Jones pair potential, 88, 91 ff

- Morse pair potential, 88
- Nosé scheme, 101 ff
- number of atoms, 88
- pair potential, 90 ff
  - empirical, 91 ff
  - Lennard–Jones, 91 ff
  - Morse, 91 ff
- Parinello scheme, 100 ff
- Pauli repulsion, 91
- polymer, 106
- solution of equations of motion, 101
- stochastics, 103
molecular field approximation, 9, 78
molecule, 53, 55, 88, 98
- crystal, 91
- orbital, 89
momentum vector, 55, 58, 87
monomer, 106
Monte Carlo method, 9, 11 f, 26, 51 f, 61 ff, 204, 208, 213, 225
- algorithm, 87
- application in materials science, 81 ff
- characteristic steps, 61 ff
- classification, 63
- direct integration, 51
- equilibrium states, 51
- Hamiltonian, 63
- Heisenberg spin model, 77
- hit-or-miss method, 66
- importance sampling, 63, 67, 71 ff
- in materials science
  - crystal growth, 81
  - diffusion, 81
  - epitaxial growth, 81
  - fracture, 81
  - heterophase interface, 81
  - phase transformation, 81
  - polymers, 81
  - surface and interface phenomena, 81
  - thermodynamics, 81
- integration, 52, 66, 68, 71 ff
- Ising lattice, 63
- kinetic, 52, 225 ff
- lattice gas spin model, 78 ff
- lattice type, 63
- mesoscale, 225
- Metropolis algorithm, 5, 51, 73 ff
- microstructure simulation, 51
- multistate, 225
- naive sampling, 63, 68
- non-overlapping random walk, 84
- path-dependent prediction, 51
- path-independent prediction, 51
- Potts model, 63, 225 ff
- quantum mechanical, 77
- random walk, 84
- sampling method, 63
- simple sampling, 63, 68
- simulation, 52, 63
- statistics, 51
Moore configuration, 206 ff, 208
morphology, 9
Morse pair potential, 88, 91 ff
MOSFET, 316
MSI, 316
multilayer
- feedforward net, 320 ff
- perceptron, 320
multiple
- instruction stream–multiple data stream, 317
- instruction stream–single data stream, 317
- integral, 68
- mechanisms, 304
multiplication register, 317
multistate Potts model, 11, 60 ff, 75 ff, 87, 225 ff
- fundamentals, 225 ff
- introduction, 225 ff

- N -

nano–microscale simulation, 51 ff, 71 f, 79, 87 ff, 98, 103
- statistical mechanics, 51
nanoscale
- dynamics, 87
- simulation, 51 ff, 71 ff, 79, 87 ff, 98, 103
nanoscopic, 5, 249
- model, 23
- simulation, 51 ff
nearest neighbor, 78, 94 ff
necking, 115
neighboring site, 117
nematic phase, 84
network model, 5, 9, 25, 115, 239 ff
- application, 241 ff
- bulging phenomena, 241
- continuous grain growth, 241
- continuous recrystallization, 241
- crystal recovery, 241
- discontinuous grain growth, 241
- equation of motion, 240
- examples, 242 ff
- incipient stages of discontinuous recrystallization, 241
- low cycle fatigue deformation, 241
- nucleation, 241
- subgrain growth, 241
- superplastic deformation, 241
- switching rules, 240
- topological recombination, 240

Neumann boundary condition, 32 ff
neural network, 319 ff
neuron layer, 319 f
neutron diffusion, 64, 66
new product, 6
Newton's equation of motion, 17, 23, 99, 156, 252
- dislocation dynamics, 17, 116 ff, 120, 152 ff
- molecular dynamics, 17, 99
non-conservative dislocation motion, 162 ff
non-equilibrium, 5
- phase transformation, 177
- statistical mechanics, 53
non-isostructural precipitation, 178, 198
non-space-discretized model, 114
non-stationary process, 32 ff, 258 ff
non-totalistic cellular automata, 207
nonconserved variable, 178, 187
nonhomogeneous differential equation, 134
nonlinear, 9, 18, 27, 43
- crystal plasticity, 11
- finite element method, 43
- materials response, 115, 257
nonweighted stochastic sampling, 68
normalization, 95
Nosé scheme, 101 ff
nucleation, 118 ff, 226 f, 233
- random, 118
- site, 118
- site saturated, 118
- spatially random, 118
nuclei, 87
number of atoms, 113
numerical
- computation, 115
- error, 34 ff
- experiment, 20, 66
- integration, 67 ff
  - hit-or-miss method, 66
  - Monte Carlo, 66
- modeling, 13, 20 ff
  - definition, 13 ff
- precision, 33
- simulation, 13
- solution, 20
- stochastic sampling, 61

- O -

object, 322
obstacle force, 156
Onsager equation, 181 ff
opposite spin, 96
order, 9, 115
organic chemistry, 89
orientation, 15, 84
orientation dependent stored elastic energy, 226
orientation distribution function, 268, 270
orthogonality, 95
oscillation period, 88
osmotic force, 156, 162
Ostwald ripening, 181 ff
outer totalistic cellular automata, 207
overdamped, 120
- glide, 120
- high stress dislocation dynamics, 164
overlap, 95
oxides, 93 f

- P -

pair potential, 17, 88 ff
- classical, 92
- hard sphere, 91
- Lennard–Jones, 88 ff
- Morse, 88 ff
- radially symmetric, 92
pair-functional
- model, 93
- potential, 92 f
parabolic partial differential equation, 32
parallel computing, 315
parameter, 18 ff
- adjustable, 91
- macroscopic, 56
- scaling, 88
- transfer, 11
Parinello scheme, 87, 100 ff
partial differential equation, 11, 32 ff, 115, 133 ff, 206, 250
- Green's function, 133 ff
- introduction, 30 ff
- numerical solution, 32 ff
- phenomenological, 116
- solution, 133
particle, 55
- interaction, 49
- motion, 29
- ripening, 25, 178, 198
- size, 15
partition function, 58 ff, 73
- canonical ensemble, 58
- grandcanonical ensemble, 59
- isobaric–isothermal ensemble, 59
- microcanonical ensemble, 59
path-dependent, 28, 51 ff, 60, 63, 225
- function, 16
- problem, 52
- process, 88
path-independent
- function, 16
- quantity, 87

Pauli principle, 96
Pauli repulsion, 91
Peach–Koehler force, 157 ff
Peierls force, 156 ff
percolation, 9
- bond, 325
- bootstrap, 325
- problem, 66
- site, 325
- theory, 325 ff
personal computer, 317
phase diagram, 78
phase field kinetic model, 5, 9, 25, 34, 177 ff, 187 ff
- discretization of space, 34
- discretization of time, 34
phase field kinetic simulation, 199
- application, 197 ff
- elastic stresses, 195 ff
- microscopic, 193 ff
phase space, 51 ff, 73, 87
- coordinates, 55 ff
- density, 58, 71
- Gibbs, 53, 55
- Helmholtz, 53, 55
- temporal evolution, 55 ff
- trajectory, 55
  - deterministic, 52 ff
  - stochastic, 52 ff
phase state, 52
phase transformation, 9, 25, 177, 179 ff
- equilibrium, 177
- isostructural, 9
- liquid-state, 178
- non-equilibrium, 177
- non-isostructural, 9
- solid-state, 178
phase transition, 84
phenomenological, 12, 89
- constitutive equation, 24
- dynamics, 118
- law, 115
- laws of diffusion, 179 ff
- model, 11, 27, 114, 120
- partial differential equation, 116
phonon drag force, 156
physical metallurgy, 89
physical parameters, 14
physical time and length scale, 12
piecewise polynomial solution, 251
Piola–Kirchhoff stress tensor, 261
plane wave, 95
plastic
- anisotropy, 268
- deformation, 120
- instability, 27
- potential, 272
plasticity, 24
plasticity finite element method, 15
point defect, 162
- extrinsic, 114
- intrinsic, 114
Poisson equation, 32, 32 ff
Poisson's ratio, 92
polar decomposition theorem, 261
pole figure, 298
polycrystal, 268 ff
- elastictiy and plasticity models, 267 ff
- fundamentals, 267
- mechanics, 270
- models, 25, 267 ff
- plasticity models, 11, 249, 291
- simulation
  - application, 296 ff
  - constitutive model, 270 ff
  - equipotential flow surface, 272 ff
  - examples, 297 ff
  - yield surface, 270 ff
polycrystalline metal, 120
polymer, 84, 104 f, 114
- amorphous, 115
- block copolymers, 115
- chain orientation, 84
- copolymers, 115
- crystalline, 115
- Monte Carlo simulation, 84
- necking, 115
- paracrystalline domain, 115
- simulation, 84, 106
- spherolites, 115
- structure, 115
polymerization, 84
polynomial
- ansatz function, 41, 46
- form function, 251
- function, 41, 250
- trial function, 33, 41, 43
Portevin–LeChatelier effect, 114
position vector, 58
potassium, 91
potential, 51, 88 ff
- atomic, 88
- bond order, 9, 94 ff
- Born–Mayer, 94
- cohesion, 92
- covalent, 93 f
- decohesion, 92
- effective medium, 9, 92 f
- embedded atom, 9, 84, 92 f
- empirical, 9, 92 ff
- energy, 98
- Finnis–Sinclair, 92
- function, 26, 88
- glue, 92 f
- hard sphere, 91
- interatomic, 88 ff

- ionic, 93 f
- isotropic many-body, 92 ff
- Lennard–Jones, 91
- many-body, 92 ff
- Morse, 91 ff
- pair, 90 ff
- pair-functional, 92 f
- pseudopotential, 90
- second moment, 9, 92 f
- semi-empirical, 92 ff
- shell, 9, 93 ff
- tight-binding, 95 ff
- weak pseudopotential, 90

Potts model, 5, 12, 26, 51, 60 f, 75 ff, 116 f, 204, 225 ff
- and cellular automata, 117
- application, 229 ff
- diffusion, 228 f
- domain, 52
- energy, 226
- examples, 229 ff
- generalized spin, 225
- grain growth, 226 ff
- interaction energy, 229
- interface curvature, 226
- kinetic, 52, 225
- multistate, 52, 87, 225 ff
- q-state, 52, 87, 225 ff
- recrystallization, 228 f
- ripening, 226
- solidification, 228 f

precipitation, 178, 198
- growth, 178, 198

prediction
- beyond the atomic scale, 14
- discrete, 53
- local, 53
- microstructure evolution, 23
- statistical, 53
- stress, 119

predictive power, 23
predictor–corrector method, 38 ff, 101
pressure, 60
primary grain boundary dislocation, 84
primary recrystallization, 226 ff
Princeton computer, 317
principal stress, 126
principle of modeling, 13 ff
probabilistic, 51 ff, 60, 87, 225
- cellular automata, 11, 26, 208
- model, 61

probability, 55
probability density, 57
- canonical ensemble, 58
- grandcanonical ensemble, 59
- isobaric–isothermal ensemble, 59
- microcanonical ensemble, 59

probability distribution, 73
process, 6
- atomistic, 88
- path-dependent, 88

processor, 315
processor speed, 316
programing, 20
- code, 20
- error, 20
- language, 12

propagation of acoustic waves, 51
properties
- electromagnetic, 5
- lattice defects, 114
- mechanical, 5
- non-average, 55

pseudo-random numbers, 65, 68, 71
pseudo-stochastic process, 61
pseudopotential, 91 ff

- Q -

q-state Potts model, 87
quadrature
- Monte Carlo, 81
- trapezoid method, 81

quantum mechanics, 89, 95
quantum-mechanical potential, 90
quasi-defects, 23
quasi-free electron, 92

- R -

radial dependence, 95
radiation, 66
random nucleation, 118
random number, 51, 64 ff
- experiment, 61
- generator, 65
- pseudo, 71
- weighted, 71

random sampling, 117
random walk, 64, 66, 84
rate equation, 17, 204
rate-dependent deformation, 270 ff
rate-independent deformation, 270 ff
reaction/interaction criterion, 154
Read–Shockley equation, 214
real
- language, 322
- physical defects, 23
- situation, 13
- system, 13
- time, 88

recovery, 9, 216
recrystallization, 9, 25, 27, 118, 233 ff
reduced instruction set, 315, 317
relaxation time, 51

relaxed-constraints model, 9, 25, 287 ff
repulsive interatomic force, 94
Reuss model, 9, 267, 274 ff
rigid-body rotation, 124, 261
ripening, 25, 195, 197, 199, 226
RISC, 315, 317
Ritz method, 44 ff
rolling process, 24
rotation, 124
rotational equilibrium, 127
round-off error, 35
round-robin test, 28 ff
Runge–Kutta method, 40 ff

- S -

Sachs model, 5, 9, 288 ff
sample necking, 115
scale, 5 ff, 12, 23, 33, 303 ff
- coupling, 304
  - linked processes, 304
  - multiple mechanisms, 304
  - spatial variation, 304
  - structure evolution, 304
- definition, 5
- diagram, 5
- discrepancies, 11
- hierarchy, 5 ff, 305
- in microstructure, 114 ff
- intrinsic, 11
- macroscopic, 5
- mesoscopic, 5
- microscopic, 5
- microstructure, 5
- nanoscopic, 5
- parameter, 11, 33, 88
- physical, 12
- space, 5
- space and time, 11
- time, 5
scale-dependent, 250, 267
scale-independent, 250, 267
Schrödinger equation, 26, 49 ff, 51, 87, 89, 97
- time-dependent, 49
- time-independent, 49
scientific abstraction, 13
screw dislocation, 139 ff
second moment model, 9, 92 f
second phase, 114
secular equation, 95
segregation, 84, 104
self force, 156
self-consistent, 267
- model, 280 ff, 291
- plasticity model, 9
- viscoplastic model, 298
self-organization, 9, 115
self-organizing map, 320
semi-empirical
- many-body potential, 92 f
- potential, 92 ff
semiconductor, 316
- field-effect transistor, 316
- transistor, 316
sequential integration, 11, 303 ff
series expansion error, 20
shape function, 41, 255 ff
shearband, 114
sheet broadening, 24
shell model, 9, 93 ff
short-range
- interaction, 11, 116
- many-body interaction, 204
- order, 115
silicates, 93 f
silicon, 93, 316
SIMD, 317
simple sampling, 63, 66
simplification, 13
simulare, 13
simulation, 9, 13, 20 ff, 28, 53
- application, 81
- atomic scale, 53
- atomistic, 51 f
- box
  - mass, 100
  - volume, 100
- Cahn–Hilliard, 34
- cell, 100, 103
- cheap, 12
- classification, 116
- competitive isostructural ripening, 197, 199
- competitive particle ripening, 178, 198
- complex alloys, 9
- crystal growth, 81
- crystal plasticity, 9
- crystal slip, 9
- decomposition, 197, 199
- definition, 13 ff, 18, 23 ff
- deterministic, 52
- diffusion, 81, 179
- dislocation dynamics, 9
- distinction from modeling, 22
- epitaxial growth, 81
- fast, 12
- fatigue, 9
- finite difference, 250 ff
- finite element, 250 ff
- flow curve, 22
- fracture, 81
- fracture mechanics, 9
- general considerations, 12 ff
- Gibbs phase space, 55
- grain growth, 9, 233 ff

- Helmholtz phase space, 55
- heterophase interface, 81
- integrated, 9
- integrative, 11
- interface phenomena, 9
- isostructural ripening, 197, 199
- kink formation, 9
- levels, 9, 11, 303
- macroscale, 249, 250 ff, 304
- many-body problem, 23
- many-particle, 64
- mesoscopic, 249 ff, 304
- mesoscopic–macroscopic scale, 9, 249 ff
- methods, 5 ff, 9 ff, 12
  - mesoscale, 115 ff
  - overview, 12 ff
- micro–mesolevel, 9, 113 ff
- microscopic, 304
- microstructure, 9, 113 ff
- microstructure mechanics, 9
- microtexture, 9
- Monte Carlo, 84
- nano–microscale, 51 ff
- nanoscale, 51 f, 304
- non-isostructural precipitation, 178, 198
- particle ripening, 178, 198
- phase transformation, 9, 81, 179
- polycrystal, 267 ff
- polymers, 81, 84
- precipitation, 178, 198
- random walk, 64
- real events, 20
- recovery, 9
- recrystallization, 9, 233 ff
- ripening, 197, 199
- segregation, 84
- semantics, 13
- single atom, 24
- solidification, 9
- spinodal decomposition, 178, 198
- static, 28
- statistical kinematical, 12
- stochastic, 52
- strain, 9
- strain rate, 9
- stress, 9
- suitability, 12
- surface and interface phenomena, 81
- Taylor factor, 9
- techniques, 12 ff
- temperature, 9
- texture, 9
- thermodynamics, 78, 81
- thin film microstructure, 84

simultaneous integrated modeling, 11, 303 ff
single instruction stream–multiple data stream, 317
single instruction stream–single data stream, 317
sink, 32
SISD, 317
site, 117
- percolation, 325
- saturated nucleation, 118

skew symmetric part
- displacement gradient tensor, 16

soap like structure, 239
sodium, 91
software algorithm, 315
solid-state
- kinematics, 258 ff
- mechanics, 43, 251
- phase transformation, 178

solidification, 9
solution
- analytical, 12
- continuous, 34
- periodic, 34

source, 32
source and drain geometry, 316
space and time scales, 9 ff, 11, 113, 305 ff
space derivative, 33
space scale, 23
space-discretized
- dislocation simulation, 118
- simulation, 23, 114

spatial
- classification, 23 ff
- dimension, 24
- discretization, 23 f
- growth, 234 f
- impingement, 234 f
- lattice, 117
- random nucleation, 118
- texture, 234 f
- variation, 304

spatial and temporal evolution of complex systems, 201
spin, 12, 76, 78, 96, 225
- domain, 12
- model, 78
- region with identical, 12

spinodal decomposition, 9, 178, 197 ff
spring model, 5
SSI, 316
stability, 35
stacking fault, 114
- energy, 90

state
- antibonding, 95 f
- bonding, 95 f

state equation, 6, 14, 17 ff, 116
state function, 51, 53

state variable, 6, 12, 14, 16 ff, 41, 55, 116, 203, 207, 250 f
- approach, 18
- concentration, 16
- concept, 9 ff, 14
- definition, 16
- dislocation density, 16
- empiricial polynomal description, 16
- explicit, 16
- extensive, 16
- fitting, 16
- implicit, 16
- intensive, 16
- interface spacing, 16
- mapping, 116
- mass-dependent, 16
- mass-independent, 16
- model, 18
- multi-variable approach, 16
- on a spatial grid, 116
- particle distribution, 16
- particle size, 16
- physical significance, 16
- update, 17
static equilibrium, 126 f
static simulation, 28
stationary, 32
- diffusion equation, 32
- ensemble, 55
- heat equation, 32
- process, 32, 258
statistical
- error, 20
- evaluation, 64
- grain interaction model, 289 ff
- kinematical simulation, 12
- kinetics, 53 ff
- mechanics, 51, 53 ff, 60, 63 f, 71
  - equilibrium, 53
  - non-equilibrium, 53, 55
- model, 26 ff, 114
- numerical solution, 51
- plasticity model, 16 f
  - three-parameter, 17
  - two-parameter, 17
- thermodynamics, 53 ff
stochastic, 52, 87, 321
- cellular automata, 208
- event, 66
- in molecular dynamics, 103
- matrix, 73
- model, 26 ff
- modeling, 117
- process, 61
- sampling, 61, 64, 66, 117
- trajectory, 52, 55
- transformation rule, 203
stored elastic energy
- orientation dependence, 226
straight dislocation, 118
strain, 16
- field, 122 ff
- Green–Lagrange, 261
- hardening, 168
- homogeneity, 270
- rate, 16
- rate sensitivity, 118, 120, 290
- rate tensor, 260
- relaxation, 25
stress
- Cauchy tensor, 261
- deviator, 126
- field, 124 ff
- fluctuation criterion, 154
- function
  - Airy's, 136 ff
- homogeneity, 270
- Piola–Kirchhoff tensor, 261
- strain
  - conjugate, 261 ff
stress–strain behavior, 120
structure, 94
- evolution, 116, 304
- evolution equation, 6, 17 ff, 162
- of models, 14
- polymer, 114
- units, 115
structure domain, 114
- amorphous, 114
- crystalline, 114
subdomain, 41
subgrain
- scale, 249
- wall, 25
sum over states, 58
superconductivity, 9, 50
superposition principle, 30
surface, 84
symmetric part
- displacement gradient tensor, 124
symmetrical matrix, 73
symmetry, 67
symmetry breaking, 252
system
- average, 55
- bus, 317
- conservative, 98
- ergodic, 52

- T -

tailoring of materials, 113, 177
Taylor expansion, 38, 102, 126
Taylor factor, 9, 17
Taylor model, 5, 25, 298
- brass shear, 288

- example, 298 ff
- full-constraints, 280 ff
- full-constraints viscoplastic, 298
- lath, 288
- pancake, 288
- relaxed-constraints, 287 ff
- relaxed-constraints pancake viscoplastic, 298

Taylor series expansion, 40
Taylor–Bishop–Hill model, 9, 250, 267, 287 ff
temporal
- discretization, 23
- evolution, 55

tensor, 16
- displacement gradient, 124
- invariants, 126
- strain, 124
- stress, 126
- stress deviator, 126

ternary alloy, 77
texture, 9, 24 f, 268, 270, 297 f
TFLOP/s, 315
theory
- of deriving models, 13 ff
- phase field, 9, 177 ff, 187 ff

thermal
- activation, 18, 164
- conductivity, 50
  - ceramics, 50
  - metals, 50
  - semiconductors, 50
- equilibrium, 73
- expansion, 51
- force, 156, 160 ff
- neutron, 66

thermionic valve, 315 f
thermodynamic limes, 60
thermodynamics, 5, 9, 53, 78, 178
- equilibrium, 5, 87, 160
- non-equilibrium, 5, 17, 113
- state function, 53
- statistical, 53 ff

thin film, 233
- deposition, 84
- microstructure, 84

three-dimensional dislocation dynamics, 5
tight-binding potential, 26, 90, 93, 95 ff
time
- average, 55
- dependent, 49
- derivative, 29, 33 ff
- evolution, 88
- interval, 34 f
- reversible Verlet algorithm, 101 ff
- scale, 23, 304
- step, 88
- trajectory, 55

time and length scale, 12
- physical, 12
- spanning, 11

topological network model, 5, 11, 25, 115, 118, 239 ff
- application, 241 ff
- examples, 242 ff

topology, 27
- thin film, 233
- Voronoi, 118
- Wigner-Seitz, 118

total differential, 17
totalistic cellular automata, 207
traction, 126
trail functions, 251
trajectory, 52
- deterministic, 52 ff
- in phase space, 55
- stochastic, 52 ff

transformation, 78, 177 f, 198, 249, 250
- in ceramics, 178, 198
- in metals, 178, 198
- in polymers, 178, 198

transformation rule, 116, 117, 207
- deterministic, 201 ff
- global, 201 ff
- local, 116, 201 ff
- long-range interaction, 203
- probabilistic, 201 ff
- short-range interaction, 203
- stochastic, 203

transistor, 315 f
transition
- matrix, 73
- metal, 92
- probability, 51
- probability matrix, 73

translational
- discrepancy, 322
- equilibrium, 127

transport
- coefficient, 53
- equation, 53

trial function, 33, 41, 43
trial state, 73
true, 321
truncation error, 20, 34 f
tungsten, 92
twist boundary, 84
two-dimensional dislocation dynamics, 5

- U -

ULSI, 316
ultra large-scale integration, 316
uncorrelated random number, 61
unit communication network, 317
upper-bound parameter, 307

- V -

vacancy, 5
vacancy formation, 92
valence electron, 94 f
van der Waals
- bond, 89, 91
- solid, 92
variable
- dependent, 12, 14, 30, 322
- energy, 55
- extensive, 15
- independent, 12, 14, 29, 322
- intensive, 15
- mass-dependent, 15
- mass-independent, 15
- particle number, 55
- pressure, 55
- state, 12, 14 f
- temperature, 55
- volume, 55
variational
- method, 44
- potential energy principle, 252
- principle, 251 f
  - Dirichlet, 251
  - virtual displacement, 251
- problem, 43
- quantum Monte Carlo method, 26
- virtual displacement principle, 251
VAX, 317
vector computing, 315
vein, 114
velocity
- atom, 102
- field, 103
- gradient tensor, 260
Verlet method, 33, 38, 52, 87 ff, 101 ff
vertex model, 5, 9 f, 25, 115, 118, 239 ff
- application, 241 ff
- bulging phenomena, 241
- continuous grain growth, 241
- continuous recrystallization, 241
- crystal recovery, 241
- discontinuous grain growth, 241
- examples, 242 ff
- incipient stages of discontinuous recrystallization, 241
- low-cycle fatigue deformation, 241
- nucleation, 241
- subgrain growth, 241
- superplastic deformation, 241
very large-scale integration, 316
virtual displacement principle, 43, 251 f
viscoplastic
- deformation, 270 ff, 272
- dislocation dynamics, 164
- dynamics, 118
- flow, 120
- model, 290, 298
viscous
- dislocation dynamics, 164
- dynamics, 118, 120
- flow, 120
VLSI, 316
Voigt model, 9, 267, 273 ff
Volterra model, D., 136
volume
- dilatation, 261
- of simulation box, 100
von Neumann configuration, 64 ff, 206 ff, 317
Voronoi topology, 118

- W -

water, 89
wave
- equation, 32 ff, 49, 252
- function, 87, 95
- mechanics, 95
weak pseudopotential, 90
weight distribution function, 58
weighted integration, 71 ff
weighting function, 44, 71, 319
Wigner-Seitz topology, 118
workstation, 88

- Y -

yield surface, 126, 257, 270 ff

- Z -

Zener anisotropy ratio, 131
zustandsintegral, 58, 60